Astrophysical Reaction Rates from In-Beam γ-Ray Spectroscopy: Experimental Studies of Proton Capture Reactions on Stable Rb Isotopes

Inaugural-Dissertation
zur
Erlangung des Doktorgrades
der Mathematisch-Naturwissenschaftlichen Fakultät
der Universität zu Köln

vorgelegt von
Svenja Elisabeth Wilden
aus Dormagen

angenommen im Jahr 2026

"We rise and we fall and we break
And we make our mistakes"

— *Hamilton, Act I, Lin-Manuel Miranda*

"The fault, dear Brutus, is not in our stars,
But in ourselves, that we are underlings."

Julius Caesar, Act I, Scene 2, William Shakespeare

Abstract

Cross sections are one of the key parameters for understanding nucleosynthesis in stars. Since the relevant energy ranges in stellar environments are very low and often involve exotic nuclei far from stability, it is often not possible to determine the reaction rates directly through experiments. Therefore, they are usually estimated by extrapolation or with the help of theoretical models. The statistical Hauser-Feshbach model, which is based on nuclear input parameters such as the nuclear level density, the γ-ray strength function, and the optical model potentials, is largely used to describe such processes.

This work investigates the extent to which proton capture processes in the stable rubidium isotopes ^{85}Rb and ^{87}Rb can be described by the Hauser–Feshbach model. The γ process, which occurs during supernova explosions, is currently considered to be the main mechanism for the nucleosynthesis of neutron-deficient p nuclei. Since the reaction network of this process mainly comprises photodisintegration reactions at unstable nuclei, the stellar reaction rates are largely calculated on the basis of theoretical models. However, the accuracy of these predictions can be significantly improved if the underlying nuclear models are verified by experimentally determined absolute cross sections.

As part of this work, two proton-induced reactions on ^{85}Rb and ^{87}Rb were therefore investigated using the in-beam method at the HORUS spectrometer at the University of Cologne. Since no published data on the cross sections of these reactions existed to date, the present measurements significantly expand the database on proton-induced reactions. In particular, the measurement on ^{87}Rb contributes to the near completion of the systematic investigation of the $N = 50$ isotone chain. Challenges arose in particular due to target stability, background suppression, and the low count rates in the relevant energy range.

For both rubidium isotopes, the measured cross sections show significant deviations from the default predictions of the Hauser–Feshbach model. The results suggest that the proton optical model potential in particular is responsible for these discrepancies. This is supported by a comparative analysis of (p, n) reaction data, which also cannot be reproduced with the default settings. Changes to the other model parameters — such as the nuclear level density or the γ-ray strength function — did not lead to any significant improvement in the theoretical description.

The results obtained in this work thus provide important experimental clues for refining optical model potentials in the mass region around $A \approx 85$. They form a basis for future work in which scattering and reaction measurements will further reduce model uncertainties and contribute to more precise astrophysical reaction rates.

Zusammenfassung

Wirkungsquerschnitte stellen eine der zentralen Größen zum Verständnis der Nukleosynthese in Sternen dar. Da die relevanten Energiebereiche in stellaren Umgebungen sehr niedrig sind und häufig exotische Kerne fernab der Stabilität beteiligt sind, ist eine direkte experimentelle Bestimmung der Reaktionsraten oftmals nicht möglich. Daher werden diese in der Regel durch Extrapolationen oder mit Hilfe theoretischer Modelle abgeschätzt. Für die Beschreibung solcher Prozesse wird größtenteils das statistische Hauser–Feshbach-Modell verwendet, das auf nuklearen Eingangsparametern wie der Kernzustandsdichte, der γ-Stärkefunktion und den optischen Modellpotentialen basiert.

Diese Arbeit untersucht, inwieweit Protoneneinfangsprozesse an den stabilen Rubidiumisotopen ^{85}Rb und ^{87}Rb durch das Hauser–Feshbach-Modell beschrieben werden können. Der γ-Prozess, der während Supernova-Explosionen abläuft, gilt nach aktuellem Stand als Hauptmechanismus für die Nukleosynthese der neutronenarmen p-Kerne. Da das Reaktionsnetzwerk dieses Prozesses überwiegend Photodesintegrationsreaktionen an instabilen Kernen umfasst, werden die stellaren Reaktionsraten weitgehend auf Basis theoretischer Modelle berechnet. Die Genauigkeit dieser Vorhersagen kann jedoch entscheidend verbessert werden, wenn die zugrunde liegenden nuklearen Modelle durch experimentell bestimmte absolute Wirkungsquerschnitte überprüft werden.

Im Rahmen dieser Arbeit wurden daher zwei protoneninduzierte Reaktionen an ^{85}Rb und ^{87}Rb mit Hilfe der In-Beam-Methode am HORUS-Spektrometer der Universität zu Köln untersucht. Da bislang keine veröffentlichten Daten zu den Wirkungsquerschnitten dieser Reaktionen existierten, erweitern die vorliegenden Messungen die Datenbasis zu protoneninduzierten Reaktionen erheblich. Insbesondere trägt die Messung an ^{87}Rb dazu bei, die systematische Untersuchung der $N = 50$ Isotonenkette nahezu abzuschließen. Herausforderungen ergaben sich insbesondere durch Targetstabilität, Untergrundunterdrückung und die niedrigen Zählraten im relevanten Energiebereich.

Für beide Rubidiumisotope zeigen die gemessenen Wirkungsquerschnitte deutliche Abweichungen von den Standardvorhersagen des Hauser–Feshbach-Modells. Die Ergebnisse deuten darauf hin, dass insbesondere das Protonen-Optische-Modellpotential für diese Diskrepanzen verantwortlich ist. Dies wird durch vergleichende Analysen von (p, n)-Reaktionsdaten gestützt, die ebenfalls nicht mit den Standardeinstellungen reproduziert werden können. Änderungen der übrigen Modellparameter – wie der Kernzustandsdichte oder der γ-Stärkefunktion – führten hingegen zu keiner signifikanten Verbesserung der theoretischen Beschreibung.

Die in dieser Arbeit erzielten Ergebnisse liefern somit wichtige experimentelle Anhaltspunkte für die Verfeinerung optischer Modellpotentiale im Massenbereich um $A \approx 85$. Sie bilden eine Grundlage für zukünftige Arbeiten, bei denen gezielte Streu- und Reaktionsmessungen die

Zusammenfassung

Modellunsicherheiten weiter reduzieren und zu präziseren astrophysikalischen Reaktionsraten beitragen sollen.

Contents

1 Introduction

For centuries, the night sky has captivated the imagination of humanity. The stars, shimmering like distant lighthouses, have served as sources of wonder, inspiration, and guidance. Myths, legends, and tales of gods and heroes from ancient cultures are based on constellations, and early navigators relied on the same pattern of stars to cross unknown oceans - the fascination with the cosmos has shaped the cultural and scientific heritage of many, if not all, civilizations. This never-ending curiosity laid the foundation for modern nuclear astrophysics, where the quest to understand the origins of stars and the elements they synthesize continues to encourage exploration.

Approximately 3600 years old and dating back to the Early Bronze Age, the Nebra Sky Disc is the oldest known representation of the sky made and one of the most precisely studied artifacts in the world [1]. It was found and looted in 1999 near the town of Nebra in Saxony-Anhalt, Germany, and has been listed on the UNESCO Memory of the World Register since 2013 [2]. It shows the Sun or full moon, a crescent moon, a cluster of seven stars, most likely the Pleiades, and two arcs, to help determine the course of the Sun between the solstices. Therefore, it is suitable to determine dates such as the spring feast on May the first [2].

The ambition of understanding the stars, their composition, and the processes that govern their behavior began with the development of early astronomy. Ancient Greek astronomers like Claudius Ptolemy cataloged the positions of stars, laying the groundwork for later astronomical studies [3]. In the 19th century, the emergence of spectroscopy established the connection between stellar light and chemical composition. The discovery of dark absorption lines in the solar spectrum by Joseph von Fraunhofer, and later the interpretation of these lines through the pioneering work of Gustav Kirchhoff and Robert Bunsen, revealed that each element produces a unique spectral fingerprint. This insight allowed astronomers to identify the chemical elements present in stars and laid the foundation for quantitative stellar spectroscopy and abundance analyses that followed in the early 20th century [4, 5].

More than one hundred years ago, the article "*Isotopes and Atomic Weights*" was published by F. W. Aston in Nature [6], where he presented atomic weights of a few elements and their isotopes. More importantly, Aston showed that the atomic weight of helium is less than four times the mass of a proton. In the same year, F. W. Aston published another article in which more weights and a minimum number of isotopes of different atoms are given [7]. As of today, more than 3300 isotopes have been identified.

It was not until the early 20th century that scientists began to uncover the processes powering stars. In 1920, Sir Arthur Eddington's groundbreaking work proposed that nuclear fusion – the

combining of hydrogen nuclei into helium – was the source of stellar energy, on the basis of Aston's findings [8]. This marked a critical moment, linking the microscopic world of nuclear reactions with the macroscopic phenomena observed in the cosmos.

Building on this theoretical foundation, the development of nuclear physics in the early 1930s provided the missing experimental pieces needed to understand stellar energy production. The discovery of the neutron by James Chadwick in 1932 [9] enabled the formulation of a consistent picture of nuclear structure and reactions within stars. Only a few years later, Hans Bethe identified the two main processes that power stars: the proton–proton (pp) chain and the carbon–nitrogen–oxygen (CNO) cycle, which describe how hydrogen is converted into helium under stellar conditions [10]. These breakthroughs linked laboratory nuclear reactions to the observed luminosities and lifetimes of stars. In parallel, early stellar abundance compilations revealed the pattern of the periodic table in nature, guiding nucleosynthesis theory [11, 12].

George Gamow's article, *Expanding Universe and the Origin of Elements* [13] from 1946, discusses the formation of chemical elements in the early universe. He stated that almost all chemical elements – light and heavy – were synthesized during the initially hot and dense state of the universe. This implied that the abundances of the elements would be approximately static over time. Building upon this idea, Gamow and his student Ralph Alpher developed a quantitative framework for nucleosynthesis in the early universe [14]. Shortly thereafter, Alpher and Robert Herman extended this model and predicted that residual thermal radiation from the Big Bang should still be present in the cosmos. This prediction was later confirmed as the cosmic microwave background [15, 16]. While Gamow's early work assumed that both light and heavy elements could be formed in the early universe, it soon became clear that the synthesis of elements heavier than lithium required stellar environments. This realization set the stage for later developments in stellar nucleosynthesis and the identification of distinct astrophysical sites for element formation.

In 1954, Fred Hoyle predicted the existence of an excited 0_2^+ state in ^{12}C. Nowadays it is known as the Hoyle state, which provides the resonant pathway for the triple-α process and allows stars to efficiently synthesize carbon from helium [17]. The experimental confirmation of this resonance followed soon [18]. The paper *Synthesis of The Elements in Stars* - also known as *B2FH* - written in 1957 by Margaret Burbidge, Geoffrey Burbidge, William A. Fowler, and Fred Hoyle was supposed to be a review article [11]. It went far beyond this: By combining theory and measurements it laid the ground for the field that is today known as *Nuclear Astrophysics*, which helps explain the origins of the elements, the life cycle of stars, and the fundamental workings of the universe. To this day, not all of these processes are fully understood and there are still uncertainties in the description of properties that are relevant for these processes as reaction rates, nuclear structure properties, and the astrophysical environments responsible for the heaviest elements [19].

As the understanding of the universe expanded, it became clear that stars are not simply luminous spheres of gas but nuclear engines where matter is continually transformed. As the saying goes, *stars don't shine, they burn.* The next section examines how these stellar cauldrons forge the elements that define the universe.

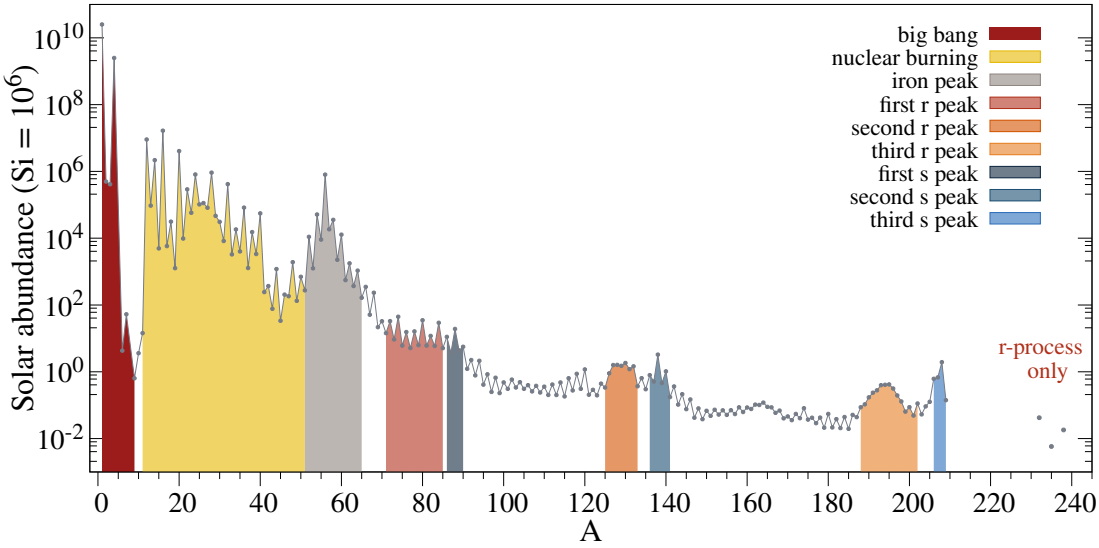

Figure 1.1: The solar abundances of the isotopes normalized to silicon ($^{28}\mathrm{Si} = 10^6$) as a function of mass number A. The lines are used to guide the eye. The shaded areas are used to mark the peaks associated with the different processes approximately. Values are taken from Ref. [22]. Details can be found in the text.

1.1 The Formation of Elements in Stars

The complex processes driving stellar nucleosynthesis require a detailed understanding of the nuclear physics that govern reaction rates, cross sections, and the behavior of atomic nuclei – sometimes very neutron or proton rich exotic nuclei – under extreme conditions. The pattern created through these properties and conditions known as the solar abundance curve is shown in Fig. 1.1. The structural features are the foundation for various theories trying to explain the origin of the elements.

The groundwork for a first solar abundance curve was laid out by Goldschmidt [20]. At the time *B2FH* was written, this curve was improved by Brown [21] and updated again by Suess and Urey [12]. These data formed the basis for *B2FH*. The most recent data set is from 2020 by Lodders [22] and forms the basis for Fig. 1.1.

The stellar burning phases are the core fusion stages that occur in stars over their lifetimes and govern how different elements are formed.

Hydrogen and helium dominate the solar abundance pattern, with a combined abundance of about 98.5 % [22]. The origin of these elements lies in the Big Bang itself, when the hot and dense Universe expanded and cooled until protons and neutrons were formed and – due to the high particle energies – were in equilibrium. After the temperature dropped more, the ratio of protons and neutrons was fixed – laying the basis for nuclear reactions and serving as fusion material – and forming ^{4}He, leaving a high share of protons, as well as traces of deuterium, ^{3}He and ^{7}Li [23].

Nucleosynthesis does not stop with this, in fact it just starts with these building blocks and is an ongoing process inside stars. Stars generate their power via nuclear reactions and the general pattern for different burning phases is similar. The reaction with the smallest Coulomb barrier advances the fastest. The pressure that is generated by the ongoing nucleosynthesis balances gravity and prevents a collapse. However, the nucleosynthesis changes the composition of the stellar plasma. As the nuclei needed for the specific burning stage are consumed by fusion, the burning region shifts outward, leading to a transition from *core burning* to *shell burning*. There is, however, one category of stars, that do not undergo shell burning. The insufficient energy production cannot compensate gravity and the star contracts. The temperature increases until it is high enough to ignite the next burning stage in the core which stabilizes the star against further contraction. The previous burning stage remains as a shell burning around the core. This cycle may repeat several times depending on the star's total mass. [24]

In general, one can differentiate between *dwarfs* – *brown* and *red* – with $0.013\ M_\odot \lesssim M \lesssim 0.08\ M_\odot$ and $0.08\ M_\odot \lesssim M \lesssim 0.4\ M_\odot$, respectively, *low mass stars* with $0.4\ M_\odot \lesssim M \lesssim 2\ M_\odot$, *intermediate mass stars* with $2\ M_\odot \lesssim M \lesssim 11\ M_\odot$ and *massive stars* with $11\ M_\odot \lesssim M$. The mass does not only influence the different burning stages and with that the nucleosynthesis as well as the death of the star but in addition the lifetime of a star. The more massive the star is the shorter its lifetime.

Brown dwarfs cannot ignite hydrogen, but they have enough mass to burn deuterium, which is what distinguishes them from massive planets.

Hydrostatic hydrogen burning is the first burning phase, where four ^{1}H nuclei fuse into a ^{4}He nucleus via sequences of interactions involving two particles. The pathways by which this proceeds are the *proton-proton chains* (*pp chains*) or *CNO cycles*, which involve heavier nuclei acting as catalysts, in particular in the C, N and O region [10, 24, 25]. Which mechanism dominates is dependent on the core temperature – consequently mass – and composition of the star [24, 25]. *Red dwarfs* can fuse hydrogen to helium via pp chains but do not have enough mass to also fuse helium. Due to the electron degeneracy, they contract up to a certain volume. The newly formed helium white dwarf cools by radiation of the thermal energy. *Low mass stars*, up to $M \approx 1.2\ M_\odot$, fuse hydrogen via the less temperature dependent pp chains possessing radiative cores while stars with $M \gtrsim 1.2\ M_\odot$ burn hydrogen via the highly temperature-dependent CNO cycles having convective cores [26].

After the hydrogen has been consumed to a certain limit, the energy generation via the pp chains stops and gravity is not counterbalanced anymore. The star contracts, which increases the central temperature to around 100 MK, until the helium in the core is ignited and *hydrostatic helium burning* starts. For light stars with masses below $1.8\ M_\odot$, the core reaches such high densities that the matter becomes electron degenerate and the increasing temperature does not affect the pressure, which results in an even higher energy generation rate. The thermal runaway releases energy which lifts the degeneracy after some time, resulting in a *core helium flash* which lasts only a few seconds and the core settling into a stable helium burning phase [24, 26]. This however does not occur in more massive stars, where the helium ignites in a much more gradual manner.

The end products of this burning stage are ^{12}C and ^{16}O, the fourth and third most abundant nuclides, respectively. A significant drop in the abundance (cf. Fig. 1.1) is found in the mass region from A = 5 – 11, with no stable nuclides for A = 5 and A = 8, where the elements Li, Be and B are located. This is a major hindrance for the synthesis of heavier elements. This gap is overcome by the so-called *triple-alpha reaction* as suggested independently by Öpik [27] and Salpeter [28, 29]. They proposed a two-step process to produce ^{12}C, where in the first step two α-particles fuse to an unstable ^{8}Be in its ground state. Occasionally, a third α-particle interacts with the ^{8}Be before decaying resulting in a ^{12}C nucleus. However, this process would be too slow unless the reaction proceeds via a resonance at 7.68 MeV in ^{12}C as Fred Hoyle proposed and Dunbar *et al.* measured [18]. This resonance is nowadays known as the *Hoyle state* and is subject of still ongoing research [30–35].

At the end of helium burning, there is still some ^{12}C left since the $^{12}\mathrm{C}(\alpha,\gamma)^{16}\mathrm{O}$ reaction is rather slow. The same goes for the succeeding $^{16}\mathrm{O}(\alpha,\gamma)^{20}\mathrm{Ne}$ reaction. ^{16}O, as mentioned above, is relatively abundant in the universe and therefore not destroyed in the aforementioned process. Stars with masses $M \lesssim 9\ M_\odot$[1] do not reach high enough temperatures in the core to start a next burning phase, but helium burns in a shell surrounding the carbon-oxygen core increasing its mass during the *asymptotic giant branch* (AGB) phase. Simultaneously, the density of the core increases due to contraction. The exhaustion of helium in the core can lead to thermally unstable helium-burning shells, undergoing *helium-shell flashes*, also known as *thermal pulses*. These cause mixing of material between different shells due to a subsequent convective transport and proton ingestion into He-burning regions. The protons form together with the ^{12}C from the He-burning shell ^{13}C through the sequence $^{12}\mathrm{C}(p,\gamma)^{13}\mathrm{N}(\beta^-)^{13}\mathrm{C}$. The reaction $^{13}\mathrm{C}(\alpha,n)^{16}\mathrm{O}$ is an important neutron source for the nucleosynthesis of heavy elements as will be explained below [37]. Another foundation of a neutron source is ^{14}N as a product from the CNO-cycle which is transformed into ^{22}Ne through the chain $^{14}\mathrm{N}(\alpha,\gamma)^{18}\mathrm{F}(e^+\nu_e)^{18}\mathrm{O}(\alpha,\gamma)^{22}\mathrm{Ne}$. ^{22}Ne in turn will be converted via the competing reactions $^{22}\mathrm{Ne}(\alpha,\gamma)^{26}\mathrm{Mg}$ and $^{22}\mathrm{Ne}(\alpha,n)^{25}\mathrm{Mg}$ [24, 38]. The latter provides neutrons towards the end of helium burning at temperatures above $T \approx 0.25$ GK influencing the synthesis of heavy elements. During the AGB phase, the star suffers mass loss via strong stellar winds, ejecting its outer layers to the interstellar medium, leaving behind a *carbon-oxygen white dwarf* [24].

After the He is consumed in the core, a new contraction due to gravity and missing radiation pressure begins, until the temperature is again high enough to fuse ^{12}C and ^{16}O of which the core is made up after helium burning, igniting the *carbon burning*. Since the fusion of $^{12}\mathrm{C} + {}^{12}\mathrm{C}$ has the lowest Coulomb barrier, it dominates the carbon burning. The newly formed ^{24}Mg is highly excited, and the emission of light particles such as p, α, and n as primary reactions is likely. These reactions mainly produce ^{23}Na and ^{20}Ne. These particles on the other hand will be involved in secondary reactions when the temperature rises. Due to the larger Coulomb barrier of reactions where ^{16}O is involved, most of the present ^{16}O nuclei survive while ^{12}C is consumed. Other abundant nuclei that exist in the core are ^{16}O, ^{20}Ne, ^{23}Na and ^{24}Mg. For stars

[1] Note, that there are limits between 8 $M_\odot$ to 9 $M_\odot$ given in literature depending on the explicit features as e. g. metallicity of the specific star as further discussed in [36].

with masses 9 $M_\odot \lesssim M \lesssim 11\ M_\odot$[2] *carbon burning* marks the last core burning stage. These stars undergo some more complicated evolutionary stages and finally end their life with strong stellar winds removing the surface becoming an *oxygen-neon white dwarf* with a mass of $\approx 1.2\ M_\odot$[24].

All of the following burning stages take place in massive stars with $M \gtrsim 11\ M_\odot$. Note that the next burning stage, after the core contracts due to gravity and the temperature and pressure rise again, is not *oxygen burning* but *neon burning*. This proceeds mostly through photodisintegration reactions on ^{20}Ne due to the relatively small α-particle separation energy [24]. The α-particles released via $^{20}\mathrm{Ne}(\gamma,\alpha)^{16}\mathrm{O}$ can react with other species of nuclei via e. g. $^{20}\mathrm{Ne}(\alpha,\gamma)^{24}\mathrm{Mg}$, $^{23}\mathrm{Na}(\alpha,p)^{26}\mathrm{Mg}$ or $^{24}\mathrm{Mg}(\alpha,\gamma)^{28}\mathrm{Si}$.

After the ^{20}Ne in the core is exhausted, ^{16}O, ^{24}Mg, and ^{28}Si are the most abundant nuclei. Again, the core contracts, temperature increases and *oxygen burning* starts. The fusion of two ^{16}O is the most likely process as it has the smallest Coulomb barrier. The highly excited ^{32}S nucleus will not de-excite via γ-ray emission but with the emission of light particles. There is a variety of exit channels due to the high excitation energy, namely protons, α particles, and deuterons. The particles are captured rapidly by secondary reactions by heavier nuclei stemming from the neon burning of the primary reactions of oxygen burning. Through different sequences, the oxygen burning primarily produces ^{28}Si and ^{32}S, namely via $^{16}\mathrm{O}(^{16}\mathrm{O,p})^{31}\mathrm{P}(\mathrm{p},\gamma)^{32}\mathrm{S}$, $^{16}\mathrm{O}(^{16}\mathrm{O,p})^{31}\mathrm{P}(\mathrm{p},\alpha)^{28}\mathrm{S}$, $^{16}\mathrm{O}(^{16}\mathrm{O},\alpha)^{28}\mathrm{Si}$ and $^{16}\mathrm{O}(^{16}\mathrm{O,n})^{31}\mathrm{S}(\gamma,\mathrm{p})^{30}\mathrm{P}(\gamma,\mathrm{p})^{29}\mathrm{Si}(\alpha,\mathrm{n})^{32}\mathrm{S}$ [24]. Note, that nuclides up to ^{42}Ca are produced depending on the mass, but with a small mass fraction compared to those of ^{28}Si and ^{32}S.

After the consumption of ^{16}O in the core, the most abundant elements in the core are ^{28}Si and ^{32}S. One last time the core contracts, the temperature increases. However, fusion reactions such as $^{28}\mathrm{Si} + {}^{28}\mathrm{Si}$ or $^{28}\mathrm{Si} + {}^{32}\mathrm{S}$ are unlikely to take place because of the Coulomb barriers. The path during *silicon burning* continues with photodisintegration of less tightly bound nuclei and the subsequent release of light particles, e. g. protons, neutrons and α particles [39]. ^{32}S will be first destroyed by being converted to ^{28}Si via $^{32}\mathrm{S}(\gamma,\alpha)^{28}\mathrm{Si}$ and $^{32}\mathrm{S}(\gamma,\mathrm{p})^{31}\mathrm{P}(\gamma,\mathrm{p})^{30}\mathrm{Si}(\gamma,\mathrm{n})^{29}\mathrm{Si}(\gamma,\mathrm{n})^{28}\mathrm{Si}$. The temperature increases further and ^{28}Si can photodisintegrate. A complex network transforming ^{28}Si from intermediate mass nuclei up to the Fe-peak is initiated since ^{56}Fe is one of the most tightly bound nuclei. Hence, this ensures the abundance of light nuclei decreases while the abundance in the iron-peak region increases. Once silicon is exhausted in the core, the star's structure resembles that of an onion, with layers of different compositions separated by their burning shells. This marks the extinction of stellar burning since the fuel is consumed and due to neutrinos escaping the star, the thermal energy decreases, leading to a *freeze-out* [40]. The central density and temperature increase and an equilibrium state, the so-called *Nuclear Statistical Equilibrium* (NSE), develops, where all reactions between nuclei are in equilibrium [24]. The core is electron degenerate, without a source of nuclear energy and is weighted by the nuclear ashes of the overlying burning shells. At some point, the iron core will reach a critical mass – the Chandrasekhar mass limit of $\approx 1.44\ M_\odot$ – where the pressure of the electron degeneracy cannot counteract gravity and collapses [26].

[2] Note, that there are lower limits as mentioned above and upper limits between 11 $\mathrm{M}_\odot$ to 12 $\mathrm{M}_\odot$ given in literature as further discussed in [36].

1.2 Nucleosynthesis of Heavy Nuclides through Neutron Capture Reactions

Beyond the iron peak, the charged-particle reaction cross-sections are far too small due to the increasing Coulomb barrier, and thus do not contribute to the observed abundance of trans-iron elements shown in Fig. 1.1. Since neutron-induced reactions are not hindered by the Coulomb force, they are the primary source of the nucleosynthesis of elements heavier than iron, because the neutron-capture cross sections are large at moderate stellar temperatures. In the groundbreaking *B2FH*-paper [11] two different neutron-capture processes were accounted for producing the vast majority of heavy elements. Furthermore, these two processes also provide an explanation for the double-peak structures in the solar abundance pattern shown in Fig. 1.1. These double-peaks are prominent around the mass numbers $A \approx 80$–90, 130–138, and 195–208 [41]. These structures correspond to the magic neutron numbers $N = 50, 82$, and 126. The sharp peaks stem from the *slow neutron-capture process* (*s-process*), whereas the broader peaks around 10 A below them stem from the *rapid neutron-capture process* (*r-process*). This is shown in more detail in Fig. 1.2. The general picture is more complex though and stars, whose elemental abundance cannot be described by these two processes, point to a third process, the *intermediate neutron-capture process* (*i-process*). These neutron-capture processes are explained in detail below.

1.2.1 The *s*-process

The first distinct confirmation that the heavy elements originate in stars was the discovery of the solely radioactive element technetium in the spectra of AGB stars by Paul Merrill in 1952 [42]. The age of the star at that point of its evolution is about 10^7 y, whereas the longest lived technetium isotope has a half-life of $\approx 4.2 \cdot 10^6$ y. Hence, the Tc must have been produced during the lifetime of the star and could not have been present when the star formed.

As ^{99}Tc, the likely most abundant isotope of Tc, about half of the heavy elements are made by the *s*-process [43]. The origin are seed nuclei, that are exposed to a neutron flux weak enough to allow β^--decays after (n, γ) reactions. This process transforms the seeds to nuclei of higher mass. Since the half-life of the β^--decays is in general shorter than the time for a neutron capture – hence, the name 'slow' – the path of the *s*-process runs closely to the valley of stability when looking at the chart of nuclei. The typical neutron densities are $\mathrm{N}_n = 10^{7-12}\mathrm{cm}^{-3}$ [44]. The heaviest nucleus that can be synthesized by the *s*-process is ^{209}Bi, as all heavier elements produced by further neutron captures are radioactive and decay via the emission of an α-particle back to stability. Branching points occur when β^--decays and neutron captures compete, i. e. $\lambda_\beta \approx \lambda_n$. They provide information on the specific conditions, e. g. temperature and neutron density, of the stellar environment. [24]

The *s*-process itself further splits up into the *main* and *weak* *s*-process components. These components, each producing a specific subset of the *s*-nuclei, operate in two distinct astrophysical environments, namely:

- main *s*-process: Thermally pulsing lower-mass ($M < 4\ M_\odot$) AGB stars produce the stable

s-nuclei with $A \geq 90$. The neutrons released by the $^{13}C(\alpha, n)^{16}O$ reaction are the main neutron source and will be captured by already existing seed nuclei. The reached neutron density amounts to $N_n = 10^7 cm^{-3}$, lasting a few thousand years. Another source during thermal pulses, acting on higher temperatures, is the $^{22}Ne(\alpha, n)^{25}Mg$ reaction, which has a neutron density of about $N_n = 10^{10} cm^{-3}$ lasting only a few years. The latter has a smaller contribution and the *s*-process abundance is rather low. Nevertheless, it influences the *s*-process branching points since some nuclei will capture a neutron before decaying back to stability due to the higher neutron densities. [24, 43–45]

- weak *s*-process: Massive stars ($M \geq 8\ M_\odot$) produce the stable *s*-nuclei with $60 < A < 90$ [24, 43–46]. These stars explode as a Type II core-collapse-supernova (CCSN). The main neutron source here is the $^{22}Ne(\alpha, n)^{25}Mg$ reaction stemming from $^{18}O(\alpha, \gamma)^{22}Ne$ that is produced at the end of helium burning as explained in Section 1.1.

1.2.2 The *r*-process

The other half of the heavy elements are made by the *r*-process [41, 47]. It is also capable of producing the long-lived radioisotopes as ^{232}Th and ^{238}U, which underlines the need for a neutron-capture process in addition to the *s*-process. The *r*-process has, in contrast to the *s*-process, a very high neutron density of $N_n = 10^{20-28} cm^{-3}$, which leads to neutron-capture timescales that are way shorter than the timescale for β^--decays, especially near stability – hence, the name 'rapid'. Therefore, the *r*-process operates far from stability near the neutron dripline until the path reaches closed neutron shells (N = 50, 80, and 126), it is halted by (γ, n) reactions on more weakly bound neutron-rich nuclei or the neutron flux terminates [24, 44]. In these cases, the nuclei decay back to stability through β^--decays.

For the *r*-process, reliable theoretical models are even more crucial than for the *s*-process, since the experimental data far from the valley of stability is limited. These models, on the other hand, need reliable experimental input for more reliable predictions that are beyond experimental reach [48]. Therefore, huge effort is made to both, experimentally and theoretically, investigate the key properties of nuclear physics, e. g. masses, level schemes, neutron-capture cross sections and β-decay rates [47, 49–54].

The precise astrophysical site of the *r*-process is less well known than for the *s*-process [47]. The most promising scenarios for high neutron densities are also the most extreme astrophysical environments. These include neutron star mergers, merging black holes and neutron stars, rare CCSN, and black hole accretion discs [47, 55]. Some more light was shed on this thanks to the observation of the kilonova that followed the gravitational wave event GW170817 from a neutron-star merger [56]. The discovery was very powerful since multi-messenger astronomy was applied using a variety of instruments to observe the multiple components of the ejecta, observing the source of the kilonova for days [57–61]. These observations led to the assumption that the *r*-process takes place in neutron star mergers, which are most likely the primary astrophysical site of *r*-process element production.

In addition to neutron-capture processes, there are more processes that are needed to describe a specific group of neutron-deficient nuclei – the so-called *p-nuclei*.

To explain the observed abundance pattern of stars, models using neutron-star mergers as the only source make it difficult to reproduce the patterns. Therefore, at least a second site is needed for the *r*-process [54, 55, 62–65]. Many open questions remain about not only the different contributions of likely astrophysical sites but the *r*-process nucleosynthesis in these sites.

1.2.3 The *i*-process

Already in 1977 Cowan and Rose [66] suggested an additional neutron-capture process, the *i*-process. This process has neutron densities of $N_n = 10^{15-17}\mathrm{cm}^{-3}$ in between those of the *r*-process and *s*-process – hence the name.

However, this suggestion was mostly forgotten about for over 30 years until Herwig *et al.* came to the same conclusions as Cowan and Rose without knowing about the publication [37]. If H is mixed into convective He-burning shells, neutrons are released through the $^{13}\mathrm{C}(\alpha, n)^{16}\mathrm{O}$ reaction, since protons are captured by $^{12}\mathrm{C}$, as explained in Section 1.1. The difference between the *i*-process and the *s*-process lies in the details of the split between the H-burning activation and the mixing of H or $^{13}\mathrm{C}$ into the He-shell flash convection-zone. If the mixing continues, neutrons are released within 1 s to 10 s, creating the neutron density needed for the *i*-process via the $^{13}\mathrm{C}(\alpha, n)^{16}\mathrm{O}$ reaction being active at higher temperatures [37, 54]. The potential astrophysical sites include rapidly accreting white dwarfs [67, 68] and thermal pulses of AGB stars [37, 69].

The *i*-process can explain the abundance patterns of some carbon-enhanced metal poor stars (CEMP), that show an enrichment in Ba and Eu, produced by the *s*-process and *r*-process, respectively, [70]. This was a long-standing problem due to the fact that these two processes occur in different astrophysical sites [71].

The paths taken by the *i*-process during the neutron captures are located closer to stability than those of the *r*-process. Since neutron-capture cross-sections are mostly[3] known for stable isotopes or isotopes close to stability, the neutron capture rates have to be deduced from models [72, 73]. These rates are important since some of them – and their uncertainties – have a strong impact on the prediction of models for the *i*-process [74, 75]. The importance of the rates and their relative vicinity to stability lead to experiments to constrain reaction rates [76, 77]. The challenge of obtaining these neutron capture rates for unstable nuclei remains high, but it is worthwhile for not only understanding the *i*-process better, but also the *r*-process.

[3] with the exception for isotopes from Ra to Fm

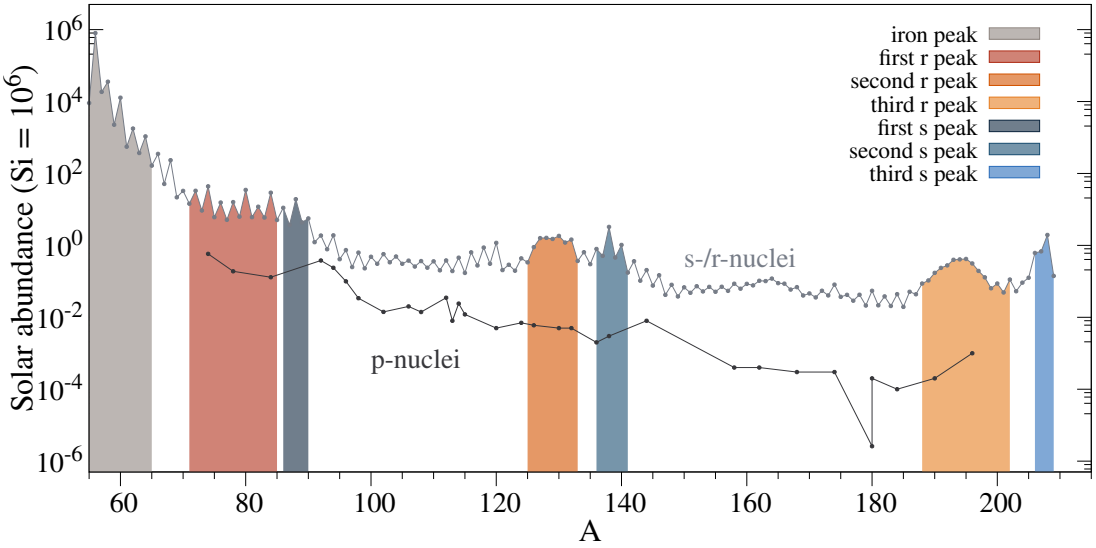

Figure 1.2: The solar abundances of the p nuclei in comparison to the s- or r-nuclei normalized to silicon (^{28}Si $= 10^6$) as a function of mass number A. The lines are used to guide the eye. The shaded areas are used to mark the peaks associated with the different processes approximately. The values are taken from Ref. [22]. Details can be found in the text.

1.3 The *p*-Nuclei and their many Production Mechanisms

As mentioned in Section 1.2, most of the nuclei are produced in neutron-capture processes except for a small group of 35[4] stable neutron-deficient nuclei[5] with $A \geq 74$ from Se to Hg. These are referred to as the *p*-nuclei and their astrophysical origin is still a question.

There are extinct radionuclides – ^{92}Nb, ^{97,98}Tc, and ^{146}Sm – that are not *p*-nuclei but are assumed to have the same origin process as the *p*-nuclei [78]. Therefore, information about the early solar system, where these radionuclides were still present and now have decayed, might be extracted from meteorites to help constrain the *p*-nuclei–nucleosynthesis [54, 78–80]. There are several hindrances, e. g. the uncertainties for the abundance predictions, to use these radionuclides as a cosmochronometer for the scenarios that formed the molecular cloud our sun originated from [54, 81].

The fact that the *p*-nuclei are (mostly) by-passed by the *r*-process or *s*-process is known since *B2FH*, who named the mechanism responsible for the synthesis *p*-process [11]. Follow-up research showed that some *p*-nuclei gain contributions from the *r*-process or *s*-process [80]. As shown in Fig. 1.2, the abundance of *p*-nuclei is usually ten to a thousand times smaller than that of the *s*- and *r*-nuclei, and further, no single *p*-nuclei is the most abundant isotope of its element.

Historically, the *p*-process was concluded by *B2FH* to be made up of (p, γ) and maybe (γ, n)

[4] Sometimes 30-35, depending on the employed models for the processes as they vary the exact contributions for the *p*-process [78].

[5] Namely: ^{74}Se, ^{78}Kr, ^{84}Sr, ^{92,94}Mo, ^{96,98}Ru, ^{102}Pd, ^{106,108}Cd, ^{112,114,115}Sn, ^{113}In, ^{120}Te, ^{124,126}Xe, ^{130,132}Ba, ^{136,138}Ce, ^{138}La, ^{144}Sm, ^{152}Gd, ^{156,158}Dy, ^{162,164}Er, ^{168}Yb, ^{174}Hf, ^{180}Ta, ^{180}W, ^{184}Os, ^{190}Pt, and ^{196}Hg.

reactions on seed nuclei, produced by the *s*- and *r*-process, in the envelope of a CCSN [11]. However, the conditions for (p,γ) captures to happen are very unlikely to occur in the H–rich layers of CCSN due to the high densities ($100\,\mathrm{g/cm^3}$), high temperatures (1.8 GK to 3.3 GK), and short time scales [11, 24, 79, 82]. Moreover, the temperatures that are needed to resolve the problem with the Coulomb barrier, would lead to photodisintegration processes destroying the nuclei.

Different astrophysical scenarios and diverse mechanisms to explain the origin of the *p*-nuclei have been suggested over the years. They will be explained in the subsections below. The expression *p*-process is used as an umbrella-term in the community for describing the diverse processes that contribute to the *p*-nuclei and not only the historically assumed (p,γ) reactions.

1.3.1 The γ-process

One of these processes, which presumably contributes the most to the synthesis of the *p*-nuclei, is the γ-process. It consists of a series of photodisintegrations – (γ,n), (γ,p), and (γ,α) – on heavy seed nuclei that can synthesize neutron-deficient nuclei [80, 82, 83]. The various processes contributing to the γ-process show the complexity of the reaction network. The starting point are sequences of (γ,n) reactions on stable isotopes, creating a flow to the neutron-deficient site of the valley of stability. This continues up to a point where the nuclei have become proton-rich enough that (γ,p) and (γ,α) reactions become comparably likely due to the increasing neutron binding energy with decreasing neutron number. Since the neutron separation energy for even neutron numbers is higher than for the neighboring nuclei, this deflection into isotopic chains of lower charge number is more likely to happen for even neutron numbers [78]. For higher mass nuclei, (γ,α) dominates over (γ,p) deflections whereas for lower mass it is the other way around, e. g. due to the Coulomb barriers [19]. Subsequent β^+-decays and electron captures can also contribute to the reaction flow [80]. The temperature dependence is different for the various types of reactions, which can shift the deflections and branchings between the photodisintegrations to other nuclei. It is worth noting that the *p*-nuclei with lower mass require higher temperature (2.5 GK to 3.5 GK) to photodisintegrate than the *p*-nuclei with higher mass (< 2.5 GK). The upper temperature limit is important because otherwise the seed nuclei would completely photodisintegrate to iron as they are less bound [78, 80]. Therefore, the γ-process sites have to hold the temperatures for a long enough time period to allow reactions but, short enough to hinder a complete photodisintegration.

A scenario, where these conditions are met, is in the ONe–rich layers of massive stars in their pre-supernovae or supernovae phase, as first suggested by Arnould in 1976 [79, 83]. The name γ-process was first brought up in a paper by Woosley and Howard in 1978 [82], who concluded that CCSN provide the needed conditions for the synthesis of *p*-nuclei via photodisintegration processes. The latter scenario, however, under-predicts the abundance of the *p*-nuclei ^{92,94}Mo and ^{96,98}Ru since the amount of seed nuclei in this mass region is not sufficient [82]. This is also confirmed by more recent studies of different CCSN models [84].

Another site that has been suggested, where the required conditions are met, is the explosion of a carbon-oxygen white dwarf that reached the Chandrasekhar limit ($\approx 1.44\ M_\odot$), i. e. Type Ia

supernovae [85, 86]. The limit is reached via the accretion of mass from a companion star. It is worth noting that nucleosynthesis via the γ-process occurs only with a s-process enrichment in SNe Ia for which it is in turn crucial to know the initial s-process seed distribution and location since this impacts the p-process nucleosynthesis [86]. This scenario could be a dominant site with a contribution of at least 50 % for the production of p-nuclei including the production of ^{92}Mo and ^{96,98}Ru [86, 87]. Calculations including the synthesis of heavy-element seeds needed for p-nuclei-nucleosynthesis confirmed that SN Ia contribute significantly in the mass range of $96 < A < 196$ [88].

Although the γ-process is the process with the presumably largest contribution to the production of p-nuclei, some questions remain open. The precise contribution – whether they contribute equally or one dominates over the other – to the p-nuclei-abundances of CCSN and SN Ia is still unclear. The precise origin of the troublesome p-nuclei ^{92,94}Mo and ^{96,98}Ru is not yet solved. And last but not least, there are many unstable nuclei involved in the γ-process. Sensitivity studies showed that theoretically predicted rates of reactions on unstable nuclei and of excited states contributions are the main uncertainties for the γ-process, since these can alter the complex reaction flows [89].

1.3.2 The νp-, rp-, and νr-process

The above mentioned discrepancies give rise to investigations of other processes contributing to the production of p-nuclei other than the γ-process.

The νp-process

The νp-process involves neutrino-driven winds of CCSNe. If the electron fraction reaches values of $Y_e > 0.5$, proton-rich neutrino-driven winds are obtained, lasting for up to 20 s after the explosion [90]. These wind ejects are hotter than 10 GK and consist mainly of free protons and neutrons. The expansion and cooling of the proton rich matter allows to build up $N = Z$ nuclei, mainly ^{56}Ni and α-particles, and an excess of protons [91]. In contrast to a neutron-rich NSE, where no free neutrons exist during the freeze-out, a small amount of 10^{-11} to 10^{-12} free neutrons exists due to the capture of electron antineutrinos on free protons via the $p(\bar{\nu_e}, e^+)n$ reaction [92]. For temperatures between 1.5 GK to 3 GK, the faster (n, p) on ^{56}Ni followed by (p, γ) reactions, bypass the waiting point nucleus ^{64}Ge with a β^+ half-life of $T_{1/2} = 64$ s as well as ^{68}Se and ^{72}Kr with half-lives of 35.5 s and 17.1 s, respectively [72, 92]. The reaction flow up to molybdenum follows the already mentioned $N = Z$ trend. Between molybdenum ($Z = 42$) and tin ($Z = 50$) this trend shifts closer to the valley of stability and with this, to more neutron-rich isotopes ($N > Z$). (p, γ) reactions begin to slow down due to the Coulomb barrier as soon as the temperature falls below 1.5 GK and nuclei decay back to stability through β^+-decays and (n, p) reactions [92]. This is a primary process since it does not need seed-nuclei from other processes.

Note, that the νp-process is sensitive to a variety of parameters, that stem from the underlying physics as well as astrophysical sites. Besides the interaction of neutrinos with the nucleons, the electron fraction is important. In general, a higher electron fraction will lead to the synthesis of

heavier elements [91, 93]. The main uncertainties from the nuclear physics input come from the masses on the νp-process pathway, the triple α-reaction and the ^{56}Ni(n,p) reaction. The latter is the first step in the νp-process and plays an important role on the following nucleosynthesis. A lower rate leads to a more efficient νp-process [92]. Despite the uncertainties, the νp-process can account for light p-nuclei with up to $A = 108$ for an Y_e about 0.6 or up to $A = 152$, if $Y_e \approx 0.65$ in the ejecta [92]. This includes the production of the troublemaking p-nuclei ^{92,94}Mo and ^{96,98}Ru [91, 92]. However, other studies imply that the stellar models need adjustment or other sources are required for the production of these p-nuclei [94]. This shows that more progress in modeling the explosion mechanism, hydrodynamic studies, neutrino transport, the progenitor star as well as the relevant nuclear physics is needed to better understand the impact of neutrinos for the p-nuclei.

The *rp*-process

The *rapid proton capture*-process (r-process) transforms nuclei produced in the CNO–cycle to ones up to and beyond the Fe – Co–region [95]. The path of the rp-process involves sequences of (p,γ) reactions on CNO–nuclei up to the proton dripline, where β^+-decays, (p,γ) and (γ,p) reactions compete [24]. As a result of the proximity to the proton dripline, huge experimental effort has been made over the years to measure the key ingredients, such as masses and half-lives, for this process (cf. [96] and references therein). Nevertheless, the important reactions are hard to measure mostly due to too low intensities of rare isotope beams.

Different astrophysical sites for the rp-process have been proposed, such as when a neutron star accretes H- and He–rich material from a companion star. This ignites a thermonuclear runaway that causes a Type I X-ray burst, which can synthesize proton-rich isotopes up to $A \approx 100$ [97–101]. These bursts can last from 10 s to 100 s recurring within hours to days, reaching temperatures in the burning region of up to 2 GK. Although this scenario is a potential site that produces light p-nuclei ^{84}Sr, ^{92,94}Mo, and ^{96,98}Ru, and possibly ^{74}Se and ^{78}Kr, the gravitational fields of the neutron star prevent the ejection of the synthesized material [79, 97, 100]. Nevertheless, radiation-driven winds could lead to ejections of some small amount of material, but it remains unclear if such winds contain material synthesized during X-ray bursts [102]. A more recent study suggests that in a common-envelope phase, where mass is accreted onto the neutron star while it passes through the envelope of its companion, material produced by the rp-process might be ejected [103].

This shows, that more detailed studies and simulations are needed to confirm or decline the role of accreting neutron stars for the production of p-nuclei.

The νr-process

The most recent suggested mechanism for nucleosynthesis of the p-nuclei is the νr-process [104]. In contrast to the already discussed processes synthesizing the p-nuclei, this process operates in neutron-rich environments, where the r-process produced seeds that experienced strong neutrino irradiation. Similar to the νp-process, the temperature in the beginning is high and the material

consists of protons and neutrons, which as the temperature decreases begin to form nuclei via charged-particle reactions. These reactions undergo a freeze-out at $T \approx 3\,\mathrm{GK}$. The nuclei act as seeds for neutron captures in a $(n,\gamma) \rightleftharpoons (\gamma,n)$ equilibrium. The absorption of neutrinos breaks the equilibrium instead of β-decays and the flow is pushed to higher charge numbers toward and beyond the valley of stability. This mechanism produces p-nuclei as well as the extinct radionuclide ^{92}Nb that is shielded by ^{92}Mo from being produced in the νp-process and the rp-process. It is important to note that this process is highly dependent on uncertainties regarding interactions involving neutrinos, and the specific astrophysical conditions required for such strong flux of neutrinos are not yet fully understood.

To summarize the discussion on the p-process with all contributing processes explained above: it is still a work in progress to fully understand the synthesis and the solar abundance of the p-nuclei.

1.4 The Importance of Nuclear Physics for Reaction Rates in Astrophysical Environments

The different processes and astrophysical sites that lead to the nucleosynthesis of elements have the same basis: a huge variety of nuclear physics data. In principal, the key ingredients can be reduced to reaction rates at low energies and binding energies. Of the approximately 3000 known nuclides today, 2500 have measured masses.

The different processes explained in Section 1.2 consist of neutron-capture reactions with subsequent β-decays. Knowing the reaction rates for them is crucial in order to model the abundance flow. The approximately 400 isotopes involved in the s-process are located close to the valley of stability which allows to obtain reliable neutron-capture rates as well as masses to determine Q-values more easily [54, 105]. It is worth noting, that there are circa 15 branching points in the s-process which can provide information on the precise stellar environment such as temperature and density. For this, the most accurate knowledge of the aforementioned rates and half-lives is needed as well as the temperature dependence of the rates [106].

The number of involved isotopes changes drastically to about 5000 when considering the r-process. Nuclei of really light to superheavy masses lying between the valley of stability and the neutron dripline play a role now. Depending on the employed mass model, the precise location of the neutron drip line and the number of predicted nuclides in bound systems (6000 to 8000) differ quite a lot [54, 105]. Note, that at least half of the predicted nuclei stay unidentified in experiments so far. The masses impact the β-decay rates and the neutron-capture rates. They are key ingredients in modeling the r-process. A precise knowledge is needed to reduce uncertainties and improve theoretical predictions [54].

The rp-process has some similarities to the r-process. Instead of neutron capture rates, proton capture rates need to be known, as well as half-lives and nuclear masses. The proton dripline, however, lies closer to the valley of stability than the neutron dripline and the Coulomb barrier plays a role when protons are involved [106]. Approximately 200 nuclei are involved in the

rp-process [54].

A huge effort has been made to measure masses precisely as they serve as an important basis to model the *rp*-process and the *r*-process [105, 107]. In addition, radioactive ion beam facilities across the world came into play and new techniques to investigate the nuclear parameters for the different nucleosynthesis processes have been developed [48].

The γ-process is a complex network of photodisintegration processes, i. e. (γ, n), (γ, p), and (γ, α), as explained in Section 1.3.1 with about 2000 involving nuclei, many of them being unstable [54]. Since the reaction rates of (γ, n) compete with β^+-decays, (γ, p)–, and (γ, α)–reactions, these rates as well as the α-, p-, and n-capture rates need to be known precisely [19, 106, 108]. It is important to stress that the process is highly sensitive to the plasma temperature and a higher temperature leads to more excited states contributing to stellar rates [109]. This is a longstanding crux since in experiments, only cross-sections in the ground-state can be measured [110]. The reactions in the stellar plasma, however, will also occur on nuclei in excited states. If the situation $A + \gamma \leftrightarrow B + x$, where states in the nuclei A and B are connected by (charged-)particle- and γ-transitions, is considered in a stellar plasma, both directions for the reaction will occur. The contributions of the excited states are not symmetrical. The capture-reaction should be studied for reactions where photons are involved, as the latter reactions most likely have a negative reaction Q-value, which is more affected by contributions of excited states. In addition, the contribution of the ground state for (γ, x) reactions, where x equals α, p, or n, is always lower than for the inverse direction (x, γ) [78]. The ground-state contribution is overall dependent on the temperature of the plasma as well as on spin and excitation energies of involved states [106, 111]. Since the photodisintegration reactions play a major role in the γ-process, the reverse stellar rates are calculated using the *detailed balance theorem*. Especially important is, that the reciprocity relations do not hold for laboratory cross-sections, why the derivation of stellar reaction rates for reaction networks require theory [112]. This will be discussed in more detail in the following chapter (cf. Chapter 2).

1.4.1 Charged-Particle induced Reaction Rates and the Gamow Window

This thesis will focus on the proton-capture reactions. A reaction $A + a \rightarrow B + b$ has a certain cross section σ that characterizes a nuclear reaction and is one of the most important quantities. It quantifies the probability that a reaction occurs with respect to center-of-mass energy. The cross section σ is defined as

$$\sigma_{ab}(E) = \frac{N_R}{N_a \cdot n_A}, \tag{1.1}$$

where N_R is the number of reactions that occurred, N_a the number of projectiles and n_A the number of target atoms per area. By this definition, the dimension of the cross section is an area, and the commonly used unit is *barn*, where 1 b $= 10^{-28}$ m^2.

As explained above, the various reactions in a stellar environment are temperature dependent. Since the temperature is not constant in most environments, particles, as well as photons, follow a distribution that is temperature dependent rather than having a sharp energy or a constant

relative velocity. Therefore, the *reaction rate per particle pair* $\langle\sigma v\rangle_{Aa}$ is a more useful quantity than the cross section itself. The reaction rate can be expressed as either energy-dependent or velocity-dependent as follows:

$$r_{Aa} = n_A n_a \langle\sigma v\rangle_{Aa} = n_A n_a \int_0^\infty v P(v) \sigma(v)\, dv, \tag{1.2}$$

where n_A and n_a are the concentrations of the respective particles expressed in cm^{-3}, $\sigma(v)$ the velocity v dependent cross section, and $P(v)$ the probability distribution of the nuclei interacting at a relative velocity between v and $v + dv$. In literature, the most commonly used quantity is $N_A\langle\sigma v\rangle_{Aa}$ in $\mathrm{cm}^3\mathrm{mol}^{-1}\mathrm{s}^{-1}$ with N_A denoting the Avogadro constant. In a stellar plasma, the energy available to the nuclei is delivered by the thermal motion, wherefore the initiated reactions are called *thermonuclear reactions*. The relative particle velocities between the interacting nuclei determine the probability of a reaction. The velocity distribution can be described by the Maxwell-Boltzmann distribution

$$P(v)\, dv = \left(\frac{\mu}{2\pi kT}\right)^{3/2} e^{-\mu v^2/(2kT)} 4\pi v^2\, dv, \tag{1.3}$$

which describes the probability that the relative velocity of particles A and a lies between v and $v+dv$. The reduced mass is $\mu = \frac{m_A m_a}{m_A + ma}$, k is the Boltzmann constant with $k = 8.6173 \times 10^{-5}$ eV K, and T is the temperature. This is possible since most stellar matter is non-degenerate and non-relativistic. The reaction rate per particle can be written as an energy distribution using $E = \mu v^2/2$ and $dE/dv = \mu v$

$$\langle\sigma v\rangle_{Aa} = \left(\frac{8}{\mu\pi}\right)^{1/2} \frac{1}{(kT)^{3/2}} \int_0^\infty E\sigma(E) e^{-E/kT}\, dE. \tag{1.4}$$

The velocity, and accordingly energy of a charged particle in a stellar or laboratory environment is usually not high enough to overcome the Coulomb barrier in a classical manner. Quantum-mechanically, however, there is a certain probability to penetrate the Coulomb barrier via tunneling. For energies low compared to the barrier height, the s-wave Coulomb barrier transmission probability is

$$P = e^{-2\pi\eta}, \tag{1.5}$$

called the *Gamow factor* with the Sommerfeld parameter

$$\eta = \frac{Z_A Z_a e^2}{\hbar v}, \tag{1.6}$$

where Z_A and Z_a are the charges of interacting particles [24, 113].

Introducing the *astrophysical S-factor* $S(E)$ defined as [24]

$$\sigma(E) = \frac{1}{E} e^{-2\pi\eta} S(E) \tag{1.7}$$

has the advantage of removing the dependence of the cross sections on $1/E$ and the s-wave

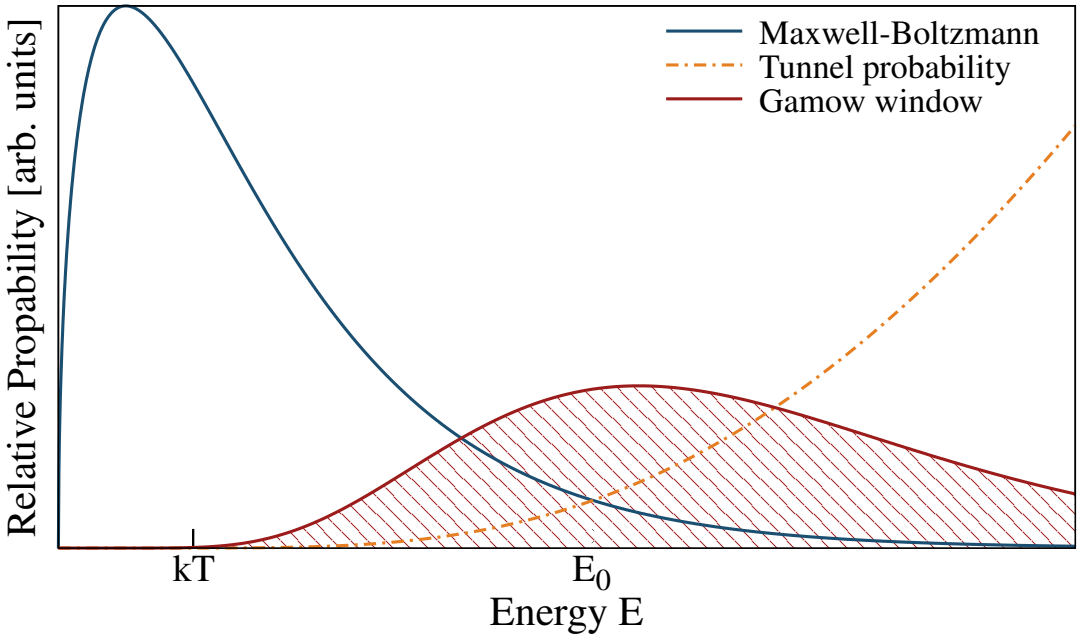

Figure 1.3: Schematic representation of the Gamow peak which corresponds to the astrophysical relevant energy window for charged-particle induced reaction. As explained in the text, it stems from the convolution of the Maxwell-Boltzmann distribution and the tunneling probability, also known as the Gamow factor. Note, that the different functions are scaled for a better representation.

Coulomb barrier transmission probability. This leads to a greatly reduced energy dependence of the S-factor in non-resonant regions compared to the cross section. With this, Eq. (1.4) can be re-written as

$$\langle \sigma v \rangle_{Aa} = \left(\frac{8}{\mu \pi} \right)^{1/2} \frac{1}{(kT)^{3/2}} S_0 \int_0^\infty e^{-2\pi\eta} e^{-E/kT} \, dE, \tag{1.8}$$

under the assumption of a constant S-factor $S(E) = S_0$. The convolution of the Maxwell-Boltzmann distribution, approaching zero for large energies, and the Gamow-factor, approaching zero for small energies, leads to a maximum contribution to the integral from energies where the product is maximal. This product forms a peak, the so-called *Gamow peak* or *Gamow window*, representing a narrow energy range, where most nuclear reactions in a stellar plasma take place [106]. This can be seen schematically in Fig. 1.3. Within the width of the Gamow peak, the cross sections have to be determined, either experimentally or theoretically.

In reality, the concept of the Gamow peak is limited due to several assumptions that are made, as, e. g. the energy dependence of the cross section is determined by the entrance channel or the S-factor has a smoothly varying dependence on the energy, and can be used as an estimator for the relevant energies [106]. Therefore, numerical calculations of the Gamow window are employed to find the relevant energy region, which can differ up to several MeV [108]. The cross sections

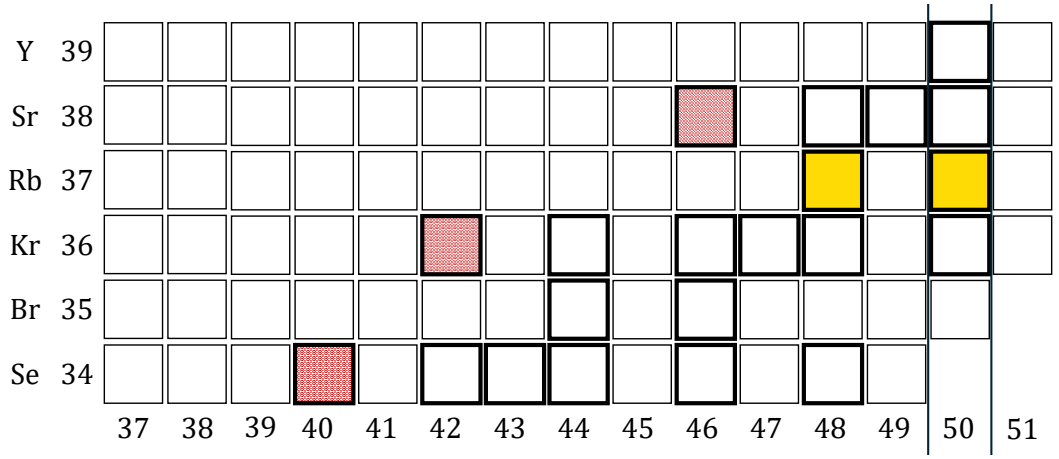

Figure 1.4: The $A = 80 - 90$ mass region around the left hand side of the valley of stability. The p-nuclei ^{74}Se, ^{78}Kr, and ^{84}Sr are marked in red. Yellow marks the proton-induced reactions on ^{85}Rb and ^{87}Rb that are investigated within the scope of this thesis.

at these energies, however, can become too small to measure and can often be lower than 10^{-9} b. This leads to direct measurements not being feasible and new techniques and setups need to be developed to improve the sensitivity. As explained above, many of the nuclei involved in the γ-process are unstable. This makes a target production unfeasible. Hence, radioactive ion beams need to be used to gain information about cross sections. Direct measurements might still be really difficult to impossible if the beam intensity and cross section are too small. So far, the number of measured cross sections for radioactive nuclei is still small. Nevertheless, these facilities enlarge the available data base and will provide more information in the future [48, 96].

For these reasons, the prediction of cross sections is heavily relying on theoretical calculations. These calculations are mainly performed using the Hauser-Feshbach framework, which will be explained in detail in Chapter 2.

1.5 Objectives of This Work

As discussed in the preceding sections, nuclear reaction rates play a fundamental role in various nucleosynthesis processes. This thesis focuses on the experimental investigation of proton-induced reactions at astrophysically relevant energies, particularly those associated with the p-process.

The motivation for this work arises from two main aspects. On the one hand, experimentally determined (p, γ) cross sections allow the calculation of the corresponding reverse photodisintegration reaction rates through the reciprocity theorem. On the other hand, the obtained data provide an essential test for the nuclear-physics input parameters used in Hauser–Feshbach statistical model calculations, contributing to their further refinement.

Figure 1.4 presents the mass region of interest. The p-nuclei ^{74}Se, ^{78}Kr, and ^{84}Sr are marked in red, while yellow highlights nuclei for which experimental data are directly connected to this

work. Within the scope of this thesis, the proton-induced reactions on ^{85}Rb and ^{87}Rb were investigated, providing the first experimental (p,γ) cross sections reported for these isotopes.

The objectives of this thesis are to provide new experimental data on proton-induced reactions in the mass region relevant to the γ-process and to test the predictive power of statistical model calculations in this context. In particular, the measured ^{85}Rb$(p,\gamma)^{86}$Sr and ^{87}Rb$(p,\gamma)^{88}$Sr reaction cross sections serve as sensitive probes of the Hauser–Feshbach model parameters, allowing a critical evaluation of their applicability near the $N = 50$ shell closure. By comparing the experimental results with theoretical predictions and systematically exploring key input parameters, this work aims to identify shortcomings in current model descriptions and to contribute to a more consistent understanding of proton-capture reactions in this mass region.

All of the nuclear reactions presented in this thesis were measured at the University of Cologne. In Chapter 2, the statistical model for nuclear reactions is briefly introduced along with the most important nuclear physics inputs. Chapter 3 gives an overview of the experimental setup and techniques used. Chapter 4 presents the complete analysis of the ^{85}Rb$(p,\gamma)^{86}$Sr reaction, while Chapter 5 summarizes the published work on ^{87}Rb$(p,\gamma)^{88}$Sr and discusses additional experimental aspects. Chapter 6 provides a more general discussion of both Rb measurements and their astrophysical implications, followed by Chapter 7, which contains a summary and an outlook on future experiments.

2 The Statistical Approach to Cross-Section Calculations

As explained in the previous chapter, the reaction networks of the different processes, that are responsible for the production of the p-nuclei, and more generally all elements, consist of thousands of involved reactions on mainly unstable nuclei. Not only are they not (easily) accessible in the laboratory, moreover, thermal excitation usually cannot be taken into account when experiments are performed on earth [106]. Therefore, it is essential to use reaction network calculations which rely on theoretical reaction rates predicted by statistical models, e. g. the Hauser-Feshbach statistical model [114, 115].

The *statistical model of compound reactions* was proposed by Bohr [116, 117], which laid the ground for the use of statistical methods to describe nuclear reactions as did e. g. Bethe [118], Weisskopf [119], and Weisskopf and Ewing [120] in forms of evaporation models. These models use that the spacing between levels of highly excited nuclei is quite small. The spacings are smaller than the widths of the states, why they might overlap and are similar to a continuum. Therefore, the individual features of each state are negligible, but statistical information including many states can be obtained [119]. This holds for reactions with an adequately large Q-value or for high beam energies.

In the beginning, the first evaporation models were designed to theoretically explain the reaction cross sections of reactions with slow neutrons. Over the years, the different models have been extended to account for charged-particles [121], conservation of total orbital momentum, and parity [114], as well as implementing the shell model and an updated view of the compound nucleus including the nuclear optical potentials [122]. The applicability of the Hauser-Feshbach theory if reactions involve γ-rays was shown by Cowan, Thielemann and Truran in 1991 [123]. Vogt [122] was the first to call the theory of Hauser and Feshbach [114] the *Hauser-Feshbach model* to credit them. The statistical model to calculate the nuclear reaction cross sections nowadays is still named in that manner. The energy range, that Hauser-Feshbach calculations cover for nuclear reactions involving e. g. neutrons, protons, and photons, is between a few keV up to several hundred MeV for nuclei between $12 \leq A \leq 339$ [124].

The Hauser-Feshbach model is extensively used in many fields of physics, e. g. for medical isotope production, nuclear fusion, nuclear energy production, radiotherapy, and, as in this thesis, (nuclear) astrophysics. A widely used nuclear reaction model code is Talys [124], which will be discussed at the end of this chapter in Section 2.3. Before, the nuclear physics input models that are important and enter the calculations will be discussed in Section 2.2, and the general concept

of the Hauser-Feshbach cross section will be explained in Section 2.1.

2.1 The Hauser-Feshbach Cross Section

As written above, the independence hypothesis of Bohr is the basis for the Hauser-Feshbach theory [116, 117]. It states that a projectile a and a target A form a compound system C, distribute the energy over all nucleons of the the compound nucleus before photons or particles b are emitted independently of its formation, i. e.

$$A + a \rightarrow C^* \rightarrow B + b. \tag{2.1}$$

For radiative capture reactions the compound nucleus is equal to the residual nucleus, and Eq. (2.1) can be written as

$$A + a \rightarrow B^* \rightarrow B + \gamma. \tag{2.2}$$

The hypothesis holds if statistical equilibrium among the nucleons is reached, which requires a long reaction time. From this it follows that the decay of the compound nucleus can be viewed as a separate process — often referred as "losing the memory of its formation" — and, therefore, only depends on conserved quantities such as energy, parity and angular momentum [116]. This process is illustrated in Figure 2.1. Still, the ejectiles can follow an angular distribution when the compound nucleus decays due to the angular momentum coupling between the compound nucleus C and the reaction product B [122, 125]. The independence of formation and decay allows to write the cross section σ_{ab} for the incident channel a and the outgoing channel b as

$$\sigma_{ab} = \sum_{J\pi} \sigma_{ab}^{J\pi}. \tag{2.3}$$

Each $\sigma_{ab}^{J\pi}$ can be written as

$$\sigma_{ab} = P_b \cdot \sigma_a, \tag{2.4}$$

where σ_a is the compound formation cross section through channel a and P_b is the probability to decay via channel b. Note, however, that σ_{ab} is the average cross section over the sum of contributions from possible states with the angular momentum J and the parity π since these quantities are conserved. To improve readability, this notation will be skipped as long as the equation holds for a certain state. P_b can be written as

$$\frac{P_b}{\sum_h P_h}, \tag{2.5}$$

where summing over all outgoing channels i obeys $\sum_h P_h = 1$.

The compound formation cross section σ_a via the channel a is

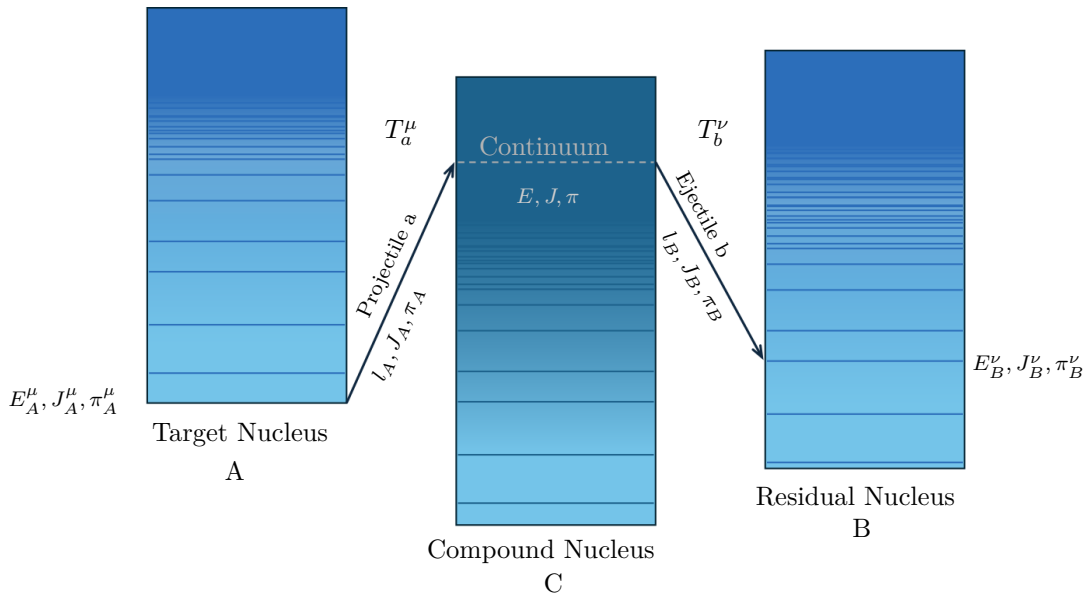

Figure 2.1: Schematic illustration of a compound nucleus reaction. The target nucleus A in its state μ forms a compound nucleus C due to the interaction with projectile a. The energy, spin, angular momentum and parity are named E, J, l and π, respectively. The compound nucleus decays via the emission of ejectile b to the state ν of the residual nucleus B. The transmission coefficients for the specific states are T_a^μ and T_b^ν. The decreasing level distance and the darker areas in the color gradient symbolize the increasing level density in the nuclei up to assumed continuum.

$$\sigma_a = \frac{\pi}{k_a^2} \sum_l (2l+1) T_l(a), \tag{2.6}$$

where k_a denotes the wavenumber of particle a and

$$T_l(a) = 1 - \left| e^{2i\delta_{al}} \right|^2 \tag{2.7}$$

is the transmission coefficient for the orbital angular momentum l, and δ_{al} the complex scattering phase shift [24, 114, 122].

The *reciprocity theorem*

$$\frac{\pi}{k_b^2} \sigma_{ab} = \frac{\pi}{k_a^2} \sigma_{ba} \tag{2.8}$$

connects forward and reverse reaction via time-reversibility of a quantum-mechanical system and is used to express the probability P_b in terms of a transmission coefficient [121, 122]. The concept of *detailed balance* in contrast to the reciprocity theorem fails to hold for nuclear reactions since the spin direction is not reversed [121]. To involve unpolarized particles with spin, Eq. (2.8) needs

to be modified to account for spin I as follows [24]:

$$\frac{\pi}{k_b^2}(2I_a+2)(2I_A+1)\sigma_{ab} = \frac{\pi}{k_a^2}(2I_b+2)(2I_B+1)\sigma_{ba}. \tag{2.9}$$

Combining Eq. (2.4), (2.5) and (2.8) leads to

$$\frac{P_b}{P_a} = \frac{k_b^2(2I_b+2)(2I_B+1)\sigma_b}{k_a^2(2I_a+2)(2I_A+1)\sigma_a}. \tag{2.10}$$

Summing over all channels h leads to

$$P_b = \frac{k_b^2(2I_b+2)(2I_B+1)\sigma_b}{\sum_h k_h^2(2I_h+2)(2I_H+1)\sigma_h}, \tag{2.11}$$

due to Eq. (2.5). The coupling involving I_a, I_A and l from the projectile and target to a total spin J is taken into account in Eq. (2.6), which leads to

$$\begin{aligned}\sigma_a =& \frac{\pi}{k_a^2}\sum_l(2l+1)\sum_s\frac{2J+1}{(2I_a+2)(2I_A+1)(2l+1)}T_l(a)\\ =& \frac{\pi}{k_a^2}\sum_l\sum_s\frac{2J+1}{(2I_a+2)(2I_A+1)}T_l(a),\end{aligned} \tag{2.12}$$

where s represents the sum from $|I_a - I_A|$ to $|I_a + I_A|$. Combining Eq. (2.3), (2.4), (2.11) and (2.12) leads to the *Hauser-Feshbach formula* [114, 122]

$$\begin{aligned}\sigma_{ab} =& \sum_{J\pi} k_b^2(2I_b+2)(2I_B+1)\frac{\sigma_a\sigma_b}{\sum_h k_h^2(2I_h+2)(2I_H+1)\sigma_h}\\ =& \frac{\pi}{k_a^2}\sum_{J\pi}\frac{2J+1}{(2I_a+2)(2I_A+1)}\frac{\sum_{sl}T_l(a)\sum_{s'l'}T'_l(b)}{\sum_h\sum_{s''l''}T''_l(h)}.\end{aligned} \tag{2.13}$$

In the majority of cases, particularly in the context of this thesis, the precise spin and parity of the levels involved in high excitations remains unknown. However, these cases can be addressed by employing level density functions, which offer predictions for levels above the highest experimentally determined level. In the instance of radiative capture, the exit channel is characterized by the γ-ray transmission coefficient, which is proportional to the gray strength function.

Section 2.2 will provide a detailed examination of the nuclear level density and γ-ray strength function.

Resonance Reactions

In contrast to the previously described "continuum capture" process, the capture of particles to resonance states of the compound nucleus is characterized by narrow widths and low excitation energies. This can be understood as *Projectile a* in Figure 2.1 being captured by one of the discrete nuclear states. The particles are "quasi-bound" to a nuclear state, exhibiting a high

probability of formation, resulting in a substantial cross section. The Breit-Wigner formula,

$$\sigma_{ab} = (2l+1)\frac{\pi}{k^2}\frac{\Gamma_a\Gamma_b}{(E-E_r)^2+\Gamma^2/4}, \tag{2.14}$$

is of particular relevance in this context, where l is the orbital angular momentum, Γ_i are the partial widths of the channels a and b, Γ is the total width, and E_r is the resonance energy. Resonant reactions are of significant importance in the field of nuclear astrophysics. The existence of such resonances facilitates reactions that would otherwise impede nucleosynthesis due to their low cross sections.

2.1.1 Reactions at Elevated Temperatures

As mentioned in Section 1.4, the nuclei in a stellar plasma will not only be in their ground state but in excited states that need to be taken into account when calculating the cross section. Therefore, the stellar reaction rate r^* is needed, which is an adaption of Eq. (1.2),

$$r^* = n_A n_a \langle \sigma v \rangle^*_{Aa} = \frac{n_A n_a}{G_0(T)} \int_0^\infty \sigma^{\text{eff}}(E) P_{MB}(E,T)\, dE, \tag{2.15}$$

and involves the effective cross section $\sigma^{\text{eff}}(E)$, the temperature and energy dependent Maxwell-Boltzmann distribution $P_{MB}(E,T)$ and the normalized partition function $G_0(\mathrm{T})$. The *effective cross section* is derived by summing all of the possible transitions from state μ in the initial nucleus to state ν in the final nucleus, weighted by the corresponding transition probabilities

$$\sigma^{\text{eff}} = \sum_\mu \sum_\nu \frac{2J_\mu + 1}{2J_0 + 1} \frac{E - E_\mu}{E} \sigma^{\mu\to\nu}(E - E_\mu). \tag{2.16}$$

J_i are the spins of ground and excited states and E_μ is the excitation energy relative to the ground state, with $\mu = 0$ and $E_0 = 0$. Note that, $\sigma^{\mu\to\nu} = 0$ for $E - E_\mu < 0$ [106, 110]. The laboratory cross section is given by $\sigma^{\text{lab}} = \sum_\nu \sigma^{0\to\nu}$ and does not include contributions from excited states. Those can be important in astrophysical environments depending on the temperature and the reaction itself. The contribution of the ground state to the stellar rate serves as an indicator of the significance of excited states in the calculation of stellar rates [110]

$$X(T) = \frac{\int_0^\infty \sigma^{\text{lab}}(E) P_{MB}(E,T)\, dE}{\int_0^\infty \sigma^{\text{eff}}(E) P_{MB}(E,T)\, dE}. \tag{2.17}$$

By definition, the ground-state contribution can take on values from $0 \leq X \leq 1$. When X equals 1, the ground-state cross section — i. e. , the one measured in a laboratory — can be used to derive the stellar reaction rate. Consequently, the smaller the value of X, the more significant the contributions of the excited states become [110]. It has been noted that, in general, the contributions of excited states are reduced for charged-particle induced reactions in comparison to photodisintegration reactions [78, 126, 127]. Stellar rates – and therefore also stellar cross

sections as well as the effective cross section –, but not laboratory rates, follow an important reciprocity relation that connects the forward and reverse reactions [106, 126, 127]. It fails for the laboratory rates since the entrance and exit channels are not symmetric, i. e. the summation is over different indices [127]. The detailed balance theorem[1] is used to calculate stellar reaction rates. The reciprocity relations – for particles as projectiles and ejectiles as well as for one of them being replaced by a photon – are important for applications in reaction networks. They prevent numerical inconsistencies that may arise during network calculations [106].

2.2 Models for Statistical Properties of Nuclei

Since the nuclei involved in many astrophysical processes such as the γ-process are unstable and experiments are (nearly) impossible to perform as explained in Section 1.4.1, the Hauser-Feshbach theory provides a tool to predict cross sections. Of course it is preferable to have reliable predictions, which depend on the accurate determination of the input models. In addition, the models should be microscopic as well as global. The latter is important since all regions of the nuclear chart need to be taken into account, especially when network calculations that cover thousands of reactions involved are performed for nucleosynthesis. Cross-section predictions have primarily relied on more or less phenomenological approaches, adjusting parameters to limited experimental data or deducing them from systematic trends. While the reliability of such predictions in cases of nuclei located beyond the scope of experimental accessibility is anticipated, the validity of these predictions becomes questionable in the context of exotic nuclei. The aforementioned challenges can be addressed by relying on methods that are as fundamental (microscopic) as possible and based on physically sound models [128]. Naturally, the ideal case would be to have one universally valid model in whose framework the nuclear physics properties are calculated and show a good consistency overall.

As mentioned during this chapter, the statistical models need certain input for the calculations which will be explained below.

2.2.1 Optical-model potentials

The term ”optical-model potential” is derived from the analogy between light passing through a medium and the scattering of a particle in nuclear potentials. The aforementioned transmission coefficients for the entrance channel are typically calculated numerically by solving the Schrödinger equation for a fitting nuclear potential. The ansatz for the potentials is:

$$U(r) = V(r) + iW(r), \tag{2.18}$$

where $V(r)$ and $W(r)$ are the real and imaginary part of the potentials, respectively. In the case of charged particles, an additional Coulomb potential term is introduced, denoted by $V_C(r)$.

[1] The *detailed balance theorem* states that all states in a nucleus are occupied according to some population factor. This fails to hold for long-lived isomeric states [106].

The fundamental principle of the phenomenological model of Koning and Delaroche [129] revolves around the notion that the complex interplay between an incident particle and a nucleus with its many nucleons can be adequately represented – and thus simplified – by an effective nuclear potential with which the projectile interacts.

The square well potential was employed in the past to reduce computing time when the well's border was sharp and its depth constant [106]. However reasonable that may have been, the potential was not capable of predicting the cross sections and the scattering precisely [130]. This lead to the use of Woods-Saxon potentials for the real and imaginary part of the form

$$V_k(r, E) = -\frac{V_k(E)}{1 + e^{\frac{r - r_k}{a_k}}}, \tag{2.19}$$

where $V_k(E)$ denotes the depth of the potential, a_k is the diffuseness parameter and r_i the radius of the nucleus, with $W_k(r, E)$ and $W_k(E)$ used for the imaginary part [131]. The division of the potential into real and imaginary parts reflects the elastic scattering of projectiles and describes all competing non-elastic channels [129]. Each part of Equation (2.18) is split into volume-central (V), spin–orbit (SO) – when particles with spin are involved – and surface-central (D) potentials, where the latter only applies for the imaginary part. The spin-orbit terms $W_{SO}(r, E)$ and $V_{SO}(r, E)$ as well as the surface-central term $W_D(r, E)$ are proportional to the derivative of Equation (2.19). The latter leads to an absorption of the projectile near the surface for low scattering energies ($< 10\,\mathrm{MeV}$), whereas the $W_V(r, E)$ term begins to dominate for higher energies [129].

In the field of nuclear astrophysics, it is desirable to develop *global* potentials that are applicable to the entire nuclear chart. Two problems must be addressed in order to determine appropriate optical potentials for astrophysical applications: the prediction of optical potentials for highly unstable nuclei and the extension to the astrophysically relevant energies. From an astrophysical perspective, the region below the Coulomb barrier is of specific interest. At such low energies, elastic scattering cross sections become indistinguishable from Rutherford scattering, making it difficult to extract information on the underlying nuclear potential [112]. It is important to note that the optical potentials commonly used in reaction calculations are typically derived from elastic scattering data at much higher energies, i. e. tens of MeV. Consequently, these potentials are not well constrained around the Coulomb barrier.

Koning and Delaroche developed a global phenomenological optical model potential for both neutrons and protons, covering an energy range from 1 keV up to 200 MeV and mass numbers $24 \leq A \leq 209$. The potential was constrained by a comprehensive experimental database, ensuring that there is no unphysical freedom of geometric parameters. The radius and diffuseness parameters of the volume, surface, and spin–orbit terms are identical for the real and imaginary parts and remain energy independent, thereby minimizing the number of free parameters [129].

While this framework provides reliable descriptions for for protons and neutrons, extending such models to composite projectiles like α particles remains challenging. In particular, at near- and sub-Coulomb energies, phenomenological approaches often fail to reproduce experimental cross sections accurately, leading to discrepancies between different models that can span several

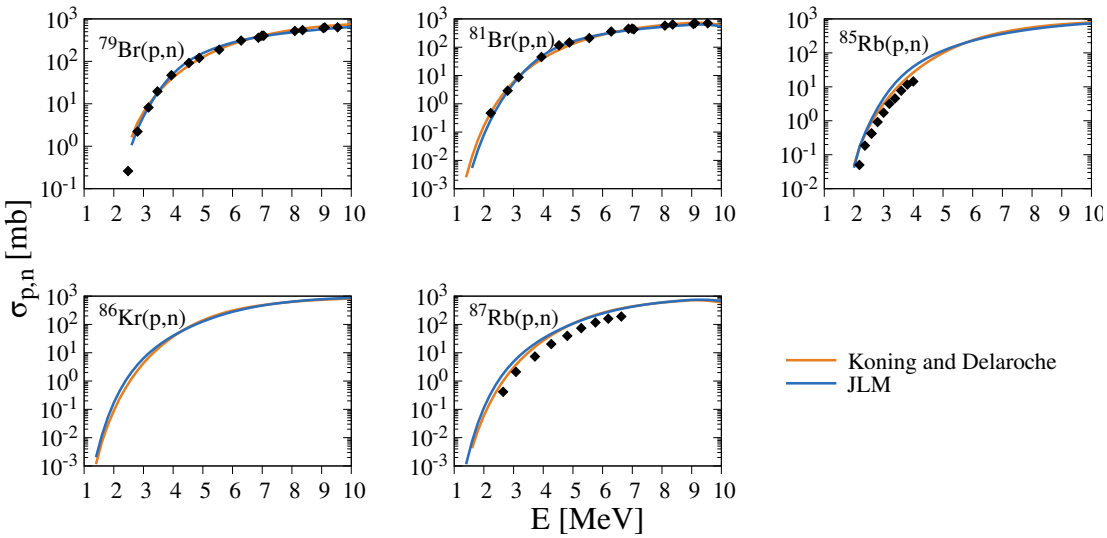

Figure 2.2: The comparison of theoretical calculations using the phenomenological optical model potential of Koning and Delaroche [129] and the semi-microscopical model JLM [135–137] to experimental data if available in the $A \approx 85$ mass region. The models give approximately the same predictions for all nuclei. The experimental data for the bromine isotopes are described well, whereas both models seem to over predict the data for the rubidium isotopes. If there was more than one experiment reporting on the data, the most recent set was used for the comparison. The experimental data is taken from [138–140]. The TALYS 2.0 code in its default settings was used to perform the calculations [124].

orders of magnitude [132–134].

Beside the phenomenological approaches, there are microscopic or microscopic-based approaches for the description of optical model potentials. Microscopic models in general provide a more physically grounded description, as they are built from nuclear structure properties, and are generally better suited for extrapolations into energy or mass regions where experimental data are scarce — a key advantage for astrophysical applications. Some microscopic approaches rely on folding a nucleon-nucleon effective interaction with the nuclear density function [135–137]. However, the energy-dependent potential depths need to be adjusted with experimental data, whereas the shape is well reproduced [137]. (Semi-)Microscopic potentials seem to predict the data quite well as demonstrated in Refs. [141–143]. A comparison of the theoretical calculations to experimental data is shown in Figure 2.2.

Another approach to describe α-induced reactions not depending on the high sensitivity on the imaginary part of the chosen α-optical model potential is the *pure barrier transmission model (PBTM)*, which has been elaborated on by P. Mohr *et al.* [144]. This model is defined by the assumption that an incoming α-particle is absorbed as soon as it tunnels through the barrier from the exterior to the interior. Since the probability of the α-particle tunneling out again is small, the assumption, that a compound nucleus is formed and only γ-rays or neutrons are emitted, is reasonable [144]. Therefore, the model does not depend on any uncertain, non-measurable part of an imaginary potential. This model was employed in recent studies [145–148] and showed good

agreement, especially for cross sections at astrophysically relevant (low) energies.

As this thesis deals with proton induced reactions, the problems arising with α-optical model potentials have only been mentioned for completeness. As shown in Figure 2.2 the phenomenological optical model potential of Koning and Delaroche [129] and the semi-microscopical model JLM [135–137] demonstrate no significant discrepancies among them for nuclei in the mass region $A \approx 85$, which is dealt with here.

2.2.2 Nuclear level density

The application of statistical-model formalism is only possible under the condition that the total level density is sufficiently high. As mentioned above, in the majority of nuclei, the precise spin and parity information are not known. Therefore, a key ingredient for statistical model calculations is the nuclear level density $\rho(E_X, J, \pi)$, which accounts for the not or incomplete known level information at high excitation energies and corresponds to the number of levels (typically) per MeV near a certain excitation energy E_X. The *total level density* can be obtained by summing $\rho(E_X, J, \pi)$ over spin and parity [52],

$$\rho^{\mathrm{tot}}(E_X) = \sum_{J,\pi} \rho(E_X, J, \pi). \tag{2.20}$$

Assuming uncorrelated functions, the nuclear level density can be separated into spin and parity dependent distributions [52]:

$$\rho(E_X, J, \pi) = \rho(E_X) \cdot g(E_x, J) \cdot f(E_X, \pi). \tag{2.21}$$

At high excitation energies, the number of states with positive and negative parity are approximately equal, thus the parity distribution is $f(E_X, \pi)$ [52]. This assumption is also implemented in some of the models introduced below. At low excitation energies, the level spacing, i. e. the inverse of the level density, is large enough to extract the nuclear level density by counting individual levels. This becomes unfeasible for high excitation energies as the nuclear level density becomes large whereas the spacing is small – too small to be resolved – and counting individual level becomes impossible. Therefore, it is important to have reliable models, notably for nuclei far away from stability, as they are important for statistical model calculations.

A variety of models for level density have been developed historically. These models include phenomenological analytical expressions and tabulated level densities derived from microscopic nuclear structure models. TALYS has several of these models implemented in its code [124], where some of them are more or less reliable and redundant to others [128]. Therefore, the models that are considered reliable and tested the most will be introduced in the following. For phenomenological level density models, the Constant Temperature Model (CTM) [149, 150] and the (Back-shifted) Fermi gas Model (BSFG) [149, 151, 152], while, to employ more microscopic approaches, the Hartree-Fock-Bogoliubov plus combinatorial method (HFB+comb) [153] as well as the Temperature-dependent HFB plus combinatorial (THFB+comb) [154] are introduced.

(Back-shifted) Fermi Gas model

In 1936 H. A. Bethe made a first attempt to describe nuclear level densities [152]. The nucleus is treated as a gas of non-interacting fermions, i. e. protons and neutrons – the Fermi gas. Although this approach is simplistic, it captures all the essential information except for the influence of pairing between nucleons. This is accounted for by the back-shifted Fermi gas model, where an additional shift in energy Δ is introduced, considering pairing and shell-model effects

$$\rho_{BSFG}(E_X) = \frac{1}{\sqrt{2\pi}\sigma}\frac{\pi}{12}\frac{\exp(2\sqrt{aU})}{a^{1/4}U^{5/4}}, \tag{2.22}$$

where $U = E_X - \Delta$ is the effective excitation energy, a the level density parameter, and σ the spin cut-off parameter [52, 124]. The spin-cut-off parameter is a measure of the width of the angular momentum distribution of the level density, dependent on the excitation energy. The level density parameter a is dependent on the excitation energy, too. This expression considers the presence of shell effects at low energy and their disappearance at high energy [124]. The parameter Δ differs for the Fermi gas

$$\Delta = \chi\frac{12}{\sqrt{A}} \tag{2.23}$$

and back-shifted Fermi gas model

$$\Delta = \chi\frac{12}{\sqrt{A}} + \delta, \tag{2.24}$$

by the free parameter δ adjusted by experimental data and the definition of χ, which depends on whether the nucleus is odd-odd, odd-even or even-even and takes integer values from 0 to 2 or -1 to 1 for the models respectively [124].

Constant Temperature Model

Another approach is the constant temperature model, where the total level density is given by

$$\rho_{CT}(E_X) = \frac{\mathrm{d}N(E_X)}{\mathrm{d}E_X} = \frac{1}{T}e^{\frac{E_X - E_0}{T}}, \tag{2.25}$$

where T and E_0 are free parameters that are connected to a constant nuclear temperature and an energy shift [52, 124, 155]. This procedure works well for fitting experimental data at low excitation energies [150].

The Gilbert-Cameron Model

A. Gilbert and A. G. W. Cameron combined both models, the CTM and the Fermi gas model into the so-called Gilbert-Cameron model. The CTM is used at low energies, whereas the Fermi gas model is applied to the high-energy part [150]. Both models have to be matched at an energy,

E_M, such that

$$\rho_{CT}(E_M) = \rho_{BSFG}(E_X). \tag{2.26}$$

Given that the matching is determined by experimental information, it is possible that the solution to the matching problem may yield values for the matching parameters that are unphysical [149].

The initial studies of the Gilbert-Cameron model and the BSFG did not take into account refinements such as energy-dependent shell effects and the explicit treatment of collective effects. All in all, experimental data is reasonably well-represented by both models, but they fail to describe fine structures in the level density. Furthermore, extrapolations to nuclei that are located far from the valley of stability, where there is a severe lack of experimental data, would be subject to a considerable degree of uncertainty [52, 149].

Microscopic level densities

The calculation of level densities should be performed using microscopic models that are based on first principles and fundamental interactions in order to have more reliable predictions, especially when extrapolating into regions, where the data is scarce. The models are calculated on the basis of the combinatorial approach. Both methods presented here start from a single-particle level scheme, calculated using the Hartree-Fock-Bogoliubov framework, and incorporate particle-hole excitations. The effective interactions, that are used in the calculations, are the Skyrme interaction [153] and the D1M parametrization of the Gogny force [154]. Afterwards, collective effects such as vibrational and rotational excitations are explicitly included. In contrast to the CTM and (BS)FG, there is no assumed parity equi-partition in these two microscopic level density models. Both models are in tabulated format for more than 8500 nuclei with excitation energies up to 200 MeV and spin values up to $J = 49$ [124]. It is important to note that these tabulated microscopic combinatorial level densities ρ_{HFM} have not been adjusted to experimental data, such as from low-lying levels and s-wave resonance spacings at the neutron separation energy S_n. The implementation of a scaling function

$$\rho(E_X, J, \pi) = e^{c\sqrt{E_x - \delta}} \rho_{HFM}(E_X - \delta, J, \pi) \tag{2.27}$$

is intended to enhance adjustment flexibility, where the default is $c = \delta = 0$ to obtain the unaltered nuclear level densities, but the parameters can be changed, where c is similar to the parameter a in the Fermi gas model. The parameter δ offsets the nuclear level density to a different energy [124].

The different above presented models are compared to experimentally known levels, presented in the upper part of Figure 2.3. It is demonstrated, that for most nuclei in the $A \approx 85$ mass region up to approximately 3 MeV to 4 MeV the experimentally determined cumulative number of levels agree with the level densitiy models. An exception is ^{88}Sr, for which up to 5 MeV to 6 MeV, the two numbers agree quite well. In general, the models give very similar results, except for the ^{79}Br$(p,\gamma)^{80}$Kr reaction and the ^{86}Kr$(p,\gamma)^{87}$Rb reaction. The THFB+comb level density model [154], which is no longer recommended to use (cf. Section 2.3 below), predicts clearly

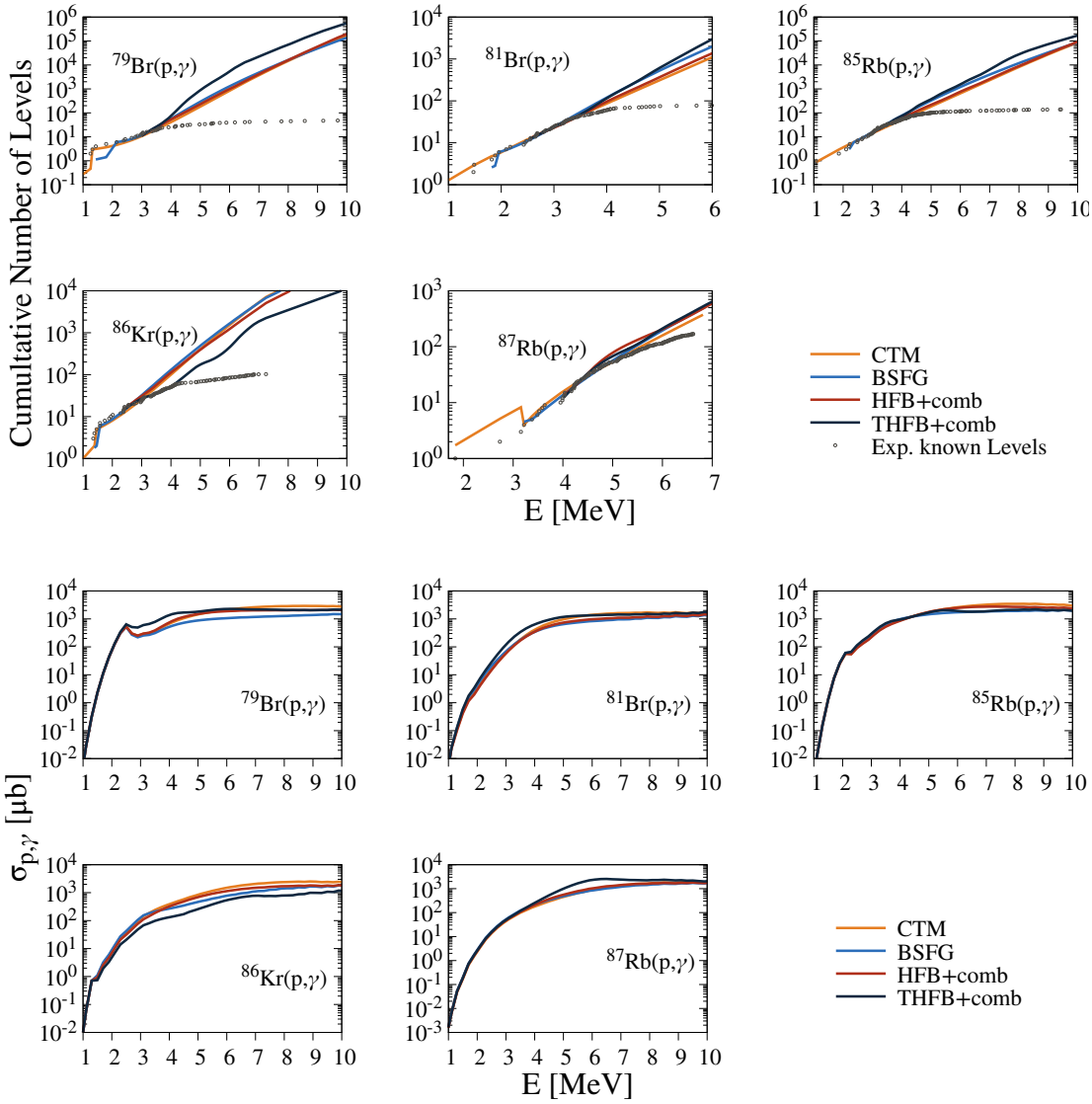

Figure 2.3: The comparison utilizing theoretical calculations using the different level density models CTM [150], BSFG [151], HFB+comb [153], and THFB+comb [154] in the $A \approx 85$ mass region is performed to experimentally known levels (upper figure) and their influence on the cross sections is shown (lower figure). The experimental data is taken from References [156–160]. The models give approximately the same predictions for all nuclei except for the $^{79}\mathrm{Br}(p,\gamma)^{80}\mathrm{Kr}$ reaction and the $^{86}\mathrm{Kr}(p,\gamma)^{87}\mathrm{Rb}$ reaction, which each differ significantly for the THFB+comh level density model [154]. Note, that this model is no longer recommended. The TALYS 2.14 code in its default settings was used to perform the calculations except for the level density models [124].

a higher level density for the first and a lower density of the second reaction. The CTM level density model [150] gives a strange result for ^{87}Rb$(p,\gamma)^{88}$Sr, since it predicts a falling number of cumulative levels around 3 MeV. Above that, the results seem to fit the data.

2.2.3 γ-ray strength function

The γ-ray strength function, also called photon strength function, $f_{Xl}(E_\gamma)$, is important to describe nuclear reactions, where γ-rays are involved [52, 124]. The absorption and emission probability for γ-rays is described by it. Therefore, it is used to obtain the transmission coefficients for γ-rays of type Xl entering the Hauser-Feshbach calculations. X denotes either electric (E) or magnetic (M) radiaton and l denotes the multipolarity. As already explained for the nuclear level density, for low energy, excited states are well separated and the individual decays can consequently be observed. Since this is not the case anymore for high energies, the γ-ray strength function is used to statistically describe the decays [124]. The transmission coefficients T_{Xl} are defined by

$$T_{Xl}(E_\gamma) = 2\pi E_\gamma^{2l+1} \overleftarrow{f_{Xl}}(E_\gamma), \tag{2.28}$$

which connects the probability of emitting a γ-ray to the downwards γ-ray strength function [122, 161]. It is defined as

$$\overleftarrow{f_{Xl}}(E_\gamma) = E_\gamma^{-(2l+1)} \frac{\langle \Gamma_{Xl}(E_\gamma) \rangle}{D_l}, \tag{2.29}$$

where T_{Xl} is expressed by the quotient of the average partial decay width $\langle \Gamma_{Xl}(E_\gamma) \rangle$ and the average level spacing D_l [161]. The upward γ-ray strength function $\overrightarrow{f_{Xl}}(E_\gamma)$ is connected to the average photo-absorption cross section via

$$\overrightarrow{f_{Xl}}(E_\gamma) = \frac{E_\gamma^{-(2l+1)}}{(\pi\hbar c)^2} \frac{\langle \sigma_{Xl}(E_\gamma) \rangle}{2l+1}, \tag{2.30}$$

where $\langle \sigma_{Xl}(E_\gamma) \rangle$ is the average photo-absorption cross section summed over all possible spins of final states [122]. In 1955, D. M. Brink proposed a hypothesis, later referred to as Brink's hypothesis, which states that the photo-absorption cross-section (or γ-ray strength function) for a nucleus in an excited state is identical to that for the nucleus in its ground state [162]. Since the targets in the laboratory are usually in their ground-state, a proof with measuring photo-absorptions cross sections on excited states is not possible. It should be noted that a more general form exists, which is referred to as the Brink-Axel hypothesis. The latter includes the independence of the initial and final spins of the transition [163, 164]. In addition, the aforementioned hypothesis includes the processes of absorption and emission of γ-rays between resonant states. The assumed validity of this hypothesis then implies

$$\overrightarrow{f_{Xl}}(E_\gamma) = \overleftarrow{f_{Xl}}(E_\gamma), \tag{2.31}$$

where the upward and downward γ-ray strength functions should be equal and only dependent on E_γ. Although the Brink hypothesis has been thoroughly established above the energy of

approximately 10 MeV, its validity remains a subject of ongoing debate, both, experimentally as well as theoretically, particularly in the context of energies below the neutron threshold [164–170].

The γ-strength function is important for describing all transitions involving γ-rays. However, they are especially significant in (n, γ) and (γ, n) reactions because neutrons are not affected by the nucleus's Coulomb force, and photon strength functions directly govern the reaction cross section. Therefore, it is one crucial ingredient when modeling stellar neutron-capture processes [171], as described in Section 1.2. As described in Section 1.3, reactions involving neutrons, especially photodisintegration of neutrons, play a significant role in the formation of p-nuclei and therefore, in the network calculations of the γ-process [79].

In the context of astrophysics, calculations of the γ-ray transmission coefficient demand the consideration of at least the most dominant $E1$ and $M1$ transitions [52, 79]. In the region of the giant dipole resonance (GDR), spanning 10 MeV to 20 MeV, therefore above the particle threshold, the photo-absorptions cross section – and hence, the γ-ray strength function – is dominated by $E1$ transitions [52, 124, 172]. An additional resonance commonly found in atomic nuclei, which is small compared to the GDR, is the $E1$ pygmy dipole resonance, located at lower energies around 6 MeV to 10 MeV [173]. Since many of the astrophysically relevant reactions happen at energies below particle separation energies, the low-energy region of the γ-ray strength function is of special interest as it influences the network calculations. As mentioned, there are debates over the validity of the Brink-Axel hypothesis in this energy region. An upend, i. e. an unexpected enhancement of the γ-ray function at low energies, was experimentally observed [172, 174–177]. Specifically, calculations based on the shell model anticipate an increase in the $M1$ de-excitation strength function as energies diminish, reaching a value of zero [178, 179]. For open shell nuclei, showing a deformation, shell model calculations in the Fe chain imply that a part of the $M1$ strength is shifted to the scissors mode [180, 181]. These findings suggest that the precise mechanism of the enhancement is not yet fully understood and that further research is required and ongoing in this area.

The oldest and phenomenological model, the so-called Brink-Axel option, employs a standard Lorentzian (SLO) form to describe the GDR shape

$$f_{Xl}(E_\gamma) = \frac{1}{(2l+1)(\pi\hbar c)^2} \frac{\sigma_{Xl} E_\gamma \Gamma_{Xl}^2}{(E_\gamma^2 - E_{Xl}^2)^2 + E_\gamma^2 \Gamma_{Xl}^2}, \tag{2.32}$$

where σ_{Xl} is the peak cross section, E_{Xl} the centroid energy of the giant resonance, and Γ_{Xl} the width of the peak, which is assumed to be constant in this approach [124, 162, 163]. The SLO demonstrates good agreement with experimental data around the resonance energy, but shows deviations in the low-energy part around the neutron threshold. To compensate for these deviations, J. Kopecky and M. Uhl proposed that the width Γ_{Xl} is temperature- and energy-dependent [182, 183]. This is called the generalized Lorentzian (GLO) and is used for $E1$ radiation. Although, the matching between experimental data and this model is improved [182], yet it has some disadvantages. The structures that occur in the low-energy tail of the strength function, such as the pygmy dipole resonance, cannot be reproduced [172]. In contrast, while a Lorentzian function can offer an adequate representation of the $E1$ strength, the position of its maximum

and the width must be predicted from a model for a particular nucleus or through experiments. Another improved model on the basis of a Lorentzian is the simplified modified Lorentzian model (SMLO), which considers a SLO-type function for both the low-energy scissors mode and the spin-flip components, which are tuned experimentally [124, 184]. Since predictions are particularly important for exotic nuclei, where the needed quantities are not accessible through experiments, microscopic models should be favored to make more reliable predictions of the γ-ray strength function [172]. The microscopic models, that have been developed, are based on the *Quasi-particle Random Phase Approximation* (QRPA). It is worth noting, that all QRPA calculations are adjusted to experimental observations [172]. The γ-ray strength function is provided by the models as a function of E_γ and, depending on the model, as a function of the temperature, or equivalently, the excitation energy of the final state. The location and width, as well as the average resonance capture data at low energies, can be reproduced by different models obtained with the Hartree-Fock-Bogoliubov method [185–187]. The relativistic mean-field framework has also been used, but only for stable nuclei with available experimental data [188]. All the models provide a $E1$, but only for tabulated values the $M1$ γ-ray strength functions are consistent with those of $E1$ [124, 186, 189]. Within the framework of this model, calculations of the photoabsorption strength are extended to the determination of the de-excitation strength function, that is expected to have an increased $M1$ contribution as the energy decreases to zero [186]. This model shows an overall good agreement with experimental data in the low energy regime but also above threshold [172].

As for the nuclear level density, TALYS has several models implemented in its code [124], some of them are more or less reliable and redundant to others [128]. The models that are considered are the SMLO [184], Gogny-HFB plus QRPA using D1M interaction (D1M+QRPA) [186], Skyrme-HFB plus QRPA using the BSk27 interaction [185], and the Relativistic mean-field + continuum RPA (RMF+cRPA) for the $E1$ supplemented by the $M1$ from D1M+QRPA [188]. A comparison of theoretical calculations using different strength models can be found in Figure 2.4.

A variety of experimental techniques – e. g. photonuclear reactions, nuclear resonance fluorescence (NRF), two-step cascade, neutron- and proton-capture and charged-particle reactions – have been developed and used to gather information on γ-ray strength functions [52, 172, 190]. The studies can be divided into measurements above and below the neutron separation energy as well as in measuring the upward or downward γ-ray strength function. The most common method used above and below the neutron separation energy are photo-nuclear reactions (for more details cf. [52, 172, 190] and References within). The NRF method is a good tool to study the upward γ-ray strength function below the neutron-separation energy [52, 172, 190]. Photo-absorption experiments on the other hand, are performed above the threshold and contain photoneutron or photoproton cross-section measurements, that are dominated by $E1$ radiation. Note, that these measurements are performed on the ground states [52]. Other methods make use of particle induced reactions as e. g. radiative neutron capture [172], proton-capture reactions [191–194], and deuteron induced reaction [195]. Some of these methods make use of the model-independent ratio

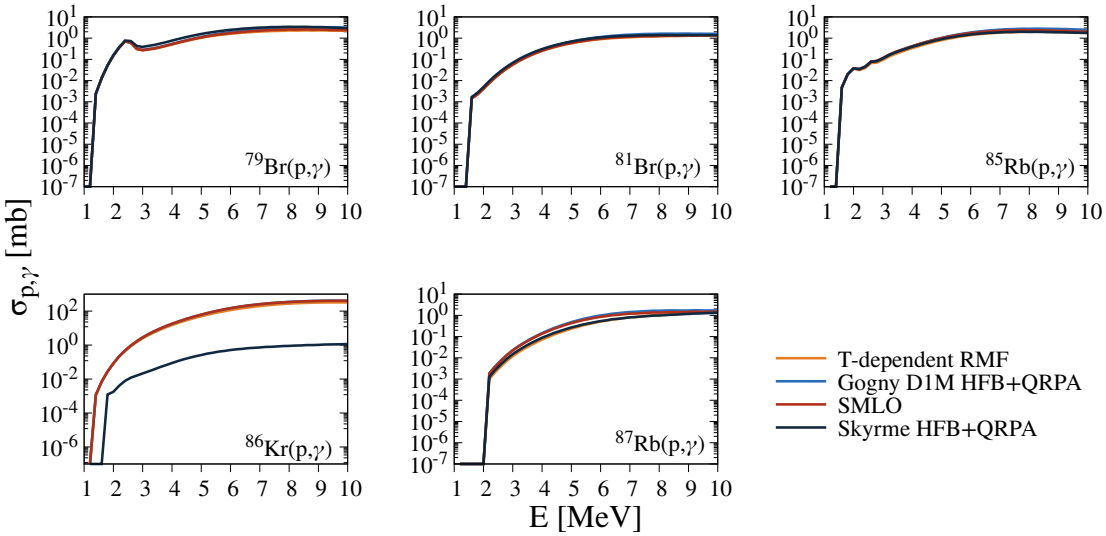

Figure 2.4: The comparison of the impact on cross section utilizing theoretical calculations using the different γ-ray strength function SMLO [184], Gogny-HFB plus QRPA using D1M interaction (D1M+QRPA) [186], Skyrme-HFB plus QRPA using the BSk27 interaction [185], and the Relativistic mean-field + continuum RPA (RMF+cRPA) for the $E1$ supplemented by the $M1$ from D1M+QRPA [188] in the $A \approx 85$ mass region. The models give approximately the same predictions for all nuclei except for the $^{86}\mathrm{Kr}(p,\gamma)^{87}\mathrm{Rb}$ reaction, which differs significantly for the Skyrme HFB+QRPA model [185]. There is no experimental data published outside of the scope of this thesis. The comparison for the two Rb isotopes to TALYS calculations will be presented in following chapters, wherefore it is left out here. The TALYS 2.0 code in its default settings was used to perform the calculations except for the γ-ray strength functions [124].

method

$$R = \frac{f(E_i - E_{L1})}{f(E_i - E_{L2})} = \frac{I(E_i - E_{L1})}{I(E_i - E_{L2})} \frac{(E_i - E_{L1})^3}{(E_i - E_{L2})^3}, \tag{2.33}$$

that can be derived from Equation (2.29), where E_i is the initial excitation energy, $E_i - E_{L1}$ and $E_i - E_{L2}$ represent two discrete low-lying levels of same spin and parity, and $I(E_i - E_{L1})$ and $I(E_i - E_{L2})$ represent the intensities for the two different primary γ-rays [172]. A schematic illustration of primary γ-rays de-exciting to discrete low-lying levels can be seen in Figure 2.5. This method has also been applied to photon-induced reactions via $(\vec{\gamma}, \gamma'\gamma'')$ [168]. The Oslo method (cf. [52] and References within) is an experimental technique, that allows, in addition to the downward γ-ray strength function, to also derive level densities in one experiment [172]. Particle-γ coincidence data is needed, which is processed in a complex iterative procedure to obtain the primary γ-ray spectrum. This spectrum is related to the level density and the γ-ray strength function by

$$P(E_\gamma, E_i) \propto \rho(E_i - E\gamma) T_\gamma(E_\gamma), \tag{2.34}$$

where $T_\gamma(E_i)$ is the total γ-ray transmission coefficient [196–198]. A normalization is needed to establish the correct slope and absolute values of the nuclear level density and the total dipole

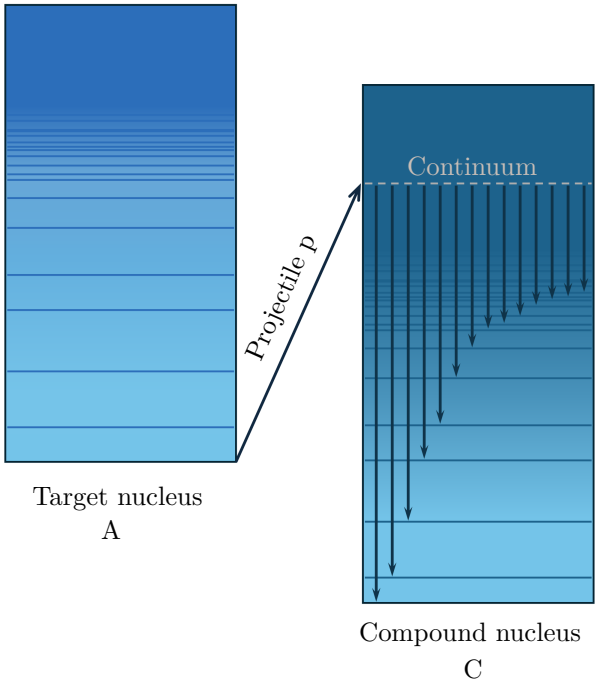

Figure 2.5: Schematic illustration of a compound nucleus decaying to different discrete levels via the emission of γ-rays after being produced by a projectile p impinging on a target A. The compound nucleus is formed at an excitation energy of $E_X = E_{p,c.m.} + Q$, where Q is the Q-value of the reaction. The excitation energy E_X is typically spread out with a width of ΔE, which corresponds to the energy loss inside the target material. The different discrete levels can then excite to the ground state of the compound nucleus C.

γ-ray strength function [52].

More information, details and methods can be found in the Review articles [52, 172].

2.3 The TALYS code

Statistical model codes do in most cases not rely solely on Hauser-Feshbach calculations, but often combine them with other model approaches, that have only become feasible in recent years due to advances in computational power. The code used in this thesis is the TALYS code, in its versions 2.0 and 2.14 [124]. It is actively developed by A. Koning, S. Hilaire, and S. Goriely [124, 189]. TALYS is a program for simulations of nuclear reactions up to 200 MeV, using, among others, the previously introduced optical model potentials, nuclear level densities and γ-ray strength functions. It is important to stress, that these are not the only input parameters, and there are models in which single input parameters can be adjusted individually. The default models

Table 2.1: The recommended models for the γ-ray strength function in TALYS [124, 128].

TALYS keyword	Model	Reference
strength 7	T-dependent RMF	[188]
strength 8	Gogny D1M HFB+QRPA	[186]
strength 9	SMLO	[184]
strength 10	Skyrme HFB+QRPA	[185]

Table 2.2: The recommended models for the nuclear level density in TALYS [124, 128].

TALYS keyword	Model	Reference
ldmodel 1	CTM	[149, 150]
ldmodel 2	BSFG	[149, 151]
ldmodel 5	HFB+comb	[153]
ldmodel 6	THFB+comb	[154]

are: Koning-Delaroche local potential, ldmodel 1, strength 9, and strength 8 if all models are microscopic. TALYS is well documented and updated as well as extended with new models on a regular basis. This thesis uses TALYS to calculate (p, γ) reaction cross sections. These calculations are based on a statistical model of compound nucleus reactions.

M. Wiedeking and S. Goriely [128] recently investigated the role of γ-ray strength functions and nuclear level densities for different reaction rates and their influence on the nucleosynthesis processes. In the article, there is a recommendation from the authors of TALYS on which models for the nuclear level density and the γ-ray strength function should be used. These recommendations can be found in Tables 2.1 and 2.2.

Note, that there is the TALYS 2.0 version [124] that is not updated and there is the TALYS git version [189], that is updated with the latest version TALYS 2.14[2]. This version has now two additional level density models as well as two additional γ-ray strength functions. The recommended models for the TALYS keyword *strength* are 8, 9, 10, 11, and 12. The latter two are with temperature dependence (D1M-Intra-E1 tables), strength 11, and based on the shell model (Shellmodel-E1 tables), strength 12. For the nuclear level density models 1, 2, 5, 7, and 8 are recommended. The latter two are the BSKG3 - Skyrme-Hartree-Fock-Bogolyubov triaxial combinatorial level densities from numerical tables, ldmodel 7, and QRPA level densities from numerical tables, ldmodel 8. Unfortunately, there are no sources given for these models in the documentation and no further information is given besides the names.

[2] As of October 2025, version 2.2 is the latest version.

3 Experimental Details and Setups - In-Beam Measurements at HORUS

As explained above, in order to simulate astrophysical scenarios and gain reliable predictions, a lot of accurate data spanning the whole chart of nuclei is needed – both from theoretical calculations and experiments [78, 96]. Various experimental techniques exist for different types of projectiles inducing nuclear reactions, as partly discussed in the previous chapter. This thesis focuses on proton-induced reactions, in particular on radiative proton capture. A range of dedicated experimental methods has been developed for this purpose.

A widely used experimental approach is the activation technique, e. g. [134, 145, 146, 199–201]. In this method, targets are irradiated with projectiles such as protons, neutrons, α-particles, or γ-rays, leading to the production of radioactive residual nuclei. The induced activity is then measured via the decay radiation of these nuclei, which provides the number of reactions and hence the reaction cross section. Therefore, a unstable reaction product is needed, which is the first constraint to consider. Second, the produced radionuclides must have suitable half-lives. Typically, it should not be too short since the activated target often needs to be transported to a counting set up after irradiation and it should not be longer than a reasonable counting time. A comprehensive review about the activation technique can be found in Reference [202].

If the reaction product is not suitable for the activation method, the 4π-summing technique [203, 204] and the so-called in-beam method with γ-ray detectors can be used to overcome this obstacle.

This chapter discusses the experimental setups for in-beam measurements within the scope of nuclear astrophysics that have been utilized in the experiments outlined in this thesis. These setups are employed at the high-efficiency γ-ray spectrometer HORUS, located at the 10 MV FN tandem accelerator, Institute for Nuclear Physics, University of Cologne. In addition, the dedicated experimental techniques will be reviewed.

3.1 Nuclear Astrophysics at HORUS

The High Efficiency Observatory for γ-ray Unique Spectroscopy – or short: HORUS – is located at the Institute for Nuclear Physics [205]. It consists of up to 14 high-purity Germanium (HPGe) detectors[1] which are positioned at two faces and the twelve vertices of an imaginary cube.

[1] It should be noted that the installation of, e. g. , lanthanum bromide detectors is also possible; however, this would not be a suitable option for the type of experiments conducted in this thesis.

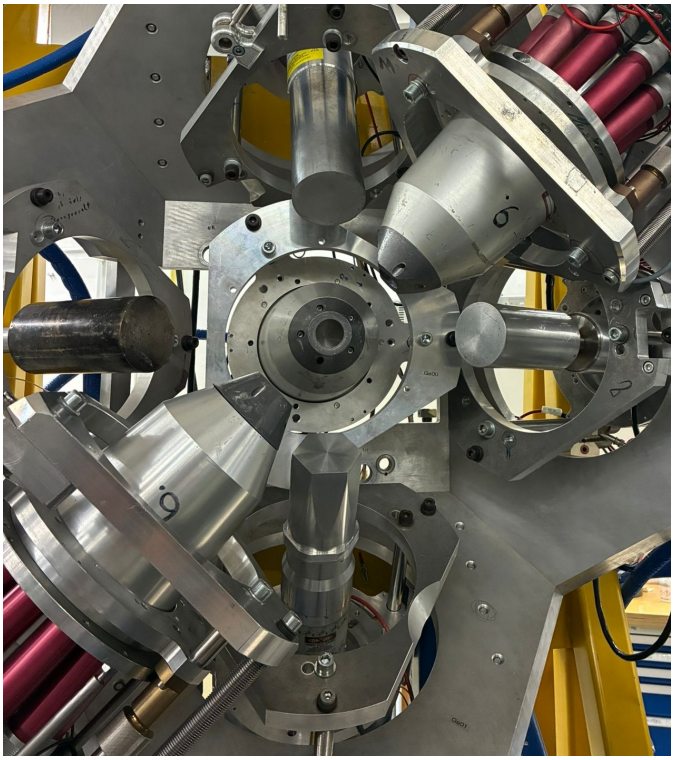

Figure 3.1: One hemisphere of HORUS without any target chamber built in. The beam comes in from the right hand side and the downstream cup is located at the left hand side of the Figure. Three BGOs and HPGe detectors are installed in this hemisphere at 45°, 90°, and 135° with respect to the beam axis. The HPGe detectors without BGOs are located at 35°, 90°, and 145°.

Six of the detectors can be equipped with bismuth germanium oxide (BGO) scintillator shields for active Compton suppression.

Angular distributions of γ-rays relative to the beam direction can be measured since the 14 HPGe detectors are mounted at five different angles with respect to the beam axis, namely 35°, 45°, 90°, 135°, and 145°. This is needed for determining the absolute reaction cross section, cf. Section 3.4 for details. The distance of the detectors to target position can be adjusted to the installed target chamber and is typically between 8 cm to 16 cm. A picture of one hemisphere with detectors and BGOs built in is shown in Figure 3.1.

The experiments presented in this thesis have been performed with two different chambers and data acquisition systems. The ^{85}Rb experiment was performed in 2015 with the signal processing of the HPGe detectors performed using the DGF-4C Rev. F modules, manufactured by the company XIA [206, 207]. The chamber that has been used for this experiment is presented in Section 3.2.1. In early 2020, a new data acquisition system, the NuDAQ system, was established with different types of modules built by CAEN S.p.A. with a corresponding software CoMPASS [208]. This, in combination with the newly designed target chamber presented in Section 3.2.2, was used in 2021 for the ^{87}Rb experiment. A detailed overview of the NuDAQ system as well as a comparison to the old data acquisition system can be found in Reference [209].

Regardless of the employed DAQ system, there exists a set of common features that are essential for the execution of nuclear astrophysics experiments. The detection of γ-rays with energies up to approximately 20 MeV is necessary. Since the data collecting takes place during the irradiation

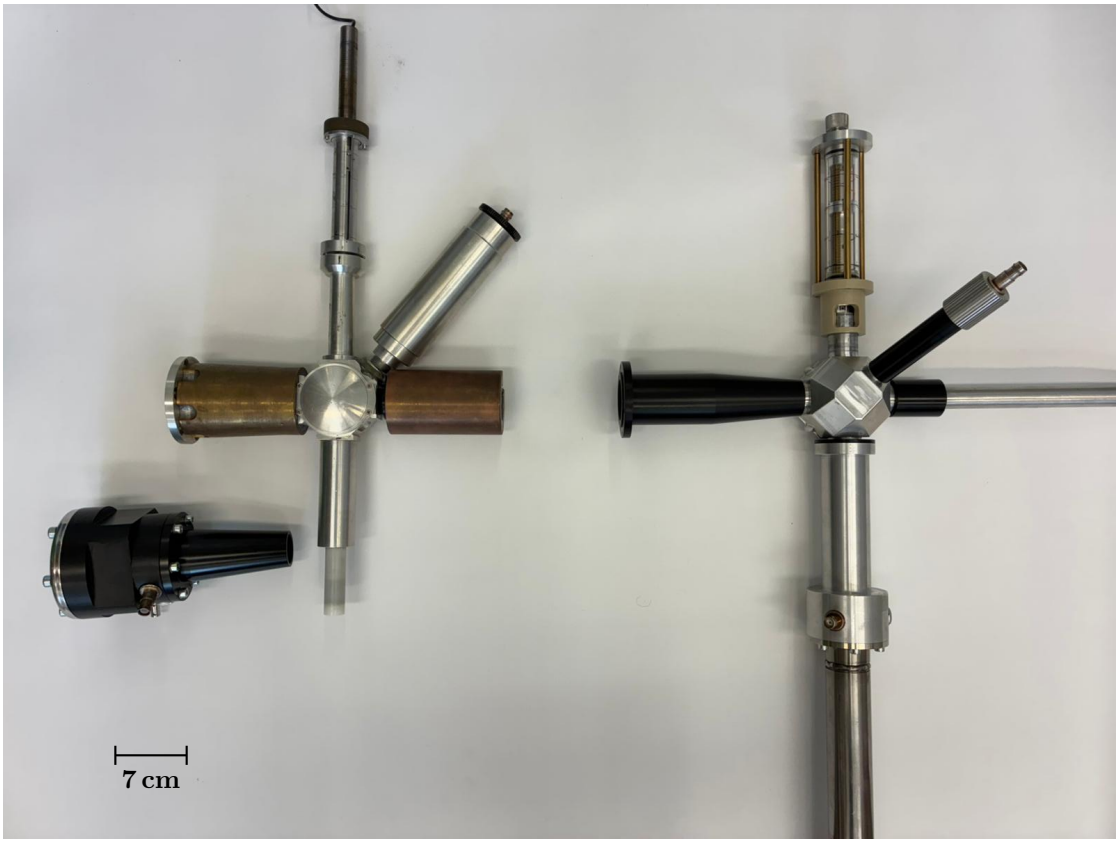

Figure 3.2: A comparison of the old and re-designed chamber for nuclear astrophysics experiments. They are on the left and right side of the photograph, respectively. The details of the similarities and differences are explained in-depth in the text. Note that the beam enters from the right side in this photograph and exits to the left if it is not stopped inside the chamber. At the left side, below the old target chamber, the short distance Faraday cup can be seen.

in contrast to the activation method, there is beam-induced background. Storing the data in a listmode format makes it possible to obtain $\gamma\gamma$-coincidence data in the offline analysis. This helps to suppress the beam-induced background when looking for the origin of peaks and determining limits of contributions of certain reactions to e. g. cross sections.

3.2 Target Chambers for Nuclear Astrophysics Experiments

Both target chambers, presented in this Section and shown in comparison in Figure 3.2, are optimized for nuclear astrophysics experiments and can be mounted in the HORUS spectrometer. Since the cross sections measured in in-beam experiments for nuclear astrophysics are often in the range of µb down to even nb, it is important to reduce the beam-produced background as much as possible. Therefore, the bodies of both chambers are made of aluminum coated with 0.1 mm

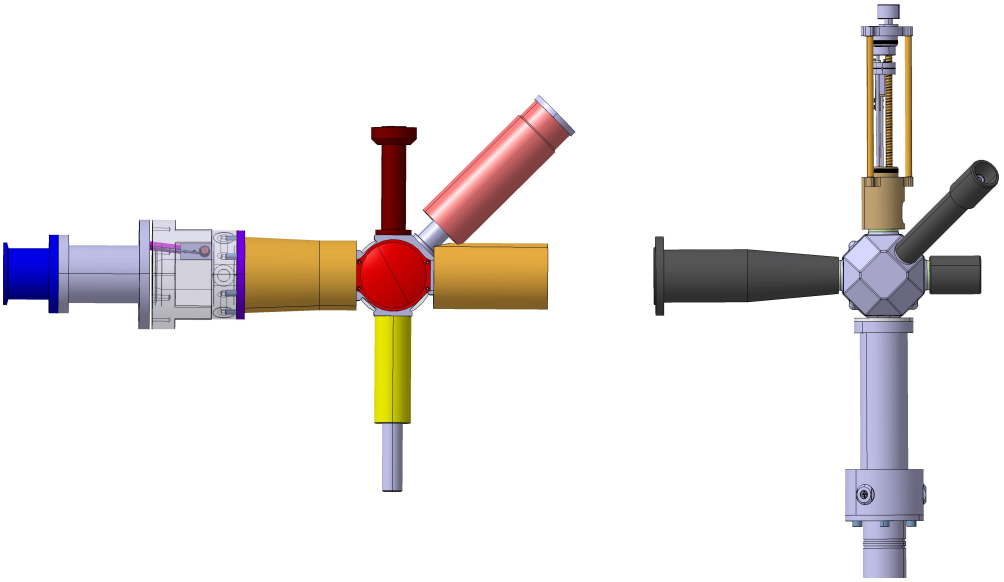

(a)

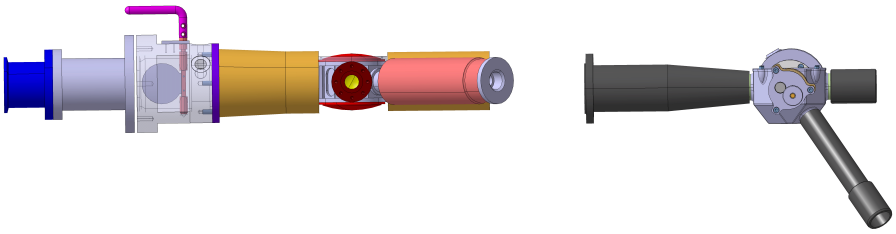

(b)

Figure 3.3: CAD drawing for comparison of the old (left) and re-designed (right) chamber for nuclear astrophysics experiments [210]. The beam direction is from right to left here. Figure 3.3a shows the same perspective as Figure 3.2 with the target ladder missing for the old chamber on the left side. Figure 3.3b shows a top view of the chambers. The re-location of the tube containing the RBS detector as well as the overall smaller volume of the tube containing the RBS detector is clearly visible. Note, that for Figure 3.3b the top view reveals part of the foot of the chamber.

tantalum on the inside. The tantalum coating reduces the competing reactions on the aluminum body, since the beam is stopped in the tantalum coating, which does not emmit γ-rays. Another important aspect is that the chambers were built as small as possible to bring the detectors closer to the target, thereby increasing the efficiency of the full-energy peak. The equation for calculating the cross section (see Equation (1.1)) not only contains the number of reactions N_R, but in addition the number of projectiles N_a, impinging on the target, and the number of target atoms per area. To get the information about the number of impinged projectiles it is necessary that the entire chamber is electrically isolated from the rest of the beam pipe and setup, which is ensured by coupling the chamber to all mounting points via plastic pieces. Both chambers are equipped with three current read outs: the target chamber (1), that is electrically isolated from the target ladder (2), and the cup (3) at the end of the beam line. During in-beam experiments, the beam is usually stopped inside the chamber at the target position with a thick gold backing behind the target. This prevents, that the beam spreads out after the target and interacts with the chamber or beam line after the passing, which would introduce more unwanted beam induced reactions and would additionally lead to a loss in the current measured in the Faraday cup. Due to the stopping of the beam, there is no current measured at the Faraday cup down the beam line. The impinging projectiles release electrons – so-called secondary or δ-electrons – during their passage through the target. These electrons are hindered to leave the chamber by a suppression voltage of $-400\,\mathrm{V}$, that is applied to a ring aperture at the entrance of the target chamber [211]. These electrons lead to the accumulated charge measured on the target ladder being higher than the actual charge deposited by the beam. Therefore, the accumulated charge measured on the chamber is negative. The details on the used current integrators are explained in Sections 3.2.1 and 3.2.2. The total number of beam particles impinging on the target can be calculated using

$$N_a = \sum_i \frac{Q_{target,i} + Q_{cup,i} + Q_{chamber,i}}{Ze}, \tag{3.1}$$

where $Q_{k,i}$ is the accumulated charge at the associated read-out point in the i-th time interval – usually 1 s, for which the current is assumed to be constant – of the measurement and the Z is the charge of the projectile.

Both contain a tube that houses a Rutherford Backscattering Spectrometry (RBS) detector to determine the number of target atoms per area either online during the experiment or in a follow-up experiment with adapted beam intensity and energy. The details for this are presented in Section 3.3.

3.2.1 Old Chamber

The ^{85}Rb measurement was performed utilizing this chamber. The old chamber, used in experiments until 2019, is visible on the left side of Figures 3.2 and 3.3. This chamber has a cylindrical geometry with a length of 7 cm and a width of 5.5 cm. The thickness of the aluminum body is 2 mm at the thinnest position. The target ladder can hold up to three targets and can be rotated by 180° without venting the chamber. There is a Faraday cup mounted at a distance of 15 cm

from the target, which can be relocated to use the Faraday cup downstream the beam line, about 2.5 m away from the target [212]. The RBS detector is placed in a tube 11 cm away from the target and the tube is under a horizontal backwards angle of 135° and an azimuthal angle of 270°. The tube has a diameter of 4.6 cm. However, the RBS detector can be equipped with narrow apertures to reduce the effective opening angle. Since the position of the RBS tube corresponds to the detector position of Ge06, this position cannot be filled with a HPGe detector, which limits the number of HPGe detectors to thirteen [211]. Lead and copper shields are installed around the beam entrance and exit pipes, resulting in the detectors being further away from the target due to the enhanced diameter. The connection for the suppression voltage is located directly at the beam entrance, where the negatively charged ring aperture is located. The read-outs for the currents on the target, the chamber and the cup are at the respective positions. Current integration is performed with two different types of current integrators are used – the ORTEC Digital Current Integrator 439 and the BIC 1000C Current Integrator with uncertainties of 0.2 % and 2 %, respectively. A pre-built scaler module from the company Meilhaus Electronic GmbH counts and records the pulses per second [211]. For more details see References [211, 212]

3.2.2 Re-designed Chamber

The measurement of the ^{87}Rb was performed in this re-designed chamber. It is presented on the right side of Figures 3.2 and 3.3. It has an asymmetric geometry, where one side is flat and the other has the shape of a polyhedron. This reduces the distance to the target, due to a relocation of the RBS detector as shown in Figures 3.3a and 3.3b. The diameter of the chamber is 7 cm and the width is 5.4 cm. The thickness of the aluminum body is thinner than that of the old chamber, with a constant thickness of 2 mm [213].[2] The target ladder can hold up to four targets and can be rotated by 360° in 5° steps without breaking the vacuum. There is no Faraday cup installed in the exit pipe anymore, only the downstream Faraday cup is used to monitor the beam current, unless a thick backing or stopper is used. The RBS detector tube, with a length of 9 cm and a diameter of 2 cm, is re-placed at a scattering angle of 114°, which allows to mount all possible fourteen HPGe detectors in the HORUS array [134, 215]. The connection between the chamber and the beam line to both sides is smaller in outside diameter, which enables the detectors to be moved closer to the chamber, and therefore the target. The detectors can be moved as close as 6 cm to 13 cm with this chamber installed [214]. The read-outs as well as the power supply for the suppression voltage have been moved to the stand of the chamber, which simplifies cable management. The current read-out system was remodeled considerably. Three *Ortec 439 Digital Current Integrators* are used to collect typically 10^{-10} C/pulse read out every 200 ms. The emitted digital signals of the current integrators are processed by a programmed dedicated *Arduino* micro-controller connected to a computer via USB. The processed data can be viewed online via a web interface, which allows to directly monitor the different currents and see trends in the behavior. The total uncertainty for the determination of the number of beam particles is

[2] Reference [214] claims, that the new chamber has a significantly thinner wall of 2 mm Al. However, Refs. [211, 212] state, that this is already the thickness of the old chamber. It was not mentioned, that is is the overall and thinnest position in the publication, respectively [210].

assumed to be 5 %. For more details see Reference [215]. All the aforementioned changes increase the detection efficiency from 0.13 % to 0.25 % at a γ-ray energy of 10 MeV [134, 214]. The overall detection efficiency for γ-rays is increased by a factor 2 compared to the old chamber, presented in Section 3.2.1, which was investigated in Reference [214]. Note, this comparison was performed with XIA's DGF-4C Rev. F modules shortly presented above.

3.3 Determination of Target Thickness

In order to determine the thickness of the target, a silicon particle detector installed in each chamber is employed, making use of Rutherford Backscattering Spectrometry [216]. This non-destructive method is utilized to measure thickness before and after, or even during, an experiment, thus facilitating comparative analysis and continuous monitoring of the thickness. The target thickness is determined by the energy loss in the material of the scattered projectiles, typically protons or α-particles.

The projectiles impinge on the target with a certain energy E_0, in the range of a few MeV. A small fraction are scattered back and hit the silicon detector, that is placed in the RBS tube as described above. This recorded spectrum is then compared to simulations, performed with e. g. the SIMNRA code [217], to extract the thickness. The lowest detected ion energy corresponds to highest energy loss in the target, i. e. the particle was scattered (nearly) at the back layer, travels trough the target again, and is then detected. This creates the edge on the left side in Figure 3.4b. The right side correlates to the scattering at the surface layer of the target. The distance of the flanks is proportional to the thickness of the target material.

To interpret the measured spectrum quantitatively, the kinematic relations governing elastic scattering must be considered. The energy of a backscattered ion depends on the scattering angle and the mass ratio of projectile and target nuclei. This is expressed by the *kinematic factor* K. It is the ratio of the energy of the projectile before (E_0) and after the collision (E_f). It can be derived, see e. g. Reference [216], that the kinematic factor for the target results in

$$K = \left(\frac{\cos(\theta) + \sqrt{\mu^2 - \sin(\theta)}}{1 + \mu} \right)^2 , \tag{3.2}$$

where $\mu = m_T/m_p$ denotes the ratio of the target nuclei mass m_T to the projectile mass m_p. There are aspects that influence the detected energy E_f. These are the kinematic factor, the energy loss in the target $\frac{\mathrm{d}E}{\mathrm{d}x}$ and the distance covered in the target, which results in

$$E_f = K \left(E_0 - \int_0^{x_1} \left(\frac{\mathrm{d}E}{\mathrm{d}x} \right) \mathrm{d}x \right) - \int_0^{x_2} \left(\frac{\mathrm{d}E}{\mathrm{d}x} \right) \mathrm{d}x, \tag{3.3}$$

where the minuend equals the energy after the scattering, the subtrahend accounts for the energy loss of the projectile leaving the target, and the distances to the surface x_1 and x_2 depend on the experimental setup [216].

Equation (3.3) has been demonstrated to be a successful solution to problems involving a

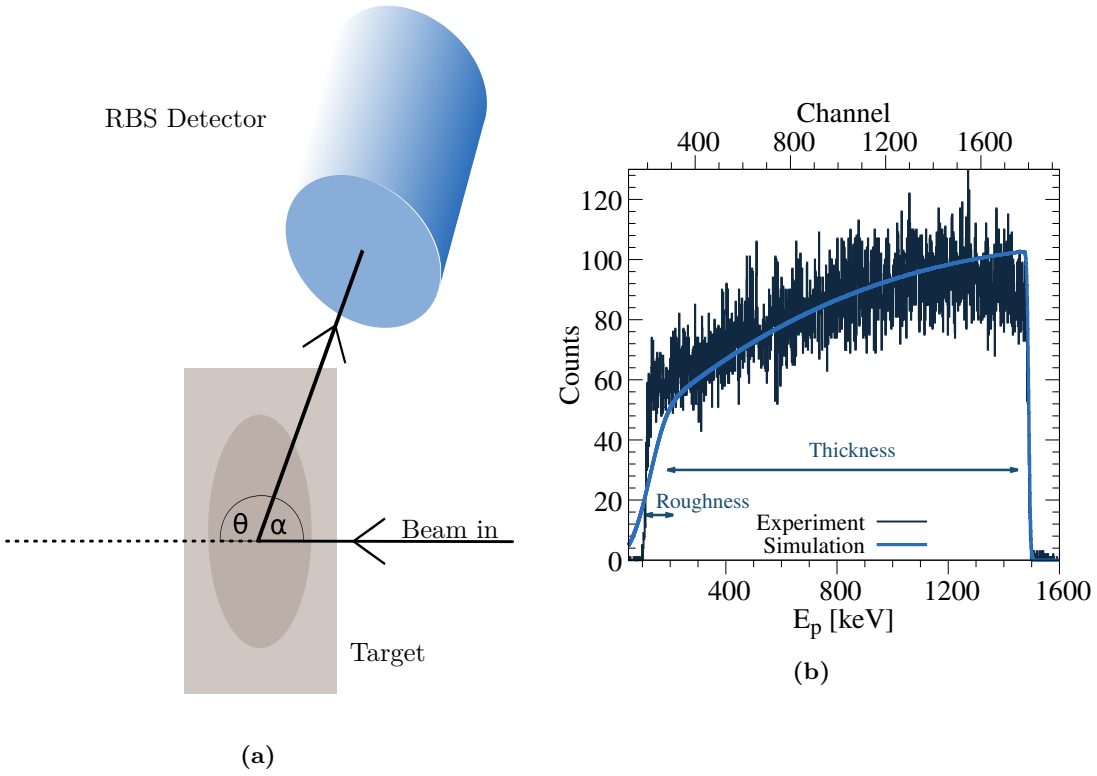

(a) (b)

Figure 3.4: Schematic illustration of the RBS detector setup and an exemplary spectrum from an RBS measurement on ^{27}Al are shown in Figures 3.4a and 3.4b, respectively. Figure 3.4a schematically illustrates the principle of Rutherford Backscattering Spectrometry (RBS). A fraction of the incident ions is backscattered toward the detector under an exit angle α, which can be derived from the fixed scattering angle θ at which the detector is mounted. This relation holds under the assumption of an incident beam at 0°. An example of an experimental RBS spectrum measured on ^{27}Al is presented in Figure 3.4b, together with a corresponding simulation performed using SIMNRA [217]. The target thickness is directly proportional to the width of the plateau in the spectrum, while the surface roughness can be inferred from the slope of the left-hand side of the peak. A smooth layer yields a sharp, steep decline, whereas surface roughness causes a broader, less steep slope, as illustrated by the simulated spectrum. The sharp edge on the right-hand side corresponds to ions backscattered from the very first layer of the target.

target composed of a single material. However, in many cases, targets are composed of multiple materials, particularly when the material is not suitable for the fabrication of foils and evaporation a stable backing, such as gold or tantalum, is necessary. Fortunately, composite layers can be handled by the SIMNRA code [217].

3.4 Determination of Reaction Yields

The detection of ground-state transitions in the reaction product is the key to determine the reaction yield for the in-beam method. This is utilized with the γ-ray spectra obtained with the HPGe detectors. To determine the total reaction yield, each γ-ray transition populating the ground-state from different levels has to be observed. This is illustrated in Figure 3.5. Summing the number of these transitions, leads to the total reaction yield. The formation and decay of a compound nucleus are independent processes. In general, the angular momentum of the compound nucleus has a preferred orientation with respect to the beam axis, such that there is an anisotropic symmetry of the system. As a result, the emitted γ-rays exhibit an angular distribution that is symmetric around 90° [24, 125].

To determine the yield $W(\theta)$ of a specific γ-ray transition, the total number of detected γ-rays of energy E_γ in the particular peak $N(E_\gamma)$ of every detector group θ has to be normalized to the efficiency $\epsilon(E_\gamma)$ and the dead time correction τ of the data acquisition for the detector group. This results in

$$W(\theta) = \frac{N(E_\gamma)}{\tau\epsilon(E_\gamma)}. \tag{3.4}$$

In order to obtain the total number of γ-rays stemming from a certain transition of a certain level i, the efficiency and dead time corrected data $W(\theta)$ are fitted with Legendre polynomials $P_k(\cos(\theta))$

$$W^i(\theta) = \sum_{k=0,2,4} a_k^i P_k(\cos(\theta)) = A_0^i \left(1 + \sum_{k=2,4} \alpha_k^i P_k(\cos(\theta))\right) \tag{3.5}$$

to obtain the angular distribution. This sum contains contributions of isotropic, dipole, and quadrupole distributions, which is sufficient for the applications here. It is assumed that transitions of dipole and quadrupole nature dominate in atomic nuclei. It has been established that, particularly in the case of the first excited state, a multitude of different γ-ray cascades populate this level. Consequently, the anisotropy that is characteristic of the de-population process to the ground state is effectively reduced, thereby resulting in an angular distribution that is nearly isotropic in nature. Examples for this are shown later during the analysis of the data, e. g. in Figure 4.10.

The total (p, γ) cross section is then given by

$$\sigma = \frac{\sum_i A_0^i}{N_p n_T}, \tag{3.6}$$

where N_p is the number of projectiles and n_T is the number of target atoms per area. This

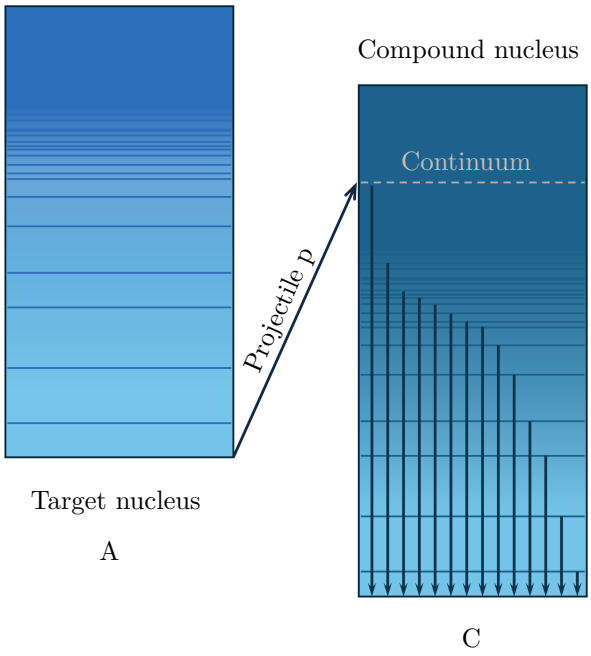

Figure 3.5: Schematic illustration of a compound nucleus decaying via γ-ray transitions to the ground state. The highly excited compound nucleus has an excitation energy of E_X after the capture reaction. It de-excites to the ground state via a direct de-excitation or via different γ-ray cascades. The de-excitation of discrete low-lying levels is observed. Note, that not always all transitions can observed in the γ-ray spectra due to low intensities or background contaminations in the spectra. If the first reason is the case, competing transitions with known intensities to other discrete lying levels can often be used to estimate the cross section.

cross section depends on the number i of observed ground state transitions. Consequently, the cross section can be interpreted as a lower limit. An upper limit for the cross section can be evaluated by estimating an upper limit of known, but not observed ground state transitions in the γ-ray spectra. $\gamma\gamma$-coincidence data can help to observe transitions, that are hidden by the (beam induced) background. With this, an estimation for an upper limit of $N(E_\gamma)$ contributing to the hidden transition can be given. In many cases, the estimations of hidden γ-ray transitions do not exceed the other uncertainties.

4 The case of ^{85}Rb

The charge-particle capture reaction ^{85}Rb$(p,\gamma)^{86}$Sr has been investigated utilizing the in-beam technique with help of the HORUS spectrometer as presented in Chapter 3. The experimental campaign was carried out in October 2015 utilizing the old chamber and the XIA data acquisition introduced in the same Chapter. Following a detailed description of the experimental method and data analysis procedure, the results of the total cross-section are discussed for the ^{85}Rb$(p,\gamma)^{86}$Sr reaction. These results are then compared to Hauser-Feshbach calculations, and the astrophysical impact is discussed.

There are three reasons why the ^{85}Rb$(p,\gamma)^{86}$Sr reaction is measured. First, there is no reported data on this reaction up to today. Second, from an astrophysical point of view, this reaction is located in a mass region $A \approx 85$, where the abundances of the p-nuclei are not well reproduced by reaction-network calculations. Third, it completes the study of proton-capture reactions on stable rubidium isotopes together with the reaction presented in Chapter 5.

Reaction cross-section values were measured at three center-of-mass energies ranging from 3.4 MeV to 4 MeV. The Q-value of this reaction is 9644.8 keV [218].

As mentioned, the main experiment was conducted in October 2015. It was documented in the Refs. [219, 220]. The main spokesperson for the ^{85}Rb-experiment, the RBS measurement and the ^{27}Al-experiment was L. Netterdon. In addition, he sorted the raw data, constructed spectra and $\gamma\gamma$-coincident matrices, performed a analysis of the data, and carried out the GEANT 4 Monte-Carlo simulations.These results had been summarized in an internal report but never have been published. Within the scope of this thesis a complete data analysis and re-evaluation of the measurements have been performed. The cross sections differ due to different derived target thicknesses and different fitting of the peaks.

4.1 Target Properties and Deterioration

The targets were prepared in the same way as the rubidium carbonate target Rb_2CO_3 presented in Chapter 5. Rb has a melting point of 39.3 °C. The targets for the investigation of the ^{85}Rb$(p,\gamma)^{86}$Sr reaction consists of rubidium chloride (RbCl) with a melting point of 718 °C. This is prepared as targets by vacuum evaporation onto a 150 mg/cm^2 thick gold backing to stop the beam inside the backing as explained in Chapter 3. The targets are shown in Figure 4.1. The RbCl target material was isotopically enriched in ^{85}Rb to 99.78(2) % [219]. RbCl is even more hygroscopic than $RbCO_3$ (cf. Chapter 5) hence storing in vacuum is preferred. The vapor

Figure 4.1: Three RbCl targets on the target ladder for RBS measurements at the RUBION facility in Bochum [222], in Octorber 2013. The targets are consecutively numbered from one to three. There is a fingerprint clearly visible on target 1, wherefore targets 2 and 3 were used in experimental campaigns.

pressure of RbCl at 390 °C is about 1.3×10^{-6} mbar and it has a rather low heat conductivity [221].

A first test experiment for the ^{85}Rb$(p,\gamma)^{86}$Sr reaction, using a target, named "target 2", has been carried out in November 2013. Before, a RBS measurements were performed at the RUBION facility in Bochum [222], in October 2013, in order to determine the target thickness of all three produced targets shown in Figure 4.1. According to notes in Ref. [219], target 2 is a homogeneous and clean target without gold admixture visible in front, which is supported by the RBS spectrum. The given thickness after the production is 0.43 mg/cm^2, which correspond to an areal density of $n_{T_2,giv} = 2.14 \cdot 10^{18}$ atoms/cm^2 [219]. The RBS measurement resulted in an areal density of $n_{T_2,meas,before} = 1.95(15) \cdot 10^{18}$ atoms/cm^2 for ^{85}Rb. This and the following target thicknesses are obtained by fitting the results of the measurement with simulations performed with SIMNRA [217]. This target was measured in an in-beam experiment with a proton beam energy of 4 MeV, with a current of 100 nA for 23 h [220, 223].

Another RBS measurement was performed at the RUBION facility in Bochum [222], in January 2014, after the experiment took place. In contrast to the first measurement, an additional layer is seen on the right hand side, corresponding to first layer scattering, in Figure 4.2. The assumption is, that there is gold diffused to the RbCl layer. The spectra is more diffuse as shown in Figure 4.2. The number of ^{85}Rb atoms stayed the same, such that the areal density is $n_{T_2,meas,after} = 1.97(16) \cdot 10^{18}$ atoms/cm^2.

This underlines how important it is to measure the thickness before and after the experiment. It seems that an admixture of gold stemming from the backing can occur during experiments. This needs to be investigated in following experiments and may need to be taken into account for the target production.

Unfortunately, target 3, used to conduct the experiment itself, was measured only before the experiment at two points in the RBS campaign in October 2013. It showed already an admixture of gold in the front layer. The given thickness after the production is 0.27 mg/cm^2, which correspond

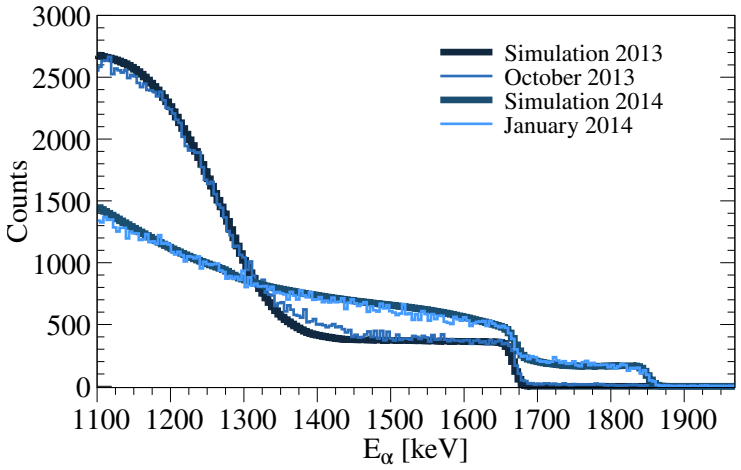

Figure 4.2: Comparison of the RBS measurements in Bochum before and after the experiment for T_2. There is a change in the target behavior. An additional layer is seen on the right hand side, most likely due to an admixture of gold, which occurred during the irradiation. The beam for the measurements was an α-beam with an energy of 2 MeV each.

to an areal density of $n_{T_3,giv} = 1.34 \cdot 10^{18}$ atoms/cm^2 [219]. The RBS measurements at the RUBION facility in Bochum gave a consistent results of $n_{T_3,meas} = 1.35(14) \cdot 10^{18}$ atoms/cm^2 as presented in Figure 4.4.[1] The slight disagreement of the RBS measurement and the simulation are likely based on inhomogeneities, that could not be modeled. During the experimental campaign using target 3 in October 2015[2], the stability of the target was monitored after observing the deterioration by determining the ratio of the γ-ray transition 767.4 keV in ^{85}Sr [224] to the 279 keV γ-ray transition stemming from Coulomb excitation in ^{197}Au [225] in intervals of 10 min. This showed a huge deterioration of the target during the irradiation, despite a limitation of the beam current to 400 nA. This current limit was set too high and heated the target up too much, which led to sublimation due to the low vapor pressure and poor heat conductivity of RbCl. The value of 390 °C at a pressure of 1.3×10^{-6} mbar suggests that, under the typical vacuum conditions of about 1×10^{-6} mbar inside the chamber, the RbCl layer was reduced in thickness by sublimation, as this temperature is approximately reached [221].

Fortunately, the RBS measurement was conducted prior to this, thereby providing a starting value for the thickness. The ratios from ^{85}Sr to ^{197}Au for each beam energy are presented in Figure 4.5. The deterioration was observed after Run 02 at $E_p = 3700$ keV. After this, the ratios change due to re-focusing of the beam or adjusting the target position such that the ratio increases again [220]. This explains the drastic changes between (sub)runs for the calculated ratios. Note, that sometimes runs were not usable for the data analysis or there were problems during the data taking as noted in Ref. [220].

The number of target nuclei was calculated with help of the ratio from ^{85}Sr to ^{197}Au for each time interval corresponding to one subrun and then multiplied by the number of protons that impinged on the target during that time interval. This helps to normalize the reaction yield, accounting for the loss of target material, discussed in Section 4.4.

[1] Note, that a note in Ref. [219] states, that the thickness determined by the RBS measurement is allegedly $n_{T_3,meas} = 1.8 \cdot 10^{18}$ atoms/cm^2, which could not be confirmed in the simulation.
[2] There is an annotation, stating that an RBS measurement took place directly before the campaign in order to rule out target deterioration without beam interaction. This data was not found.

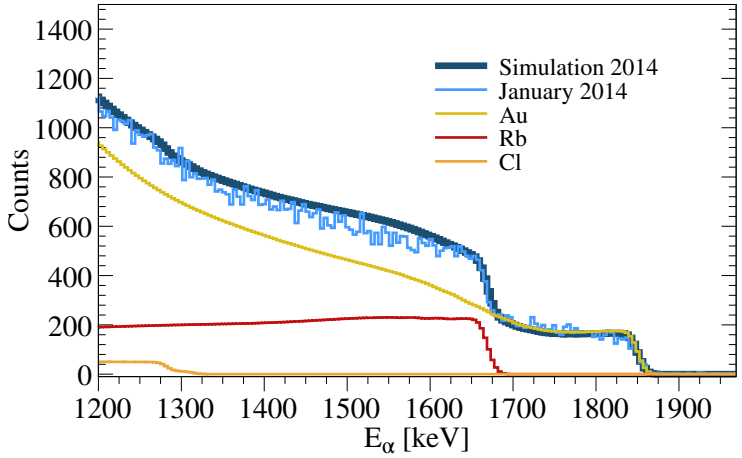

Figure 4.3: Comparison of the RBS measurements in Bochum after the experiment for T_2 to the simulation, showing the single components of the target. There is a change in the target behavior. An additional layer is seen on the right hand side, due to an admixture of gold, which occurred during the irradiation. The beam for the measurements was an α-beam with an energy of 2 MeV each.

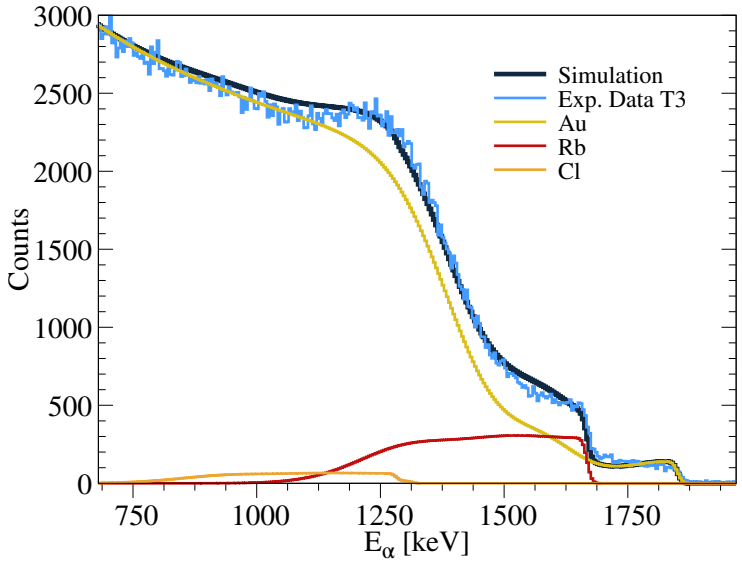

Figure 4.4: Comparison of the RBS measurement in Bochum to a SIMNRA simulation [217] for T_3. An additional layer is seen on the right hand side, due to an admixture of gold, which occurred most likely during the production. The beam for the measurements was an α-beam with an energy of 2 MeV.

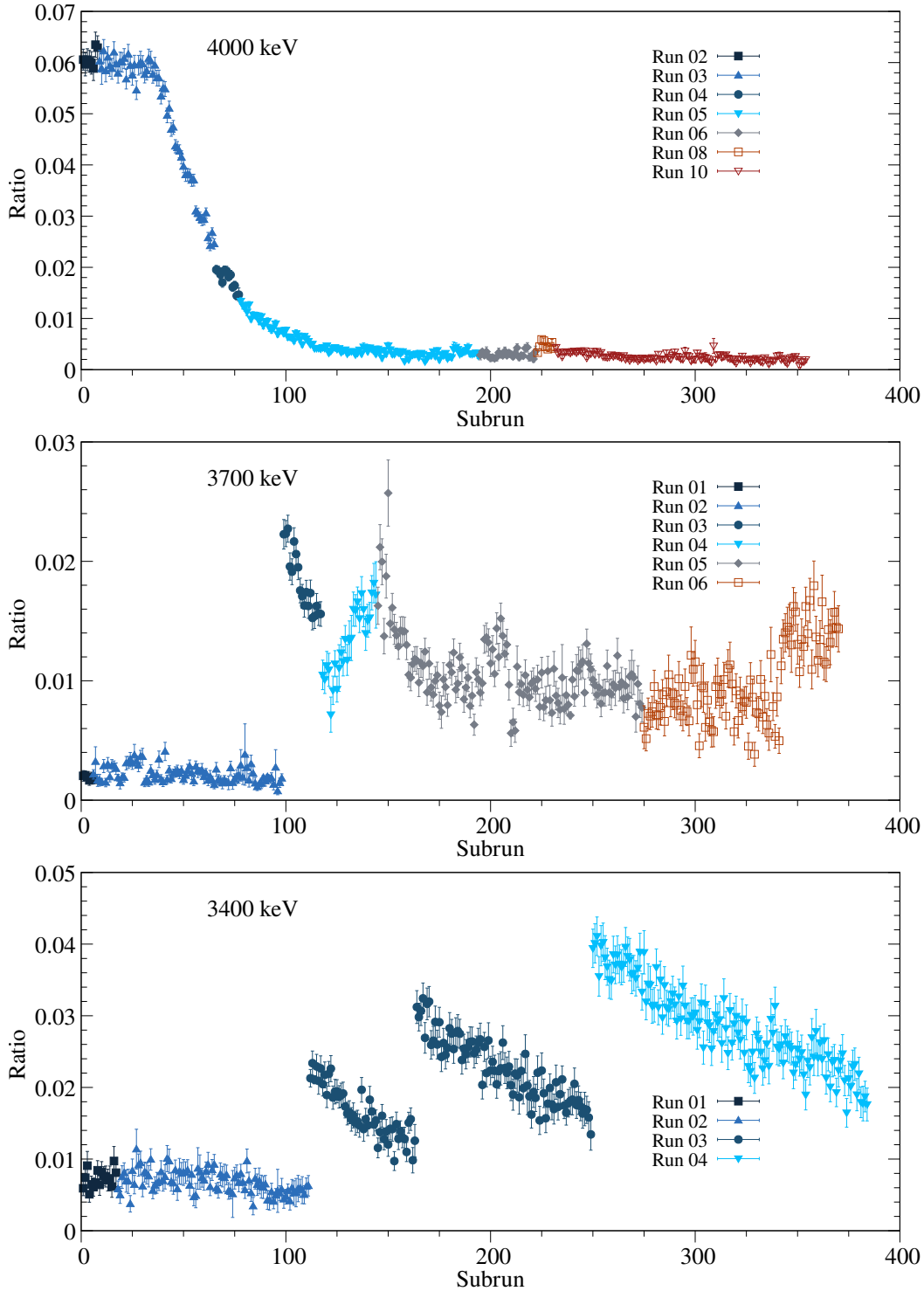

Figure 4.5: The ratios from ^{85}Sr to ^{197}Au for each beam energy monitoring the target deterioration due to sublimation of the material. The ratio stays the same after some time since no more material will sublimate due to a better contact to the gold backing which conducts heat very well, such that the temperature does not get too high [221]. Each subrun is 10 min long. The deterioration was observed after Run 02 at $E_p = 3700$ keV. After this, the ratios changes due to re-focusing of the beam or adjusting the target position such that the ratio increases again [220].

4.2 Experimental setup and procedure

The proton beam was delivered by the 10 MV FN tandem accelerator at the Institute for Nuclear Physics, Cologne. To utilize the in-beam technique, the HORUS spectrometer, the old chamber for nuclear astrophysics experiments, and the XIA data aqcuisition were employed, more details are given in Chapter 3. HORUS was equipped with 13 HPGe detectors. The experiment was conducted using six detectors at 90°, two detectors per angle at 35°, 45°, and 145°, and one detector at 135°. This is done to measure the γ-ray angular distribution of the compound nucleus decay. The beam was stopped in the thick Au backing, wherefore no charge was measured at the Faraday cup further downstream. The uncertainty of the charge collection is 3 %. Note, that not all runs presented in Figure 4.5 during the measurement of a proton beam energy of 4000 keV are used for the data evaluation due to different problems, e. g. cut off data, empty listmode files, and problems with the current read out [220]. The data in Table 4.1, showing the beam properties, takes this into account for the measuring time t and the average current I.

The center-of-mass energies $E_{c.m}$ given in Table 4.1 are the effective beam energies in the center-of-mass frame, obtained from

$$E_{eff} = E_p - \frac{\delta E}{2}, \tag{4.1}$$

where E_p is the proton beam energy, δE is the maximal energy loss in the target material, ranging from 19 keV to 21 keV varying due to the different proton energies. The loss of the target material changes the energy loss over time. However, this is quite extensive to simulate, so that the maximum value for the energy loss was used. The simulation of the energy loss inside the target is performed using the SRIM code [226]. The total energy uncertainty ΔE is then given by the Gaussian sum of the proton beam spread and the straggling inside the target.

4.3 Determination of the Full-Energy Peak Efficiency

To determine the full-energy peak efficiency, usually calibrated radioactive sources as ^{56}Co up to 3.5 MeV. Since the expected energy for the γ-ray directly de-exciting the compound nucleus (γ_0) is $E_{\gamma_0} = E_{p,c.m.} + Q$, a precise efficiency of γ-ray energies of approximately up to 15 MeV is

Table 4.1: The detailed beam characteristics for the different proton beam energies, given as the center-of-mass-energy $E_{c.m}$, the energy uncertainty ΔE, the average current $\bar{I}$, and the irradiation duration t. More details are given in the text.

$E_{c.m}$ [keV]	ΔE [keV]	$\bar{I}$ [nA]	t [h]
3349	16	102	64
3646	16	140	61.7
3944	16	224	41.5

Table 4.2: Absolute γ-ray branching ratios of the $^{27}\mathrm{Al}(p,\gamma)$ resonance at a proton energy of $E_p = 3674.4\,\mathrm{keV}$. The listed γ-ray transitions are used to perform the efficiency calibration. The data are from Ref. [227].

E_γ [keV]	E_X [MeV]	branching ratio [%]
10509	4618	85(3)
8239	6888	8.1(2)
6182	8945	1.8(1)
4458	10669	1.55(40)

needed. Therefore, the $^{27}\mathrm{Al}(p,\gamma)^{28}\mathrm{Si}$ reaction is used to generate high energy γ-ray lines with known relative intensities.

The ^{27}Al target is produced as a self-supporting foil by rolling natural aluminum to a thickness of $708(28)\,\mu\mathrm{g/cm^2}$. This corresponds to an areal density of $1.58(6)\cdot 10^{19}$ atoms/cm^2, which was measured at the RUBION facility in Bochum, Germany [222]. The target was installed in the old target chamber in HORUS, presented in Chapter 3. The experiment was carried out at a proton beam of $E_p = 3.69\,\mathrm{MeV}$. This was determined by scanning the resonance with $E_p = 3674.4\,\mathrm{keV}$ as explained in Refs. [212, 214].

The full-energy peak efficiency is firstly determined using the standard calibration sources ^{226}Ra and ^{56}Co with γ-ray energies up to 3.5 MeV [72]. Subsequent, the relative full-energy peak efficiencies are determined through the decay of the $^{27}\mathrm{Al}(p,\gamma)$ resonance up to approximately 10.5 MeV [227]. This relative efficiency is then scaled to the absolute efficiency from the calibration sources and to the γ-rays with energies shown in Table 4.2. The extension to approximately 15 MeV is obtained by measuring the angular distributions of the de-excitation of the ^{28}Si compound nucleus to the ground and excited states. The high-energy part for an in-beam γ-ray spectrum with detectors placed at 90° is presented in Figure 4.6.

Combining Equations (3.4), (3.5), and (3.6) lead to the expression

$$\sigma(\gamma_i) = \frac{N(E_\gamma^i)}{N_p\, m_T\, \tau\, \epsilon(E_\gamma^i)} \cdot \frac{1}{1+\sum_{k=2,4} \alpha_k^i P_k(\cos(\theta))} \tag{4.2}$$

for the partial cross section $\sigma(\gamma_i)$. This can then be rewritten as an expression for the full energy peak efficiency $\epsilon(E_\gamma^i)$ for each detector under an angle θ

$$\epsilon(E_\gamma^i,\theta) = \frac{N(E_\gamma^i,\theta)}{N_p\, m_T\, \tau\, \sigma(\gamma_i)} \cdot \frac{1}{1+\sum_{k=2,4} \alpha_k^i P_k(\cos(\theta))}. \tag{4.3}$$

The information are presented in Table 4.3. Where the partial cross section has been measured, the full energy peak efficiency can be determined for that γ-ray. It is critical to underscore the dependence between the estimation of the partial cross-sections and the subsequent determination of the full-energy peak efficiency. The reliability of the former is directly linked to the accuracy of the determination of the relative efficiency through the $^{27}\mathrm{Al}(p,\gamma)$ resonance. Note, that the

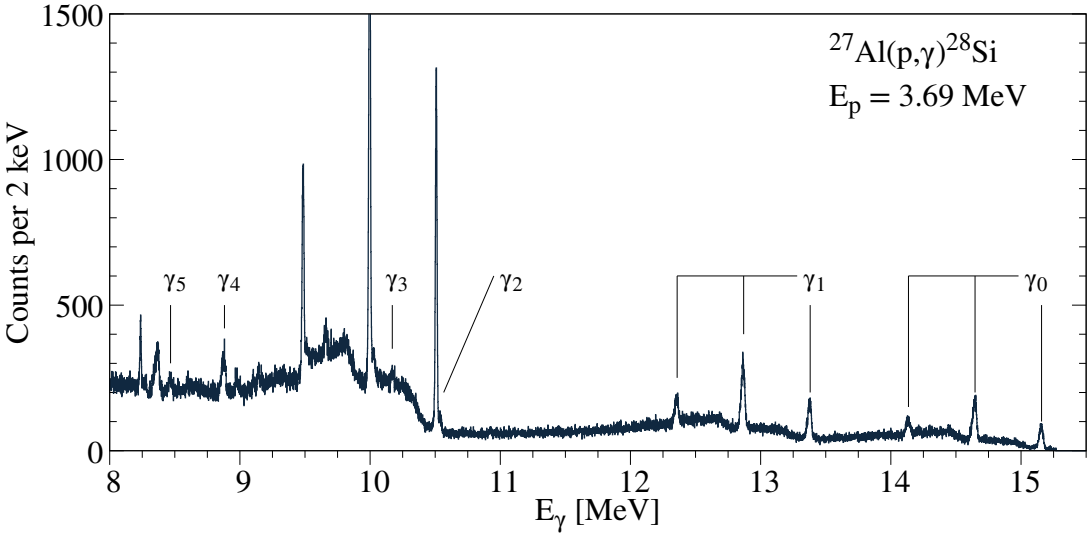

Figure 4.6: High energy part of the in-beam γ-ray spectrum of the $^{27}\mathrm{Al}(p,\gamma)^{28}\mathrm{Si}$ reaction for detectors placed at 90° with respect to the beam axis for a proton-beam energy of $E_p = 3.69\,\mathrm{MeV}$. The γ-rays to the ground state and different excited states in ^{28}Si are marked with their single and double escape peaks, if visible. The most prominent peaks around $E_\gamma \approx 10.5\,\mathrm{MeV}$ are the single and double escape peaks from resonant proton capture on ^{27}Al at a proton energy of $E_p = 3.674\,\mathrm{MeV}$ [227].

coefficients, that are determined in Ref. [227] have large uncertainties, which influences the full energy peak efficiency directly. The transitions with γ-ray energies of 4 MeV to 6 MeV to higher-lying states, that are used to scale the efficiencies have smaller uncertainties, but exhibit a statistical uncertainty of approximately 20 %. This can also be seen in Figure 4.7a and with a closer look at this region in Figure 4.7b.

Table 4.3: Experimental partial cross sections $\sigma(\gamma_i)$ of the$^{27}\mathrm{Al}(p,\gamma)^{28}\mathrm{Si}$ reaction with their uncertainties $\Delta\sigma(\gamma_i)$ and the coefficients for their angular distribution [227]. The spin and parities of the populated states in ^{28}Si are taken from Ref. [228]. The γ-ray energies are not Doppler-corrected.

	E_γ [MeV]	J^π	E_X [MeV]	$\sigma(\gamma_i)$ [μb]	$\Delta\sigma(\gamma_i)$ [μb]	$A_0\,[10^{-11}]$	$\alpha_2\,[10^{-18}]$	$\alpha_4\,[10^{-18}]$
γ_0	15.10	0^+	0	17.83	2.05	28.1(9)	13.5(18)	3.59(46)
γ_1	13.32	2^+	1.779	12.07	1.29	19.0(4)	-24.8(21)	-22.5(27)
γ_2	10.48	4^+	4.618	4.26	0.51	6.69(25)	-13.8(20)	13.2(19)
γ_3	10.12	0^+	4.979	1.56	0.23	2.46(4)	-18.9(58)	19.4(63)
γ_4	8.82	3^+	6.276	3.52	0.38	4.67(12)	-2.50(25)	18.4(26)
γ_5	8.41	0^+	6.691	0.73	0.09	1.15(5)	4.55(52)	6.68(54)

Monte-Carlo simulations utilizing the GEANT 4 toolkit have been performed to evaluate the full peak efficiency calibration [229, 230]. The detection efficiency between 0 MeV to 16 MeV is simulated in steps of 50 keV, where for each step 10^6 γ-rays are emitted from a point-like source [230]. A comparison between the experimental data and the simulation is shown in

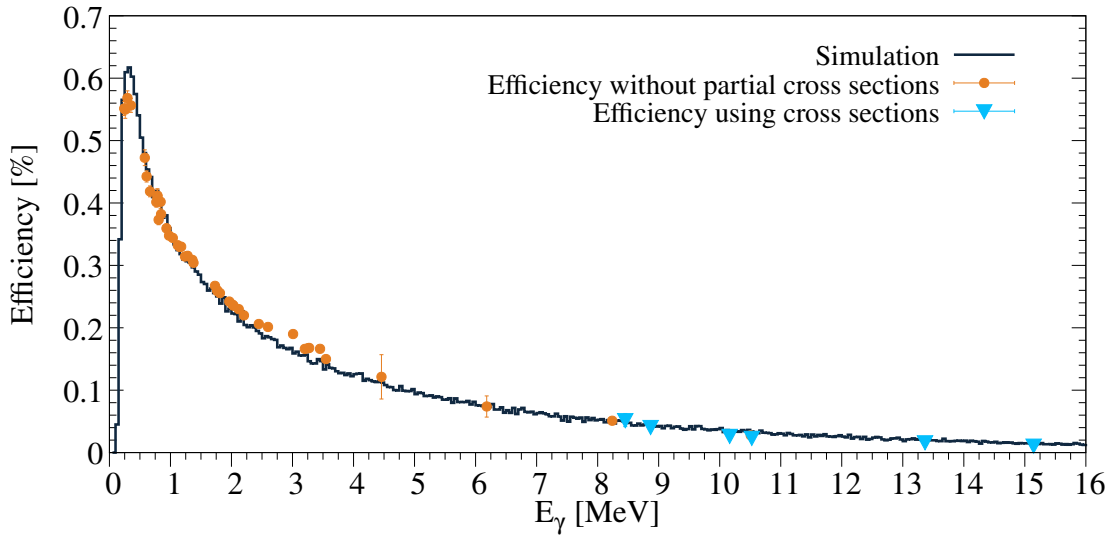

(a) The comparison between the GEANT 4 simulation and the experimentally obtained experimental full peak efficiencies with and without using cross sections over the whole energy range.

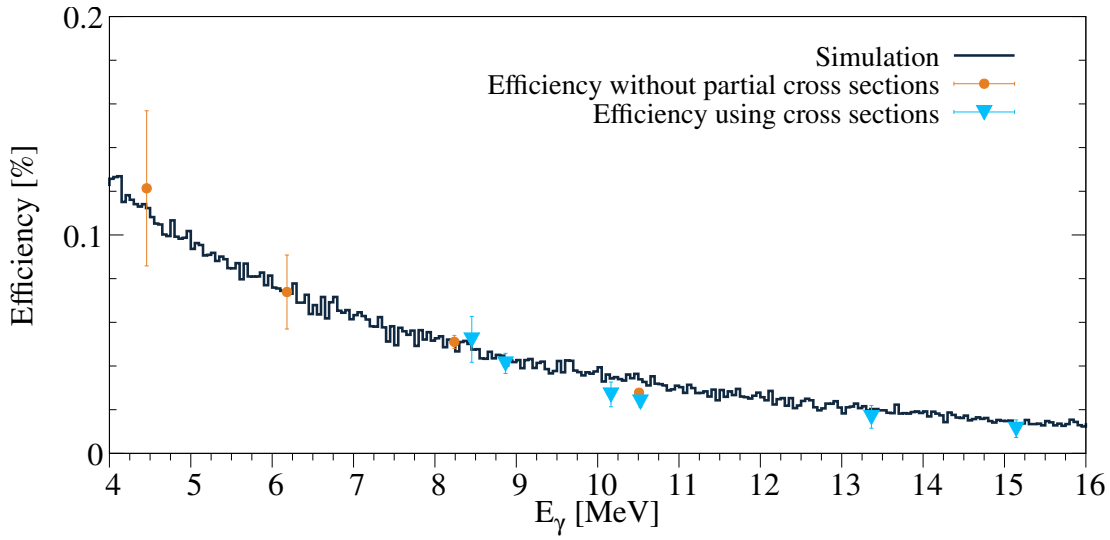

(b) A closer view on the high-energy part of the full energy peak efficiency, where efficiencies of partial cross sections are scaled to absolute full energy peak efficiencies. They show a good agreement.

Figure 4.7: Comparison between the GEANT 4 simulation [229] and the experimental full energy peak efficiencies for one detector placed at 90° with respect to the beam axis. The experimental data are well produced up to high γ-ray energies of $E_\gamma = 15.5\,\mathrm{MeV}$.

Figure 4.7a. The overall agreement is quite good. Taking a closer look to energies above 6 MeV, shown in Figure 4.7b, where there is no standard calibration source available, the agreement between the simulation and the experimental data are satisfactory. Beyond that, the effect of coincidental detected γ-rays was investigated using the GEANT 4 toolkit [229], to take a closer look at coincidence summing. The γ-rays de-exciting the compound nucleus ^{28}Si are emitted coincidentally with strong ground-state transitions or other γ-ray cascades. Since the detectors are located at distances of 9 cm to 16 cm, coincidence summing is assumed to be negligible. This is confirmed by the simulation, showing an effect of about 0.1 % or less [230].

4.4 Data Analysis

To determine the cross sections for the $^{85}\mathrm{Rb}(p,\gamma)^{86}\mathrm{Sr}$ reaction, that is of actual interest, a slight change to the method described in Section 3.4 is needed, since the target deteriorated as described in Section 4.1. The usual procedure is to normalize the summed reaction yield of the observed γ-ray transitions to the ground state to the number of target nuclei and number of projectiles. However, this is not possible due to the deterioration. Therefore, the adjustment is the following: the experimental yield $N(E_\gamma)$ is normalized to the efficiency $\epsilon(E_\gamma)$ and the dead time of the data acquisition

$$\hat{W}(\theta) = \frac{N(E_\gamma)}{\tau \cdot \epsilon(E_\gamma)}. \tag{4.4}$$

Subsequently, a sum of Legendre polynomials is fitted to the data. The obtained parameters A_0^i for each ground state transition i are summed and normalized to the product of target nuclei n_T and the number of projectiles N_p summed over k time intervals of 10 min:

$$\sigma = \frac{\sum_i A_0^i}{\sum_j n_{T,j} N_{p,j}}. \tag{4.5}$$

Besides the 3 % uncertainty of the charge collection and 5 % of the RBS measurement, an uncertainty of 10 % is added as a systematic uncertainty to the aforementioned procedure.

Figure 4.8 show the γ-ray spectra for the $^{85}\mathrm{Rb}(p,\gamma)^{86}\mathrm{Sr}$ reaction for γ-ray energies between 0.6 MeV to 3 MeV for all beam energies in comparison. They are obtained by summing all spectra of the HPGe detectors located at 90° with respect to the beam axis. As typical for the in-beam method, the background mainly stems from beam-induced background. It consists of proton-induced reactions on Cl such as $^{35,37}\mathrm{Cl}(p,p'\gamma)$, $^{35,37}\mathrm{Cl}(p,\alpha)^{32,34}\mathrm{S}$, and $^{37}\mathrm{Cl}(p,n)^{37}\mathrm{Ar}$, as well as $^{19}\mathrm{F}(p,p'\gamma)$, and $^{19}\mathrm{F}(p,\alpha)^{16}\mathrm{O}$. The Coulomb excitation of ^{197}Au of the backing is located at energies smaller than 600 keV and, hence, not visible in Figure 4.8.

The strongest γ-rays de-exciting from the ^{86}Sr compound nucleus to the ground state of ^{86}Sr are 1076.7 keV, 1854.4 keV, and 2641.3 keV [158]. These are clearly visible in the spectra. Note, that for 3.7 MeV and 4 MeV, the γ-ray transition of 2641.3 keV of the $^{85}\mathrm{Rb}(p,\gamma)$ reaction is strongly overlapping with the 2645.7 keV γ-ray transition of the $^{35}\mathrm{Cl}(p,p'\gamma)$ reaction [158, 231]. Since the level at $E_X = 2641.3$ keV not only de-excites with a γ-ray transition of 2641.3 keV, but

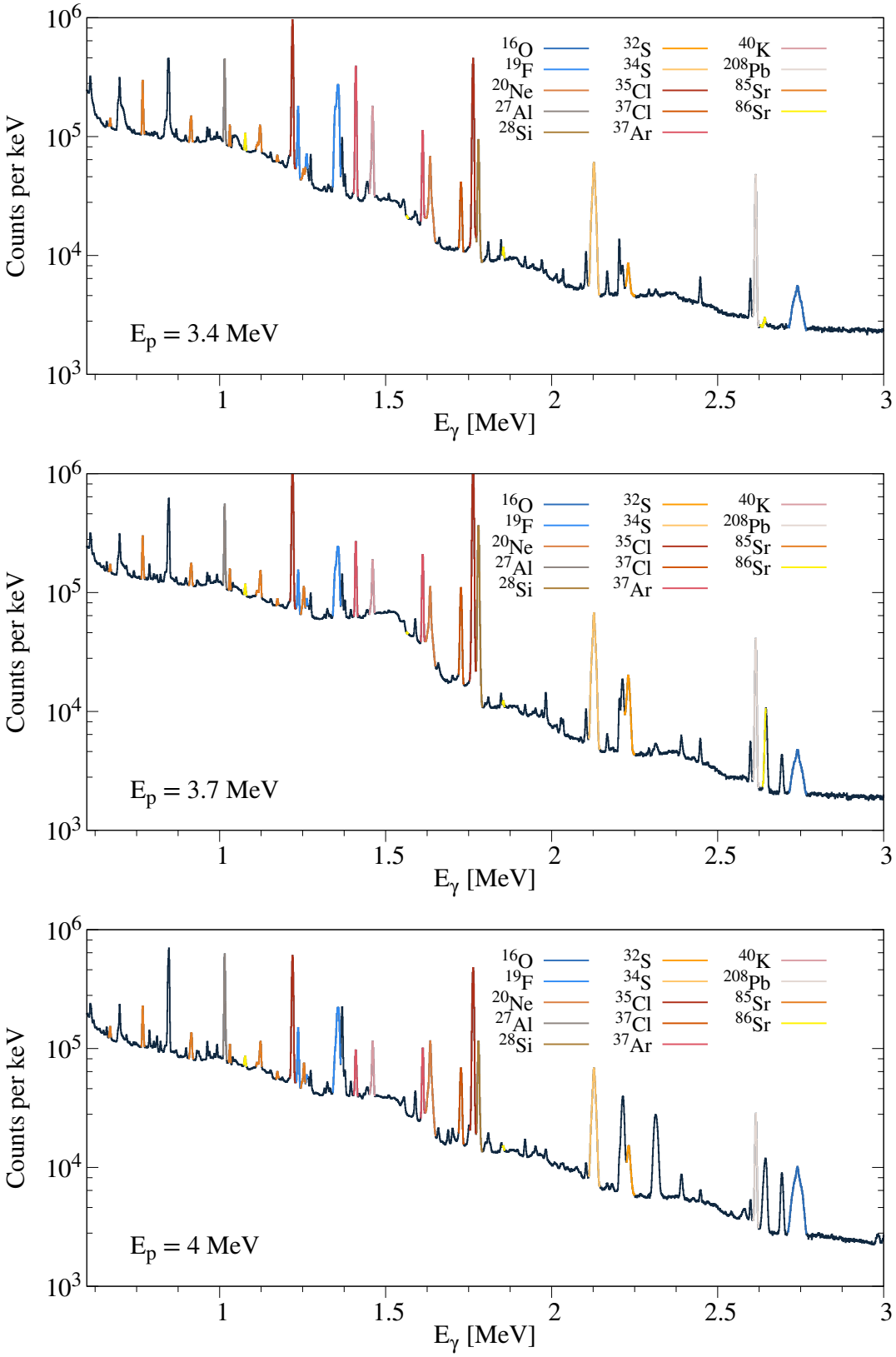
Counts per keV
10^6
10^5
10^4
10^3
1
1.5
2
2.5
3
E_γ [MeV]
^{16}O
^{19}F
^{20}Ne
^{27}Al
^{28}Si
^{32}S
^{34}S
^{35}Cl
^{37}Cl
^{37}Ar
^{40}K
^{208}Pb
^{85}Sr
^{86}Sr
E_p = 3.4 MeV
E_p = 3.7 MeV
E_p = 4 MeV

Figure 4.8

Figure 4.8: Comparison of the γ-ray spectra for the $^{85}\mathrm{Rb}(p,\gamma)^{86}\mathrm{Sr}$ reaction for γ-ray energies between 0.6 MeV to 3 MeV. The spectra are obtained by summing all single spectra of the HPGe detectors located at 90° with respect to the beam axis. The dominant beam-induced background stems from proton induced reactions on ^{35,37}Cl and ^{19}F. Ground-state transitions in the compound nucleus ^{86}Sr that were used for data analysis are marked in bright yellow. In addition, the de-excitation for the 2_3^+ level at $E_X = 2641.25$ keV with $E_\gamma = 1564.49$ keV and a branching ratio of 62 % is marked, since this γ-ray transition was used to disentangle and cross-check the contribution of the direct ground state transition of $E_\gamma = 2641.12$ keV. This ground state transition is overlaid with a peak stemming from the $^{35}\mathrm{Cl}(p,p'\gamma)$ reaction. This disentanglement was not possible for the highest proton beam energy of 4 MeV.

in addition with a branching of 62 % with a γ-ray transition of 1564.5 keV to the first 2^+ level, this level including its branching is then used to estimate the number of de-excitations to the ground-state as well. The method provides consistent results, why the fit to the data are assumed to be correct.

The direct de-excitation of the ^{86}Sr compound nucleus to the ground state via γ_0 has not been observed in this experimental campaign. The reasons are twofold. First, the full energy peak efficiencies around 13 MeV to 14 MeV, where γ_0 is expected, are very small. In addition, the significant target loss of target material during the irradiation directly reduces the detectable number of γ-rays in the particular peak $N(E_{\gamma_0})$. It should be noted that this is applicable to all peaks, of course. The combination of both lead to a non-observable γ_0, as well as not observed decays to other low-lying levels. An upper limit of 4 % to 6 % for the contribution of the γ_0 transition to the cross section was determined. This contribution depends on the proton beam energy. Thus, the uncertainties of the cross section evaluation due to unobserved γ-ray transitions are smaller than the quoted uncertainties for the cross section values.

All possible known ground-state transitions taken from Rerence [160] are listed in Table 4.4. It should be noted that this information has been updated very recently (July 2025). Previously, only seven ground-state transitions had been documented, marked with an asterisk *. However, recent findings have expanded this number to twelve ground-state transitions. A re-examination of the γ-ray spectra has been conducted. The levels for the unobserved ground-state transitions can – in addition to ground-state de-excitations – de-excite to other excited levels, which in turn de-excite. These de-excitations have not been detected, if not noted otherwise in Table 4.4. In the following, the data for ^{86}Sr are taken from Ref. [158].

The strongest ground state γ-ray transitions, that are visible in the single γ-ray spectra for all proton beam energies, are at 1076.79 keV, 1854.12 keV, and 2641.25 keV. The order of these transitions is decreasing in the number of detected γ-ray transitions. The peaks of the first two were easy to identify in the γ-ray spectra. The de-excitation for the 2_3^+ level at $E_X = 2641.25$ keV with a γ-ray transition of $E_\gamma = 1564.49$ keV and a branching ratio of 62 % was used to disentangle and cross-check the contribution of the direct ground state transition of $E_\gamma = 2641.12$ keV. Since the branching corrected number of counts is supposed to be equal, the procedure is reliable. This ground state transition is overlaid with a peak at $E_\gamma = 2645$ keV stemming from the $^{35}\mathrm{Cl}(p,p'\gamma)$ reaction.

Using the $\gamma\gamma$ coincidence matrices, it can be investigated whether the transitions contribute

Table 4.4: In the literature reported ground-state γ-ray transitions in ^{86}Sr. The information are taken from Ref. [158]. Note, that this has been updated very recently (July 2025). Before, there were only seven ground-state transitions known, marked with an asterisk *, now there are given twelve ground-state transitions. The γ-ray spectra have been looked through anew. The levels for the unobserved ground-state transitions de-excite also to other excited levels. These de-excitations have also not been observed.

#	E_{level} [keV]	J^π	E_γ [keV]	I [%]	Xl	Note
	0	0^+				ground state of ^{86}Sr
1	1077	2^+	1077*	100	$E2$	observed
2	1854	2^+	1854*	79.2	$E2$	observed
6	2482	3^-	2482*	0.450	$(E3)$	
9	2641	2^+	1564	62	$M1+E2$	observed
			2641*	100	$E2$	observed
11	2787	2^+	1711	100	$M1+E2$	
			2788*	29	$E2$	
16	2997	3^-	2997*	0.17	$E3$	
31	3430	2^+	3430	1.67	$E2$	
40	3687	3^-	3687	0.107	$(E3)$	
47	3871	3^-	3871	<0.47	$(E3)$	
60	4145	$(3,4^+)$	4145	<0.043		
104	4409	3^-	4409	<0.068	$(E3)$	
168	7821	(1)	7821*	100		

to the cross section and if the states in ^{86}Sr are at all populated by the (p,γ) reaction. For this, the γ-ray transitions are discussed separately in the following. The corresponding $\gamma\gamma$-coincidence spectra are presented in Figure 4.9.

2481.72 keV: The dominant decay channel for the $J^\pi = 3_1^-$ state with an excitation energy of $E_X = 2481.30\,\text{keV}$ is to the 2_2^+ state at $E_X = 1854.12\,\text{keV}$ by emitting a 627.56 keV γ-ray. After applying a gate on the 1854.12 keV γ-ray transition, that de-populates the state, the populating γ-ray 627.56 keV is visible in the coincidence spectra. Therefore, this state is excited by the (p,γ) reaction. However, the branching ratio of the direct population to the ground state is 0.450 %, which is too weak to detect and, in addition, should not contribute significantly to the cross section.

2787.45 keV: This state decays dominantly by emitting a γ-ray with an energy of 1710.80 keV to the 2_4^+ state at $E_X = 1076.79\,\text{keV}$. Applying a coincidence gate on the depopulating 2_1^+ state to the ground state of $E2$ character should reveal the 1710.80 keV γ-ray transition. Since there is no corresponding transition, that is clearly visible, this state was most likely not excited or populated via the (p,γ) reaction.

2997.01 keV: This $J^\pi = 3_2^-$ state at 2997.01 keV decays to the 2_1^+ state via the emission of a 1919.91 keV γ-ray with a branching ratio of 100 %. The coincidence spectra hardly show this transition when applying a gate on the 1076.79 keV γ-ray depopulating the first 2^+ state. Because the direct decay to the grounds state with a γ-ray of 2997.01 keV has a branching ratio of 0.17 % and is not visible in the single γ-ray spectra, this state is only weakly excited and the contribution

of the ground state transition is negligible.

3429.9 keV: The dominate decay of this $J^\pi = 2^+$ state with a γ-ray energy of 2353.5 keV of unknown parity decays with 100 % to the the first 2^+ state. A gate on the de-population of this 1076.79 keV state does not reveal a clear peak of the γ-ray of 2353.5 keV. Therefore, this state is most likely not populated. Since, in addition, the branching ratio of the direct ground state decay is 1.67 %, this decay does not contribute to the cross section at all.

3686.5 keV: The dominant decay channel for the $J^\pi = 3^-$ state with a excitation energy of $E_X = 3686.66$ keV is to the 2_1^+ state at $E_X = 1076.79$ keV by emitting a 2609.74 keV γ-ray. Applying a coincidence gate on the depopulating 2_1^+ state to the ground state of $E2$ character reveals the 2609.74 keV γ-ray transition. Since there is no or only a very weak corresponding transition, this state was most likely not excited or populated via the (p, γ) reaction. If there was a weak population, this state does not contribute to the ground state, because the branching ratio is only 0.107 %.

3871.2 keV: This $J^\pi = 3^-$ state at 3871.2 keV decays to the 2_1^+ state via the emission of a 2794.24 keV γ-ray with a branching ratio of 100 %. A gate on the de-population of this 1076.79 keV state does not clearly reveal the γ-ray of 2794.24 keV, expect for a proton energy of 4000 keV, wherefore this state is most probably not excited in the (p, γ) reaction with the exception for the highest proton beam energy. Since the branching ratio of the direct ground state decay is less than 0.47 % this contribution, if there was an excitation of the state, is negligible.

4144.7 keV: This $J^\pi = (3, 4^+)$ state has no clear assignment of spin and parity. The dominate decay to the first 2^+ state is via emitting a γ-ray of 3086.02 keV of unknown parity with a branching of 100 %. No coincident γ-ray of 3086.02 keV is observed when a gate is applied to this de-excitation. Since the branching of the direct ground state decay is less than 0.043 %, this should not contribute to the cross section nor should the state be populated at all.

4409 keV: The excitation energy of this $J^\pi = 3^-$ state is $E_X = 4408.97$ keV and it decays with a branching of 100 % to the the 2_1^+ state with an excitation energy of 1076.79 keV. The decay of this de-excitation, however, does not reveal a coincidental γ-ray with 3332.02 keV. The branching of the direct transition to the ground state is less than 0.068 %, wherefore the contribution to the ground state of this transition is insignificant.

7820 keV: This highly excited state with $J = (1)$ at $E_X = 7821.2$ keV has various states, that it branches into. The range of the emitted γ-rays is 4718 keV to 7820 keV. None of these de-excitations are observed in the coincidence spectra. A reason for this could be the quite low efficiency for $\gamma\gamma$-coincidences at these high energies. The single γ-ray spectra do not show a clear peak at 7820 keV. However, the upper limit of the contribution to the cross section is estimated as less than 1 %.

The cross section values have been determined with the observed ground state transitions in ^{86}Sr. Figure 4.10 shows the angular distributions to which the Legendre polynomials have been fitted for a proton energy of $E_p = 3.4$ MeV as an example. Since only one detector is placed at an angle of 135 %, the uncertainty here is larger due to lower statistics at this position. Around $E_\gamma = 1854.12$ keV there is a double peak structure, where at 1847.42 keV a line is visible, stemming from the natural radioactive background originating from the nuclide ^{214}Bi. Since this transition

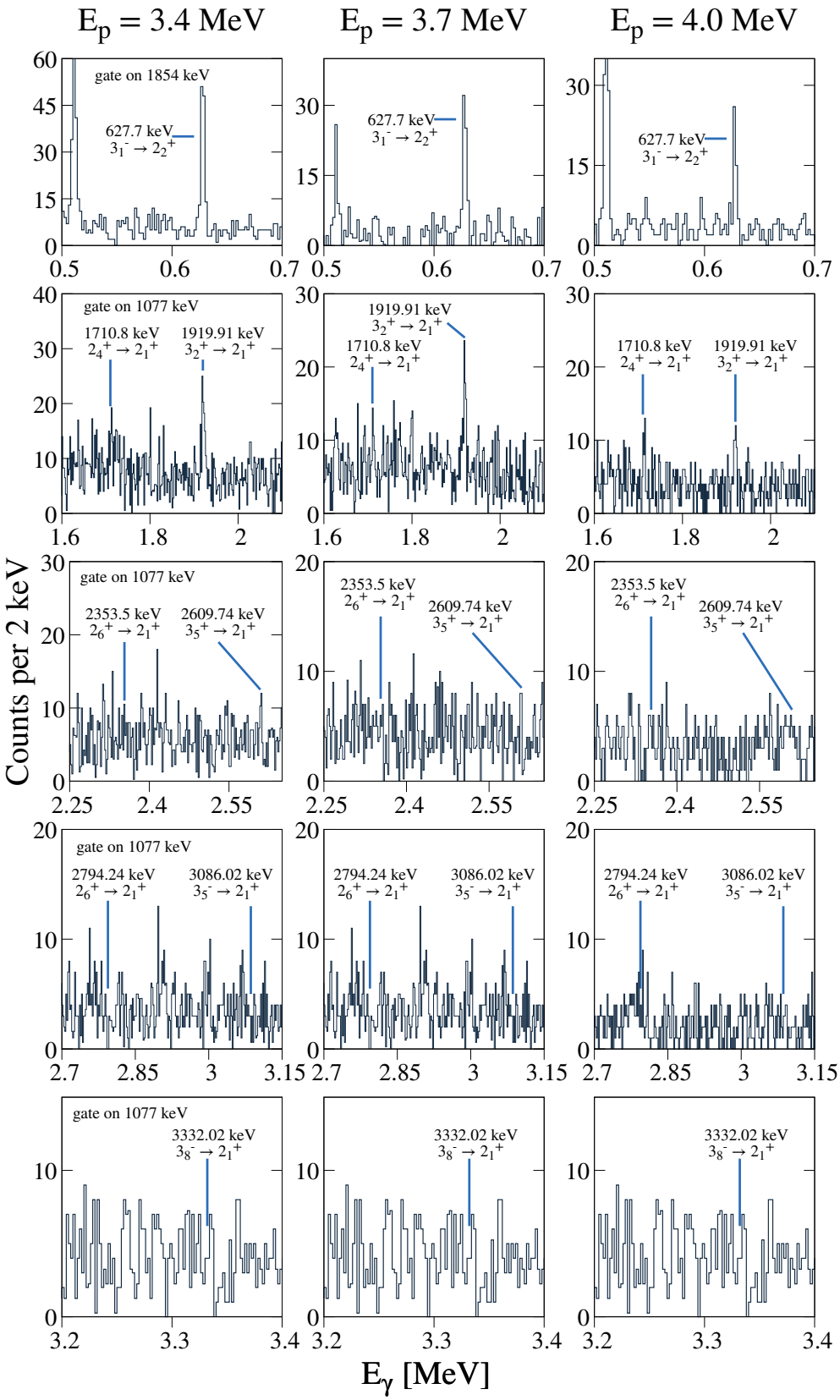
E_p = 3.4 MeV
E_p = 3.7 MeV
E_p = 4.0 MeV
gate on 1854 keV
627.7 keV
3_1^- → 2_2^+
gate on 1077 keV
1710.8 keV
2_4^+ → 2_1^+
1919.91 keV
3_2^+ → 2_1^+
2353.5 keV
2_6^+ → 2_1^+
2609.74 keV
3_5^+ → 2_1^+
2794.24 keV
2_6^+ → 2_1^+
3086.02 keV
3_5^- → 2_1^+
3332.02 keV
3_8^- → 2_1^+
Counts per 2 keV
E_γ [MeV]

Figure 4.9

Figure 4.9: $\gamma\gamma$-coincidence spectra for the different γ-ray transitions de-populating states, that also have ground-state transitions. These ground state transitions have not been observed in the single γ-ray spectra, wherefore the coincidence method was applied. Each column represents the different proton beam energies. The applied gates are given in the first figure of the line. They are valid for the entire line. The γ-ray transitions, that are (not) coincidental observed, are discussed in detail in the text. Information about excitation energies, spins, and parities are adopted from Ref. [158].

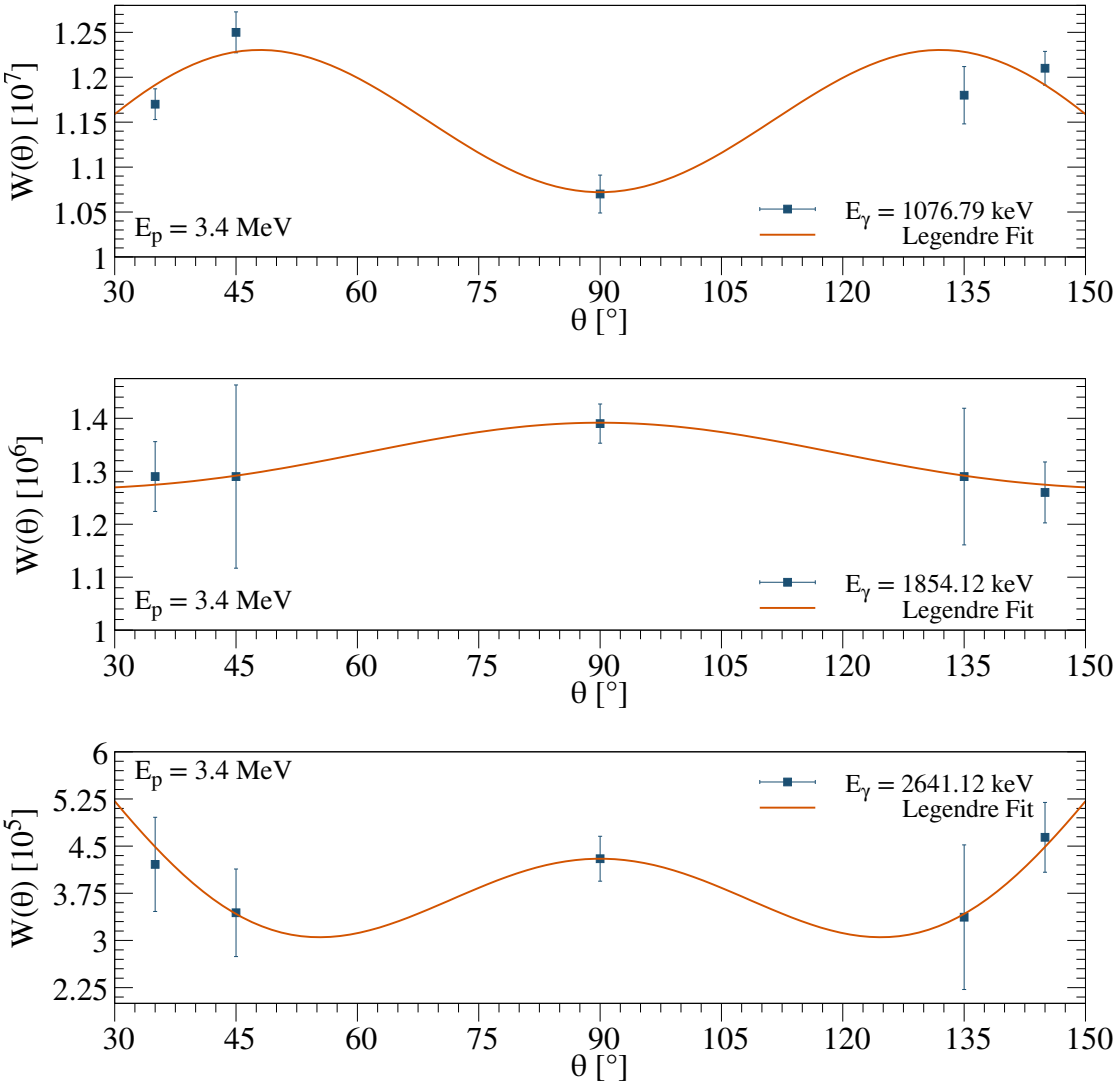

Figure 4.10: Angular distributions to which the Legendre polynomials have been fitted for a proton energy of $E_p = 3.4\,\mathrm{MeV}$. The line represents the fit of the the Legendre polynomials to the experimental data $W(\theta)$ obtained in the scope of the analysis.

Table 4.5: Experimental $^{85}\mathrm{Rb}(p,\gamma)$ reaction cross sections for the different center-of-mass energies.

$E_{c.m.}$ [keV]	$\Delta E_{c.m.}$ [keV]	σ [μb]	$\Delta\sigma$ [μb]
3349	16	162	27
3646	16	321	49
3944	16	518	74

is more dominant than the ground state transition of the (p,γ) reaction on ^{86}Sr and the statistic at 45° for the 1854.12 keV ground state transition is poor, the error of the fit dominates the error of $W(\theta)$.

The obtained cross section values are given in Table 4.5. The uncertainties, that contribute, are the target thickness and charge collection with 12 %, 5 % from the detection efficiency, and 6 % to 10 % from statistical uncertainties.

4.5 Cross-section Results and Calculations

The experimentally determined $^{85}\mathrm{Rb}(p,\gamma)^{86}\mathrm{Sr}$ reaction cross sections are given in Table 4.5 and are shown in Figure 4.11. As discussed in Chapter 2, reactions leading to a compound nucleus with high nuclear level densities are described using the Hauser-Feshbach statistical model, which is implemented in the TALYS code. For this, many information on the nuclear properties of involved nuclei needs to be known. These properties include, as explained before, e. g. low-lying excited states, optical-model potentials for the particle channels, and nuclear level densities and γ-rays strength functions for the photon channel.

An exemplary input file for the TALYS code 2.14 for the calculation utilizing γ-ray strength model 12 and level density model 2 is given below. If not stated otherwise, this input is used for all different combinations presented in Figure 4.11, only changing the γ-ray strength model and level density model. The descriptions are taken from Ref. [189].

```
projectile p
element Rb
mass 85
energy 1.3 5.5 0.010
maxlevelsbin g 40 # number of included discrete levels for given ejectile
xseps 1.0e-18   # limit for considering cross sections
transeps 1.0e-19 # limit for considering transmission coefficients
transpower 20   # limit for considering transmission coefficients
popeps 1.0e-22  # limit for considering population cross sections
outdiscrete y   # output of cross sections to each individual discrete state
outspectra y    # output of angle-integrated emission spectra
outdensity y    # output of level density parameters and level densities for
```

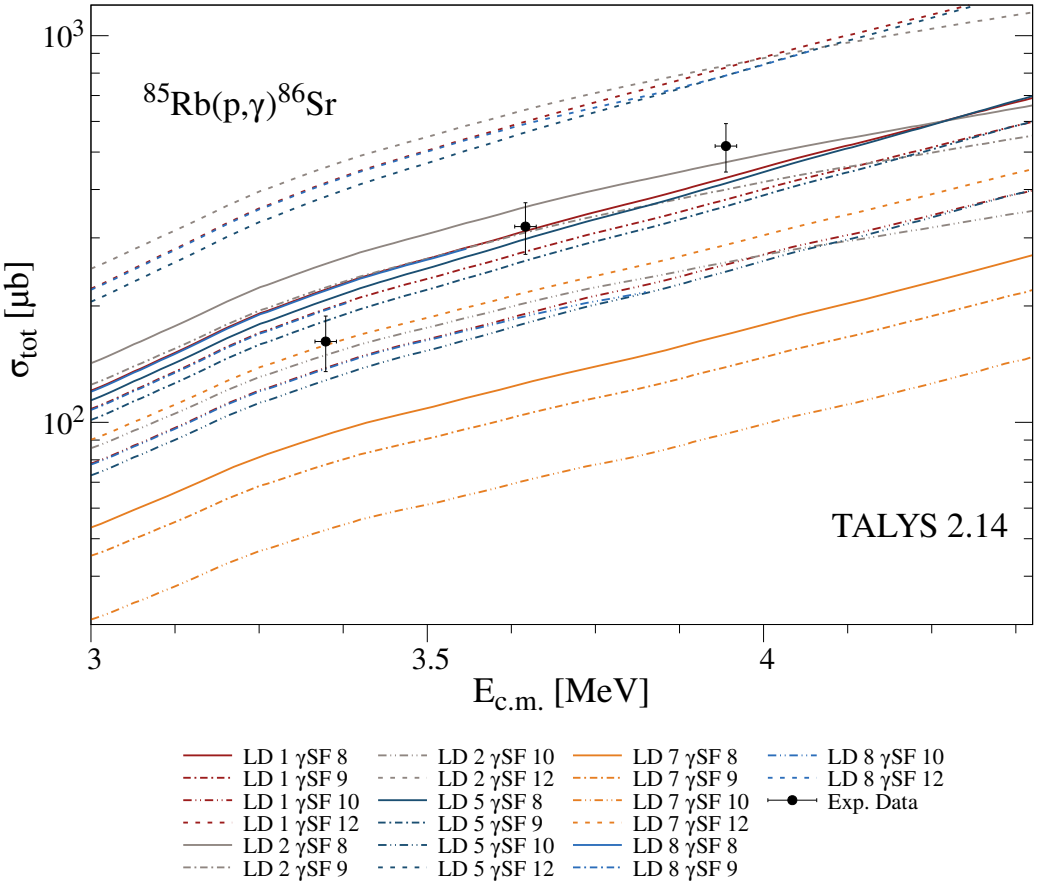

Figure 4.11: Comparison of the experimentally determined cross sections to TALYS version 2.14 calculations. For the calculations the former recommended level density and γ-ray strength function models, as explained in Section 2.3, are used. As can be seen, no model can describe all cross-section values, much less two values.

```
                 each residual nucleus
outgamma y       # output of gamma-ray parameters, strength functions,
                 transmission coefficients and reaction cross sections
outpopulation y  # output of the population of each compound nucleus
outgamdis y      # output of discrete gamma-ray intensities
outlevels y      # output of discrete level information for each nucleus
channels y       # calculation and output of all exclusive reaction channel
                 cross sections
filechannels y   # write the exclusive channel cross sections as a function
                 of incident energy on separate files
strength 12      # model for E1 gamma-ray strength function
ldmodel 2        # model for level densities
```

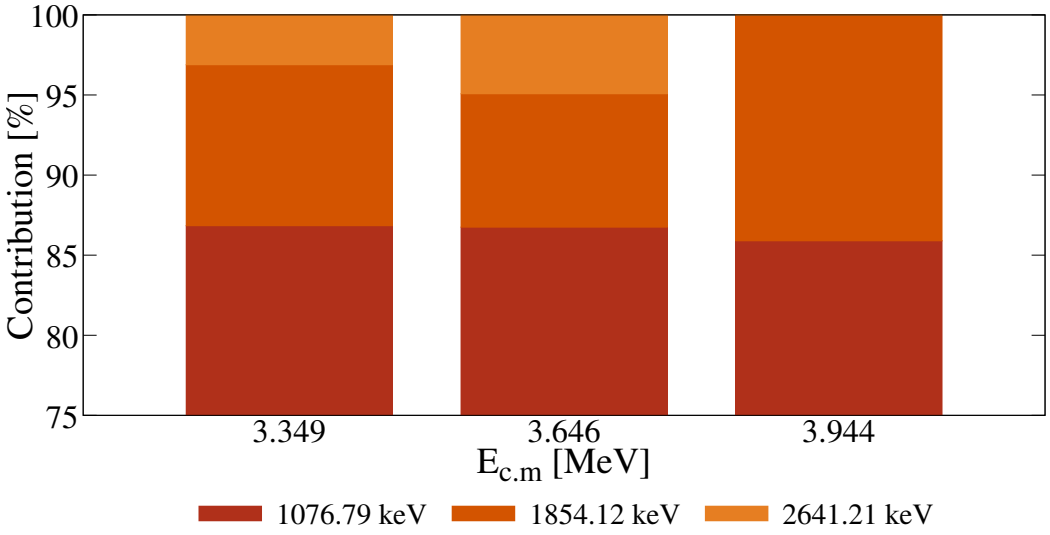

Figure 4.12: The different contributions to the population of the ground state from different excited states of the ^{85}Rb(p,γ) reaction at the three beam energies. About 86 % of the observed population of the ground state stem from the $2_1^+ \rightarrow g.s.$ transition at $E_\gamma = 1076.7$ keV. The γ-ray transition at $E_\gamma = 2641.25$ keV was not clearly distinguishable from the overlaying peak at $E_\gamma = 2645$ keV stemming from the ^{35}Cl$(p,p'\gamma)$ reaction for the highest proton beam energy.

Table 4.6: Experimental ^{85}Rb(p,γ) reaction cross sections from discrete levels for the different center-of-mass energies.

$E_{c.m.}$ [keV]	$\sigma_{1076keV}$ [μb]	$\sigma_{1854keV}$ [μb]	$\sigma_{2641keV}$ [μb]
3349(16)	133(20)	15.5(24)	4.78(73)
3646(16)	258(40)	24.7(38)	14.6(22)
3944(16)	292(45)	66.6(101)	

The different combinations for the recommended models (cf. Section 2.3), for the latter two are shown in comparison to the experimentally determined values in Figure 4.11. Model 11 of the γ-ray strength does not produce any results[3]. Due to the limited documentation, the reason for this remains unknown. As can be seen in Figure 4.11, no model can describe all cross-section values, and only one can describe two.

The experimental cross sections in comparison to to TALYS version 2.14 calculations utilizing all recommended γ-ray strength and level density models[4] for the three observed ground state transitions are presented in Chapter A.1. The corresponding Figures A.1, A.2, and A.3 show, that the trend of the discrete level cross sections is also not produced by the given models. The values are given in Table 4.6. The corresponding percentages of the discrete levels contributing to the

[3]However, it does reproduce results for the ^{87}Rb$(p,\gamma)^{88}$Sr reaction. The tables for ^{85}Rb seem to be corrupted.
[4]These recommendations are given by the authors of TALYS [124].

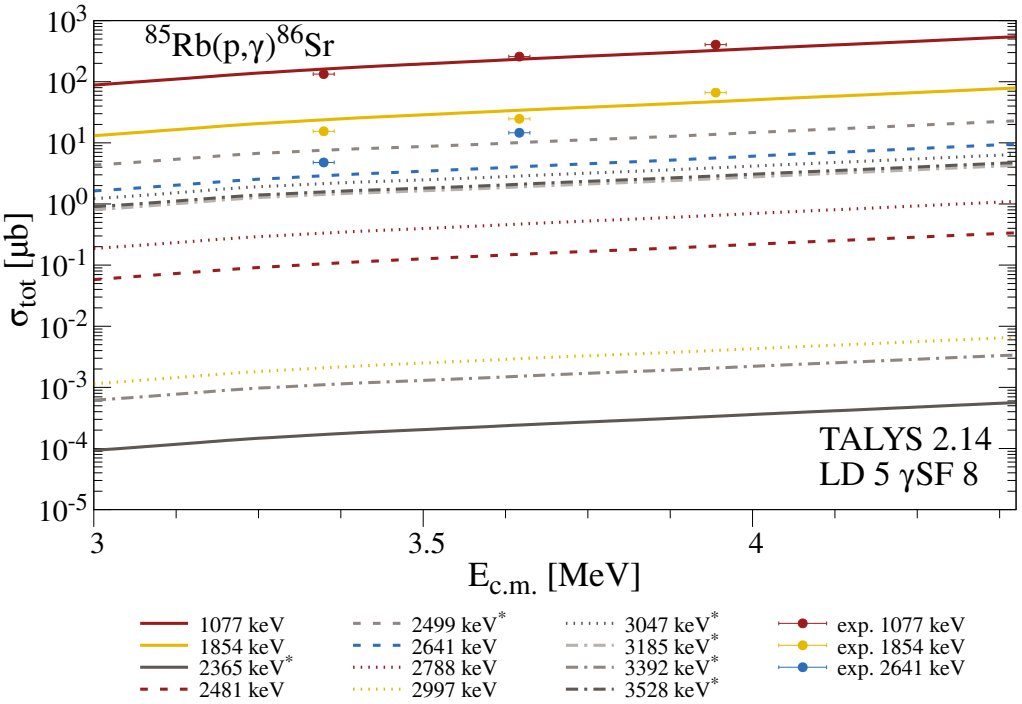

Figure 4.13: Cross sections for ground state transitions obtained by calculations with the TALYS code 2.14. Calculations for states, that are not reported (to have a ground state transition) in Reference [158], are in gray shades, whereas reported states are displayed in color. The experimentally obtained cross sections values are shown in comparison. The combination of level density model 5 and γ-ray strength function 8 is used as an example.

cross section are shown in Figure 4.12. As expected, the greatest percentage with approximately 86 % of the observed population of the ground state stem from the $2_1^+ \rightarrow g.s.$ transition at $E_\gamma = 1076.7\,\text{keV}$. The 2_1^+ state is populated by a considerable contribution of different γ-ray cascades. As a result, the decay into the ground state shows a more or less isotropic behavior, and the effect of the angular correlation is rather small, as can be seen in Figure 4.10. The γ-ray transition at $E_\gamma = 2641.25\,\text{keV}$ was not clearly distinguishable from the overlaying peak at $E_\gamma = 2645\,\text{keV}$ stemming from the $^{35}\text{Cl}(p, p'\gamma)$ reaction at the highest proton beam energy.

Taking a look at the in TALYS implemented list of levels for ^{86}Sr, there are 113 levels given. In Ref. [158], there are 132 levels reported. There are levels given, that have not been reported on in the literature [158]. This applies also for ground state transitions as shown in Figure 4.13. The cross sections for transitions, that are given in TALYS, but are not reported in Ref. [158], are in gray shades, whereas the reported transitions are colorful. In comparison, the experimental cross sections are shown for the observed transitions. The combination of level density model 5 and γ-ray strength function 8 is used as an example. TALYS [124] predicts a state at $E_X = 2499\,\text{keV}$, that show a cross section for the decay to the ground state in between of the observed transitions of the states $E_X = 1854\,\text{keV}$ and $E_X = 2641\,\text{keV}$. In addition, these three states are

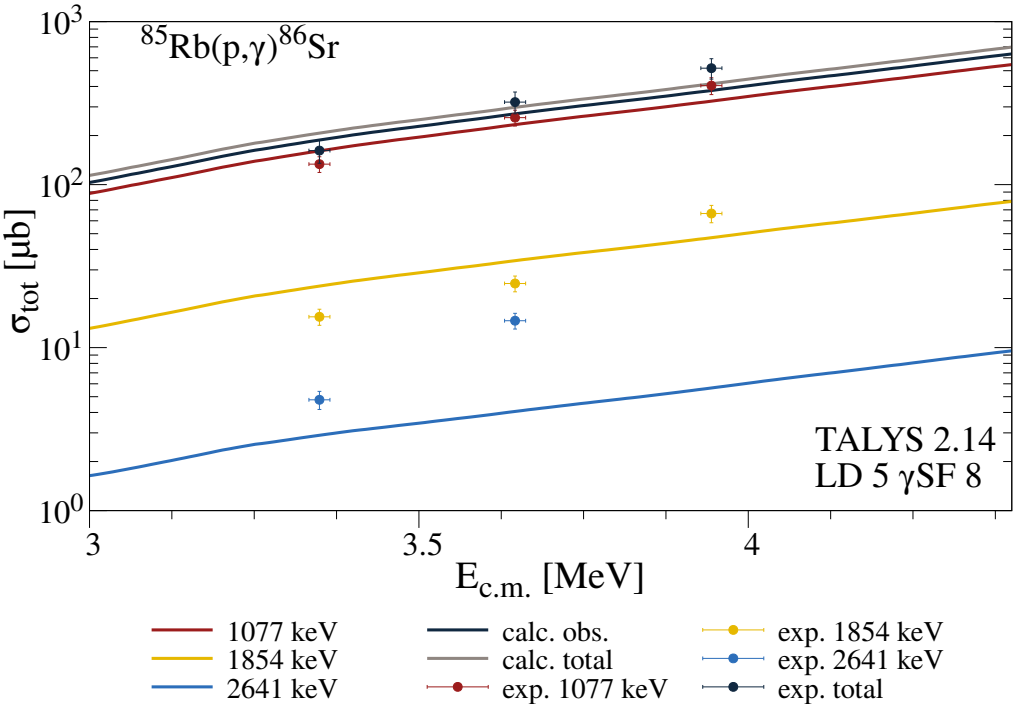

Figure 4.14: Cross sections for ground state transitions obtained by calculations with the TALYS code 2.14. Only the cross sections for states, that are observed are shown. The dark blue shows the summed calculation for the corresponding observed ground state transitions. The combination of level density model 5 and γ-ray strength function 8 is used as an example. The data for the highest proton beam energy are well reproduced. However, the experimentally obtained cross section seem to drop steeper than predicted by the model.

located at an approximately similar energy. Note that, in Reference [158], there is a state given at $E_X = 2498\,\text{keV}$, without any information beside the energy. Since there is no γ-ray transition observed in the single spectra obtained in this experiment, the calculation can not reproduce the experimental observations. Only for the highest proton beam energy, the calculations and the experimental data agree well. However, for the lower beam energies the experimentally obtained cross section seem to drop steeper than predicted by the model. Taking only the calculated cross sections into account, as shown in Figure 4.14, and summing over them, the cross section is smaller than the total calculated cross section for the (p, γ) reaction. The trend, however, is not changed.

4.5.1 Varying the Nuclear Level Density parameters

As explained in Chapter 2, there are many parameters, that influence the Hauser-Feshbach calculations, e. g. the nuclear level density, that is explained in detail in Section 2.2.2. The different recommended models are displayed in Figure 4.15 by comparing their predicted cumulative number of levels to experimentally known levels. The calculations are in good agreement with

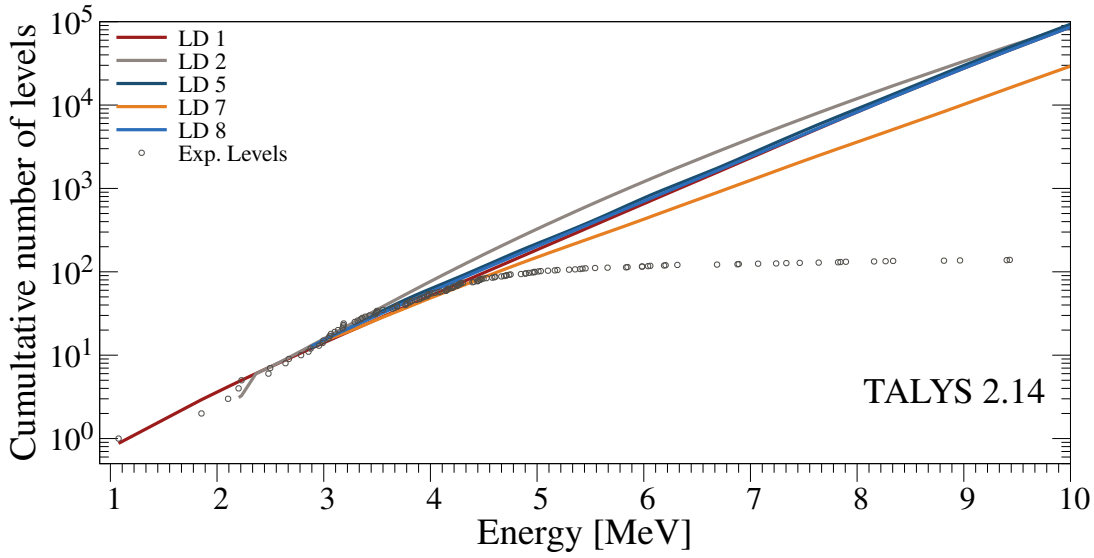

Figure 4.15: Cumulative number of levels in ^{86}Sr. The experimentally known levels are taken from Reference [158]. The predicted number of levels for the five recommended end level density models in TALYS [124]. They are in good agreement up to an energy of 4 MeV. Level density model 2 predicts a higher density starting from 3.7 MeV, whereas model 7 predicts the lowest level density above an energy of 3.2 MeV. The results obtained from the other models are similar.

the experimentally known levels up to an energy of approximately 4 MeV. Level density model 2 predicts a higher density starting from 3.7 MeV, whereas model 7 predicts the lowest level density above an energy of 3.2 MeV. The results obtained from the other models demonstrate a high degree of similarity.

There are microscopic level density models, that can be adjusted quite flexibly with two parameters. Since level density model 6 is no longer recommended and model 5 is chosen for a further analysis since it gave consistent results over the last years (see References [194, 232, 233]). According to Equation (2.27), the parameters c and δ are used to adjust the level density, since the tabulated data are normally not adjusted to experimental data. Both values can be varied between -10 and 10 in calculations utilizing the TALYS version 2.14 [124]. The default values for the parameters used in calculations are $c = 0.3719$ and $\delta = 1.4689$. The experimentally known levels and the different level density models seem to agree rather well utilizing the in TALYS implemented values. Therefore, another approach is followed. The default values, which seem to fit well for the level density here are varied from 0.360 to 0.380 for c with the keyword *ctable* and δ between 1.4590 and 1.4790 with the keyword *ptable*. These scans of parameters are shown in Chapter A.2.1. As an example the combination of $c = 0.3720$ and the different values for δ is shown in Figure 4.16. Varying the parameters in the given range does have a small influence.

The parameters are varied systematically to find the best agreement between the low-lying level scheme up to energies of 4 MeV. Note, that the level density for energies lower than approximately 2.4 MeV deviate significantly, since the lowest level considered is level number 6. Since the range

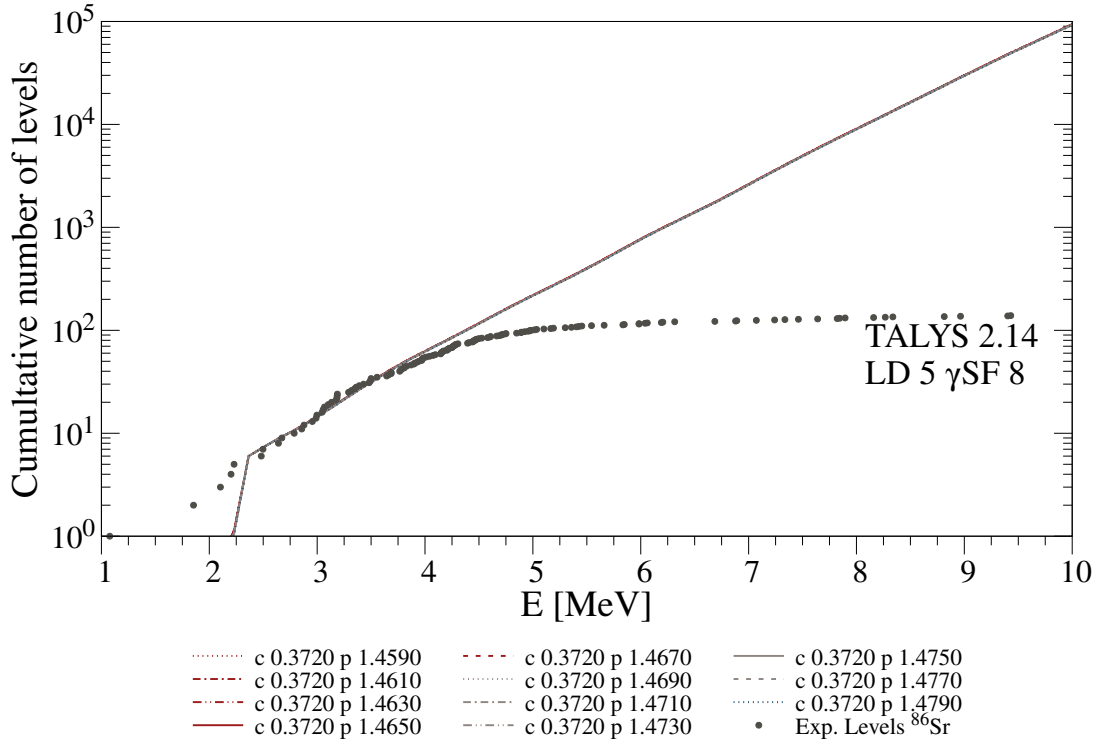

Figure 4.16: The cumulative number of levels for the combination of $c = 0.3720$ and the different values for δ. Below approximately 2.4 MeV the cumulative number of levels deviate significantly. The experimentally known levels are well described up to circa 4 MeV. The influence of varying δ in the given range of 1.4590 to 1.4790 is negligible.

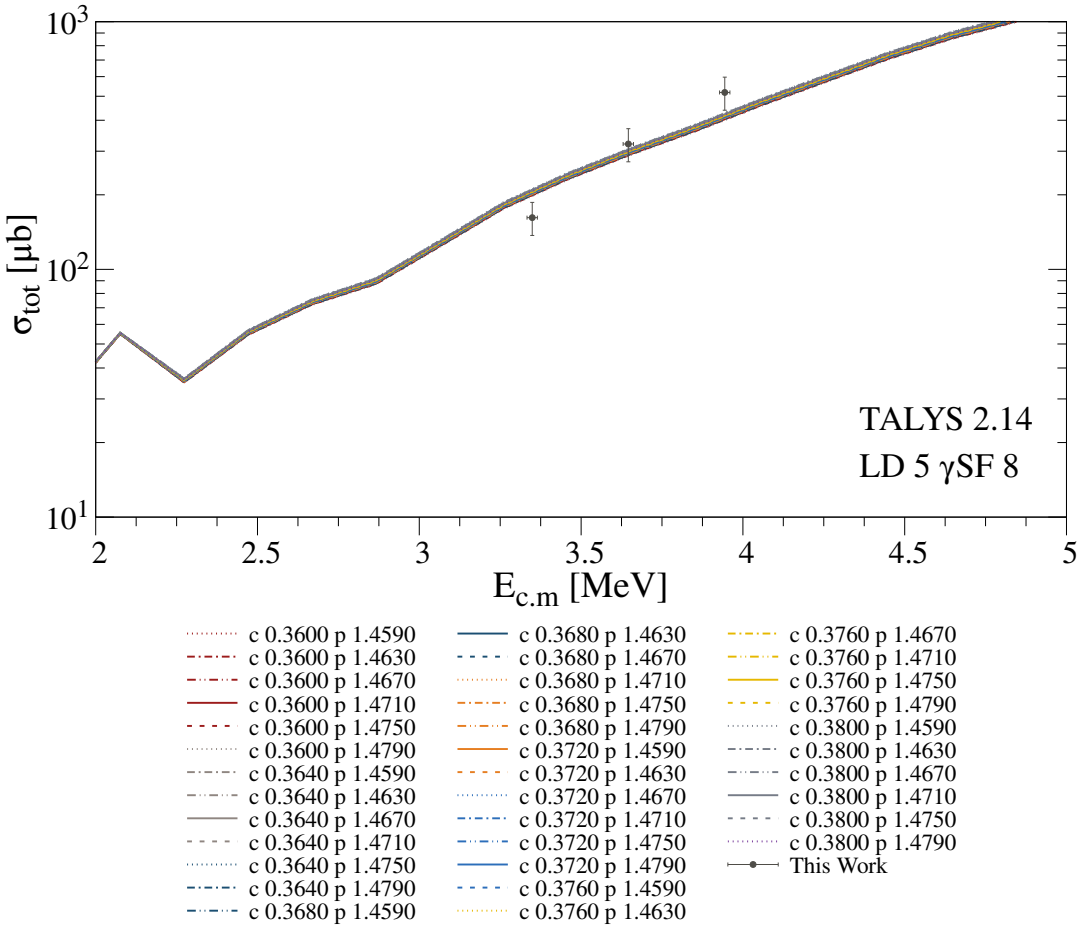

Figure 4.17: Cross sections of the ^{85}Rb$(p,\gamma)^{86}$Sr reaction compared to calculations varying c and δ. The corresponding cumulative number of levels are shown in Chapter A.2.1. It is shown, that the cross section is rather shifted up or down than increasing steeper, which would be needed to describe the data.

of the parameters is quite narrow, different combinations of parameters lead to very similar results. It can be seen, that the steepness of the cumulative number of levels varies slightly. This, of course, influenced the cross section prediction. Figure 4.17 shows the corresponding cross section to different combinations of c and δ as shown in Section A.2.1. The general trend for the cross sections is still not steep enough that all three values are described.

Therefore, level density model 1 was modified by varying the parameter T and E_0, as given in Equation (2.25). The given default values by TALYS are $T = 0.7879581$ and $E_0 = 0.889099$. T was varied between 0.700 and 0.850 and E_0 from 0.80 to 0.96. The results of the cumulative numbers of levels in comparison to the experimentally known levels as well as the calculated cross sections in comparison to the experimentally obtained ones are shown in Chapter A.2.2. It can be seen, that the combinations give results for the cumulative number of levels, that agree with

the experimentally known levels up to 4 MeV. Taking a closer look at the resulting cross sections, the general trend is still not steep enough that all three values are described.

Since varying two different level density models using two different approaches, the phenomenological constant temperature level density model (CTM) [149, 150] and the microscopic Hartree-Fock-Bogoliubov model using Skyrme interaction [153], cannot reproduce the cross sections in the measured energy range, it is assumed, that the nuclear level density is most likely not the cause for the deviation. Consequently, the next step in the process of describing the data involves the next ingredient for the calculations: the γ-ray strength function.

4.5.2 Varying the γ-ray strength parameters

TALYS provides keywords to adjust γ-ray strength functions. There are three scaling parameters to move the γ-ray strength function up and down ($ftable$), move it left or right ($etable$) by reading the γ-ray strength function at a different energy, and the $wtable$ parameter, that leaves the γ-ray strength function around its peak the same and has effects below S_n [124]. The parameter $wtable$ is recommended for adjustment and can be adjusted for the type of radiation with values between 0 to 10. It is stated, that adjusted $wtable$ values are in a 15 %-range of 1 [124]. The values of $wtable$ for $E1$, $M1$ and $E2$, if possible, have been varied between 0.85 and 1.15 for the default parameters of c and δ, which show a reasonable level density. Examples for this are shown in Chapter A.3 and in Figures 4.18 and 4.19.

Figure 4.18 shows exemplary a value of $wtable = 0.99$ for $E1$ and variations of $\pm 15\%$ for $M1$ and $E2$ for the level density model 5 and the γ-ray strength function 8. The influence of the latter two is insignificant in the energy region of interest. Varying the $E1$ strength has the greatest impact and shifts the cross sections up the greater $wtable$ is. It does not change the steepness how the cross section changes with energy.

γ-ray strength function 9 is used in Figure 4.19. Since this function is not tabulated, it does not have a consistent $M1$ strength as explained in Section 2.2.3, wherefore only the $E1$ strength can be affected with the keyword $wtable$. As for level density model 5, the shape is not changed and a greater value shifts the cross sections up.

Again, neither a microscopic approach utilizing γ-ray strength model 8 [186] nor the phenomenological model 9 [184] are changed in a way with the keyword $wtable$ that the data are described in a better way. Therefore, the sensitivity for the different widths is contemplated to gain a better understanding of the deviation between the data and the different models.

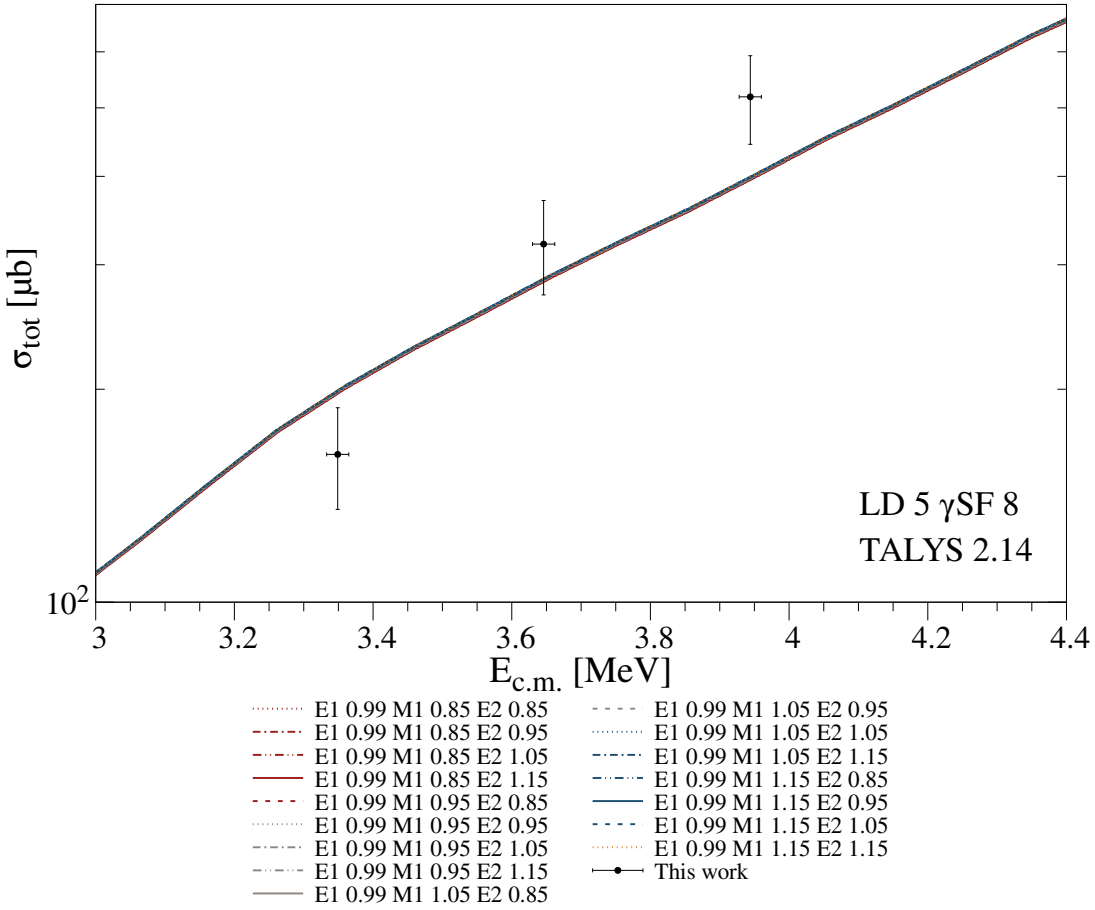

Figure 4.18: Varying the γ-ray strength function for strength model 8 with help of the parameter *wtable*. The influence of traditionally varying $M1$ and $E2$ is negligible. Varying $E1$ shifts the cross sections up and down and does not change the shape in the energy region of interest.

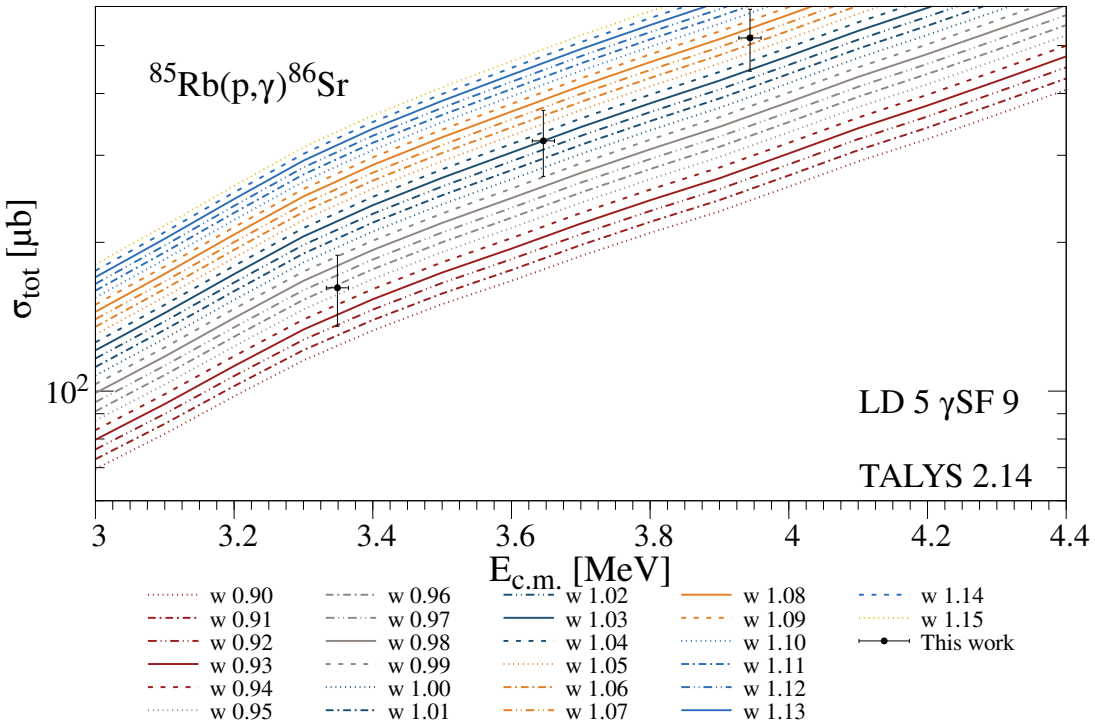

Figure 4.19: γ-ray strength function 9 is varied utilizing the keyword *wtable* in combination with level density model 5. This is applied to $E1$, since this strength function has no tabulated $M1$ values. The greater the value of *wtable*, the greater is the resulting cross section. The shape is preserved, wherefore the data are still not described by the model calculations.

4.5.3 Sensitivities to different Widths

Figure 4.20 shows the different absolute values of the sensitivities for when the γ, neutron (n), proton (p), and α widths are varied by a factor of two. Also shown in the neutron threshold (vertical line) as well as the Gamow window (dark shaded area), and the experimentally covered energy range (striped area). The cross sections in the experimentally covered area are approximately equally sensitive to variations in the different widths with exception to the α width. These widths cannot be changed with a parameter in the TALYS code unfortunately. However, there are certain quantities, that have an impact on different widths. The nuclear level density and the γ-ray strength function have an influence on the γ-widths [110]. The optical model potentials and properties of the different states influence the particle widths [110]. As can be seen in Figure 4.20 in the astrophysical relevant energy window below the (p, n)-threshold, the cross sections are determined by the proton width. In the experimentally covered energy window, the cross sections are additionally sensitive to the γ and neutron widths [110]. Since varying different aspects of the nuclear level density and the γ-ray strength function did not solve the discrepancies between the data and the model calculations, the assumption is, that the optical model potential might cause the deviation.[5]

4.5.4 Optical model potentials

The uncertainty regarding the role of different widths in explaining the difference between experiment and prediction can be partially resolved, because the proton width has been accurately measured in a previous study of the ^{85}Rb$(p, n)^{86}$Sr reaction [111, 140]. Earlier findings had led to a proposal to adjust the proton optical model potential (JLM) [137], which increases the isovector imaginary part of the potential by 70 % in order to reproduce (p, n) and (p, γ) reaction data [234]. Note, that all the calculations in the References were performed utilizing the NONSMOKER code [235]. In Reference [236], a comparison between calculated and experimentally obtained cross sections is shown. The calculations seem to agree well with the calculation, maybe underestimating the experimental data a bit. The comparison of the experimental S-factor to calculations shows a greater deviation, which is resolved using the modified JLM potential [111, 140, 236]. It should be noted, that the ^{85}Rb(p, n) cross section is predominantly sensitive to variations in the proton width in the energy range covered. This is a discrepancy to the (p, γ)-reaction that is additionally sensitive to the γ and neutron widths as shown in Figure 4.20. The default optical model potential implemented in the TALYS code [124] is the one of Koning and Delaroche [129]. This has been used up to now for the different calculations presented above.

[5] In most proton-induced experiments over the last years (see References [192, 194] and references therein), the optical model potential by Koning and Delaroche provided a good agreement with the experiments, wherefore varying this is considered as a last resort.

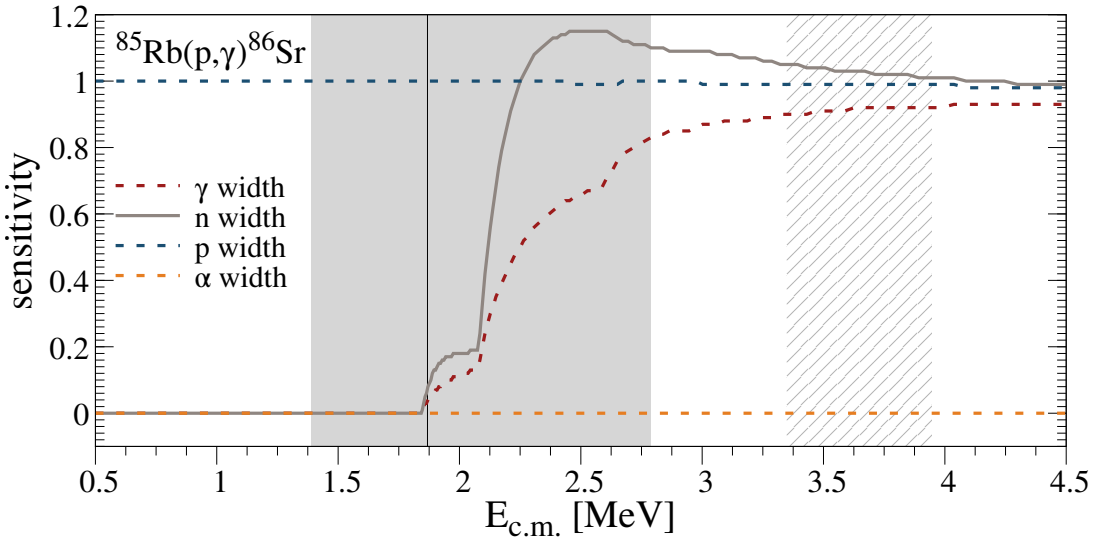

Figure 4.20: Absolute value of the sensitivity of the ^{85}Rb$(p,\gamma)^{86}$Sr laboratory cross section, when the γ, neutron (n), proton (p), and α widths are varied by a factor of 2, as a function of center-of-mass energy. The data are taken from Ref. [110]. The dark shaded area represents the Gamow window for a typical γ-process temperature of 3 GK. The vertical line shows the location of the neutron threshold. The striped area shows the experimentally covered energy region. The cross sections, that are experimentally obtained are approximately equally sensitive to changes in the proton, neutron, or γ widths. This, however, can not be changed as a parameter in TALYS unfortunately.

4.5.5 The Koning and Delaroche Optical Model potential

Due to the dependence of the (p,γ)-reaction on both γ- and neutron-widths, and the fact, that the (p,n)-reaction data are not well reproduced either, varying this potential alone might not resolve the discrepancy between experimental data and theoretical cross section predictions for the (p,γ) data. Unfortunately, there is no clear guidance provided on how to locally adjust the phenomenological optical model potential by Koning and Delaroche [129] – the default option in TALYS– to achieve a consistent description of (p,n) and (p,γ) data. Although a local parametrization for the neutron optical model potential exists and is implemented in the code, no corresponding local parameterization is available for protons [129]. This suggests that the global proton potential may not adequately describe the ^{85}Rb nucleus, resulting in the observed discrepancies between calculated and measured cross sections.

Consequently, a thorough examination of this potential is conducted. Since the (p,γ) reaction depends on three different widths in the studied energy region, the difference utilizing the Koning and Delaroche optical model potential [129] for cross section calculations to experimentally observed (p,n)-data are shown in Figure 4.21. It can be seen, that the potential overestimates the predicted cross sections compared to the data. As described in Section 2.2.1, the complete optical model potential of Koning and Delaroche [129] consists of several individual potentials. In total, TALYS provides 27 adjustable parameters for this model. Since this potential is split

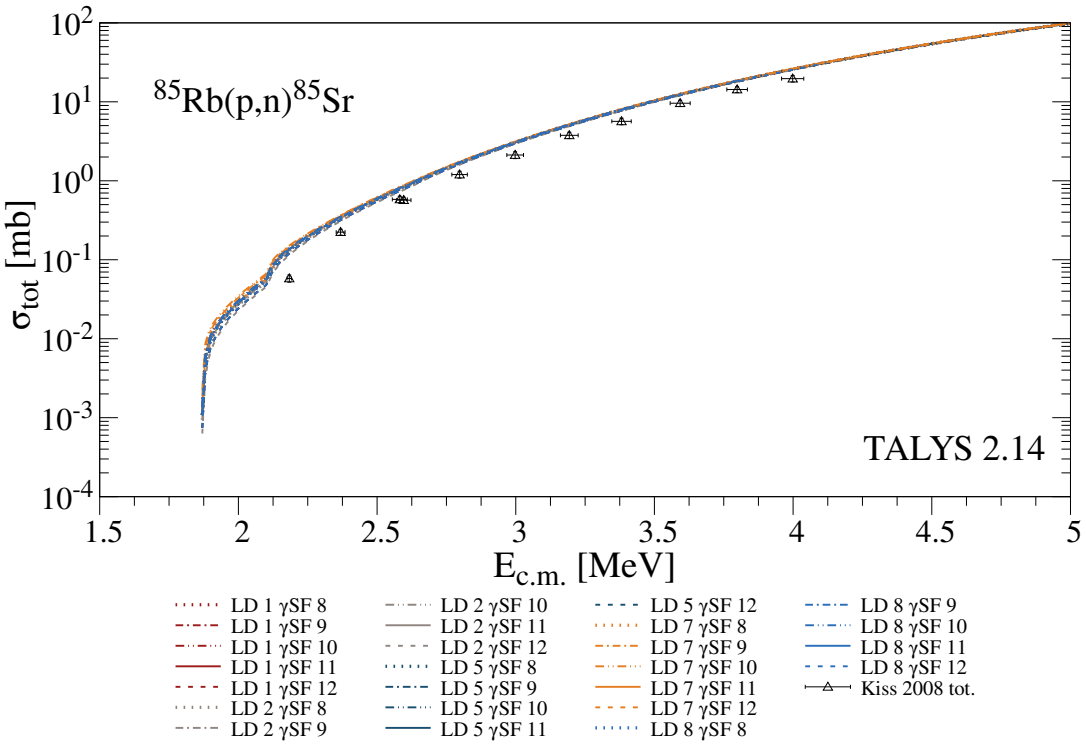

Figure 4.21: Utilizing the Koning and Delaroche optical model potential for comparing calculated cross sections to experimentally obtained (p, n)-data for different combinations of γ-ray strength models and nuclear level density models. As the calculations utilizing the JLM optical model potential [137], the predicted cross sections are again very similar for the different combinations and are overestimated in the energy region shown.

Table 4.7: The different parameters affecting the imaginary part of the optical model potential of Koning and Delaroche [129].

Affected Potential	Parameter keyword
Volume-central $W_V(E,r)$	rw, aw, $w1$, $w2$
Spin-orbit $W_{SO}(E,r)$	$rwso$, $awso$, $wso1$, $wso2$
Surface-central $W_D(r,E)$	rw, aw, $d1$, $d2$, $d3$

into imaginary and real parts as the JLM [135] potential, the assumption is made, that varying the imaginary part for this potential can also help to better describe the data as explained above. This reduces the parameters to 13. Taking a closer look in the TALYS description shows, that six parameters out of 13 describe the diffuseness a_i and the radius r_i of the nucleus as presented in Equation (2.19), which are given as not energy dependent but depend on the mass number A and are other than that constants for the volume-central, the spin-orbit, and the surface-central potential. Three of the remaining seven parameters directly scale the aforementioned potentials. For the remaining four, three influence the potentials in an inverse quadratic way ($\propto 1/x^2$) and one influences the surface-central potential in a $\exp(-d)$ way. The local neutron optical potential from [129] is used for neutrons, while the global parameterization is employed for protons, since no local fit exists for this case.

Table 4.7 summarizes the keywords used to modify the imaginary components of the KD potential. As discussed in Section 2.2.1, for scattering energies below 10 MeV, projectile absorption occurs mainly near the nuclear surface. Therefore, the surface-central potential $W_D(r,E)$ is expected to dominate in the present energy range.

All parameters were scaled within the range $x = 0.5$–2.0 using the `keywordadjust projectile x` command in TALYS, which multiplies the internal default value by x without requiring explicit knowledge of the original parameter value. The r and a parameters the rest are varied together for each part. This leads to the examples given in Figures 4.22 to 4.27. An overview of the remaining calculations are presented in Sections A.4.1 to A.4.5. The most pronounced sensitivity occurs for parameters related to the surface-central potential (rwd, awd, $d1$–$d3$), verifying the expected influence of $W_D(r,E)$ at low projectile energies. Variations of the volume-central parameters (rw, aw) produce only moderate shifts in absolute cross-section values, while changes in the spin–orbit terms ($rwso$, $awso$, $wso1$, $wso2$) have negligible impact.

Although the overall magnitude of the predicted cross sections can be influenced to some extent, none of these variations succeeds in reproducing the experimental data, indicating that imaginary-part adjustments alone are insufficient.

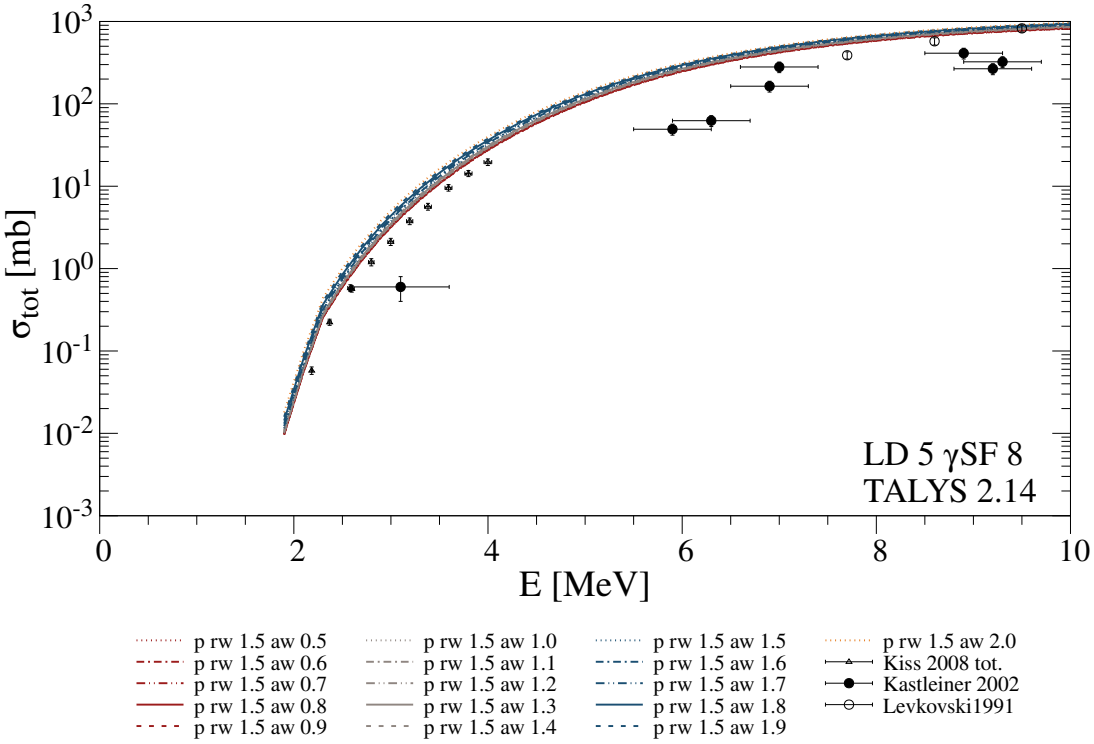

Figure 4.22: Varying the parameters rw and aw utilizing the TALYS [124] code version 2.14 in comparison to experimental obtained (p,n)-reaction cross sections from References [140, 237, 238]. Shown exemplary is $rw = 1.5$ with varying aw between 0.5 and 2.0. It is shown, that the main effect is a small up and down shift of the calculated cross sections.

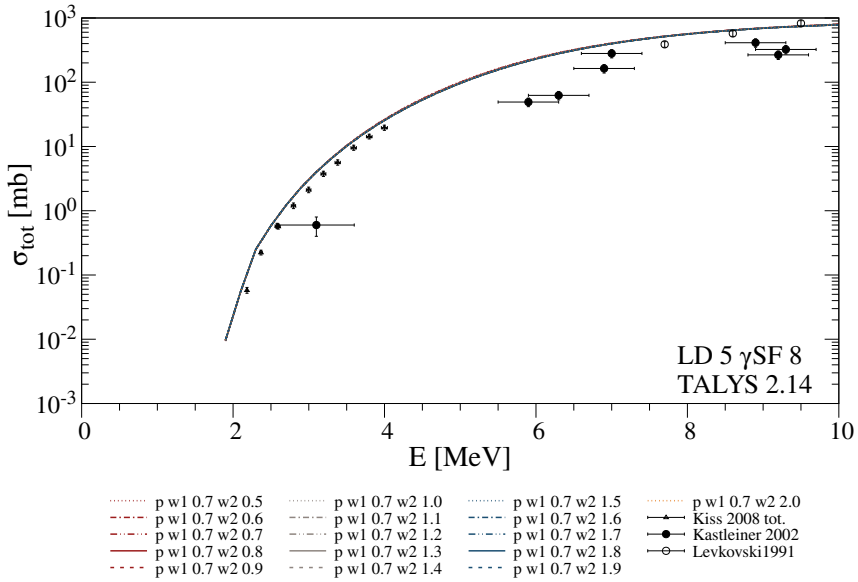

Figure 4.23: Varying the parameters $w1$ and $w2$ utilizing the TALYS [124] code version 2.14 in comparison to experimental obtained (p, n)-reaction cross sections from References [140, 237, 238]. Shown exemplary is $w1 = 0.7$ with varying $w2$ between 0.5 and 2.0. It is shown, that the effect is negligible for the calculated cross sections.

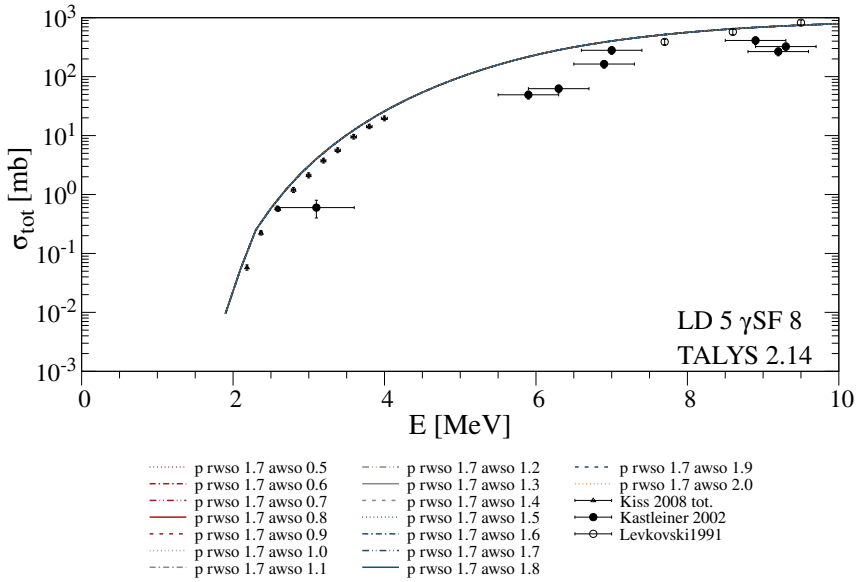

Figure 4.24: Varying the parameters $rwso$ and $awso$ utilizing the TALYS [124] code version 2.14 in comparison to experimental obtained (p, n)-reaction cross sections from References [140, 237, 238]. Shown exemplary is $rwso = 1.7$ with varying $awso$ between 0.5 and 2.0. It is shown, that the effect is negligible for the calculated cross sections.

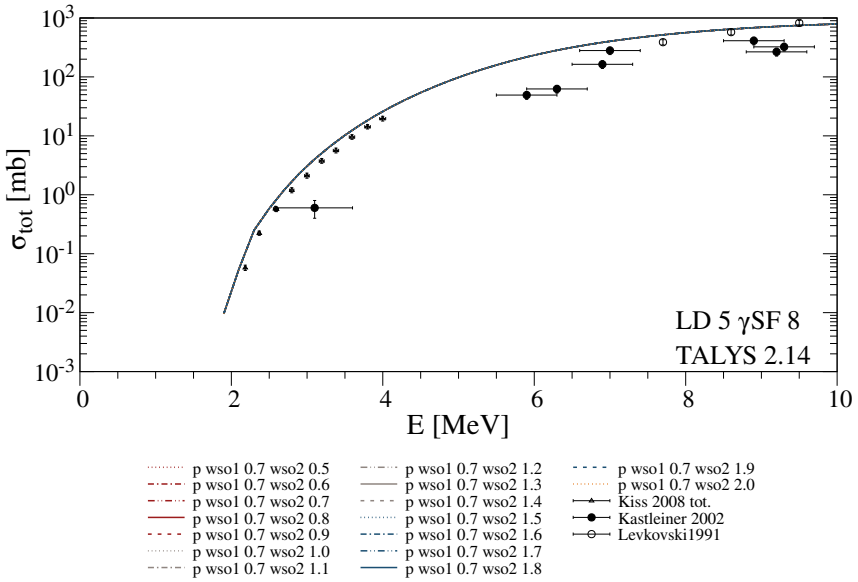

Figure 4.25: Varying the parameters $wso1$ and $wso2$ utilizing the TALYS [124] code version 2.14 in comparison to experimental obtained (p, n)-reaction cross sections from References [140, 237, 238]. Shown exemplary is $wso1 = 0.7$ with varying $wso2$ between 0.5 and 2.0. It is shown, that the effect is negligible for the calculated cross sections.

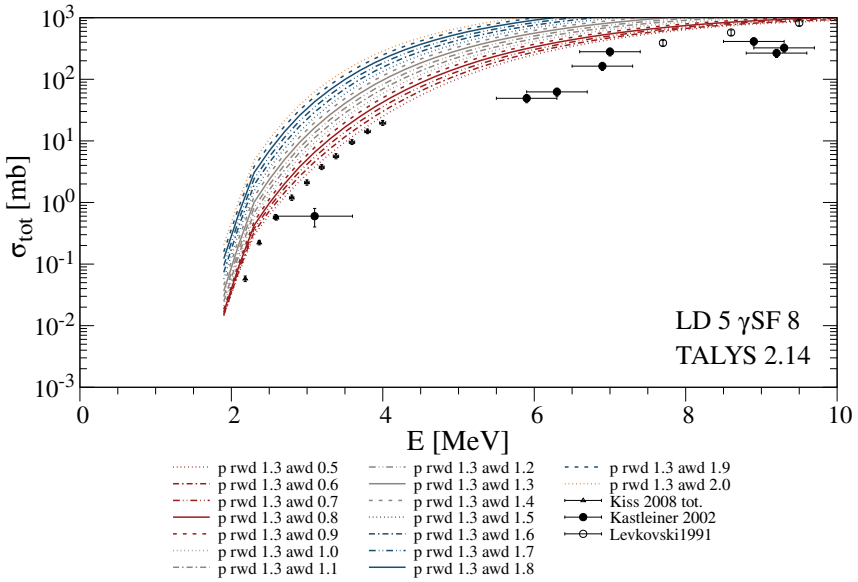

Figure 4.26: Varying the parameters rwd and awd utilizing the TALYS [124] code version 2.14 in comparison to experimental obtained (p, n)-reaction cross sections from References [140, 237, 238]. Shown exemplary is $rwd = 1.3$ with varying awd between 0.5 and 2.0. It is shown, that the effect is shifting the the calculated cross sections up with increasing the value of the awd parameter.

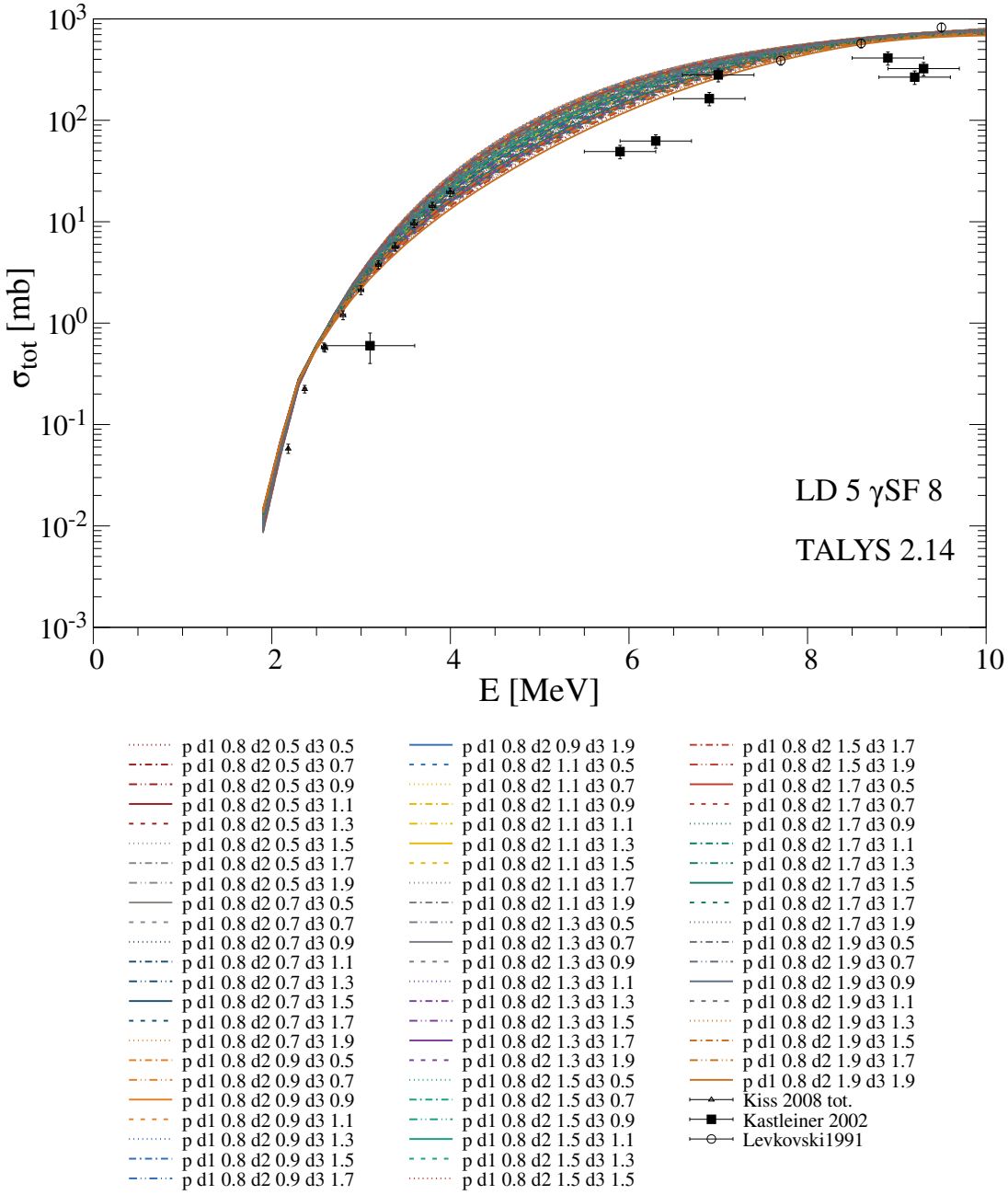

Figure 4.27: Varying the parameters $d1$, $d2$ and $d3$ utilizing the TALYS [124] code version 2.14 in comparison to experimental obtained (p, n)-reaction cross sections from References [140, 237, 238]. Shown exemplary is $d1 = 0.8$ with varying $d2$ and $d3$ between 0.5 and 2.0. The effect is most prominent for the energy range 3 MeV to 8 MeV, where it influences how steep the calculated cross sections change.

This leads to the conclusion, that the parameters of the real part of the proton optical model potential should be examined closer. The respective parameters are given in Table 4.8. The range to scale the parameters are the same as given above and are varied in a similar way as the parameters for the imaginary part.

As for the imaginary part of the potential, varying the different parts of the real part vary the cross sections differently. Among the real-part parameters, the strongest influence on the calculated cross sections arises from variations of rv, av, and $v1$. In contrast, modifications of the spin–orbit ($rvso$, $vso1$, $vso2$) and volume terms ($v2$, $v3$, $v4$) yield negligible changes. The parameters rvd and avd are also varied and show a change in the cross sections. However, they are normally kept at the default value in standard TALYS calculations and, thus, are not considered further [124]. The effect of varying rc is shown in Figure 4.28. As can be seen, the effect is not too strong and supporting that the description for the Coulomb term is valid. The variation of all other parameters described above are shown for chosen combinations in Sections A.4.6 to A.4.11.

It is worth noting, that there are combinations when varying rv together with av, that lead to a description of the experimental cross sections of the (p, n)-reaction. However, when investigating the influence on the cross section predictions of the (p, γ)-reaction, they do not describe the trend of the data as presented in Figure 4.29. This demonstrates that constraining the potential using only a single reaction channel is insufficient. Multiple channels must be simultaneously considered to properly define the model parameters.

To explore potential correlations, rv, av, and $v1$ were next varied together to see the simultaneous effect this has on the cross sections. This was chosen since varying these parameters alone achieve a fitting of the low lying experimental data, which is not given varying the remaining parameters regarding both potential parts, real and imaginary. rv is varied between 0.5 and 1.5, av between 0.5 to 1.3, and $v1$ between 0.5 and 2.0. This is presented Section A.4.12 for the different combinations of values rv, av, and $v1$. Varying all three parameters together lead to an improved fit to the data, but fails to describe the cross sections for the different reaction channels at once as presented in Figure 4.30. Consequently, the imaginary component must also be included to achieve a consistent description.

Table 4.8: The different parameters affecting the real part of the optical model potential of Koning and Delaroche [129].

Affected Potential	Parameter keyword
Volume-central $V_V(E, r)$	rv, av, $v1$, $v2$, $v3$, $v4$
Spin-orbit $V_{SO}(E, r)$	$rvso$, $vso1$, $vso2$
Coulomb $V_C(r)$	rc
Surface-central (?)	rvd*, avd*

*usually not used

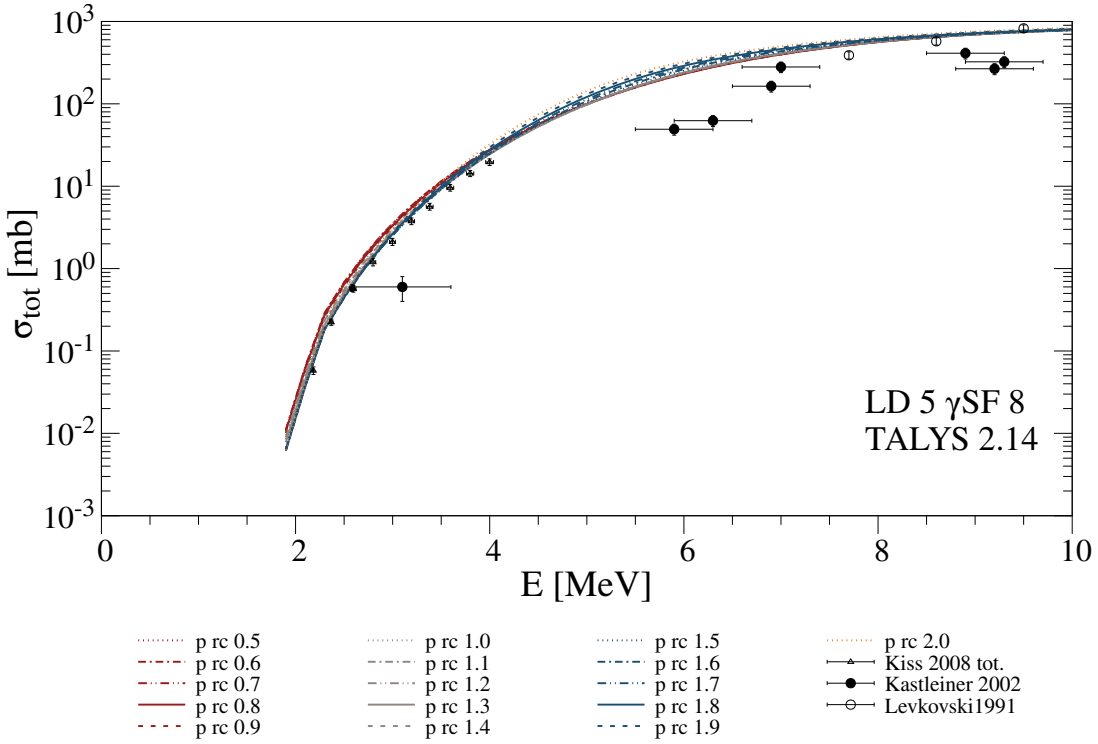

Figure 4.28: Varying the parameter *rc* utilizing the TALYS [124] code version 2.14 in comparison to experimental obtained (p, n)-reaction cross sections from References [140, 237, 238]. The variation seems to influence the calculated cross sections not too much. It is assumed that the description of the Coulomb potential part in the optical model potential is valid, wherefore this is not considered in the following.

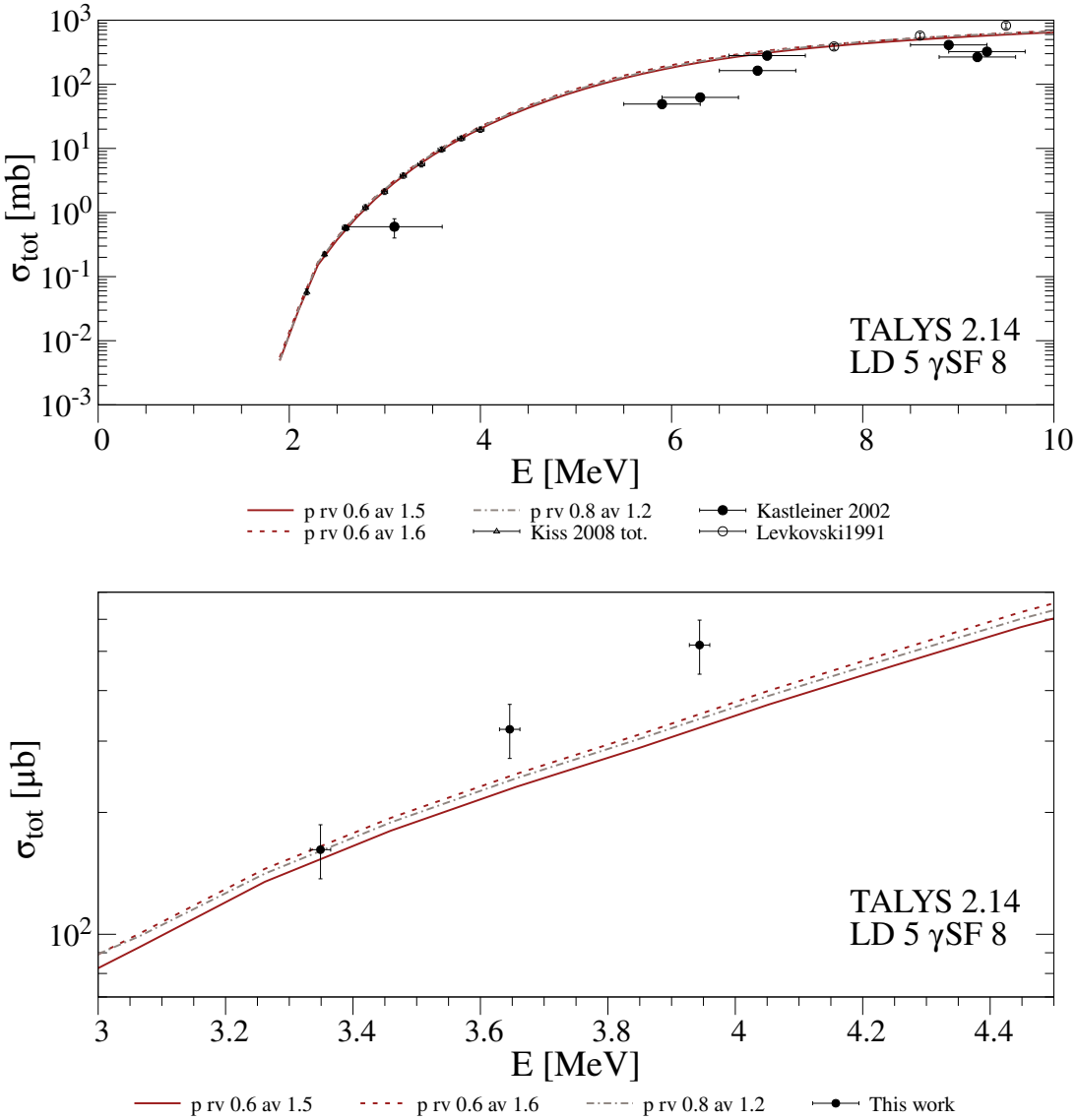

Figure 4.29: Combinations of rv and av that reproduce the (p, n) data (upper) but fail to describe the (p, γ) data (lower). The predicted (p, γ) cross sections exhibit a slope that is not steep enough compared to the experimental trend. This demonstrates that comparing only a single reaction channel is insufficient, wherefore multiple reaction channels need to be considered to properly constrain the model parameters.

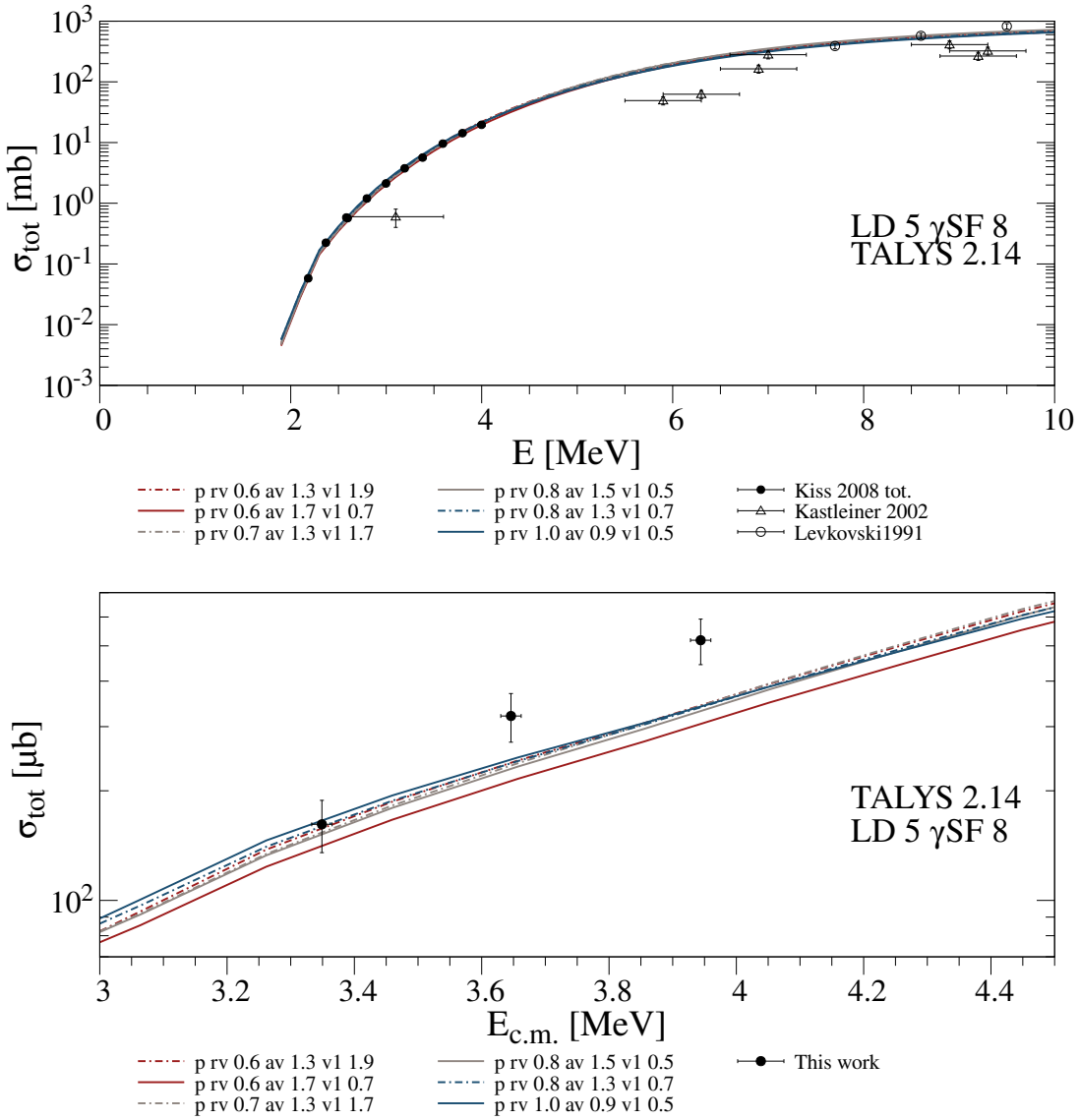

Figure 4.30: Combinations of rv, av and $v1$ that predict cross sections of the (p, n) data (upper), but fail to reproduce the cross sections of the (p, γ) data (lower). The predicted (p, γ) cross sections exhibit a slope that is not steep enough compared to the experimental trend. Therefore, additional parameters need to be taken into account.

A subsequent analysis therefore varied *rwd*, *awd*, *d*1, *d*2, and *d*3 simultaneously. This adjustment improved the fit to the data, but fails in describing the cross sections at low and high energies at once. These variations are shown in Section A.4.13. Among these, the *awd* parameter again showed the largest impact, consistent with previous results for the surface-central term.

As a consequence, all eight parameters, that have been varied together in different subcombinations are now varied at once to see the total influence it has on describing the data. For this, each parameter was varied in steps of 0.15 in the range of 0.85 to 1.15. The different combinations that resulted in describing the (p, n) data are presented in Section A.4.14. An exemplary combination is shown here in Figure 4.31. Although many combinations result in a good cross section prediction of the (p, n) data, non of them predict the cross sections of the (p, γ)-reaction. However, an improvement of describing the two different reaction channels is definitely made.

Taking a step back from varying eight parameters simultaneously, a final approach was to adapt the model by varying only the parameters *rwd*, *awd*, *rv*, and *av* in order to investigate their direct influence on the predicted cross sections. Each parameter was varied in steps of 0.2 within the range from 0.5 to 2.0. This approach yielded two parameter combinations for which the predicted cross sections almost reproduce both experimental datasets for the different reaction channels, as presented in Figure 4.32. A finer parameter grid and the inclusion of additional variables could further improve the agreement. However, with 27 parameters and a vast number of possible combinations, such an optimization becomes computationally demanding and beyond the scope of this work.

In summary, the systematic variation of the Koning and Delaroche [129] optical model potential at low energies reveals clear limitations of the global parameterization when applied to proton-induced reactions on ^{85}Rb. While adjustments of the surface and volume terms can improve the agreement with (p, n) data, no single parameter set reproduces both (p, n) and (p, γ) cross sections simultaneously. The analysis indicates that the surface-central potential, particularly the diffuseness parameter *awd* and the real volume parameters r_v and a_v have the strongest influence on the calculated results, emphasizing the need for improved constraints on the proton optical model potential for ^{85}Rb. The results underscore that purely phenomenological scaling of the existing global potentials is insufficient. Instead, dedicated optical model potential studies and complementary elastic-scattering data are required to achieve a consistent and predictive description of both reaction channels in this mass region.

The analysis of the phenomenological Koning and Delaroche [129] optical model potential has shown that, despite its flexibility, the adjustment of up to 27 interdependent parameters remains computationally demanding and does not yield a consistent description of both reaction channels with the tested parameter combinations. To overcome these limitations, the focus is now shifted to the microscopic JLM optical model potential [135, 136], which is derived from nucleon–nucleon interactions in nuclear matter and thus offers a more physically grounded framework with fewer effective parameters to vary.

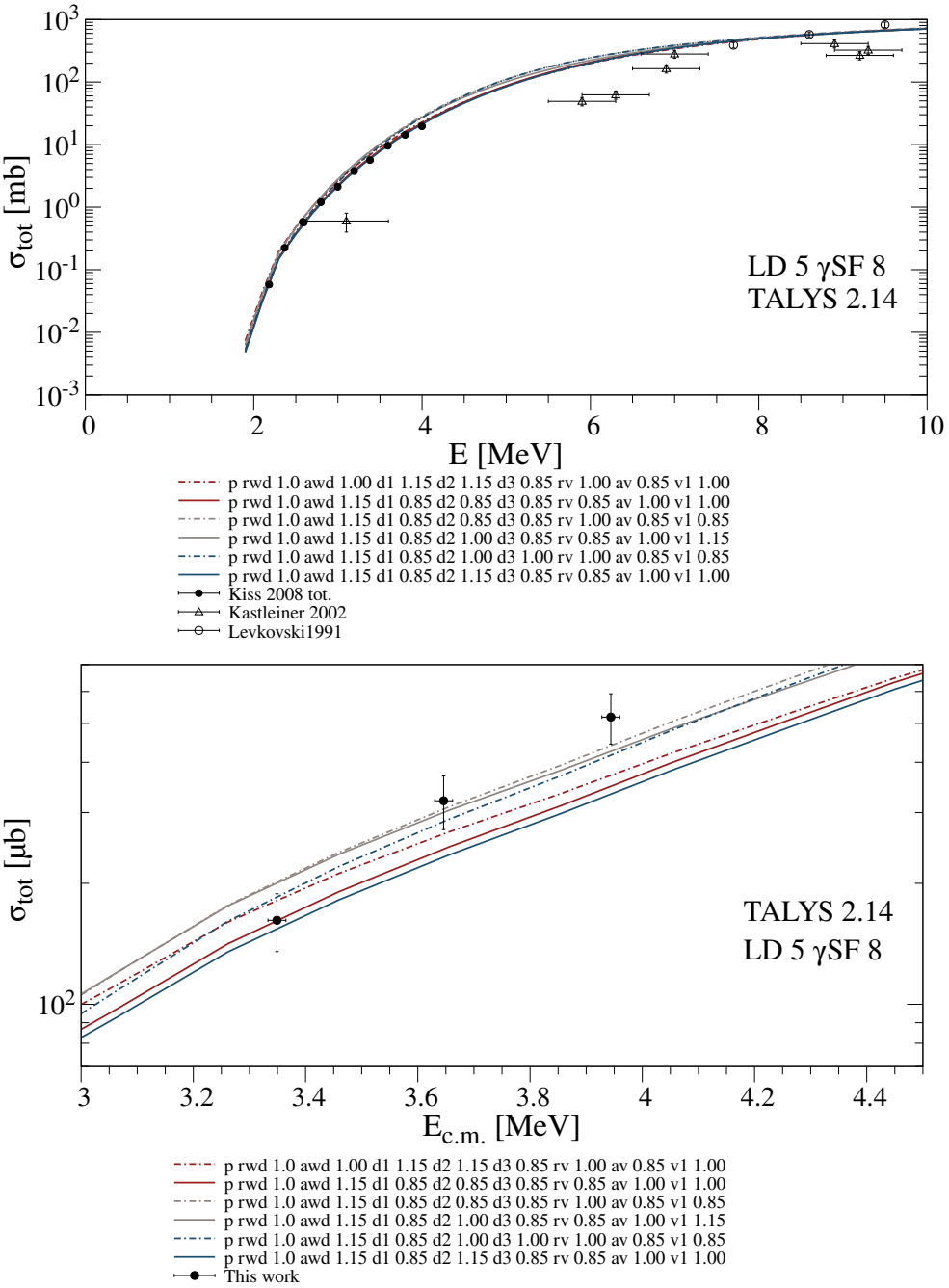

Figure 4.31: Exemplary parameter combinations describing the (p, n) data obtained by varying eight parameters of the Koning–Delaroche optical model potential, together with their corresponding predictions for the (p, γ) data. Although several parameter combinations yield comparable agreement for the (p, n) data, none successfully reproduce the experimental (p, γ) results.

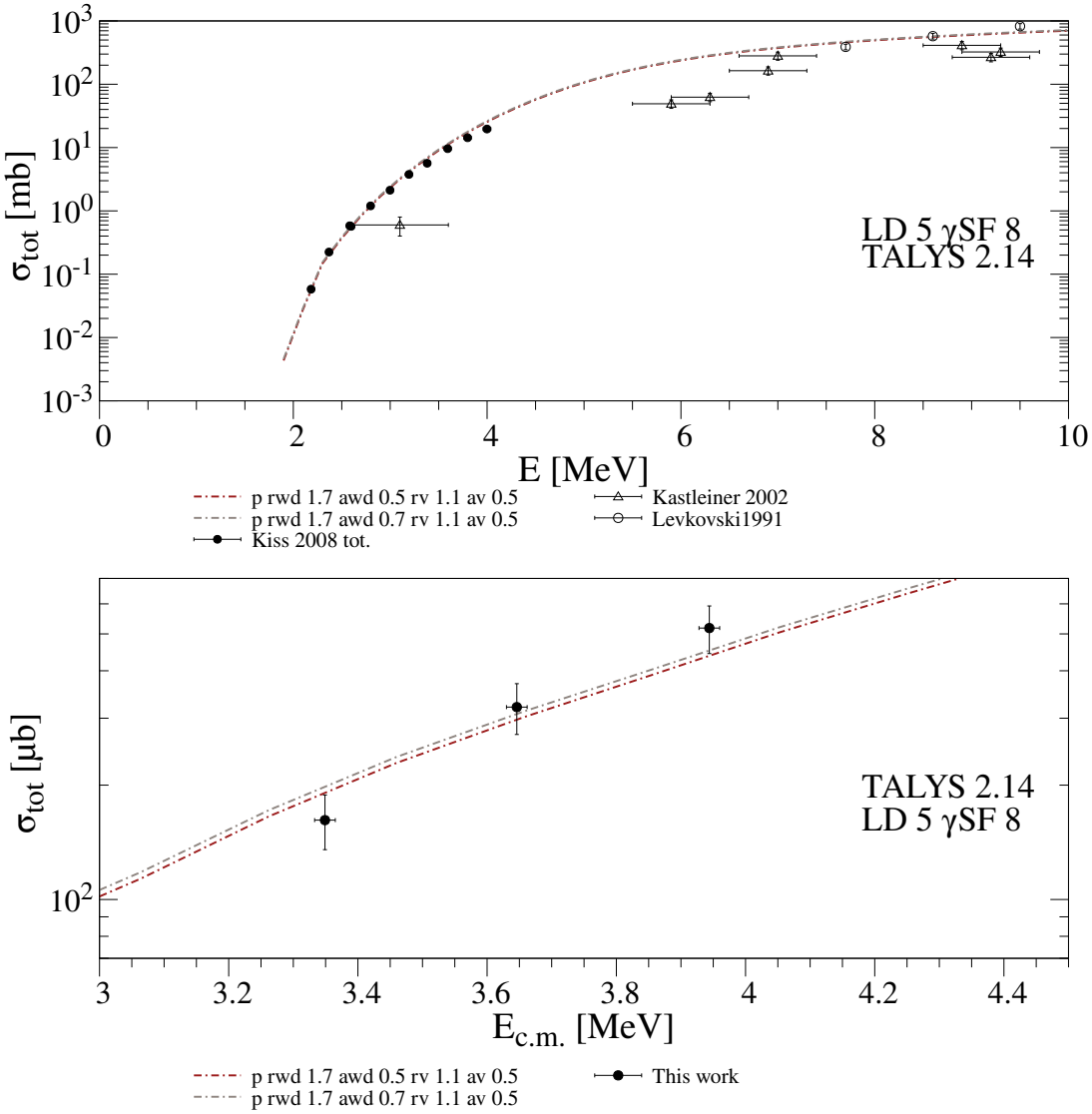

Figure 4.32: Variation of the parameters *rwd*, *awd*, *rv*, and *av* of the Koning–Delaroche optical model potential to investigate their direct influence on the predicted cross sections. Each parameter was varied in steps of 0.2 within the range from 0.5 to 2.0. Two parameter combinations were found for which the predicted cross sections almost reproduce both experimental data sets for the (p, n) and (p, γ) reaction channels.

4.5.6 The JLM optical model potential

Because the implemented γ-ray strength function and the nuclear level density significantly influence the cross section predictions, especially for (p,γ)-reactions, these parameters were varied in the same way as before (cf. Figure 4.11) utilizing the JLM optical model potential for cross section calculations comparing both the experimentally obtained (p,n)- and (p,γ)-cross-section data as shown in Figures 4.33 and 4.34. The (p,n)-cross section data from References [234, 237, 238] in the energy range below 8 MeV presented in Figure 4.33 are overpredicted. It is, however, interesting, that both the JLM [137] and the Koning and Delaroche [129] (cf. Figure 4.21) optical model potential over estimate the cross sections for the (p,n)-reaction compared to the data in Reference [140] in their default settings. Note, that the data obtained in Reference [238] show significant scatter due to large uncertainties in the beam energies and the cross sections and, therefore, are not used for the comparison directly. They serve as a lower limit when varying the model parameters. The different combinations of γ-ray strength models and nuclear level density models give nearly similar results. This is a contrast to the (p,γ)-data obtained in this thesis and presented in Figure 4.34. These combinations give very different results, deviating up to an order of magnitude. The obtained data are not described by one combination, since the experimentally determined cross section has a much steeper trend than the combinations predict. In the experimentally investigated energy region, the general trend is similar to the predictions for the optical model potential by Koning and Delaroche [129] as presented in Figure 4.11.

Since the optical model potential JLM implemented in the TALYS code has some freedom to be adjusted, different keywords influencing the imaginary and real part of the potential have been investigated. The keywords are *lwadjust*, *lw1adjust*, and *lwsoadjust* being multiplication factors to the implemented default values in a range from 0.5 to 1.5 and serve as normalization factors for the imaginary central potential, the imaginary isovector potential, and the imaginary spin-orbit potential, respectively [124]. The respective real parts are described by the same keywords by exchanging w with v. Note, that with the given range, an adjustment with a factor 1.7 as described above is not possible. Reference [234] states, that adopting the original real strength a bit lead to the best agreement for (p,n) and (p,γ) data in their study. The number of keywords compared to the Koning and Delaroche model is significantly lower, which reduces computing time.

Be aware, that the variation of the real and imaginary parts of the central potential through the parameters *lvadjust* and *lwadjust* represents a local adjustment of the JLM optical model to the experimental data in the astrophysically relevant energy range. This approach follows the general philosophy of Bauge *et al.* [137], where the global normalization factors of the real and imaginary, isoscalar and isovector components of the potential were iteratively tuned to reproduce proton and neutron elastic scattering, quasielastic (p,n), and reaction data in the 20 MeV to 50 MeV range. In contrast to that global optimization, the present work explores localized variations of the real and imaginary normalization factors to improve the agreement with reaction cross sections at low energies, where the model is less constrained. Due to the absence of experimental elastic-scattering data for the studied nucleus, these parameter adjustments

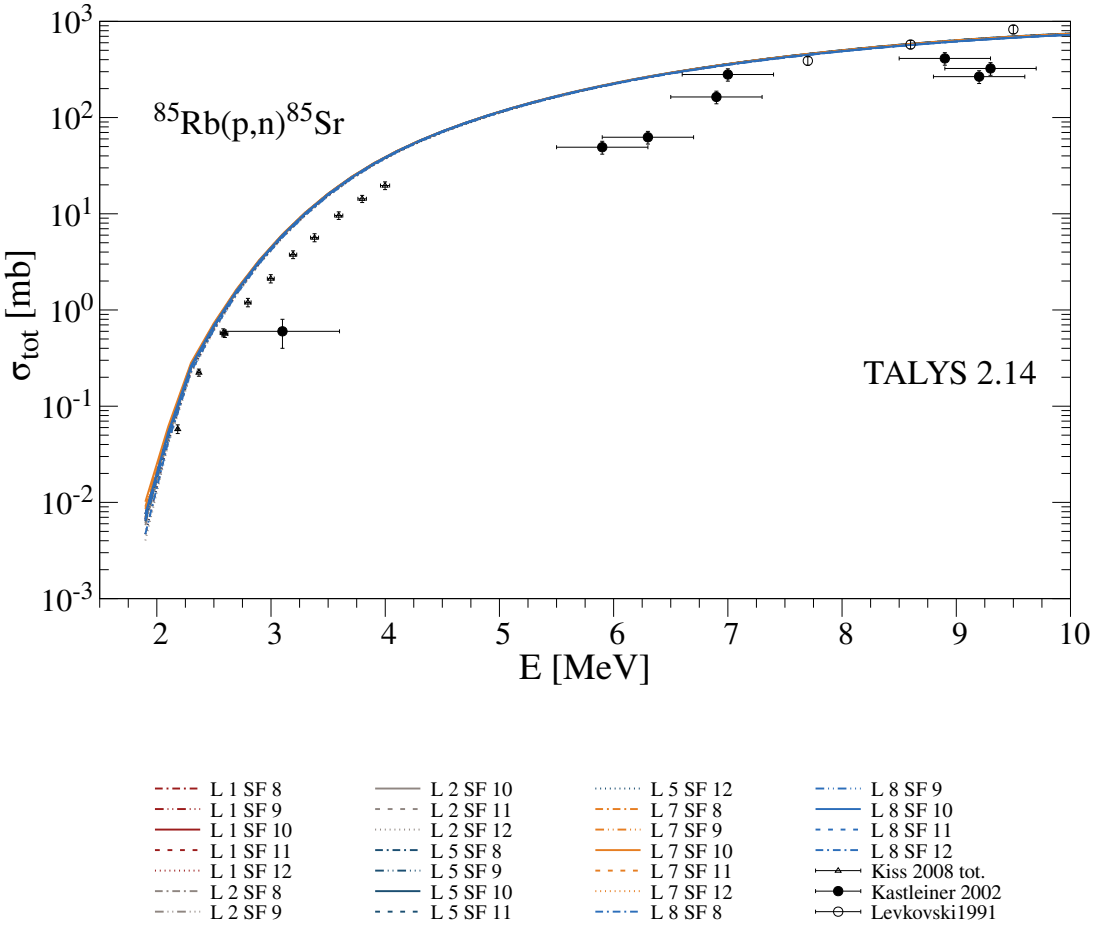

Figure 4.33: The comparison is performed between the optical model potential JLM [137] explained in the text and the (p, n)-data obtained in References [140, 237, 238]. The cross sections in the energy range below 8 MeV are overpredicted. The data from Reference [238] is scattering a lot due to large uncertainties both, in the energy and the cross section. Therefore, the calculated cross sections are compared to the data in References [140, 237], which seem to predict the trend of the cross sections more reliable. The combinations of level density models and γ-ray strength models were chosen according to the recommendations in Section 2.3. It is worth noting, that all the models give nearly similar results with the same deviation from the experimental data.

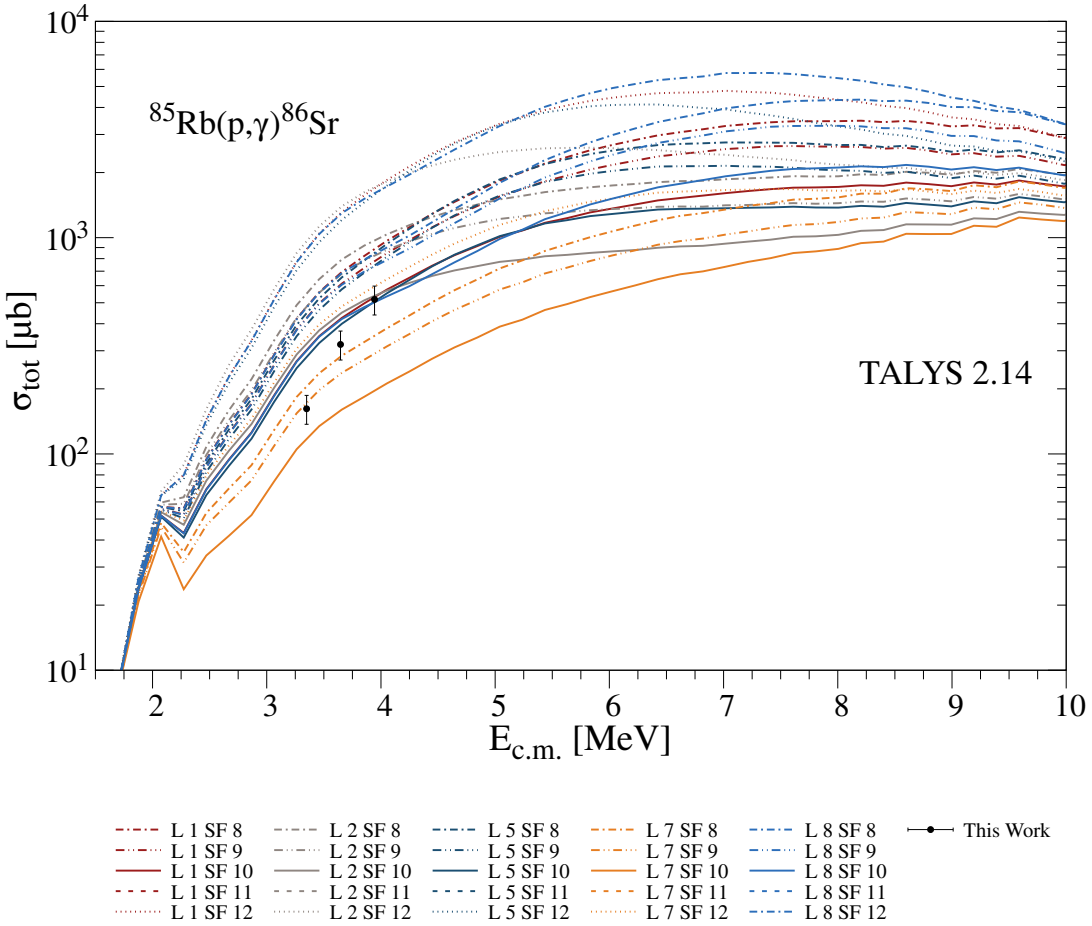

Figure 4.34: The comparison is performed between the optical model potential JLM [137] explained in the text and the (p, γ)-data obtained in this thesis. The combinations of level density models and γ-ray strength models were chosen according to the recommendations in Section 2.3. It is worth noting, that all the combinations give very different results, deviating up to an order of magnitude. The general trend up to 4.5 MeV is similar. At higher energies some models predict a more constant cross section than others. The obtained data are not described utilizing one combination. In the experimentally investigated energy region, the trend is similar to the predictions for the optical model potential by Koning and Delaroche [129] as presented in Figure 4.11.

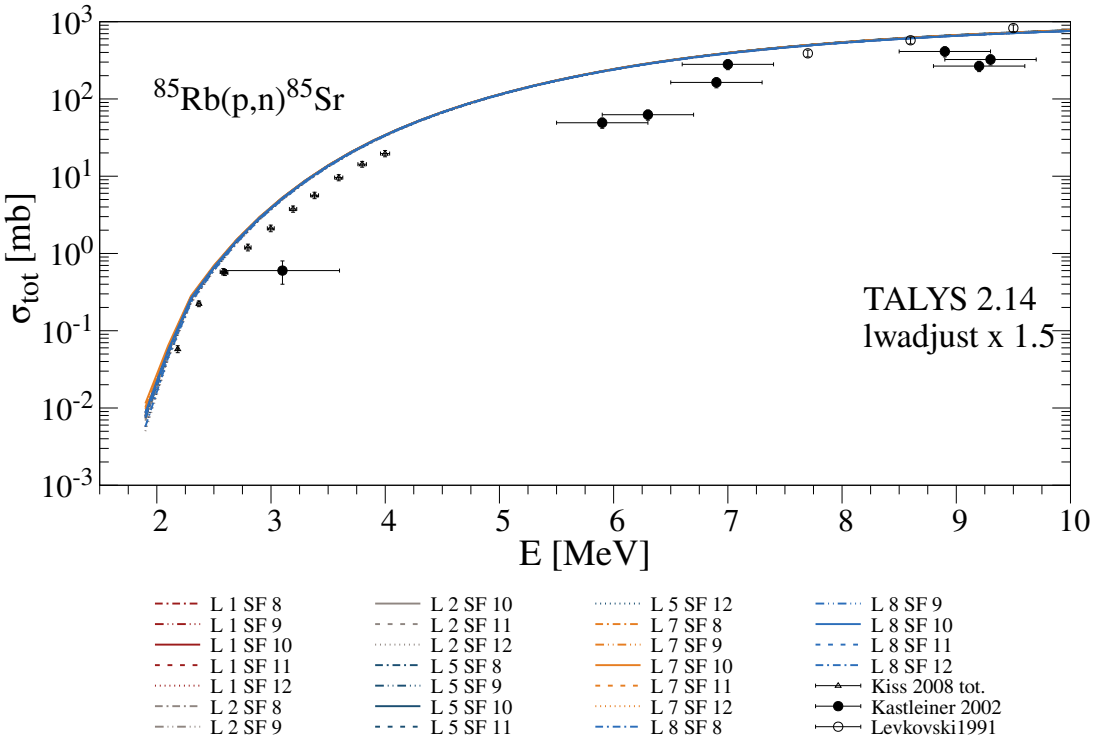

Figure 4.35: The influence of varying the imaginary central potential with *lwadjust* = 1.5 on the cross sections for the (p, n)-reaction. The cross sections are lower compared to not adjusting the imaginary central potential. The overall trend of the cross section calculations is in agreement with the trend of the experimentally obtained cross sections. However, the predictions overestimate the experimental data of Kiss [140].

cannot be independently validated, and their applicability remains limited to a phenomenological refinement within the framework of the JLM potential. Nevertheless, such localized tuning provides valuable insight into the model sensitivities and may guide future experimental efforts, particularly elastic-scattering measurements that would allow a more direct constraint of the optical potential at astrophysical energies.

The influence of varying the imaginary central potential with *lwadjust* = 1.5 on the cross sections for both reactions is shown in Figures 4.35 and 4.36. The cross sections are shifted a bit down for both reaction types. However, this adjustment still does not describe the experimental data. The overall trend in Figure 4.35 is good. The steepness of the experimental data presented in Figure 4.36 is still not represented by the model calculations. Changing the imaginary central potential alone, does not solve the differences between the data and the model calculations.

Varying the real central potential as a whole leads to a significant reduction of the calculated cross-section values. In the present case, both data sets (cf. Figures 4.37 and 4.38) are better reproduced when the real central potential is increased. In general, the agreement with the experimental data improves for *lvadjust* values greater than the default of 1. In addition to the

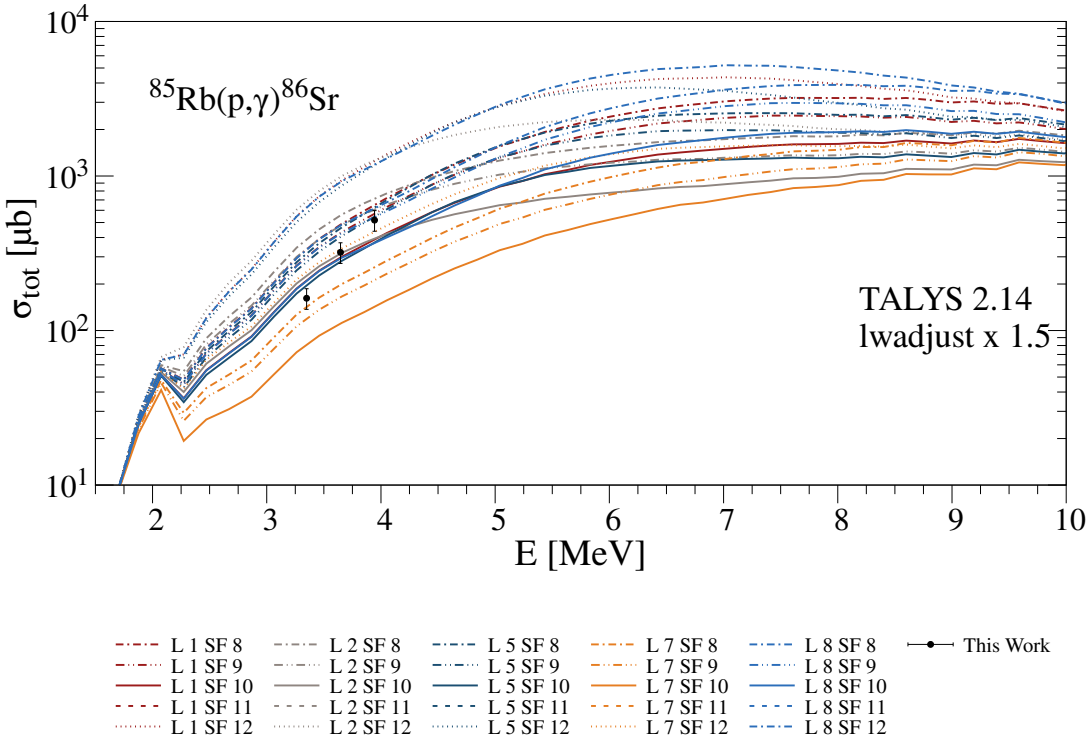

Figure 4.36: The influence of varying the imaginary central potential with $lwadjust = 1.5$ on the cross sections for the (p,γ)-reaction. Compared to not adjusting the JLM potential at all, the cross sections are lower. Since the general trend is not changed, the steepness of the experimental data are still not reproduced by the cross section calculations utilizing this adjustment.

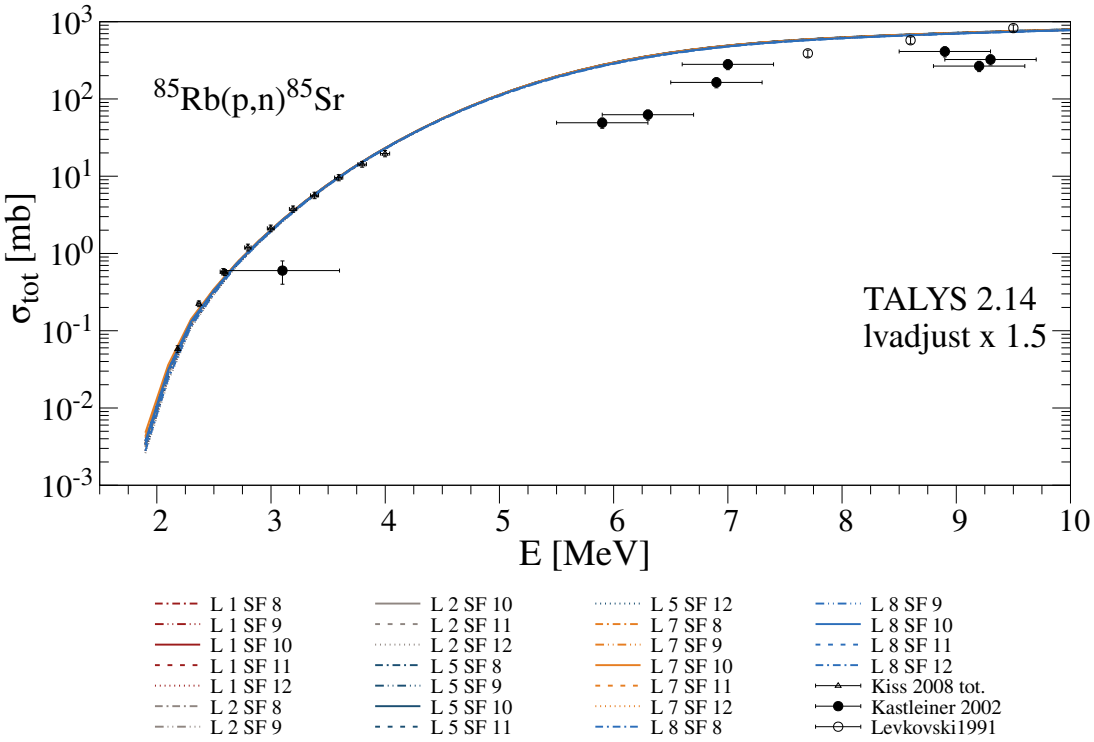

Figure 4.37: The influence of varying the real central potential with *lvadjust* = 1.5 on the cross sections for the (p, n)-reaction. Again, the calculated cross sections are lower for the lower half of the shown energy region compared to not adjusting the imaginary central potential. The predictions describe the experimental data of Kiss [140] within their uncertainties. The calculations would fit the experimental data better if the trend of the predicted cross sections were steeper around 2.5 MeV and slightly flatter around 4 MeV.

overall lower cross-section predictions for the lower half of the shown energy region, the shape of the calculated (p, γ) cross sections changes towards a steeper energy dependence, which follows the experimentally observed trend much more closely. However, none of the tested combinations of level-density models and γ-ray strength functions is able to fully reproduce the experimentally obtained (p, γ)-data.

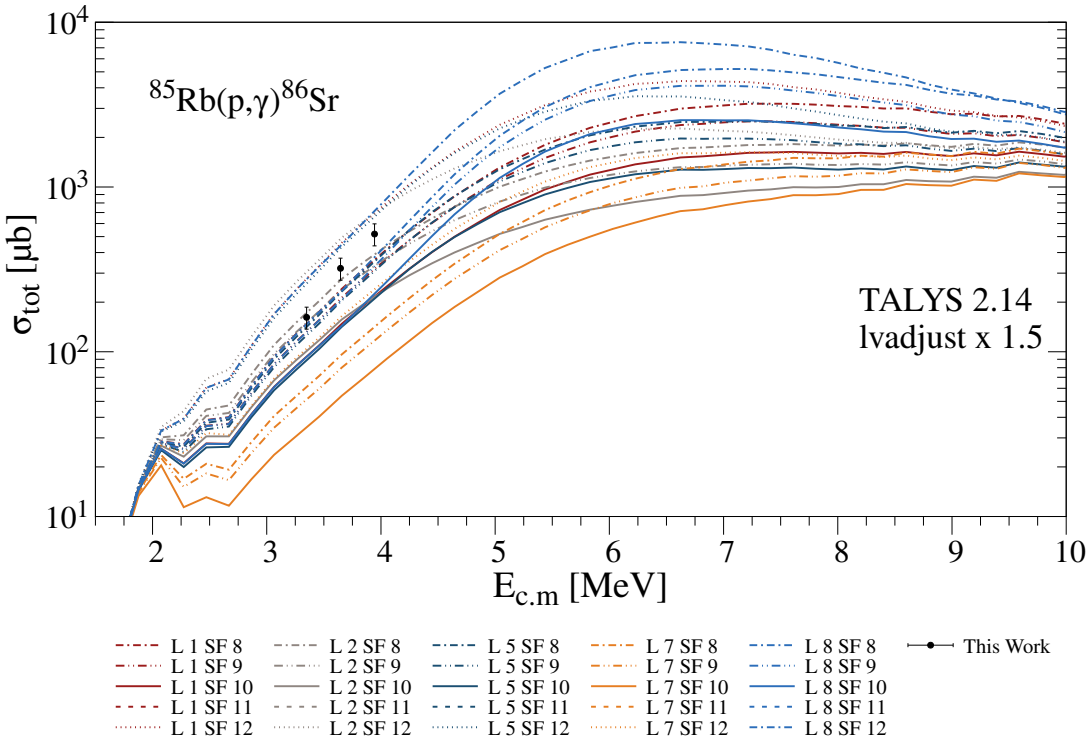

Figure 4.38: The influence of varying the real central potential with *lvadjust* = 1.5 on the cross sections for the (p,γ)-reaction. Compared to not adjusting the JLM potential at all, the cross section predictions are reduced for the lower part of the shown energy range. The general trend is changed, the steepness of the experimental data are reproduced by the cross section calculations utilizing this adjustment. However, still no single combination of level density model and γ-ray strength function describes the obtained data.

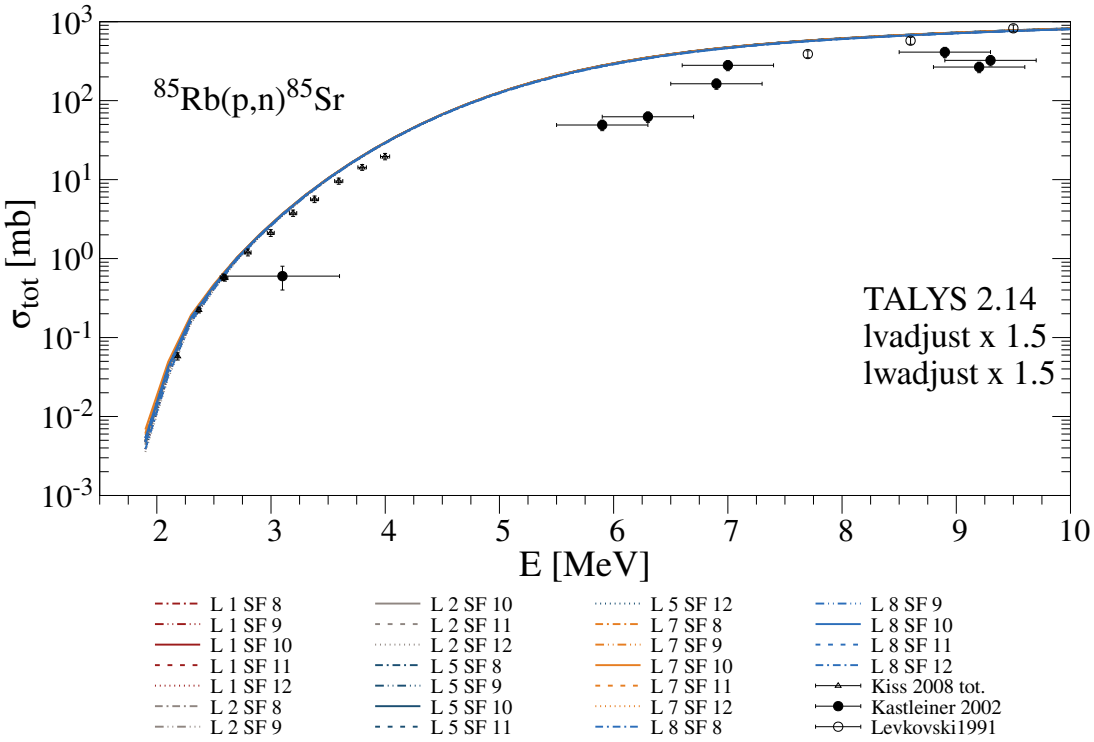

Figure 4.39: Scaling of the real and imaginary parts of the central potential by a factor of 1.5 using the parameters *lvadjust* and *lwadjust* for (p, n)-reaction. This reduces the agreement between the predictions and the data in the energy range of 3 MeV to 4 MeV. Up to 3 MeV, the experimental data and the predictions agree within the uncertainties.

As a next step, both the real and imaginary parts of the central potential were scaled by a factor of 1.5 using the parameters *lvadjust* and *lwadjust*. The results are shown in Figures 4.39 and 4.40. The predicted cross sections for the (p, n) reaction are significantly lower, as shown in Figure 4.39. Up to 3 MeV, the experimental data and the predictions agree within the uncertainties. Between 3 MeV to 4 MeV, however, the calculated cross sections exceed the experimentally determined values, resulting in a slope that is too steep. Taking a closer look at Figure 4.40, the (p, γ) data are now described by three different combinations of level density models and γ-ray strength functions, namely *ldmodel* 1 and *strength* 8, *ldmodel* 5 and *strength* 8, and *ldmodel* 7 and *strength* 8. The combination of level density model 5 and γ-ray strength model 8, since they show a good agreement to the data as presented above, strengthens its reliable predictions in experiments over the last years ([194, 233]). Up to an energy of 4 MeV, these combinations show a very similar trend. Above 4 MeV, they reach their respective maximum cross sections at different energies. Due to the limited energy range covered in this experiment, it cannot be determined which combination provides the best overall description of the data.

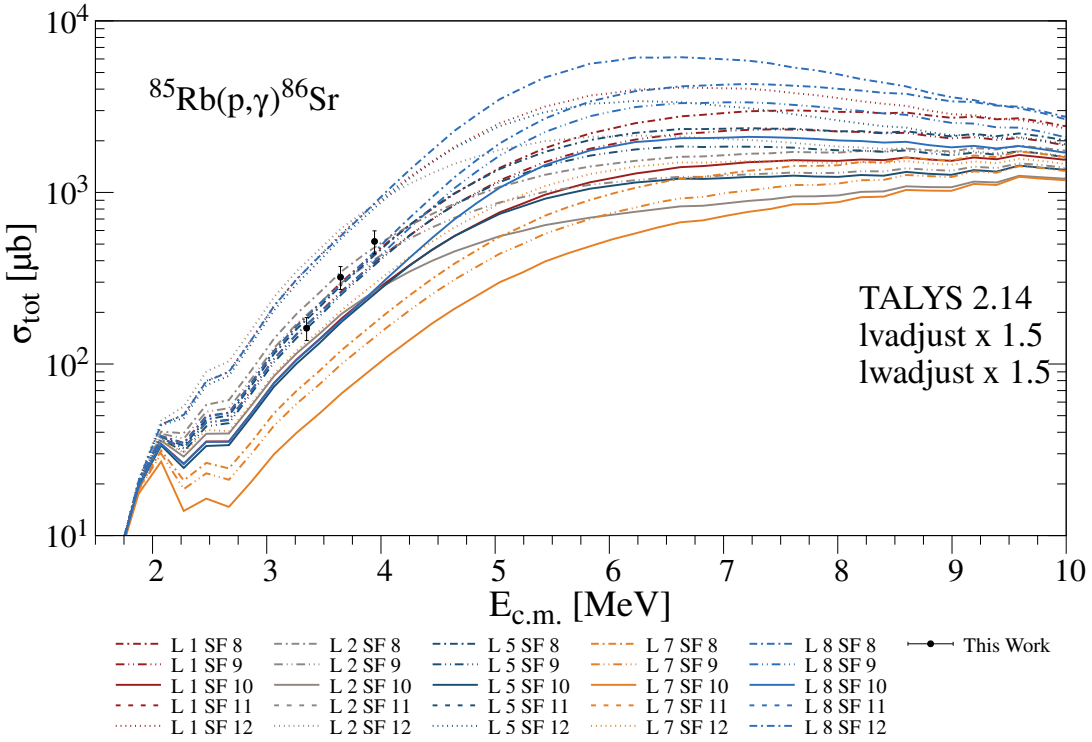

Figure 4.40: Scaling of the real and imaginary parts of the central potential by a factor of 1.5 using the parameters *lvadjust* and *lwadjust* for (p,γ)-reaction. Up to an energy of 4 MeV, these combinations show a very similar trend. Above 4 MeV, they reach their respective maximum cross sections at different energies. Due to the limited energy range covered in this experiment, it cannot be determined which combination provides the best overall description of the data.

Since the calculated (p, n) cross sections are not in agreement with the data from Reference [140], overestimating the experimental values in the measured energy range, the combination of *ldmodel* 5 and *strength* 8 was selected for systematic variation of *lwadjust* and *lvadjust* in steps of 0.1. The influence of the parameter combinations on cross section predictions are presented in Chapter A.5. Those yielding consistent results for both the (p, n) and (p, γ) reactions are shown in Figures 4.41 and 4.42. A good agreement is obtained for *lwadjust* values between 1.0 and 1.4 and $lvadjust = 0.6$.

A finer parameter scan, varying *lwadjust* between 1.0 and 1.4 in steps of 0.05 and *lvadjust* between 0.5 and 0.7 in steps of 0.02, indicates the best agreement for *lwadjust* values between 1.20 and 1.40 at $lvadjust = 0.60$. Unfortunately, no elastic-scattering cross-section data are available to confirm or challenge any of these parameter combinations.

In summary, the systematic study of the JLM optical model potential in the low-energy regime relevant for the γ-process has demonstrated to be more efficient that the study of the Koning and Delaroche [129] optical model potential. The JLM model provides a reasonable overall description for the trend of the (p, n) data, but overestimates them in the energy region between 2 MeV to 4 MeV and does not reproduce the general energy dependence of the measured (p, γ) cross sections when used in its default settings. None of the tested combinations of level density and γ-ray strength models achieves a consistent description of the experimental results.

The variation of the real and imaginary normalization factors (*lvadjust*, *lwadjust*) reveals a strong influence on the calculated cross sections. Local adjustments can improve the agreement with experimental data in certain energy intervals, yet they cannot simultaneously describe both reaction channels with a single parameter set, when only varying *lwadjust* or *lvadjust*. This underlines that the standard JLM potential — originally optimized for higher energies — may require further refinement or energy-dependent modifications to reliably describe reactions at low energies.

The lack of experimental elastic-scattering data for the studied nuclei prevents an independent validation of the adjusted parameters. Consequently, the present variations should be seen as a sensitivity analysis rather than a full re-parametrization of the potential. Nonetheless, the results highlight which parts of the model have the strongest influence on the calculated reaction cross sections.

Overall, the adjustment of the JLM potential improves the agreement with the measured cross sections, yet a consistent description of both (p, n) and (p, γ) data remains challenging, highlighting the need for further experimental and theoretical constraints in this mass region.

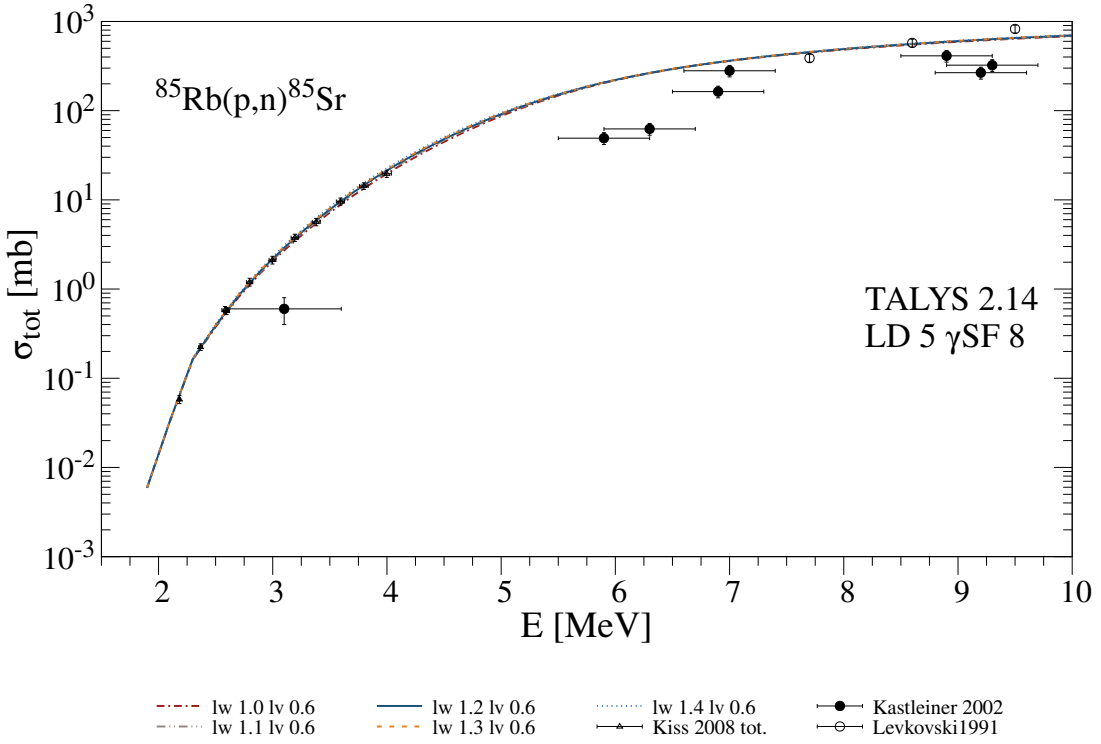

Figure 4.41: Scaling of the real and imaginary parts of the central potential by a factor of 0.6 for the real part (*lvadjust*) and by factors between 1.0 and 1.4 for the imaginary part (*lwadjust*) for the (p, n) reaction. The predicted cross sections show minor variations in the energy range of 3 MeV to 6 MeV, while overall they are in good agreement with one another.

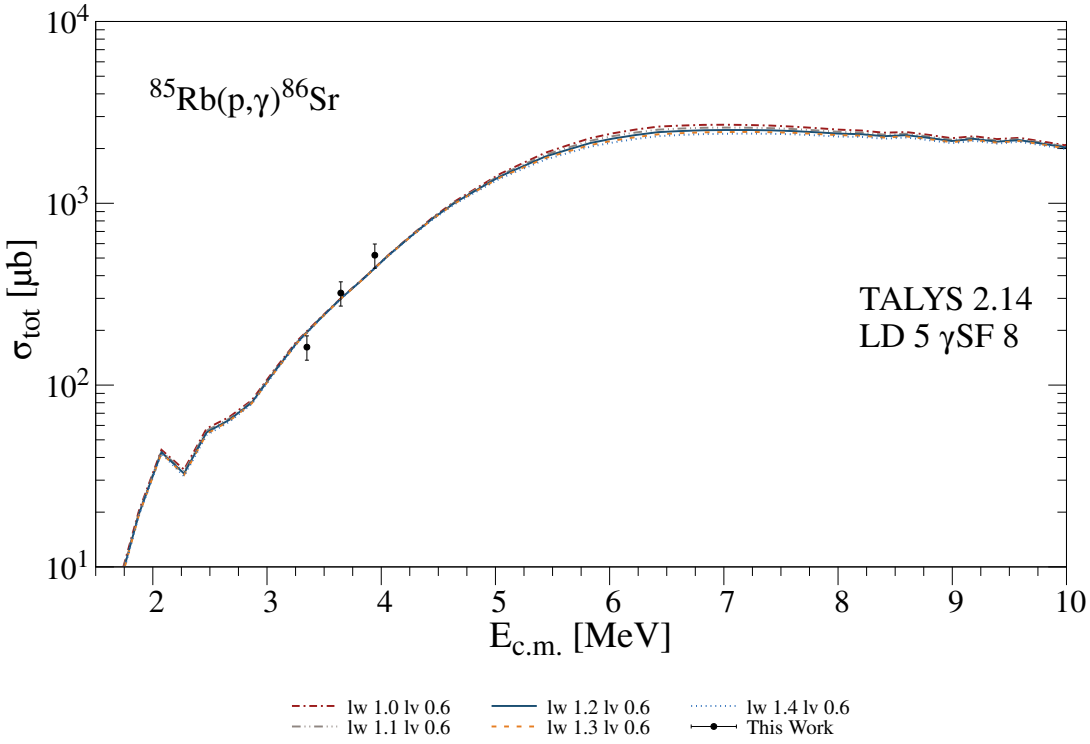

Figure 4.42: Scaling of the real and imaginary parts of the central potential by a factor of 0.6 for the real part (*lvadjust*) and by factors between 1.0 and 1.4 for the imaginary part (*lwadjust*) for the (p, γ) reaction. The predicted cross sections show minor variations in the energy range of 2 MeV to 3 MeV and greater variations starting at 5 MeV.

4.6 Summary ^{85}Rb

To summarize this Chapter: The analysis of the ^{85}Rb(p,γ) reaction brought many different challenges. The first was the deterioration of the target during the experiment. This could be taken into account during the analysis by determining the ratio of the γ-ray transition at 767.4 keV in ^{86}Sr [224] to the 279 keV γ-ray transition of the Coulomb excitation in ^{197}Au [225] in order to normalize the reaction yield. Since the target was produced with RbCl, there are many reactions, that contribute to the beam induced background, sometimes overlaying peaks stemming from the reaction of interest. This increases the challenge since the cross sections of interest are in the order of µb. Only twelve ground-state transitions are known, from which three were observed in this experiment. Nevertheless, results for the cross sections could be determined and were compared to Talys calculations.

Since none of the different combinations of level density models and γ-ray strength in their default setting was able to describe the data, a thorough examination of both has been performed. This did not lead to an adequate description of the data, wherefore the sensitivity to different widths were looked at. This resulted in the last resort of varying the optical model potentials, both the phenomenological Koning and Delaroche [129] as well as the semi-microscopic JLM [135] optical model potential. The variation was utilized using (p,n) cross section data from References [140, 237, 238] in addition to the obtained (p,γ) data from this thesis. The (p,n) data are mostly sensitive to variations in the proton widths in the energy region. Therefore, this helps to constrain the optical model potential more reliable than only considering the (p,γ) data, which are additionally sensitive to the γ and neutron widths. The modulation of the Koning and Delaroche [129] with its 27 parameters turned out to not give suiting results easily. Since the parameter space is huge, the calculations take time when varying many parameters at once. It was found, that many variations lead to a decent description of the (p,n) data, but fail to reproduce the (p,γ) data simultaneously. Therefore, adapting the Koning and Delaroche [129] optical model potential was not investigated further and instead the semi-microscopic JLM [135] optical model potential was utilized to align both (p,n) and (p,γ) cross section predictions with the experimentally obtained data. This model has a much lower parameter space of only six, making calculations faster. For this model, there are also suggestions on how to adapt it to (p,n) and (p,γ) data as presented in References [140, 234]. This quickened the search for a parameter combination that fit both the experimental (p,n) and (p,γ) cross sections. A publication with L. Netterdon on the results of the ^{85}Rb(p,γ) study is in preparation.

5 The case of ^{87}Rb

In the context of this thesis, the charged-particle capture reaction ^{87}Rb$(p,\gamma)^{88}$Sr has been examined using the in-beam technique with HPGe detectors. Measurements were performed using the γ-ray spectrometer HORUS, which is presented in detail in Chapter 3. The re-designed chamber and the NuDAQ system were utilized for this campaign in February, 2021. Following a thorough description of the experimental procedure and data analysis, the total cross-section results for the ^{87}Rb$(p,\gamma)^{88}$Sr reaction are presented. The experimental data are then compared to Hauser-Feshbach calculations, after which the astrophysical impact is discussed. Some of these aspects are discussed in the publication presented in Section 5.1 [239].

The ^{87}Rb(p,γ) reaction is located in a mass region where the abundances of the p-nuclei are not well reproduced by reaction-network calculations. To gain a better understanding of the astrophysical scenarios and the underlying physics, this reaction is investigated. So far, there is no reported data on this reaction. In addition, this reaction helps to complete the systematic studies of the $N = 50$ isotonic chain, where – for now – the only proton-capture reaction on stable isotopes that has not been measured yet, is ^{86}Kr$(p,\gamma)^{87}$Rb.

5.1 Publication I: Total cross sections of the ^{87}Rb(p,γ)^{86}Sr reaction measured via in-beam gamma-ray spectroscopy

This monograph thesis contains the following publication, which has been published in the peer-reviewed journal *The European Physical Journal A*. It is part of a more systematic measuring campaign in the $A \approx 85$ mass region, where (p,γ) reactions are investigated. The study has been planned by F. Heim. The target was produced by A. Blashev. The experiment was carried out by S. Wilden as the main spokesperson, and with the help of F. Heim and M. Müller. S. Wilden is the main author of the publication and did all the data analysis, which contains the sorting of the raw data, constructing $\gamma\gamma$-coincidence matrices, and the determination of the beam intensity, and wrote the first complete draft of the manuscript. The RBS measurement was carried out by the RUBION facility in Bochum, Germany, after the measurement in Cologne showed diffused layer. M. Müller and A. Zilges contributed with discussing the results and improving, especially, the comparison to Talys calculations. B. Machliner, M. Müller and A. Zilges did proof reading.

Eur. Phys. J. A (2025) 61:142
https://doi.org/10.1140/epja/s10050-025-01609-2

THE EUROPEAN PHYSICAL JOURNAL A

Regular Article - Experimental Physics

Total cross sections of the ^{87}Rb(p, γ)^{88}Sr reaction measured via in-beam gamma-ray spectroscopy

Svenja Wilden [a], **Benedikt Machliner** [b], **Martin Müller** [c], **Andreas Zilges** [d]

Institute for Nuclear Physics, University of Cologne, Zülpicher Straße 77, 50937 Cologne, Germany

Received: 17 December 2024 / Accepted: 1 June 2025

Communicated by Navin Alahari

Abstract The ^{87}Rb(p, γ)^{88}Sr reaction was measured for the first time at astrophysically relevant energies in an in-beam experiment at the high-efficiency HPGe γ-ray spectrometer HORUS at the University of Cologne. To determine total cross sections of the ^{87}Rb(p, γ)^{88}Sr reaction, proton beams at six different energies between E_p = 2.0 MeV and 5.0 MeV were provided by a 10 MV FN tandem accelerator, spanning nearly the entire Gamow window relevant for the astrophysical γ-process. These total experimentally obtained cross sections were then compared to calculations performed using the TALYS 2.0 code. In comparison, the measured total cross-sections are found to be lower than those predicted by different models used as input parameters for the TALYS 2.0 code for E_p = 2.0 MeV to 3.5 MeV.

1 Introduction

The majority of nuclei heavier than iron are produced via neutron capture processes. These processes bypass the so-called *p*-nuclei, a set of 35 stable, neutron-deficient nuclei [1]. The *p*-process describes a variaty of processes that account for the production of the *p*-nuclei. One of these is the γ-process which is mainly responsible for producing *p*-nuclei via different combinations of photodisintegration reactions such as (γ, *p*), (γ, *n*) and (γ, α). The number of involved reactions for describing the synthesis of *p*-nuclei is often higher than 10 000. The most favoured sites for this process, where the required temperatures of 2 GK to 3 GK for photodisintegration reactions are reached, are O-Ne layers of type II supernovae [2,3].

However, lighter *p*-nuclei in the $A \approx 90$ mass region, such as ^{92}Mo, are significantly underproduced [4]. A process that has been proposed to resolve this issue is the νp-process [5]. The *p*-nuclide ^{92}Mo lies in the $N = 50$ isotonic chain and shields ^{92}Nb, an extinct radionuclide, from being produced in the *rp*- and νp-processes [6], if one neglects (*n*, *p*)-processes. Recently, the influence of exploding massive stars has been discussed [7].

As the ^{87}Rb(p,γ) reaction is also located in the $A \approx 80-100$ mass region as five of the *p*-nuclei and as ^{92}Mo in the $N = 50$ isotonic chain, the results might help to understand the production mechanisms of those and help to improve theoretical model calculations by constraining the cross sections and the input parameters in this mass region relevant for the *p*-process. The latter is crucial since statistical model calculations are often the only way to predict the cross sections for all the reactions involved in the huge network of reactions. As sensitivity studies show, there is a strong (γ, *n*) and (γ, *p*) flux towards the $N = 50$ isotonic chain followed by a series of (γ, *p*) photodisintegrations [8].

When calculating the stellar reaction rates from cross-sections it needs to be taken into account that due to high temperatures in a stellar plasma, a considerable thermal population of excited states is expected. However, the cross-sections measured in the laboratory are only on the ground states, why the ground-state contributions to the stellar rates need to be known. Combining theory and experimental data can be used to calculate the stellar reaction rate, if there is a contribution from excited states. Since the ground-state contributions are in general higher, if not ≈ 1, for the reaction direction with positive *Q*-value depending on the temperature, measurement of these reactions, as in our case (p, γ) instead of (γ, *p*), help to constrain the stellar reaction rates more precisely [6,9].

An increased production of ^{87}Rb and ^{88}Sr, with +47% and +7% respectively, has been found in massive-star mod-

[a] e-mail: swilden@ikp.uni-koeln.de (corresponding author)
[b] e-mail: bmachli@ikp.uni-koeln.de
[c] e-mail: mmueller@ikp.uni-koeln.de
[d] e-mail: zilges@ikp.uni-koeln.de

Published online: 19 June 2025

els using new neutron-capture cross sections on Kr-isotopes, which also leads to an increase of +24% for the p-nucleus ^{84}Sr during the O-shell burning [10]. During the C-O shell merger, the temperature is about 2.5 GK and ^{87}Rb and ^{88}Sr are abundant, which indicates, that a better understanding of the ^{87}Rb(p, γ)^{88}Sr or its inverse reaction, can as well help to constrain the stellar reaction rates for ^{84}Sr since ^{87}Rb and ^{84}Sr are linked by a sequence of reactions [11,12].

2 Experimental setup and method

The ^{87}Rb(p, γ)^{88}Sr reaction was investigated at the 10 MV FN tandem accelerator at the University of Cologne's Institute for Nuclear Physics, Germany. The HORUS γ-ray spectrometer, which is equipped with a dedicated target chamber for nuclear astrophysics experiments, was used for the investigation of the reaction [13]. Fourteen HPGe detectors were employed, positioned at the six faces and eight vertices of a cube. Six of the HPGe detectors were equipped with BGO shields for active Compton suppression. The current was read out at the target, the chamber and a Faraday cup situated further downstream behind the target. To prevent δ electrons from exiting the chamber, a suppression voltage of −400 V was applied to it.

2.1 Target properties

Due to the low melting point of pure rubidium of only 39.3°C, rubidium carbonate (Rb_2CO_3) with a melting point of 837°C was used. The target, with an isotopic enrichment in ^{87}Rb of 99.2(1)%, was produced by evaporating Rb_2CO_3 onto a gold backing in our in-house target laboratory. The gold backing with a thickness of 90 mg/cm^2 was used to stop the beam to avoid further beam induced background due to widening of the beam behind the target. In the following, this target will be referred to as T_1. After the experiment, Rutherford Backscattering Spectrometry (RBS) [14] was performed at the RUBION facility in Bochum, Germany [15], to determine the Rb target thickness. The results of this measurement indicated that gold from the backing had diffused into the Rb_2CO_3 layer during irradiation, thereby making it more challenging to determine the thickness for T_1, as can be seen in Fig. 1. The thickness of a second similar target of Rb_2CO_3, in the following denoted as T_2, that had not been exposed to a beam prior to this experiment, was determined to be 642(64) µg/cm^2 and showed no gold admixture visible in the RBS spectra. Its gold backing has a thickness of 85 mg/cm^2. Note, that the thickness of each gold backing was not measured via RBS but given after the target production, since it solely needs to be thick enough to stop the beam. In a subsequent experiment, T_2 was irradiated with protons at $E_p = 3.5$ MeV. Consequently, the thickness of

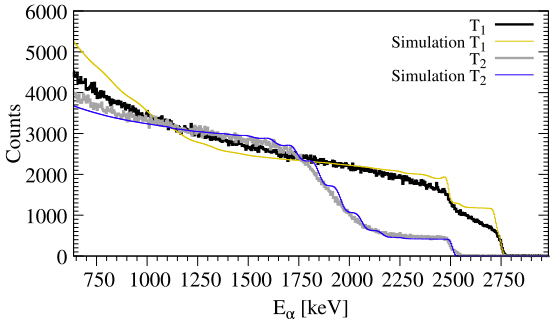

Fig. 1 Relevant part of the RBS spectra measured at the RUBION facility in Bochum, Germany [15], to determine the Rb target thickness for the targets T_1 and T_2. The spectra are well reproduced by simulations performed with SIMNRA [16]. T_1 displays an additional layer that is not present in T_2. The simulation of this layer proved to be a significant challenge. Consequently, the method outlined in the text was employed to determine the thickness of T_1

T_1 could be determined by normalizing the reaction yield for the ^{87}Rb(p,n) ^{87}Sr reaction obtained with T_1, at the same beam energy, to that obtained with T_2. This leads to the following equation:

$$\frac{N_{\gamma_i,2}}{N_{p_2} \cdot N_{T_2}} = \frac{N_{\gamma_i,1}}{N_{p_1} \cdot N_{T_1}} \quad \Leftrightarrow N_{T_1} = \frac{N_{\gamma_i,1}}{N_{\gamma_i,2}} \cdot \frac{N_{p_2}}{N_{p_1}} \cdot N_{T_2}, \tag{1}$$

where $N_{\gamma_i,j}$ is the γ-ray yield observed in the detectors placed at 90°, N_{p_j} is the number of projectiles, N_{T_j} is the number of target nuclei per area with $j \in \{1, 2\}$ and i denotes the used γ-ray transitions. The effective thickness of T_1 has thus been determined to be 727(72) µg/cm^2.

2.2 Beam properties

During the continuous irradiation of the ^{87}Rb target nuclei with protons of different energies $E_{c.m.}$ as given in Tab. 1, highly excited compound nuclei are formed with an excitation energy of

$$E_x = E_{c.m.} + Q, \tag{2}$$

where Q is the Q value of 10 612.8 keV for the radiative proton-capture reaction on ^{87}Rb [17] and $E_{c.m.}$ denotes the center-of-mass-energy. The effective proton-beam energy assuming an energy loss of ΔE in the target is given by

$$E_{\text{eff}} = E_p - \frac{\Delta E}{2}, \tag{3}$$

Table 1 The detailed beam characteristics for the different effective proton-beam energies E_{eff}, where $E_{c.m.}$ denotes the center-of-mass-energy, I denotes the total current and t denotes the irradiation duration for the in-beam measurement

E_{eff} [MeV]	$E_{c.m.}$ [MeV]	I [nA]	t [h]
1.970(23)	1.947(23)	620(31)	14.8
2.776(23)	2.744(23)	610(31)	20.3
3.480(22)	3.440(22)	430(22)	9.9
3.982(22)	3.936(22)	360(18)	11.8
4.483(22)	4.432(22)	170(9)	8.2
4.984(22)	4.928(22)	140(7)	15.6

which has been used to calculate the center-of-mass-energy $E_{c.m.}$. Here, E_p is the proton-beam energy provided by the accelerator. SRIM [18] was used to calculate the average energy loss ΔE in the target, which ranges between 34 keV to 64 keV depending on the proton-beam energy. If statistics are high enough, $E_{c.m.}$ can also be determined using prompt γ rays and the formula

$$E_{c.m.} = E_\gamma - Q + E_{state}, \tag{4}$$

where E_γ is the energy of the prompt γ ray and E_{state} is the energy of the state that is populated by the prompt γ-ray transition. With this knowledge, the offset of the proton-beam energy from the accelerator can be estimated. For the uncertainty of the beam energy we assume 20 keV. The uncertainty of the energy loss in the target is the standard deviation of the SRIM [18] simulation and is almost insignificant compared to the other uncertainties. More details can be found in Ref. [13].

The de-excitation of the compound nucleus was investigated via high-resolution in-beam γ-ray spectroscopy to determine total cross sections for six different proton-beam energies between $E_p = 2$ MeV and $E_p = 5$ MeV. These proton-beam energies have been selected to cover the region of the astrophysically relevant Gamow window for the ^{87}Rb(p, γ)^{88}Sr reaction, which lies between 1.28 MeV and 3.17 MeV at a temperature of $T = 3.0$GK.

The proton-beam energy, proton current, and irradiation time details for the six measured beam energies can be found in Tab. 1. Note that the current is increased with decreasing beam energy in order to partly compensate for the decreasing cross section. This was possible because with smaller beam energy the heat deposition in the target backing, which stops the beam, is smaller and the rate of undesired reactions, and especially the neutron production, is also reduced.

2.3 Spectra

Accurate knowledge of the full-energy peak efficiency for γ rays up to 16 MeV is required for determining total and partial cross sections. The efficiency of the low-energy part, up to 2.5 MeV, has been calibrated using a ^{226}Ra standard calibration source. By in addition using ^{56}Co and ^{66}Ga standards the detection efficiency of γ-rays can be determined precisely up to an energy of 4.8 MeV. The half-lives of these sources are 77.2 days [20] and 9.3 h [21], respectively. Fitting the efficiencies determined from these standards with a function of the form

$$\epsilon\left(E_\gamma\right) = a \cdot \exp\left(-b \cdot E_\gamma\right) + c \cdot \exp\left(-d \cdot E_\gamma\right) \tag{5}$$

leads to the full-energy peak efficiencies. This function is then used to extrapolate up to γ-ray energies of up to 16 MeV, where the uncertainty of the full-energy peak efficiency is about 12% in contrast to the uncertainty of 2% at $E_\gamma = 1.3$ MeV. For this experiment the total detection efficiency of HORUS is about 2.2% at $E_\gamma = 1.3$ MeV.

The digital data acquisition that is used at the HORUS γ-ray spectrometer consists of two CAEN S.p.A. V1782 digitizers for which details can be found in Refs. [22,23]. The events are stored in ROOT-tree format.

A schematic illustration of the reaction and the γ decays to the ground state that have been observed in ^{88}Sr [19] are shown in Fig. 2.

3 Data analysis

The experimental yield $Y(E_\gamma)$ of the ^{87}Rb(p, γ)^{88}Sr reaction is obtained by determining the peak volume for each ground-state transition visible in the γ-ray spectra. Two typical spectra are shown in Fig. 3 for beam energies of $E_p = 2.0$ MeV and $E_p = 5.0$ MeV with irradiation times of 14.8 h and 15.6 h, respectively. Given that ^{87}Rb has no stable isotopic neighbours, the only competing reaction at these energies is ^{87}Rb(p,n)^{88}Sr. As expected, for a proton-beam energy of 2.0 MeV the contribution of the (p, n) reaction is significantly lower than for higher beam energy. This behavior is consistent with statistical model calculations performed using the TALYS 2.0 code [24], which predict a reduction by approximately a factor of 2000. Other transitions being visible stem from proton-induced reactions on ^{197}Au used as

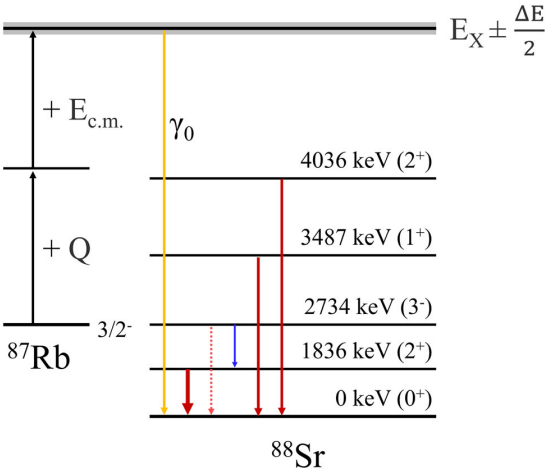

Fig. 2 Schematic illustration of the proton-capture reaction on ^{87}Rb. The highly excited compound nucleus contains many unresolved resonances and has a width of about $\frac{\Delta E}{2}$, with ΔE being the energy loss. It can de-excite directly to the ground state of ^{88}Sr via a single transition (γ_0) or into excited states followed by various γ-ray cascades. Here, only states for which the ground-state transition was observed are displayed. The thicker the arrow the more dominant are the branchings. The data are taken from Ref. [19]

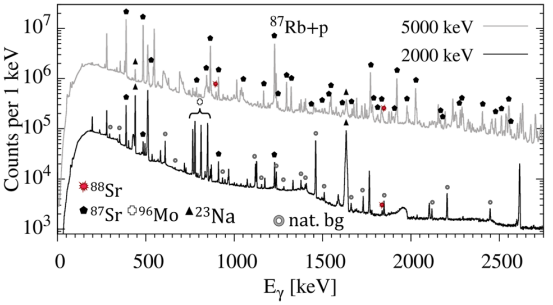

Fig. 3 Comparison of γ-ray spectra obtained at beam energies of E_p = 2000 keV and 5000 keV. The different symbols represent the different origins of some peaks. A noticeable decrease in the (p, n) reaction cross section with decreasing energy is observed. Note that the ^{96}Mo lines stem from an old contamination inside the target chamber and not the target itself

backing. Since the cross sections are very small, especially at low beam energies, lines resulting from natural background radiation, such as that of, e.g., ^{40}K and ^{226}Ra, as well as from target contaminants like ^{23}Na, are clearly visible. The ^{96}Mo lines stem from a contamination inside the target chamber caused by a previous experiment. At higher beam energies, however, transitions in the (p, n) product ^{87}Sr dominate the γ-ray spectra.

In order to obtain the total cross sections, it is necessary to determine the peak volumes of all ground-state transitions

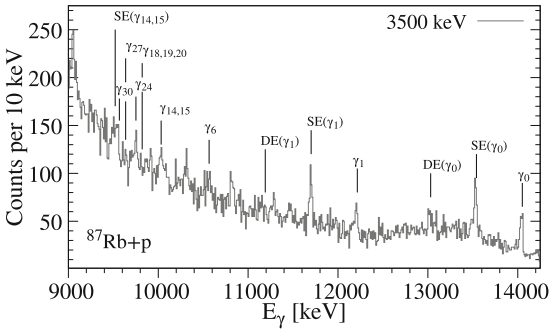

Fig. 4 High energy part of the in-beam γ-ray spectrum for the detectors placed at 90° for a proton-beam energy of E_p = 3.5 MeV. The positions of primary γ-rays to certain discrete states in ^{88}Sr are labeled

for each beam energy. Figure 2 shows the relevant part of the level scheme in ^{88}Sr for this analysis.

3.1 γ-ray spectra

The γ-ray line at E_γ = 1836 keV from the ^{87}Rb(p,γ) reaction is partially contaminated with the de-excitation of the excited $\frac{3}{2}^+$ state at E_x = 3602 keV stemming from the ^{87}Rb(p,n) reaction. This level de-excites to the $\frac{5}{2}^+$ level at E_x = 1770 keV with E_γ = 1832 keV [25]. This line is clearly visible in the γ-ray spectra for E_p = 5.0 MeV and E_p = 4.5 MeV and makes the determination of the number of γ-ray transitions stemming from the proton-capture reaction for the 1836 keV transition more challenging.

The de-excitation of the 3_1^- level in ^{88}Sr to the 2_1^+ level could be observed via a transition with E_γ = 898 keV. Due to the known branching ratio the contribution of the direct decay to the ground state could be estimated to be about 0.7% to 1.7%.

The nucleus ^{87}Rb has a ground-state spin of $J_0^\pi = \frac{3}{2}^-$. Consequently, the majority of states populated after the s-wave proton capture are those with $J^\pi = 1^-$ and 2^- decaying into the ground state with *E1* and *M2* transitions, respectively. The former is a likely decay and thus, the prompt γ decay to the ground state could be observed if the statistics in the γ-ray spectra were high enough. This was used as explained in Sec. 2 to approximate the offset of the accelerator since the direct decay of the compound nucleus to the ground state of ^{88}Sr, known as γ_0, could be observed for beam energies between E_p = 2.8 MeV and E_p = 5 MeV. A high energy spectrum for the measurement with a proton-beam of E_p = 3.5 MeV is shown in Fig. 4, where the γ_0 and other primary γ-rays to certain discrete states in ^{88}Sr are visible. In addition, this limits the uncertainty for the beam energy since with an approximated offset, $E_{c.m.}$ can be determined in two ways as explained.

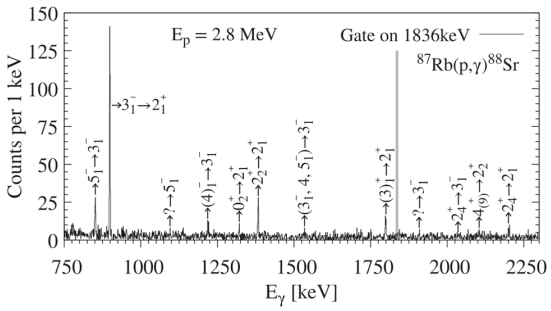

Fig. 5 Application of the $\gamma\gamma$-coincidence method on the ^{87}Rb(p, γ)^{88}Sr reaction for a proton-beam energy of $E_p = 2.8$ MeV. Gating on the $2^+_1 \rightarrow$ g.s. transition at $E_\gamma = 1836$ keV in the original spectrum reveals many transitions feeding this state. The width of the gate is marked with light grey lines. Different γ-ray cascades of higher lying states that de-excite into the 2^+_1 level can be identified. They are labeled in the figure

With the NuDAQ system [23] single spectra as well as $\gamma\gamma$-coincidence matrices can be generated. The latter are used to identify γ-ray cascades and consequently correlate these γ-ray transitions to a certain isotope. Further details on the used hardware and software for the analysis can be found in Ref. [23].

Moreover, they can be used to reduce beam-induced background and identify γ-ray transitions buried in the Compton background and estimate the intensity of these transitions. An example of the application of the $\gamma\gamma$-coincidence method with a gate on the $2^+_1 \rightarrow$ g.s. transition at $E_\gamma = 1836$ keV for a proton-beam energy of $E_p = 2.8$ MeV is shown in Fig. 5. As explained before, there is a noticeable background reduction such that the population of the different states can be observed in detail.

3.2 Angular Distribution

The total cross-section of the (p,γ) reaction is given by

$$\sigma_{(\mathrm{p},\gamma)_{\mathrm{tot}}} = \frac{N_{(\mathrm{p},\gamma)}}{N_p \cdot N_{T_1}}, \tag{6}$$

where $N_{(\mathrm{p},\gamma)}$ is the number of proton capture reactions, N_p is the number of projectiles and N_{T_1} is the number of target nuclei per area. The de-excitation of the highly excited compound nucleus occurs via the emission of γ rays, which follow an angular distribution $W(\theta)$ with respect to the beam axis [26]. This angular distribution $W(\theta)$ was sampled by groups of detectors placed at five different angles relative to the beam axis. The experimental yield of each detector group was determined as follows:

$$W(\theta) = \frac{Y(E_\gamma)}{\epsilon(E_\gamma) \cdot \tau}, \tag{7}$$

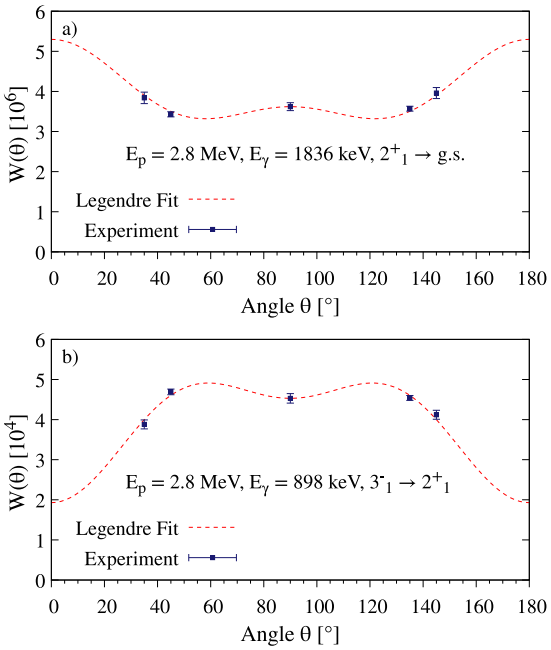

Fig. 6 The de-excitation of the highly excited compound nucleus via γ rays follows an angular distribution. The experimental yield is measured at five different angles and a sum of Legendre polynomials it fitted to it. The upper figure a) shows the measured angular distribution $W(\theta)$ for the $2^+_1 \rightarrow$ g.s. transition, whereas the lower figure b) shows the measured angular distribution $W(\theta)$ for the $3^-_1 \rightarrow 2^+_1$ transition in ^{88}Sr for a proton-beam energy of $E_p = 2.8$ MeV

where $Y(E_\gamma)$ is the total number of detected γ-rays of energy E_γ at the angle θ, $\epsilon(E_\gamma)$ is the full-energy peak efficiency and τ is the dead time correction of the data acquisition.

A sum of Legendre polynomials is fitted to the experimental values in order to obtain the angular distribution

$$W(\theta) = A_0 \cdot \left(1 + \sum_{k=2,4} \alpha_k P_k(\cos(\theta))\right) \tag{8}$$

and especially its integral A_0. The angular distributions for all γ-ray transitions at each beam energy are obtained. Figure 6 shows the experimentally determined angular distributions $W(\theta)$ for the $2^+_1 \rightarrow$ g.s. and the $3^-_1 \rightarrow 2^+_1$ transitions in ^{88}Sr for a proton-beam energy of $E_p = 2.8$ MeV at five different angles.

4 Results and Analysis

The different measured contributions to the population of the ground state can be seen in Fig. 7. For this, all A_0 coefficients of Eq. (8) for one beam energy for the observed ground state

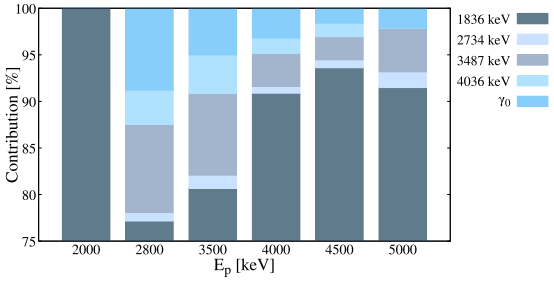

Fig. 7 The different contributions to the population of the ground state from different excited states of the ^{87}Rb(p, γ)^{88}Sr reaction at the six beam energies. Between 80% and 95% of the observed population of the ground state originate from the $2_1^+ \rightarrow$ g.s. transition at $E_\gamma = 1836$ keV. Note that for $E_p = 2.0$ MeV only the $2_1^+ \rightarrow$ g.s. transition was visible in the spectra due to low statistics. Therefore, only a reliable lower limit can be given

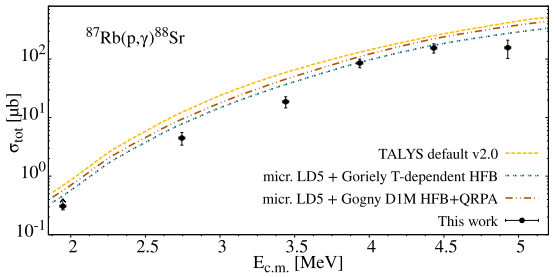

Fig. 8 Total experimental cross-section values $\sigma_{tot,exp}$ for the ^{87}Rb(p, γ)^{88}Sr reaction obtained in this work (black circles). For more details see text. The results are compared to different statistical model calculations using the TALYS 2.0 code [24]. The microscopic level density from the combinatorial model by Hilaire and Goriely [28] and two different photo strength functions [29,30] have been used in addition to the TALYS 2.0 default to compare experimental data to calculations. The different models are in fair agreement with the measured cross-section values

transitions are summed. This represents the total number of proton captures $N_{(p,\gamma)}$. As expected from the funnel effect [27], the contribution of the $2_1^+ \rightarrow$ g.s. transition yields the greatest contribution to the total cross section since many high-lying levels de-excite via γ-ray cascades that end up in the 2_1^+ state, which de-excites with $E_\gamma = 1836$ keV to the ground state. Since the 2_1^+ state is populated by a considerable contribution of different γ-ray cascades, the decay into the ground state shows a more or less isotropic behavior and the effect of the angular correlation is rather small as can be seen in Fig. 6 a). Due to the very low cross section at a $E_p = 2$ MeV, statistics are only sufficient to observe the $2_1^+ \rightarrow$ g.s. transition. Considering the trend in Fig. 7, we have to assume that about 25% of the produced ^{88}Sr nuclei de-excite via different ground-state transitions and therefore cannot be accounted for. Consequently, the cross section determined at this energy is a lower limit.

4.1 Total cross-section values

The measured total cross-section values obtained in this work are listed in the second column in Tab. 2. The uncertainties of the experimentally obtained cross-section values $\sigma_{\text{tot,exp}}$ are influenced by the uncertainties of the number of projectiles ($\approx 5\%$), the target thickness ($\approx 10\%$), the full-energy peak efficiency ($\approx 0.5 - 11\%$) and the statistical uncertainty for the fit of the Legendre polynomials ($\approx 1 - 10\%$). It should be noted that some of these uncertainties are energy dependent. Until now there are no other reported experimental data on this reaction. Figure 8 shows the results of this work in comparison with different statistical model calculations using the TALYS 2.0 code [24].

Table 2 Total experimentally obtained cross-section values $\sigma_{tot,exp}$ for the ^{87}Rb(p, γ)^{88}Sr reaction depending on the center-of-mass energy $E_{c.m.}$. For the beam energies between $E_p = 2.8$ MeV and $E_p = 4.5$ MeV five ground-state transitions have been observed, for the beam energy of $E_p = 5.0$ MeV four ground-state transitions have been observed, and for the beam energy of $E_p = 2.0$ MeV only the $2_1^+ \rightarrow$ g.s. transition with $E_\gamma = 1836$ keV has been observed. The single cross-sections for the observed ground-state decays are listed for each observed de-excitation. In the scope of TALYS calculations using version 2.0, the cross-section of the de-excitation $2_1^+ \rightarrow$ g.s. has been calculated [24] and is listed in the fourth column. For this calculation the microscopic level density from the combinatorial model by Hilaire and Goriely [28] and the temperature-dependent Skyrme-Hartree-Fock-Bogoliubov model [29] have been used

$E_{c.m.}$ [MeV]	$\sigma_{\text{tot,exp}}[\mu b]$	$\sigma_{1836\text{keV}}[\mu b]$	$\sigma_{\text{TALYS},2_1^+}[\mu b]$	$\sigma_{2734\text{keV}}[\mu b]$	$\sigma_{3485\text{keV}}[\mu b]$	$\sigma_{4035\text{keV}}[\mu b]$	$\sigma_{\gamma 0}[\mu b]$
1.947(23)	0.307(41)*	0.307(41)	0.298				
2.744(23)	4.5(11)	3.45(39)	5.27	0.041(5)	0.42(5)	0.164(33)	0.39(6)
3.440(22)	18.7(40)	15.1(17)	28.9	0.26(3)	1.64(20)	0.77(10)	0.93(18)
3.936(22)	85(14)	78(8)	70.9	0.61(7)	3.06(34)	1.38(18)	2.7(4)
4.432(22)	154(27)	144(26)	135	1.31(14)	3.82(50)	2.24(29)	2.4(4)
4.928(22)	156(54)	143(17)	207	2.6(3)	7.4(24)		3.3(5)

* lower limit

4.2 Statistical model analysis and discussion

The results of the calculations and their outcome depends mainly on the selected models for the nuclear input parameters. The most important input parameters are the nuclear level density (NLD) and the γ-ray strength function (γ-SF), which contain fundamental information about nuclear structure and decay behavior. As sensitivity studies as performed in Ref. [9] show, the ^{87}Rb(p, γ)^{88}Sr reaction is very sensitive to the γ-width, which is derived from the γ-SF. In the TALYS 2.0 code [24], a variety of models for NLD and γ-SF are implemented. The following models have been selected since they are reliable and have proven their predictive power in previous studies [31–34]: The microscopic level density stems from the combinatorial model by Hilaire and Goriely [28]. Two different photon strength functions have been chosen, namely the temperature-dependent Skyrme-Hartree-Fock-Bogoliubov model [29] and the Gogny-Hartree-Fock-Bogoliubov model [30].

The experimental cross-section values $\sigma_{tot,exp}$ for the ^{87}Rb(p, γ)^{88}Sr reaction obtained in this work are presented in Fig. 8 together with different statistical model calculations utilising the TALYS 2.0 [24] code. The models employed for the level-density and the γ-SF have been selected in accordance to the above mentioned criteria. The different models are in fair agreement with the experimentally determined cross-section values. The choice of the NLD and the γ-SF deviating from the TALYS 2.0 [24] default seem to improve the agreement slightly. All calculations seem to overestimate the cross sections at lower beam energies.

In addition to these calculations, the cross-section of different levels de-exiting to the ground state have been calculated using the TALYS 2.0 code [24] utilizing the microscopic level density from the combinatorial model by Hilaire and Goriely [28] and the temperature-dependent Skyrme-Hartree-Fock-Bogoliubov model [29]. These calculated cross-sections are compared to the measured cross-sections tabulated in Tab. 2 and shown in Fig. 9. The comparison shows that the TALYS 2.0 code [24] predictions for the different observed levels for the cross-sections are in fair agreement. Furthermore, TALYS [24] predicts additional de-excitations from discrete level to the ground-state. This is especially interesting since the states at $E_x = 3378$ keV and $E_x = 3485$ keV are located at a similar energy and show a similar cross-section for the decay to the ground-state, but experimentally only the de-excitation of $E_x = 3485$ keV to the ground-state was observed. Similar applies for the following levels: $E_x = 3218$ keV, $E_x = 3522$ keV, $E_x = 4035$ keV, $E_x = 4226$ keV and $E_x = 4262$ keV. They all share a similar calculated cross-section σ_{E_γ} and for some similar energy for the decay to the ground-state, however, only the de-excitation to the ground-state of $E_x = 4035$ keV was observed in the experiment. This indicates that the calculations using the TALYS 2.0 code [24] cannot reproduce the experimental observations. It seems that TALYS takes too many ground-state decays into account for the cross-section calculation. Moreover, as shown in Fig. 4 for $E_p = 3.5$ MeV no primary γ-rays have been observed to discrete levels that the TALYS 2.0 code [24] predicts in addition to the observed levels, that de-excite to the ground-state.

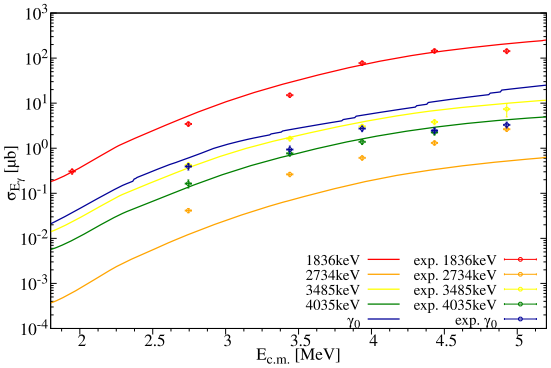

Fig. 9 The cross-sections of different levels de-exciting to the ground-state from calculations using the TALYS 2.0 code [24] utilizing the microscopic level density from the combinatorial model by Hilaire and Goriely [28] and the temperature-dependent Skyrme-Hartree-Fock-Bogoliubov model [29] compared to the measured cross-sections σ_{E_γ} of the observed de-excitations. The measured and calculated cross-sections σ_{E_γ} are in fair to good agreement, depending on the de-exciting level E_x. The trend for the different energies $E_{c.m.}$ is reproduced well for most of the energies E_γ

Previous studies of ^{92}Mo and ^{88}Sr showed deviations for the low-energy part of the measurement, too, as shown in Fig. 10. Therefore, a re-evaluation of the NLD and the γ-SF in this region could be useful to better understand the production mechanisms of ^{92}Mo and ^{92}Nb. Most likely, no enhancement in the low-energy limit is observed in the γ-SF for ^{88}Sr. This is in contrast to ^{94}Mo, where the low-energy enhancement is required [32].

5 Summary and conclusion

In this work, the total cross-sections of the ^{87}Rb(p, γ)^{88}Sr reaction have been studied experimentally at six proton-beam energies between $E_p = 2$ MeV to 5 MeV for the first time. By studying the radiative proton-capture on ^{87}Rb the nuclear physics characteristics of ^{88}Sr can be accessed. It has been demonstrated that the employed level-density model from the combinatorial model by Hilaire and Goriely [28] provides decent predictions regarding ^{88}Sr. The total cross sections for the ^{87}Rb(p, γ)^{88}Sr reaction can be described by statistical model calculations using the previously mentioned set of parameters. It was concluded that a possible low-energy

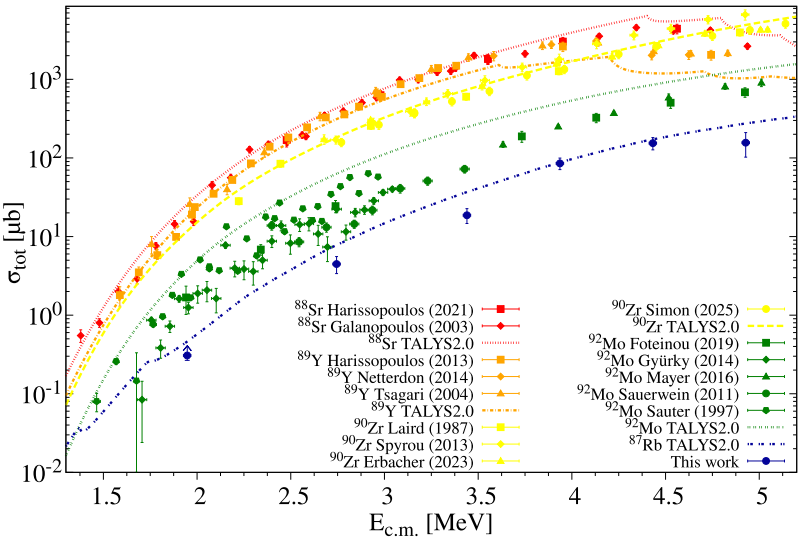

Fig. 10 Comparison between different measured total cross section values σ_{tot} for (p, γ) reactions on the following nuclei in the $N = 50$ isotonic chain: ^{87}Rb (This work), ^{88}Sr [35,36], ^{89}Y [37–39], ^{90}Zr [40–43], and ^{92}Mo [44–48]. The results are compared to statistical model calculations using the TALYS 2.0 code [24], where the microscopic level density from the combinatorial model by Hilaire and Goriely [28] and the photo strength function from Ref. [29] have been used

enhancement of the γ-SF in ^{88}Sr would have at most a negligible effect on the cross-section values. A more systematic comparison between the various measured cross-sections of the stable N = 50 nuclei as shown in Fig. 10 can deepen the understanding of the underlying nuclear physics and can help to improve the underlying models for the statistical model calculations within a certain mass region. Therefore, a comparison of cross-sections and the robustness of the used models for the ^{87}Rb(p, γ)^{88}Sr reaction with the ^{85}Rb(p,γ)^{86}Sr reaction is planned. The influence of the obtained cross sections $\sigma_{tot,exp}$ on the stellar reactions rates will be studied in detail in the future.

Acknowledgements We gratefully thank A. Blazhev for the target preparation and F. Heim for discussion. The authors thank the accelerator team at the Institute for Nuclear Physics in Cologne. This project has been supported by the Deutsche Forschungsgemeinschaft under the contracts ZI 510/12-1. SW is supported by the Hans-Böckler-Stiftung.

Author contributions All authors contributed to the study conception and design. Material preparation, data collection and analysis were performed by Svenja Wilden, Martin Müller, and Benedikt Machliner. The first draft of the manuscript was written by Svenja Wilden and all authors commented on previous versions of the manuscript. All authors read and approved the final manuscript.

Funding Open Access funding enabled and organized by Projekt DEAL. This project has been supported by the Deutsche Forschungsgemeinschaft under the contract ZI 510/12-1 (project 544767130). SW is supported by the Hans-Böckler-Stiftung.

Data Availability Statement Data sets generated and/or analyzed during the current study are available from the corresponding author on reasonable request.

Code Availability Statement This manuscript has no associated code/software.

Declarations

Conflict of interest The authors have no conflict of interest to declare that are relevant to the content of this article.

References

1. E.M. Burbidge, G.R. Burbidge, W.A. Fowler, F. Hoyle, Rev. Mod. Phys. **29**(4), 547 (1957)
2. S.E. Woosley, W.M. Howard, Astrophys. J. Suppl. **36**, 285 (1978). https://doi.org/10.1086/190501
3. M. Arnould, S. Goriely, Phys. Rep. **384**, 1 (2003). https://doi.org/10.1016/S0370-1573(03)00242-4
4. M. Arnould, S. Goriely, Prog. Part. Nucl. Phys. **112**, 103766 (2020). https://doi.org/10.1016/j.ppnp.2020.103766
5. C. Fröhlich, G. Martínez-Pinedo, M. Liebendörfer, F.-K. Thielemann, E. Bravo, W.R. Hix, K. Langanke, N.T. Zinner, Phys. Rev. Lett. **96**, (2006). https://doi.org/10.1103/physrevlett.96.142502

6. T. Rauscher, N. Dauphas, I. Dillmann, C. Fröhlich, Z. Fülöp, G. Gyürky, Rep. Prog. Phys. **76**, 066201 (2013). https://doi.org/10.1088/0034-4885/76/6/066201
7. A. Choplin, S. Goriely, R. Hirschi, N. Tominaga, G. Meynet, Astron. Astrophys. **661**, 86 (2022). https://doi.org/10.1051/0004-6361/202243331
8. W. Rapp, J. Gorres, M. Wiescher, H. Schatz, F. Kappeler, Astrophys. J. **653**, 474–489 (2006). https://doi.org/10.1086/508402
9. T. Rauscher, Astrophys. J. Suppl. **201**, 26 (2012). https://doi.org/10.1088/0067-0049/201/2/26
10. M. Tessler, J. Zappala, S. Cristallo, L. Roberti, M. Paul, S. Halfon, T. Heftrich, W. Jiang, D. Kijel, A. Kreisel, M. Limongi, Z.-T. Lu, P. Müller, R. Purtschert, R. Reifarth, A. Shor, D. Veltum, D. Vescovi, M. Weigand, L. Weissman, Phys. Rev. C **104**, 015806 (2021). https://doi.org/10.1103/PhysRevC.104.015806
11. L. Roberti, M. Limongi, A. Chieffi, Astrophys. J. Suppl. **270**, 28 (2024). https://doi.org/10.3847/1538-4365/ad1686
12. Roberti, L. Private communication (2025)
13. F. Heim, J. Mayer, M. Müller, P. Scholz, M. Weinert, A. Zilges, Nucl. Instrum. Methods A **966**, 163854 (2020). https://doi.org/10.1016/j.nima.2020.163854
14. Chu, W.-K., Mayer, J., Nicolet, M.-A. Backscattering Spectrometry. Academic Press, Inc., Heidelberg (1978). https://doi.org/10.1016/B978-0-121-73850-1.X5001-7
15. RUBION - Zentrale Einrichtung für Ionenstrahlen und Radionuklide. https://www.rubion.rub.de/methods/41/
16. M. Mayer, *SIMNRA User's Guide, Report IPP 9/113* (Max-Planck-Institut für Plasmaphysik, Garching, Germany, 1997)
17. M. Wang, W.J. Huang, F.G. Kondev, G. Audi, S. Naimi, Chin. Phys. C **45**, 030003 (2021). https://doi.org/10.1088/1674-1137/abddaf
18. J. Ziegler, J. Biersack, and M. Ziegler, SRIM – The Stopping and Range of Ions in Matter. http://srim.org/
19. E.A. McCutchan, A.A. Sonzogni, Nucl. Data Sheets **115**, 135 (2014). https://doi.org/10.1016/j.nds.2013.12.002
20. H. Junde, H. Su, Y. Dong, Nucl. Data Sheets **112**, 1513 (2011). https://doi.org/10.1016/j.nds.2011.04.004
21. E. Browne, J.K. Tuli, Nucl. Data Sheets **111**, 1093 (2010). https://doi.org/10.1016/j.nds.2010.03.004
22. CAEN S.p.A. - *User Manual UM6875 - V1782 Octal Digital MCA*. http://www.caen.it/products/v1782/
23. Weinert, M. Investigation of Microscopic Structures in the Low-Energy Electric Dipole Response of 120Sn using Consistent Experimental and Theoretical Observables and Digital Signal Processing for Nuclear Physics Experiments. PhD thesis, University of Cologne (2022)
24. Koning, A., Hilaire, S., Goriely, S. Eur. Phys. J. A **59** (2023) https://doi.org/10.1140/epja/s10050-023-01034-3
25. Johnson, T.D., Kulp, W.D. Nucl. Data Sheets **129** (2015) https://doi.org/10.1016/j.nds.2015.09.001
26. T. Mayer-Kuckuk, *Kernphysik*, 4th edn. (Teubner Studienbücher. Vieweg & Teubner, Wiesbaden, Germany, 1984)
27. A. Zilges, D.L. Balabanski, J. Isaak, N. Pietralla, Prog. Part. Nucl. Phys. **122**, 103903 (2022). https://doi.org/10.1016/j.ppnp.2021.103903
28. S. Goriely, S. Hilaire, A.J. Koning, Phys. Rev. C **78**, 064307 (2008). https://doi.org/10.1103/PhysRevC.78.064307
29. S. Goriely, E. Khan, M. Samyn, Nucl. Phys. A **739**, 331 (2004). https://doi.org/10.1016/j.nuclphysa.2004.04.105
30. S. Goriely, S. Hilaire, S. Péru, K. Sieja, Phys. Rev. C **98**, 014327 (2018). https://doi.org/10.1103/PhysRevC.98.014327
31. Wiedeking, M., Goriely, S. Philos. Trans. R. Soc. A **382** (2024) doi:https://doi.org/10.1098/rsta.2023.0125
32. Heim, F., Scholz, P., Mayer, J., Müller, M., Zilges, A. Phys. Rev. C. **101** (2020) https://doi.org/10.1103/PhysRevC.101.035807
33. Heim, F., Scholz, P., Körschgen, M., Mayer, J., Müller, M., Zilges, A. Phys. Rev. C. **101** (2020) https://doi.org/10.1103/PhysRevC.101.035805
34. Heim, F., Mayer, J., Müller, M., Scholz, P., Zilges, A. Phys. Rev. C. **103** (2021) https://doi.org/10.1103/PhysRevC.103.055803
35. S. Harissopulos, E. Vagena, P. Dimitriou, M. Axiotis, S. Galanopoulos, V. Foteinou, A. Lagoyannis, Phys. Rev. C **104**, 025804 (2021). https://doi.org/10.1103/PhysRevC.104.025804
36. S. Galanopoulos, P. Demetriou, M. Kokkoris, S. Harissopulos, R. Kunz, M. Fey, J.W. Hammer, G. Gyürky, Z. Fülöp, E. Somorjai, S. Goriely, Phys. Rev. C **67**, 015801 (2003). https://doi.org/10.1103/PhysRevC.67.015801
37. S. Harissopulos, A. Spyrou, A. Lagoyannis, M. Axiotis, P. Demetriou, J.W. Hammer, R. Kunz, H.-W. Becker, Phys. Rev. C **87**, 025806 (2013). https://doi.org/10.1103/PhysRevC.87.025806
38. L. Netterdon, V. Derya, J. Endres, C. Fransen, A. Hennig, J. Mayer, C. Müller-Gatermann, A. Sauerwein, P. Scholz, M. Spieker, A. Zilges, Nucl. Instrum. Methods Phys. Res. A **754**, 94–100 (2014). https://doi.org/10.1016/j.nima.2014.04.025
39. P. Tsagari, M. Kokkoris, E. Skreti, A.G. Karydas, S. Harissopulos, T. Paradellis, P. Demetriou, Phys. Rev. C **70**, 015802 (2004). https://doi.org/10.1103/PhysRevC.70.015802
40. C.E. Laird, D. Flynn, R.L. Hershberger, F. Gabbard, Phys. Rev. C **35**, 1265–1274 (1987). https://doi.org/10.1103/PhysRevC.35.1265
41. A. Spyrou, S.J. Quinn, A. Simon, T. Rauscher, A. Battaglia, A. Best, B. Bucher, M. Couder, P.A. DeYoung, A.C. Dombos, X. Fang, J. Görres, A. Kontos, Q. Li, L.Y. Lin, A. Long, S. Lyons, B.S. Meyer, A. Roberts, D. Robertson, K. Smith, M.K. Smith, E. Stech, B. Stefanek, W.P. Tan, X.D. Tang, M. Wiescher, Phys. Rev. C **88**, 045802 (2013). https://doi.org/10.1103/PhysRevC.88.045802
42. Erbacher, P., Heftrich, T., Endres, A., Glorius, J., Netterdon, L., Just, D., Göbel, K., Krtička, M., Reifarth, R., Sonnabend, K., Thomas, B., Weigand, M., Zilges, A. Eur. Phys. J. A **59**(4) (2023) https://doi.org/10.1140/epja/s10050-023-00984-y
43. Simon, A., Koros, J., Olivas-Gomez, O., Kelmar, R., Churchman, E., Clark, A.M., Harris, C., Henderson, S.L., Kelly, S.E., Millican, P., Palmisano-Kyle, A., Reingold, C.S., Robertson, D., Stech, E., Spyrou, A., Tan, W.P. Eur. Phys. J. A **61**(3) (2025) https://doi.org/10.1140/epja/s10050-025-01521-9
44. Foteinou, V., Axiotis, M., Harissopulos, S., Dimitriou, P., Provatas, G., Lagoyannis, A., Becker, H.-W., Rogalla, D., Zilges, A., Schreckling, A., Endres, A. Eur. Phys. J. A **55**(5) (2019) https://doi.org/10.1140/epja/i2019-12738-x
45. G. Gyürky, M. Vakulenko, Z. Fülöp, Z. Halász, G.G. Kiss, E. Somorjai, T. Szücs, Nucl. Phys. A **922**, 112–125 (2014). https://doi.org/10.1016/j.nuclphysa.2013.12.003
46. Mayer, J., Goriely, S., Netterdon, L., Péru, S., Scholz, P., Schwengner, R., Zilges, A. Phys. Rev. C. **93** (2016) https://doi.org/10.1103/PhysRevC.93.045809
47. A. Sauerwein, M. Elvers, J. Endres, J. Hasper, A. Hennig, L. Netterdon, A. Zilges, P. Demetriou, R. Julin, S. Harissopulos, AIP Conf. Proc. **1377**, 423–425 (2011). https://doi.org/10.1063/1.3628433
48. T. Sauter, F. Käppeler, Phys. Rev. C **55**, 3127–3138 (1997). https://doi.org/10.1103/PhysRevC.55.3127

5.2 Experimental Details beyond the Publication

Two aspects that should be addressed in more detail are not or only briefly mentioned in the publication. The first is the dead time correction of detectors installed in BGO shields and the second one is the determination of the target thickness.

5.2.1 Dead Time correction for Detectors with BGO shields

As mentioned in Sections 3.4 and 5.1, the total number of detected γ-ray transitions of energy E_γ need to be corrected for various factors, including the dead time of the data acquisition. This is the time during which the data acquisition system, including the detectors, cannot process signals. The dead time is determined for each detector channel separately, such that it can be distinguished between detectors with a BGO shield and without. The CoMPASS software provides a dead time estimation after the data acquisition, hence, the measurement, has been stopped. To calculate the dead time, CoMPASS takes several outputs and events into account, namely the number of output events N_{out}, the pile-up events N_{pile}, rejected events due to the saturation of the digitizer input state N_{Sat}, the events rejected by user selection N_{user}, and poissonian events N_{poi}, that are explained in detail in [240]. This leads to the dead time (percentage) τ_{dead} for each detector of

$$\tau_{dead} = 1 - \frac{N_{out} + N_{user} + N_{Sat}}{N_{in}} = 1 - \frac{N_{out} + N_{user} + N_{Sat}}{N_{out} + N_{user} + N_{Sat} + N_{pile} + N_{poi}}. \tag{5.1}$$

Problems arise when online BGO vetos are applied. The dead time percentage is far higher than it should be. This is due to N_{out} missing events. The signal of the HPGe detector, that has been vetoed by the BGO, counts as dead time, which it is not. The data in Section 5.1 has been mostly analyzed, before the workaround using the raw data presented in Ref. [209] was established. Therefore, another workaround was used, explained in the following. A problem is, that the output count rate (OCR) and the input count rate (ICR) are not written in a file for the whole measuring time. The OCR can be calculated using

$$OCR = \frac{N_{int,spec}}{t_{mess}}, \tag{5.2}$$

where $N_{int,spec}$ is the obtained γ-ray spectrum integrated over the whole energy range and t_{mess} is the total measuring time. It is assumed, that for the detectors with a BGO, τ_{dead} and the ICR are affected equally and that they are linearly dependent for detectors without BGOs. It holds

$$\tau_{live} = 1 - \tau_{dead} = \frac{OCR}{ICR}, \tag{5.3}$$

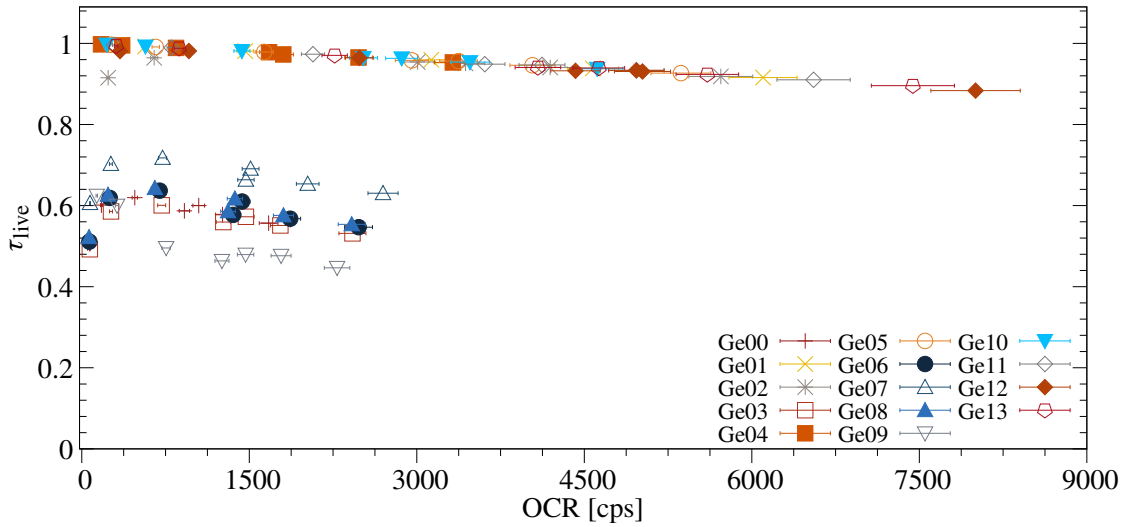

Figure 5.1: The uncorrected live time τ_{live} and OCR for the detectors used in the experiment over multiple runs with varying count rate conditions is shown in this figure. The detectors with BGOs show a divergent behavior in contrast to the detectors without BGOs, that have an approximately linear dependence.

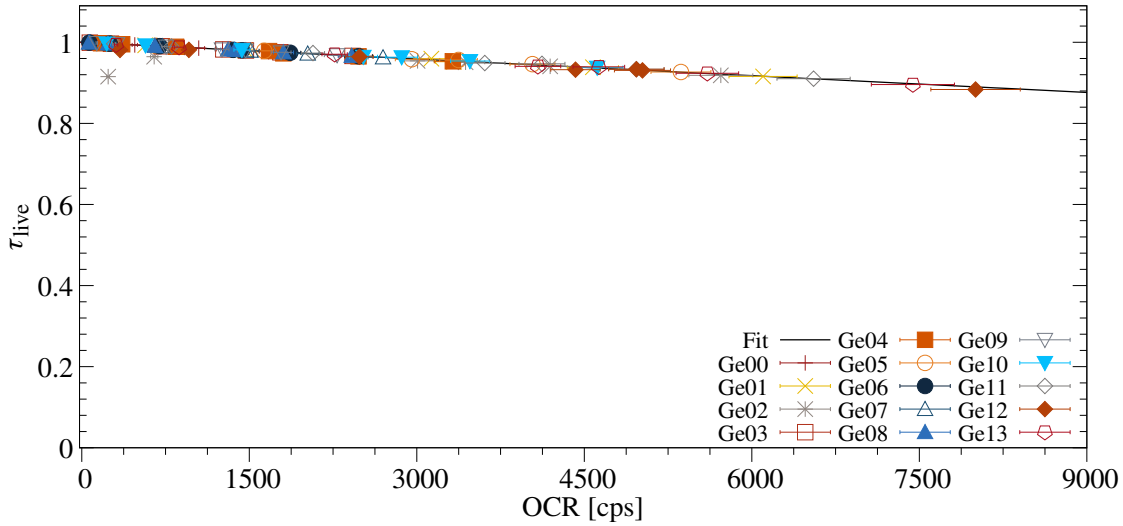

Figure 5.2: The corrected live time τ_{live} and OCR for the detectors used in the experiment. After applying the correction from Equation (5.4), the detectors with BGO align on the same straight line as the others. This corrected live time is then used to analyze the data.

wherefore τ_{live} and the OCR are likewise linearly dependent. τ_{dead} is the dead time from

CoMPASS in the following. CoMPASS stores the realtime and livetime in ms for each channel of a run into a *ROOT* file. τ_{dead} is then derived by taking the ratio of the life time and real time for each detector. With Equation (5.3), τ_{live} can be determined for each detector. Figure 5.1 shows the results of this method. The detectors with the BGO vetos – Ge00, Ge03, Ge06, Ge07, Ge08, and Ge09 – are clearly off, whereas the other detectors lie approximately on a straight line. Ge02, without a BGO, shows a deviation for the lowest OCR. It is worth noting that each detector equipped with BGO exhibits an approximately linear behavior on its own, with deviations occurring only at very low input count rates, as shown in Figure 5.1. The error for the OCR is assumed to be 5 %. Fitting the data of the detectors without BGOs leads to the linear equation

$$\tau_{live}(OCR) = 1.374(11) \cdot 10^{-5} \cdot OCR + 0.999971(68). \tag{5.4}$$

With this, the data of the detectors with BGOs can be corrected. The result is shown in Figure 5.2. The data analysis was subsequently performed using the corrected τ_{live}.

5.2.2 Determination of the Target Thickness

The rubidium carbonate Rb_2CO_3 with an isotopic enrichment of 99.2(1) % was produced in house by evaporation onto gold backings with thicknesses of 90 mg/cm^2 and 85 mg/cm^2 for targets T_1 and T_2, respectively. The thickness of the Rb_2CO_3 layer estimated after the target production is 0.8 mg/cm^2 and 0.65 mg/cm^2, respectively. Figure 5.3 show the targets T_1 and T_2. For the experiment, T_1 was used, whereas T_2 served as a reference target to determine the thickness of T_1.

As the number of target atoms per unit area has a direct influence on the cross-section, as defined in Equation (1.1), a precise determination is crucial. In order to account for target loss during the irradiation process, it is helpful to determine the target thickness both before and after the experiment. As the targets were completed shortly before the experimental campaign started, it was not possible to conduct an RBS measurement at the RUBION facility in Bochum, Germany, beforehand [222]. Since the experiment was performed in February 2021, Covid-related regulations were still in place, meaning that scheduling an RBS measurement in Cologne in advance was not possible. A first RBS measurement performed in October 2021 in Cologne already hinted, that there was an additional layer in front for target T_1 similar to the target behavior in the ^{85}Rb(p,γ) measurement, but the resolution was not high enough to see all the details. This is shown in Figure 5.4. Therefore, a RBS measurement at the RUBION facility in Bochum, Germany, was performed in 2022. This data is presented in Fig. 1 of the publication in Section 5.1 [239].

It was quite challenging to fit the target T_1 properly despite the very good resolution of the measurement at the RUBION facility in Bochum, Germany [222]. The thickness of T_2 was determined at four different points to account for a possible roughness and non equal distribution of the target material during the evaporation. Figure 5.5 shows these measurement points. There is a small additional structure visible in front of the target. However, this can be simulated quite well as shown in Fig. 1 in the publication. It can also be seen, that the thickness at

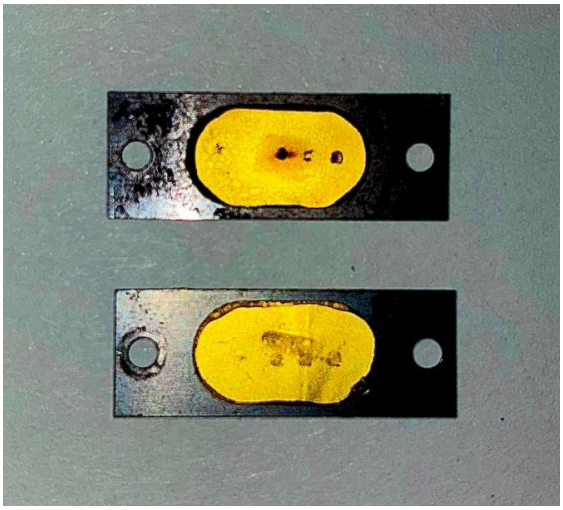

Figure 5.3: Photo of the Rb_2CO_3 targets T_1 and T_2, named from top to bottom, taken in 2025. The beam spots are prominent on both targets. Additional non centered beam spots can be seen stemming from the RBS measurement at the RUBION facility in Bochum, Germany [222].

the different points does not vary by a lot. The RBS measurement results in an average areal density of $n_{T_2,meas} = 3.35(33) \cdot 10^{18}$ 1/cm^2, which agrees well with the given value after the target production of $n_{T_2,giv} = 3.39 \cdot 10^{18}$ 1/cm^2. T_2 was irradiated in a follow-up experiment with protons at $E_p = 3.5\,\text{MeV}$, one of the proton beam energies used in the experiment with T_1. Using target thickness for T_2, the known number of projectiles N_{p_j} with $j \in \{1, 2\}$, the reaction yield for different γ-ray transitions i at six detectors at 90° of the ^{87}Rb(p,n)^{87}Sr and the ^{87}Rb(p,p')^{87}Rb reactions and the relation

$$\begin{aligned} \frac{N_{\gamma_i,2}}{N_{p_2} \cdot n_{T_2}} &= \frac{N_{\gamma_i,1}}{N_{p_1} \cdot n_{T_1}} \\ \Leftrightarrow n_{T_1} &= \frac{N_{\gamma_i,1}}{N_{\gamma_i,2}} \cdot \frac{N_{p_2}}{N_{p_1}} \cdot n_{T_2}, \end{aligned} \tag{5.5}$$

the target thickness of T_1 can be determined. In total eight different γ-ray transitions in ^{87}Sr and one in ^{87}Rb have been used to average over T_1. They are given in Table 5.1. Averaging over the calculated T_1 for each γ-ray transition leads to a target thickness of $n_{T_1,calc} = 3.79(38) \cdot 10^{18}$ 1/cm^2, which deviates from the given thickness of $n_{T_1,giv} = 4.17(42) \cdot 10^{18}$ 1/cm^2 by about 10 %. It is worth noting, that T_2 was only irradiated at a beam energy of $E_p = 3.5\,\text{MeV}$, whereas T_1 was irradiated with three different beam energies before of $E_p = 5\,\text{MeV}$, 4.5 MeV, and 4 MeV. There is a possibility that the thickness of T_1 was affected at one of the beam energies. However, since the overall uncertainty of the cross sections given in Table 2 of the publication in Section 5.1, exceeds 10 %, the method to extract the thickness of the target is still valid and should give reasonable results.

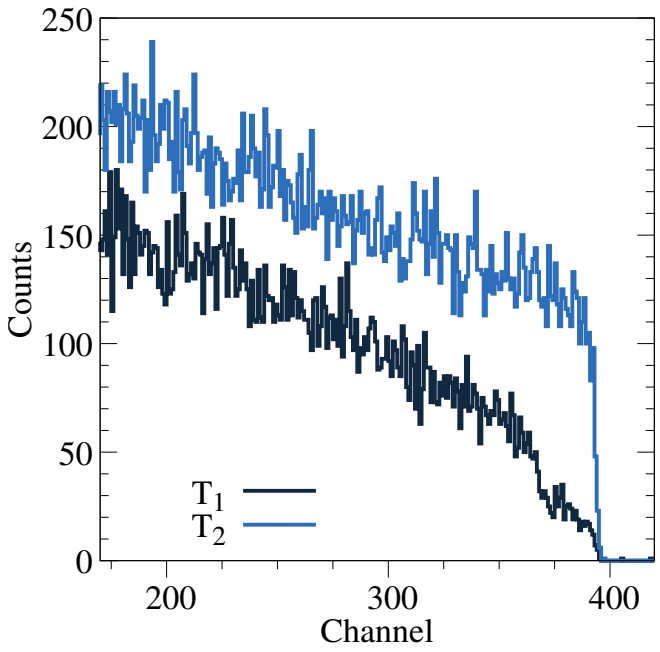

Figure 5.4: Comparison of the RBS measurement performed in Cologne in October 2021 for targets T_1 and T_2. On the right flank of T_1 an additional structure can be seen, which is not the case for the straight falling flank of T_2. The beam for the measurements was an α-beam with an energy of 4 MeV.

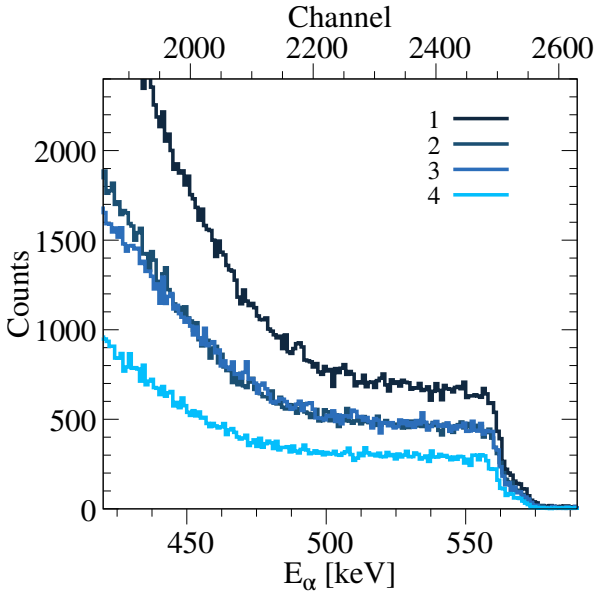

Figure 5.5: Comparison of the RBS measurement performed at the RUBION facility in Bochum, Germany, in April 2022 for the four measurement point of target T_2. On the right flank of T_2 an additional structure can be seen, which is small compared to that of T_1. The thickness of T_2 can still be simulated well, as explained in the text. The beam for the measurements was an α-beam with an energy of 3 MeV.

Table 5.1: The γ-ray transitions and further information of ^{87}Sr and ^{87}Rb, that are used to average over T_1 [159]. The yield is observed with six detectors at 90° for each target. Equation (5.5) is then used to calculate the thickness of T_1 for each transition. This is used to average over the thickness, which results in $n_{T_1,calc} = 3.79(38) \cdot 10^{18}$ atoms/cm^2.

#	E_{level} [keV]	J^π	E_γ [keV]	Xl	Note
	0	$3/2^-$			ground state of ^{87}Rb
1	403	$5/2^-$	403	$M1+E2$	
	0	$9/2^+$			ground state of ^{87}Sr
1	388	$1/2^-$	388	$M4$	not used, since isomeric state with $T_{1/2}$ =2.8 h
2	873	$3/2^-$	485	$M1+E2$	
3	1228	$5/2^+$	355	$E1(+M2)$	
			1228	$E2$	
4	1254	$5/2^-$	380		Multipolarity unknown
			865	$E2$	
7	1770	$5/2^+$	517	$(E1)$	
			542	$M1(+E2)$	
			1770	$E2$	

5.3 TALYS calculations utilizing different Optical model Potentials

The following investigation took place in more detail after the paper was published. The deviations observed for the proton-induced reactions on ^{85}Rb for two reaction channels lead to a deeper analysis of the cross section predictions by TALYS for both stable Rb isotopes.

For the ^{87}Rb target, calculations with TALYS 2.14, even when varying the level density and γ-ray strength function models, do not satisfactorily describe the experimental data for either the (p,γ) or (p,n) reactions, as shown in Figures 5.6 and 5.7. For this first comparison, the optical model potential of Koning and Delaroche was employed [129].

The comparison to experimental (p,n) data was performed using the results from Reference [139]. Unfortunately, no individual uncertainties are provided for these data, apart from an estimated overall uncertainty of about 20 % for the cross sections. Moreover, the original publication specifies that the reported values correspond exclusively to the production of the isomeric state, rather than the total cross section σ_{tot}. Consequently, the comparison presented below refers to the ^{87}Rb$(p,n)^{87\text{m}}$Sr reaction channel. When only the isomeric branch of a reaction, such as ^{87}Rb$(p,n)^{87\text{m}}$Sr, is used to constrain or adjust an optical model potential, this introduces systematic uncertainties, since the branching between $\sigma_{g.s}$ and σ_m has to be predicted correctly in the model calculations.

Notably, while the predicted (p,γ) cross sections exhibit significant variation depending on the chosen model combinations, the (p,n) reaction is considerably less sensitive to these model inputs. Across the investigated energy range, all combinations of level-density and γ-ray strength models yield nearly identical (p,n) cross section predictions.

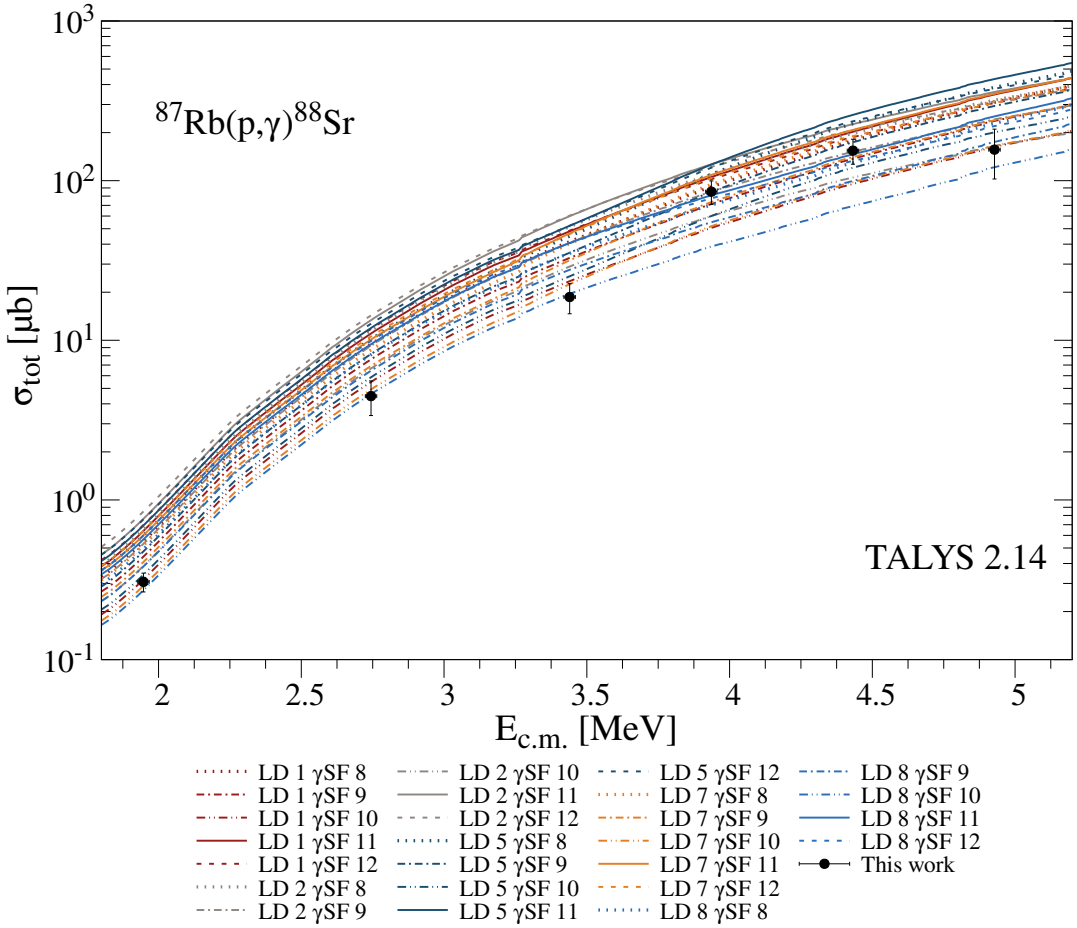

Figure 5.6: Comparison of the experimentally determined cross sections for the ^{87}Rb(p,γ) reaction with TALYS version 2.14 calculations. For the calculations, the previously recommended level density and γ-ray strength function models, as explained in Section 2.3, are used. The optical model potential of Koning and Delaroche was employed [129]. As can be seen, no model can describe all cross-section values and fails to describe the structure between 4 MeV to 4.5 MeV.

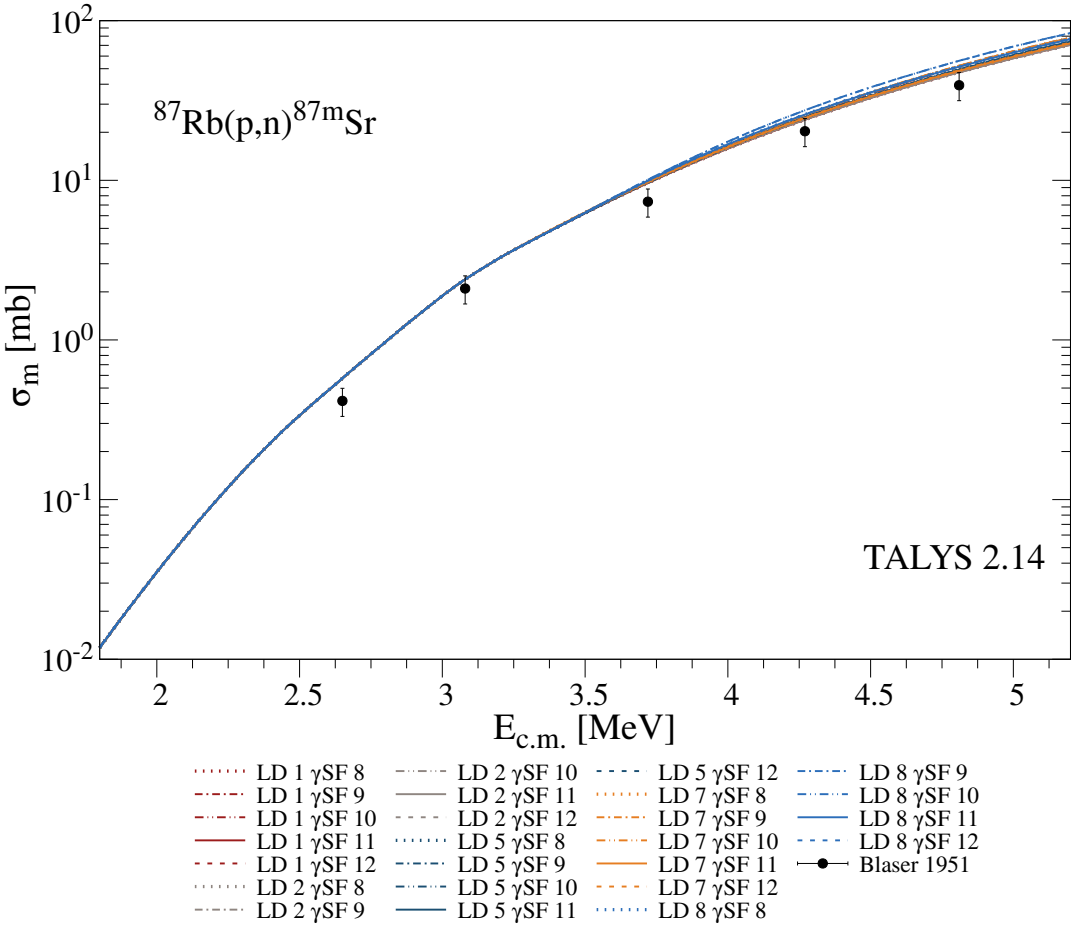

Figure 5.7: Comparison of the experimental determined cross sections for the ^{87}Rb(p,n) reaction to TALYS version 2.14 calculations. The data are taken from Reference [139]. For the calculations, the previously recommended level density and γ-ray strength function models, as explained in Section 2.3, are used. The optical model potential of Koning and Delaroche was employed [129]. All combinations of level density and γ-ray strength models yield a similar result for the (p,n) cross section data.

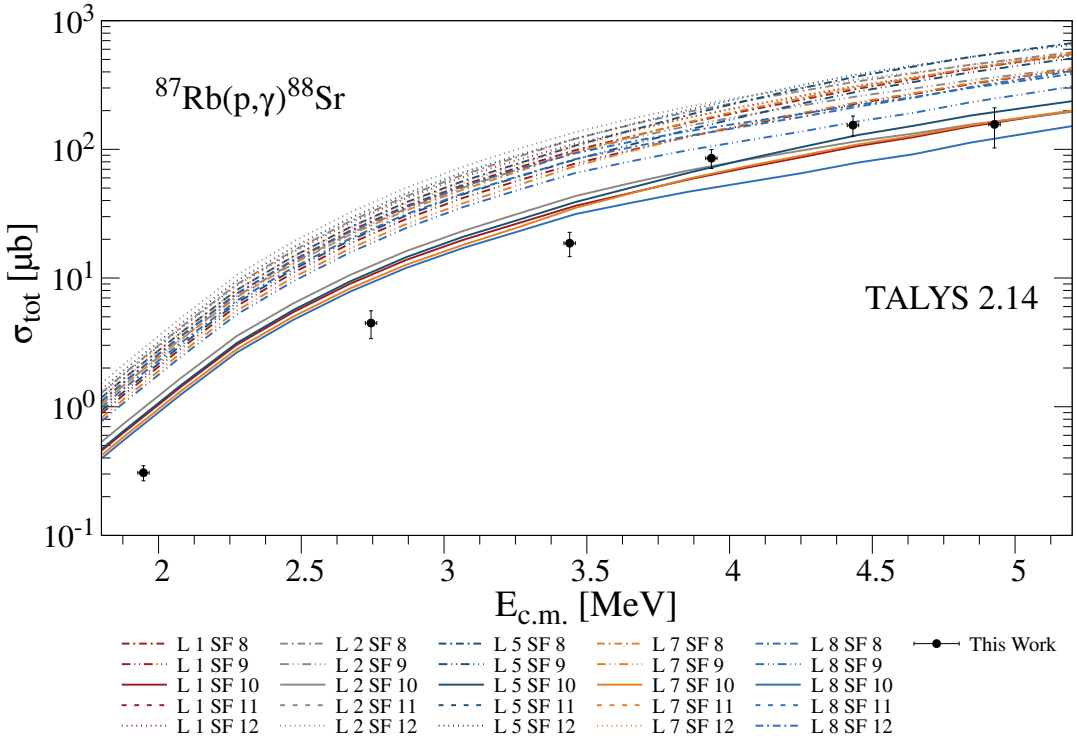

Figure 5.8: Comparison of the experimental determined cross sections for the ^{87}Rb(p,γ) reaction to TALYS version 2.14 calculations utilizing the JLM optical model potential. The different combinations do not describe the data. In the range of 1.9 MeV to 3.6 MeV all models predict a higher cross section than experimentally obtained. Combinations emloying γ-ray strength model 10 show the smallest cross section predictions and are able to describe data for energies greater than 3.5 MeV, whereas it fails to describe the structure in the cross sections.

Figures 5.8 and 5.9 present the comparison of the experimentally obtained cross sections to the predictions utilizing the JLM [135] optical model potential. As for the calculations with the Koning and Delaroche [129] optical model potential, the (p,n) data are overpredicted. The deviations between the predicted (p,γ) cross sections to the data are greater than for the phenomenological one.

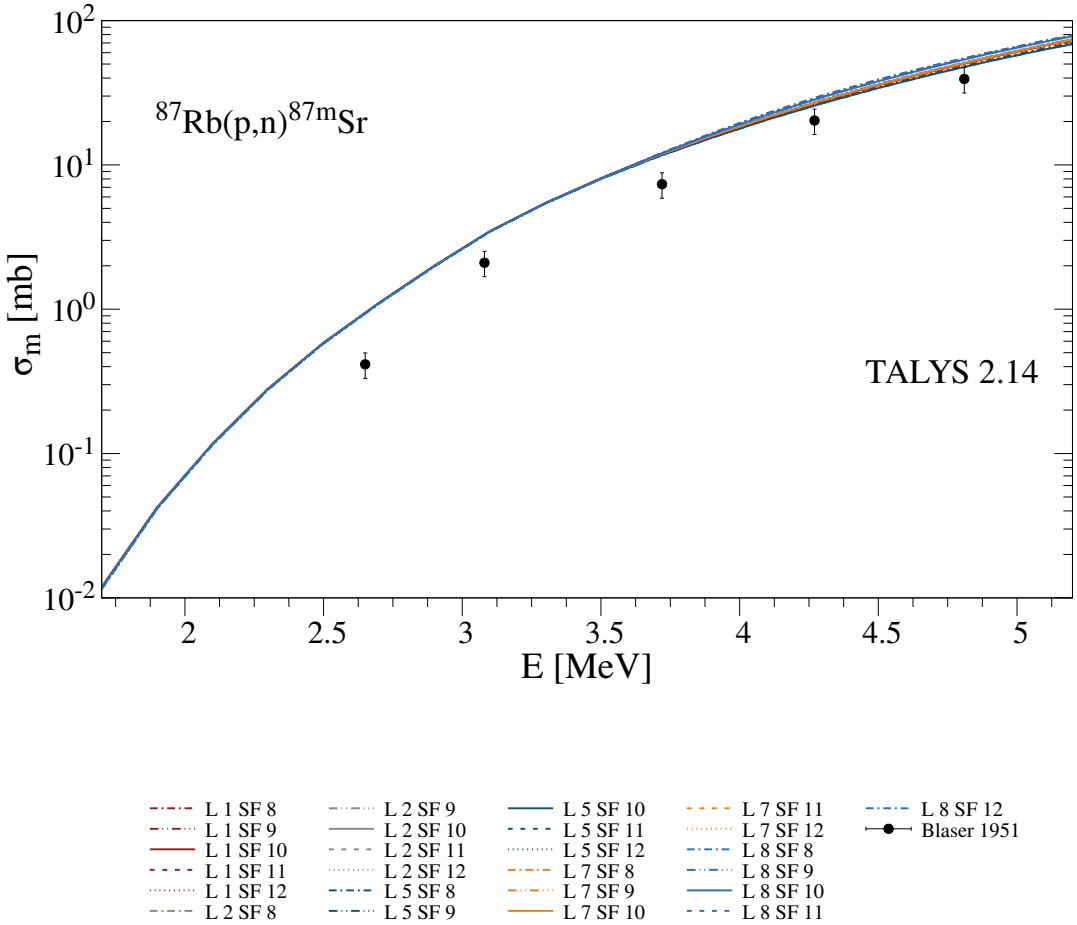

Figure 5.9: Comparison of the experimental determined cross sections for the $^{87}\mathrm{Rb}(p,n)$ reaction to TALYS version 2.14 calculations utilizing the JLM optical model potential. While the statistical model calculations reproduce the general energy dependence of the experimental cross sections, they fail to reproduce the absolute magnitude of the data. The data are taken from Reference [139].

5.4 Widths and Sensitivities

As explained in Section 4.5.3, the different absolute values of the sensitivities for when the γ, neutron (n), proton (p), and α widths are varied by a factor of two [110], are presented in Figure 5.10. The Gamow window (dark shaded area to the vertical line), and the experimentally covered energy range (striped area). The cross sections in the experimentally covered area are approximately equally sensitive to variations in the different widths with exception to the α width. These widths cannot be changed with a parameter in the TALYS code unfortunately. Since varying only the models of the nuclear level density and the γ-ray strength function did not solve the discrepancies between the data and the model calculations and the (p, n) data show similar deviations as for the ^{85}Rb, the assumption is, that the optical model potential cause the deviation for the $^{87}\mathrm{Rb}(p, \gamma)$ reaction as it did for $^{85}\mathrm{Rb}(p, \gamma)$. Thus, the JLM [135] optical model potential is, in the following, varied similarly to that presented in Section 4.5.6. Note, the $^{87}\mathrm{Rb}(p, n)$ reaction is fortunately only sensitive to the proton widths [110]. Unfortunately, no elastic scattering data are available for ^{87}Rb.

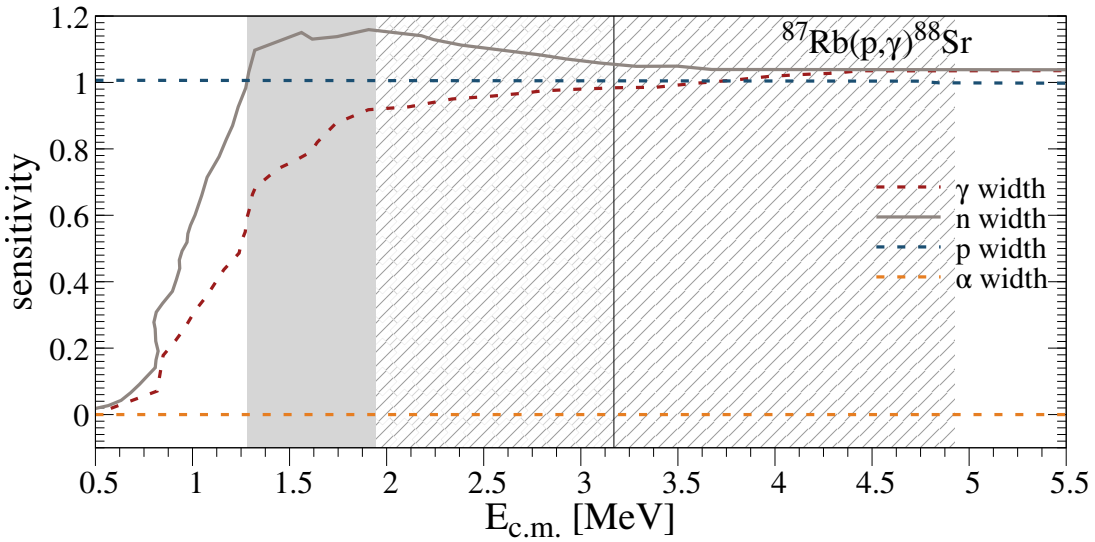

Figure 5.10: Absolute value of the sensitivity of the $^{87}\mathrm{Rb}(p, \gamma)^{88}\mathrm{Sr}$ laboratory cross section, when the γ, neutron (n), proton (p), and α widths are varied by a factor of two, as a function of center-of-mass energy. The data are taken from Ref. [110]. The dark shaded area represents the Gamow window for a typical γ-process temperature of 3 GK. The vertical line shows the right side of the Gamow window. The striped area shows the experimentally covered energy region. The cross sections, that are experimentally obtained are approximately equally sensitive to changes in the proton, neutron, or γ widths. This, however, can not be changed as a parameter in TALYS unfortunately.

5.5 Predicting Cross Sections Utilizing Variations to the JLM Optical Model Potential

Since the combination of level density model 5 with γ-ray strength model 8 yielded good agreement with the experimental data for proton-induced reactions on ^{85}Rb, the same combination was adopted for the ^{87}Rb analysis when varying the JLM optical model potential [135].

The parameters *lwadjust* and *lvadjust* were each varied between 0.5 and 1.5. The results obtained for $lwadjust = 1.1$, which gave good agreement for ^{85}Rb, are shown in Figure 5.11. In general, the energy dependence of the predicted cross sections is reproduced reasonably well, but the absolute values are overestimated compared to the experimental (p, n) [139] and (p, γ) data. Thus, the parameter combination that improved the description of proton-induced reactions on ^{85}Rb does not resolve the discrepancies observed for ^{87}Rb. A lower value of $lwadjust = 0.5$, shown in Figure 5.12, leads to an improved overall description but still fails to accurately reproduce the (p, n) data above 4.5 MeV. For the (p, γ) reaction, the general trend is captured, yet the absolute cross sections are not reproduced, and particularly the data point at 5 MeV is overpredicted. The remaining parameter combinations are presented in Chapter B.1. Overall, lower *lwadjust* values tend to yield better agreement, but no single parameter combination can simultaneously reproduce both (p, n) and (p, γ) data by varying only *lwadjust* and *lvadjust*.

Introducing an additional variation of *lw1adjust*, the normalization factor for the imaginary isovector potential, has a minor influence on the predicted cross sections compared to *lwadjust* and *lvadjust* by shifting them slightly up and or down. Representative results of these parameter variations are presented in Chapter B.2. Conversely, varying *lv1adjust* appears to have a similar influence and still fails to reproduce the absolute cross-section values as shown for different examples in Chapter B.3.

Finally, varying *lwsoadjust*, the normalization factor of the imaginary spin–orbit potential, has only a negligible effect on the calculated cross sections and is therefore not further discussed here. Two examples are shown in Chapter B.4. Varying the *lvsoadjust* value instead, has a small influence on the cross section predictions compared to *lwadjust* and *lvadjust*. Examples are presented in Chapter B.5.

Since the predicted cross sections are too high, but the energy dependence seem to be described well for some combinations of *lwadjust* and *lvadjust*, the γ-ray strength function is changed to *strength* 10. This model shows the lowest predicted cross sections for this reaction as presented in Figure 5.8.

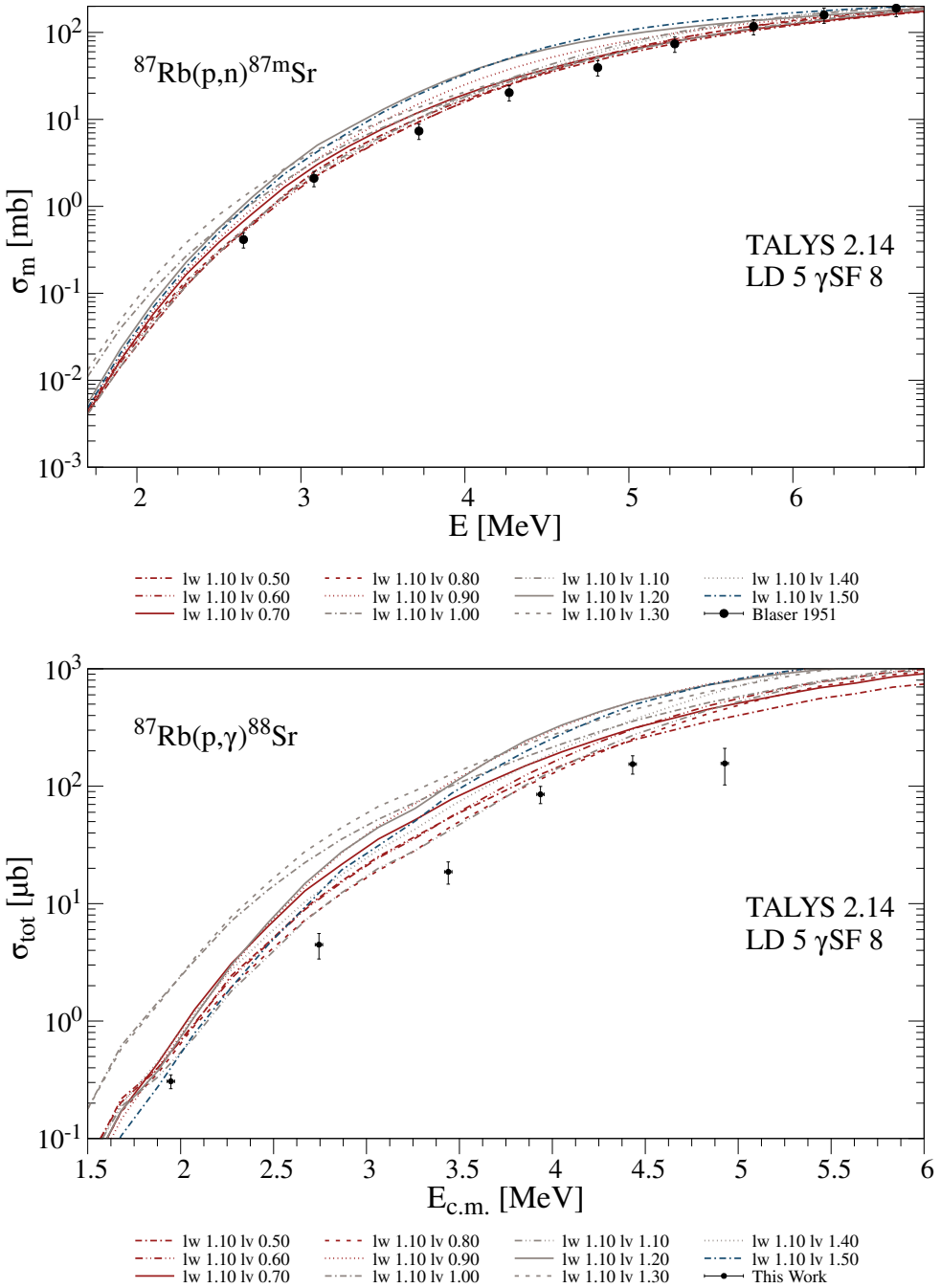

Figure 5.11: Variation of *lwadjust* = 1.1 with different values of *lvadjust* for proton-induced reactions on ^{87}Rb. The upper panel shows the predicted ^{87}Rb$(p,n)^{87m}$Sr cross sections in comparison with the experimental data from Reference [139]. While the general energy dependence is reproduced for the different combinations of *lwadjust* = 1.1 and *lvadjust*, not all parameter sets describe the absolute values satisfactorily. The lower panel presents the comparison between the experimentally obtained ^{87}Rb(p,γ) data and the statistical model predictions. Although some combinations reproduce the trend of the data more accurately than others, none of them succeeds in reproducing the absolute magnitude of the experimental cross sections.

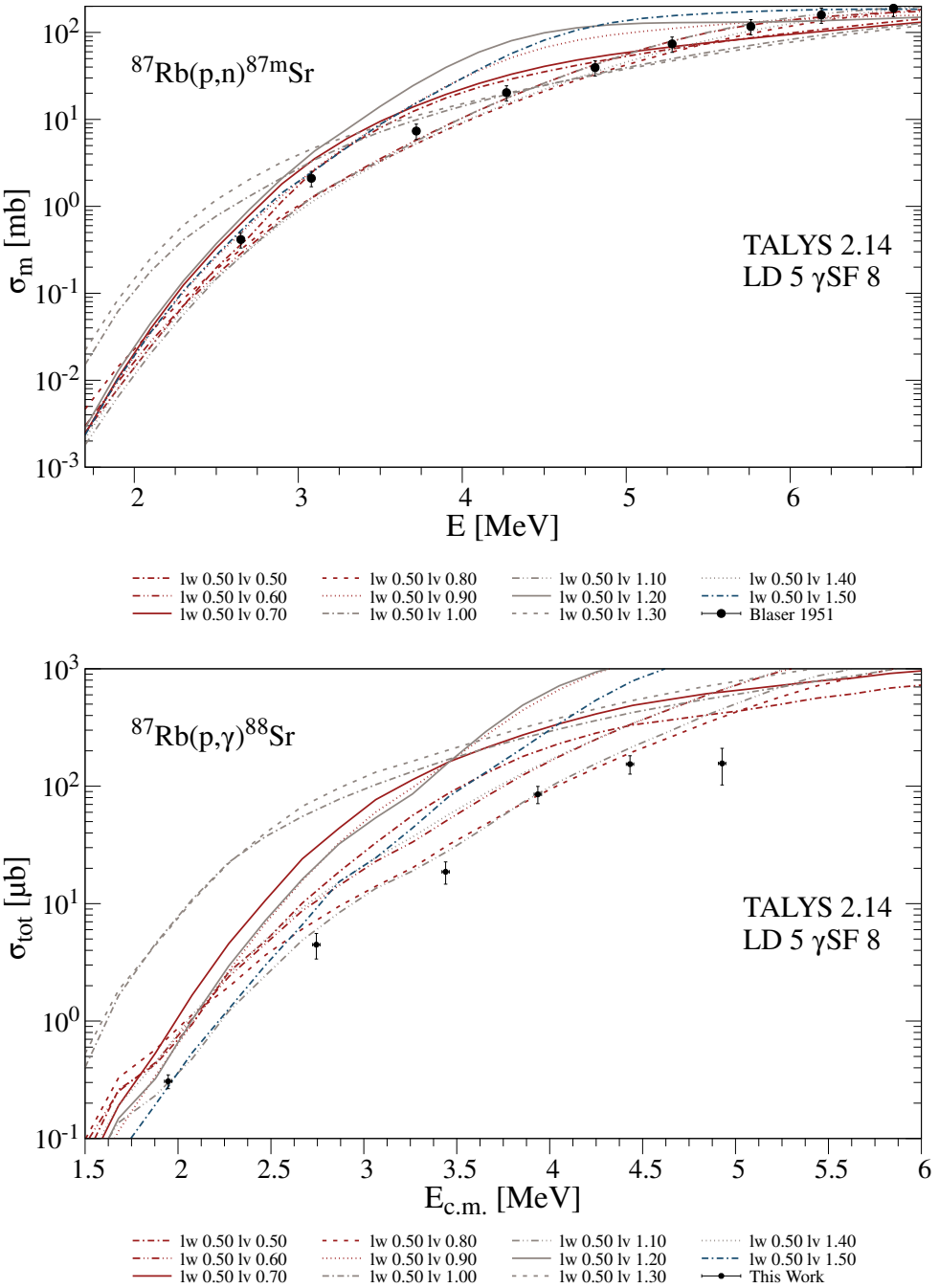

Figure 5.12: Variation of *lwadjust* = 0.5 with the altered *lvadjust* for proton-induced reactions on ^{87}Rb. The upper panel shows the predicted $^{87}\mathrm{Rb}(p,n)^{87\mathrm{m}}\mathrm{Sr}$ cross sections in comparison with the experimental data from Reference [139]. While the general energy dependence is reproduced for the different combinations of *lwadjust* = 0.5 and *lvadjust*, not all parameter sets describe the absolute values satisfactorily. The lower panel presents the comparison between the experimentally obtained $^{87}\mathrm{Rb}(p,\gamma)$ data and the statistical model predictions. Although some combinations reproduce the trend of the data more accurately than others, none of them succeeds in reproducing the experimental cross sections at all energies.

Doing so increases the agreement between the predicted and the experimentally determined cross sections, as demonstrated in Figure 5.13. The remaining parameter combinations obtained by varying *lwadjust* and *lvadjust* in steps of 0.1 between 0.5 and 1.5 are presented in Chapter B.6. The most promising overall agreement for describing both reaction channels simultaneously is achieved for a combination of *lwadjust* and *lvadjust* values of 0.5.

There are, however, other parameter combinations employing γ-ray strength model 10 that reproduce one of the two data sets reasonably well but fail to describe the other. Since the experimental data for the ^{87}Rb$(p,n)^{87m}$Sr reaction correspond to the population of the isomeric state rather than the total reaction cross section, the comparison between model predictions and data must be interpreted with caution.

The variation of only *lwadjust* and *lvadjust* does not lead to a fully satisfactory description. Therefore, in a next step, the parameters *lw1adjust* and *lv1adjust* were varied separately, using the same step size and range as before. The combination of $lwadjust = lvadjust = 0.5$ and $lw1adjust = 1.5$ provides a reasonable agreement for both the (p,γ) and the isomeric (p,n) data, as shown in Figure 5.14, with additional examples presented in Chapter B.2. Again, some parameter sets reproduce one reaction channel slightly better but worsen the description of the other.

When varying *lwadjust*, *lvadjust*, and *lv1adjust* simultaneously, the influence on the predicted cross sections becomes more pronounced than in the case of *lw1adjust*. This variation was again performed in steps of 0.1 across the range from 0.5 to 1.5 for each parameter. The resulting predictions describe both data sets better than when varying only *lwadjust* and *lvadjust*, and show an improvement compared to the *lw1adjust* variations, as illustrated in Figure 5.15 (see Chapter B.8 for additional examples).

Since both additional parameter variations improved the simultaneous description of the (p,γ) and (p,n) reactions, the next logical step was to explore the combined effect of all four parameters. In this extended parameter study, *lwadjust* was varied in steps of 0.02 between 0.50 and 0.54, *lvadjust* in steps of 0.02 between 0.50 and 0.60, and both *lw1adjust* and *lv1adjust* were scanned in the range from 0.50 to 1.50 in steps of 0.10. The best agreement was obtained for $lwadjust = lvadjust = lv1adjust = 0.5$ and *lw1adjust* between 0.5 and 0.8. This is presented in Figure 5.16. Other combinations are presented in Chapter B.9. The different parameter combinations result in only minor deviations and provide an overall reasonable agreement with the experimental data. For the isomeric (p,n) data [139], discrepancies remain in the energy range between 3.5 MeV to 4.5 MeV, while for the (p,γ) reaction, the lowest data point is slightly underestimated with the employed parameter combinations.

In total, the adaptation of the JLM optical model potential proved to be more challenging than for the ^{85}Rb investigation presented in Chapter 4. The obtained results require confirmation through measurements of total cross sections for the (p,n) reaction. Ideally, a simultaneous fit to (p,n), as well as elastic proton and neutron scattering data, should be performed to further constrain the potential parameters and improve the reliability of the model in this mass region.

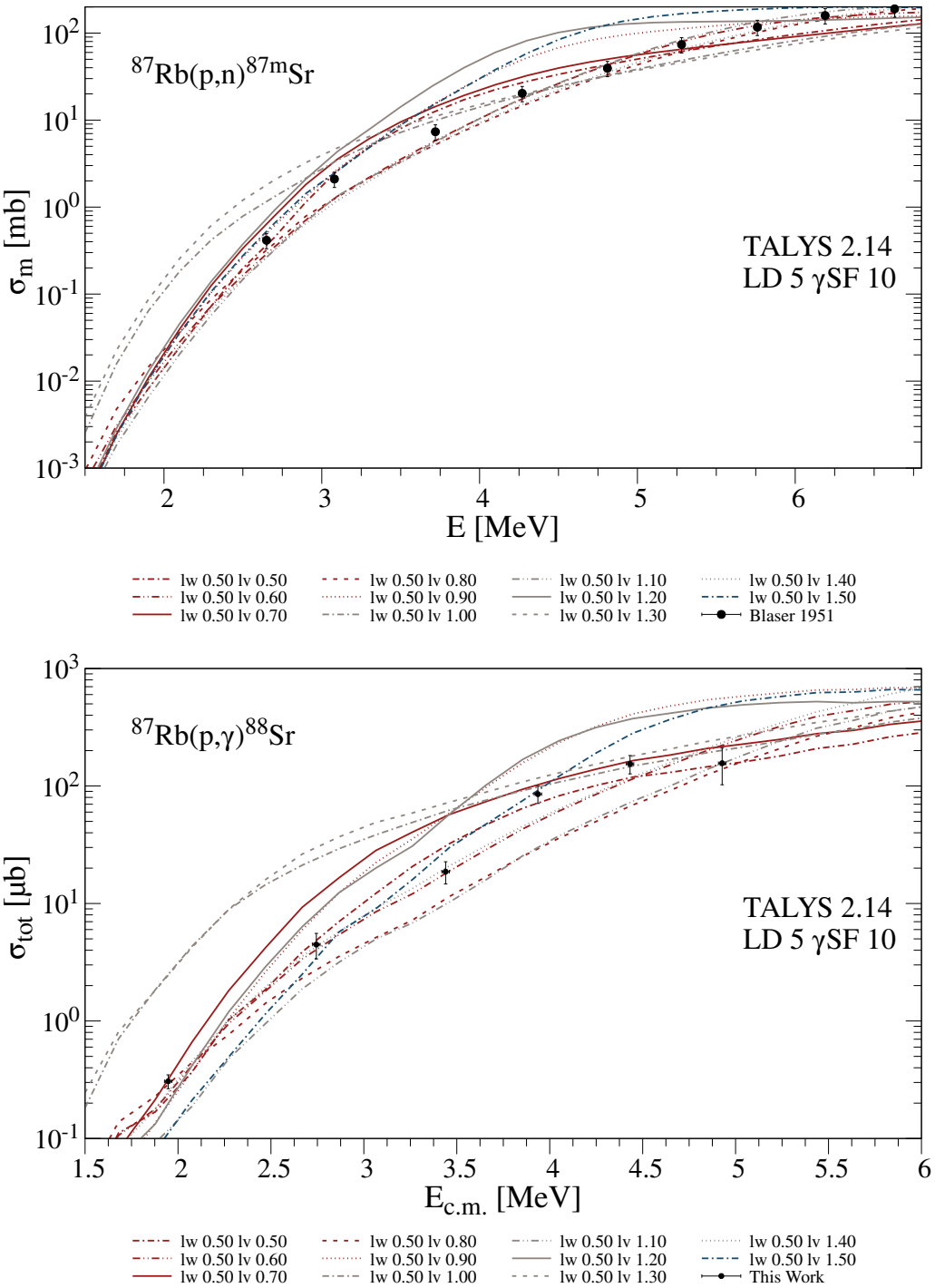

Figure 5.13: Same as Figure 5.12, but employing γ-ray strength model 10 instead of model 8. The predicted cross sections are overall lower than those obtained with model 8, and the magnitude of the (p, γ) data is reproduced more accurately.

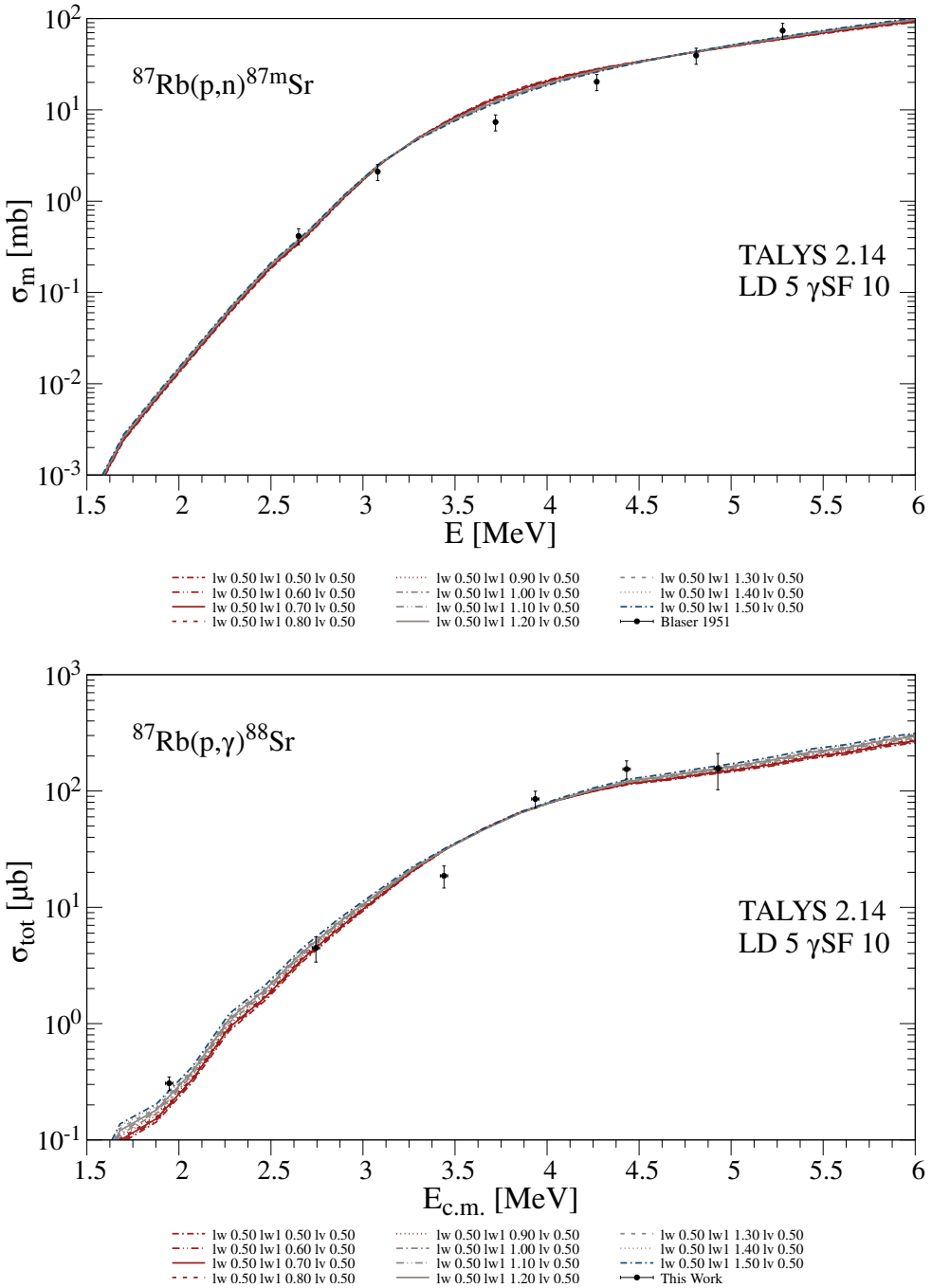

Figure 5.14: Variation of $lwadjust = lvadjust = 0.5$ with different values of $lw1adjust$, employing γ-ray strength model 10 for proton-induced reactions on ^{87}Rb. The upper panel shows the predicted isomeric (p, n) cross sections in comparison with the experimental data from Reference [139]. The overall energy dependence is reproduced reasonably well, although not all data points are accurately described. A similar behavior is observed in the lower panel, which compares the predicted and experimental cross sections for the (p, γ) reaction.

.

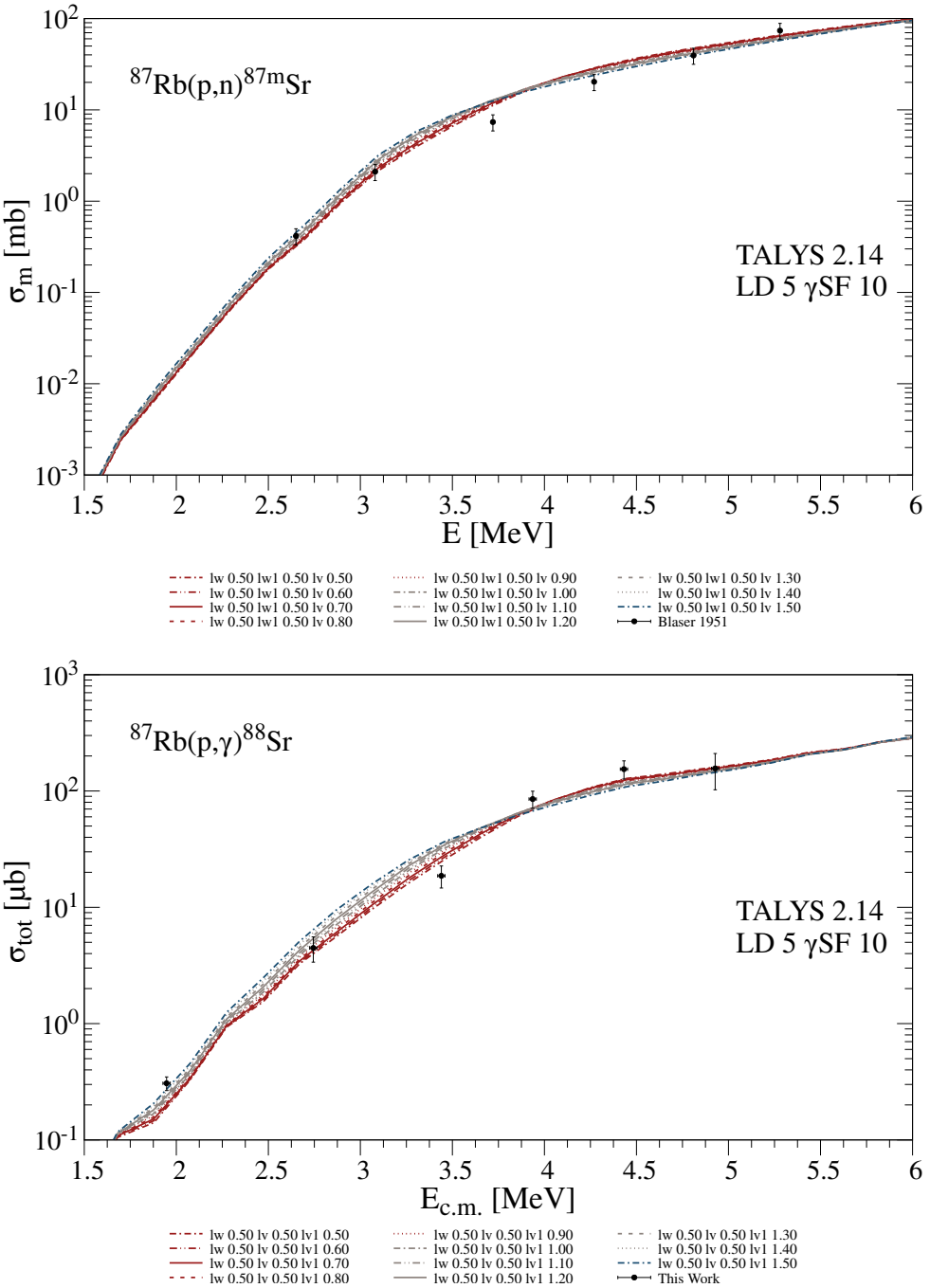

Figure 5.15: Variation of $lwadjust = lvadjust = 0.5$ with different values of $lv1adjust$, employing γ-ray strength model 10 for proton-induced reactions on ^{87}Rb. The influence on predicted cross sections is slightly greater than for variations of $lw1adjust$ in the presented energy region. The upper panel shows the predicted isomeric (p, n) cross sections in comparison with the experimental data from Reference [139]. The overall energy dependence is reproduced reasonably well, although not all data points are accurately described. A similar behavior is observed in the lower panel, which compares the predicted and experimental cross sections for the (p, γ) reaction.

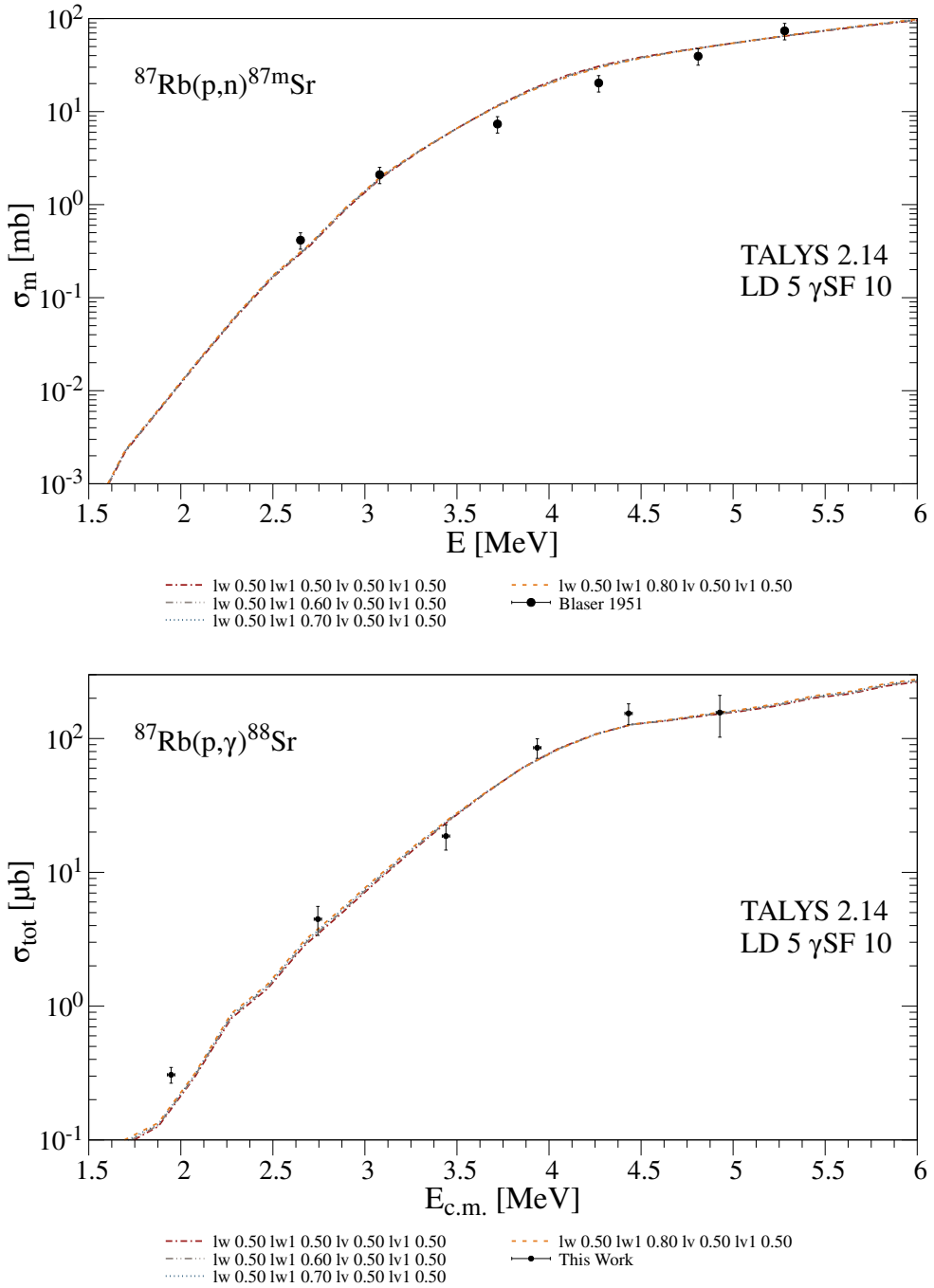

Figure 5.16: Best-fitting variation of $lwadjust = lvadjust = lv1adjust = 0.5$ with the altered $lw1adjust$, employing γ-ray strength model 10 for proton-induced reactions on ^{87}Rb. The different parameter combinations result in only minor deviations and provide an overall reasonable agreement with the experimental data. For the isomeric (p, n) data [139], discrepancies remain in the energy range between 3.5 MeV to 4.5 MeV, while for the (p, γ) reaction, the lowest data point is slightly underestimated with the employed parameter combinations.

5.6 Summary ^{87}Rb

In this chapter, the radiative proton-capture reaction $^{87}\mathrm{Rb}(p,\gamma)^{88}\mathrm{Sr}$ was investigated experimentally for the first time at astrophysically relevant energies between 2 MeV and 5 MeV using in-beam γ-ray spectroscopy with the HORUS spectrometer. The measurement provides total cross sections covering almost the entire Gamow window of the γ process, thereby constraining theoretical model predictions for reactions along the $N = 50$ isotonic chain.

A detailed analysis of the target preparation, beam properties, detection efficiencies, and angular distributions enabled a reliable extraction of total cross sections.

The dominant contribution to the total cross section originates from the de-excitation of the first excited 2_1^+ state at 1836 keV to the ground state. The obtained experimental cross sections are generally lower than those predicted by the TALYS calculations, although the overall trend and magnitude are reasonably well reproduced when employing microscopic level densities from the combinatorial model of Hilaire and Goriely (*ldmodel* 5) and Gogny–Hartree–Fock–Bogoliubov + QRPA dipole γ-ray strength functions. Remaining discrepancies, particularly at lower energies, indicate a possible need for refined input parameters, especially concerning the γ-ray strength function.

In addition to the published analysis, additional details and further studies were carried out to address systematic effects and model dependencies. A correction approach for the live-time behavior of BGO-shielded detectors was developed, to gain reasonable life times. Furthermore, the determination of the target thickness based on Rutherford Backscattering Spectrometry (RBS) and comparative yield analysis ensured the robustness of the extracted cross sections. Subsequent TALYS 2.14 calculations with various optical model potentials showed that neither the default Koning–Delaroche nor the JLM potentials could simultaneously reproduce both the (p,γ) and (p,n) reaction channels in their default settings, motivating the parameter adaptations discussed in detail above.

Overall, the new $^{87}\mathrm{Rb}(p,\gamma)^{88}\mathrm{Sr}$ data help to close an important gap in the systematic investigation of proton-capture reactions along the $N = 50$ isotones and provide valuable constraints for statistical model calculations and nucleosynthesis simulations within the γ process. Future work will include a detailed evaluation of the impact of these data on stellar reaction rates and a comparison with the $^{85}\mathrm{Rb}(p,\gamma)^{86}\mathrm{Sr}$ reaction to further improve the consistency of the employed nuclear-physics models.

6 Discussion of the Cross Section Results for ^{85,87}Rb(p,γ)^{86,88}Sr and the Astrophysical Impact

The overprediction of proton-induced reaction cross sections in the mass region $A = 82$–87, spanning from Kr to Sr, as observed for the isotopes ^{85}Rb and ^{87}Rb studied in this work, has been reported in several experimental studies (e. g. [241–243]). These deviations indicate systematic uncertainties in the statistical Hauser–Feshbach model.

Reference [243] attributes the discrepancies to uncertainties in both the optical model potential and the nuclear level density. Whereas Reference [242] relates the overprediction directly to an inaccurately calculated proton width [110]. Reference [241] emphasizes that (p, γ) cross sections are sensitive to the choice of the proton optical model potential and to width-fluctuation corrections. Owing to the employed experimental setup, that study was also able to place constraints on the nuclear level density and γ-ray strength function.

In their analysis, Tsantiri *et al.* [241], investigating the ^{82}Kr(p, γ) reaction in inverse kinematics, adjusted the Talys input by modifying the width-fluctuation factor (*widthmode* 2) and by adopting an alternative mode of the JLM [135] optical model potential, namely (*jlmmode* 3). Such modifications were not applicable to the present experiments, since the neutron channel opens already at 1.8 MeV and 0.5 MeV for proton-induced reactions on ^{85}Rb and ^{87}Rb, respectively. In contrast, this channel remained closed in their study due to a threshold of 5.1 MeV. For this, they chose the upper limit for the energy deliberately [244] and also applied this limitation for another experiment to avoid problems with particle emission channels [245].

6.1 The stable Rb isotopes and their role in Supernova models

Figures 6.1 and 6.2 present the integrated reaction flux in the $A \approx 75 - 90$ mass region for a $25\,M_\odot$ supernova model. The data are taken from Reference [246]. The nucleosynthesis in such a supernova environment depends sensitively on the adopted nuclear reaction rates, particularly on the (p, γ) and (γ, p) branchings around the $N = 50$ shell closure.

For both temperatures, this region of the chart of nuclei exhibits a complex reaction flux pattern, including single neutron and proton captures as well as their inverse photodisintegration

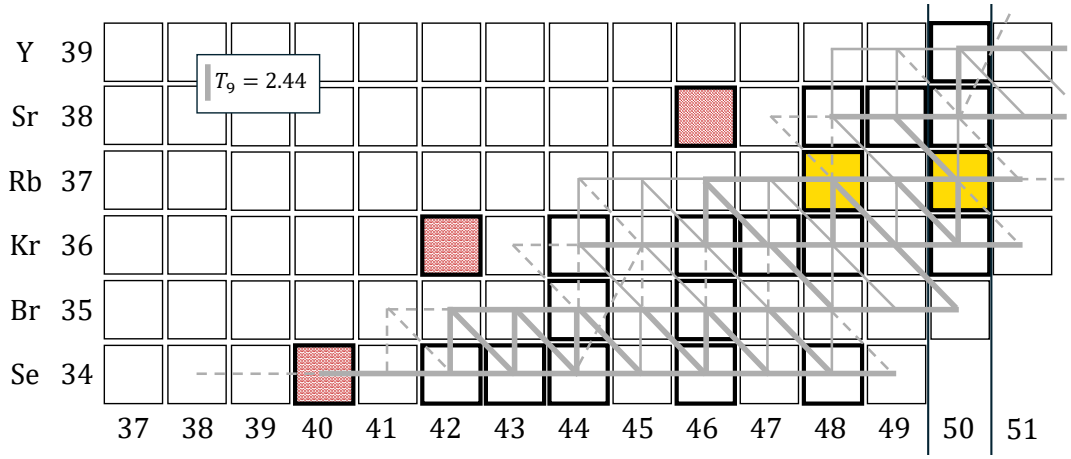

Figure 6.1: Integrated reaction flux for the first second of a Type II SN explosion for a peak temperature of 2.44 GK in the Ne/O layer of a $25M_{\odot}$ star. The thickness of the respective lines correspond to the reaction flux as follows: thick solid – $> 10^{-10}$, thin solid – $> 10^{-11}$, dashed – $> 10^{-12}$. Figure adapted from Reference [246]. The *p*-nuclei ^{74}Se, ^{78}Kr, and ^{84}Sr are marked in red. The two stable Rb isotopes, for which proton-induced reactions have been investigated in this thesis, are marked in yellow.

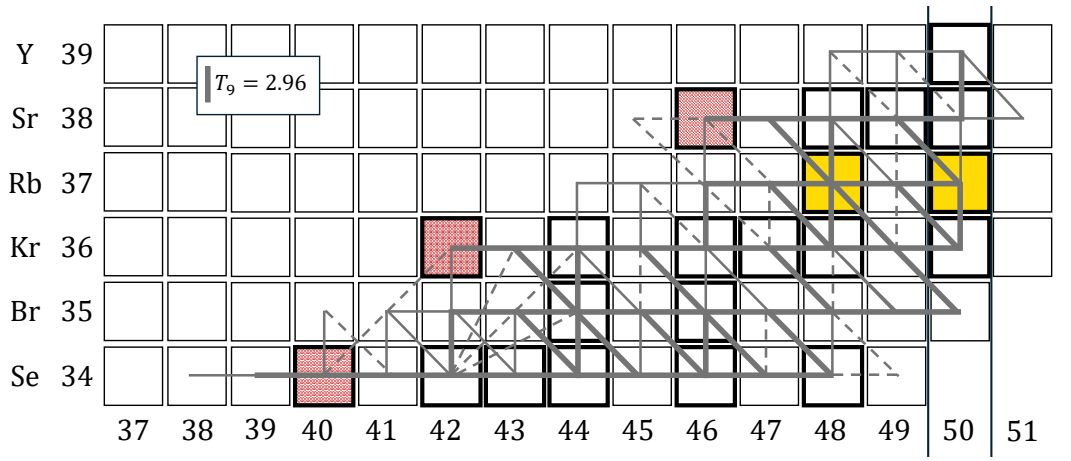

Figure 6.2: Integrated reaction flux for the first second of a Type II SN explosion for a peak temperature of 2.96 GK in the Ne/O layer of a $25M_{\odot}$ star. The thickness of the respective lines correspond to the reaction flux as follows: thick solid – $> 10^{-10}$, thin solid – $> 10^{-11}$, dashed – $> 10^{-12}$. Figure adapted from Reference [246]. The *p*-nuclei ^{74}Se, ^{78}Kr, and ^{84}Sr are marked in red. The two stable Rb isotopes, for which proton-induced reactions have been investigated in this thesis, are marked in yellow.

Table 6.1: The ground state contribution for calculating stellar reaction rates for the investigated reactions at two different plasma temperatures of 2.5 GK and 3.0 GK. Values are given for both reaction directions. The data is taken from Reference [110].

Temperature	**^{85}Rb$(p,\gamma)^{86}$Sr**		**^{87}Rb$(p,\gamma)^{88}$Sr**	
T [GK]	(p,γ)	(γ,p)	(p,γ)	(γ,p)
2.50	0.683	0.004 90	0.841	0.0164
3.00	0.627	0.005 04	0.752	0.0138

reactions. Due to the relatively low single particle thresholds, (p,n) and (n,p) reactions also contribute to the reaction network, further complicating the overall flow. The three p-nuclei ^{74}Se, ^{78}Kr, and ^{84}Sr, located in this mass region, are marked in red, whereas the two stable Rb isotopes investigated in this thesis are indicated in yellow.

The comparison between the high-temperature (2.96 GK) and the low-temperature (2.44 GK) temperature layers reveals distinct reaction flow patterns. At lower temperature, the reaction flux proceeds mainly towards the proton-rich side of the $N = 50$ isotonic chain via consecutive (n,γ) captures. In contrast, at higher temperatures, the reaction flux is dominated by strong (γ,p) and (γ,n) reactions, that drive the material towards the $N = 50$ neutron shell closure and then down along the isotonic chain, predominantly through (γ,p) reactions, without crossing the closed shell (except for the Sr isotopic chain).

At 2.96 GK, all three p-nuclei are part of the reaction network, whereas at the lower temperature only ^{74}Se is included. Naturally, the overall reaction flux is determined by the initial seed abundance and the reaction rates. Between ^{85}Rb and ^{86}Sr, and ^{87}Rb and ^{88}Sr there is always a reaction flux, but it depends on the temperature.

Reference [110] investigated the ground state contributions of laboratory cross sections for calculating the stellar reaction rate. The closer the value is to unity, the greater its influence on the stellar reaction rate. This topic was shortly introduced in Section 1.4. Ground state contributions for the investigated reactions are presented in Table 6.1 at two different plasma temperatures of 2.5 GK and 3.0 GK similar to the temperatures in Figures 6.1 and 6.2. The corresponding values are shown for both the forward and inverse reactions. As explained above, the ground state contribution of the (p,γ) direction is significantly higher than the contribution of the inverse reaction.

6.2 From Nuclear Data to Stellar Abundances

Observational evidence further constrains the nucleosynthesis of elements in the mass region around $A \approx 85$, which includes Rb, Sr, Y, and Zr. Roederer *et al.* [247] presented a detailed abundance study of the metal-poor, r-process–enhanced star HD 222925, deriving abundances for 46 elements using high-resolution spectroscopy. While the heavy r-process elements (e.g.,

Ba, Eu, Th) show strong enhancements, the light trans-iron elements exhibit significantly lower abundances. For rubidium, only an upper limit could be derived.

The experimental investigations of $^{85,87}\mathrm{Rb}(p,\gamma)$ and $^{85,87}\mathrm{Rb}(p,n)$ reactions presented in this thesis provide essential nuclear-physics input for refining these rates, thereby improving the predictive power of network calculations that aim to reproduce the observed Rb abundances in stellar and supernova environments. Paired with the next generation telescopes, more actual measurements of Rb in stars will be achievable, helping to improve abundance analysis.

6.3 Inverse Reactions

As explained above, the ground-state contribution for (p,γ) reactions is far higher than for (γ,p)-reactions. The adaptions to the calculations with the TALYS 2.14 code [124], that showed the best agreements to the experimental data are used to additionally calculate the inverse reaction cross sections for the investigated nuclei on their ground state.

6.3.1 $^{85}\mathrm{Sr}(n,p)$ and $^{86}\mathrm{Sr}(\gamma,p)$

The calculated cross sections for the inverse reactions on ^{85}Rb, obtained using the modified JLM optical model potential [135] as described in Section 4.5.6, and computed with the TALYS 2.14 code [124], are shown in Figures 6.3 and 6.4.

For the $^{85}\mathrm{Sr}(n,p)$ reaction, the predicted cross sections differ notably between the default and the adapted JLM potentials. The default calculation exhibits a more complex structure than the adapted ones: it shows a dip around 0.1 MeV, followed by an increase reaching a maximum near 0.6 MeV, and another minimum around 1.4 MeV. A second maximum appears at approximately 3.2 MeV, after which the cross section becomes nearly constant above 4.5 MeV.

In contrast, the adapted JLM potentials predict only a single flat minimum around 1 MeV and yield higher cross sections above 4.5 MeV. Below 0.5 MeV, the adapted models predict cross sections up to a factor of five higher than those obtained with the default potential. From 2.5 MeV onward, the cross section remains approximately constant. The absolute magnitude of the predicted values increases with the *lwadjust* parameter, while the overall trend of the different adaptations remains consistent.

The photodisintegration reaction $^{86}\mathrm{Sr}(\gamma,p)$ show no difference when utilizing the different versions of the JLM models computing the cross sections with the TALYS 2.14 code [124] in the presented energy range. The predicted cross section increases with some structure visible around 8 MeV.

Unfortunately, no experimental data are available for these reactions for a direct comparison. The pronounced deviations of the predicted cross sections, particularly at low neutron energies, may have a direct impact on supernova nucleosynthesis models, as illustrated in Figures 6.1 and 6.2. An inaccurate prediction of the (n,p) rate could alter the balance between proton- and neutron-induced channels, potentially modifying the resulting isotopic abundances in supernova nucleosynthesis models [246].

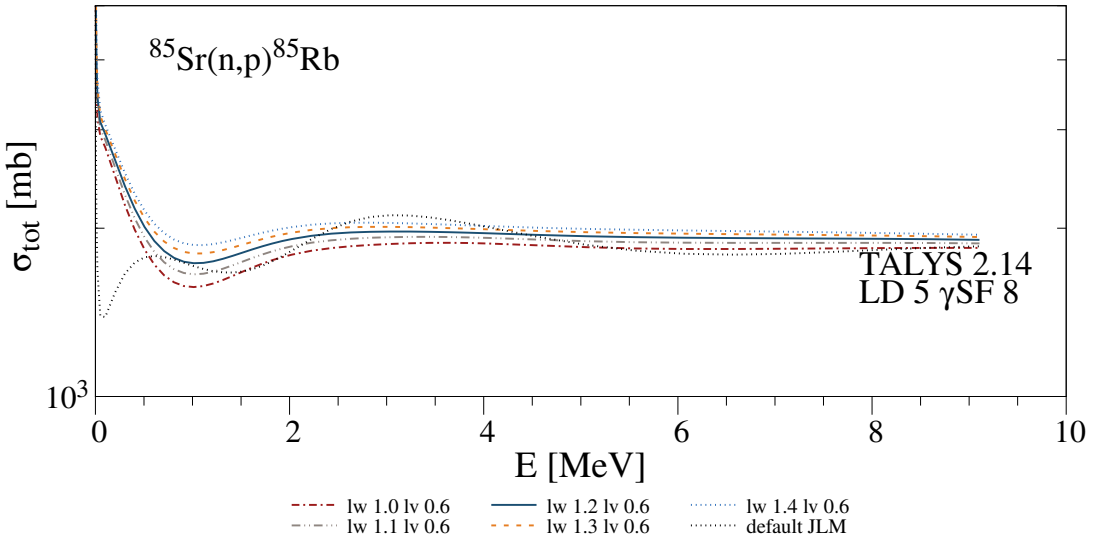

Figure 6.3: Predicted cross sections for the inverse $^{85}\mathrm{Rb}(p,n)$ reaction utilizing the parameters found for the forward reaction. The predicted cross sections differ between the default and the adapted JLM potentials. The adapted potentials predict smoother energy dependencies and higher cross sections at low neutron energies, with higher predicted cross sections for larger *lwadjust* values.

6.3.2 $^{87}\mathrm{Sr}(n,p)$ and $^{88}\mathrm{Sr}(\gamma,p)$

The calculated cross sections for the inverse reactions on ^{87}Rb, obtained using the modified JLM optical model potential [135] as described in Section 5.5 and computed with the TALYS 2.14 code [124], are shown in Figures 6.5 and 6.6.

For the $^{87}\mathrm{Sr}(n,p)$ reaction, the predicted cross sections differ notably between the default and the adapted JLM potentials. These cross sections correspond to reactions on the ground state of ^{88}Sr. The default calculation exhibits a more complex structure: it shows a dip around 0.1 MeV, followed by a rise reaching a saddle point near 1 MeV. A second maximum appears at approximately 3 MeV, after which the cross section becomes nearly constant above 6 MeV.

In contrast, the adapted JLM potentials predict a smoother behavior, with a single minimum around 2 MeV and generally lower cross sections above 1.5 MeV, reaching a maximum near 5.5 MeV. At neutron energies below 1.5 MeV, however, the adapted potentials yield cross sections up to a factor of four higher than those from the default model, with a maximum around 0.5 MeV. From about 8 MeV onward, the cross sections remain approximately constant. The absolute magnitude of the predictions increases slightly with higher *lw1adjust* values, whereas the overall energy dependence remains consistent across the tested parameter combinations.

For the $^{88}\mathrm{Sr}(\gamma,p)$ reaction, no significant differences are observed between the default and adapted JLM potentials in the investigated energy range when using the TALYS 2.14 code. The predicted cross sections increase gradually with energy, exhibiting minor structure around 4 MeV.

Since no experimental data are available for these inverse reactions, a direct validation of the

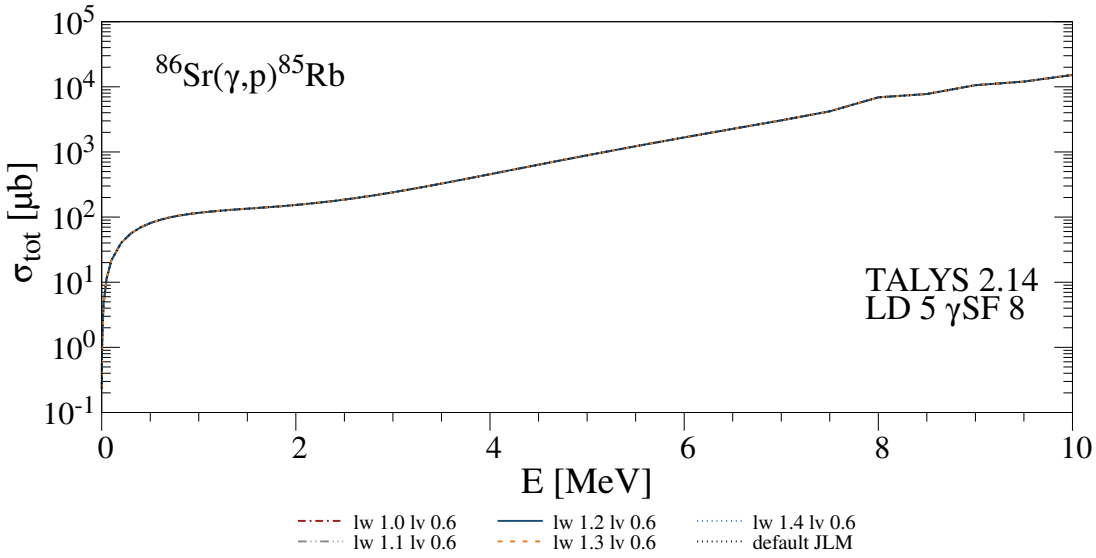

Figure 6.4: Predicted cross sections for the inverse $^{85}\mathrm{Rb}(p,\gamma)$ reaction utilizing the parameters found for the forward reaction. No difference when utilizing the different versions of the JLM models computing the cross sections with the TALYS 2.14 code [124] is observed in the presented energy range. The predicted cross section increases over the energy range with some small structure around 8 MeV.

predictions is currently not possible. Nevertheless, the pronounced deviations at low neutron energies suggest that such differences could influence supernova nucleosynthesis models, as illustrated in Figures 6.1 and 6.2. An inaccurate prediction of the (n,p) reaction rate would affect the balance between proton- and neutron-induced channels, potentially altering the final isotopic abundances in γ-process simulations [246]. Given that the optical potential was adapted to reproduce the isomeric component of the (p,n) cross section, future work should verify these results against total and ground state (p,n) cross sections to ensure model consistency.

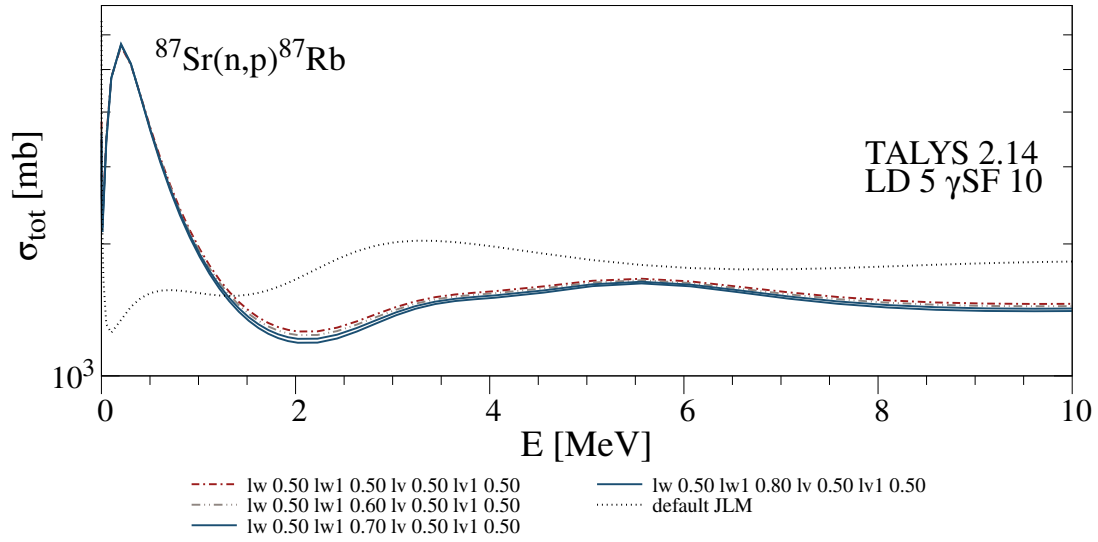

Figure 6.5: Predicted cross sections for the inverse $^{87}\mathrm{Rb}(p,n)$ reaction utilizing the best parameters found for the forward reaction. The predicted cross sections differ between the default and the adapted JLM potentials. The adapted potentials predict smoother energy dependencies and higher cross sections at low neutron energies.

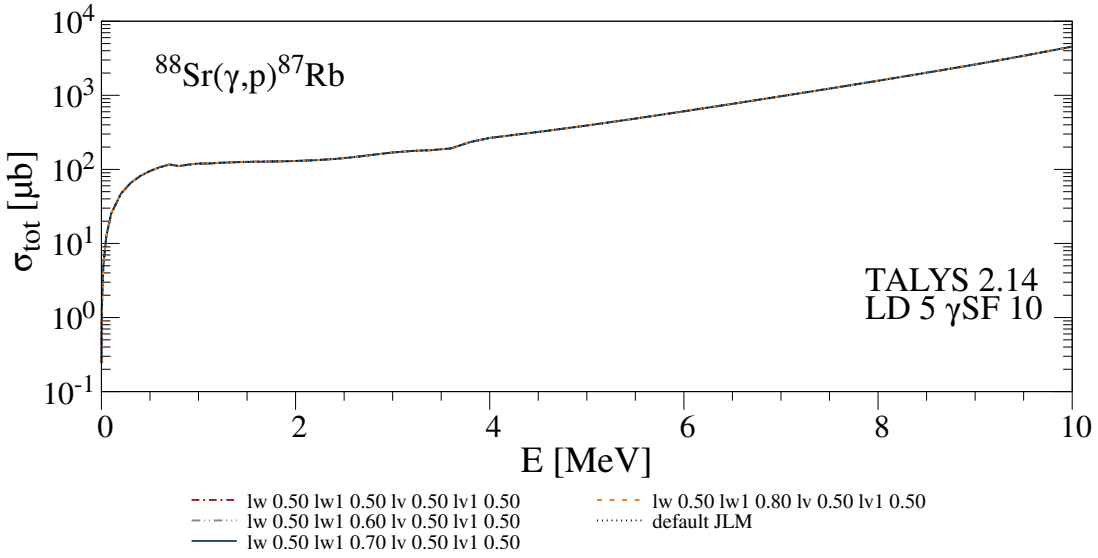

Figure 6.6: Predicted cross sections for the inverse $^{87}\mathrm{Rb}(p,\gamma)$ reaction utilizing the best parameters found for the forward reaction. No difference when utilizing the different versions of the JLM models computing the cross sections with the TALYS 2.14 code [124] is observed in the presented energy range. The predicted cross section increases over the energy range with some small structure around 4 MeV.

7 Summary and Outlook

This thesis presents experimental investigations of the reactions ^{85}Rb$(p,\gamma)^{86}$Sr and ^{87}Rb$(p,\gamma)^{88}$Sr, both of which are relevant to the astrophysical γ-process. The measurements were carried out at the HORUS spectrometer at the 10 MV Tandem accelerator at the Institute for Nuclear Physics, University of Cologne. Both experiments aimed to provide the first experimental cross-section data for these reactions in the energy range of the astrophysically relevant Gamow energy between approximately 1.4 MeV to 3.2 MeV for the investigated reactions and to test the predictive power of statistical model calculations in the mass region near the $N = 50$ shell closure.

The ^{85}Rb$(p,\gamma)^{86}$Sr reaction was investigated using RbCl targets enriched in ^{85}Rb on thick gold backing. During both target preparation and beam irradiation, interdiffusion of the Rb compound into the gold layer occurred, complicating the precise determination of the effective target thickness. In addition to that, the target was deteriorated during the irradiation, wherefore a normalization to 10 min time intervals to the product of the number of projectiles and number of target nuclei had to be performed. Therefore, a systematic uncertainty dominating the overall uncertainties was introduced into final cross section values. The proton beam energies were selected between 3.4 and 4.0 MeV, and the reaction γ rays were measured utilizing the chamber for nuclear astrophysics experiments, that was used until 2019, installed in the HORUS spectrometer. The complex spectra due to the beam induced background required detailed $\gamma\gamma$ coincidence analysis to extract reliable total cross sections.

For the ^{87}Rb$(p,\gamma)^{88}$Sr reaction, Rb_2CO_3 enriched in ^{87}Rb was used to prepare targets for the experimental campaign by evaporation onto thick gold backings. A similar behavior regarding the interdiffusion of the target and backing layer was observed when performing RBS measurements after the experiment. Since the ratio of the 279 keV peak stemming from the Coulomb excitation in ^{197}Au [225] and the 484 keV peak from the ^{87}Rb(p,n) reaction [159], chosen to monitor the target during the experiment, was constant, it is assumed that no deterioration took place. Due to the complex target behavior, a second, not exposed to the beam before RBS measurements took place, target was used to normalize the reaction yield for the ^{85}Rb(p,γ) reaction for thickness determination. This experiment provided the first experimental (p,γ) data on this isotope and served as an important benchmark to test the consistency of statistical model predictions along the $N = 50$ isotonic chain. It further demonstrated that total cross sections as low as 300 nb can be measured utilizing the combination of the re-designed Astrochamber and the NuDAQ system.

Since both target materials, $RbCO_3$ and RbCl, tend to intermix with the gold backing, either during target preparation or during irradiation in the experiment, this interdiffusion makes it very difficult, if not impossible, to determine the target thicknesses with an appropriate level of

accuracy. Therefore, alternative backing materials should be investigated in future studies to reduce the uncertainties associated with the target thickness determination. This has a direct influence on the cross section determinations.

In both experimental campaigns, the measured cross sections were compared to Hauser–Feshbach model calculations performed with the TALYS version 2.0 and 2.14 code. The calculations were systematically varied with respect to the nuclear level density, γ-ray strength function, and optical model potentials. None of the tested parameter combinations in their default settings reproduced both data sets consistently. The strongest sensitivity for the shape of the cross section was observed if one varied the the proton optical model potential, whereas the variations in the nuclear level density and γ-strength function mainly affected the absolute scale.

The Hauser–Feshbach calculations were compared with both experiments as well as (p, n) data from References [139, 140, 237, 238] and further explored by systematically varying and adapting key model parameters. The measured ^{85}Rb and ^{87}Rb cross sections could not be described consistently within the standard framework. This discrepancy points to remaining uncertainties in the description of nuclear properties relevant to the γ-process in this mass region. The optical model potential JLM [135] was further tested by adjusting its real and imaginary normalization parameters. These local modifications improved the agreement, providing a consistent description of both (p, n) and (p, γ) data simultaneously. The case for ^{87}Rb was more difficult, since only cross section data for the isomeric (p, n) channel are reported [139]. Therefore, the results should be confirmed with total cross section data for the (p, n) channel. This demonstrates that comparing only a single reaction channel is insufficient, wherefore multiple reaction channels need to be considered to properly constrain the model parameters. The lack of elastic-scattering data for ^{85,87}Rb prevents an independent validation of these adjustments. Furthermore, as demonstrated in the publication on ^{87}Rb, significant deviations and non-uniform trends are observed along the $N = 50$ isotonic chain, indicating that a coherent description across these nuclei is still lacking.

The newly obtained reaction data represent an important step toward improving nuclear-physics input for the γ-process in the $N = 50$ mass region. Future work should focus on complementary experiments on neighboring isotones such as ^{86}Kr and on constraining the optical model potentials through elastic-scattering measurements. These efforts will reduce current model uncertainties and enhance the reliability of nucleosynthesis simulations in explosive stellar environments.

The HORUS spectrometer provides detectors at five different angles with respect to the beam axis, symmetrically distributed around 90°. Since the observed γ-ray de-excitations of the excited states exhibit an angular distribution symmetric about 90°, only three independent angles remain when fitting the data with Legendre polynomials. The two angles other than 90° differ by only about 10°, which is not ideal for extracting reliable angular distributions.

Another γ-ray spectrometer, which was recently commisioned, available at the University of Cologne is the Cologne CATHEDRAL. It consists of up to 24 detectors arranged in five angular groups at 30°, 55°, 90°, 125°, and 155° with respect to the beam axis, with an optional detector at 0°. This configuration provides a much broader angular coverage. A test experiment installing the re-designed Astrochamber in the Cologne CATHEDRAL setup could therefore evaluate whether

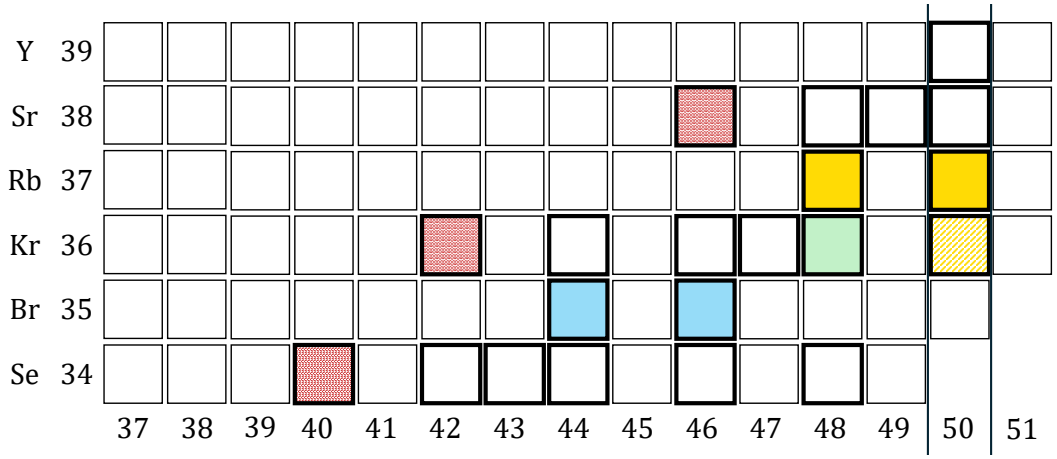

Figure 7.1: The $A = 80 - 90$ mass region around the left hand side of the valley of stability. The p-nuclei ^{74}Se, ^{78}Kr, and ^{84}Sr are marked in red. Yellow marks the nuclei that have been measured or investigated within the scope of this thesis. The proton-induced reactions on ^{85}Rb and ^{87}Rb have been analyzed, and a test measurement with $^{\text{nat}}$TlBr has been performed as a feasibility study. ^{86}Kr, marked with yellow stripes is the last stable isotone in the $N = 50$ chain, that was not investigated regarding (p, γ)-reactions. There are plans to perform the measurement in 2026. Measuring ^{84}Kr (green) can help to resolve discrepancies of two experiments performed in inverse kinematics.

the increased angular range and the larger number of detectors per angle improve the precision of the cross-section measurements. However, the greater detector-to-target distance compared to the HORUS setup is expected to reduce the detection efficiency, which represents a potential drawback of this configuration.

Future investigations could focus on constraining the optical model potentials through elastic and quasielastic proton scattering experiments. The new ALPACA setup at the University of Cologne [248] provides the opportunity to measure angular distributions for (p, p') and (p, n) reactions with high precision at energies below 10 MeV. Such measurements are particularly valuable for improving the isoscalar component of the Jeukenne–Lejeune–Mahaux (JLM) optical model potential [137], since in this energy regime experimental data are scarce and global potentials remain poorly constrained. Refining the real and imaginary parts of the potential by comparison with elastic-scattering data would directly improve the reliability of Hauser–Feshbach calculations of proton-induced cross sections. This is especially relevant for the γ-process, where (p, γ) and (γ, p) reactions play a key role and their predicted cross sections are highly sensitive to the chosen proton optical model potential. Thus, low-energy angular distribution data such as from ALPACA could significantly reduce the current nuclear-physics uncertainties that limit the accuracy of γ-process nucleosynthesis models.

Figure 7.1 presents the mass region of interest for this thesis. The p-nuclei ^{74}Se, ^{78}Kr, and ^{84}Sr are marked in red, while yellow presents nuclei where experimental data is directly linked to this work. Within the scope of this thesis, the proton-induced reactions on ^{85}Rb and ^{87}Rb were analyzed, and a test measurement using a $^{\text{nat}}$TlBr target [249] was conducted as a feasibility study

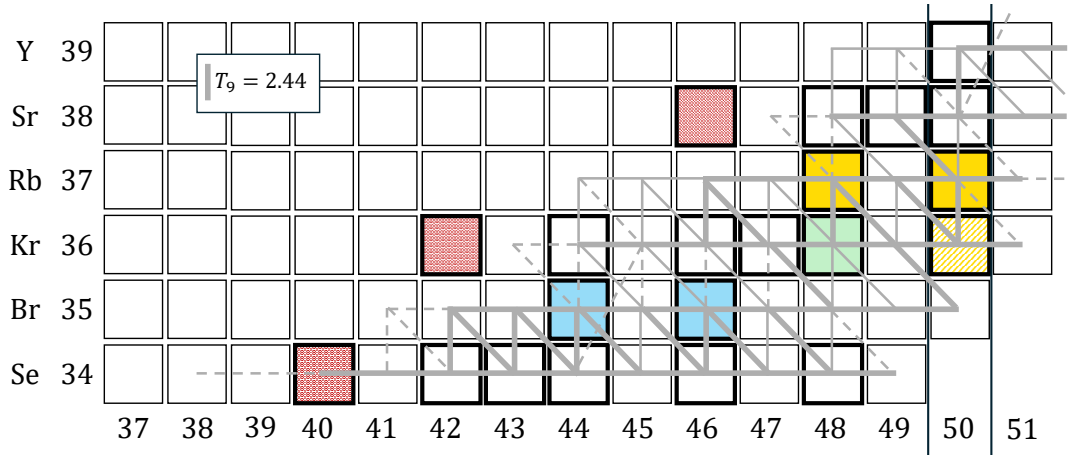

Figure 7.2: Integrated reaction flux for the first second of a Type II SN explosion for a peak temperature of 2.44 GK in the Ne/O layer of a $25M_\odot$ star. The thickness of the respective lines correspond to the reaction flux as follows: thick solid – $> 10^{-10}$, thin solid – $> 10^{-11}$, dashed – $> 10^{-12}$. Figure adapted from Reference [246]. The p-nuclei ^{74}Se, ^{78}Kr, and ^{84}Sr are marked in red. The two stable Rb isotopes, for which proton-induced reactions have been investigated in this thesis, are marked in yellow. A planned in-beam experiment on ^{86}Kr is marked with yellow stripes. The two stable Br isotopes are marked in blue. A test experiment for the feasibility has been performed on $^{\text{nat}}$Br.

for future measurements on ^{79}Br(p,γ) and ^{81}Br(p,γ). The ^{79}Br(p,γ) reaction was identified as an important reaction in sensitive branchings [19]. The isotope ^{86}Kr, shown with yellow stripes, is the last stable isotone in the $N = 50$ chain that has not yet been investigated in terms of (p,γ) reactions. A dedicated measurement is planned for early 2026. For these three (p,γ) reactions there are no reported data so far. As it is shown in Figures 7.2 and 7.3, these reactions all are quite cross-linked in the reaction network of the supernova model [246].

Measuring ^{84}Kr, colored in green, can help to resolve discrepancies of two experiments both performed in inverse kinematics utilizing two different measurement techniques, where the results deviate by a factor of two [250, 251]. Due to the possibility of implanting Kr into a backing, it is possible to perform a direct measurement to hopefully resolve these deviations. Since the (p,n) channel is open and ^{84}Rb has a half-life of 32.8 d, it would be suitable for an experiment combining the in-beam technique to investigate the (p,γ) reaction with back to back activation measurement to gain insight of the (p,n) reaction. The latter could be interesting for the νp-process [252].

There are plans to review all literature on reported experimental data to implement the newest findings into network reaction models and study the impact of these new data on the reaction network predictions [252]. This will hopefully bring us closer to a greater understanding on how and where the elements, especially the p-nuclei are produced. The experiments presented in this thesis as well as the proposed future experiments can help to achieve this goal.

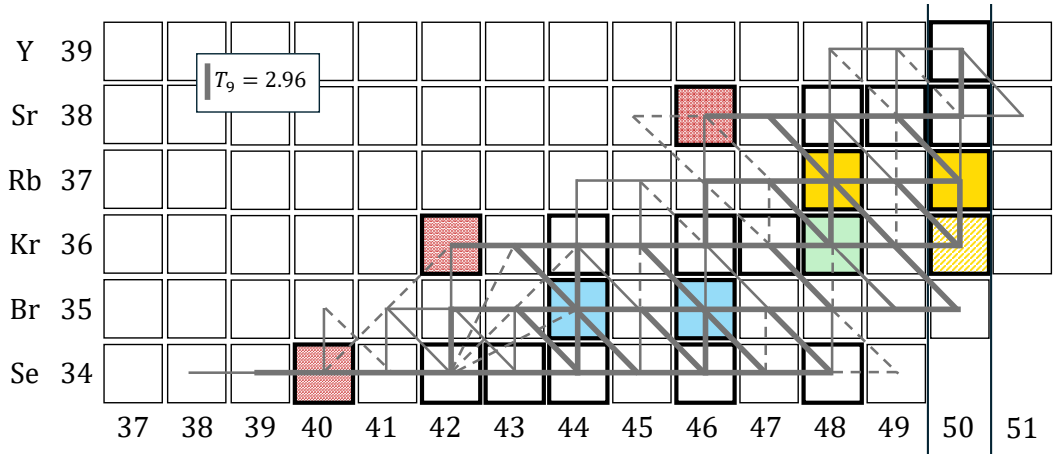

Figure 7.3: Integrated reaction flux for the first second of a Type II SN explosion for a peak temperature of 2.96 GK in the Ne/O layer of a $25 M_{\odot}$ star. The thickness of the respective lines correspond to the reaction flux as follows: thick solid – $> 10^{-10}$, thin solid – $> 10^{-11}$, dashed – $> 10^{-12}$. Figure adapted from Reference [246]. The *p*-nuclei ^{74}Se, ^{78}Kr, and ^{84}Sr are marked in red. The two stable Rb isotopes, for which proton-induced reactions have been investigated in this thesis, are marked in yellow. A planned in-beam experiment on ^{86}Kr is marked with yellow stripes. The two stable Br isotopes are marked in blue. A test experiment for the feasibility has been performed on $^{\text{nat}}$Br.

List of Figures

List of Tables

Bibliography

[1] S. Dieck, O. Michael, M. Wilke, T. Halle, C.-H. Wunderlich, J.-H. Bunnefeld, H. R. Bauer, and H. Meller, *Archaeometallurgical investigation of the Nebra Sky Disc*, Sci. Rep. **14** (2024).

[2] *UNESCO - Memory of the World - Nebra Sky Disk*. https://www.unesco.org/en/memory-world/nebra-sky-disc?hub=1081. (Last accessed 06.11.2025).

[3] C. Ptolemy, *Ptolemy's Almagest*, ed. and trans. by G. J. Toomer. English translation and commentary of Ptolemy's *Almagest*. Princeton, NJ: Princeton University Press, 1984. ISBN: 978-0-691-00260-6.

[4] G. Kirchhoff, *Über den Zusammenhang zwischen Emission und Absorption von Licht und Wärme*, Annalen der Physik **185** (1860) 275.

[5] C. Payne, *Stellar Atmospheres: A Contribution to the Observational Study of High Temperature in the Reversing Layers of Stars*, PhD thesis. Radcliffe College, Harvard University, 1925.

[6] F. W. Aston, *Isotopes and Atomic Weights*, Nature **105** (1920) 617.

[7] F. W. Aston, *The Constitution of the Elements*, Nature **106** (1920) 468.

[8] A. S. Eddington, *The Internal Constitution of the Stars*, The Scientific Monthly **11** (1920) 297.

[9] J. Chadwick, *The Existence of a Neutron*, Proc. R. Soc. Lond. A Math. Phys. Sci **136** (1932) 692.

[10] H. A. Bethe, *Energy Production in Stars*, Phys. Rev. **55** (1939) 434.

[11] E. M. Burbidge, G. R. Burbidge, W. A. Fowler, and F. Hoyle, *Synthesis of the Elements in Stars*, Rev. Mod. Phys. **29** (1957) 547.

[12] H. E. Suess and H. C. Urey, *Abundances of the Elements*, Rev. Mod. Phys. **28** (1956) 53.

[13] G. Gamow, *Expanding Universe and the Origin of Elements*, Phys. Rev. **70** (1946) 572.

[14] R. A. Alpher, H. A. Bethe, and G. Gamow, *The Origin of Chemical Elements*, Physical Review **73** (1948) 803.

[15] R. A. Alpher and R. C. Herman, *Evolution of the Universe*, Nature **162** (1948) 774.

[16] R. A. Alpher and R. C. Herman, *Remarks on the Evolution of the Expanding Universe*, Physical Review **75** (1949) 1089.

[17] F. Hoyle, *On Nuclear Reactions Occurring in Very Hot Stars. I. The Synthesis of Elements from Carbon to Nickel*, Astrophys. J. Suppl. Ser. **1** (1954) 121.

[18] D. N. F. Dunbar, R. E. Pixley, W. A. Wenzel, and W. Whaling, *The 7.68-MeV State in ^{12}C*, Phys. Rev. **92** (1953) 649.

[19] T. Rauscher, *Branchings in the γ process path revisited*, Phys. Rev. C **73** (2006).

[20] V. Goldschmidt, *Geochemische Verteilungsgesetze der Elemente*, Norske Vidensk. Akad. Skrifter I Mat. Naturv. Kl. 4 **1** (1937).

[21] H. Brown, *A Table of Relative Abundances of Nuclear Species*, Rev. Mod. Phys. **21** (1949) 625.

[22] K. Lodders, *Solar Elemental Abundances*, Oxford Research Encyclopedia of Planetary Science (2020).

[23] J. A. Johnson, B. D. Fields, and T. A. Thompson, *The origin of the elements: a century of progress*, Philos. Trans. R. Soc. A **378** (2020) 20190301.

[24] C. Iliadis, *Nuclear Physics of Stars*, Wiley, 2007. ISBN: 9783527618750.

[25] E. G. Adelberger *et al.*, *Solar fusion cross sections. II. The pp chain and CNO cycles*, Rev. Mod. Phys. **83** (2011) 195.

[26] B. W. Carroll and D. A. Ostlie, *An Introduction to Modern Astrophysics*, Cambridge University Press, 2017. ISBN: 9781108380980.

[27] E. J. Öpik, *Stellar Models with Variable Composition. II. Sequences of Models with Energy Generation Proportional to the Fifteenth Power of Temperature*, Math. Proc. R. Ir. Acad. **54** (1951) 49.

[28] E. E. Salpeter, *Nuclear Reactions in the Stars. I. Proton-Proton Chain*, Phys. Rev. **88** (1952) 547.

[29] E. E. Salpeter, *Nuclear Reactions in Stars. Buildup from Helium*, Phys. Rev. **107** (1957) 516.

[30] D. E. Alburger, *Gamma-Ray Decay of the 7.66-Mev Level of ^{12}C*, Phys. Rev. **124** (1961) 193.

[31] J. A. Nolen and S. M. Austin, *Measurement of the excitation energy of the 7.654 MeV state of* ^{12}C *and the rate of the* 3α *reaction*, Phys. Rev. C **13** (1976) 1773.

[32] T. A. Lähde, U.-G. Meissner, and E. Epelbaum, *An update on fine-tunings in the triple-alpha process*, Eur. Phys. J. A **56** (2020).

[33] S. Jin, L. F. Roberts, S. M. Austin, and H. Schatz, *Enhanced triple-α reaction reduces proton-rich nucleosynthesis in supernovae*, Nature **588** (2020) 57.

[34] J. Bishop *et al.*, *Neutron-upscattering enhancement of the triple-alpha process*, Nat. Commun. **13** (2022).

[35] D. Werner, *Study of the Hoyle State in ^{12}C using the Lund-York-Cologne-Calorimeter (LYCCA) array*, PhD thesis. Köln, Deutschland: Universität zu Köln, 2024.

[36] S. E. Woosley, A. Heger, and T. A. Weaver, *The evolution and explosion of massive stars*, Rev. Mod. Phys. **74** (2002) 1015.

[37] F. Herwig, M. Pignatari, P. R. Woodward, D. H. Porter, G. Rockefeller, C. L. Fryer, M. Bennett, and R. Hirschi, *Convective-Reactive Proton-12C Combustion in Sakurai's Object (V4334 Sagittarii) and Implications for the Evolution and Yields from the First Generation of Stars*, Astrophys. J. **727** (2011) 89.

[38] A. Choplin, S. Ekström, G. Meynet, A. Maeder, C. Georgy, and R. Hirschi, *Pre-supernova mixing in CEMP-no source stars*, Astron. Astrophys. **605** (2017) A63.

[39] F. K. Thielemann and W. D. Arnett, *Hydrostatic Nucleosynthesis - Part Two - Core Neon to Silicon Burning and Presupernova Abundance Yields of Massive Stars*, Astrophys. J. **295** (1985) 604.

[40] C. Bertulani and T. Kajino, *Frontiers in nuclear astrophysics*, Prog. Part. Nucl. Phys. **89** (2016) 56.

[41] M. Arnould, S. Goriely, and K. Takahashi, *The r-process of stellar nucleosynthesis: Astrophysics and nuclear physics achievements and mysteries*, Phys. Rep. **450** (2007) 97.

[42] S. P. W. Merrill, *Spectroscopic Observations of Stars of Class*, Astrophys. J. **116** (1952) 21.

[43] F. Käppeler, R. Gallino, S. Bisterzo, and W. Aoki, *The s process: Nuclear physics, stellar models, and observations*, Rev. Mod. Phys. **83** (2011) 157.

[44] R. Reifarth, C. Lederer, and F. Käppeler, *Neutron reactions in astrophysics*, J. Phys. G: Nucl. Part. Phys **41** (2014) 053101.

[45] M. Lugaro, M. Pignatari, R. Reifarth, and M. Wiescher, *The s Process and Beyond*, Annu. Rev. Nucl. Part. Sci. **73** (2023) 315.

[46] M. Pignatari, R. Gallino, M. Heil, M. Wiescher, F. Käppeler, F. Herwig, and S. Bisterzo, *The weak s-Pocess in massive Stars and its Dependence on the Neutron Capture Cross Sections*, Astrophys. J. **710** (2010) 1557.

[47] J. J. Cowan, C. Sneden, J. E. Lawler, A. Aprahamian, M. Wiescher, K. Langanke, G. Martínez-Pinedo, and F.-K. Thielemann, *Origin of the heaviest elements: The rapid neutron-capture process*, Rev. Mod. Phys. **93** (2021).

[48] C. J. Horowitz *et al.*, *r-process nucleosynthesis: connecting rare-isotope beam facilities with the cosmos*, J. Phys. G **46** (2019) 083001.

[49] T. Marketin, L. Huther, and G. Martínez-Pinedo, *Large-scale evaluation of β-decay rates of r-process nuclei with the inclusion of first-forbidden transitions*, Phys. Rev. C **93** (2016).

[50] M. R. Mumpower, R. Surman, D.-L. Fang, M. Beard, P. Möller, T. Kawano, and A. Aprahamian, *Impact of individual nuclear masses on r-process abundances*, Phys. Rev. C **92** (2015).

[51] J. E. Escher, J. T. Harke, R. O. Hughes, N. D. Scielzo, R. J. Casperson, S. Ota, H. I. Park, A. Saastamoinen, and T. J. Ross, *Constraining Neutron Capture Cross Sections for Unstable Nuclei with Surrogate Reaction Data and Theory*, Phys. Rev. Lett. **121** (2018).

[52] A. Larsen, A. Spyrou, S. Liddick, and M. Guttormsen, *Novel techniques for constraining neutron-capture rates relevant for r-process heavy-element nucleosynthesis*, Prog. Part. Nucl. Phys. **107** (2019) 69.

[53] A. V. Voinov *et al.*, *Reduction of the neutron imaginary potential off the stability line and its possible impact on neutron capture rates*, Phys. Rev. C **104** (2021).

[54] M. Arnould and S. Goriely, *Astronuclear Physics: A tale of the atomic nuclei in the skies*, Prog. Part. Nucl. Phys. **112** (2020) 103766.

[55] A. Arcones and F.-K. Thielemann, *Origin of the elements*, Astron. Astrophys. Rev. **31** (2022).

[56] D. Kasen, B. Metzger, J. Barnes, E. Quataert, and E. Ramirez-Ruiz, *Origin of the heavy elements in binary neutron-star mergers from a gravitational-wave event*, Nature **551** (2017) 80.

[57] B. P. Abbott *et al.*, *Multi-messenger Observations of a Binary Neutron Star Merger**, Astrophys. J. Lett. **848** (2017) L12.

[58] B. P. Abbott *et al.*, *GW170817: Observation of Gravitational Waves from a Binary Neutron Star Inspiral*, Phys. Rev. Lett. **119** (2017).

[59] M. Nicholl *et al.*, *The Electromagnetic Counterpart of the Binary Neutron Star Merger LIGO/Virgo GW170817. III. Optical and UV Spectra of a Blue Kilonova from Fast Polar Ejecta*, Astrophys. J. Lett. **848** (2017) L18.

[60] M. R. Drout *et al.*, *Light curves of the neutron star merger GW170817/SSS17a: Implications for r-process nucleosynthesis*, Science **358** (2017) 1570.

[61] B. J. Shappee *et al.*, *Early spectra of the gravitational wave source GW170817: Evolution of a neutron star merger*, Science **358** (2017) 1574.

[62] M. Safarzadeh, R. Sarmento, and E. Scannapieco, *On Neutron Star Mergers as the Source of r-process-enhanced Metal-poor Stars in the Milky Way*, The Astrophysical Journal **876** (2019) 28.

[63] Á. Skúladóttir, C. J. Hansen, S. Salvadori, and A. Choplin, *Neutron-capture elements in dwarf galaxies: I. Chemical clocks and the short timescale of ther-process*, Astron. Astrophys. **631** (2019) A171.

[64] B. Côté *et al.*, *Neutron Star Mergers Might Not Be the Only Source of r-process Elements in the Milky Way*, Astrophys. J. **875** (2019) 106.

[65] D. M. Siegel, *r-Process nucleosynthesis in gravitational-wave and other explosive astrophysical events*, Nat. Rev. Phys. **4** (2022) 306.

[66] J. J. Cowan and W. K. Rose, *Production of C-14 and neutrons in red giants*, Astrophys. J. **212** (1977) 149.

[67] P. A. Denissenkov, F. Herwig, U. Battino, C. Ritter, M. Pignatari, S. Jones, and B. Paxton, *i-process Nucleosynthesis and Mass Retention Efficiency in He-shell Flash Evolution of Rapidly Accreting White Dwarfs*, Astrophys. J. Lett. **834** (2017) L10.

[68] B. Côté, P. Denissenkov, F. Herwig, A. J. Ruiter, C. Ritter, M. Pignatari, and K. Belczynski, *i-process contribution of rapidly accreting white dwarfs to the solar composition of first-peak neutron-capture elements*, Astrophys. J. **854** (2018) 105.

[69] A. Choplin, L. Siess, and S. Goriely, *The intermediate neutron capture process*, Astron. Astrophys. **667** (2022) A155.

[70] M. Hampel, R. J. Stancliffe, M. Lugaro, and B. S. Meyer, *The intermediate neutron-capture process and carbon-enhanced metal-poor stars*, Astrophys. J. **831** (2016) 171.

[71] M. Lugaro, A. I. Karakas, R. J. Stancliffe, and C. Rijs, *The s-Process in Asymptotic Giant Branch Stars of low Matellicity and the Composition of Carbon-Enhanced Metal-Poor Stars*, Astrophys. J. **747** (2012) 2.

[72] *National Nuclear Data Center, information extracted from the NuDat database.* https://www.nndc.bnl.gov/nudat/. (Last accessed 06.11.2025).

[73] I. Dillmann *et al.*, *Measuring neutron capture cross sections of radioactive nuclei: From activations at the FZK Van de Graaff to direct neutron captures in inverse kinematics with a storage ring at TRIUMF*, Eur. Phys. J. A **59** (2023) 105.

[74] P. A. Denissenkov, F. Herwig, G. Perdikakis, and H. Schatz, *The impact of (n,γ) reaction rate uncertainties of unstable isotopes on the i-process nucleosynthesis of the elements from Ba to W*, Mon. Not. R. Astron. Soc. **503** (2021) 3913.

[75] P. Denissenkov, G. Perdikakis, F. Herwig, H. Schatz, C. Ritter, M. Pignatari, S. Jones, S. Nikas, and A. Spyrou, *The impact of (n,γ) reaction rate uncertainties of unstable isotopes near N=50 on the i-process nucleosynthesis in He-shell flash white dwarfs*, J. Phys. G Nucl. Part. Phys. **45** (2018) 055203.

[76] A. Spyrou *et al.*, *First Study of the* ^{139}Ba$(n,\gamma)^{140}$Ba *Reaction to Constrain the Conditions for the Astrophysical i Process*, Phys. Rev. Lett. **132** (2024) 202701.

[77] V. W. Ingeberg *et al.*, *Nuclear level density and* γ*-ray strength function of* ^{67}Ni *and the impact on the i process*, Phys. Rev. C **111** (1 2025) 015803.

[78] T. Rauscher, N. Dauphas, I. Dillmann, C. Fröhlich, Z. Fülöp, and G. Gyürky, *Constraining the astrophysical origin of the p-nuclei through nuclear physics and meteoritic data*, Rep. Prog. Phys. **76** (2013) 066201.

[79] M. Arnould and S. Goriely, *The p-process of stellar nucleosynthesis: astrophysics and nuclear physics status*, Phys. Rep. **384** (2003) 1.

[80] M. Pignatari, K. Göbel, R. Reifarth, and C. Travaglio, *The production of proton-rich isotopes beyond iron: The* γ*-process in stars*, Int. J. Mod. Phys. E **25** (2016) 1630003.

[81] M. Lugaro, M. Pignatari, U. Ott, K. Zuber, C. Travaglio, G. Gyürky, and Z. Fülöp, *Origin of the p-process radionuclides* ^{92}*Nb and* ^{146}*Sm in the early solar system and inferences on the birth of the Sun*, Proc. Natl. Acad. Sci. U. S. A. **113** (2016) 907.

[82] S. E. Woosley and W. M. Howard, *The p-process in supernovae*, Astrophys. J. Suppl. **36** (1978) 285.

[83] M. Arnould, *Possibility of synthesis of proton-rich nuclei in highly evolved stars. II*, Astronomy and Astrophysics **46** (1976) 117.

[84] L. Roberti, M. Pignatari, A. Psaltis, A. Sieverding, P. Mohr, Z. Fülöp, and M. Lugaro, *The* γ*-process nucleosynthesis in core-collapse supernovae*, Astron. Astrophys. **677** (2023) A22.

[85] W. M. Howard, B. S. Meyer, and S. E. Woosley, *A new site for the astrophysical gamma-process*, Astrophys. J. **373** (1991) L5.

[86] C. Travaglio, F. K. Röpke, R. Gallino, and W. Hillebrandt, *Type Ia Supernovae as Sites of the p-Process: Two-Dimensional Models Coupled To Nucleosynthesis*, Astrophys. J. **739** (2011) 93.

[87] C. Travaglio, R. Gallino, T. Rauscher, F. K. Röpke, and W. Hillebrandt, *Testing the Role of SNe Ia for Galactic Chemical Evolution of p-Nuclei With Two-Dimensional Models and With s-Process Seeds at Different Metallicities*, Astrophys. J. **799** (2015) 54.

[88] U. Battino, M. Pignatari, C. Travaglio, C. Lederer-Woods, P. Denissenkov, F. Herwig, F. Thielemann, and T. Rauscher, *Heavy elements nucleosynthesis on accreting white dwarfs: building seeds for the p-process*, Mon. Not. R. Astron. Soc. **497** (2020) 4981.

[89] T. Rauscher, N. Nishimura, R. Hirschi, G. Cescutti, A. S. J. Murphy, and A. Heger, *Uncertainties in the production of p-nuclei in massive stars obtained from Monte Carlo variations*, Mon. Not. R. Astron. Soc. **463** (2016) 4153.

[90] T. Fischer, S. C. Whitehouse, A. Mezzacappa, F.-K. Thielemann, and M. Liebendörfer, *Protoneutron star evolution and the neutrino-driven wind in general relativistic neutrino radiation hydrodynamics simulations*, Astron. Astrophys. **517** (2010) A80.

[91] C. Fröhlich, G. Martínez-Pinedo, M. Liebendörfer, F.-K. Thielemann, E. Bravo, W. R. Hix, K. Langanke, and N. T. Zinner, *Neutrino-Induced Nucleosynthesis of* $A > 64$ *Nuclei: The* νp *Process*, Phys. Rev. Lett. **96** (2006).

[92] S. Wanajo, H.-T. Janka, and S. Kubono, *Uncertainties in the p-Process: Supernova Dynamics Versus Nuclear Physics*, Astrophys. J. **729** (2011) 46.

[93] A. Arcones and J. Bliss, *Nucleosynthesis of elements between Sr and Ag in neutron- and proton-rich neutrino-driven winds*, J. Phys. G Nucl. Part. Phys. **41** (2014) 044005.

[94] L. Y. Zhang, J. J. He, S. Wanajo, D. Dell'Aquila, S. Kubono, and G. Zhao, *New thermonuclear $^{10}B(\alpha,p)^{13}C$ rate and its astrophysical implication in the νp-process*, Astrophys. J. **868** (2018) 24.

[95] R. K. Wallace and S. E. Woosley, *Explosive hydrogen burning*, Astrophys. J. Suppl. Ser. **45** (1981) 389.

[96] H. Schatz *et al.*, *Horizons: nuclear astrophysics in the 2020s and beyond*, J. Phys. G Nucl. Part. Phys. **49** (2022) 110502.

[97] H. Schatz *et al.*, *rp-process nucleosynthesis at extreme temperature and density conditions*, Phys. Rep. **294** (1998) 167.

[98] S. E. Woosley, A. Heger, A. Cumming, R. D. Hoffman, J. Pruet, T. Rauscher, J. L. Fisker, H. Schatz, B. A. Brown, and M. Wiescher, *Models for type I X-ray bursts with improved nuclear physics*, Astrophys. J. Suppl. Ser. **151** (2004) 75.

[99] H. Schatz, A. Aprahamian, V. Barnard, L. Bildsten, A. Cumming, M. Ouellette, T. Rauscher, F. K. Thielemann, and M. Wiescher, *End point of the rp process on accreting neutron stars*, Phys. Rev. Lett. **86** (2001) 3471.

[100] J. José, F. Moreno, A. Parikh, and C. Iliadis, *Hydrodynamic models of Type I X-Ray Bursts: Metallicity effects*, Astrophys. J. Suppl. Ser. **189** (2010) 204.

[101] H. Schatz and W.-J. Ong, *Dependence of X-ray burst models on nuclear masses*, Astrophys. J. **844** (2017) 139.

[102] A. Parikh, J. José, G. Sala, and C. Iliadis, *Nucleosynthesis in type I X-ray bursts*, Prog. Part. Nucl. Phys. **69** (2013) 225.

[103] J. Keegans, C. L. Fryer, S. W. Jones, B. Côté, K. Belczynski, F. Herwig, M. Pignatari, A. M. Laird, and C. A. Diget, *Nucleosynthetic yields from neutron stars accreting in binary common envelopes*, Mon. Not. R. Astron. Soc. **485** (2019) 620.

[104] Z. Xiong, G. Martínez-Pinedo, O. Just, and A. Sieverding, *Production of p Nuclei from r-Process Seeds: The νr Process*, Phys. Rev. Lett. **132** (2024) 192701.

[105] D. Lunney, *New mass measurements with trapped (radioactive) ions and related fundamental physics*, Hyperfine Interact. **240** (2019).

[106] T. Rauscher, *Essentials of nucleosynthesis and theoretical nuclear astrophysics*, AAS-IOP Astronomy. London, England: Institute of Physics Publishing, 2020.

[107] K. Blaum, J. Dilling, and W. Nörtershäuser, *Precision atomic physics techniques for nuclear physics with radioactive beams*, Phys. Scr. **T152** (2013) 014017.

[108] T. Rauscher, *Relevant energy ranges for astrophysical reaction rates*, Phys. Rev. C Nucl. Phys. **81** (2010).

[109] T. Rauscher, *Photonuclear reactions in astrophysics*, Nucl. Phys. News **28** (2018) 12.

[110] T. Rauscher, *Sensitivity of Astrophysical Reaction Rates to Nuclear Uncertainties*, Astrophys. J. Suppl. **201** (2012) 26.

[111] T. Rauscher, G. G. Kiss, G. Gyürky, A. Simon, Z. Fülöp, and E. Somorjai, *Suppression of the stellar enhancement factor and the reaction $^{85}Rb(p,n)^{85}Sr$*, Phys. Rev. C Nucl. Phys. **80** (2009).

[112] T. Rauscher, *The path to improved reaction rates for astrophysics*, Int. J. Mod. Phys. E **20** (2011) 1071.

[113] G. Gamow, *Zur Quantentheorie des Atomkernes*, Eur. Phys. J. A **51** (1928) 204.

[114] W. Hauser and H. Feshbach, *The inelastic scattering of neutrons*, Phys. Rev. **87** (1952) 366.

[115] H. Feshbach, *Unified theory of nuclear reactions*, Ann. Phys. (N. Y.) **5** (1958) 357.

[116] N. Bohr, *Neutron capture and nuclear constitution*, Nature **137** (1936) 344.

[117] N. Bohr, *Transmutations of atomic nuclei*, Science **86** (1937) 161.

[118] H. A. Bethe, *Nuclear physics B. nuclear dynamics, theoretical*, Rev. Mod. Phys. **9** (1937) 69.

[119] V. Weisskopf, *Statistics and nuclear reactions*, Phys. Rev. **52** (1937) 295.

[120] V. F. Weisskopf and D. H. Ewing, *On the yield of nuclear reactions with heavy elements*, Phys. Rev. **57** (1940) 472.

[121] J. M. Blatt and V. F. Weisskopf, *Theoretical Nuclear Physics*, 1979th ed. New York, NY: Springer, 2012. ISBN: 978-1-4612-9959-2.

[122] M. Baranger and E. W. Vogt, *Advances in nuclear physics*, ed. by M. Baranger and E. Vogt. Advances in Nuclear Physics. New York, NY: Springer, 2012. ISBN: 978-1-4757-0105-0.

[123] J. J. Cowan, F.-K. Thielemann, and J. W. Truran, *The R-process and nucleochronology*, Phys. Rep. **208** (1991) 267.

[124] A. Koning, S. Hilaire, and S. Goriely, *TALYS: modeling of nuclear reactions*, Eur. Phys. J. A **59** (2023).

[125] T. Mayer-Kuckuk, *Kernphysik*, 7th ed. Teubner Studienbücher Physik. Vieweg+teubner Verlag, 2002. ISBN: 978-3-519-13223-3.

[126] T. Rauscher and F.-K. Thielemann, *Astrophysical reaction rates from statistical model calculations*, At. Data Nucl. Data Tables **75** (2000) 1.

[127] J. A. Holmes, S. E. Woosley, W. A. Fowler, and B. A. Zimmerman, *Tables of thermonuclear-reaction-rate data for neutron-induced reactions on heavy nuclei*, At. Data Nucl. Data Tables **18** (1976) 305.

[128] M. Wiedeking and S. Goriely, *Photon strength functions and nuclear level densities: invaluable input for nucleosynthesis*, Phil. Trans. R. Soc. A. **382** (2024) 20230125.

[129] A. J. Koning and J. P. Delaroche, *Local and global nucleon optical models from 1 keV to 200 MeV*, Nucl. Phys. A **713** (2003) 231.

[130] H. Feshbach, *The optical model and its justification*, Annu. Rev. Nucl. Sci. **8** (1958) 49.

[131] R. D. Woods and D. S. Saxon, *Diffuse surface optical model for nucleon-nuclei scattering*, Phys. Rev. **95** (1954) 577.

[132] R. Capote *et al.*, *RIPL – reference input parameter library for calculation of nuclear reactions and nuclear data evaluations*, Nucl. Data Sheets **110** (2009) 3107.

[133] A. Kumar, S. Kailas, S. Rathi, and K. Mahata, *Global alpha-nucleus optical potential*, Nucl. Phys. A **776** (2006) 105.

[134] P. Scholz *et al.*, *Measurement of the* $^{187}Re(\alpha,n)^{190}Ir$ *reaction cross section at sub-Coulomb energies using the Cologne Clover Counting Setup*, Phys. Rev. C Nucl. Phys. **90** (2014).

[135] E. Bauge, J. P. Delaroche, and M. Girod, *Semimicroscopic nucleon-nucleus spherical optical model for nuclei with A> 40 at energies up to 200 MeV*, Phys. Rev. C Nucl. Phys. **58** (1998) 1118.

[136] J.-P. Jeukenne, A. Lejeune, and C. Mahaux, *Optical-model potential in finite nuclei from Reid's hard core interaction*, Phys. Rev. C Nucl. Phys. **16** (1977) 80.

[137] E. Bauge, J. P. Delaroche, and M. Girod, *Lane-consistent, semimicroscopic nucleon-nucleus optical model*, Phys. Rev. C Nucl. Phys. **63** (2001).

[138] H. I. West Jr, R. M. Nuckolls, B. Hudson, B. Ruiz, R. G. Lanier, and M. G. Mustafa, *Bromine and iodine excitation-function measurements with protons and deuterons at 3-17 MeV*, Phys. Rev. C Nucl. Phys. **47** (1993) 248.

[139] J. P. Blaser, F. Boehm, P. Marmier, and P. Scherrer, *Excitation functions and cross sections of the (p,n) reaction (II)*, Helvetica Physica Acta **24** (1951) 441.

[140] G. G. Kiss, T. Rauscher, G. Gyürky, A. Simon, Z. Fülöp, and E. Somorjai, *Coulomb suppression of the stellar enhancement factor*, Phys. Rev. Lett. **101** (2008) 191101.

[141] M. Avrigeanu, A. C. Obreja, F. L. Roman, V. Avrigeanu, and W. von Oertzen, *Complementary optical-potential analysis of α-particle elastic scattering and induced reactions at low energies*, At. Data Nucl. Data Tables **95** (2009) 501.

[142] M. Avrigeanu and V. Avrigeanu, *α-particle optical potential tests below the Coulomb barrier*, Phys. Rev. C Nucl. Phys. **79** (2009).

[143] P. Demetriou, C. Grama, and S. Goriely, *Improved global α-optical model potentials at low energies*, Nucl. Phys. A **707** (2002) 253.

[144] P. Mohr, Z. Fülöp, G. Gyürky, G. G. Kiss, and T. Szücs, *Successful prediction of total α-induced reaction cross sections at astrophysically relevant sub-Coulomb energies using a novel approach*, Phys. Rev. Lett. **124** (2020) 252701.

[145] M. Müller, F. Heim, Y. Wang, S. Wilden, and A. Zilges, *Determination of ^{170,172}Yb(α,n) ^{173,175}Hf reaction cross sections in a stacked-target experiment*, Phys. Rev. C. **107** (2023).

[146] Z. Mátyus, G. Gyürky, P. Mohr, A. Angyal, Z. Halász, G. G. Kiss, Á. Tóth, T. Szücs, and Z. Fülöp, *Low-energy α -nucleus optical potential studied via (α,n) cross section measurements on Te isotopes*, Phys. Rev. C. **109** (2024).

[147] G. G. Kiss *et al.*, *Low-energy measurement of the ^{86}Kr(α,n)^{89}Sr reaction cross section and its impact on weak r-process nucleosynthesis*, Astrophys. J. **988** (2025) 170.

[148] P. Mohr, Z. Fülöp, G. Gyürky, Z. Halász, G. G. Kiss, S. R. Kovács, Z. Mátyus, T. N. Szegedi, and T. Szücs, *The α-nucleus potential: towards a solution of a long-standing problem*, Eur. Phys. J. A **61** (2025).

[149] A. J. Koning, S. Hilaire, and S. Goriely, *Global and local level density models*, Nucl. Phys. A **810** (2008) 13.

[150] A. Gilbert and A. G. W. Cameron, *A composite nuclear-level density formula with shell corrections*, Can. J. Phys. **43** (1965) 1446.

[151] W. Dilg, W. Schantl, H. Vonach, and M. Uhl, *Level density parameters for the back-shifted fermi gas model in the mass range $40 < A < 250$*, Nucl. Phys. A **217** (1973) 269.

[152] H. A. Bethe, *An attempt to calculate the number of energy levels of a heavy nucleus*, Phys. Rev. **50** (1936) 332.

[153] S. Goriely, S. Hilaire, and A. J. Koning, *Improved microscopic nuclear level densities within the Hartree-Fock-Bogoliubov plus combinatorial method*, Phys. Rev. C Nucl. Phys. **78** (2008).

[154] S. Hilaire, M. Girod, S. Goriely, and A. J. Koning, *Temperature-dependent combinatorial level densities with the D1M Gogny force*, Phys. Rev. C Nucl. Phys. **86** (2012).

[155] T. Ericson, *A statistical analysis of excited nuclear states*, Nucl. Phys. **11** (1959) 481.

[156] B. Singh, *Nuclear data sheets for A = 80*, Nucl. Data Sheets **105** (2005) 223.

[157] J. K. Tuli and E. Browne, *Nuclear data sheets for A=82*, Nucl. Data Sheets **157** (2019) 260.

[158] A. Negret and B. Singh, *Nuclear structure and decay data for A=86 isobars*, Nucl. Data Sheets **203** (2025) 283.

[159] T. Johnson and W. Kulp, *Nuclear Data Sheets for A = 87*, Nucl. Data Sheets **129** (2015).

[160] E. McCutchan and A. Sonzogni, *Nuclear Data Sheets for A = 88*, Nucl. Data Sheets **115** (2014) 135.

[161] R. Capote *et al.*, *RIPL – reference input parameter library for calculation of nuclear reactions and nuclear data evaluations*, Nucl. Data Sheets **110** (2009) 3107.

[162] D. Brink, *Some aspects of the interaction of light with matter*, PhD thesis. University of Oxford, 1955.

[163] P. Axel, *Electric dipole ground-state transition width strength function and 7-Mev photon interactions*, Phys. Rev. **126** (1962) 671.

[164] M. Guttormsen, A. C. Larsen, A. Görgen, T. Renstrøm, S. Siem, T. G. Tornyi, and G. M. Tveten, *Validity of the generalized Brink-Axel hypothesis in* ^{238}Np, Phys. Rev. Lett. **116** (2016) 012502.

[165] K. Sieja, *Brink-Axel hypothesis in the pygmy-dipole resonance region*, Eur. Phys. J. A **59** (2023).

[166] J. Isaak *et al.*, *Constraining nuclear photon strength functions by the decay properties of photo-excited states*, Phys. Lett. B **727** (2013) 361.

[167] C. T. Angell, S. L. Hammond, H. J. Karwowski, J. H. Kelley, M. Krtička, E. Kwan, A. Makinaga, and G. Rusev, *Erratum: Evidence for radiative coupling of the pygmy dipole resonance to excited states [Phys. Rev. C86, 051302(R) (2012)]*, Phys. Rev. C Nucl. Phys. **91** (2015).

[168] J. Isaak *et al.*, *The concept of nuclear photon strength functions: A model-independent approach via ($\vec{\gamma}$,γ'γ") reactions*, Phys. Lett. B **788** (2019) 225.

[169] M. Markova *et al.*, *Comprehensive test of the Brink-Axel hypothesis in the energy region of the pygmy dipole resonance*, Phys. Rev. Lett. **127** (2021) 182501.

[170] D. Martin *et al.*, *Test of the brink-Axel hypothesis for the pygmy dipole resonance*, Phys. Rev. Lett. **119** (2017).

[171] S. N. Liddick *et al.*, *Experimental neutron capture rate constraint far from stability*, Phys. Rev. Lett. **116** (2016).

[172] S. Goriely *et al.*, *Reference database for photon strength functions*, Eur. Phys. J. A **55** (2019).

[173] D. Savran, T. Aumann, and A. Zilges, *Experimental studies of the Pygmy Dipole Resonance*, Prog. Part. Nucl. Phys. **70** (2013) 210.

[174] A. Voinov, E. Algin, U. Agvaanluvsan, T. Belgya, R. Chankova, M. Guttormsen, G. E. Mitchell, J. Rekstad, A. Schiller, and S. Siem, *Large enhancement of radiative strength for soft transitions in the quasicontinuum*, Phys. Rev. Lett. **93** (2004) 142504.

[175] M. Guttormsen *et al.*, *Radiative strength functions in* $^{93-98}Mo$, Phys. Rev. C Nucl. Phys. **71** (2005).

[176] L. C. Campo *et al.*, *Test of the generalized Brink-Axel hypothesis in* $^{64,65}Ni$, Phys. Rev. C. **98** (2018).

[177] P. Fanto and Y. Alhassid, *Low-energy enhancement in the magnetic dipole γ -ray strength functions of heavy nuclei*, Phys. Rev. C. **109** (2024).

[178] K. Sieja, *Electric and magnetic dipole strength at low energy*, Phys. Rev. Lett. **119** (2017).

[179] R. Schwengner, S. Frauendorf, and A. C. Larsen, *Low-energy enhancement of magnetic dipole radiation*, Phys. Rev. Lett. **111** (2013) 232504.

[180] R. Schwengner, S. Frauendorf, and B. A. Brown, *Low-energy magnetic dipole radiation in open-shell nuclei*, Phys. Rev. Lett. **118** (2017).

[181] S. P. E. Magagula *et al.*, *Investigating the strength of the scissors mode in* ^{151}Sm, J. Phys. Conf. Ser. **2586** (2023) 012070.

[182] J. Kopecky and M. Uhl, *Test of gamma-ray strength functions in nuclear reaction model calculations*, Phys. Rev. C **41** (5 1990) 1941.

[183] J. Kopecky, M. Uhl, and R. E. Chrien, *Radiative strength in the compound nucleus* ^{157}Gd, Phys. Rev. C **47** (1 1993) 312.

[184] S. Goriely and V. Plujko, *Simple empirical E1 and M1 strength functions for practical applications*, Phys. Rev. C. **99** (2019).

[185] Y. Xu, S. Goriely, and E. Khan, *Systematical studies of the $E1$ photon strength functions combining the Skyrme-Hartree-Fock-Bogoliubov plus quasiparticle random-phase approximation model and experimental giant dipole resonance properties*, Phys. Rev. C **104** (4 2021) 044301.

[186] S. Goriely, S. Hilaire, S. Péru, and K. Sieja, *Gogny-HFB+QRPA dipole strength function and its application to radiative nucleon capture cross section*, Phys. Rev. C **98** (2018) 014327.

[187] S. Goriely, E. Khan, and M. Samyn, *Microscopic HFB + QRPA predictions of dipole strength for astrophysics applications*, Nucl. Phys. A **739** (2004) 331.

[188] I. Daoutidis and S. Goriely, *Large-scale continuum random-phase approximation predictions of dipole strength for astrophysical applications*, Phys. Rev. C **86** (3 2012) 034328.

[189] A. Koning, S. Hilaire, and S. Goriely, *TALYS — nuclear reaction software*. https://github.com/arjankoning1/talys/. (Last accessed 01.10.2025). 2025.

[190] A. Zilges, D. L. Balabanski, J. Isaak, and N. Pietralla, *Photonuclear reactions—From basic research to applications*, Prog. Part. Nucl. Phys. **122** (2022) 103903.

[191] J. Mayer, S. Goriely, L. Netterdon, S. Péru, P. Scholz, R. Schwengner, and A. Zilges, *Partial cross sections of the* $^{92}Mo(p,\gamma)$ *reaction and the γ-strength in* ^{93}Tc, Phys. Rev. C. **93** (2016).

[192] L. Netterdon, A. Endres, S. Goriely, J. Mayer, P. Scholz, M. Spieker, and A. Zilges, *Experimental constraints on the γ-ray strength function in* ^{90}Zr *using partial cross sections of the* $^{89}Y(p,\gamma)^{90}Zr$ *reaction*, Phys. Lett. B **744** (2015) 358.

[193] F. Heim, J. Mayer, M. Müller, P. Scholz, and A. Zilges, *Deducing primary γ-ray intensities and the dipole strength function in* ^{94}Mo *via radiative proton capture*, Phys. Rev. C **103** (2 2021) 025805.

[194] F. Heim, P. Scholz, M. Körschgen, J. Mayer, M. Müller, and A. Zilges, *Insights into the statistical γ-decay behavior of* ^{108}Cd *via radiative proton capture*, Phys. Rev. C. **101** (2020).

[195] M. Wiedeking *et al.*, *Low-energy enhancement in the photon strength of* ^{95}*Mo*, Phys. Rev. Lett. **108** (2012) 162503.

[196] A. Schiller, L. Bergholt, M. Guttormsen, E. Melby, J. Rekstad, and S. Siem, *Extraction of level density and γ strength function from primary γ spectra*, Nucl. Instrum. Methods Phys. Res. A **447** (2000) 498.

[197] M. Guttormsen, T. Ramsøy, and J. Rekstad, *The first generation of γ-rays from hot nuclei*, Nucl. Instrum. Methods Phys. Res. A **255** (1987) 518.

[198] M. Guttormsen, T. S. Tveter, L. Bergholt, F. Ingebretsen, and J. Rekstad, *The unfolding of continuum γ-ray spectra*, Nucl. Instrum. Methods Phys. Res. A **374** (1996) 371.

[199] S. R. Kovács *et al.*, *Measurement of β-particles to determine cross sections relevant to the weak r-process*, Nucl. Instrum. Methods Phys. Res. A **1073** (2025) 170272.

[200] F. Heim, M. Müller, S. Wilden, and A. Zilges, *Absolute* ^{96}Mo$(p,n)^{96m+g}$Tc *cross sections and a new branching for the* ^{96m}Tc *decay*, Phys. Rev. C **103** (5 2021) 054613.

[201] L. Netterdon, P. Demetriou, J. Endres, U. Giesen, G. G. Kiss, A. Sauerwein, T. Szücs, K. O. Zell, and A. Zilges, *Investigation of α-induced reactions on the p nucleus*, Nucl. Phys. A **916** (2013) 149.

[202] G. Gyürky, Z. Fülöp, F. Käppeler, G. G. Kiss, and A. Wallner, *The activation method for cross section measurements in nuclear astrophysics*, Eur. Phys. J. A **55** (2019).

[203] A. Simon *et al.*, *SuN: Summing NaI(Tl) gamma-ray detector for capture reaction measurements*, Nucl. Instrum. Methods Phys. Res. A **703** (2013) 16.

[204] A. Spyrou, H.-W. Becker, A. Lagoyannis, S. Harissopulos, and C. Rolfs, *Cross-section measurements of capture reactions relevant to the p process using a 4π γ-summing method*, Phys. Rev. C **76** (1 2007) 015802.

[205] A. Linnemann, *Das HORUS-Würfelspektrometer und Multiphononanregungen in* ^{106}*Cd*, PhD thesis. Universität zu Köln, 2006.

[206] W. Skulski, M. Momayezi, B. Hubbard-Nelson, P. Grudberg, J. Harris, and W. Warburton, *Towards Digital X-Ray and Particle Spectroscopy*, Acta. Phys. Pol. B **31** (2000) 47.

[207] B. Hubbard-Nelson, M. Momayezi, and W. K. Warburton, *A module for energy and pulse shape data acquisition*, Nucl. Instrum. Methods Phys. Res. A **422** (1999) 411.

[208] CAEN S.p.A. – Tools for Discovery. https://www.caen.it/.

[209] M. Weinert, *Investigation of Microscopic Structures in the Low-Energy Electric Dipole Response of 120Sn using Consistent Experimental and Theoretical Observables and Digital Signal Processing for Nuclear Physics Experiments*, PhD thesis. Universität zu Köln, Fakultät für Mathematik und Naturwissenschaften, Institut für Kernphysik, 2022.

[210] S. Thiel. Private communication. 2025.

[211] A. Sauerwein, *Experimental studies of charged-particle induced reactions and their impact on the nucleosynthesis of p nuclei*, PhD thesis. Universität zu Köln, 2012.

[212] L. Netterdon *et al.*, *The γ-ray spectrometer HORUS and its applications for nuclear astrophysics*, Nucl. Instrum. Methods Phys. Res. A **754** (2014) 94.

[213] P. Scholz, *Exploring statistical properties of nuclei for explosive stellar nucleosynthesis*, PhD thesis. Universität zu Köln, 2018. ISBN: 978-3-8439-3784-9.

[214] F. Heim, J. Mayer, M. Müller, P. Scholz, M. Weinert, and A. Zilges, *Experimental techniques to study the γ process for nuclear astrophysics at the Cologne accelerator laboratory*, Nucl. Instrum. Methods A **966** (2020) 163854.

[215] F. Heim, *The statistical gamma-decay behavior and nuclear reaction rates of heavy nuclei relevant for explosive nucleosynthesis*, PhD thesis. Universität zu Köln, 2021.

[216] W.-K. Chu, J. Mayer, and M.-A. Nicolet, *Backscattering spectrometry*, Heidelberg: Academic Press, Inc., 1978.

[217] M. Mayer, *SIMNRA User's Guide*, Garching, Germany: Max-Planck-Institut für Plasmaphysik, 2024.

[218] M. Wang, G. Audi, A. H. Wapstra, F. G. Kondev, M. MacCormick, X. Xu, and B. Pfeiffer, *The Ame2012 atomic mass evaluation*, Chin. Phys. C **36** (2012) 1603.

[219] "HORUS Strahlzeit Oktober 2012 bis Februar 2014". Laboratory notebook. AG Zilges, Institut für Kernphysik, Universität zu Köln. 2014.

[220] "Nukleare Astrophysik Strahlzeitbuch 07/2015". Laboratory notebook. AG Zilges, Institut für Kernphysik, Universität zu Köln. 2015.

[221] A. Blazhev. Private communication. 2025.

[222] *RUBION - Zentrale Einrichtung für Ionenstrahlen und Radionuklide*. https://www.rubion.rub.de/methods/41/.

[223] M. Baldenhofer, *Bestimmung des Wirkungsquerschnitts der astrophysikalisch relevanten Reaktion $^{85}Rb(p,\gamma)$*. Bachelor's thesis. 2014.

[224] B. Singh and J. Chen, *Nuclear data sheets for $A = 85$*, Nucl. Data Sheets **116** (2014) 1.

[225] X. Huang and C. Zhou, *Nuclear data sheets for $A=197$*, Nucl. Data Sheets **104** (2005) 283.

[226] *J. Ziegler, J. Biersack, and M. Ziegler, SRIM – The Stopping and Range of Ions in Matter*. http://srim.org/.

[227] J. Brenneisen, D. Grathwohl, M. Lickert, R. Ott, H. Röpke, J. Schmälzlin, P. Siedle, and B. H. Wildenthal, *The structure of ^{28}Si above 10 MeV excitation energy I: gamma-decay modes and radiative widths of levels*, Z. Physik A - Hadrons and Nuclei **352** (1995) 149.

[228] M. Shamsuzzoha Basunia, *Nuclear data sheets for $A = 28$*, Nucl. Data Sheets **114** (2013) 1189.

[229] S. Agostinelli *et al.*, *Geant4—a simulation toolkit*, **506** (2003) 250.

[230] L. Netterdon. Private communication. 2025.

[231] J. Chen, J. Cameron, and B. Singh, *Nuclear data sheets for $A = 35$*, Nucl. Data Sheets **112** (2011) 2715.

[232] F. Heim, J. Mayer, M. Müller, P. Scholz, and A. Zilges. Phys. Rev. C. **103** (2021).

[233] F. Heim, P. Scholz, J. Mayer, M. Müller, and A. Zilges, *Constraining nuclear properties in ^{94}Mo via a $^{93}Nb(p,\gamma)^{94}Mo$ total cross section measurement*, Phys. Rev. C. **101** (2020).

[234] G. G. Kiss, G. Gyürky, Z. Elekes, Z. Fülöp, E. Somorjai, T. Rauscher, and M. Wiescher, *$^{70}Ge(p,\gamma)^{71}As$ and $^{76}Ge(p,n)^{76}As$ cross sections for the astrophysical p process: Sensitivity of the optical proton potential at low energies*, Phys. Rev. C Nucl. Phys. **76** (2007).

[235] T. Rauscher and F.-K. Thielemann, *Tables of nuclear cross sections and reaction rates: An addendum to the paper "astrophysical reaction rates from statistical model calculations"*, At. Data Nucl. Data Tables **79** (2001) 47.

[236] G. G. Kiss, *Proton Induced Reactions and the Astrophysical P Process*, PhD thesis. University of Debrecen, 2008. ISBN: 9798346320180.

[237] V. N. Levkovskij, *Cross-sections of medium mass nuclide activation (A=40–100) by medium energy protons and alpha-particles (E=10–50 MeV)*. Tech. rep. Act. Cs. by Protons and Alphas, Moscow, 1991.

[238] S. Kastleiner, S. M. Qaim, F. M. Nortier, G. Blessing, T. N. van der Walt, and H. H. Coenen, *Excitation functions of $^{85}Rb(p,xn)^{85m,g,83,82,81}Sr$ reactions up to 100MeV: integral tests of cross section data, comparison of production routes of ^{83}Sr and thick target yield of ^{82}Sr*, Appl. Radiat. Isot. **56** (2002) 685.

[239] S. Wilden, B. Machliner, M. Müller, and A. Zilges, *Total cross sections of the $^{87}Rb(p,\gamma)^{88}Sr$ reaction measured via in-beam gamma-ray spectroscopy*, Eur. Phys. J. A **61** (2025).

[240] CAEN S.p.A. – Tools for Discovery, *User Manual UM5960 – CoMPASS Multiparametric DAQ Software for Physics Applications*. https://www.caen.it/.

[241] A. Tsantiri *et al.*, *Cross-section measurement of the $^{82}Kr(p,\gamma)^{83}Rb$ reaction in inverse kinematics*, Phys. Rev. C. **107** (2023).

[242] G. Lotay *et al.*, *First direct measurement of an astrophysical p-process reaction cross section using a radioactive ion beam*, Phys. Rev. Lett. **127** (2021) 112701.

[243] G. Gyürky, E. Somorjai, Z. Fülöp, S. Harissopulos, P. Demetriou, and T. Rauscher, *Proton capture cross section of Sr isotopes and their importance for nucleosynthesis of proton-rich nuclides*, Phys. Rev. C Nucl. Phys. **64** (2001).

[244] A. Tsantiri. Private communication. 2025.

[245] A. Tsantiri and *et al.*, *Constraining the synthesis of the lightest p nucleus ^{74}Se*, Phys. Rev. Lett. (2025).

[246] W. Rapp, J. Gorres, M. Wiescher, H. Schatz, and F. Kappeler, *Sensitivity of p-process nucleosynthesis to nuclear reaction rates in a $25M_{\odot}$ Supernova model*, Astrophys. J. **653** (2006) 474.

[247] I. U. Roederer, C. M. Sakari, V. M. Placco, T. C. Beers, R. Ezzeddine, A. Frebel, and T. T. Hansen, *The R-process alliance: A comprehensive abundance analysis of HD 222925, a metal-poor star with an Extreme R-process enhancement of [Eu/H] = −0.14*, Astrophys. J. **865** (2018) 129.

[248] G. Huppelsberg, *Development of a particle-γ coincidence setup for the investigation of proton angular distributions in (d,pγ) reactions*, MA thesis. Universität zu Köln, Institut für Kernphysik, 2024.

[249] N. M. Florea, D. Tofan, and A. Radu. ^{nat}TlBr target produced at IFIN-HH. 2024.

[250] A. Palmisano-Kyle *et al.*, *Constraining the astrophysical p process: Cross section measurement of the $^{84}Kr(p,\gamma)^{85}Rb$ reaction in inverse kinematics*, Phys. Rev. C. **105** (2022).

[251] M. Williams *et al.*, *Cross sections of the $^{83}Rb(p,\gamma)^{84}Sr$ and $^{84}Kr(p,\gamma)^{85}Rb$ reactions at energies characteristic of the astrophysical γ process*, Phys. Rev. C. **107** (2023).

[252] T. Psaltis. Private communication. 2025.

Appendices

A ^{85}Rb

A.1 Cross section calculation of discrete levels in ^{86}Sr

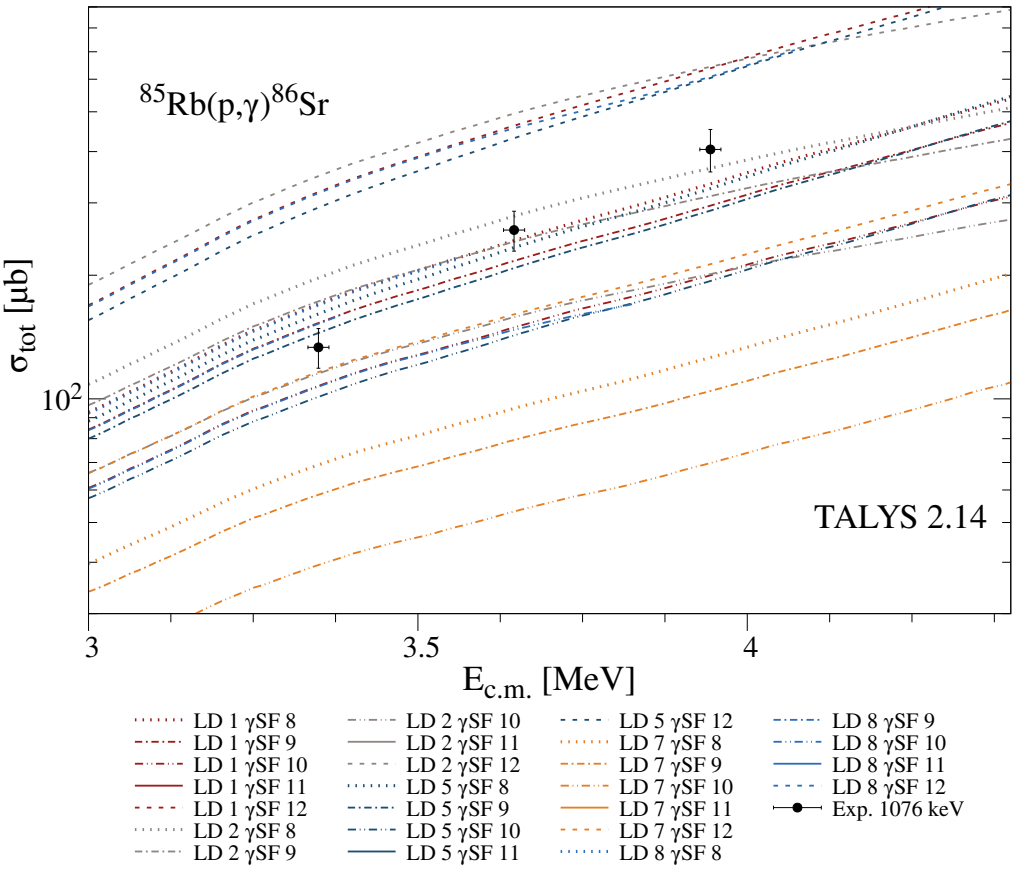

Figure A.1: Cross section calculation for the de-excitation of of the first 2^+ level with $E_\gamma = 1076.78\,\text{keV}$ in comparison with experimental cross sections. The calculations are performed with the TALYS code version 2.14 [124, 189].

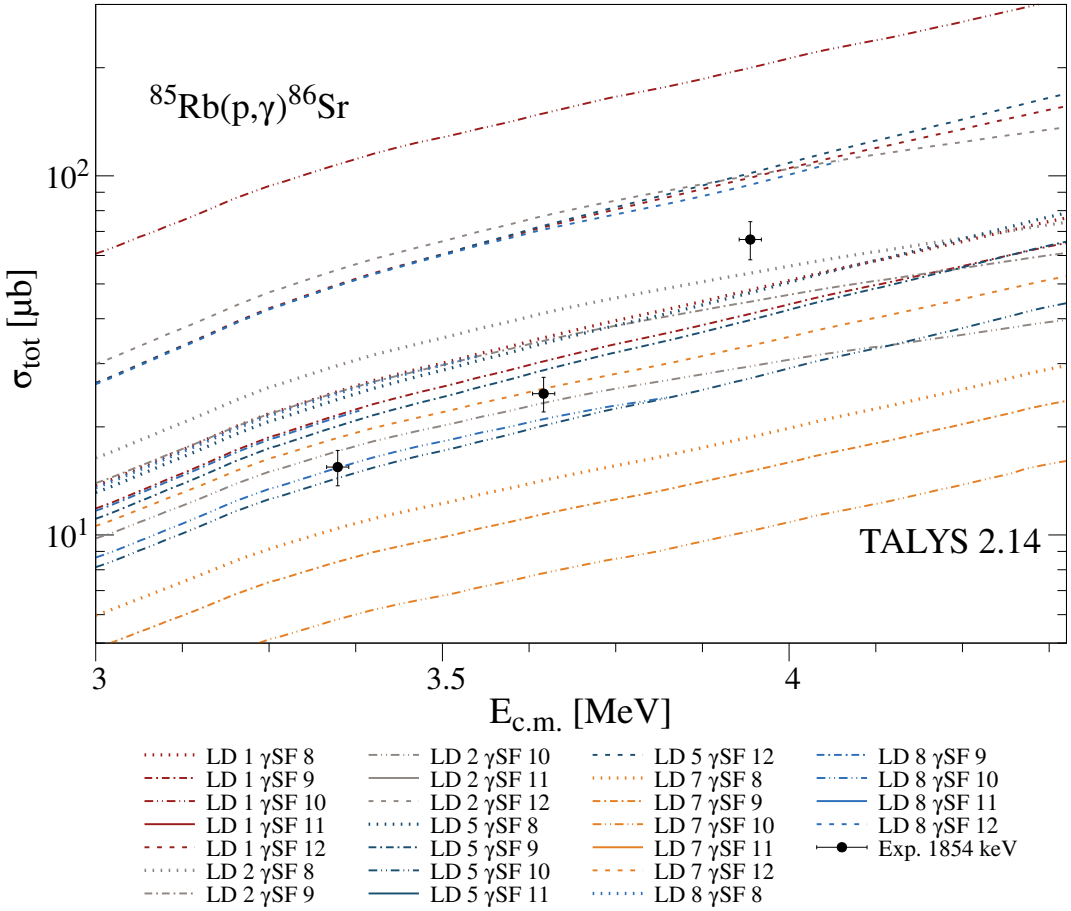

Figure A.2: Cross section calculation for the de-excitation of of the second 2^+ level with E_γ = 1854.01 keV in comparison with experimental cross sections. The calculations are performed with the TALYS code version 2.14 [124, 189].

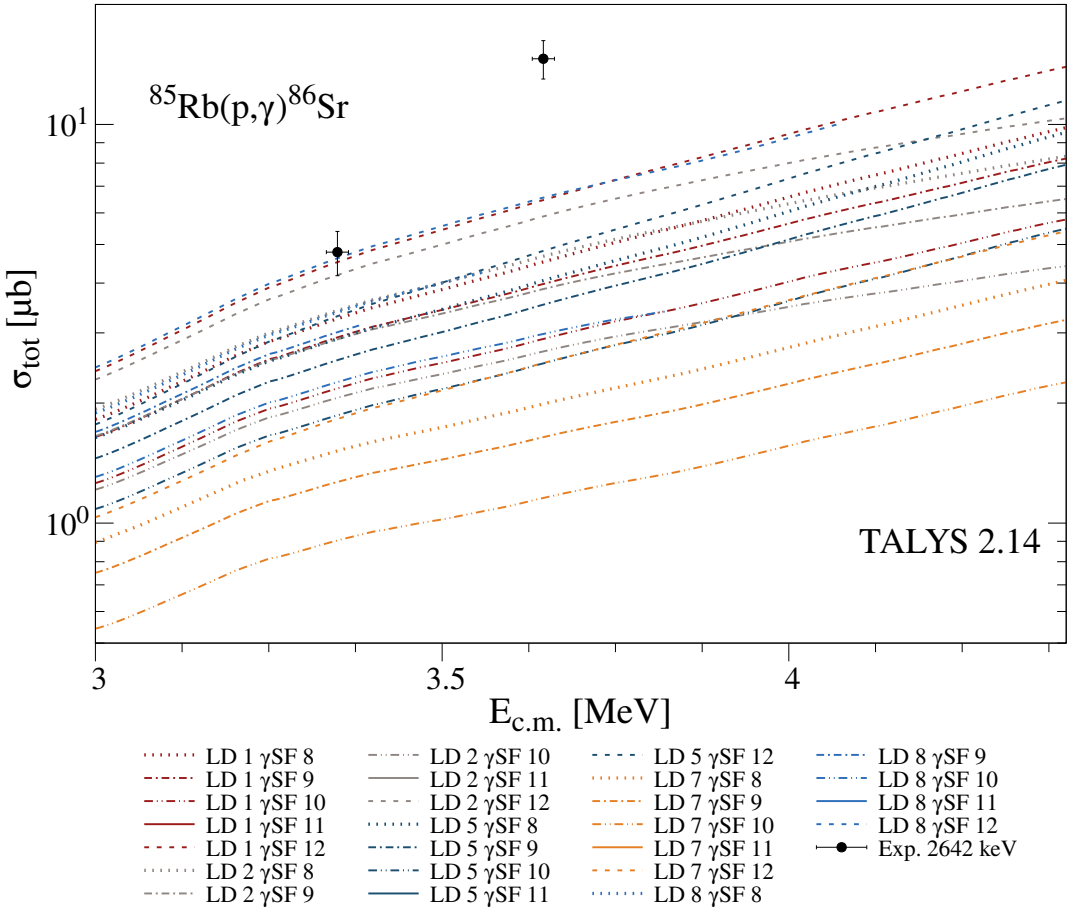

Figure A.3: Cross section calculation for the de-excitation of of the third 2^+ level with E_γ = 2641.12 keV in comparison with experimental cross sections. The calculations are performed with the TALYS code version 2.14 [124, 189].

A.2 Systematic studies of Microscopic Level Density Parameters

The different combinations of the parameters, that can adjust the microscopic level density model 5, as explained in Section 2.2.2. The parameter c and δ have been varied in the range of the in TALYS implemented default values with adjustment values between 0.360 and 0.380 for c and 1.459 and 1.479 for δ. The different cumulative number of levels, that are obtained from different combinations are plotted against the experimentally known cumulative number of levels. This is under the assumption that the experimentally cumulative number of levels is reasonable in an energy range up to approximately 4.5 MeV.

A.2.1 Calculations varying c and δ with TALYS 2.14 code

It can be seen that for c between 0.360 and 0.372, the combinations of c and δ give reasonable results in an energy range of 3.3 MeV to 4.5 MeV.

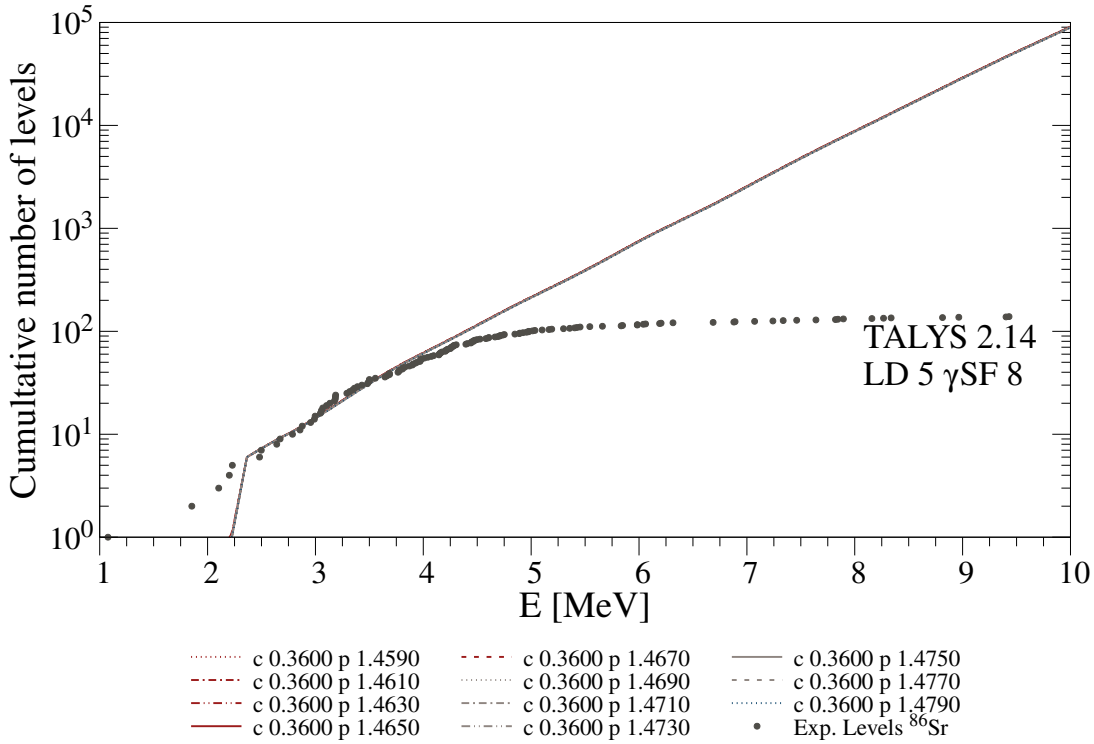

Figure A.4: The cumulative number of levels for the combination of $c = 0.3600$ and the different values for δ. Below approximately 2.4 MeV the cumulative number of levels deviate significantly. The experimentally known levels are well described up to circa 4 MeV. The influence of varying δ in the given range of 1.4590 to 1.4790 is negligible.

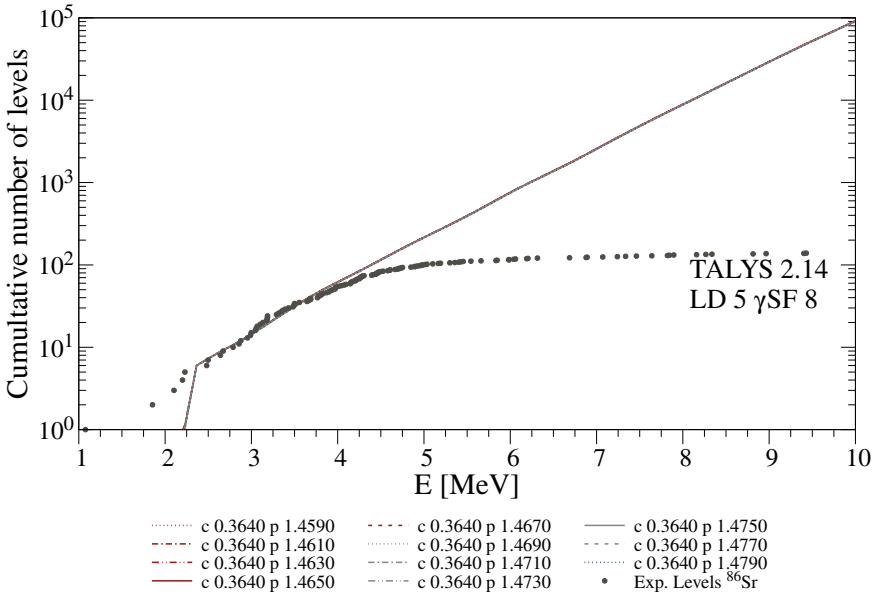

Figure A.5: Same as before with $c = 0.3640$.

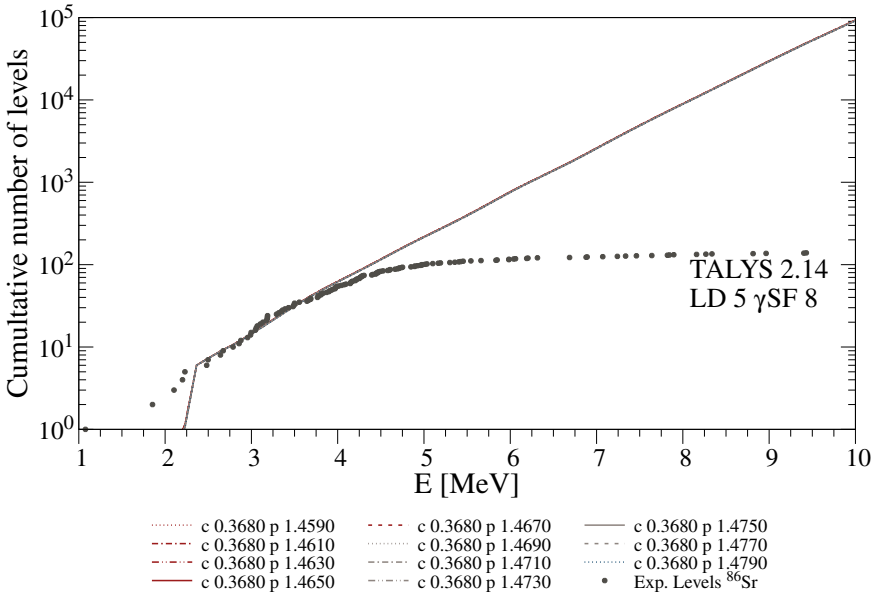

Figure A.6: Same as before with $c = 0.3680$.

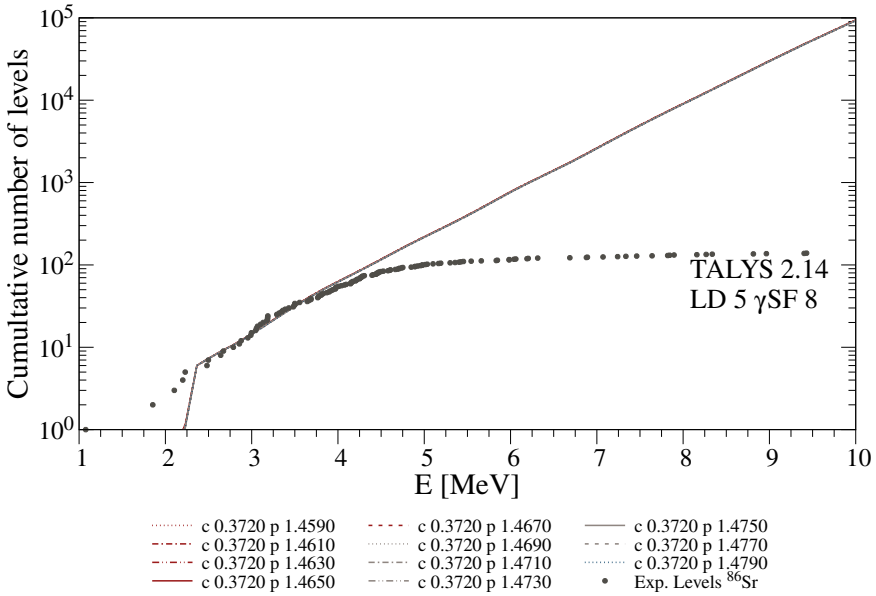

Figure A.7: Same as before with $c = 0.3720$.

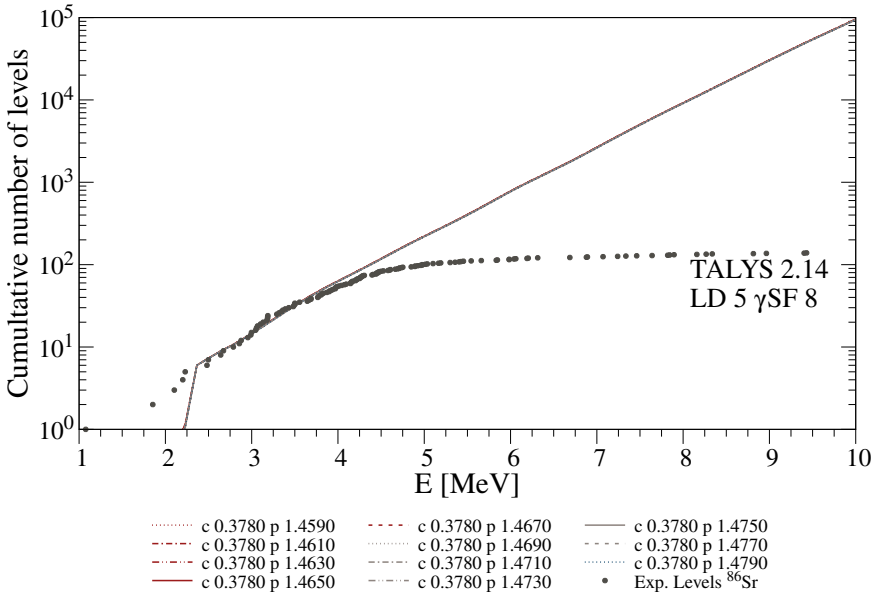

Figure A.8: Same as before with $c = 0.3780$.

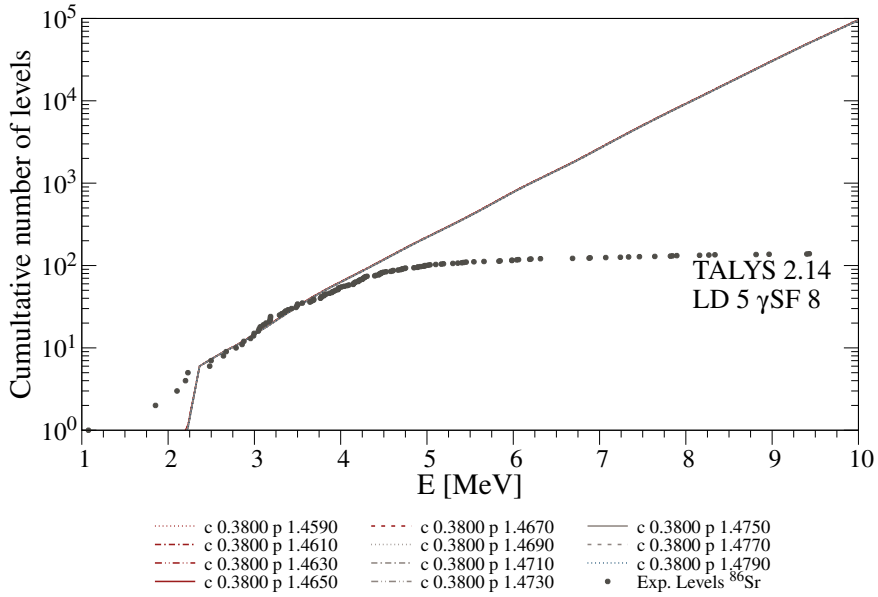

Figure A.9: Same as before with $c = 0.3800$.

A.2.2 Calculations varying T and E_0 with TALYS 2.14 code

Level density model 1 in combination with γ-ray strength function 9 is tested by varying the parameters T and E_0. On the left side, the experimental level density is compared to the variations of E_0.

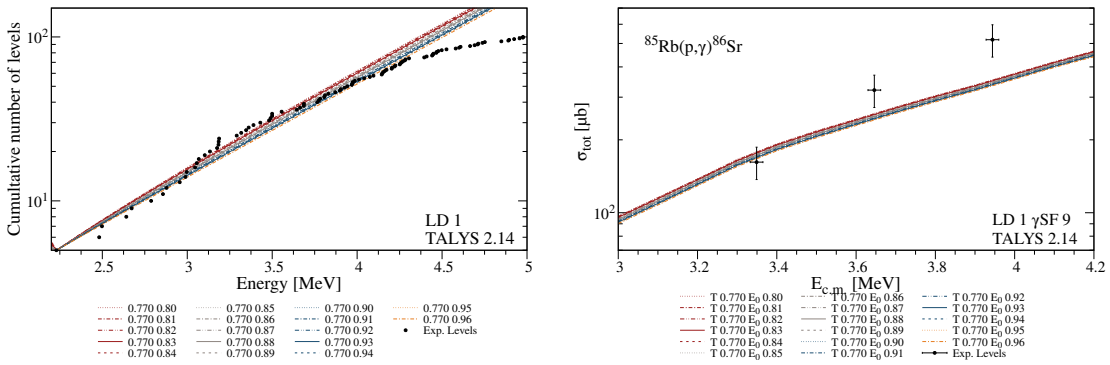

Figure A.10: Figures for $T = 0.770$

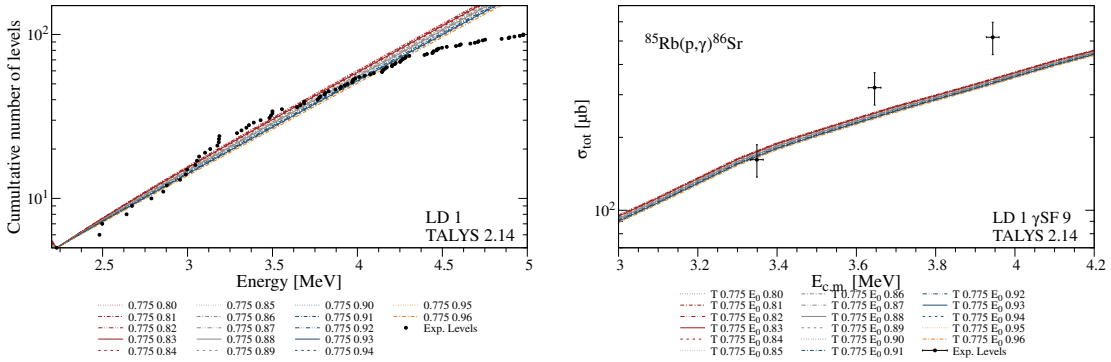

Figure A.11: Figures for $T = 0.775$

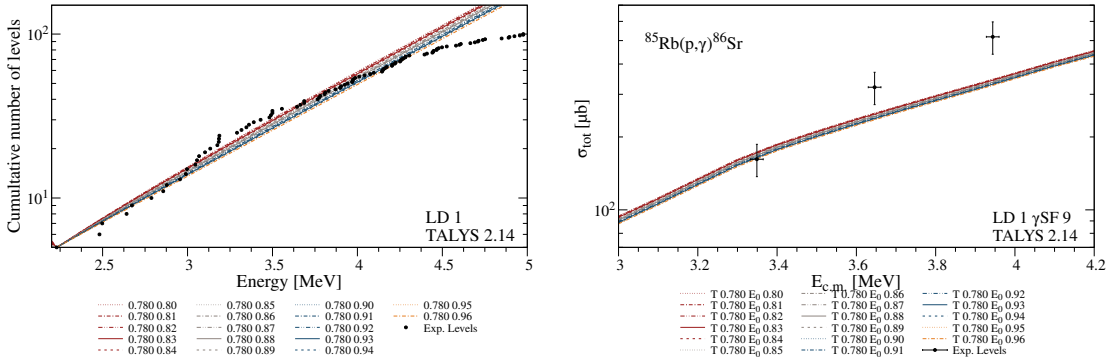

Figure A.12: Figures for $T = 0.780$

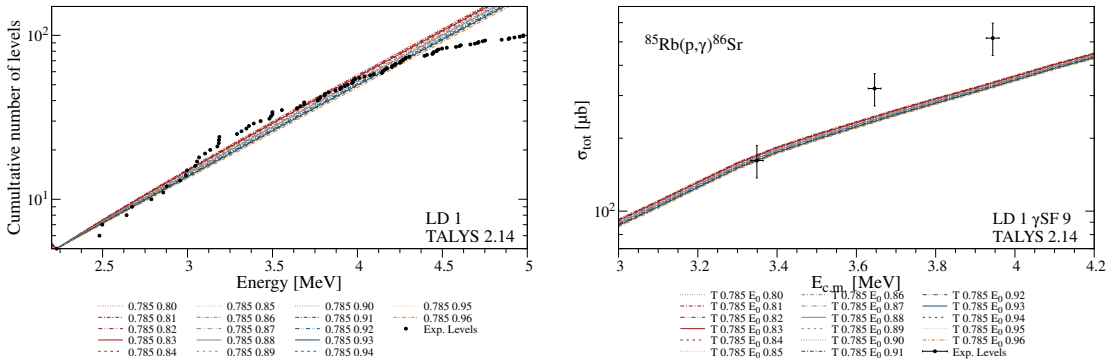

Figure A.13: Figures for $T = 0.785$

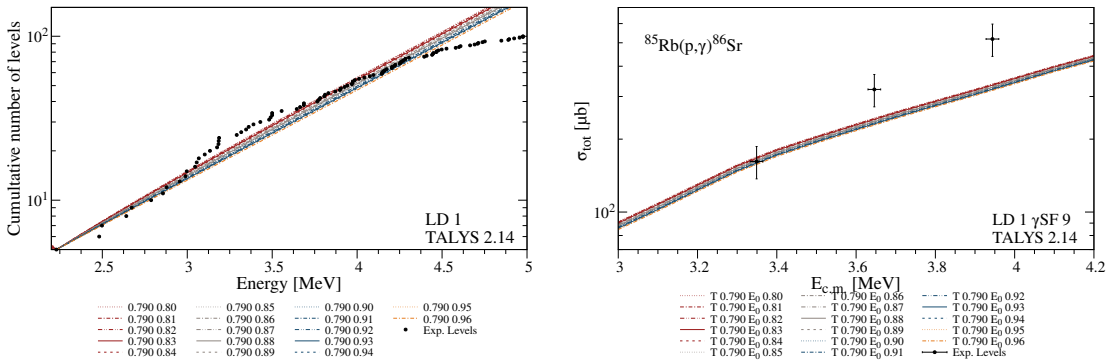

Figure A.14: Figures for $T = 0.790$

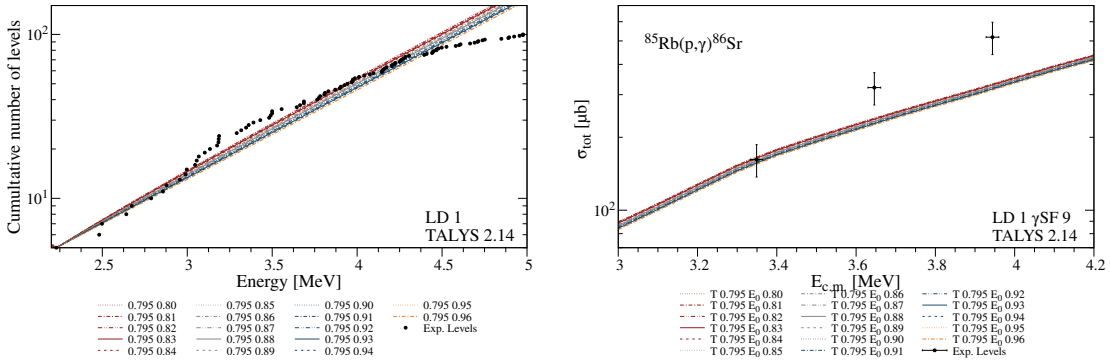

Figure A.15: Figures for $T = 0.795$

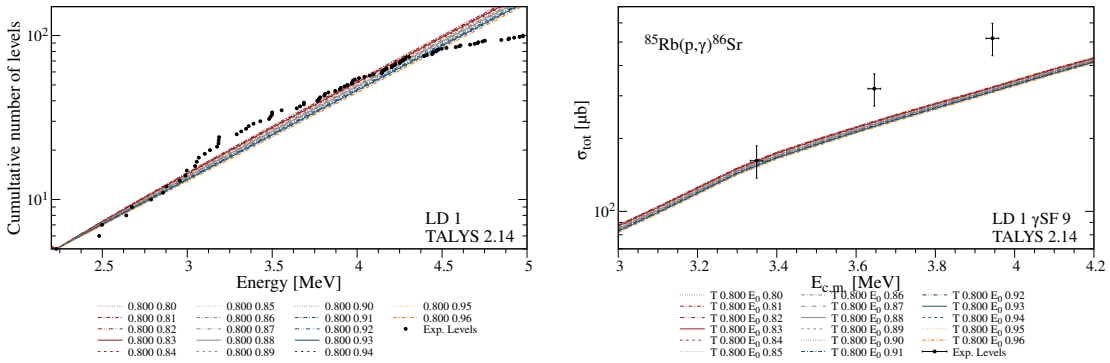

Figure A.16: Figures for $T = 0.800$

A.3 Systematic studies of γ-ray strength Parameters *wtable*

Variation of the *wtable* parameter influencing the γ-ray strength function. The influence of varying the $M1$ strength is negligible compared to the influence of the $E1$ strength. The greater the value of *wtable*, the greater are the predicted cross sections.

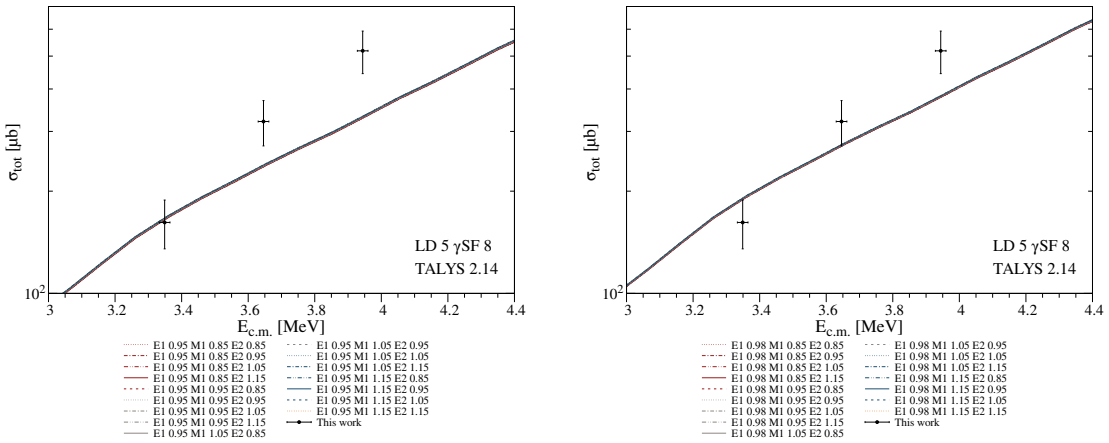

Figure A.17: Varying the γ-ray strength function for strength model 8 with help of the parameter *wtable*. The influence of traditionally varying $M1$ and $E2$ is negligible. Varying $E1$ shifts the cross sections up and down and does not change the shape in the energy region of interest. Shown are *wtable* $E1$ 0.95 on left hand side and 0.98 on the right hand side.

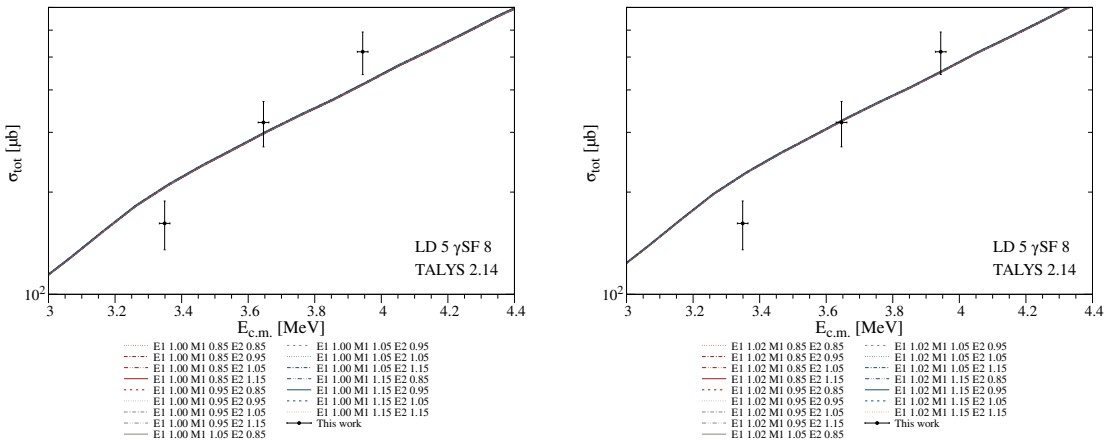

Figure A.18: Same as before with *wtable* $E1$ 1.00 on left hand side and 1.02 on the right hand side.

A.4 Systematic studies of the Koning and Delaroche Optical Model Potential

A thorough examination of this potential is conducted, since it is the default optical model potential in the TALYS code. It provides 27 adjustable parameters, that are varied as described in detail in Chapter 4. Details on each of the parameters are given in the TALYS documentation.

A.4.1 Varying *rw* and *aw*

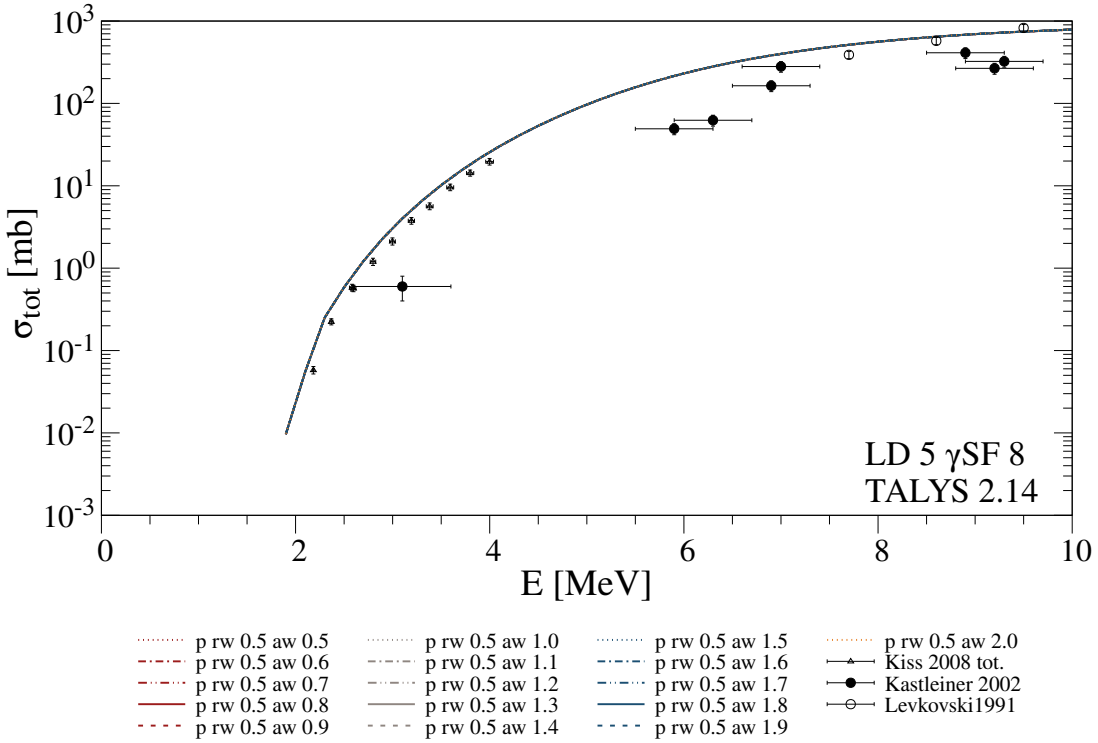

Figure A.19: Varying the parameters rw and aw utilizing the TALYS [124] code version 2.14 in comparison to experimental obtained (p, n)-reaction cross sections from References [140, 237, 238]. Shown is $rw = 0.5$ with varying aw between 0.5 and 2.0.

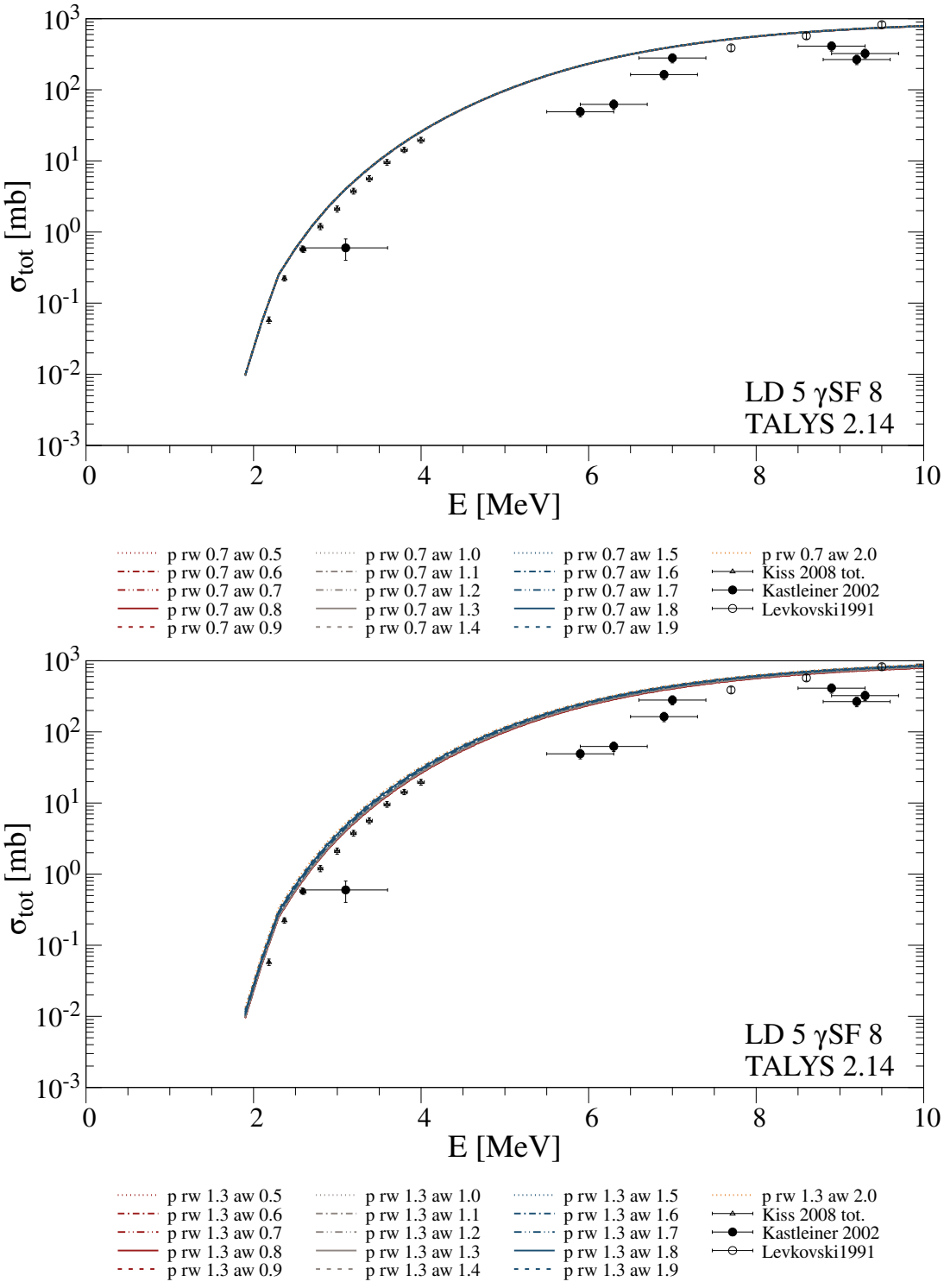

Figure A.20: Same as before. Shown are $rw = 0.7$ and 1.3 with varying aw between 0.5 and 2.0.

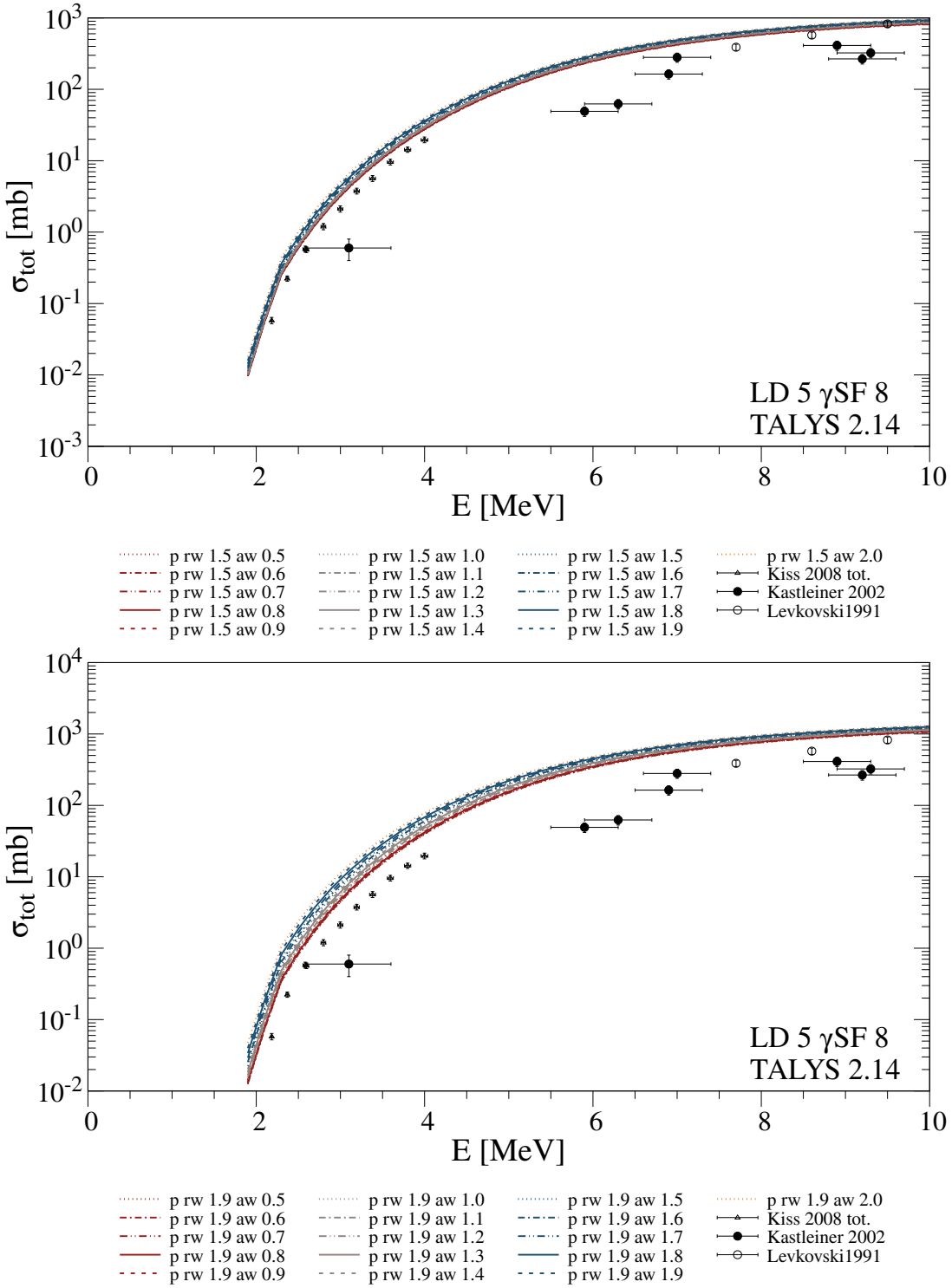

Figure A.21: Same as before. Shown are $rw = 1.5$ and 1.9 with varying aw between 0.5 and 2.0.

A.4.2 Varying *w1* and *w2*

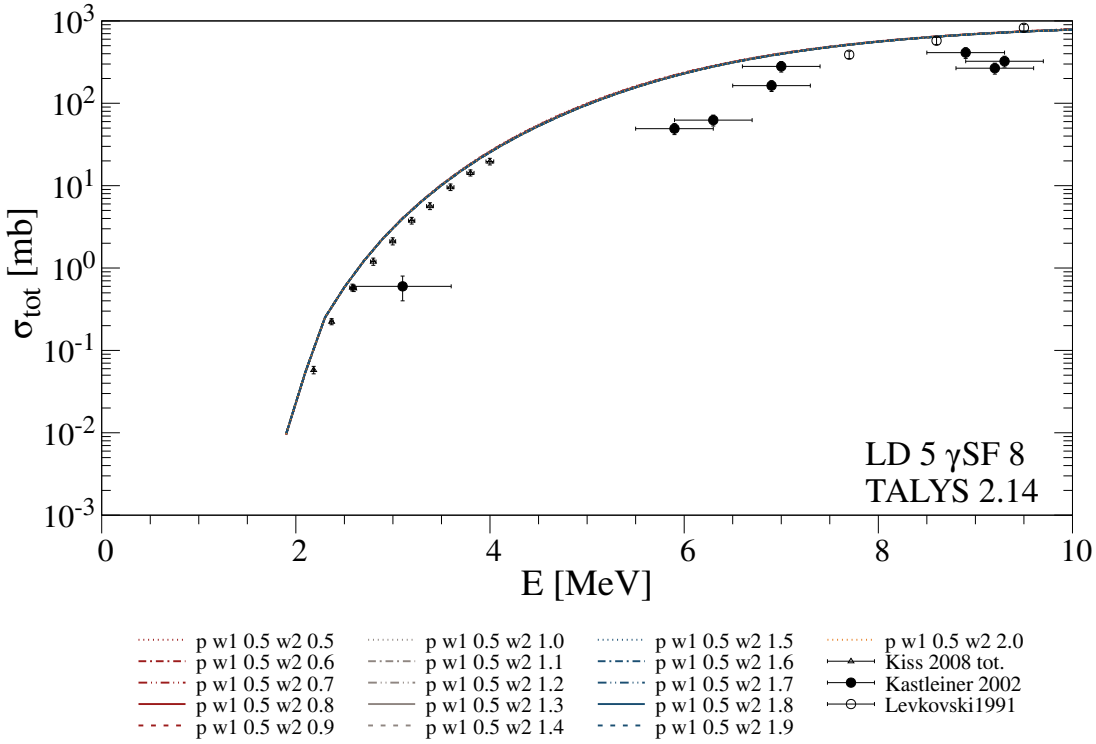

Figure A.22: Varying the parameters $w1$ and $w2$ utilizing the TALYS [124] code version 2.14 in comparison to experimental obtained (p, n)-reaction cross sections from References [140, 237, 238]. Shown exemplary is $w1 = 0.5$ with varying $w2$ between 0.5 and 2.0. It is shown, that the effect is negligible for the calculated cross sections.

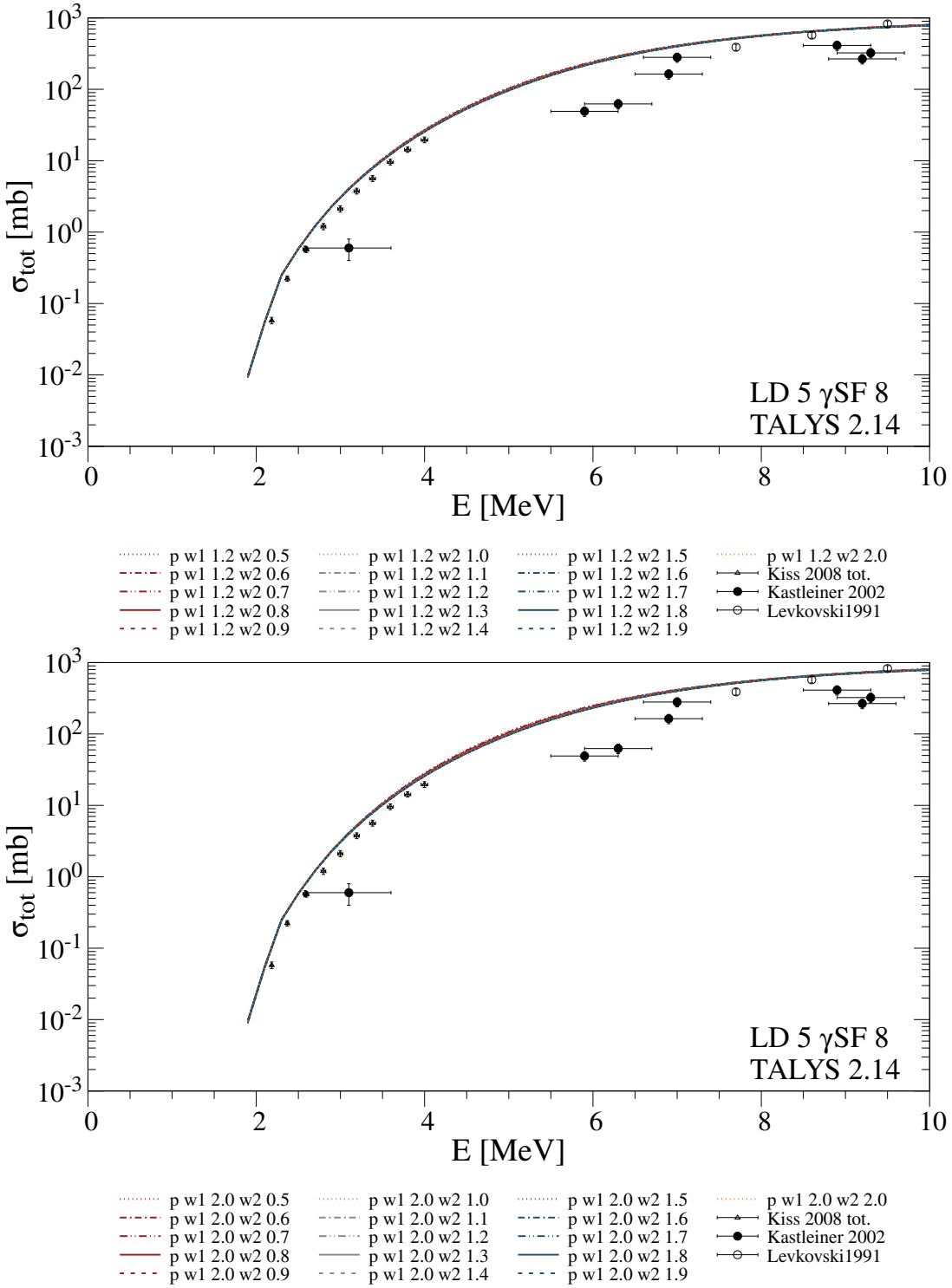

Figure A.23: Same as before. Shown are $w1 = 1.2$ and $w1 = 2.0$ with varying $w2$ between 0.5 and 2.0.

A.4.3 Varying *rwso* and *awso*

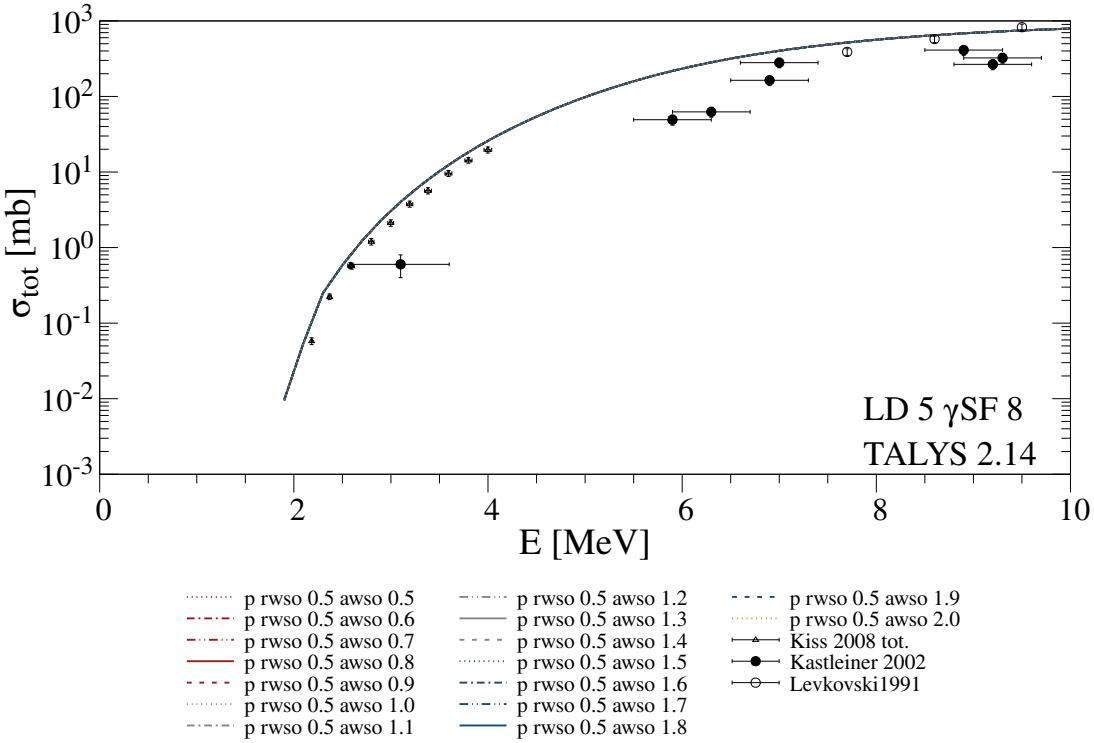

Figure A.24: Varying the parameters *rwso* and *awso* utilizing the TALYS [124] code version 2.14 in comparison to experimental obtained (p, n)-reaction cross sections from References [140, 237, 238]. Shown exemplary is $rwso = 0.5$ with varying *awso* between 0.5 and 2.0. It is shown, that the effect is negligible for the calculated cross sections.

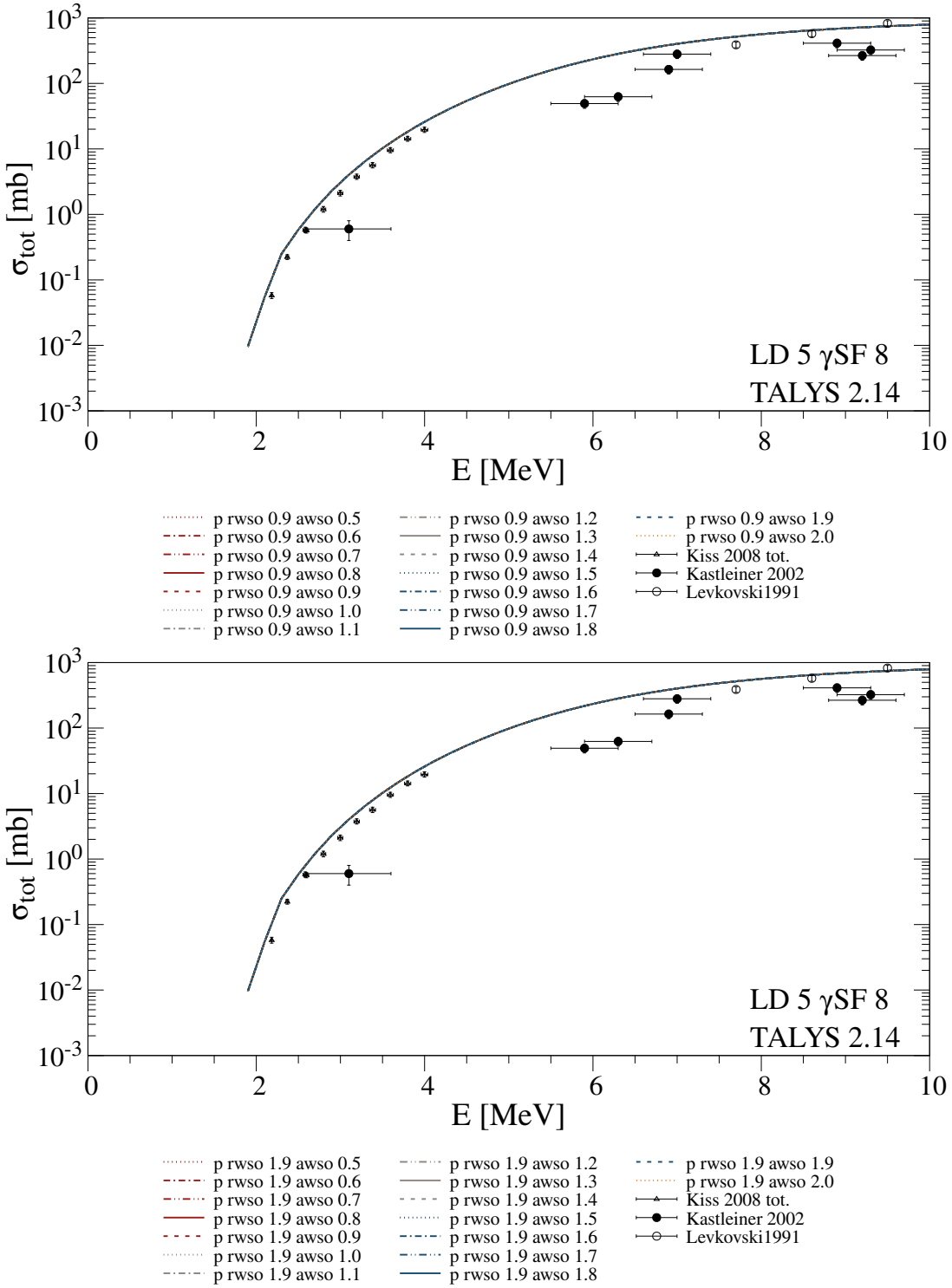

Figure A.25: Same as before. Shown are $rwso = 0.9$ and $rwso = 1.9$ with varying $awso$ between 0.5 and 2.0.

A.4.4 Varying *rwd* and *awd*

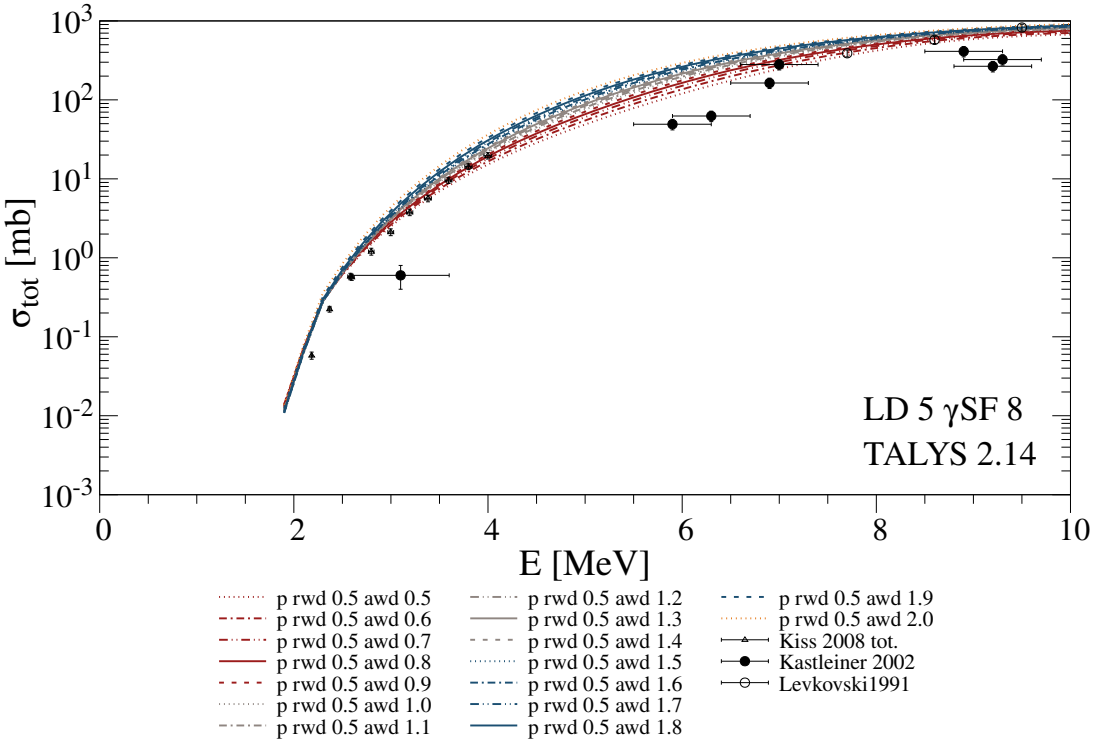

Figure A.26: Varying the parameters *rwd* and *awd* utilizing the TALYS [124] code version 2.14 in comparison to experimental obtained (p, n)-reaction cross sections from References [140, 237, 238]. Shown exemplary is $rwd = 0.5$ with varying *awd* between 0.5 and 2.0. It is shown, that the effect is shifting the the calculated cross sections up with increasing the value of the *awd* parameter.

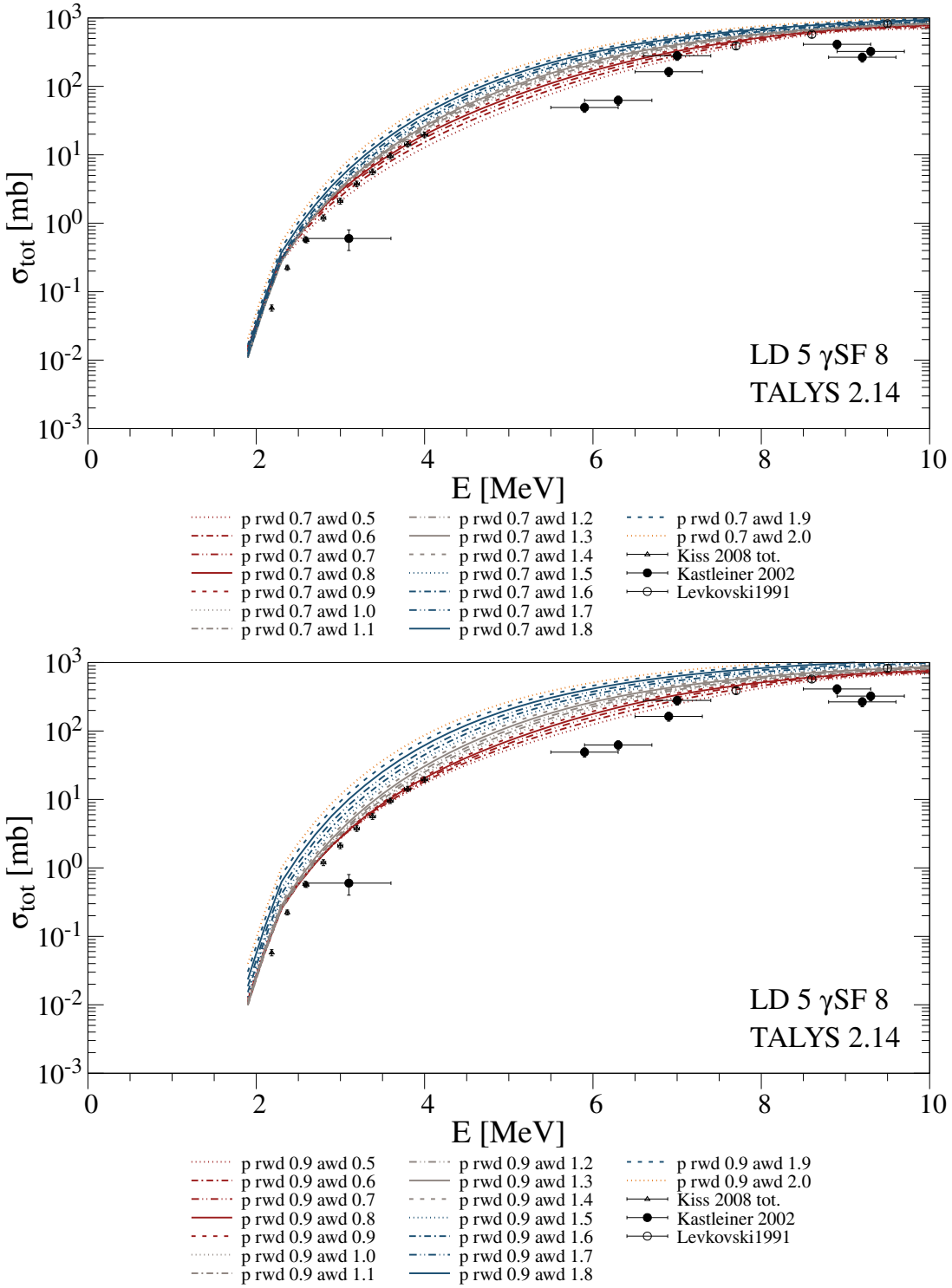

Figure A.27: Same as before with $rwd = 0.7$ and $rwd = 0.9$.

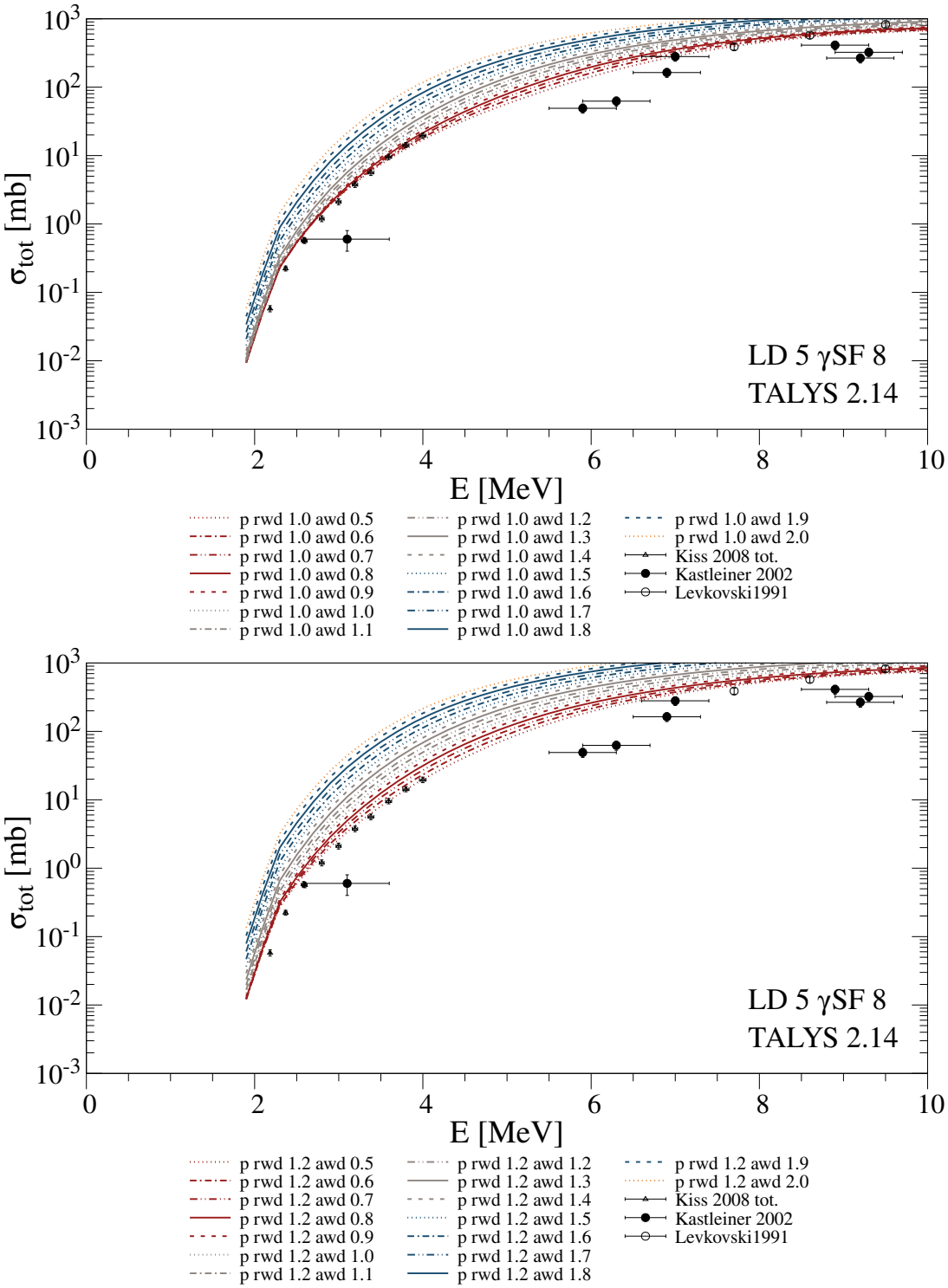

Figure A.28: Same as before with $rwd = 1.0$ and $rwd = 1.2$.

A.4.5 Varying *d1*, *d2* and *d3*

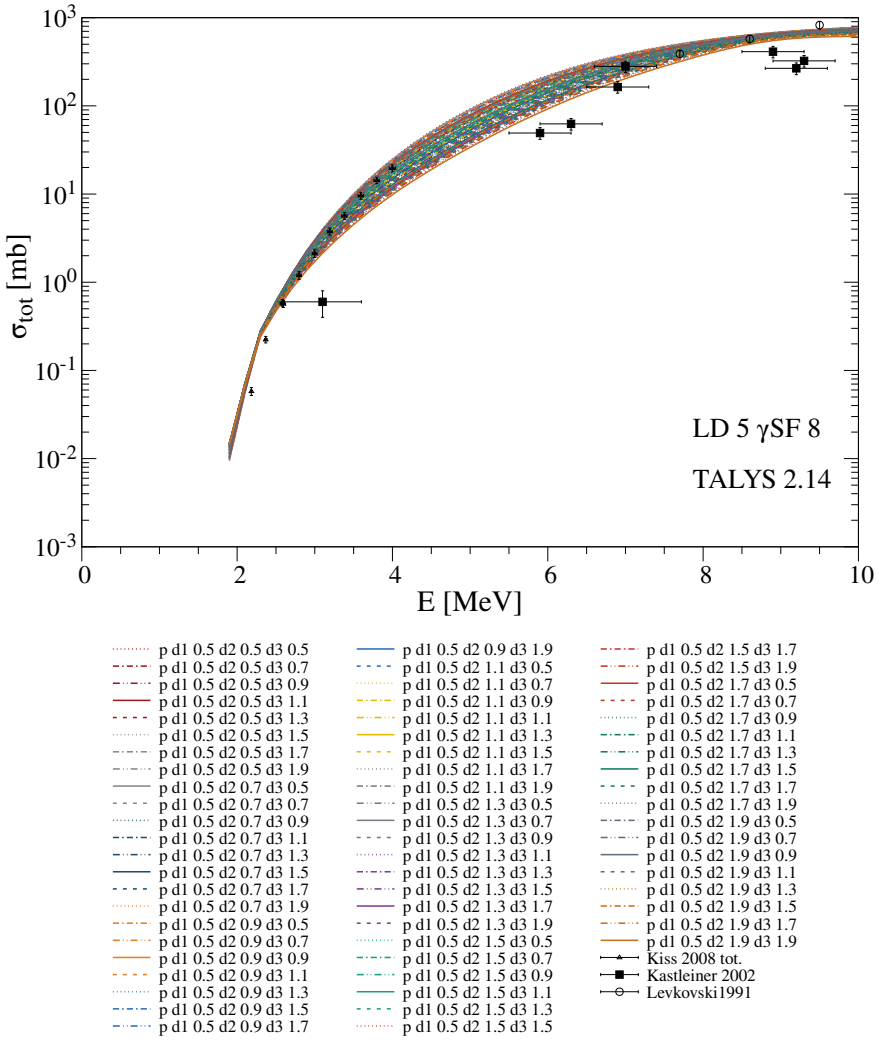

Figure A.29: Varying the parameters $d1$, $d2$ and $d3$ utilizing the TALYS [124] code version 2.14 in comparison to experimental obtained (p, n)-reaction cross sections from References [140, 237, 238]. Shown exemplary is $d1 = 0.5$ with varying $d2$ and $d3$ between 0.5 and 2.0. The effect is most prominent for the energy range 3 MeV to 8 MeV, where it influences how steep the calculated cross sections change.

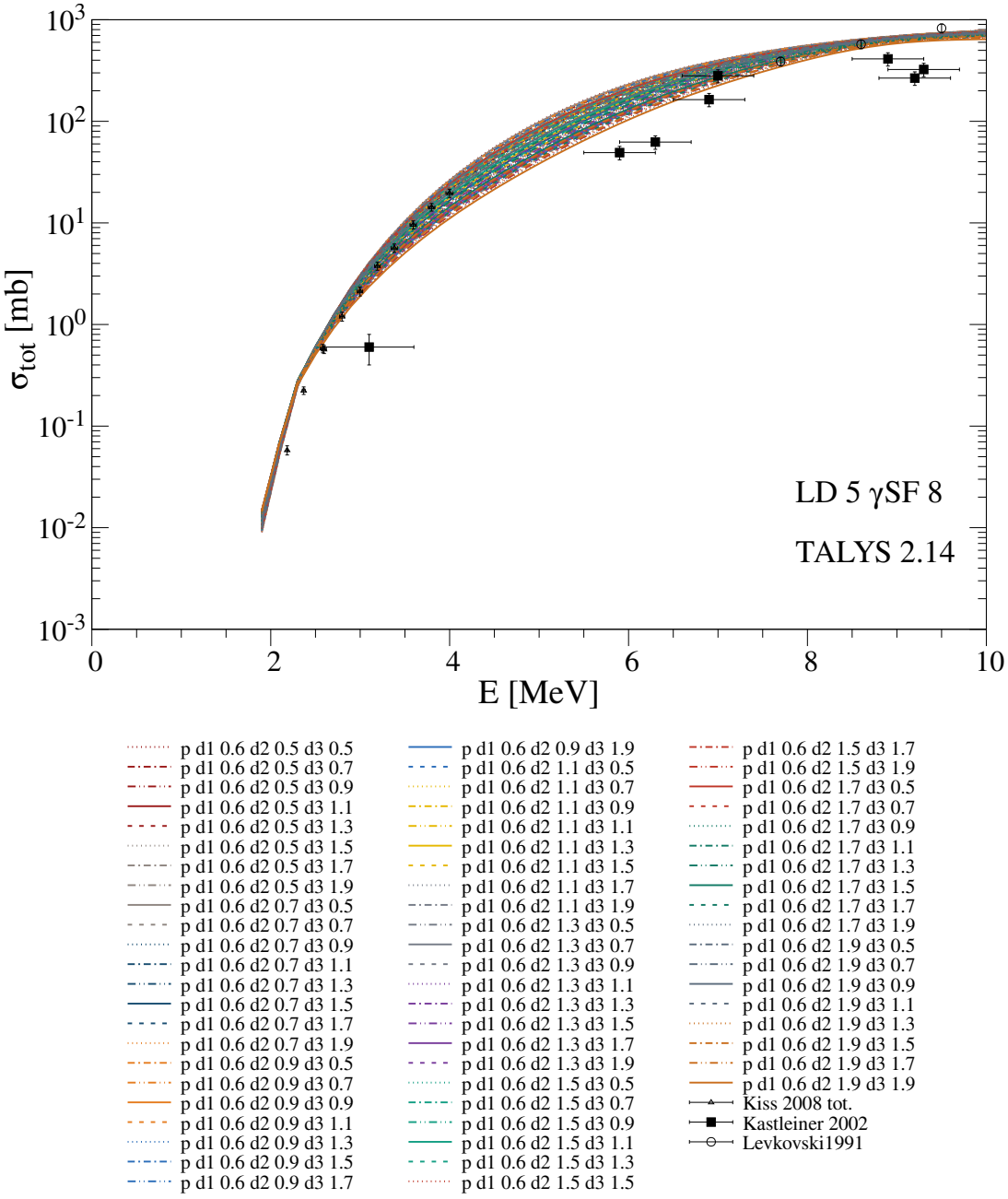

Figure A.30: Same as before with $d1 = 0.6$.

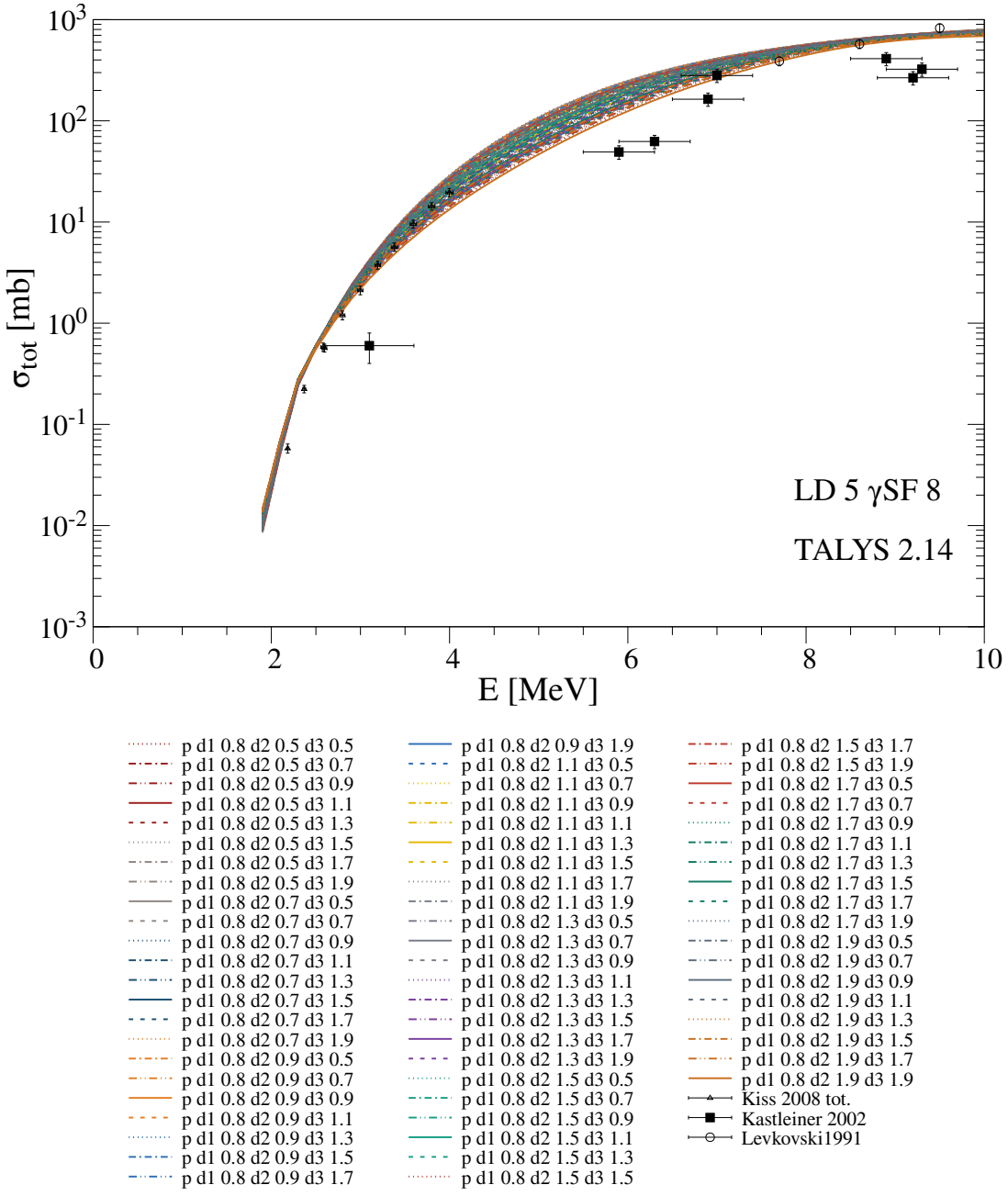

Figure A.31: Same as before with $d1 = 0.8$.

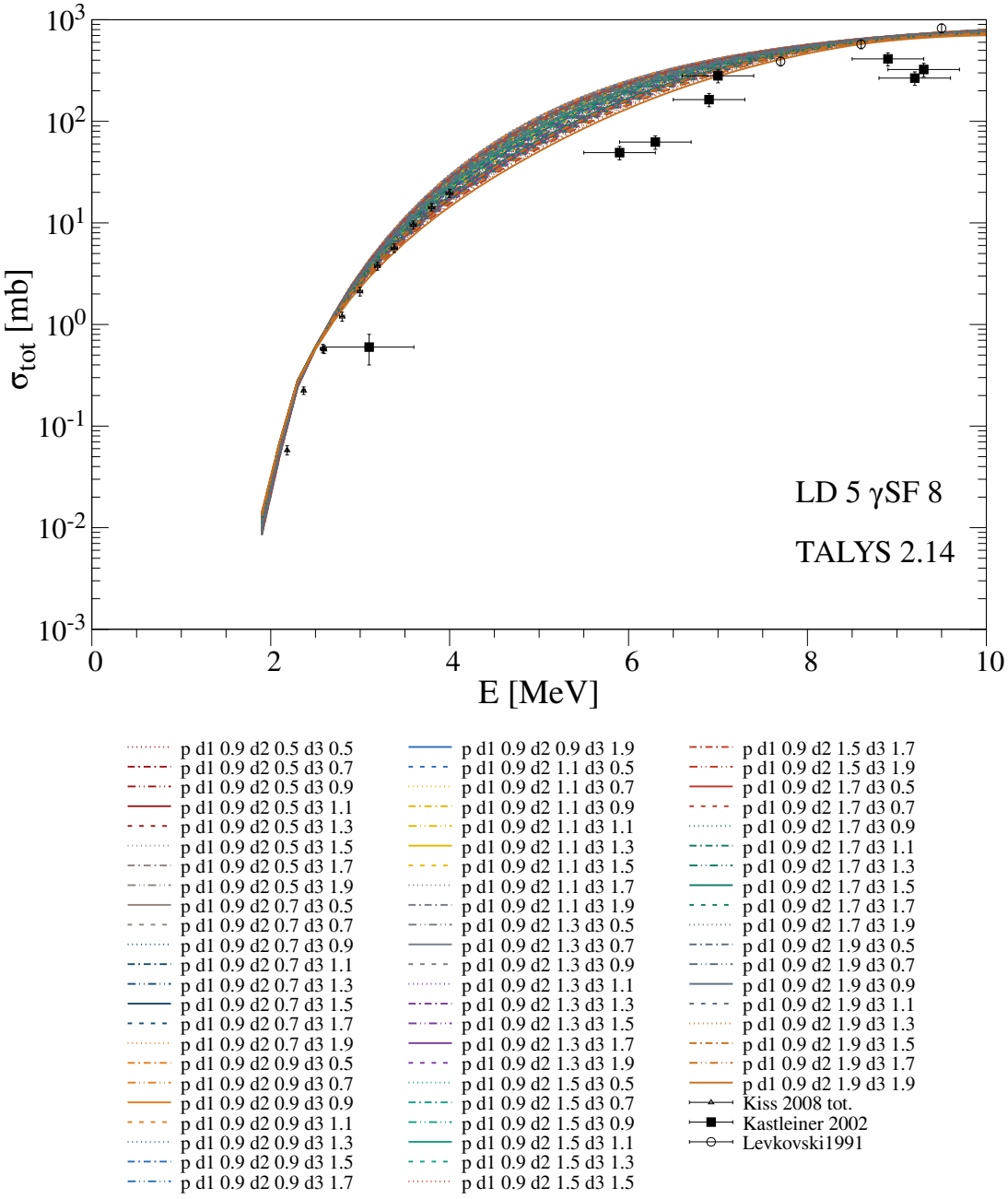

Figure A.32: Same as before with $d1 = 0.9$.

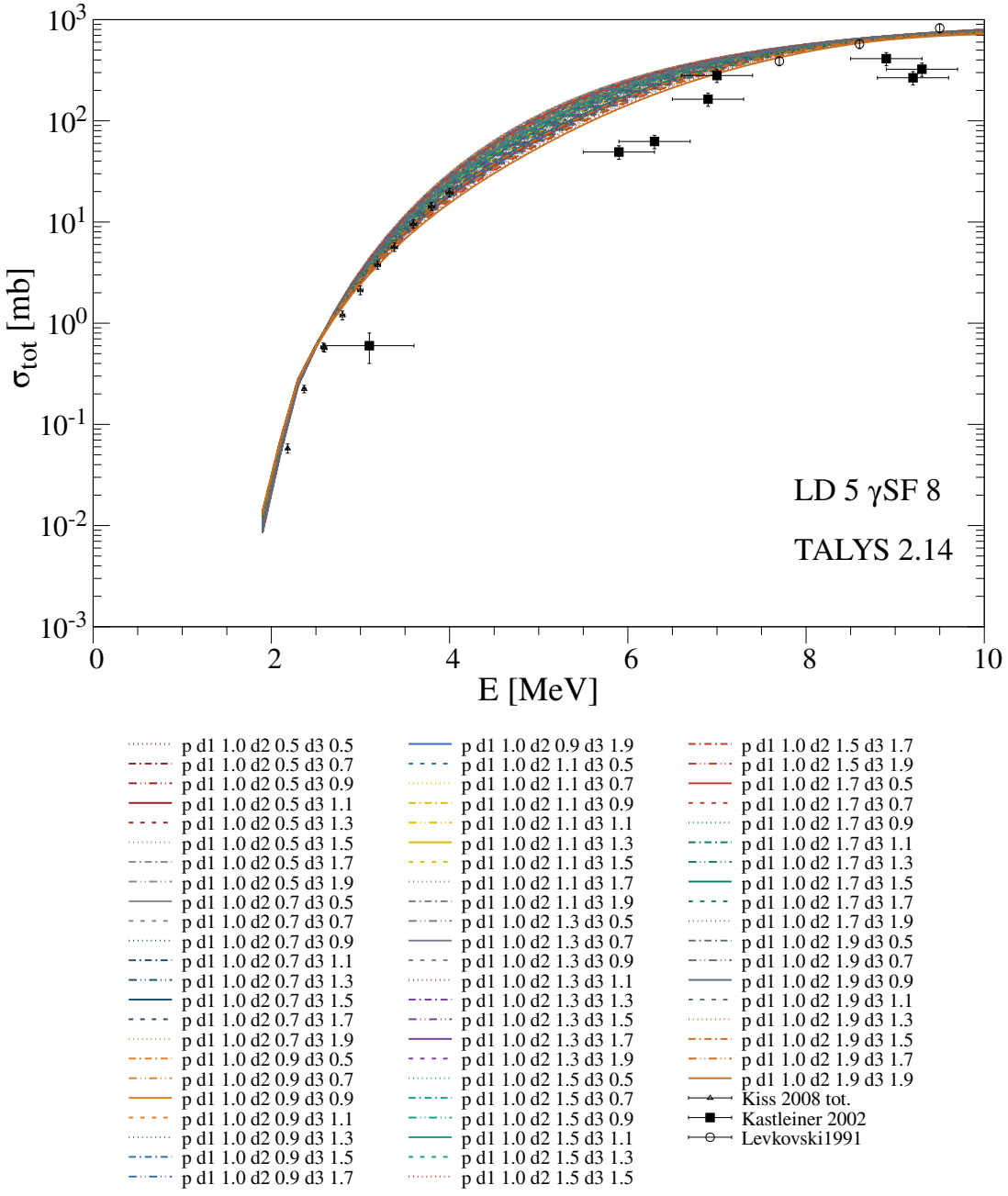

Figure A.33: Same as before with $d1 = 1.0$.

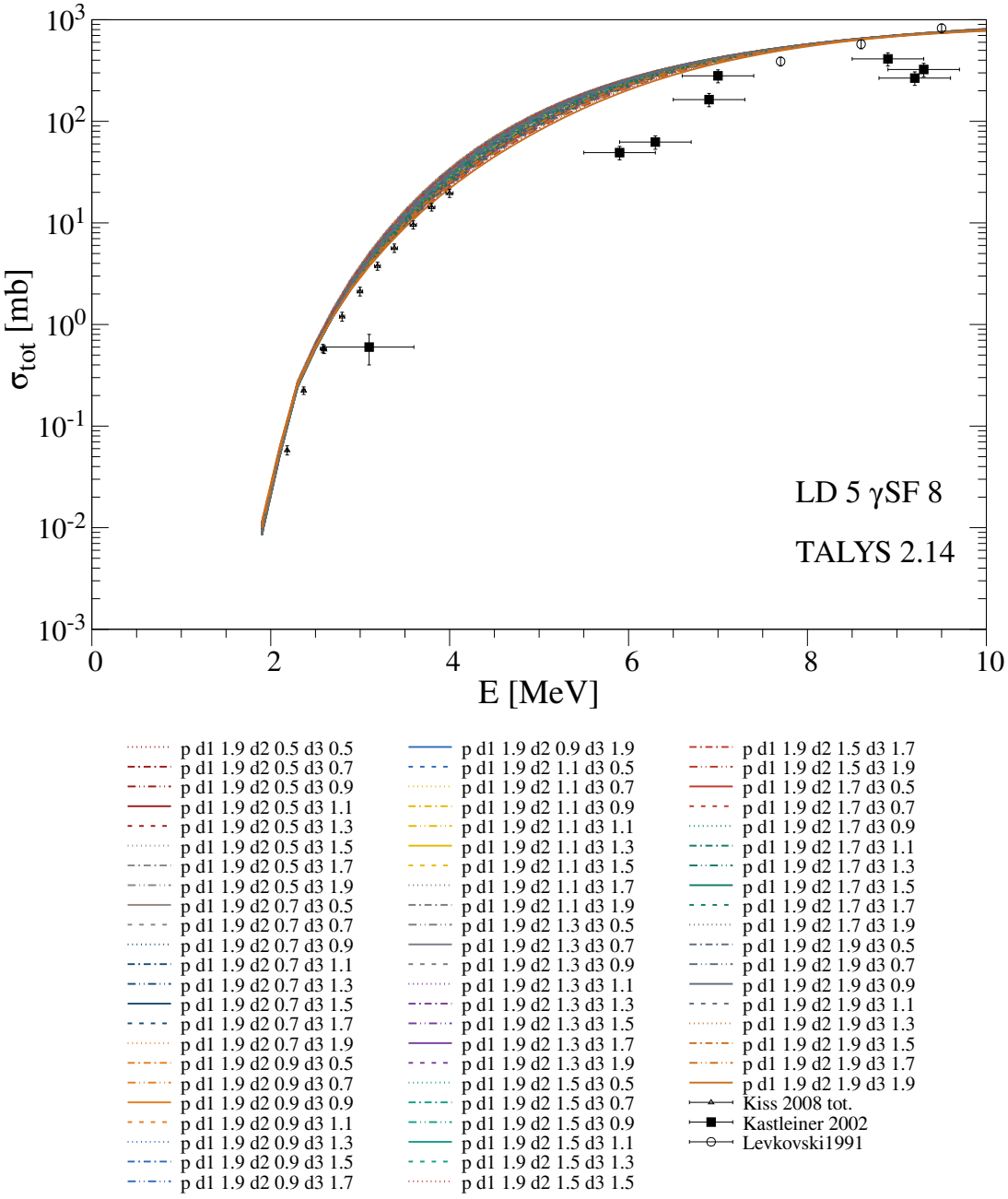

Figure A.34: Same as before with $d1 = 1.9$.

A.4.6 Varying *rv* and *av*

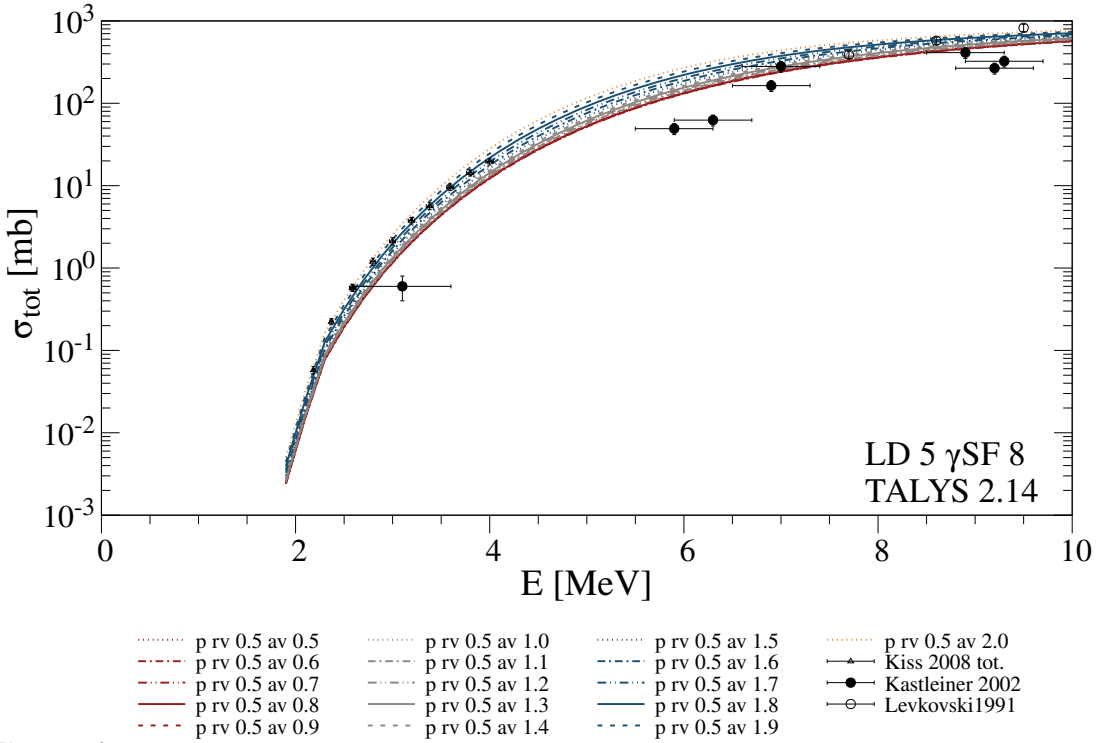

Figure A.35: Varying the parameters rv and av utilizing the TALYS [124] code version 2.14 in comparison to experimental obtained (p, n)-reaction cross sections from References [140, 237, 238]. Shown exemplary is $rv = 0.5$ with varying av between 0.5 and 2.0. The variation is mostly shifting the calculated cross sections up and down.

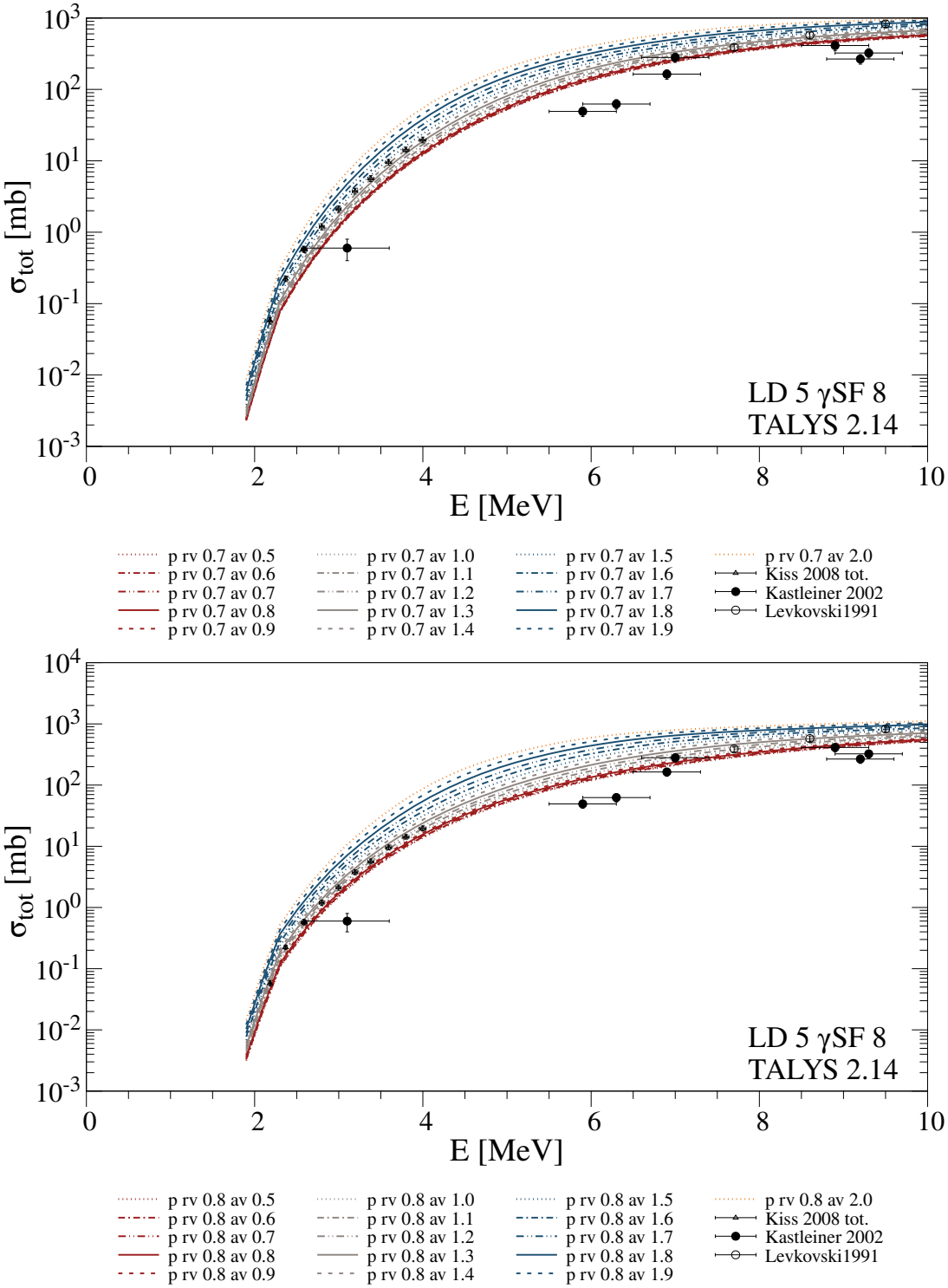

Figure A.36: Same as before with $rv = 0.7$ and $rv = 0.8$.

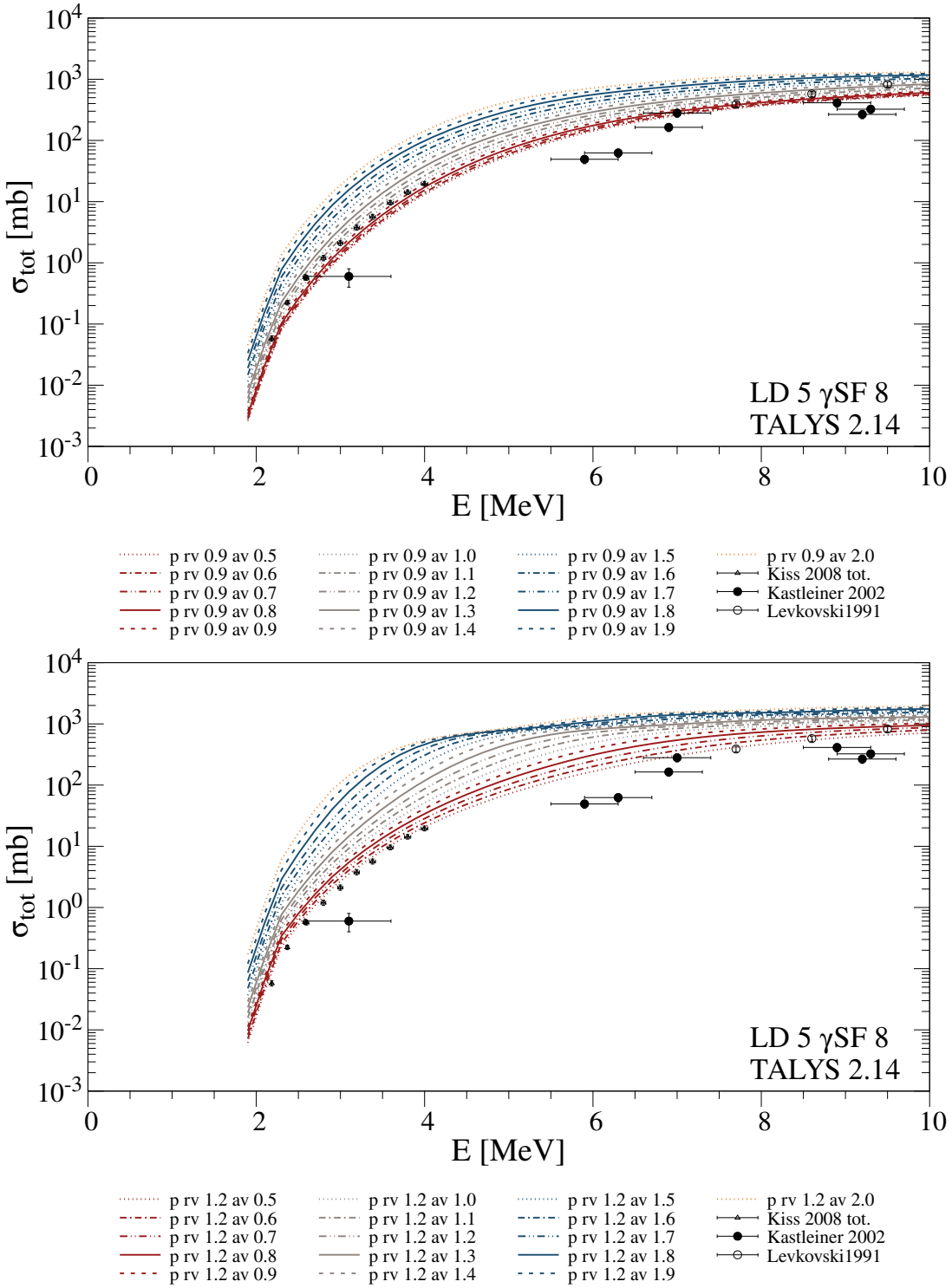

Figure A.37: Same as before with $rv = 0.9$ and $rv = 1.2$.

A.4.7 Varying *v1*

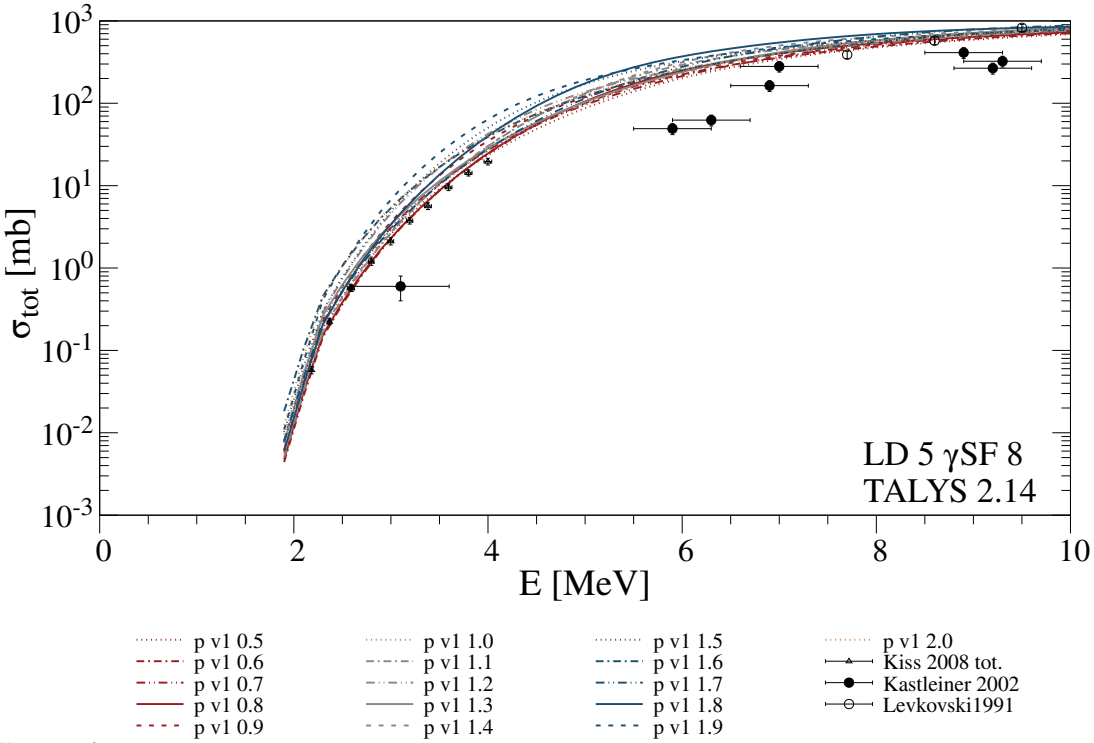

Figure A.38: Varying the parameter $v1$ utilizing the TALYS [124] code version 2.14 in comparison to experimental obtained (p, n)-reaction cross sections from References [140, 237, 238]. Shown is varying $v1$ between 0.5 and 2.0. The variation is mostly shifting the calculated cross sections up and down.

A.4.8 Varying *v2*, *v3* and *v4*

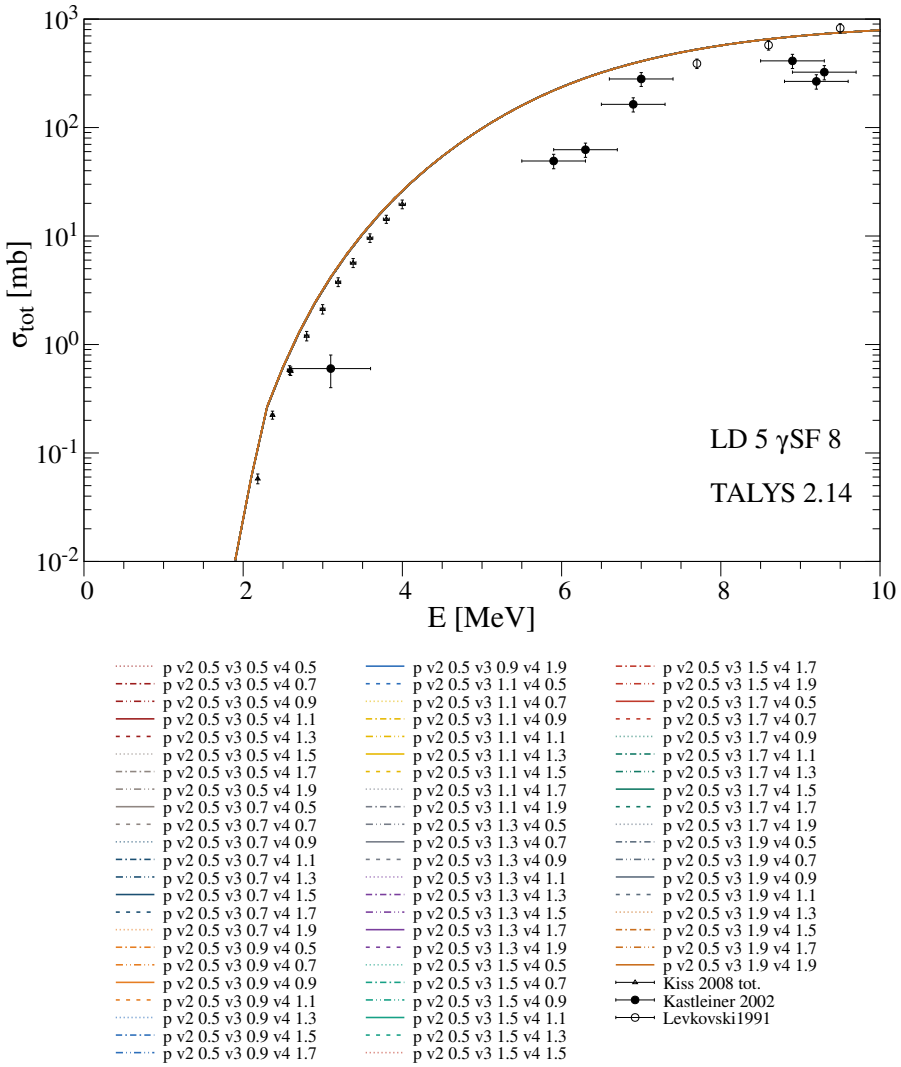

Figure A.39: Varying the parameters $v2$, $v3$ and $v4$ utilizing the TALYS [124] code version 2.14 in comparison to experimental obtained (p, n)-reaction cross sections from References [140, 237, 238]. Shown exemplary is $v2 = 0.5$ with varying $v3$ and $v4$ between 0.5 and 2.0.

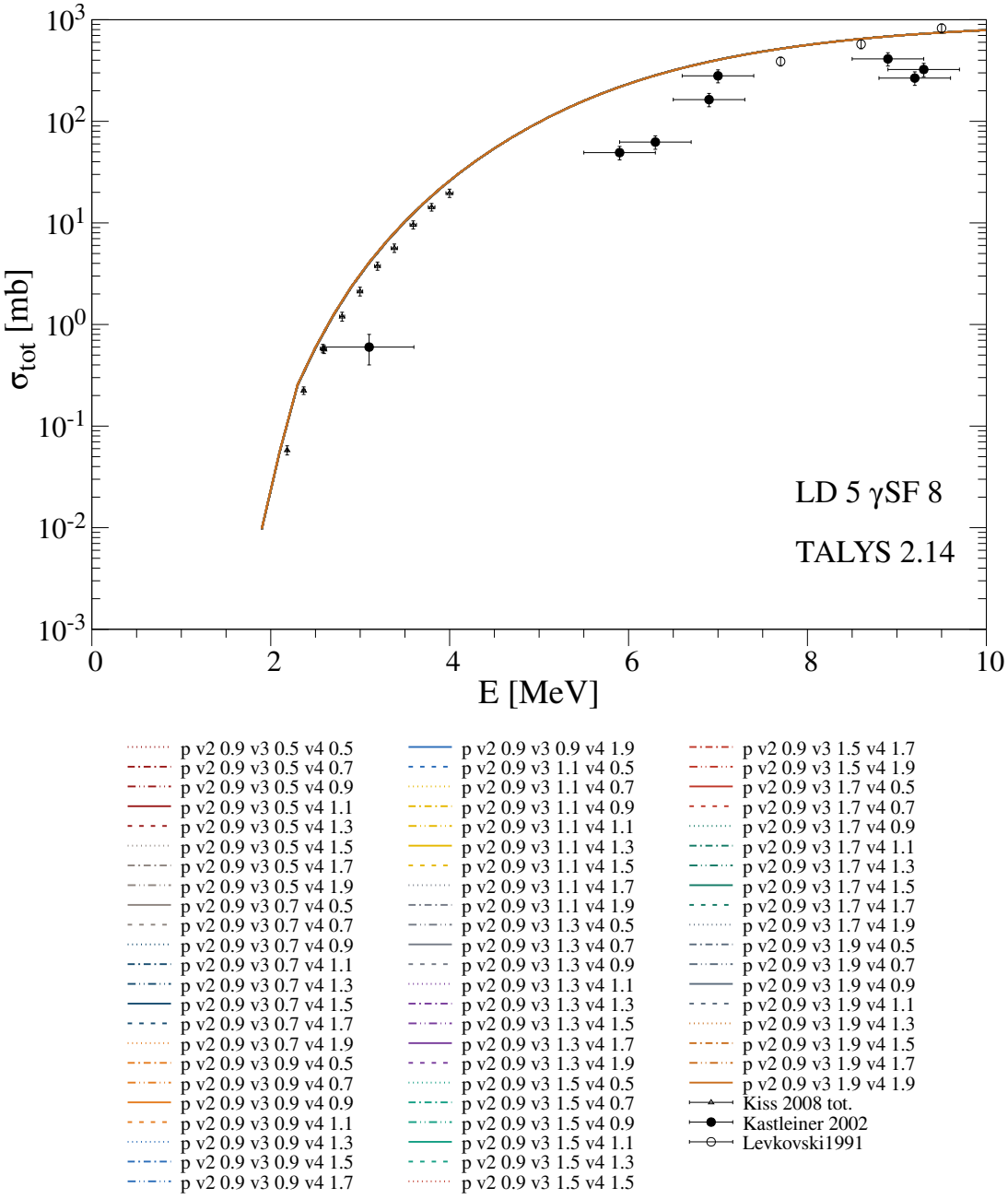

Figure A.40: Same as before with $v2 = 0.9$.

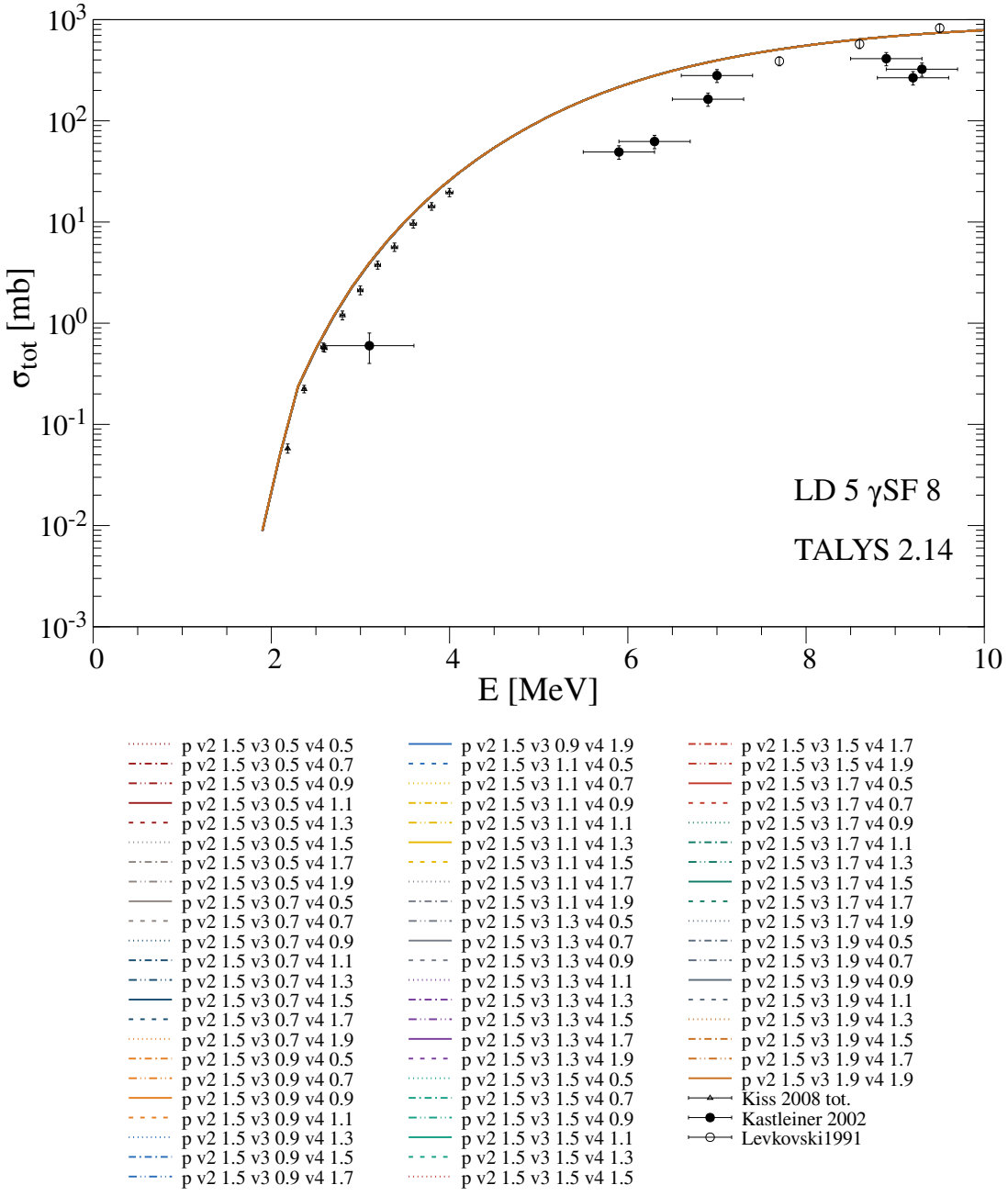

Figure A.41: Same as before with $v2 = 1.5$.

A.4.9 Varying *rvso*

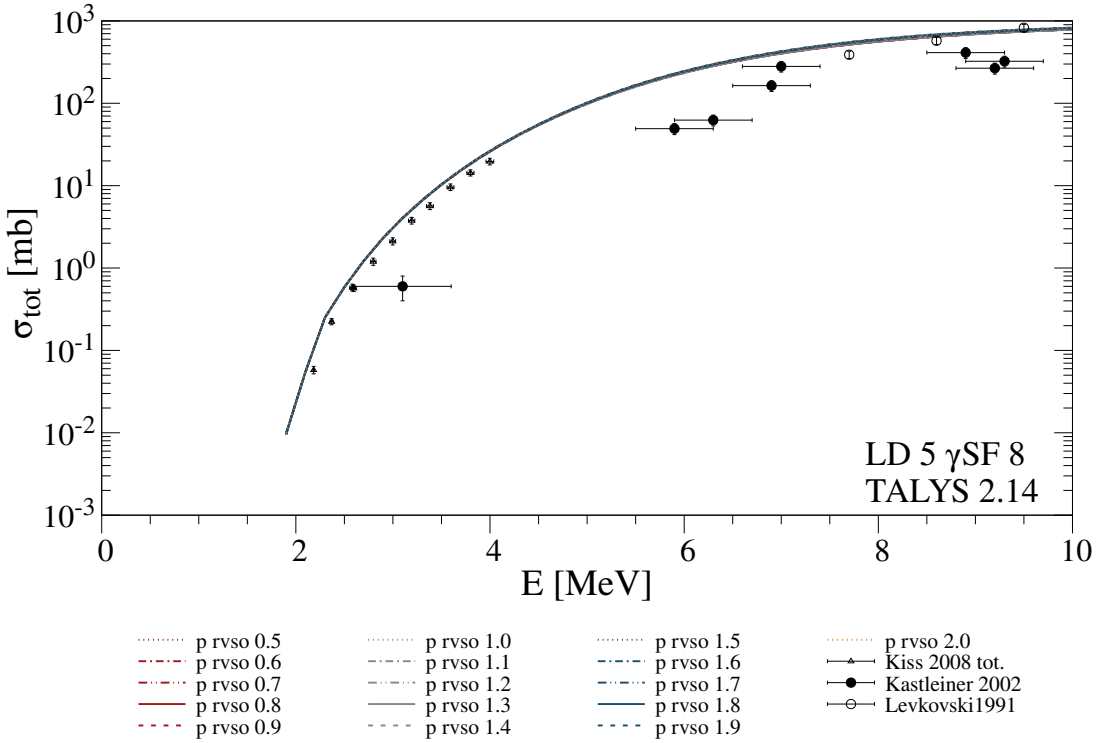

Figure A.42: Varying the parameter *rvso* utilizing the TALYS [124] code version 2.14 in comparison to experimental obtained (p, n)-reaction cross sections from References [140, 237, 238]. Shown is varying *rvso* between 0.5 and 2.0. The variation is mostly shifting the calculated cross sections up and down.

A.4.10 Varying *vso1* and *vso2*

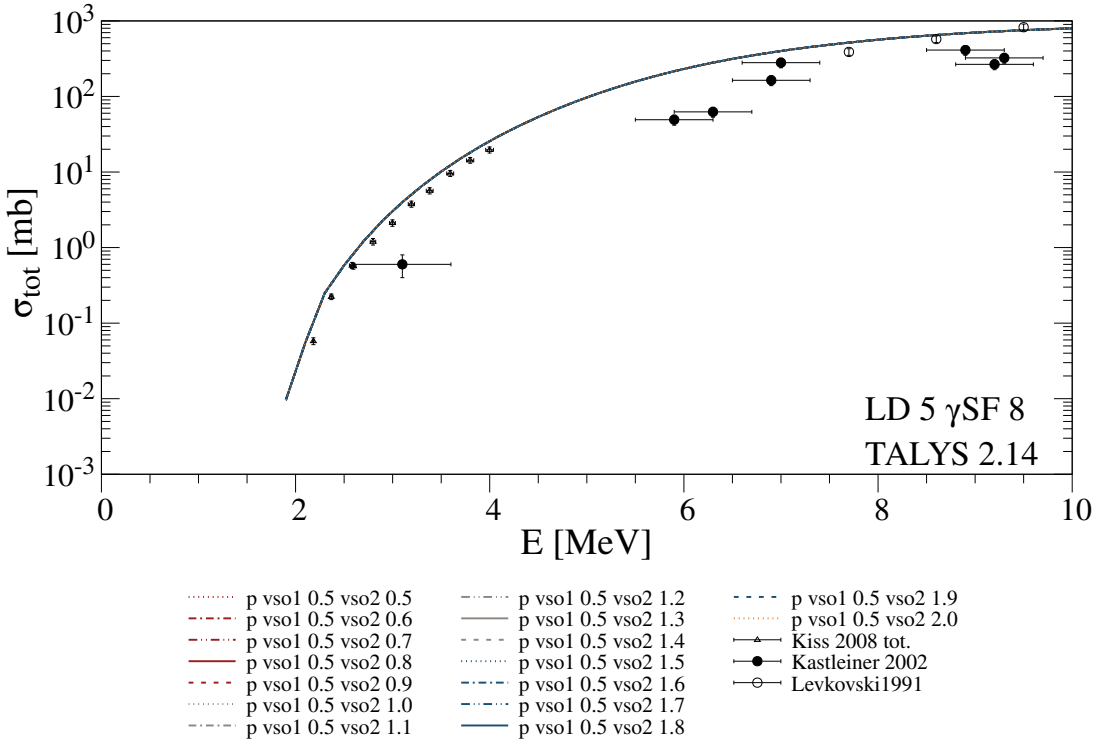

Figure A.43: Varying the parameters $vso1$ and $vso2$ utilizing the TALYS [124] code version 2.14 in comparison to experimental obtained (p, n)-reaction cross sections from References [140, 237, 238]. Shown exemplary is $vso1 = 0.5$ with varying $vso2$ between 0.5 and 2.0. The variation is no effecting the predicted cross sections.

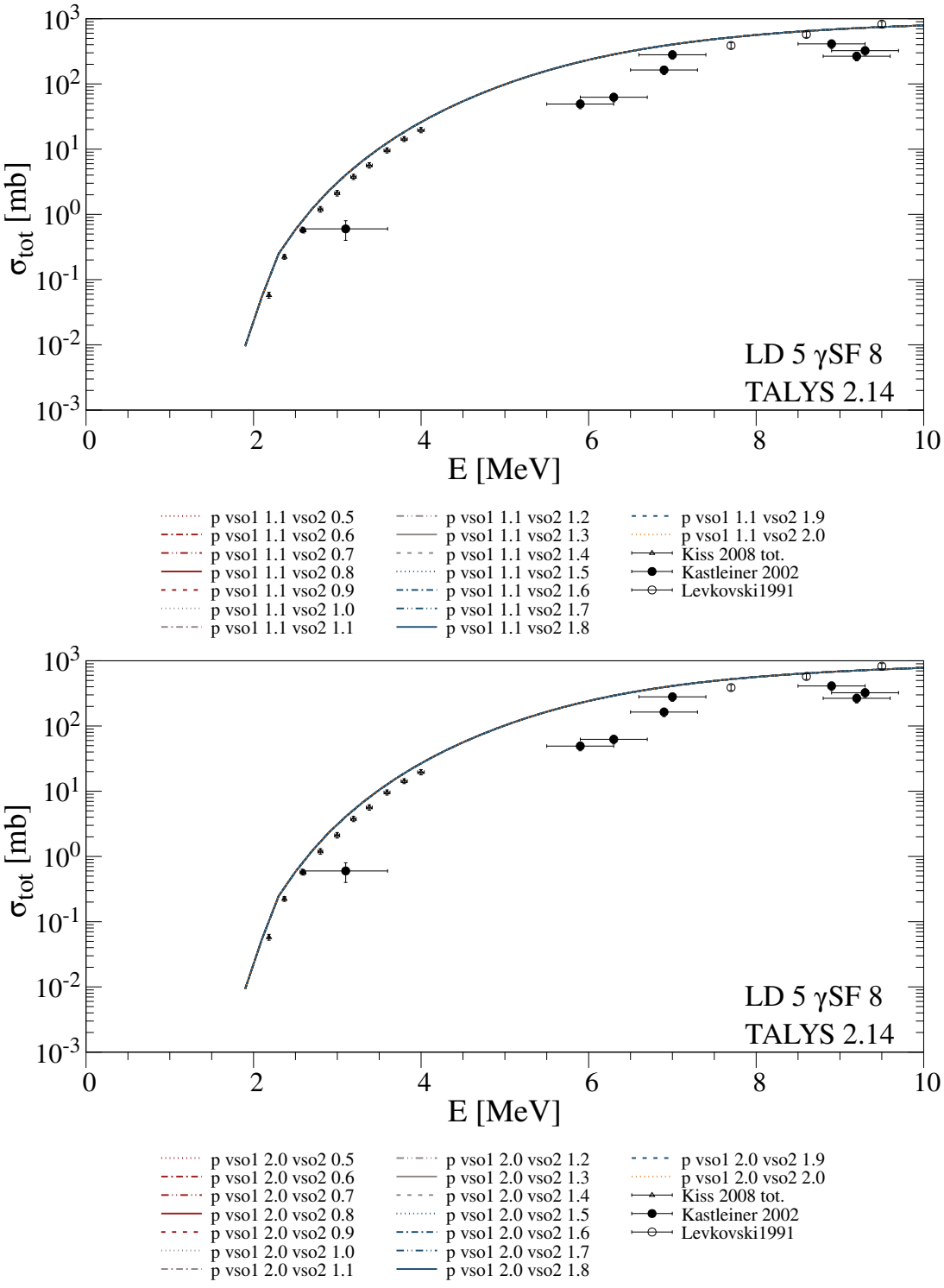

Figure A.44: Same as before with $vso1 = 1.1$ and $vso1 = 2.0$.

A.4.11 Varying *rvd* and *avd*

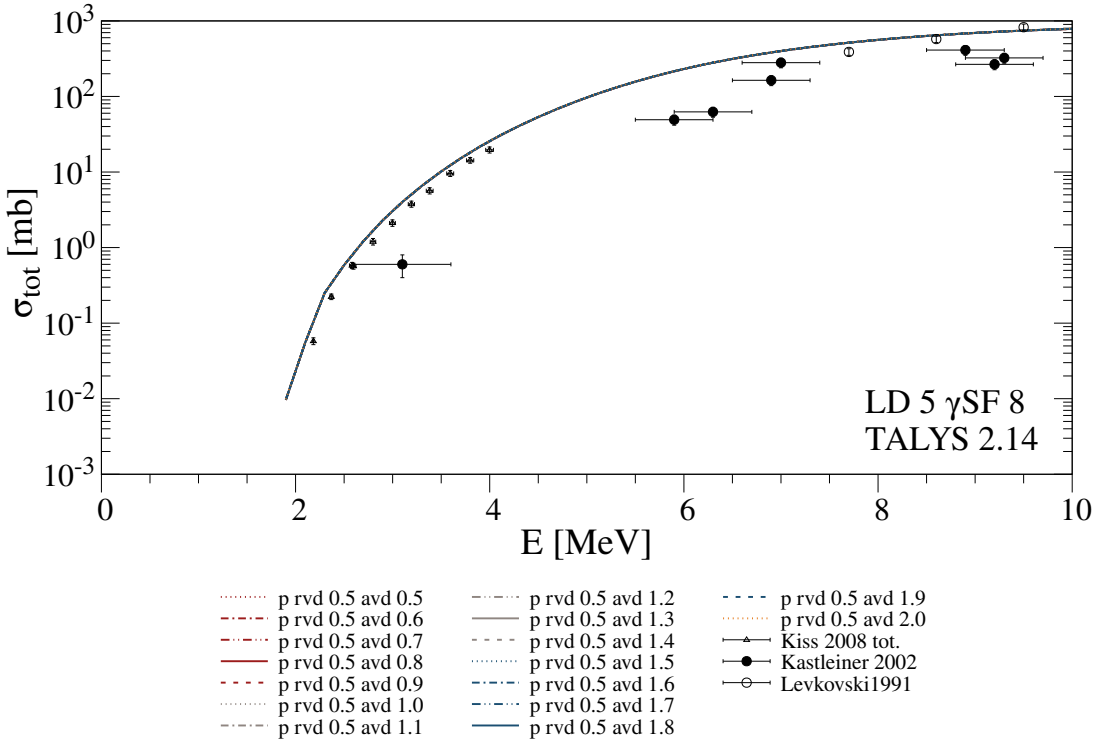

Figure A.45: Varying the parameters *rvd* and *avd* utilizing the TALYS [124] code version 2.14 in comparison to experimental obtained (p, n)-reaction cross sections from References [140, 237, 238]. Shown exemplary is $rvd = 0.5$ with varying *avd* between 0.5 and 2.0. The variation is no effecting the predicted cross sections.

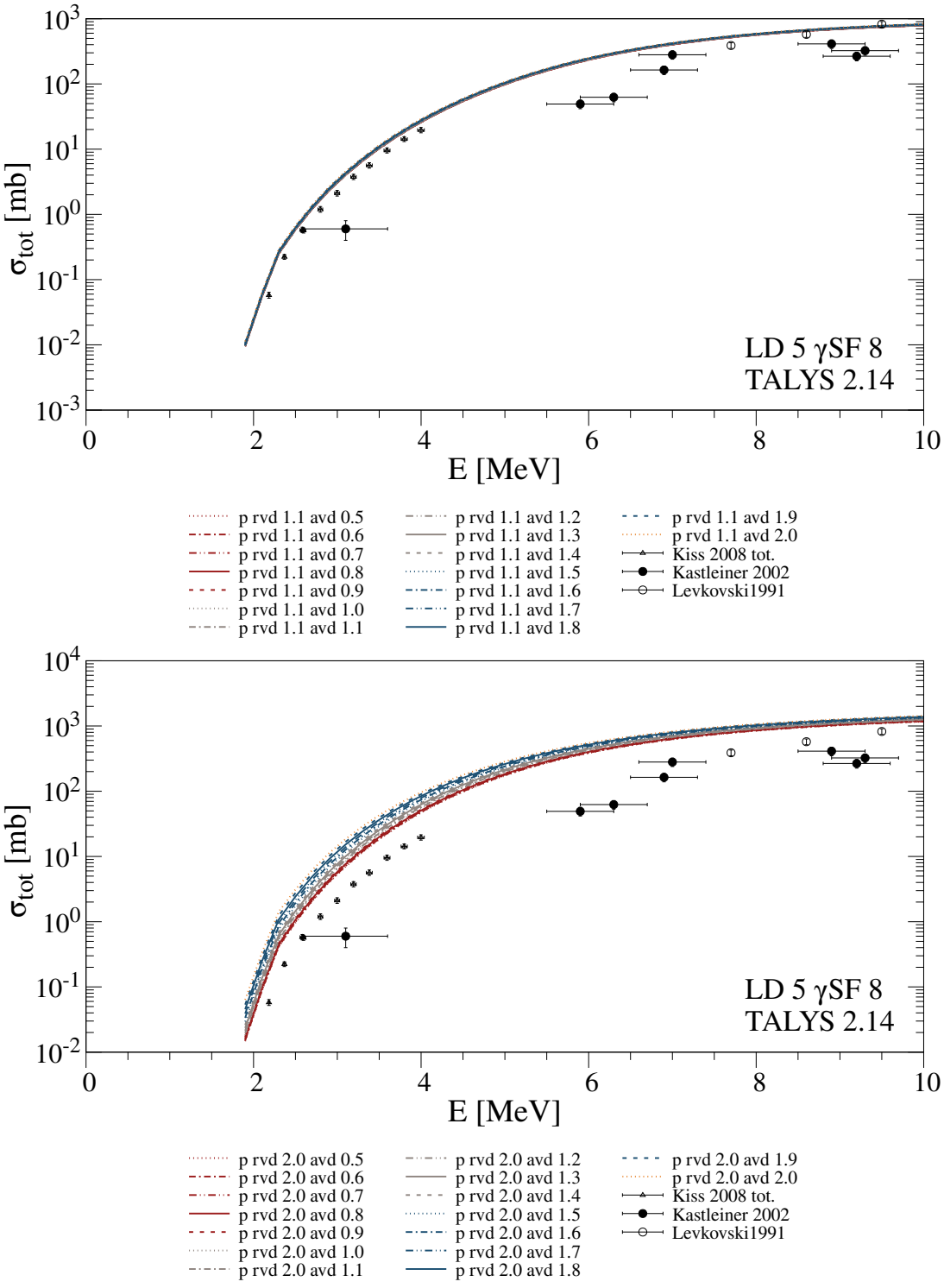

Figure A.46: Same as before with $rvd = 1.1$ and $rvd = 2.0$.

A.4.12 Varying *rv*, *av* and *v1*

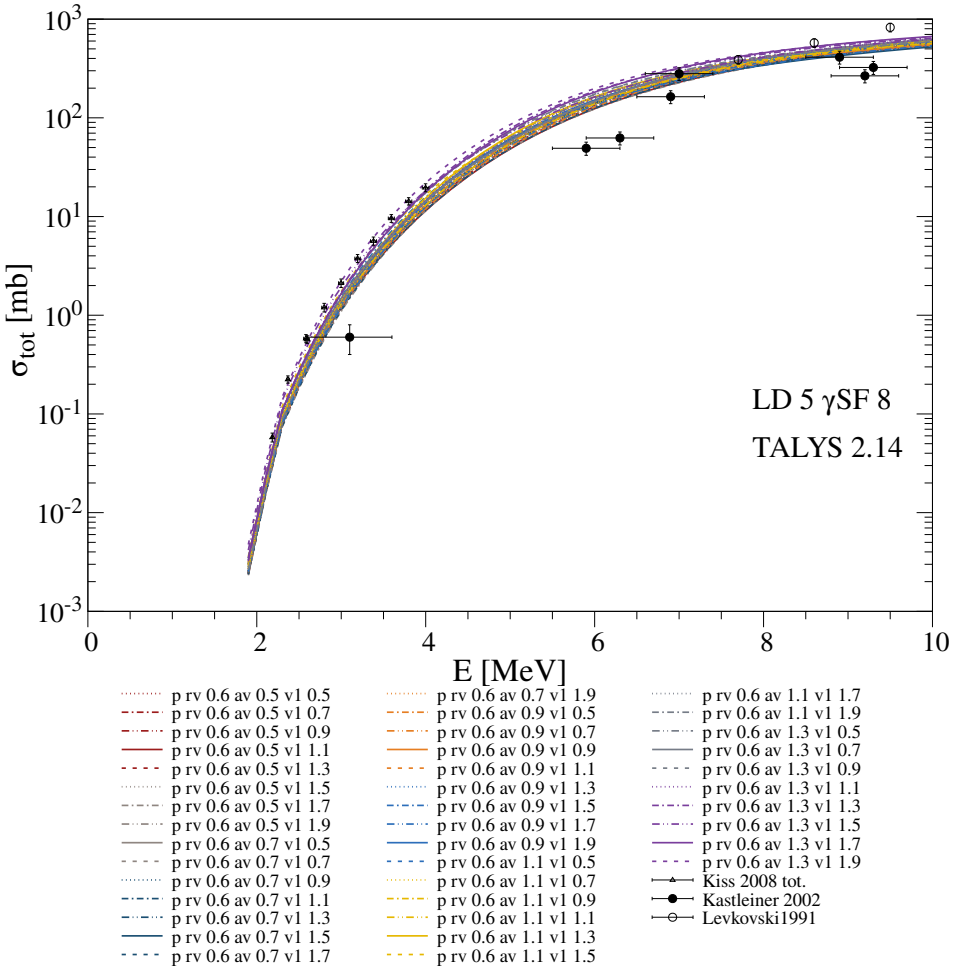

Figure A.47: Varying the parameters rv, av, and $v1$ utilizing the TALYS [124] code version 2.14 in comparison to experimental obtained (p, n)-reaction cross sections from References [140, 237, 238]. Shown are exemplary the variations of rv between 0.6 to 1.1, here $rv = 0.6$, with varying av and $v1$ between 0.5 and 2.0. It is shown, that this improves the description of the data for the lower energies.

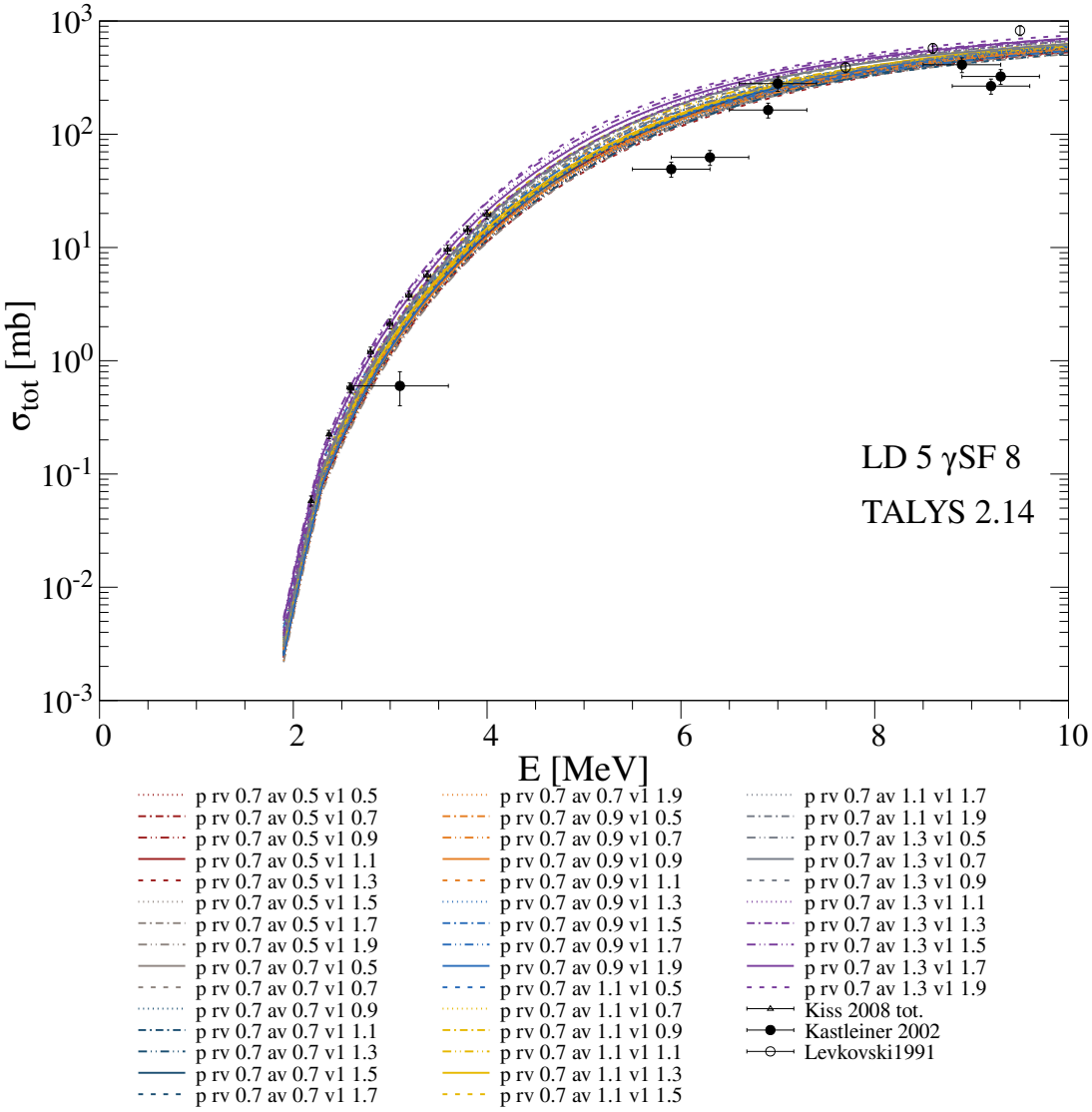

Figure A.48: Same as before with $rv = 0.7$.

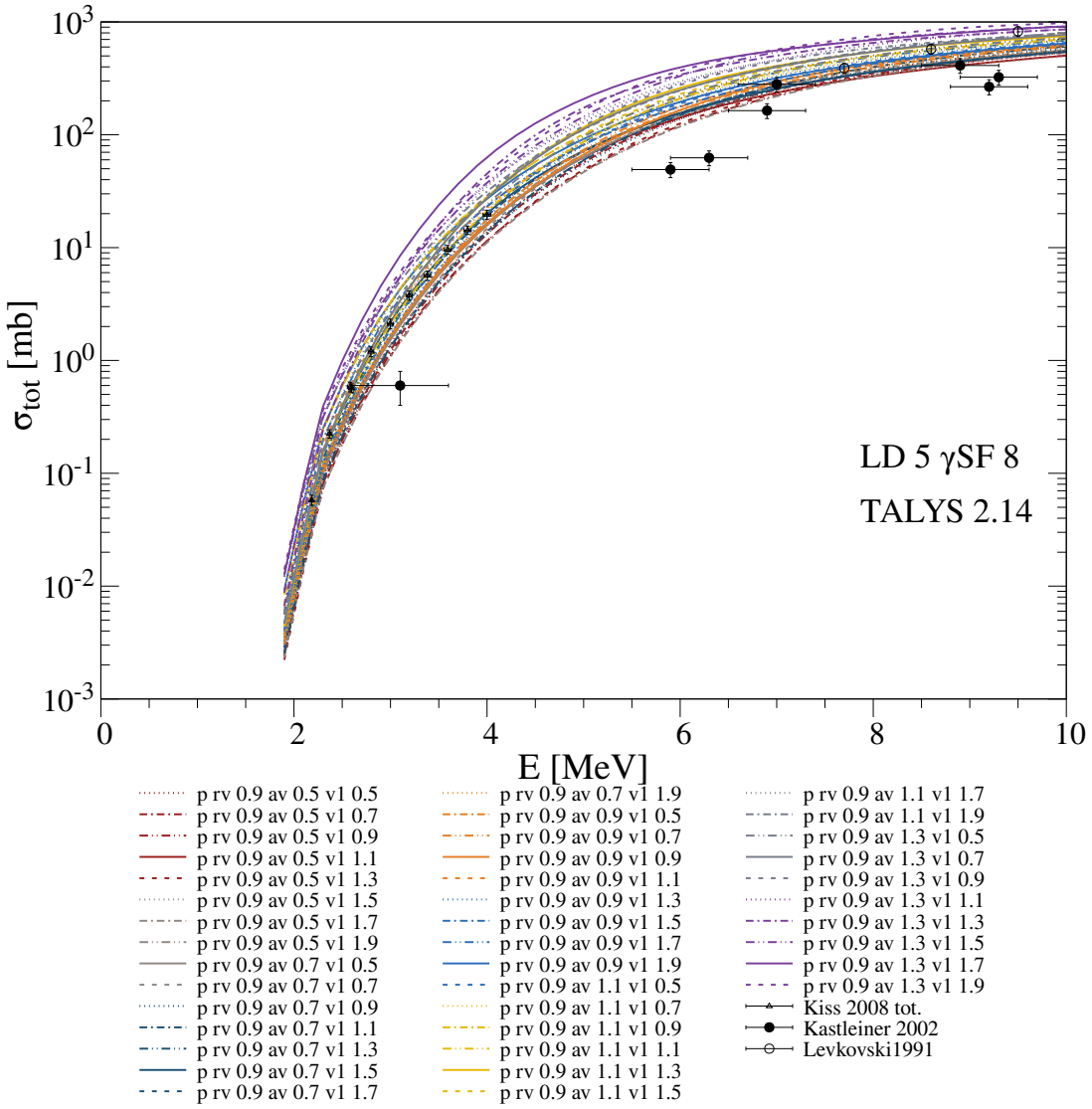

Figure A.49: Same as before with $rv = 0.9$.

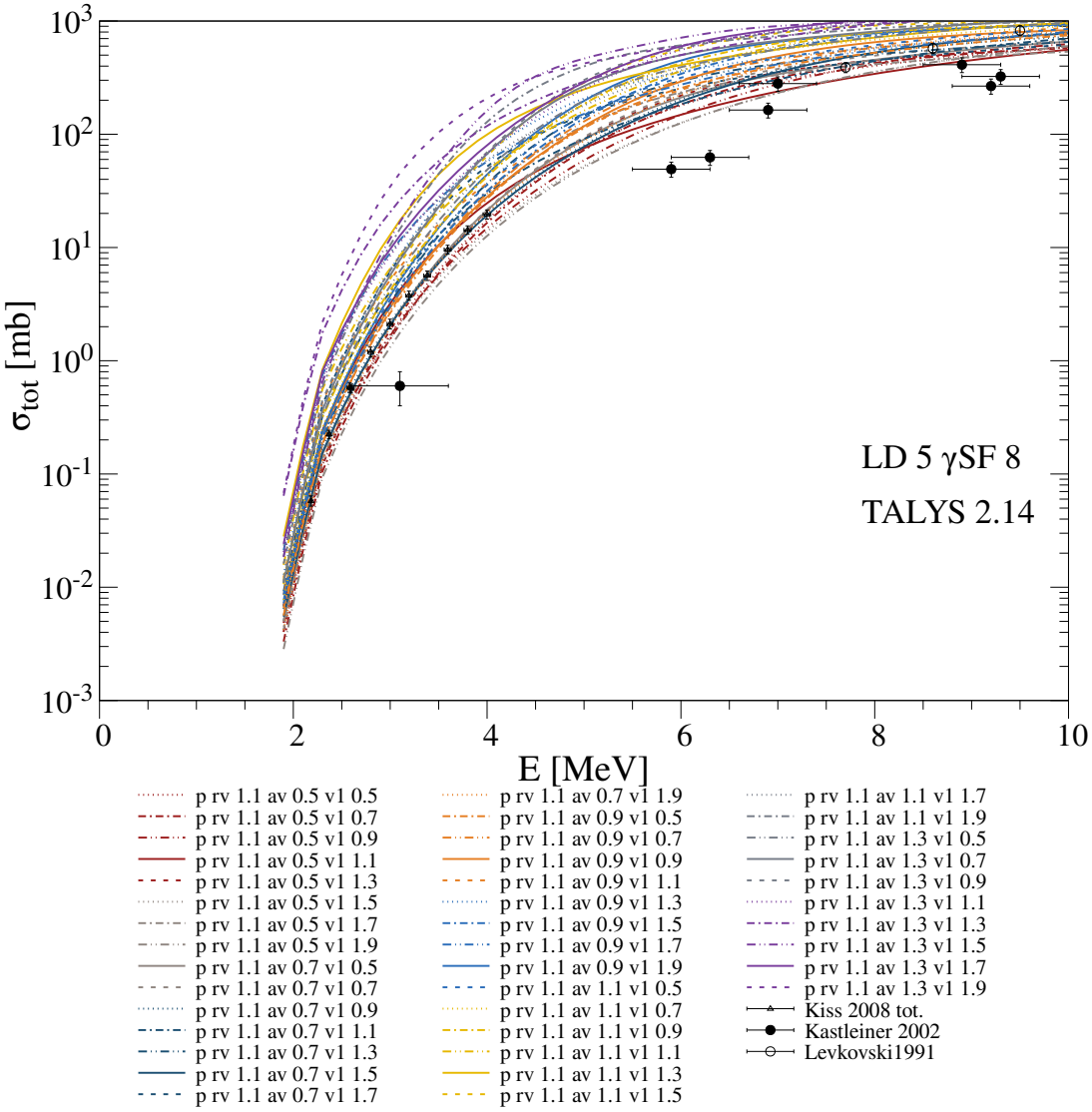

Figure A.50: Same as before with $rv = 1.1$.

A.4.13 Varying *rwd*, *awd*, *d1*, *d2* and *d3*

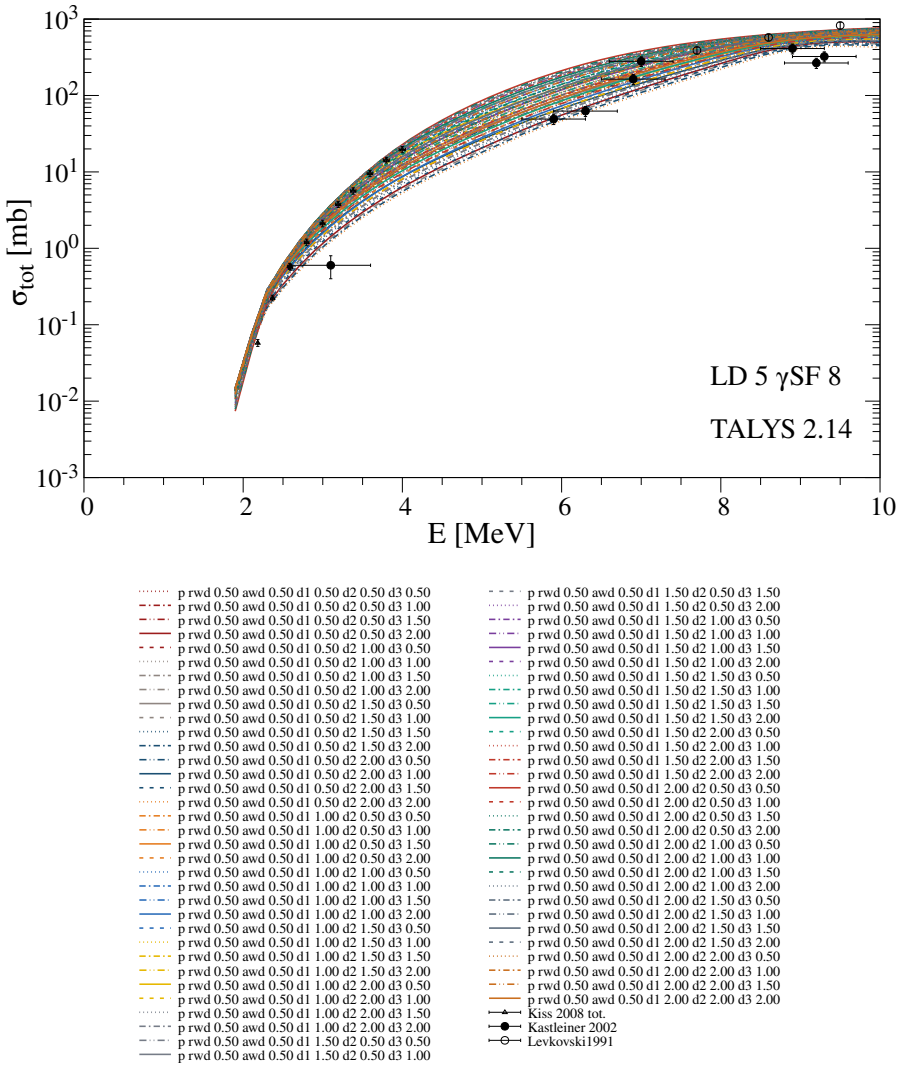

Figure A.51: Parameter combinations describing the (p, n) data obtained by varying eight parameters of the Koning–Delaroche optical model potential. Thee parameters are varied between 0.5 and 2.0. Shown are the variations with $rwd = awd = 0.5$

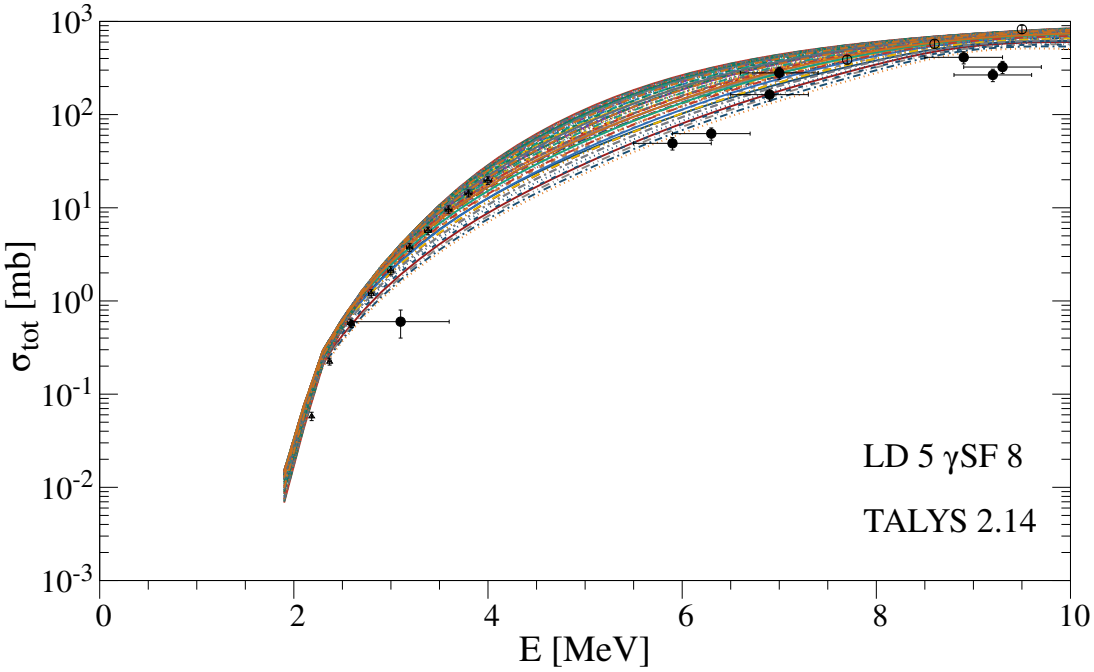

p rwd 0.50 awd 1.00 d1 0.50 d2 0.50 d3 0.50
p rwd 0.50 awd 1.00 d1 0.50 d2 0.50 d3 1.00
p rwd 0.50 awd 1.00 d1 0.50 d2 0.50 d3 1.50
p rwd 0.50 awd 1.00 d1 0.50 d2 0.50 d3 2.00
p rwd 0.50 awd 1.00 d1 0.50 d2 1.00 d3 0.50
p rwd 0.50 awd 1.00 d1 0.50 d2 1.00 d3 1.00
p rwd 0.50 awd 1.00 d1 0.50 d2 1.00 d3 1.50
p rwd 0.50 awd 1.00 d1 0.50 d2 1.00 d3 2.00
p rwd 0.50 awd 1.00 d1 0.50 d2 1.50 d3 0.50
p rwd 0.50 awd 1.00 d1 0.50 d2 1.50 d3 1.00
p rwd 0.50 awd 1.00 d1 0.50 d2 1.50 d3 1.50
p rwd 0.50 awd 1.00 d1 0.50 d2 1.50 d3 2.00
p rwd 0.50 awd 1.00 d1 0.50 d2 2.00 d3 0.50
p rwd 0.50 awd 1.00 d1 0.50 d2 2.00 d3 1.00
p rwd 0.50 awd 1.00 d1 0.50 d2 2.00 d3 1.50
p rwd 0.50 awd 1.00 d1 0.50 d2 2.00 d3 2.00
p rwd 0.50 awd 1.00 d1 1.00 d2 0.50 d3 0.50
p rwd 0.50 awd 1.00 d1 1.00 d2 0.50 d3 1.00
p rwd 0.50 awd 1.00 d1 1.00 d2 0.50 d3 1.50
p rwd 0.50 awd 1.00 d1 1.00 d2 0.50 d3 2.00
p rwd 0.50 awd 1.00 d1 1.00 d2 1.00 d3 0.50
p rwd 0.50 awd 1.00 d1 1.00 d2 1.00 d3 1.00
p rwd 0.50 awd 1.00 d1 1.00 d2 1.00 d3 1.50
p rwd 0.50 awd 1.00 d1 1.00 d2 1.00 d3 2.00
p rwd 0.50 awd 1.00 d1 1.00 d2 1.50 d3 0.50
p rwd 0.50 awd 1.00 d1 1.00 d2 1.50 d3 1.00
p rwd 0.50 awd 1.00 d1 1.00 d2 1.50 d3 1.50
p rwd 0.50 awd 1.00 d1 1.00 d2 1.50 d3 2.00
p rwd 0.50 awd 1.00 d1 1.00 d2 2.00 d3 0.50
p rwd 0.50 awd 1.00 d1 1.00 d2 2.00 d3 1.00
p rwd 0.50 awd 1.00 d1 1.00 d2 2.00 d3 1.50
p rwd 0.50 awd 1.00 d1 1.00 d2 2.00 d3 2.00
p rwd 0.50 awd 1.00 d1 1.50 d2 0.50 d3 0.50
p rwd 0.50 awd 1.00 d1 1.50 d2 0.50 d3 1.00
p rwd 0.50 awd 1.00 d1 1.50 d2 0.50 d3 1.50
p rwd 0.50 awd 1.00 d1 1.50 d2 0.50 d3 2.00
p rwd 0.50 awd 1.00 d1 1.50 d2 1.00 d3 0.50
p rwd 0.50 awd 1.00 d1 1.50 d2 1.00 d3 1.00
p rwd 0.50 awd 1.00 d1 1.50 d2 1.00 d3 1.50
p rwd 0.50 awd 1.00 d1 1.50 d2 1.00 d3 2.00
p rwd 0.50 awd 1.00 d1 1.50 d2 1.50 d3 0.50
p rwd 0.50 awd 1.00 d1 1.50 d2 1.50 d3 1.00
p rwd 0.50 awd 1.00 d1 1.50 d2 1.50 d3 1.50
p rwd 0.50 awd 1.00 d1 1.50 d2 1.50 d3 2.00
p rwd 0.50 awd 1.00 d1 1.50 d2 2.00 d3 0.50
p rwd 0.50 awd 1.00 d1 1.50 d2 2.00 d3 1.00
p rwd 0.50 awd 1.00 d1 1.50 d2 2.00 d3 1.50
p rwd 0.50 awd 1.00 d1 1.50 d2 2.00 d3 2.00
p rwd 0.50 awd 1.00 d1 2.00 d2 0.50 d3 0.50
p rwd 0.50 awd 1.00 d1 2.00 d2 0.50 d3 1.00
p rwd 0.50 awd 1.00 d1 2.00 d2 0.50 d3 1.50
p rwd 0.50 awd 1.00 d1 2.00 d2 0.50 d3 2.00
p rwd 0.50 awd 1.00 d1 2.00 d2 1.00 d3 0.50
p rwd 0.50 awd 1.00 d1 2.00 d2 1.00 d3 1.00
p rwd 0.50 awd 1.00 d1 2.00 d2 1.00 d3 1.50
p rwd 0.50 awd 1.00 d1 2.00 d2 1.00 d3 2.00
p rwd 0.50 awd 1.00 d1 2.00 d2 1.50 d3 0.50
p rwd 0.50 awd 1.00 d1 2.00 d2 1.50 d3 1.00
p rwd 0.50 awd 1.00 d1 2.00 d2 1.50 d3 1.50
p rwd 0.50 awd 1.00 d1 2.00 d2 1.50 d3 2.00
p rwd 0.50 awd 1.00 d1 2.00 d2 2.00 d3 0.50
p rwd 0.50 awd 1.00 d1 2.00 d2 2.00 d3 1.00
p rwd 0.50 awd 1.00 d1 2.00 d2 2.00 d3 1.50
p rwd 0.50 awd 1.00 d1 2.00 d2 2.00 d3 2.00
Kiss 2008 tot.
Kastleiner 2002
Levkovski1991

Figure A.52: Same as before with with $rwd = 0.5$ and $awd = 1.0$.

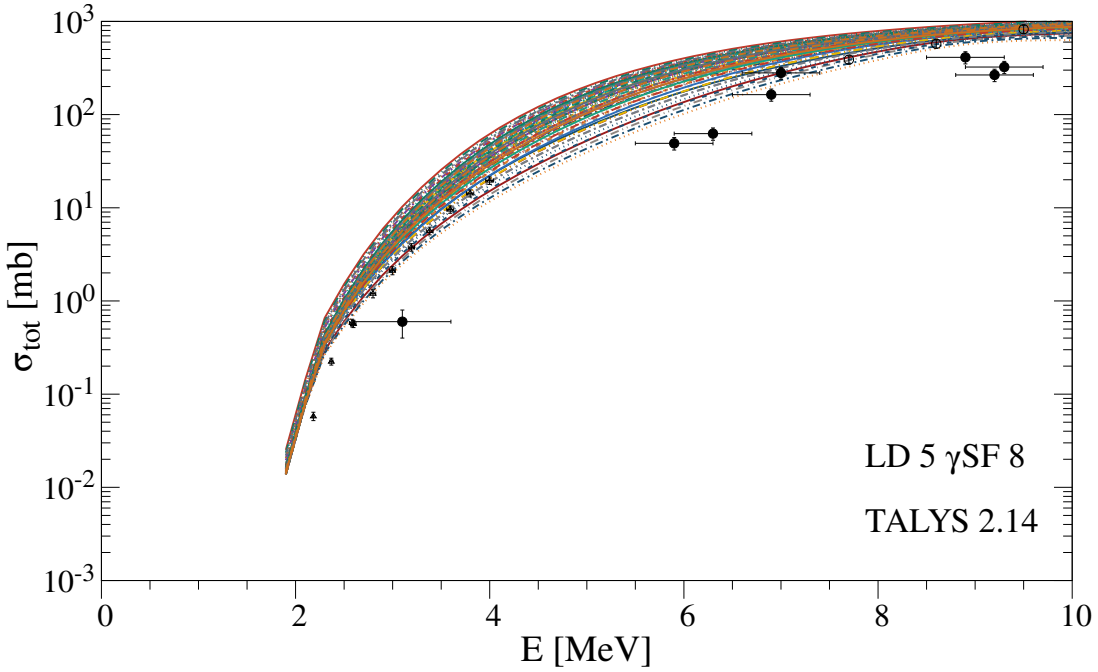

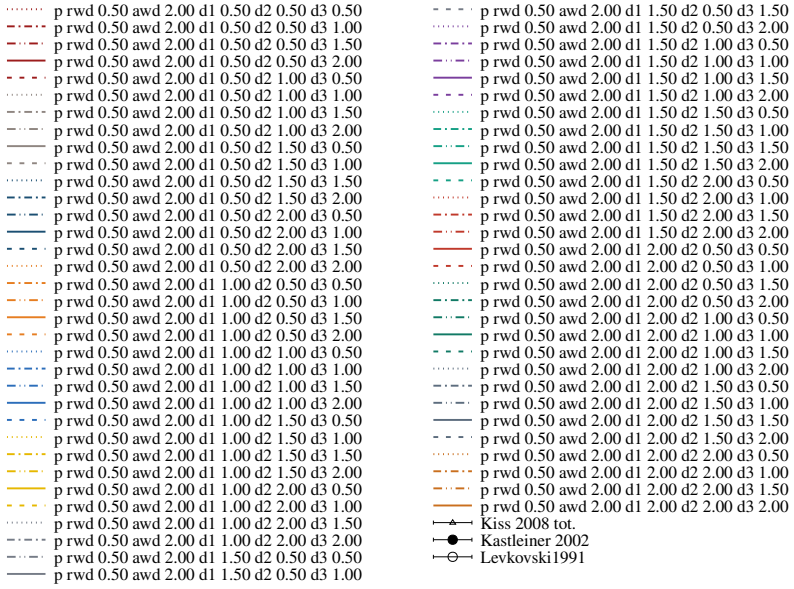

Figure A.53: Same as before with with $rwd = 0.5$ and $awd = 2.0$.

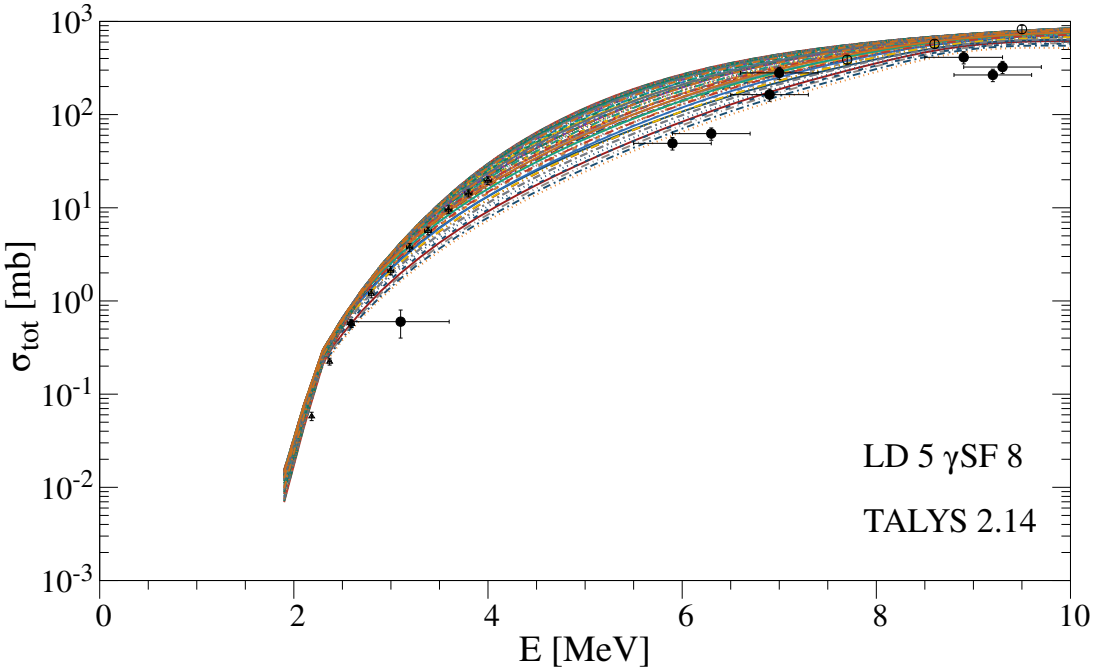

p rwd 0.75 awd 1.00 d1 0.50 d2 0.50 d3 0.50
p rwd 0.75 awd 1.00 d1 0.50 d2 0.50 d3 1.00
p rwd 0.75 awd 1.00 d1 0.50 d2 0.50 d3 1.50
p rwd 0.75 awd 1.00 d1 0.50 d2 0.50 d3 2.00
p rwd 0.75 awd 1.00 d1 0.50 d2 1.00 d3 0.50
p rwd 0.75 awd 1.00 d1 0.50 d2 1.00 d3 1.00
p rwd 0.75 awd 1.00 d1 0.50 d2 1.00 d3 1.50
p rwd 0.75 awd 1.00 d1 0.50 d2 1.00 d3 2.00
p rwd 0.75 awd 1.00 d1 0.50 d2 1.50 d3 0.50
p rwd 0.75 awd 1.00 d1 0.50 d2 1.50 d3 1.00
p rwd 0.75 awd 1.00 d1 0.50 d2 1.50 d3 1.50
p rwd 0.75 awd 1.00 d1 0.50 d2 1.50 d3 2.00
p rwd 0.75 awd 1.00 d1 0.50 d2 2.00 d3 0.50
p rwd 0.75 awd 1.00 d1 0.50 d2 2.00 d3 1.00
p rwd 0.75 awd 1.00 d1 0.50 d2 2.00 d3 1.50
p rwd 0.75 awd 1.00 d1 0.50 d2 2.00 d3 2.00
p rwd 0.75 awd 1.00 d1 1.00 d2 0.50 d3 0.50
p rwd 0.75 awd 1.00 d1 1.00 d2 0.50 d3 1.00
p rwd 0.75 awd 1.00 d1 1.00 d2 0.50 d3 1.50
p rwd 0.75 awd 1.00 d1 1.00 d2 0.50 d3 2.00
p rwd 0.75 awd 1.00 d1 1.00 d2 1.00 d3 0.50
p rwd 0.75 awd 1.00 d1 1.00 d2 1.00 d3 1.00
p rwd 0.75 awd 1.00 d1 1.00 d2 1.00 d3 1.50
p rwd 0.75 awd 1.00 d1 1.00 d2 1.00 d3 2.00
p rwd 0.75 awd 1.00 d1 1.00 d2 1.50 d3 0.50
p rwd 0.75 awd 1.00 d1 1.00 d2 1.50 d3 1.00
p rwd 0.75 awd 1.00 d1 1.00 d2 1.50 d3 1.50
p rwd 0.75 awd 1.00 d1 1.00 d2 1.50 d3 2.00
p rwd 0.75 awd 1.00 d1 1.00 d2 2.00 d3 0.50
p rwd 0.75 awd 1.00 d1 1.00 d2 2.00 d3 1.00
p rwd 0.75 awd 1.00 d1 1.00 d2 2.00 d3 1.50
p rwd 0.75 awd 1.00 d1 1.00 d2 2.00 d3 2.00
p rwd 0.75 awd 1.00 d1 1.50 d2 0.50 d3 0.50
p rwd 0.75 awd 1.00 d1 1.50 d2 0.50 d3 1.00
p rwd 0.75 awd 1.00 d1 1.50 d2 0.50 d3 1.50
p rwd 0.75 awd 1.00 d1 1.50 d2 0.50 d3 2.00
p rwd 0.75 awd 1.00 d1 1.50 d2 1.00 d3 0.50
p rwd 0.75 awd 1.00 d1 1.50 d2 1.00 d3 1.00
p rwd 0.75 awd 1.00 d1 1.50 d2 1.00 d3 1.50
p rwd 0.75 awd 1.00 d1 1.50 d2 1.00 d3 2.00
p rwd 0.75 awd 1.00 d1 1.50 d2 1.50 d3 0.50
p rwd 0.75 awd 1.00 d1 1.50 d2 1.50 d3 1.00
p rwd 0.75 awd 1.00 d1 1.50 d2 1.50 d3 1.50
p rwd 0.75 awd 1.00 d1 1.50 d2 1.50 d3 2.00
p rwd 0.75 awd 1.00 d1 1.50 d2 2.00 d3 0.50
p rwd 0.75 awd 1.00 d1 1.50 d2 2.00 d3 1.00
p rwd 0.75 awd 1.00 d1 1.50 d2 2.00 d3 1.50
p rwd 0.75 awd 1.00 d1 1.50 d2 2.00 d3 2.00
p rwd 0.75 awd 1.00 d1 2.00 d2 0.50 d3 0.50
p rwd 0.75 awd 1.00 d1 2.00 d2 0.50 d3 1.00
p rwd 0.75 awd 1.00 d1 2.00 d2 0.50 d3 1.50
p rwd 0.75 awd 1.00 d1 2.00 d2 0.50 d3 2.00
p rwd 0.75 awd 1.00 d1 2.00 d2 1.00 d3 0.50
p rwd 0.75 awd 1.00 d1 2.00 d2 1.00 d3 1.00
p rwd 0.75 awd 1.00 d1 2.00 d2 1.00 d3 1.50
p rwd 0.75 awd 1.00 d1 2.00 d2 1.00 d3 2.00
p rwd 0.75 awd 1.00 d1 2.00 d2 1.50 d3 0.50
p rwd 0.75 awd 1.00 d1 2.00 d2 1.50 d3 1.00
p rwd 0.75 awd 1.00 d1 2.00 d2 1.50 d3 1.50
p rwd 0.75 awd 1.00 d1 2.00 d2 1.50 d3 2.00
p rwd 0.75 awd 1.00 d1 2.00 d2 2.00 d3 0.50
p rwd 0.75 awd 1.00 d1 2.00 d2 2.00 d3 1.00
p rwd 0.75 awd 1.00 d1 2.00 d2 2.00 d3 1.50
p rwd 0.75 awd 1.00 d1 2.00 d2 2.00 d3 2.00
Kiss 2008 tot.
Kastleiner 2002
Levkovski1991

Figure A.54: Same as before with with $rwd = 0.75$ and $awd = 1.0$.

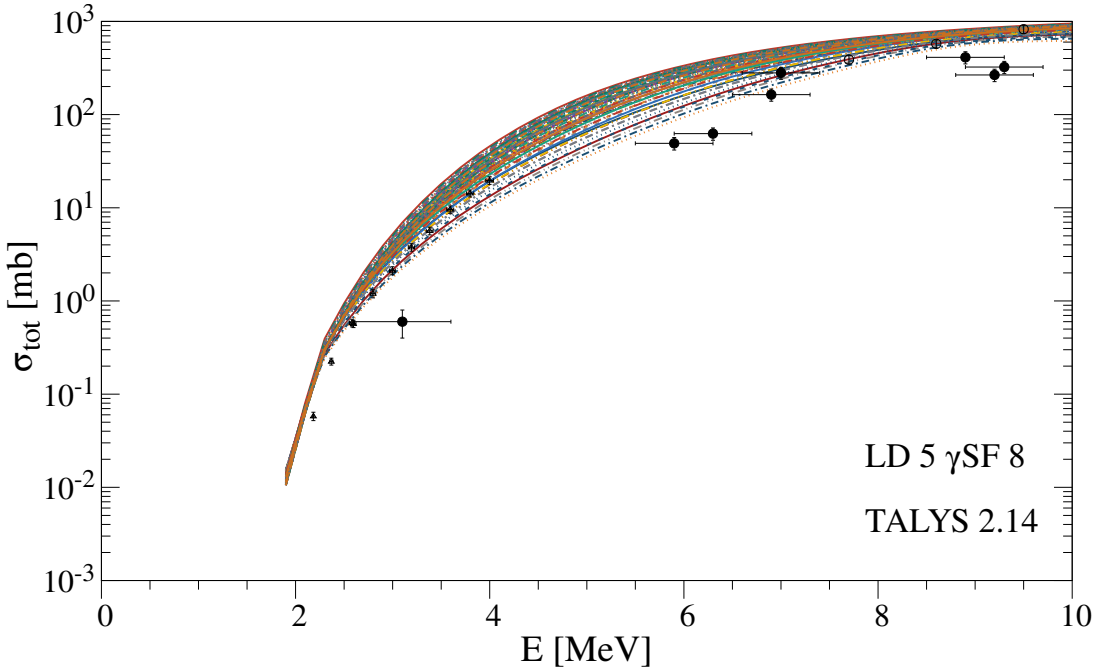

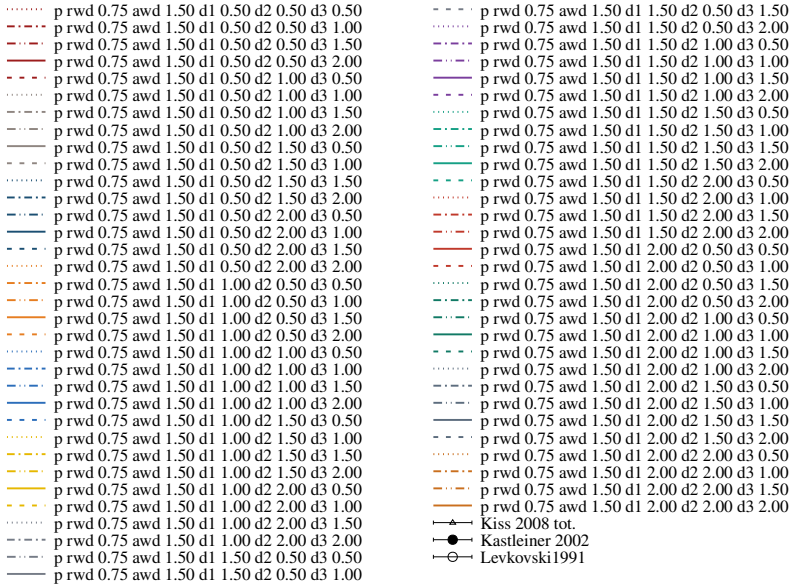

Figure A.55: Same as before with with $rwd = 0.75$ and $awd = 1.5$.

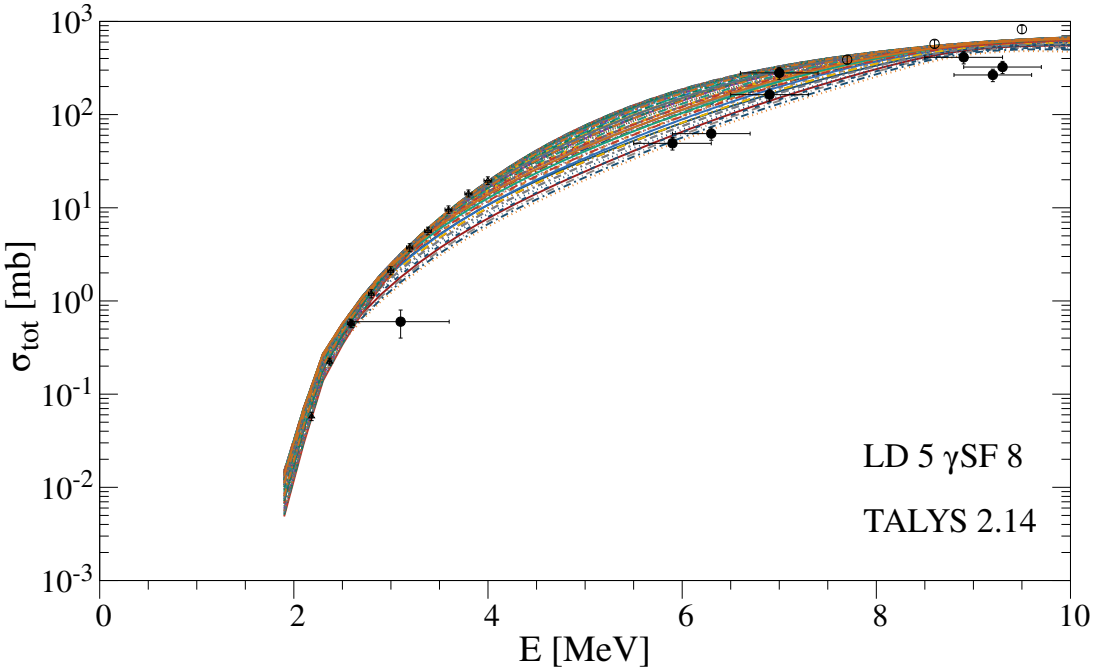

p rwd 1.00 awd 0.50 d1 0.50 d2 0.50 d3 0.50
p rwd 1.00 awd 0.50 d1 0.50 d2 0.50 d3 1.00
p rwd 1.00 awd 0.50 d1 0.50 d2 0.50 d3 1.50
p rwd 1.00 awd 0.50 d1 0.50 d2 0.50 d3 2.00
p rwd 1.00 awd 0.50 d1 0.50 d2 1.00 d3 0.50
p rwd 1.00 awd 0.50 d1 0.50 d2 1.00 d3 1.00
p rwd 1.00 awd 0.50 d1 0.50 d2 1.00 d3 1.50
p rwd 1.00 awd 0.50 d1 0.50 d2 1.00 d3 2.00
p rwd 1.00 awd 0.50 d1 0.50 d2 1.50 d3 0.50
p rwd 1.00 awd 0.50 d1 0.50 d2 1.50 d3 1.00
p rwd 1.00 awd 0.50 d1 0.50 d2 1.50 d3 1.50
p rwd 1.00 awd 0.50 d1 0.50 d2 1.50 d3 2.00
p rwd 1.00 awd 0.50 d1 0.50 d2 2.00 d3 0.50
p rwd 1.00 awd 0.50 d1 0.50 d2 2.00 d3 1.00
p rwd 1.00 awd 0.50 d1 0.50 d2 2.00 d3 1.50
p rwd 1.00 awd 0.50 d1 0.50 d2 2.00 d3 2.00
p rwd 1.00 awd 0.50 d1 1.00 d2 0.50 d3 0.50
p rwd 1.00 awd 0.50 d1 1.00 d2 0.50 d3 1.00
p rwd 1.00 awd 0.50 d1 1.00 d2 0.50 d3 1.50
p rwd 1.00 awd 0.50 d1 1.00 d2 0.50 d3 2.00
p rwd 1.00 awd 0.50 d1 1.00 d2 1.00 d3 0.50
p rwd 1.00 awd 0.50 d1 1.00 d2 1.00 d3 1.00
p rwd 1.00 awd 0.50 d1 1.00 d2 1.00 d3 1.50
p rwd 1.00 awd 0.50 d1 1.00 d2 1.00 d3 2.00
p rwd 1.00 awd 0.50 d1 1.00 d2 1.50 d3 0.50
p rwd 1.00 awd 0.50 d1 1.00 d2 1.50 d3 1.00
p rwd 1.00 awd 0.50 d1 1.00 d2 1.50 d3 1.50
p rwd 1.00 awd 0.50 d1 1.00 d2 1.50 d3 2.00
p rwd 1.00 awd 0.50 d1 1.00 d2 2.00 d3 0.50
p rwd 1.00 awd 0.50 d1 1.00 d2 2.00 d3 1.00
p rwd 1.00 awd 0.50 d1 1.00 d2 2.00 d3 1.50
p rwd 1.00 awd 0.50 d1 1.00 d2 2.00 d3 2.00
p rwd 1.00 awd 0.50 d1 1.50 d2 0.50 d3 0.50
p rwd 1.00 awd 0.50 d1 1.50 d2 0.50 d3 1.00
p rwd 1.00 awd 0.50 d1 1.50 d2 0.50 d3 1.50
p rwd 1.00 awd 0.50 d1 1.50 d2 0.50 d3 2.00
p rwd 1.00 awd 0.50 d1 1.50 d2 1.00 d3 0.50
p rwd 1.00 awd 0.50 d1 1.50 d2 1.00 d3 1.00
p rwd 1.00 awd 0.50 d1 1.50 d2 1.00 d3 1.50
p rwd 1.00 awd 0.50 d1 1.50 d2 1.00 d3 2.00
p rwd 1.00 awd 0.50 d1 1.50 d2 1.50 d3 0.50
p rwd 1.00 awd 0.50 d1 1.50 d2 1.50 d3 1.00
p rwd 1.00 awd 0.50 d1 1.50 d2 1.50 d3 1.50
p rwd 1.00 awd 0.50 d1 1.50 d2 1.50 d3 2.00
p rwd 1.00 awd 0.50 d1 1.50 d2 2.00 d3 0.50
p rwd 1.00 awd 0.50 d1 1.50 d2 2.00 d3 1.00
p rwd 1.00 awd 0.50 d1 1.50 d2 2.00 d3 1.50
p rwd 1.00 awd 0.50 d1 1.50 d2 2.00 d3 2.00
p rwd 1.00 awd 0.50 d1 2.00 d2 0.50 d3 0.50
p rwd 1.00 awd 0.50 d1 2.00 d2 0.50 d3 1.00
p rwd 1.00 awd 0.50 d1 2.00 d2 0.50 d3 1.50
p rwd 1.00 awd 0.50 d1 2.00 d2 0.50 d3 2.00
p rwd 1.00 awd 0.50 d1 2.00 d2 1.00 d3 0.50
p rwd 1.00 awd 0.50 d1 2.00 d2 1.00 d3 1.00
p rwd 1.00 awd 0.50 d1 2.00 d2 1.00 d3 1.50
p rwd 1.00 awd 0.50 d1 2.00 d2 1.00 d3 2.00
p rwd 1.00 awd 0.50 d1 2.00 d2 1.50 d3 0.50
p rwd 1.00 awd 0.50 d1 2.00 d2 1.50 d3 1.00
p rwd 1.00 awd 0.50 d1 2.00 d2 1.50 d3 1.50
p rwd 1.00 awd 0.50 d1 2.00 d2 1.50 d3 2.00
p rwd 1.00 awd 0.50 d1 2.00 d2 2.00 d3 0.50
p rwd 1.00 awd 0.50 d1 2.00 d2 2.00 d3 1.00
p rwd 1.00 awd 0.50 d1 2.00 d2 2.00 d3 1.50
p rwd 1.00 awd 0.50 d1 2.00 d2 2.00 d3 2.00
Kiss 2008 tot.
Kastleiner 2002
Levkovski1991

Figure A.56: Same as before with with $rwd = 1.00$ and $awd = 0.50$.

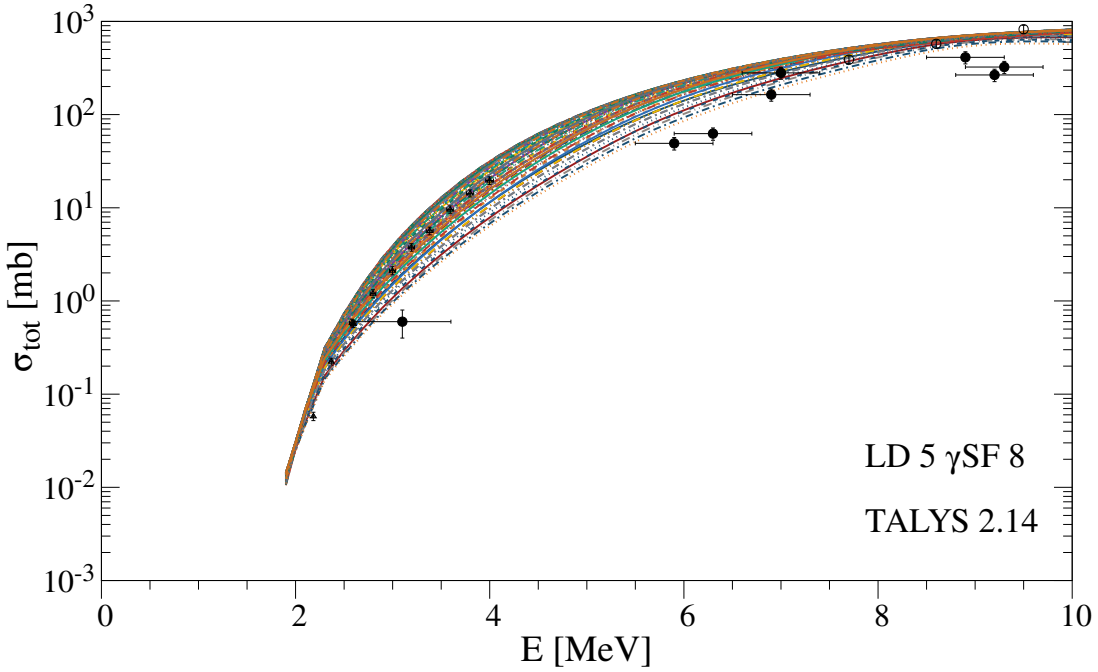

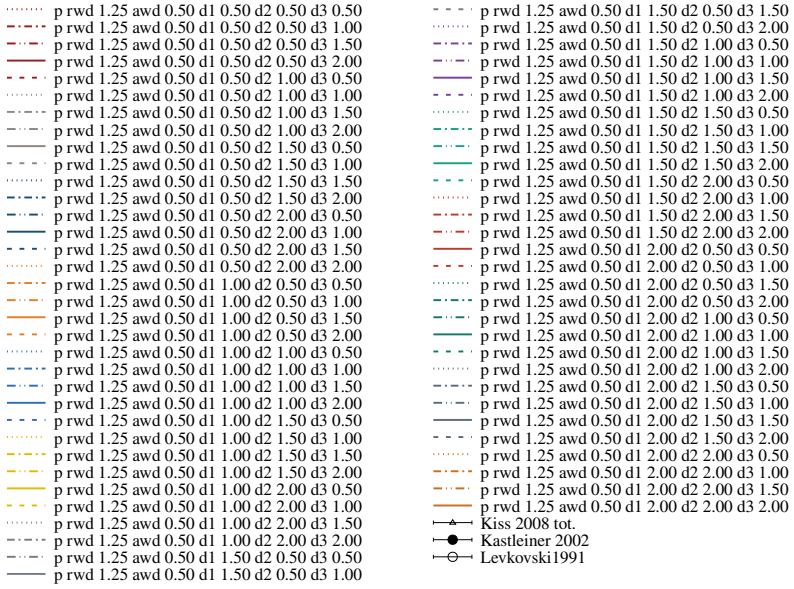

Figure A.57: Same as before with with $rwd = 1.25$ and $awd = 0.50$.

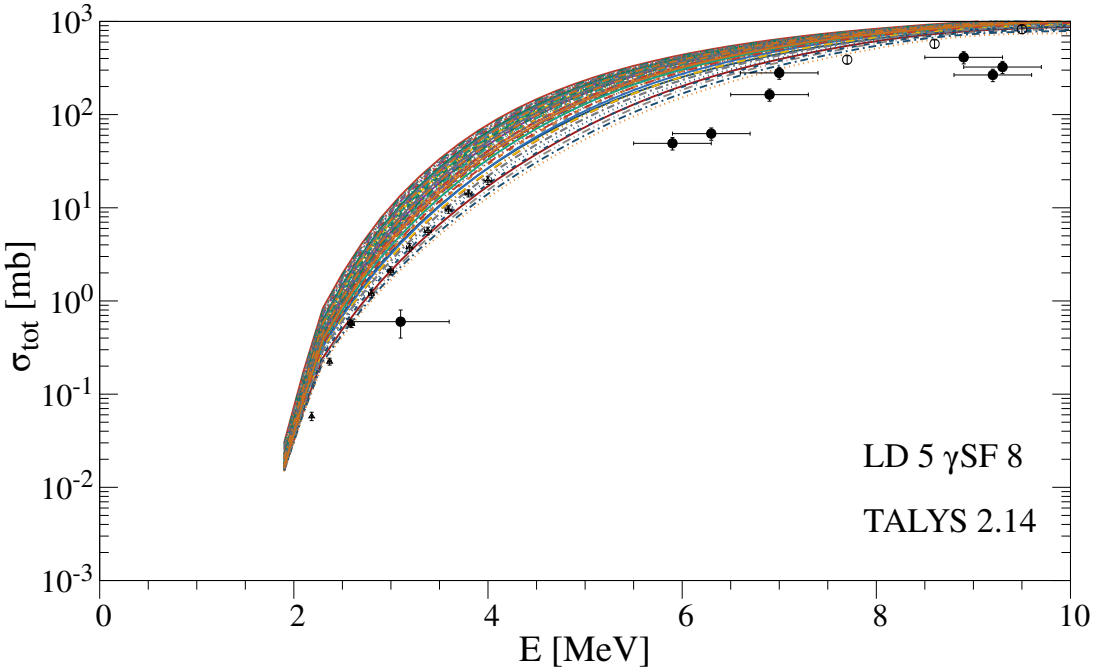

p rwd 1.25 awd 1.00 d1 0.50 d2 0.50 d3 0.50
p rwd 1.25 awd 1.00 d1 0.50 d2 0.50 d3 1.00
p rwd 1.25 awd 1.00 d1 0.50 d2 0.50 d3 1.50
p rwd 1.25 awd 1.00 d1 0.50 d2 0.50 d3 2.00
p rwd 1.25 awd 1.00 d1 0.50 d2 1.00 d3 0.50
p rwd 1.25 awd 1.00 d1 0.50 d2 1.00 d3 1.00
p rwd 1.25 awd 1.00 d1 0.50 d2 1.00 d3 1.50
p rwd 1.25 awd 1.00 d1 0.50 d2 1.00 d3 2.00
p rwd 1.25 awd 1.00 d1 0.50 d2 1.50 d3 0.50
p rwd 1.25 awd 1.00 d1 0.50 d2 1.50 d3 1.00
p rwd 1.25 awd 1.00 d1 0.50 d2 1.50 d3 1.50
p rwd 1.25 awd 1.00 d1 0.50 d2 1.50 d3 2.00
p rwd 1.25 awd 1.00 d1 0.50 d2 2.00 d3 0.50
p rwd 1.25 awd 1.00 d1 0.50 d2 2.00 d3 1.00
p rwd 1.25 awd 1.00 d1 0.50 d2 2.00 d3 1.50
p rwd 1.25 awd 1.00 d1 0.50 d2 2.00 d3 2.00
p rwd 1.25 awd 1.00 d1 1.00 d2 0.50 d3 0.50
p rwd 1.25 awd 1.00 d1 1.00 d2 0.50 d3 1.00
p rwd 1.25 awd 1.00 d1 1.00 d2 0.50 d3 1.50
p rwd 1.25 awd 1.00 d1 1.00 d2 0.50 d3 2.00
p rwd 1.25 awd 1.00 d1 1.00 d2 1.00 d3 0.50
p rwd 1.25 awd 1.00 d1 1.00 d2 1.00 d3 1.00
p rwd 1.25 awd 1.00 d1 1.00 d2 1.00 d3 1.50
p rwd 1.25 awd 1.00 d1 1.00 d2 1.00 d3 2.00
p rwd 1.25 awd 1.00 d1 1.00 d2 1.50 d3 0.50
p rwd 1.25 awd 1.00 d1 1.00 d2 1.50 d3 1.00
p rwd 1.25 awd 1.00 d1 1.00 d2 1.50 d3 1.50
p rwd 1.25 awd 1.00 d1 1.00 d2 1.50 d3 2.00
p rwd 1.25 awd 1.00 d1 1.00 d2 2.00 d3 0.50
p rwd 1.25 awd 1.00 d1 1.00 d2 2.00 d3 1.00
p rwd 1.25 awd 1.00 d1 1.00 d2 2.00 d3 1.50
p rwd 1.25 awd 1.00 d1 1.00 d2 2.00 d3 2.00
p rwd 1.25 awd 1.00 d1 1.50 d2 0.50 d3 0.50
p rwd 1.25 awd 1.00 d1 1.50 d2 0.50 d3 1.00
p rwd 1.25 awd 1.00 d1 1.50 d2 0.50 d3 1.50
p rwd 1.25 awd 1.00 d1 1.50 d2 0.50 d3 2.00
p rwd 1.25 awd 1.00 d1 1.50 d2 1.00 d3 0.50
p rwd 1.25 awd 1.00 d1 1.50 d2 1.00 d3 1.00
p rwd 1.25 awd 1.00 d1 1.50 d2 1.00 d3 1.50
p rwd 1.25 awd 1.00 d1 1.50 d2 1.00 d3 2.00
p rwd 1.25 awd 1.00 d1 1.50 d2 1.50 d3 0.50
p rwd 1.25 awd 1.00 d1 1.50 d2 1.50 d3 1.00
p rwd 1.25 awd 1.00 d1 1.50 d2 1.50 d3 1.50
p rwd 1.25 awd 1.00 d1 1.50 d2 1.50 d3 2.00
p rwd 1.25 awd 1.00 d1 1.50 d2 2.00 d3 0.50
p rwd 1.25 awd 1.00 d1 1.50 d2 2.00 d3 1.00
p rwd 1.25 awd 1.00 d1 1.50 d2 2.00 d3 1.50
p rwd 1.25 awd 1.00 d1 1.50 d2 2.00 d3 2.00
p rwd 1.25 awd 1.00 d1 2.00 d2 0.50 d3 0.50
p rwd 1.25 awd 1.00 d1 2.00 d2 0.50 d3 1.00
p rwd 1.25 awd 1.00 d1 2.00 d2 0.50 d3 1.50
p rwd 1.25 awd 1.00 d1 2.00 d2 0.50 d3 2.00
p rwd 1.25 awd 1.00 d1 2.00 d2 1.00 d3 0.50
p rwd 1.25 awd 1.00 d1 2.00 d2 1.00 d3 1.00
p rwd 1.25 awd 1.00 d1 2.00 d2 1.00 d3 1.50
p rwd 1.25 awd 1.00 d1 2.00 d2 1.00 d3 2.00
p rwd 1.25 awd 1.00 d1 2.00 d2 1.50 d3 0.50
p rwd 1.25 awd 1.00 d1 2.00 d2 1.50 d3 1.00
p rwd 1.25 awd 1.00 d1 2.00 d2 1.50 d3 1.50
p rwd 1.25 awd 1.00 d1 2.00 d2 1.50 d3 2.00
p rwd 1.25 awd 1.00 d1 2.00 d2 2.00 d3 0.50
p rwd 1.25 awd 1.00 d1 2.00 d2 2.00 d3 1.00
p rwd 1.25 awd 1.00 d1 2.00 d2 2.00 d3 1.50
p rwd 1.25 awd 1.00 d1 2.00 d2 2.00 d3 2.00
Kiss 2008 tot.
Kastleiner 2002
Levkovski1991

Figure A.58: Same as before with with $rwd = 1.25$ and $awd = 1.00$.

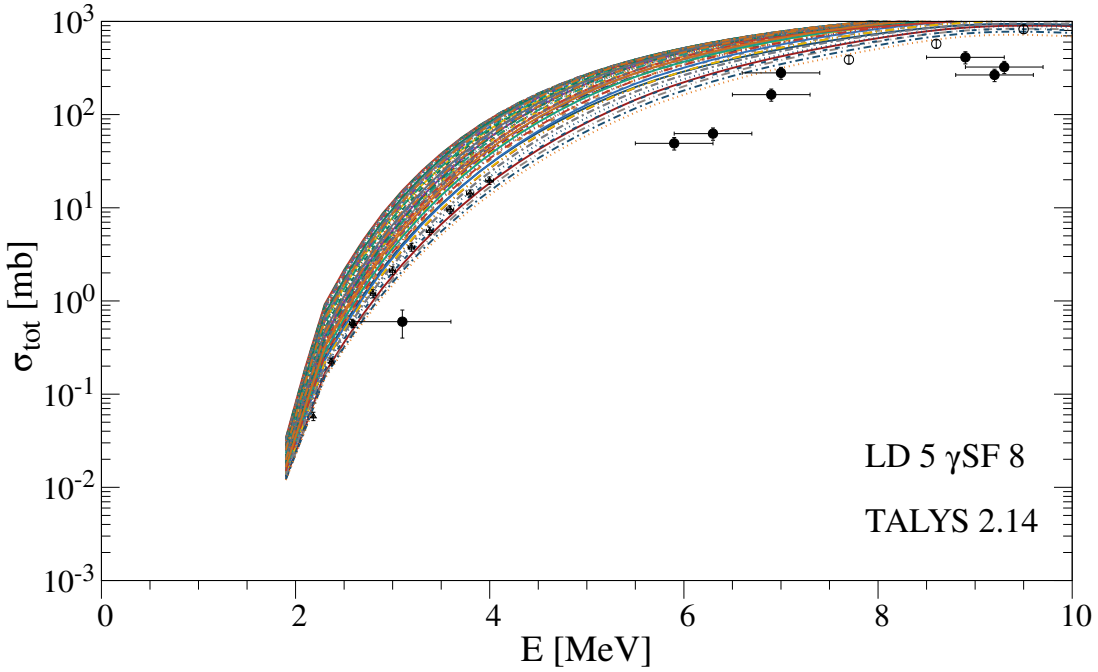

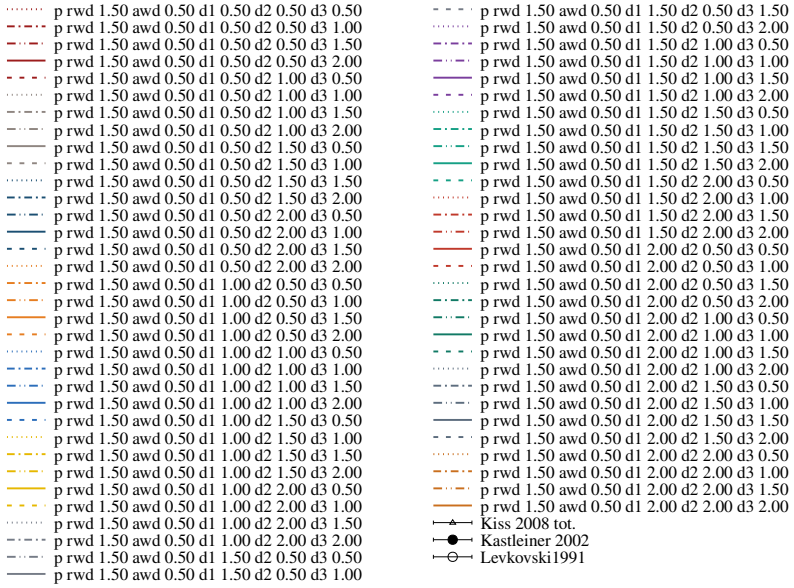

Figure A.59: Same as before with with $rwd = 1.50$ and $awd = 0.5$.

A.4.14 Varying *rwd*, *awd*, *d1*, *d2*, *d3*, *rv*, *av*, and *v1*

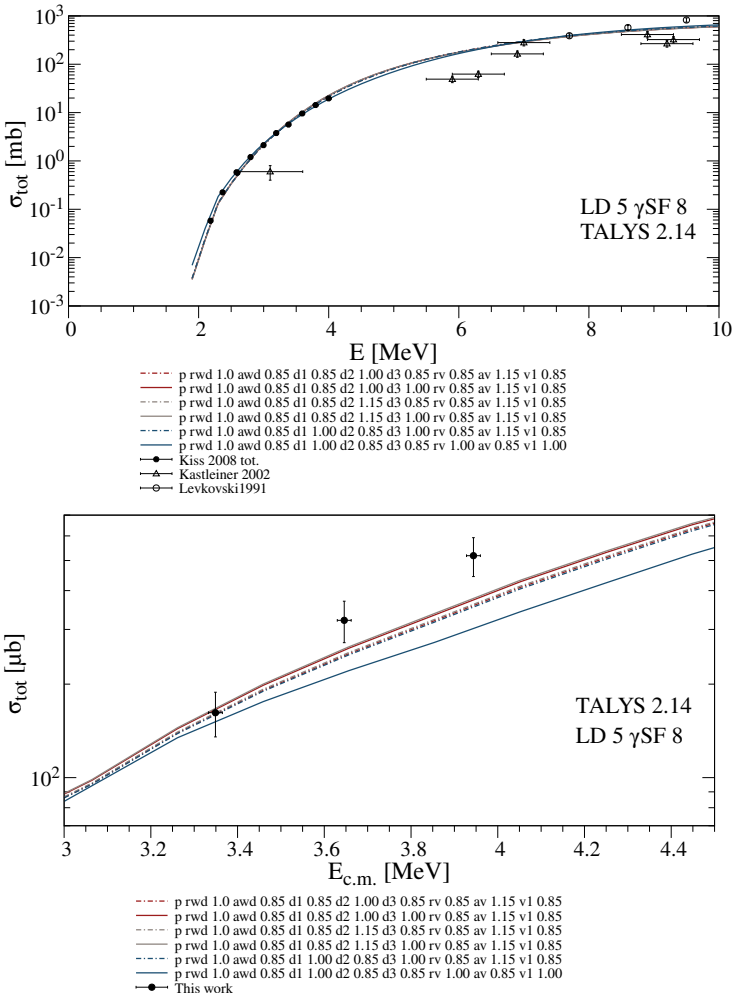

Figure A.60: Exemplary parameter combinations describing the (p, n) data obtained by varying eight parameters of the Koning–Delaroche optical model potential, together with their corresponding predictions for the (p, γ) data. Although several parameter combinations yield comparable agreement for the (p, n) data, none successfully reproduce the experimental (p, γ) results.

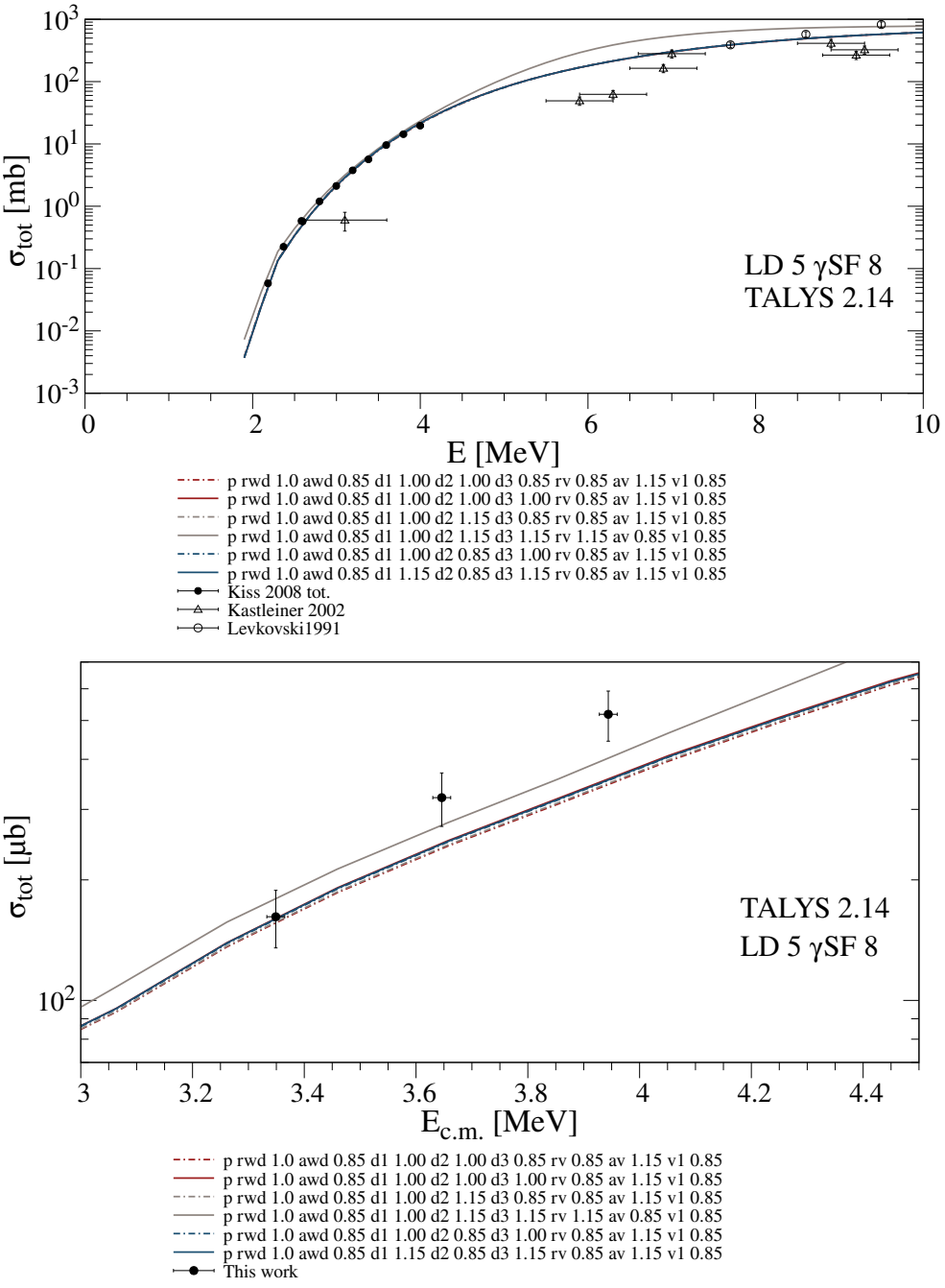

Figure A.61: Same as before for other combinations.

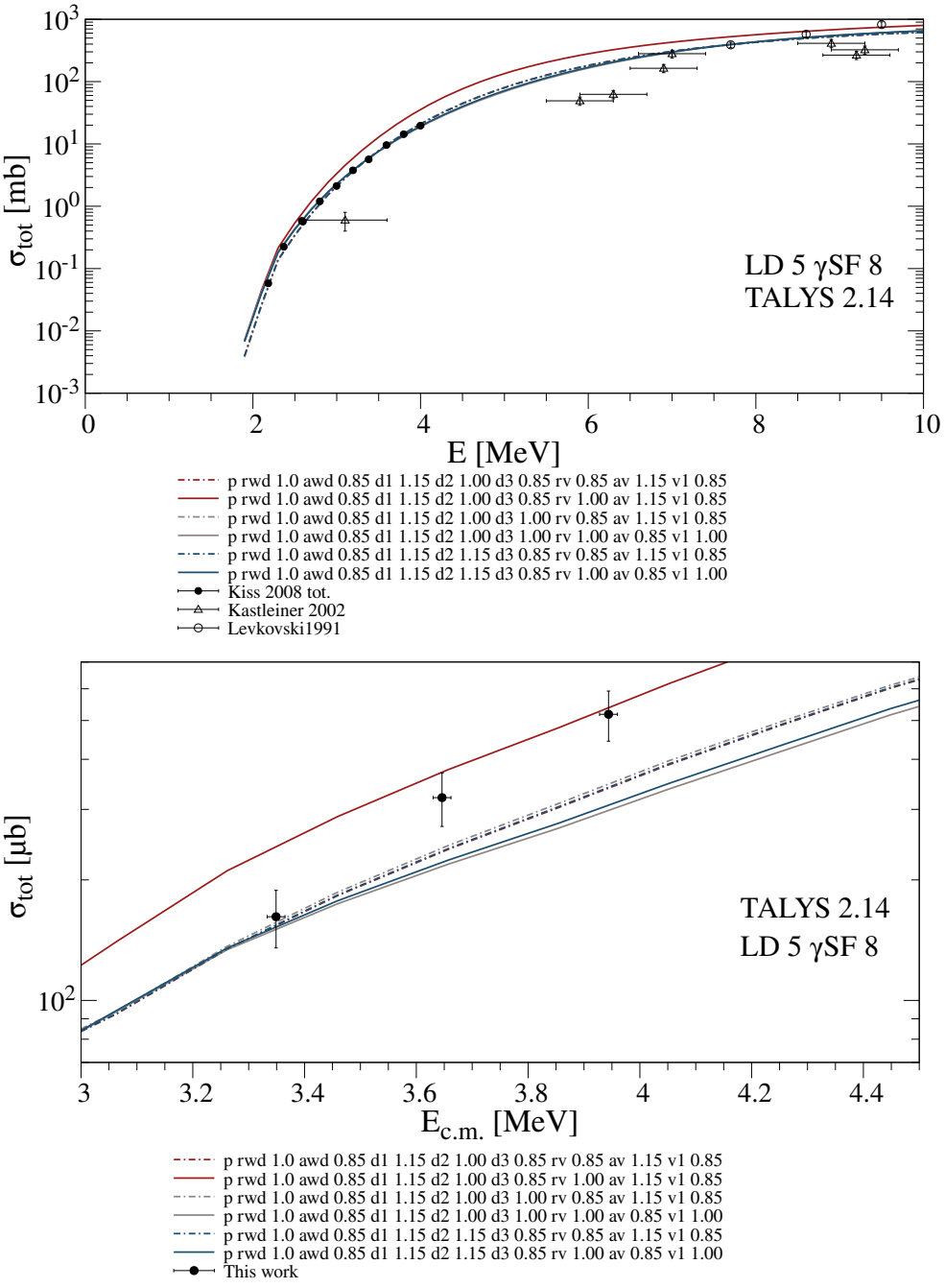

Figure A.62: Same as before for other combinations.

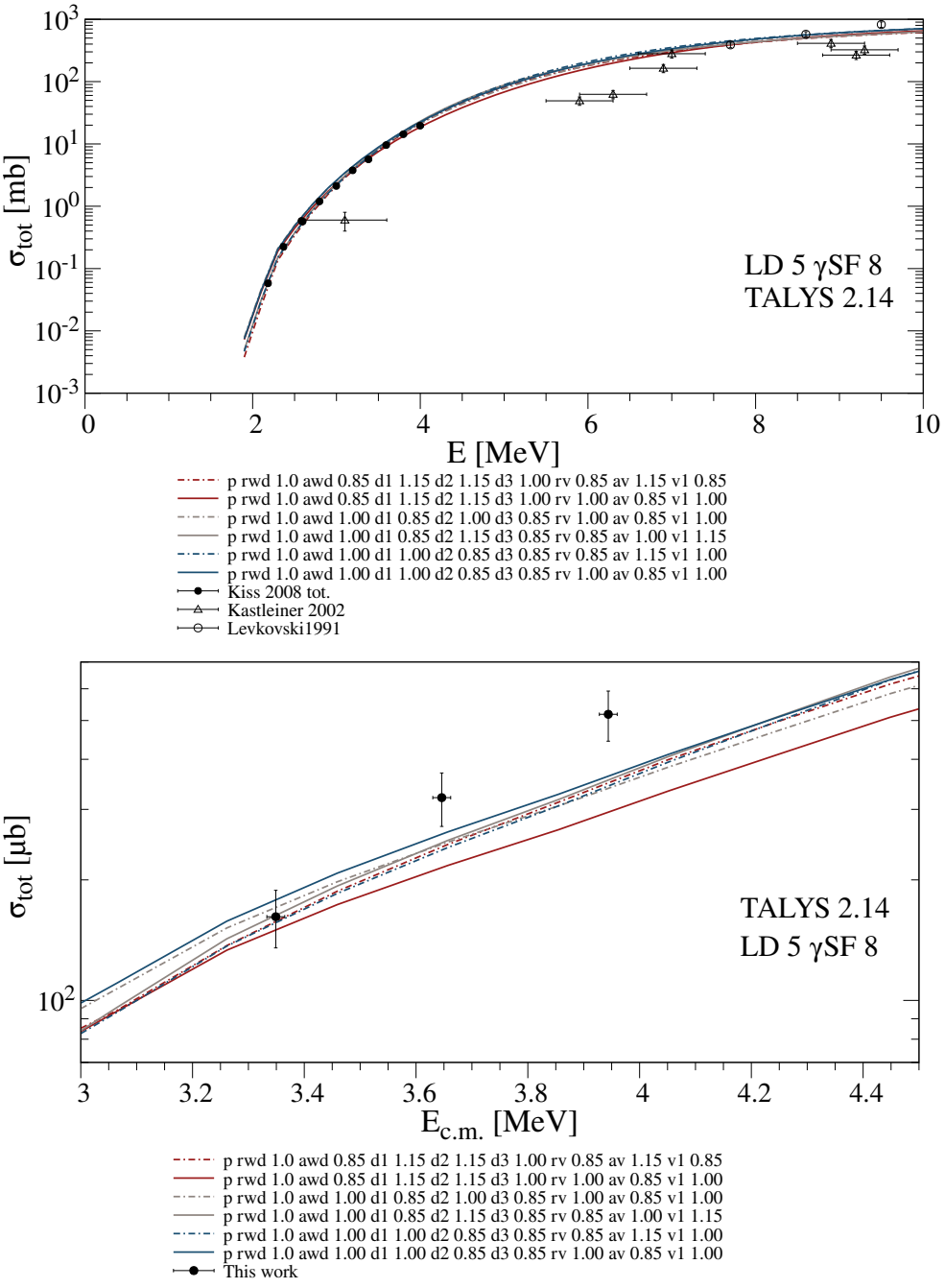

Figure A.63: Same as before for other combinations.

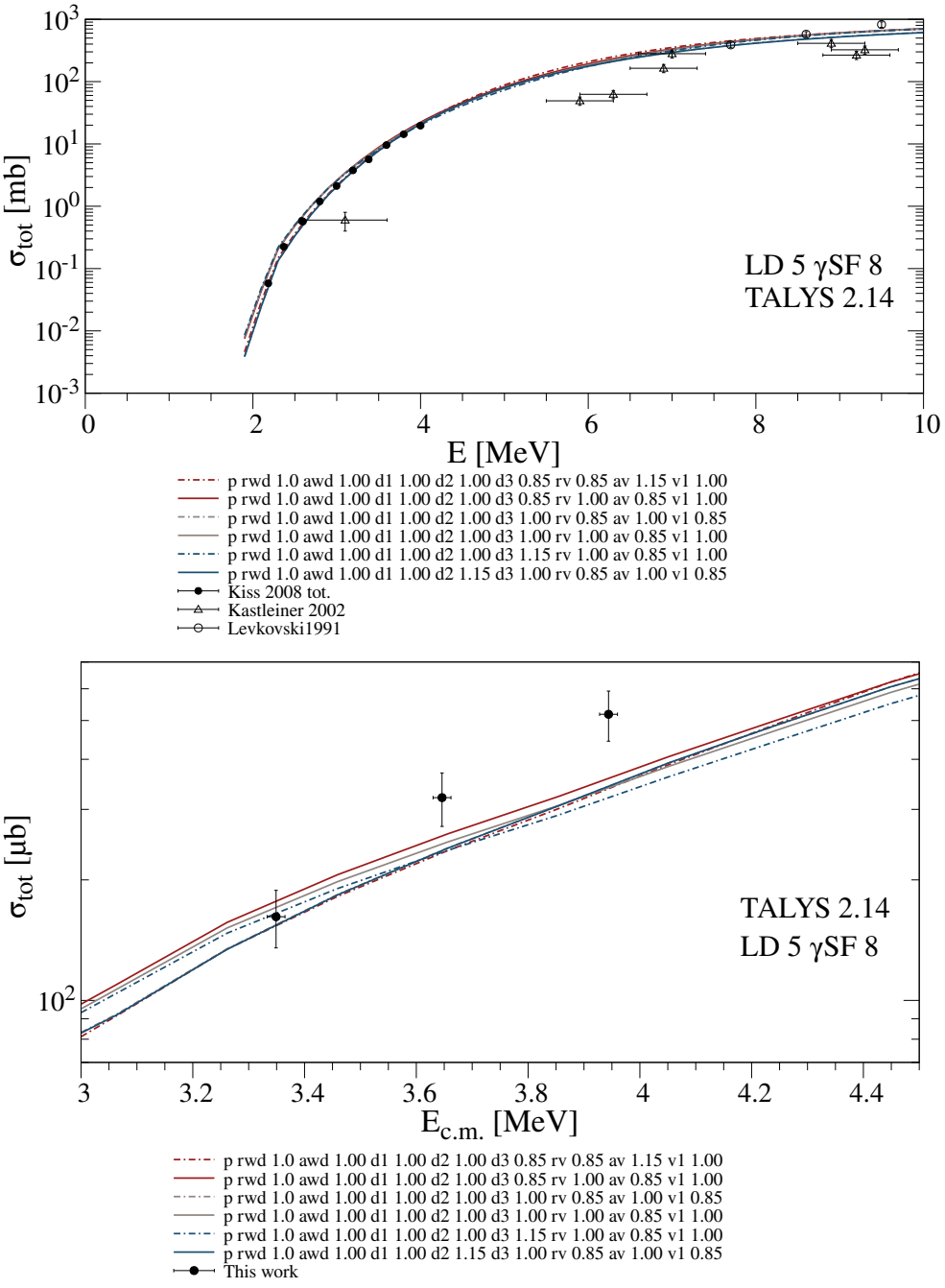

Figure A.64: Same as before for other combinations.

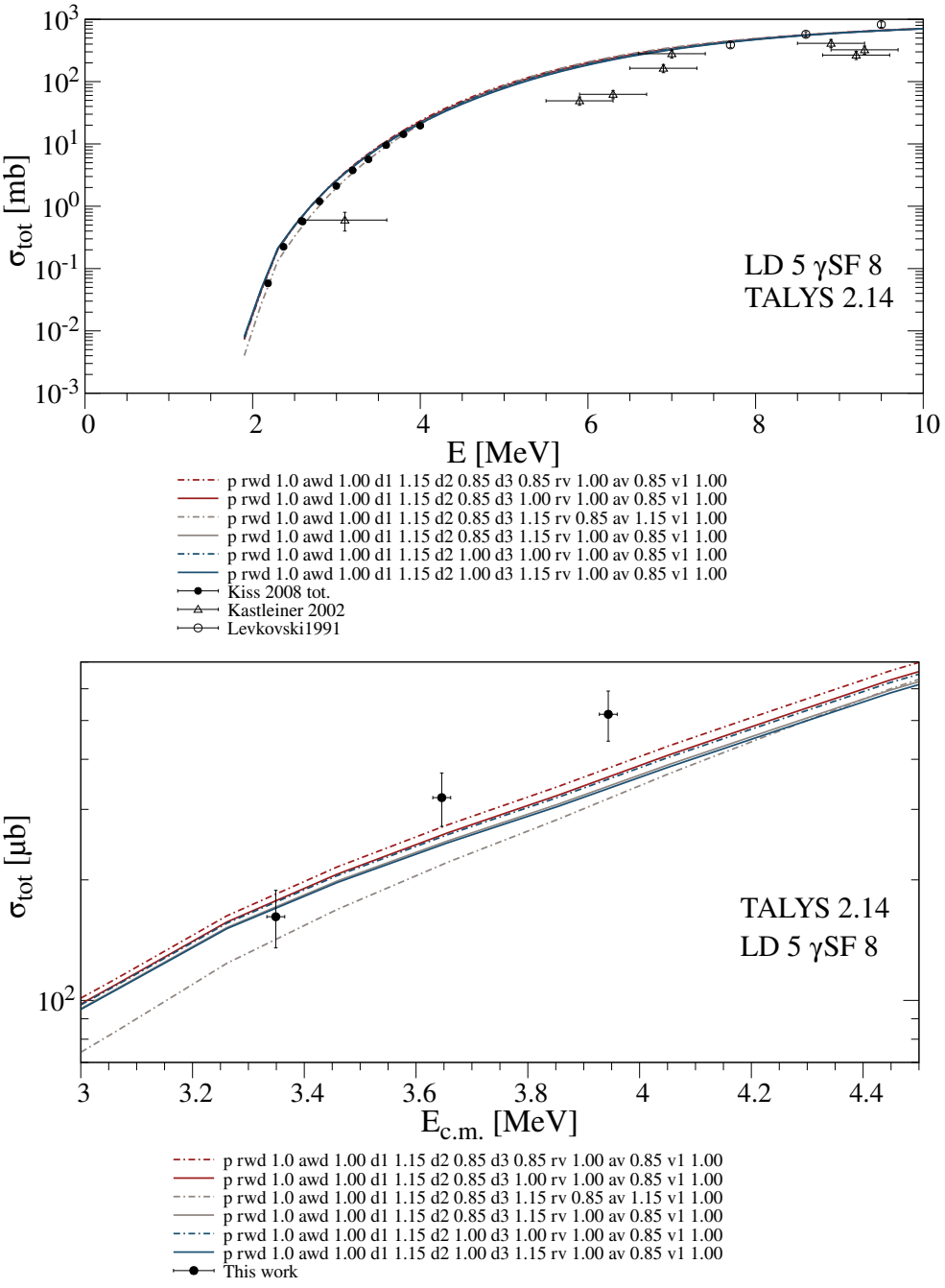

Figure A.65: Same as before for other combinations.

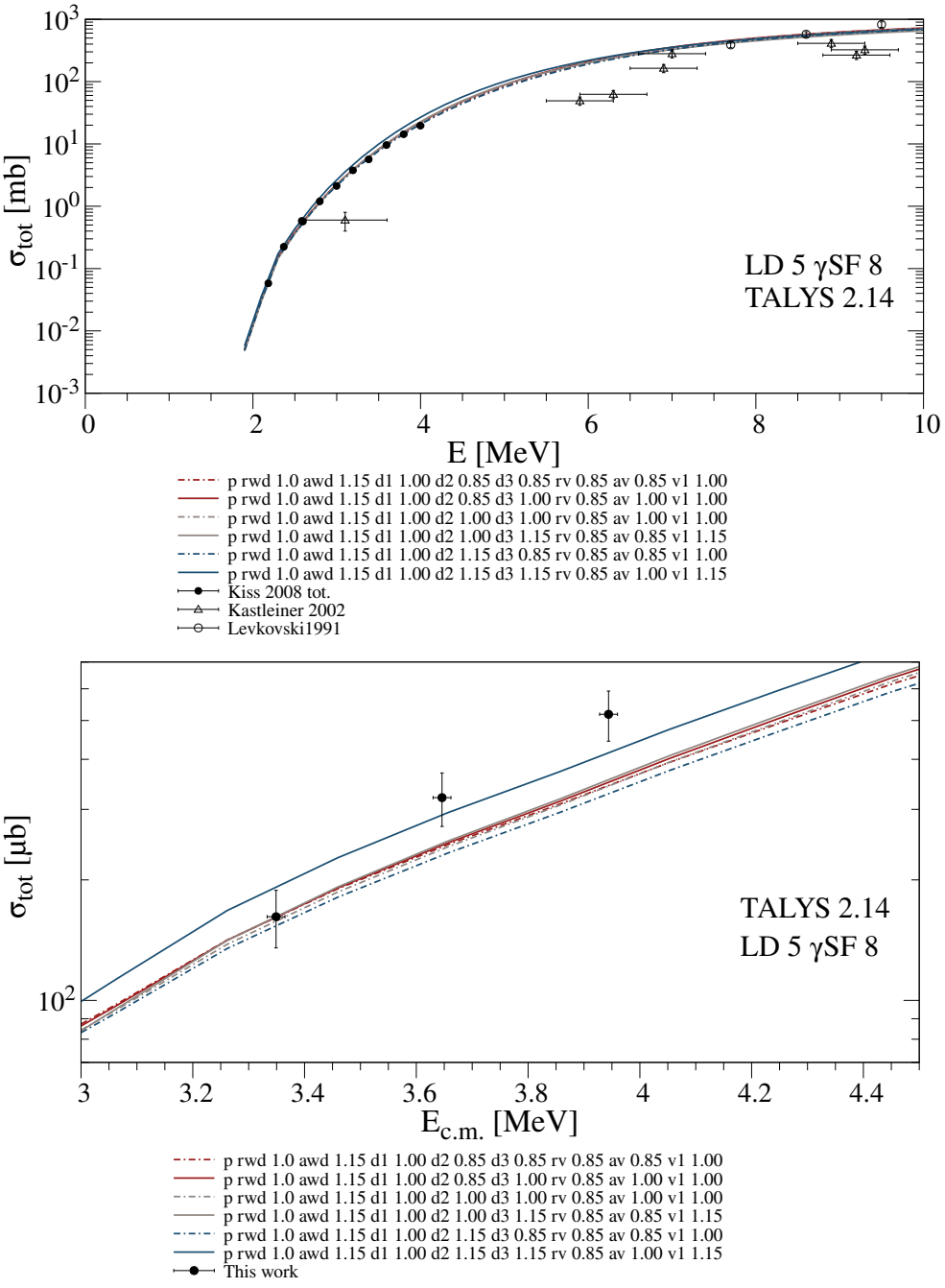

Figure A.66: Same as before for other combinations.

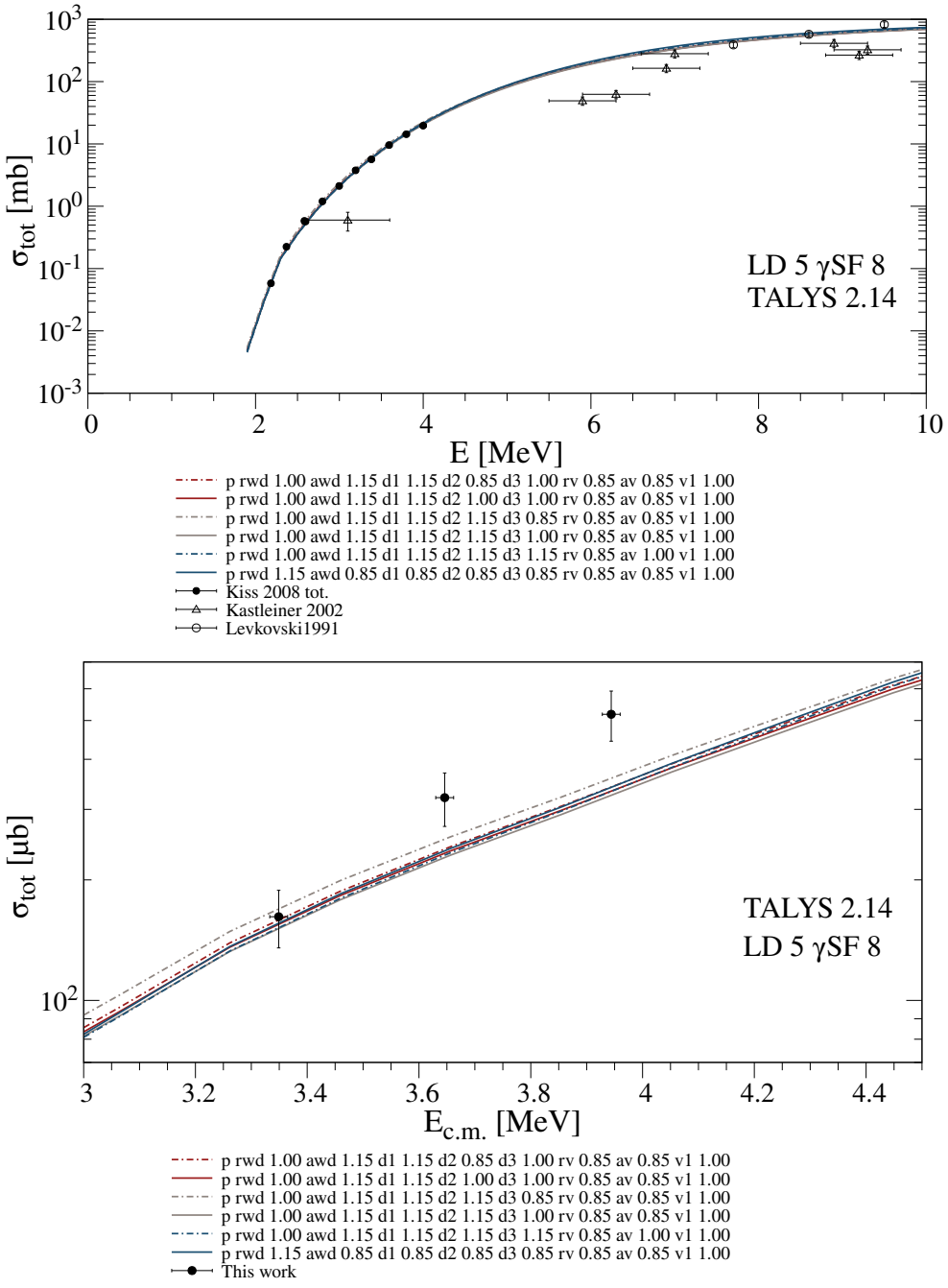

Figure A.67: Same as before for other combinations.

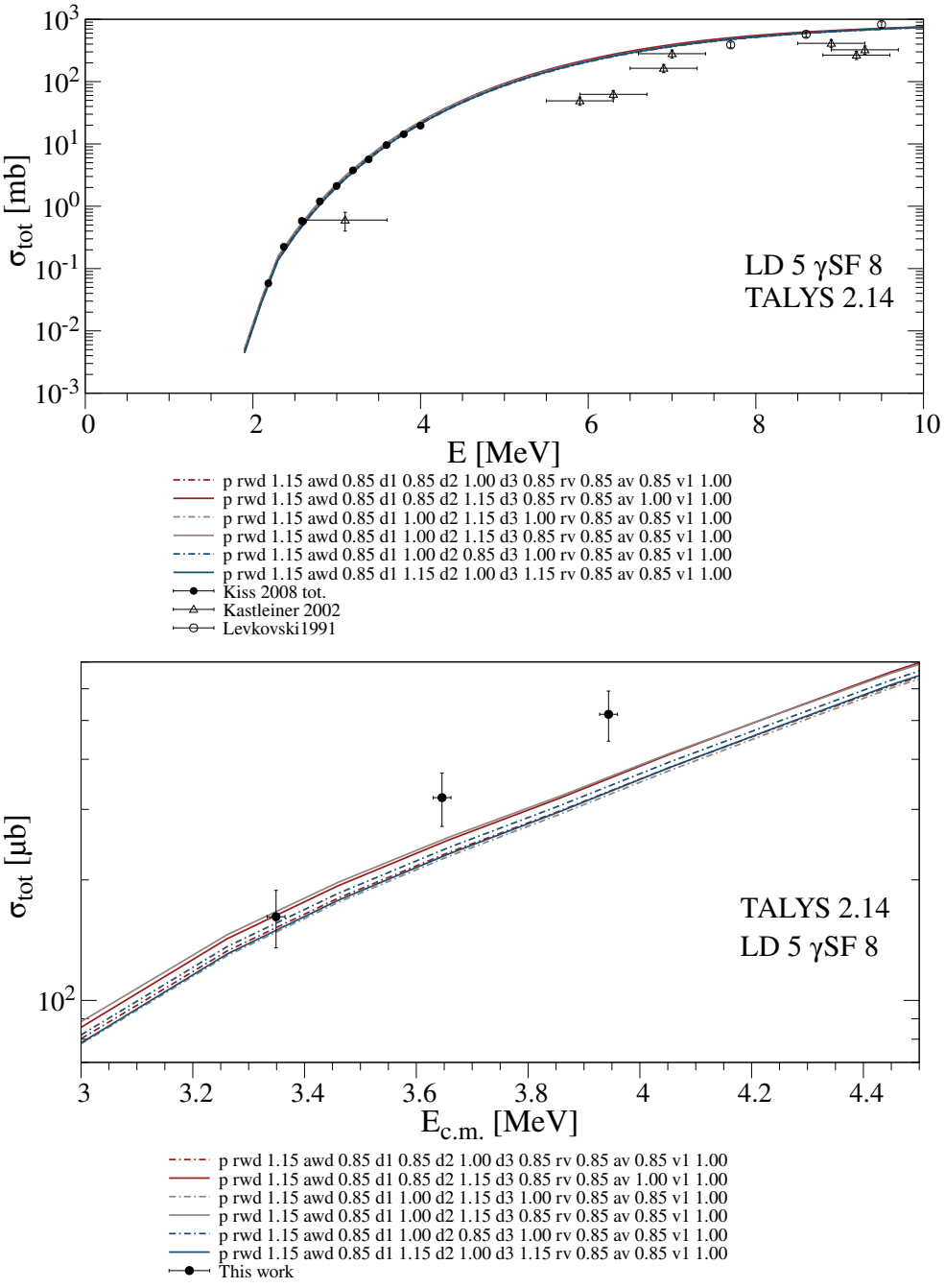

Figure A.68: Same as before for other combinations.

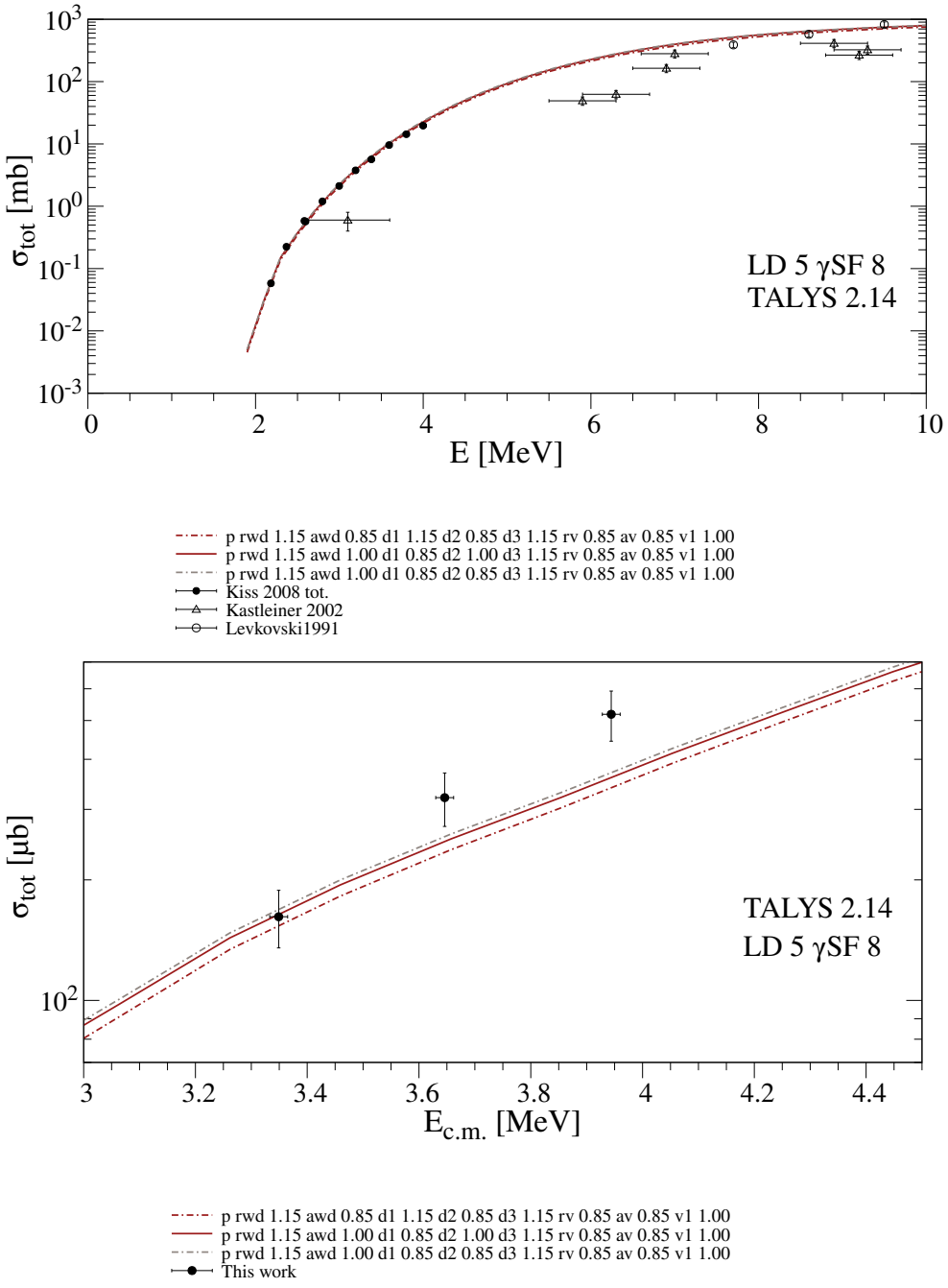

Figure A.69: Same as before for other combinations.

A.4.15 Varying *rwd*, *awd*, *rv*, and *av*

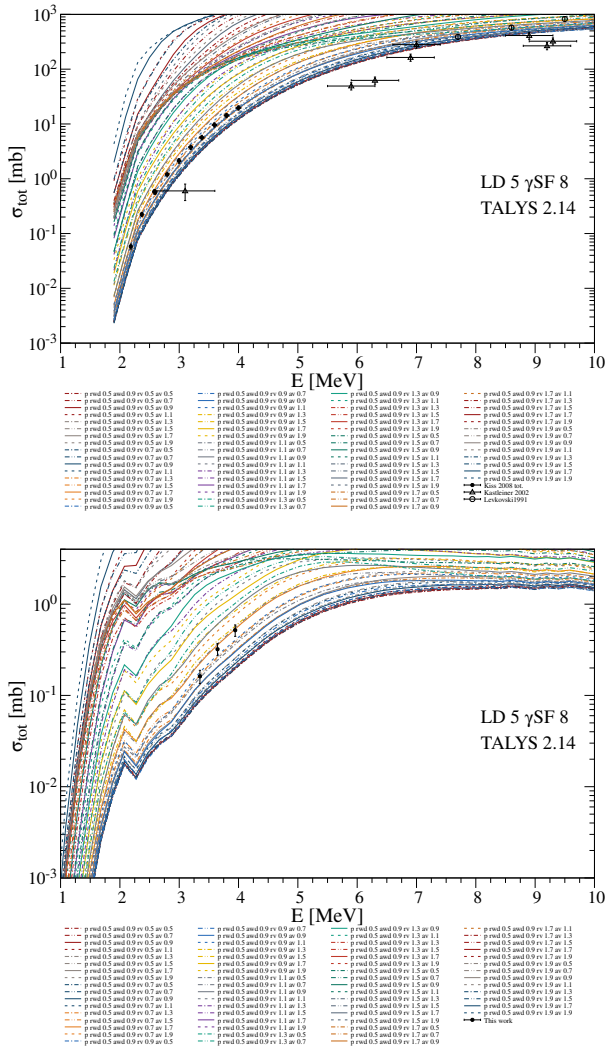

Figure A.70: Variation of the parameters *rwd*, *awd*, *rv*, and *av* of the Koning–Delaroche optical model potential to investigate their direct influence on the predicted cross sections. Each parameter was varied in steps of 0.2 within the range from 0.5 to 2.0. Shown are the combinations for $rwd = 0.5$ and $awd = 0.9$.

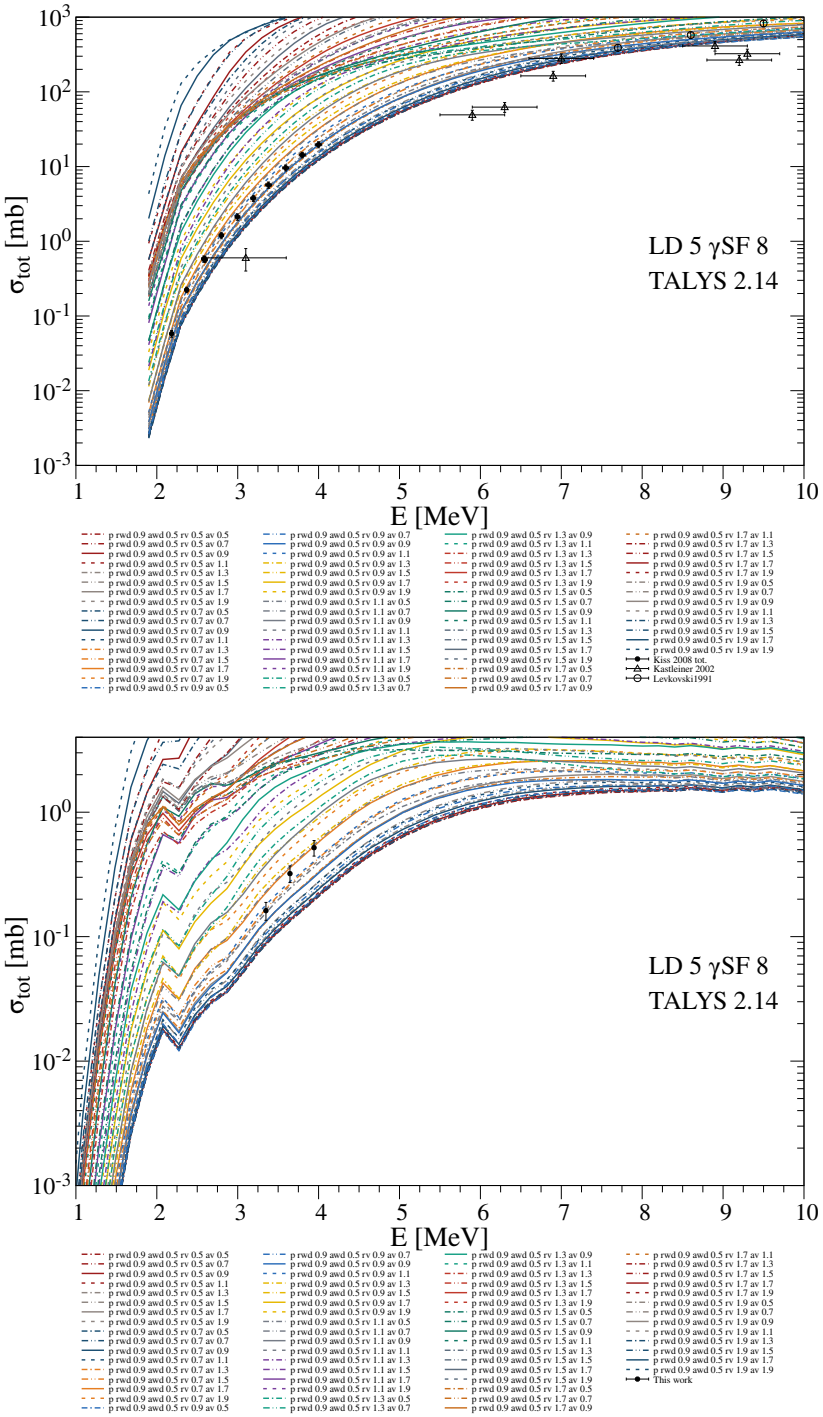

Figure A.71: Same as before with $rwd = 0.9$ and $awd = 0.5$.

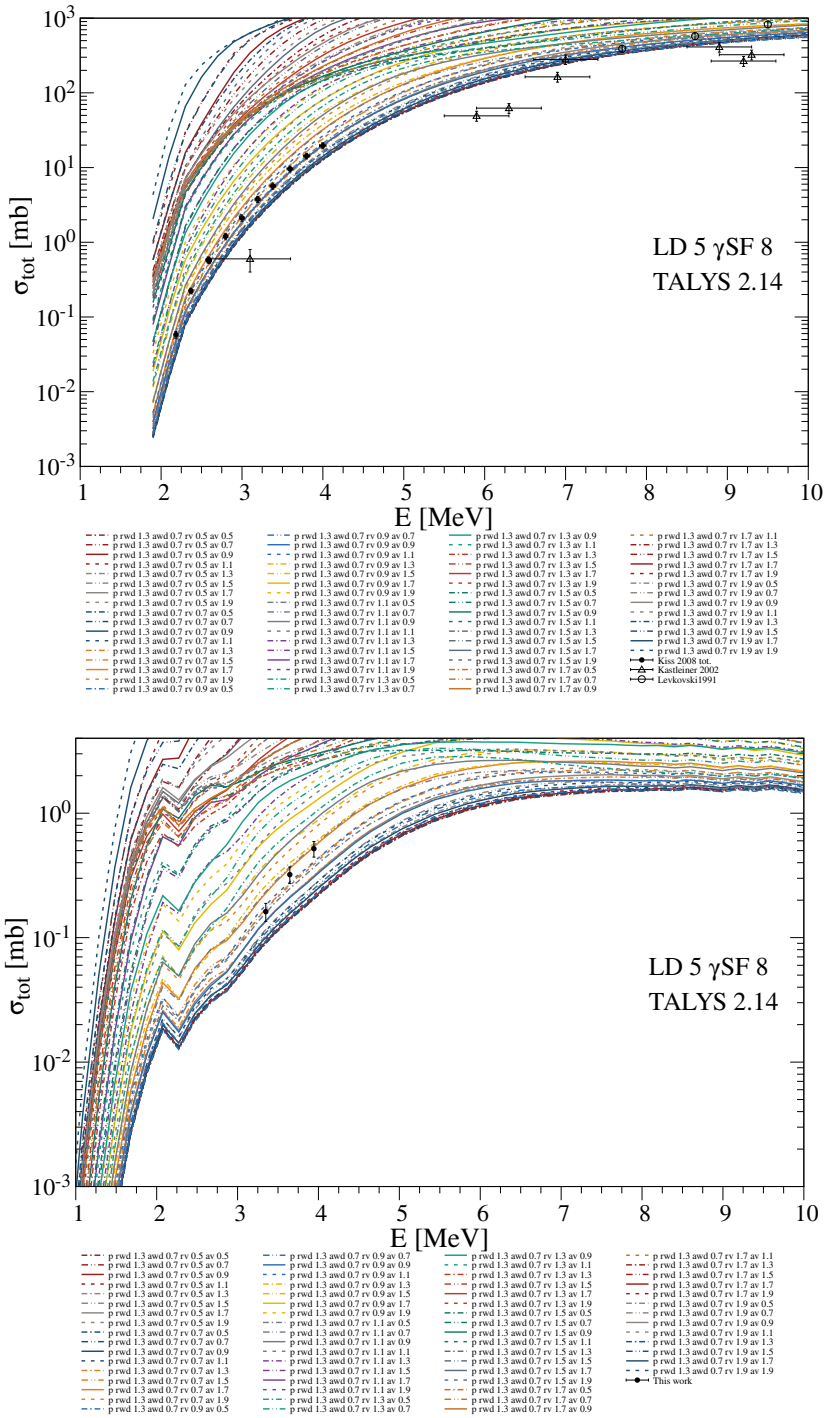

Figure A.72: Same as before with $rwd = 1.3$ and $awd = 0.7$.

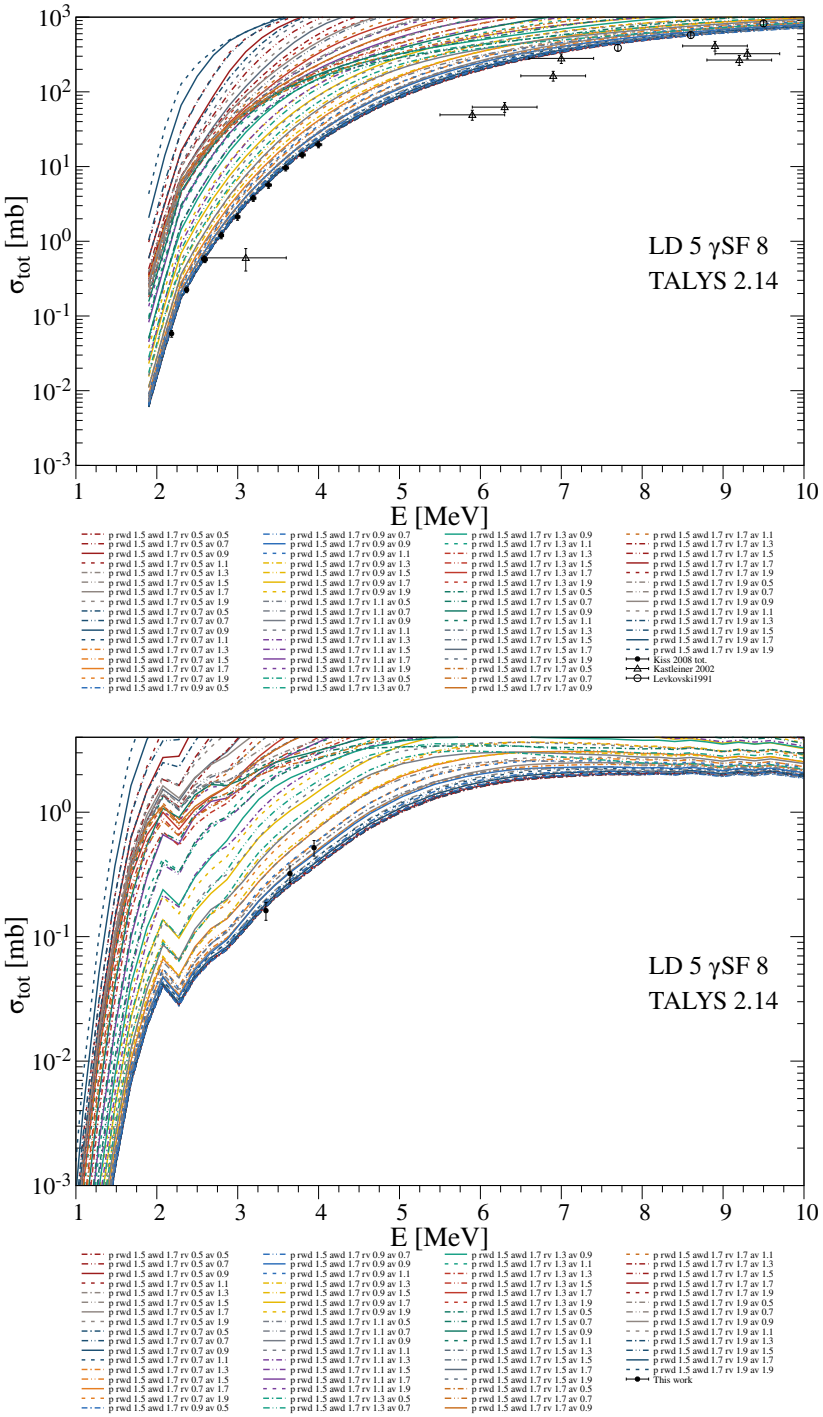

Figure A.73: Same as before with $rwd = 1.5$ and $awd = 1.7$.

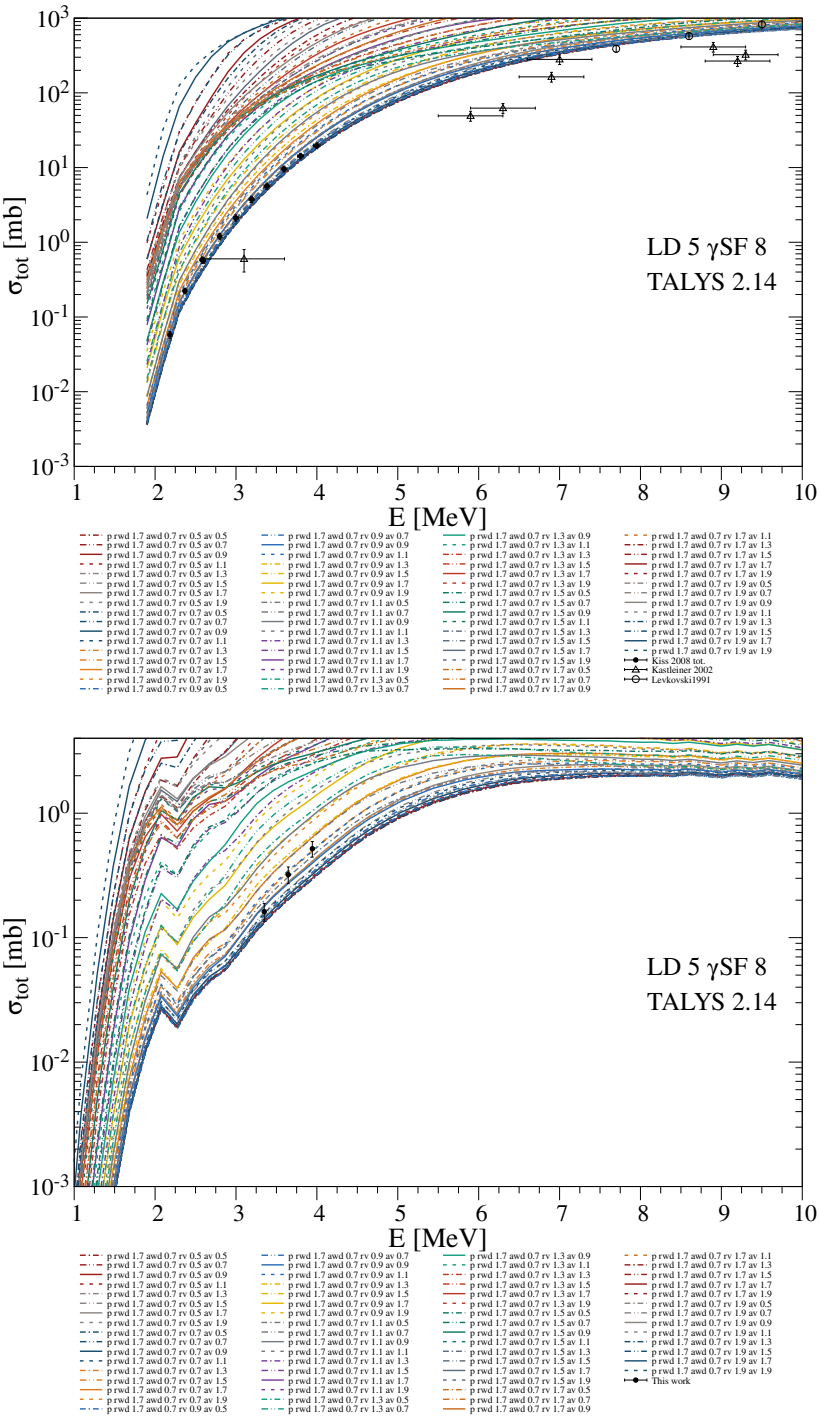

Figure A.74: Same as before with $rwd = 1.7$ and $awd = 0.7$.

A.5 Systematic studies of the JLM Optical Model Potential

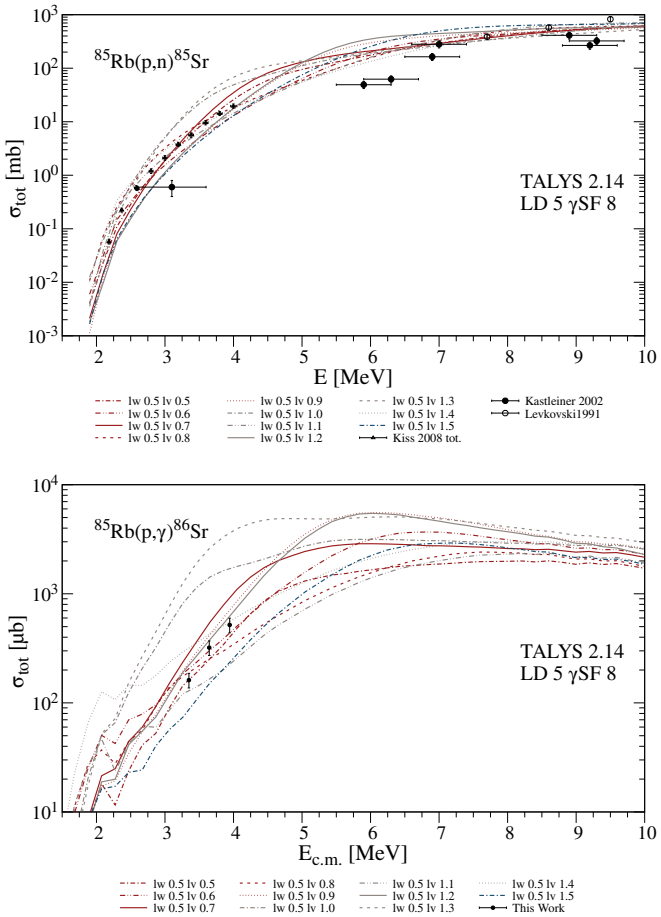

Figure A.75: Variation of *lwadjust* = 0.5 with the altered *lvadjust* for proton-induced reactions on ^{87}Rb. The upper panel shows the predicted $^{87}\mathrm{Rb}(p,n)^{85}\mathrm{Sr}$ cross sections in comparison with the experimental data from References [140, 237, 238]. While the general energy dependence is reproduced for the different combinations of *lwadjust* = 0.5 and *lvadjust*, not all parameter sets describe the absolute values satisfactorily. The lower panel presents the comparison between the experimentally obtained $^{87}\mathrm{Rb}(p,\gamma)$ data and the statistical model predictions. Although some combinations reproduce the trend of the data more accurately than others, none of them succeeds in reproducing the experimental cross sections at all energies.

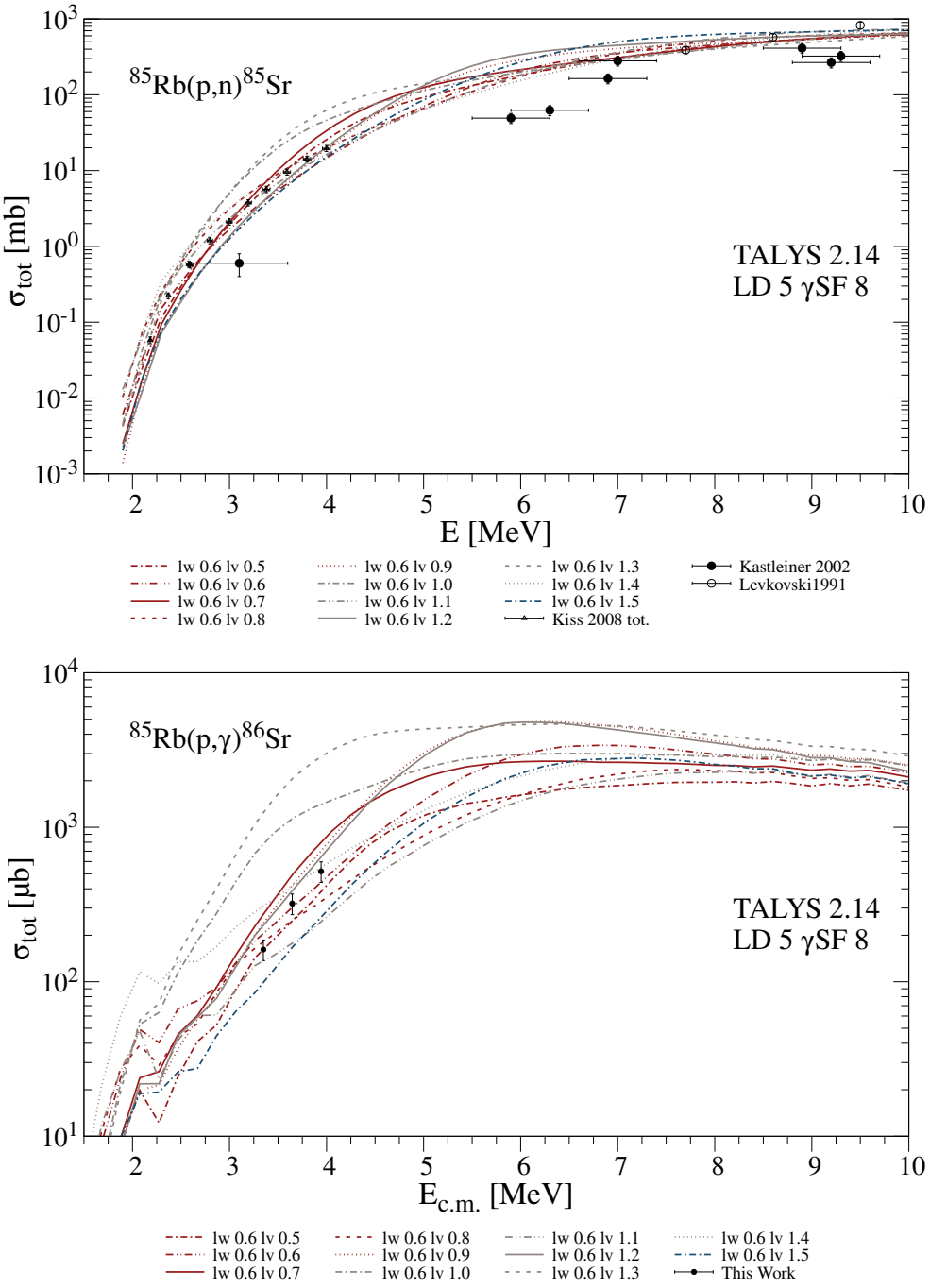

Figure A.76: Same as before with *lwadjust* = 0.6.

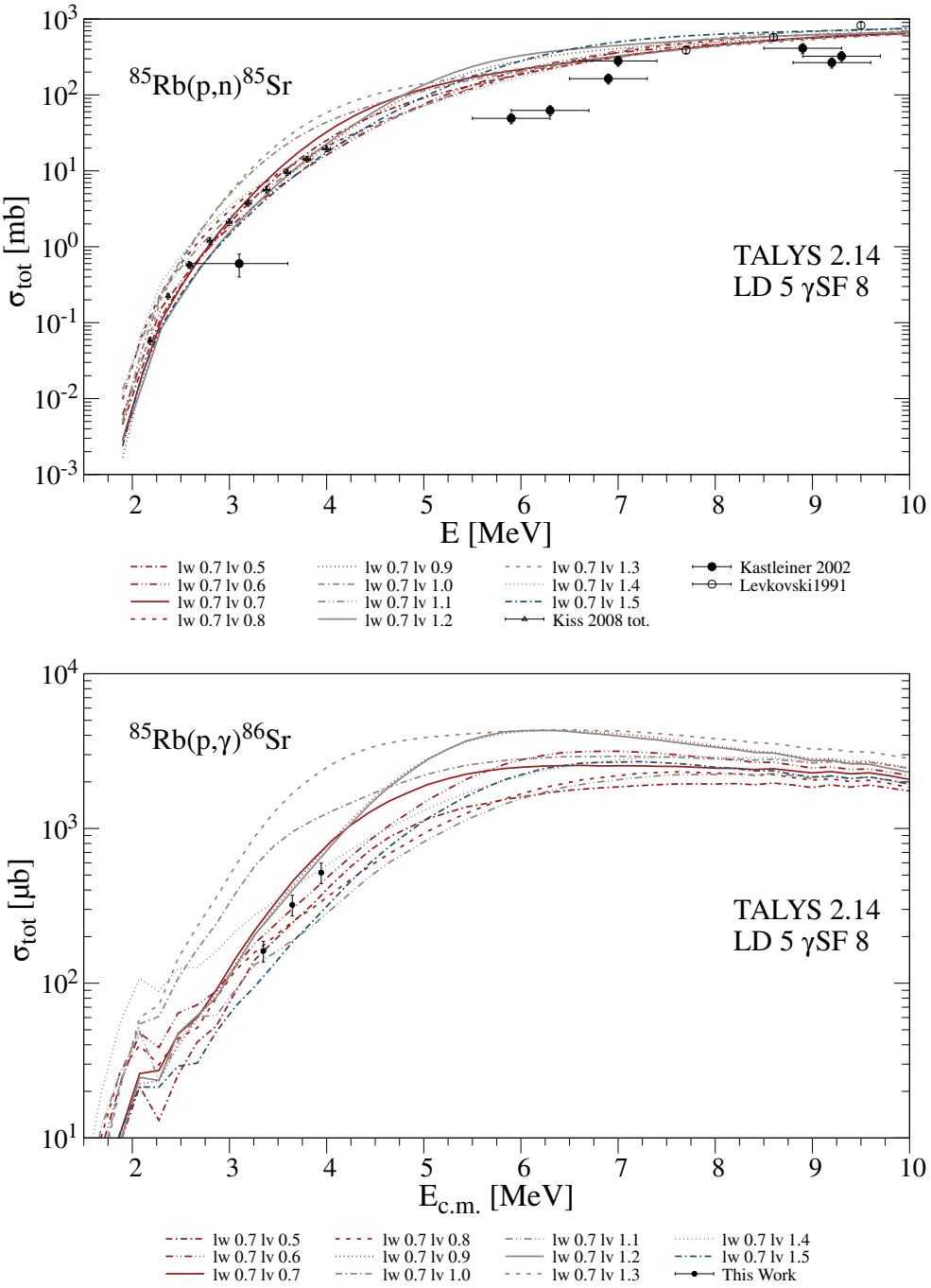

Figure A.77: Same as before with *lwadjust* = 0.7.

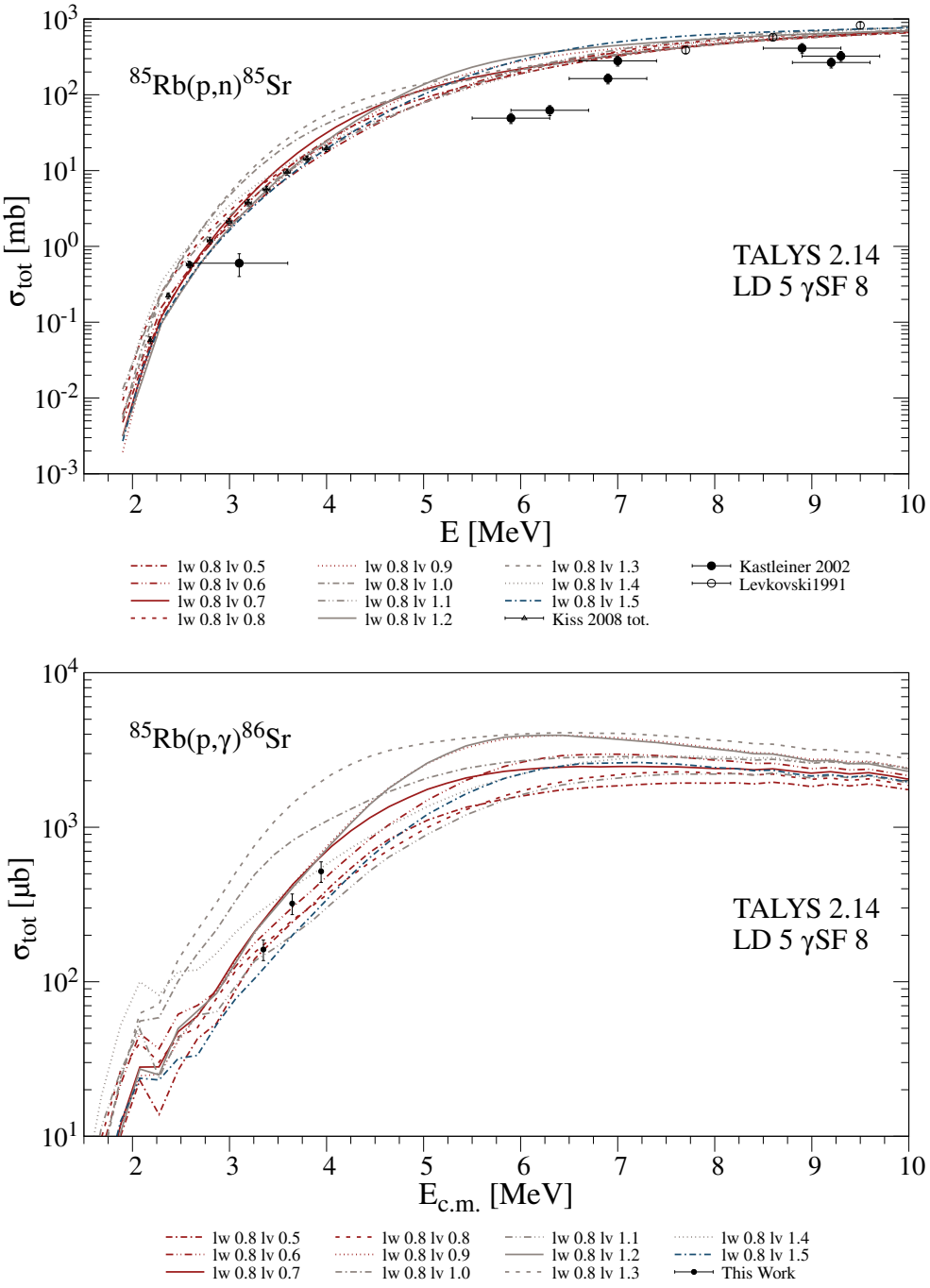

Figure A.78: Same as before with *lwadjust* = 0.8.

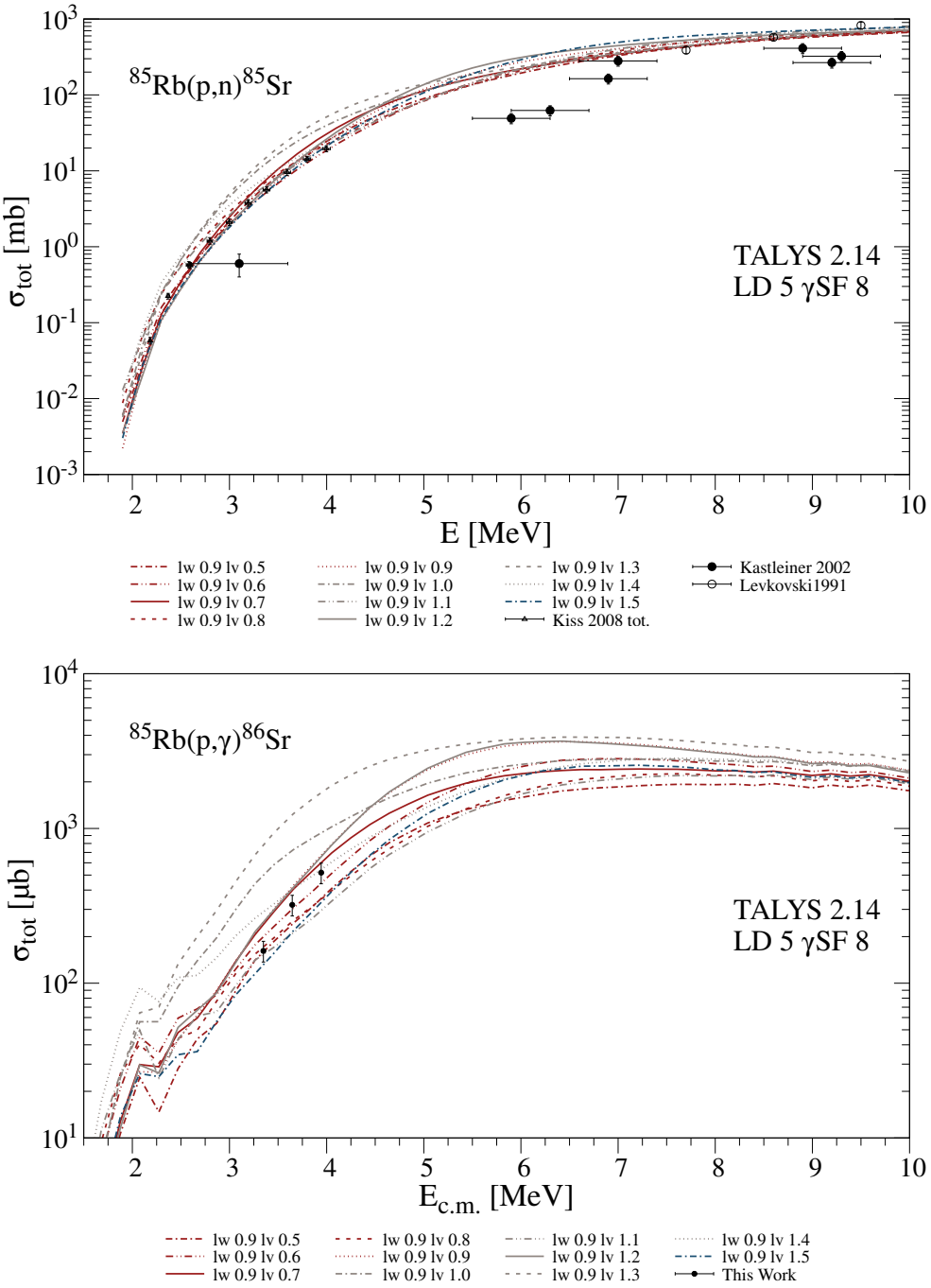

Figure A.79: Same as before with *lwadjust* = 0.9.

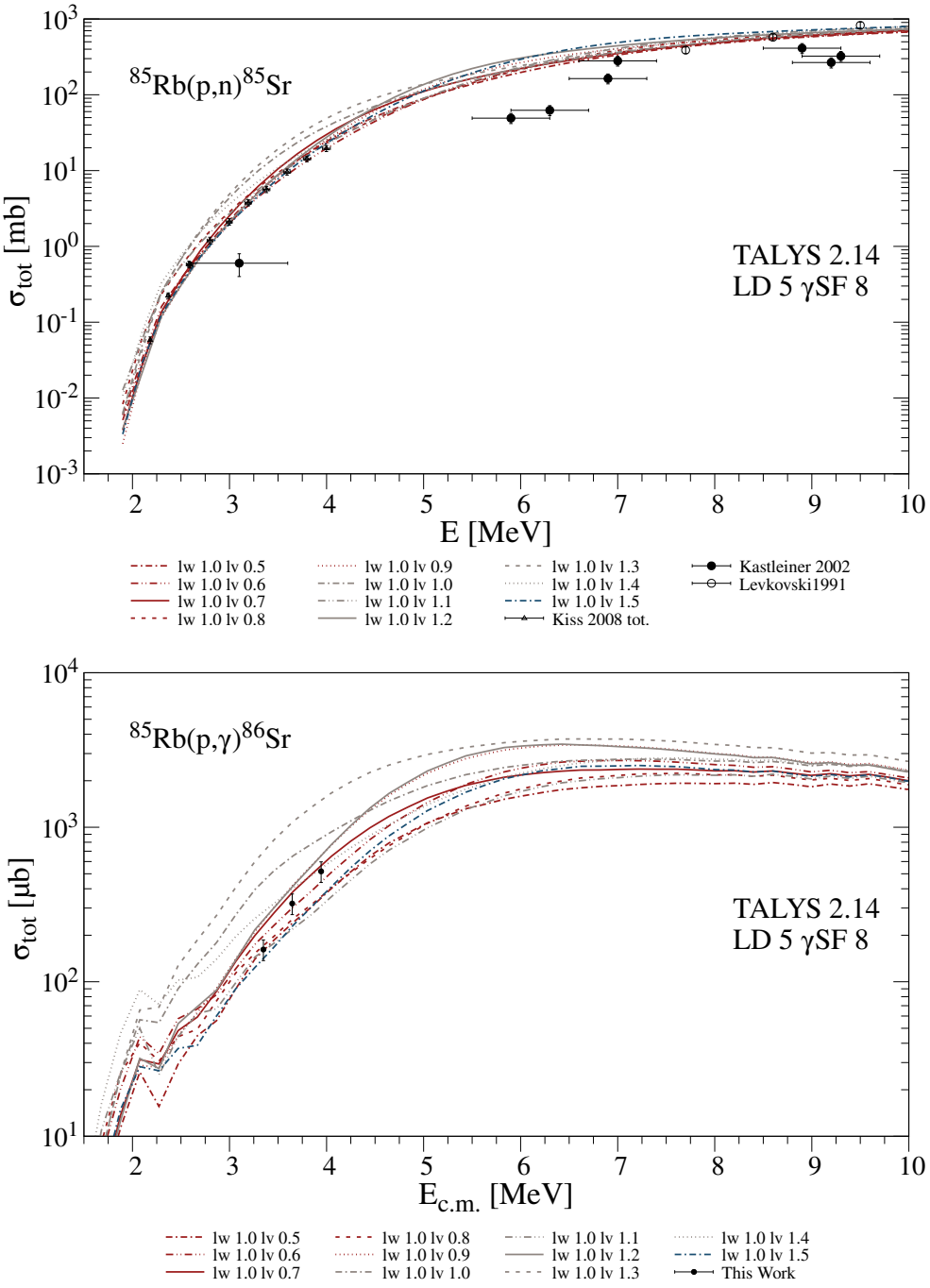

Figure A.80: Same as before with *lwadjust* = 1.0.

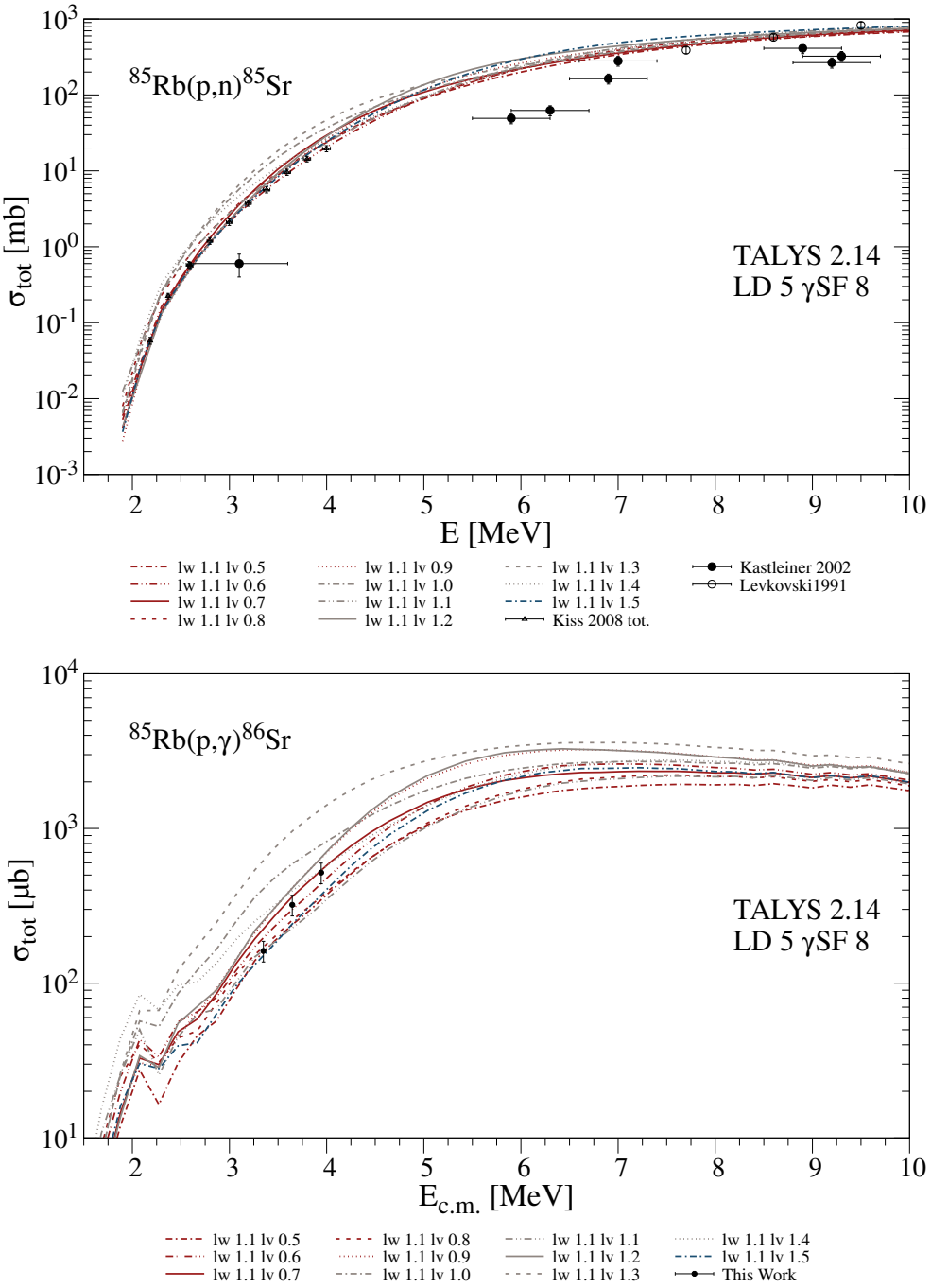

Figure A.81: Same as before with *lwadjust* = 1.1.

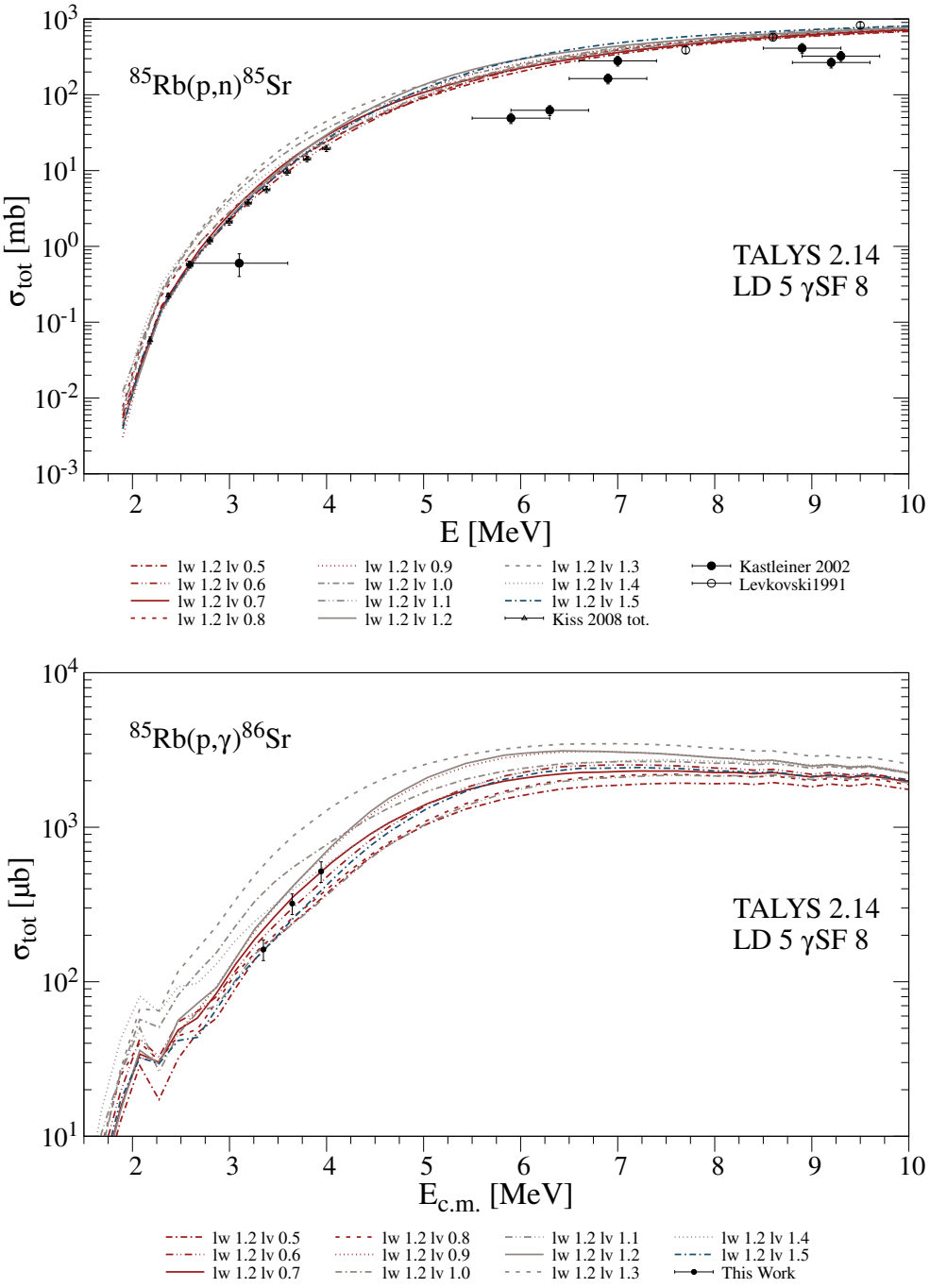

Figure A.82: Same as before with *lwadjust* = 1.2.

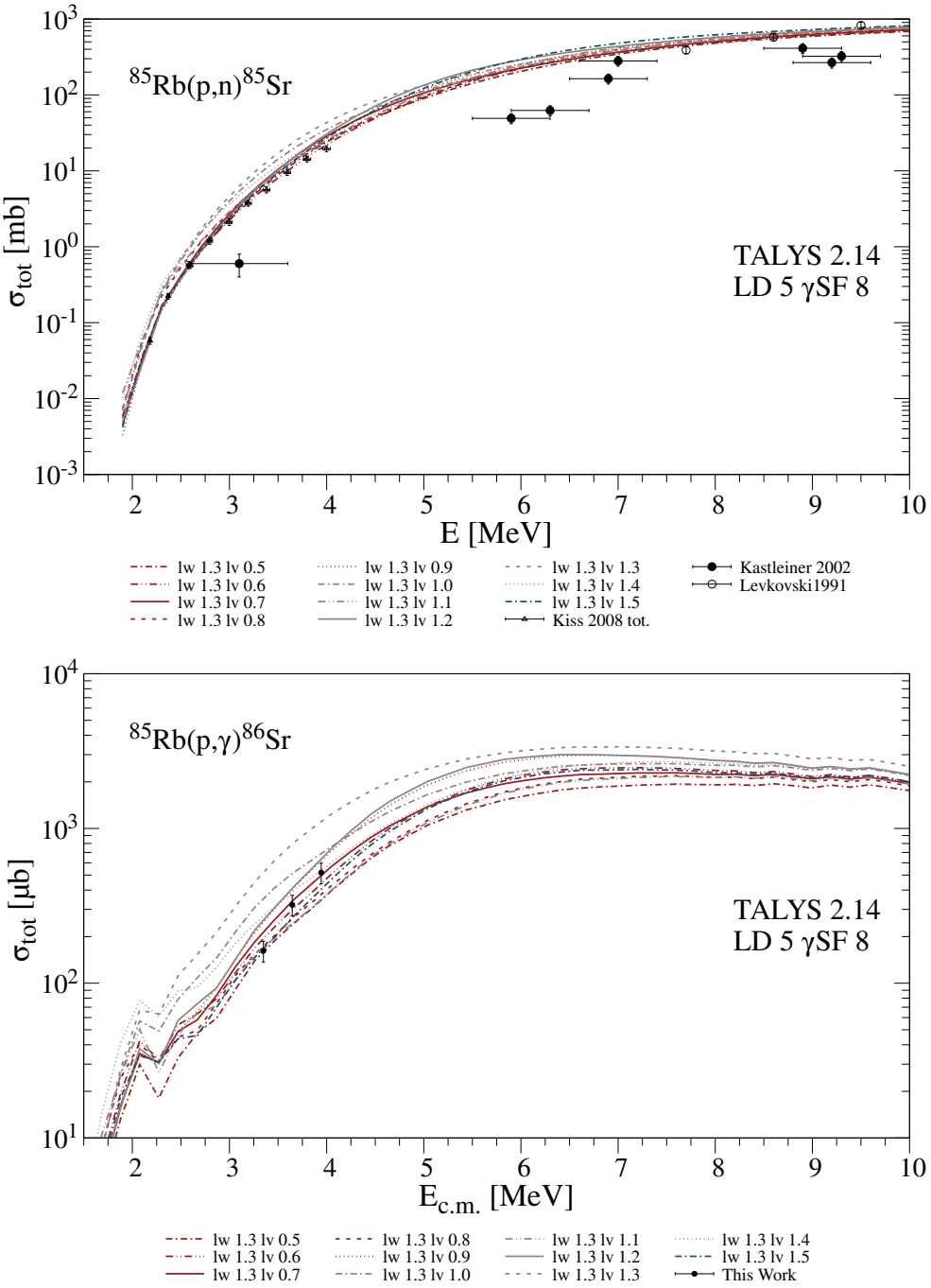

Figure A.83: Same as before with *lwadjust* = 1.3.

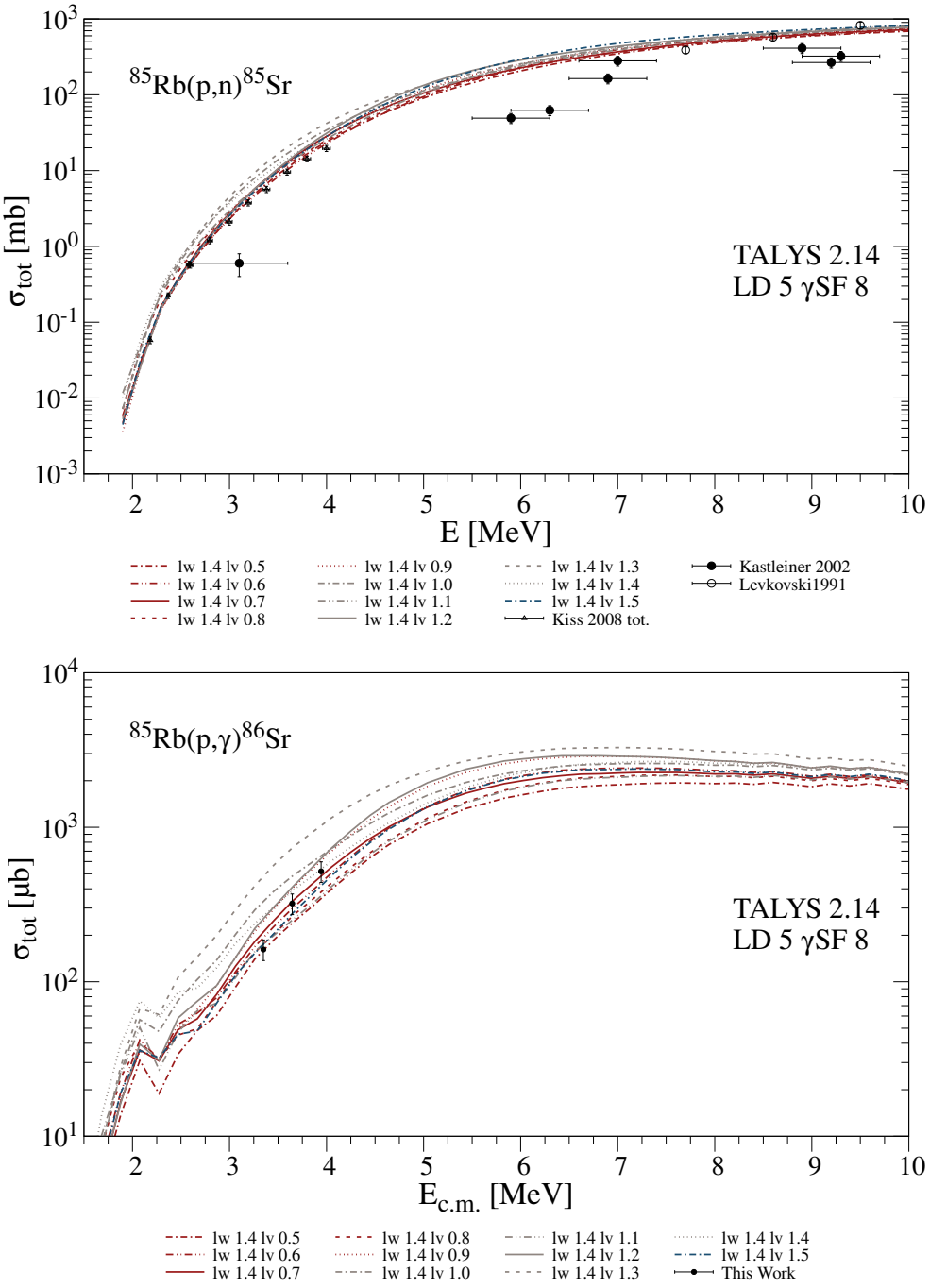

Figure A.84: Same as before with *lwadjust* = 1.4.

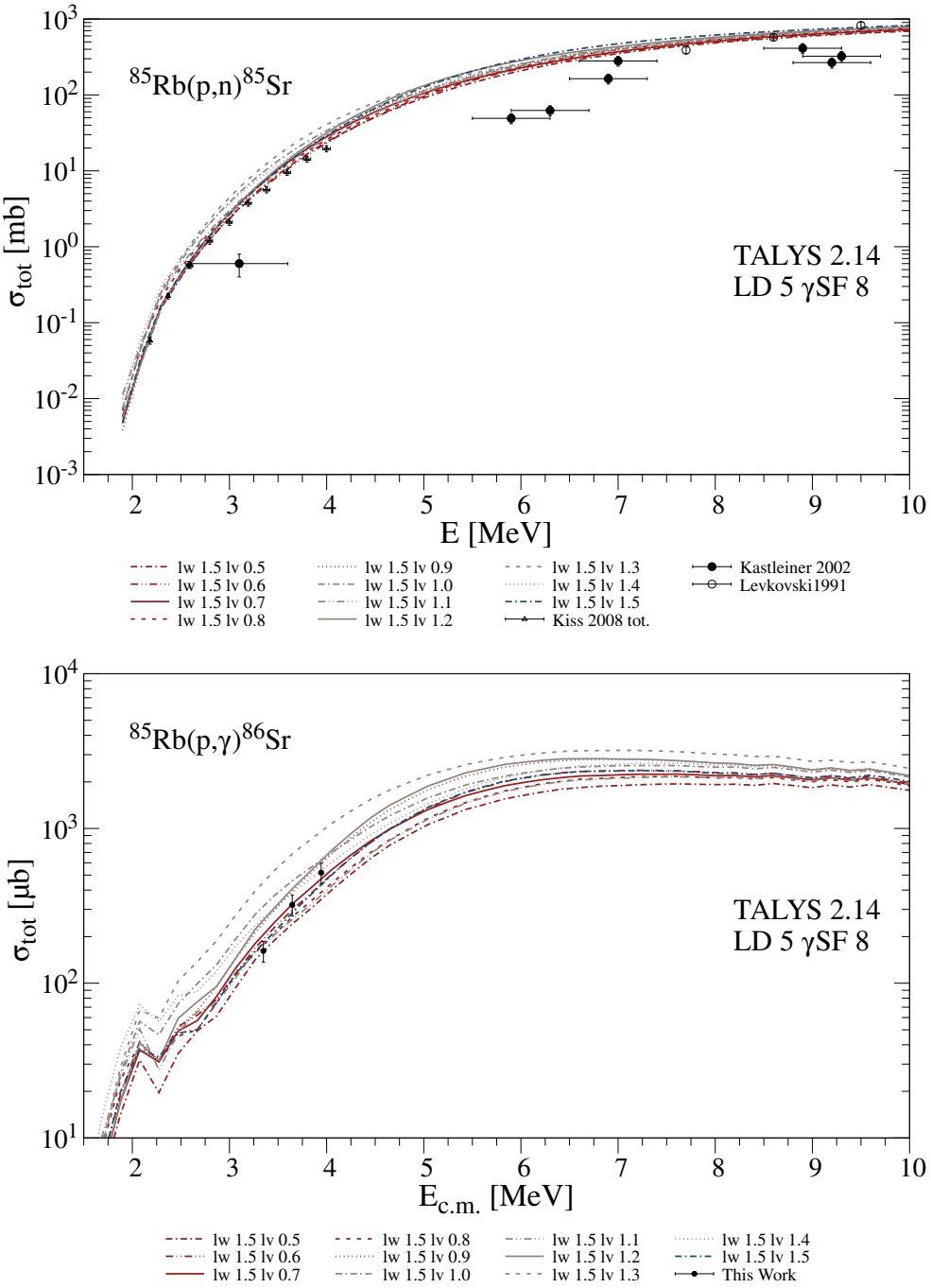

Figure A.85: Same as before with *lwadjust* = 1.5.

B ^{87}Rb

B.1 Systematic Variations of the JLM Optical Model Potential parameters *lwadjust* and *lvadjust*

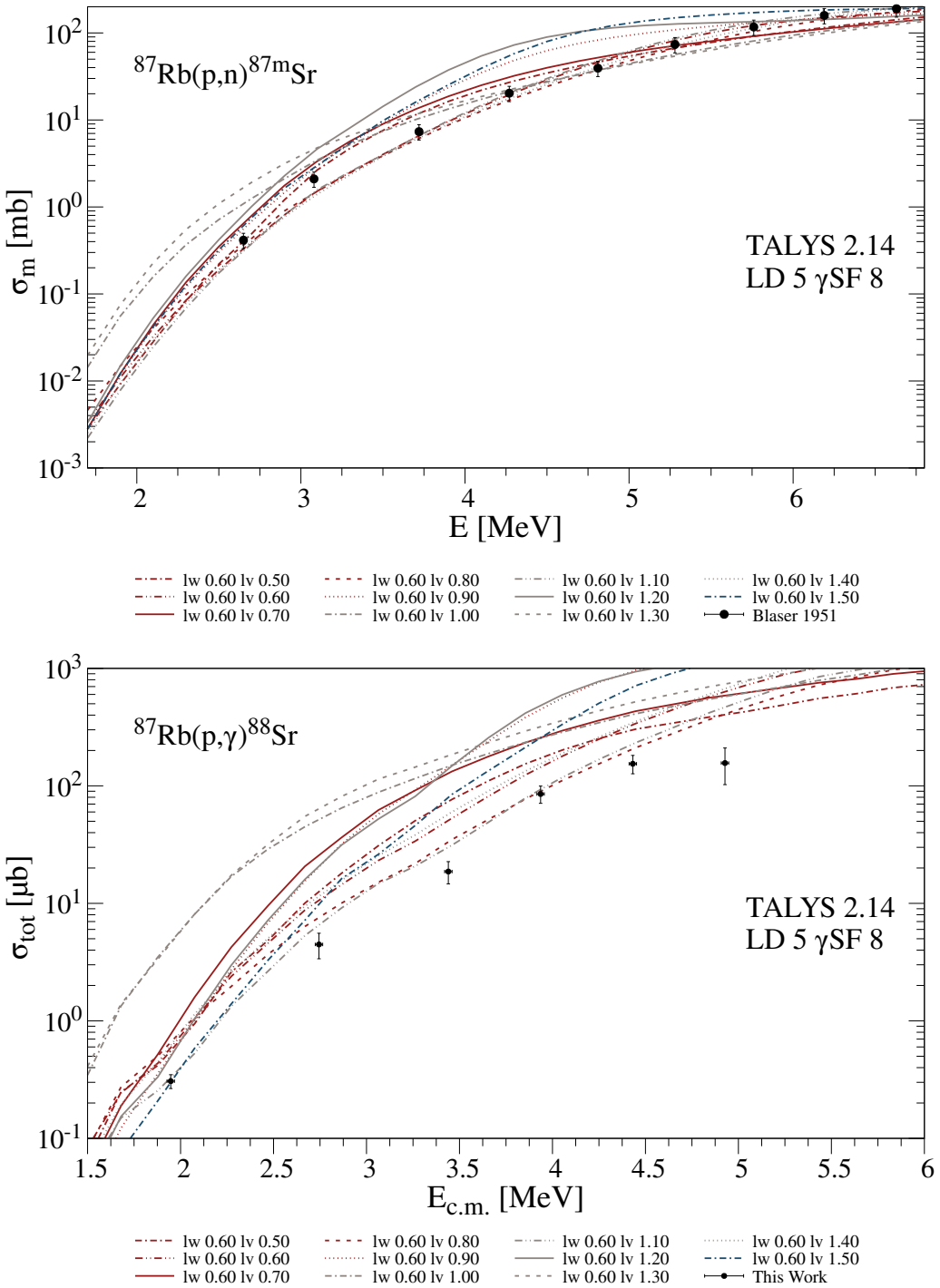

Figure B.1: Variation of *lwadjust* = 0.6 with the altered *lvadjust* for proton-induced reactions on ^{87}Rb.

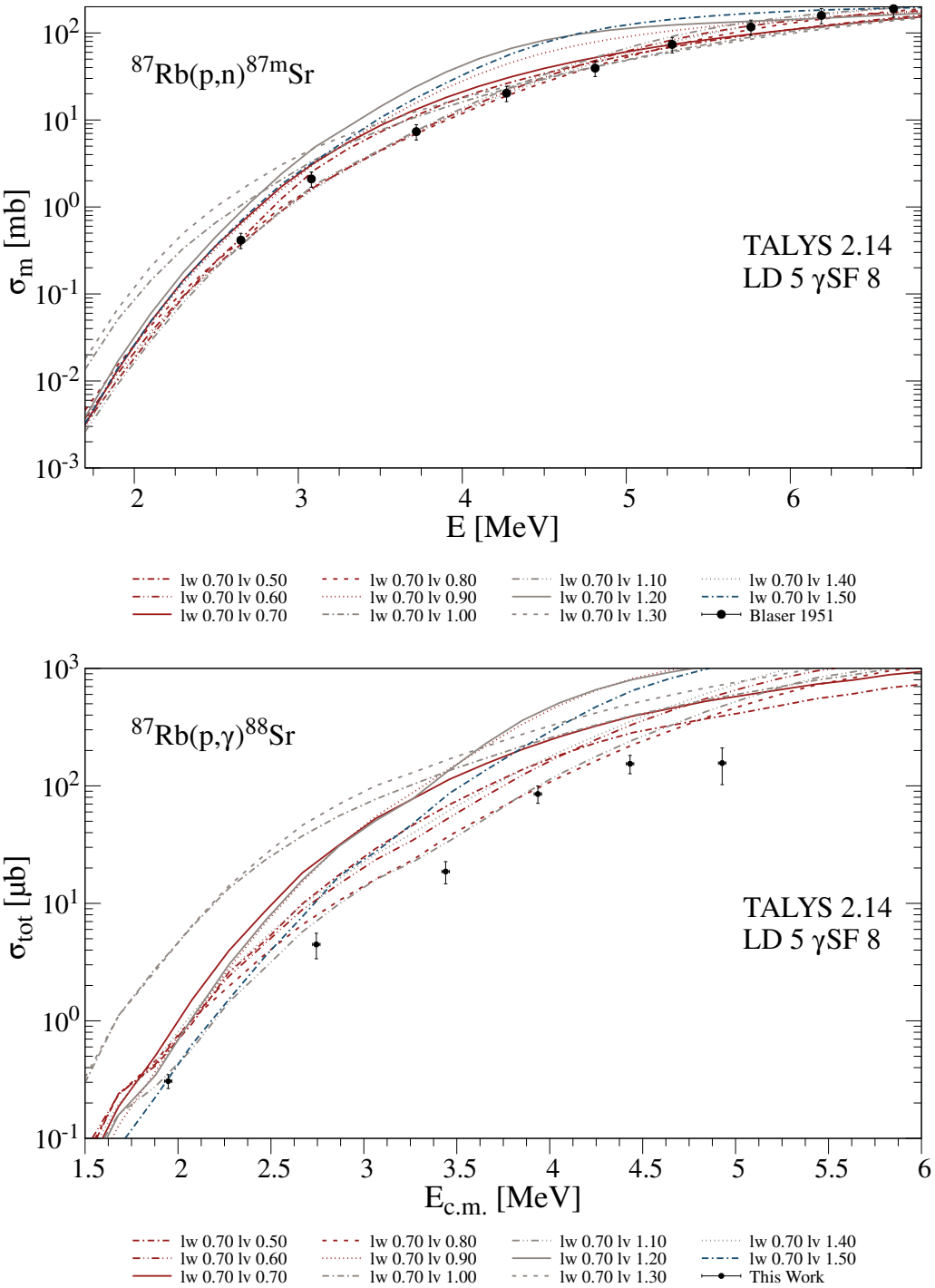

Figure B.2: Variation of *lwadjust* = 0.7 with the altered *lvadjust* for proton-induced reactions on ^{87}Rb.

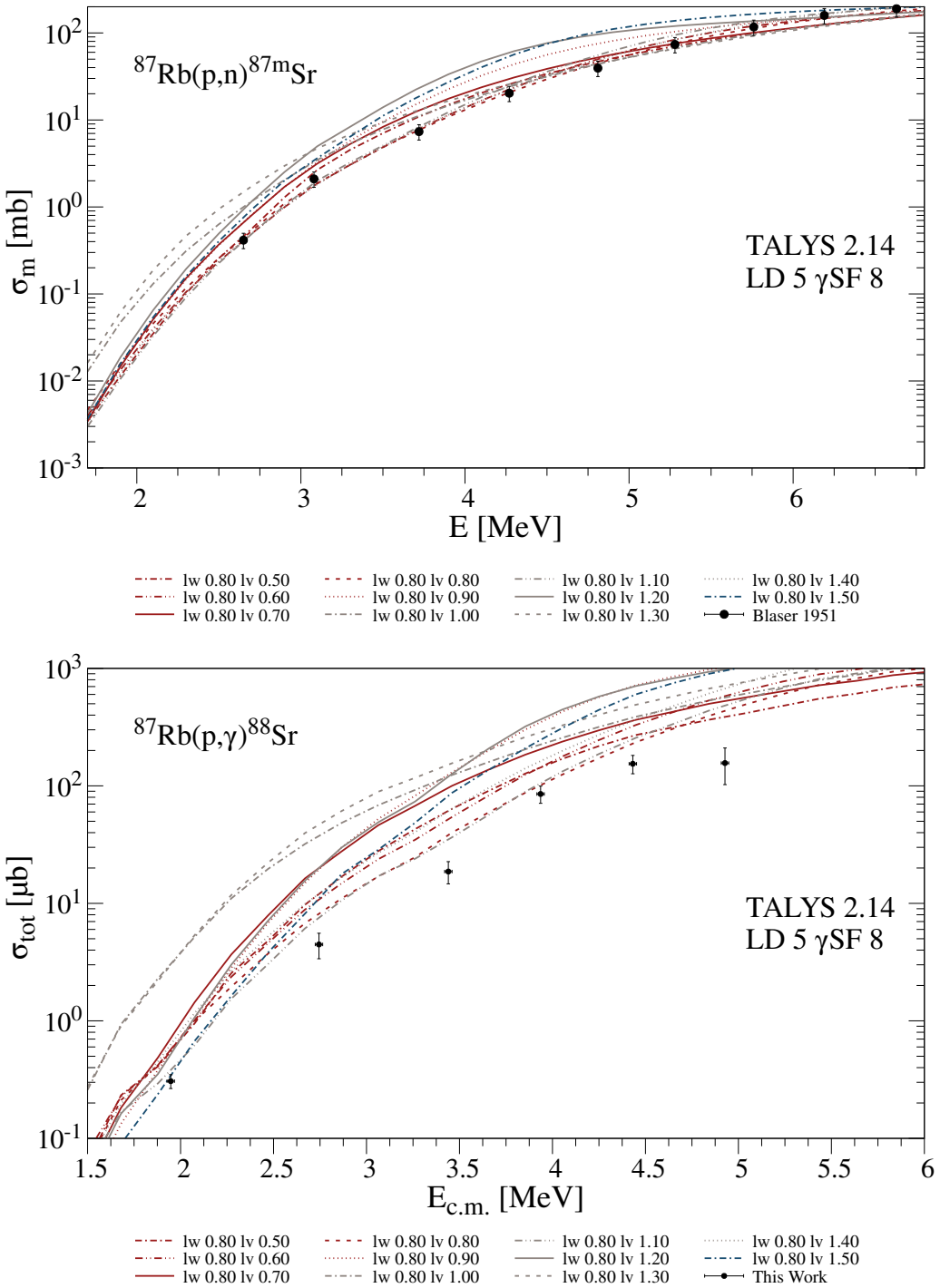

Figure B.3: Variation of *lwadjust* = 0.8 with the altered *lvadjust* for proton-induced reactions on ^{87}Rb.

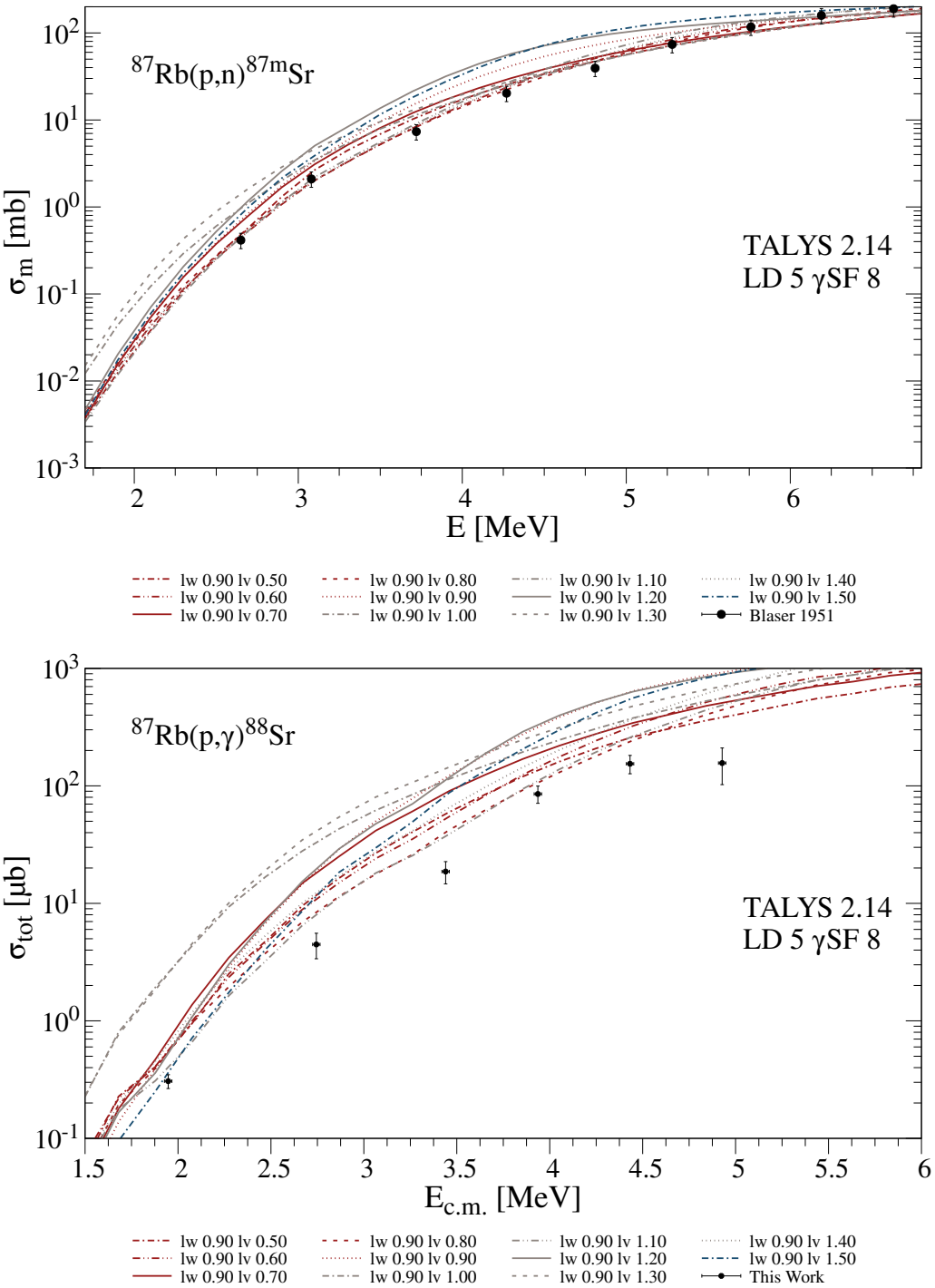

Figure B.4: Variation of *lwadjust* = 0.9 with the altered *lvadjust* for proton-induced reactions on ^{87}Rb.

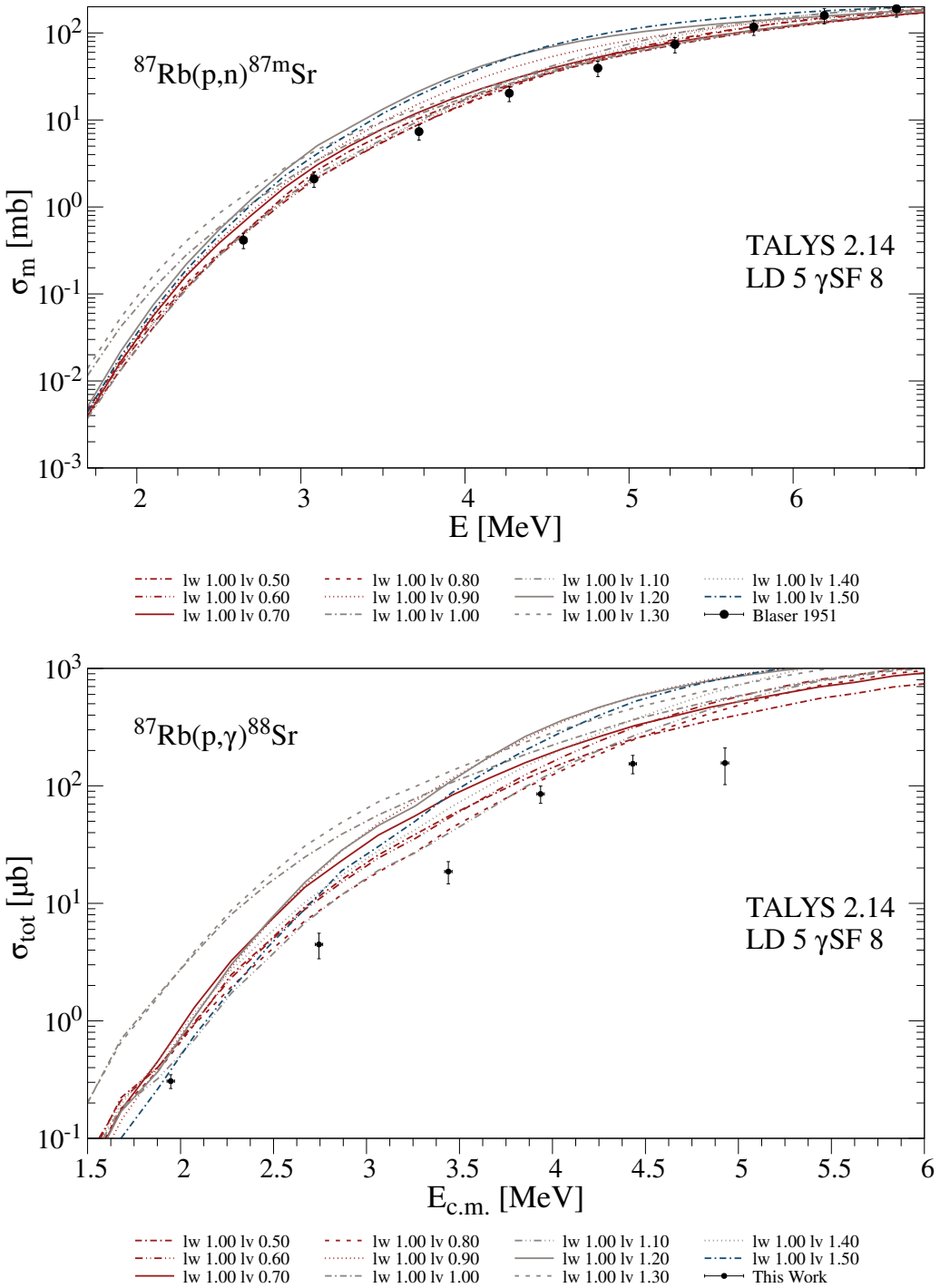

Figure B.5: Variation of *lwadjust* = 1.0 with the altered *lvadjust* for proton-induced reactions on ^{87}Rb.

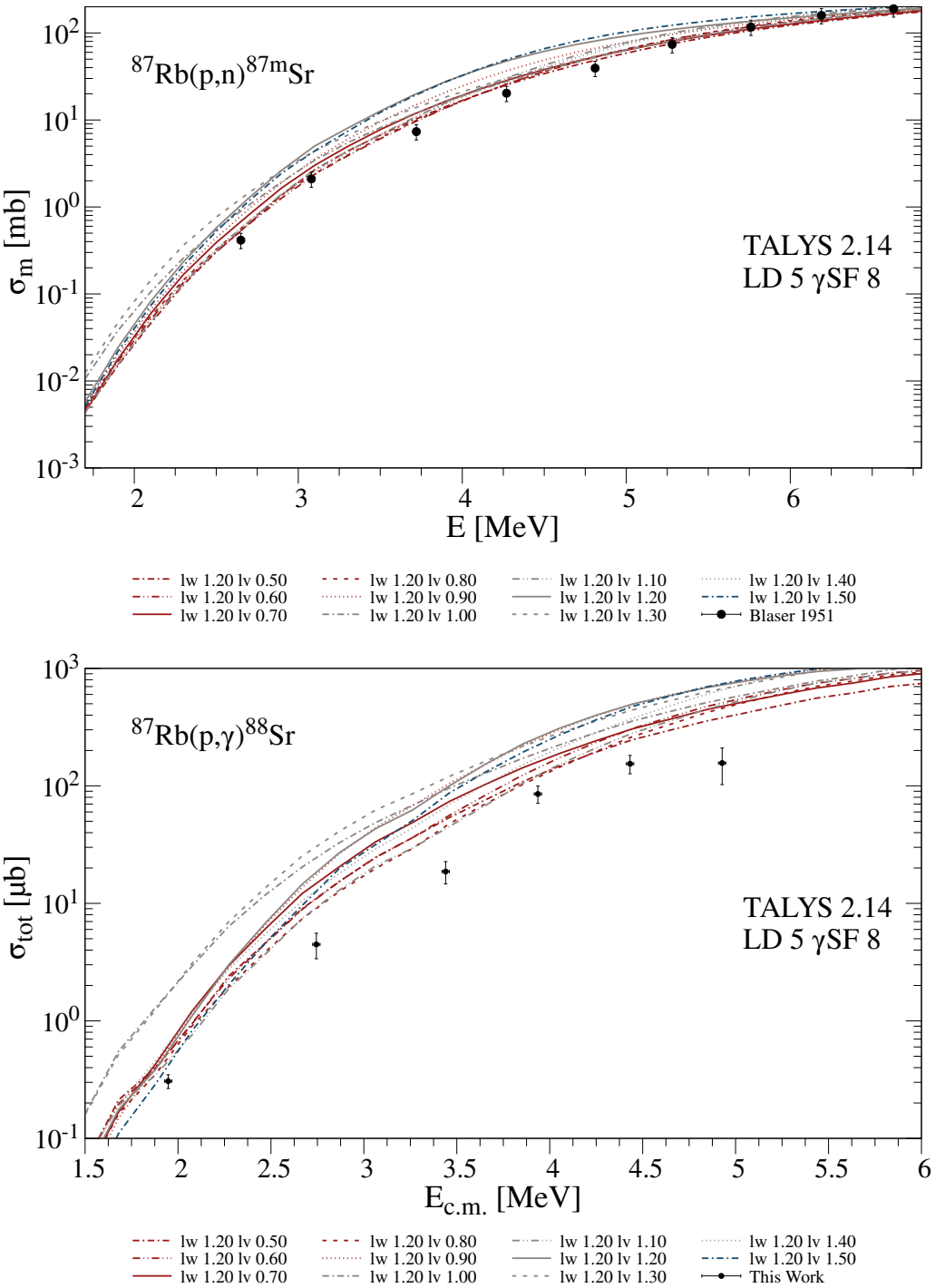

Figure B.6: Variation of *lwadjust* = 1.2 with the altered *lvadjust* for proton-induced reactions on ^{87}Rb.

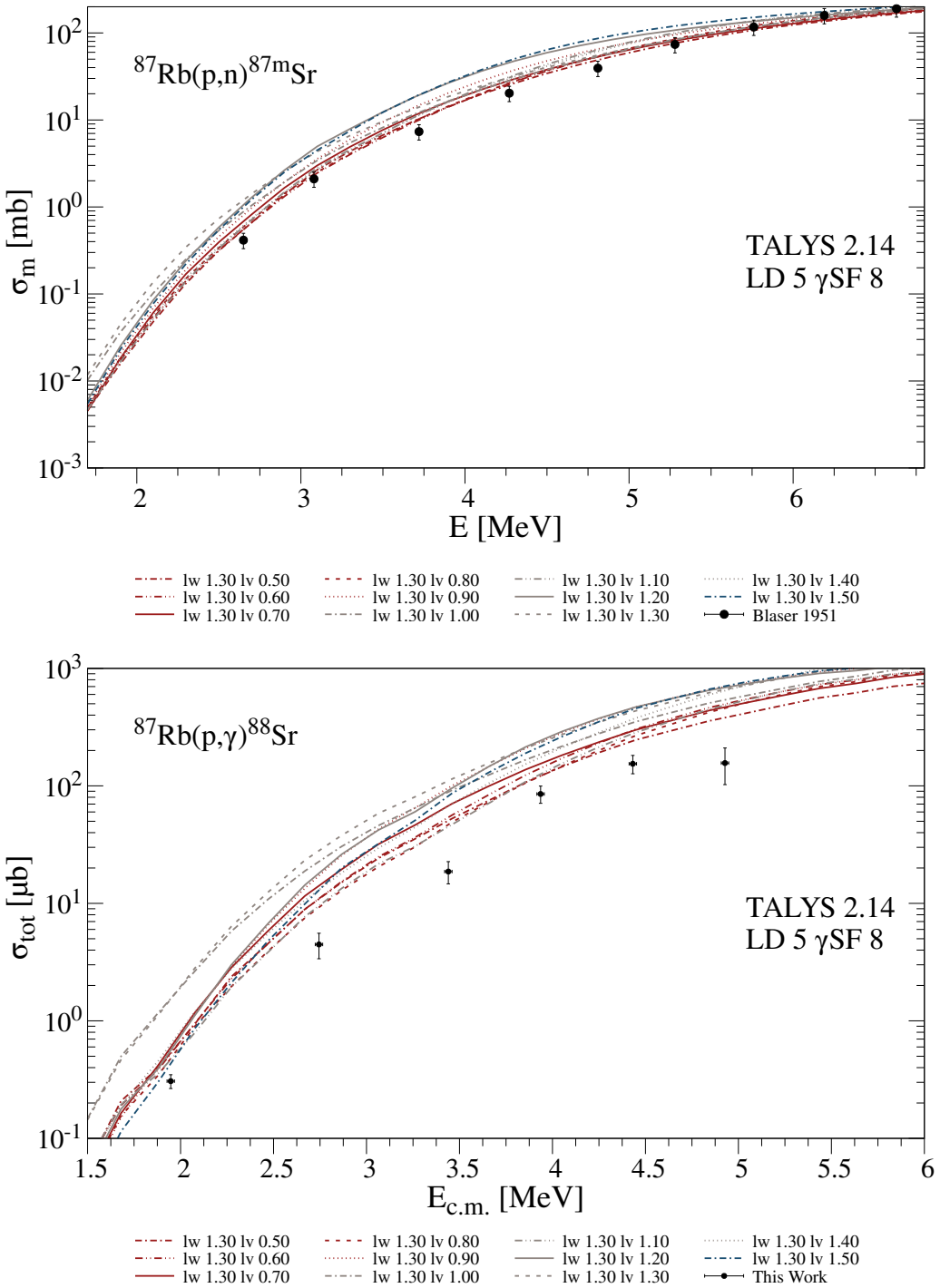

Figure B.7: Variation of *lwadjust* = 1.3 with the altered *lvadjust* for proton-induced reactions on ^{87}Rb.

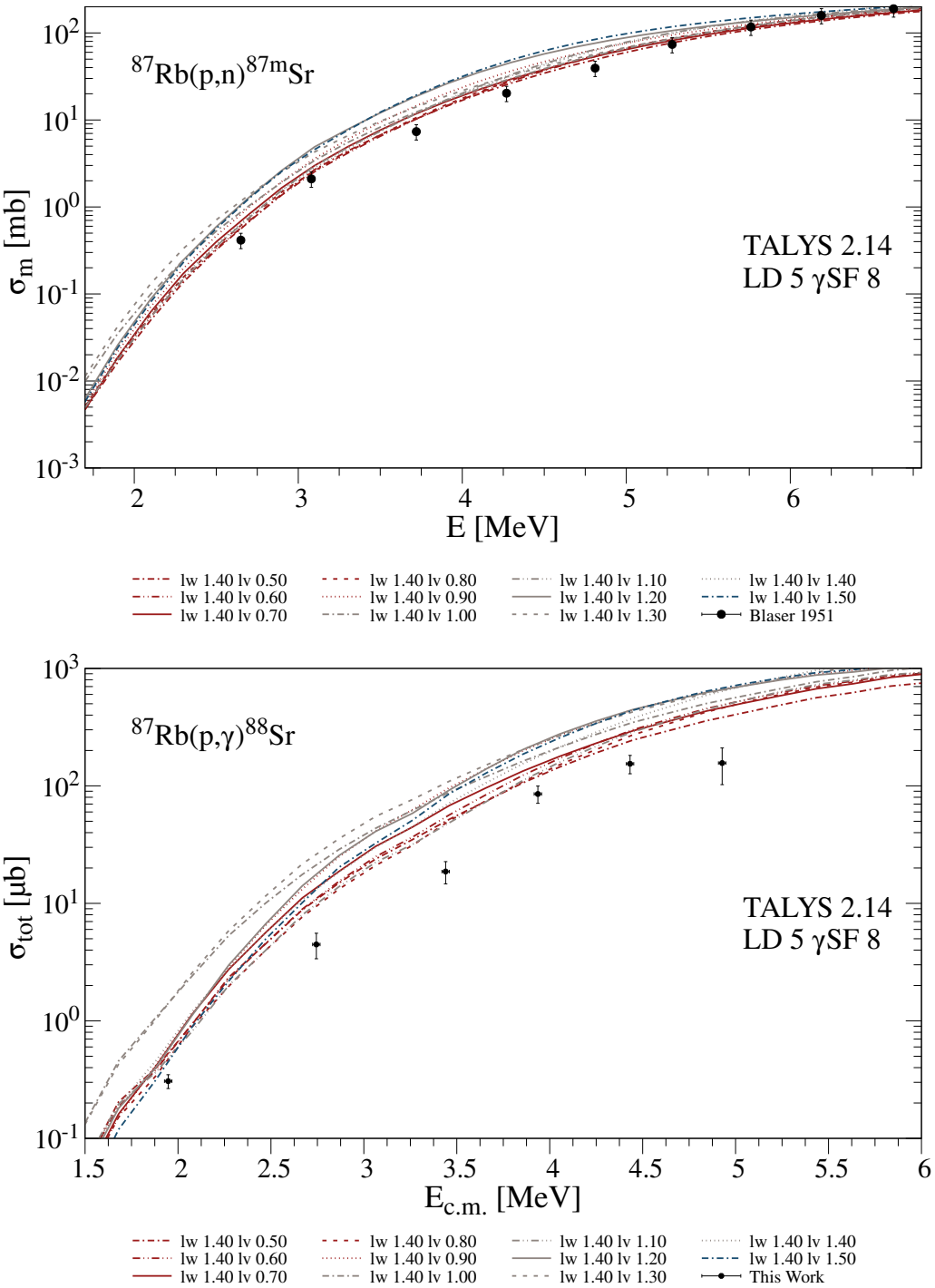

Figure B.8: Variation of *lwadjust* = 1.4 with the altered *lvadjust* for proton-induced reactions on ^{87}Rb.

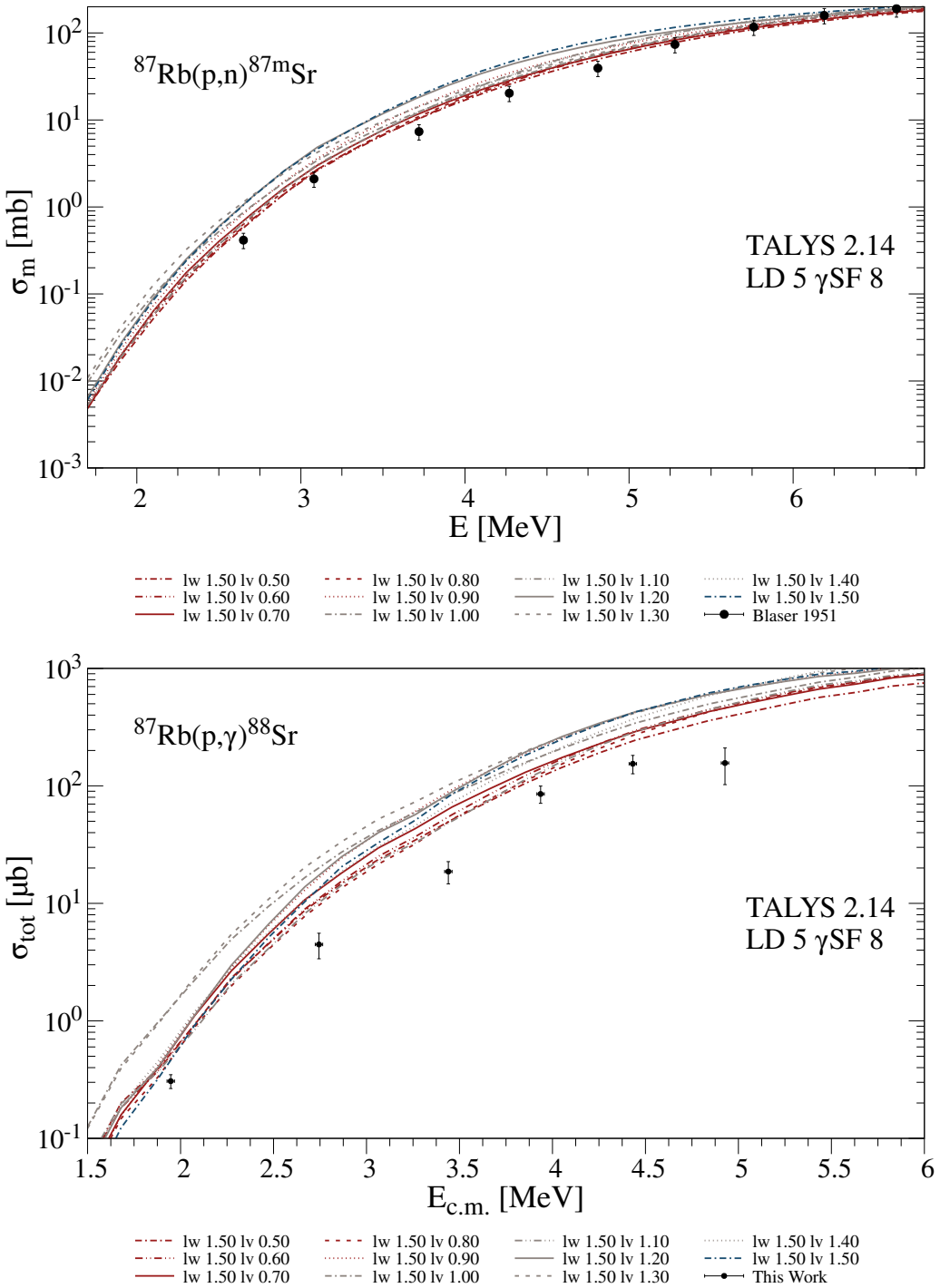

Figure B.9: Variation of *lwadjust* = 1.5 with the altered *lvadjust* for proton-induced reactions on ^{87}Rb.

B.2 Variations of *lwadjust*, *lw1adjust* and *lvadjust*

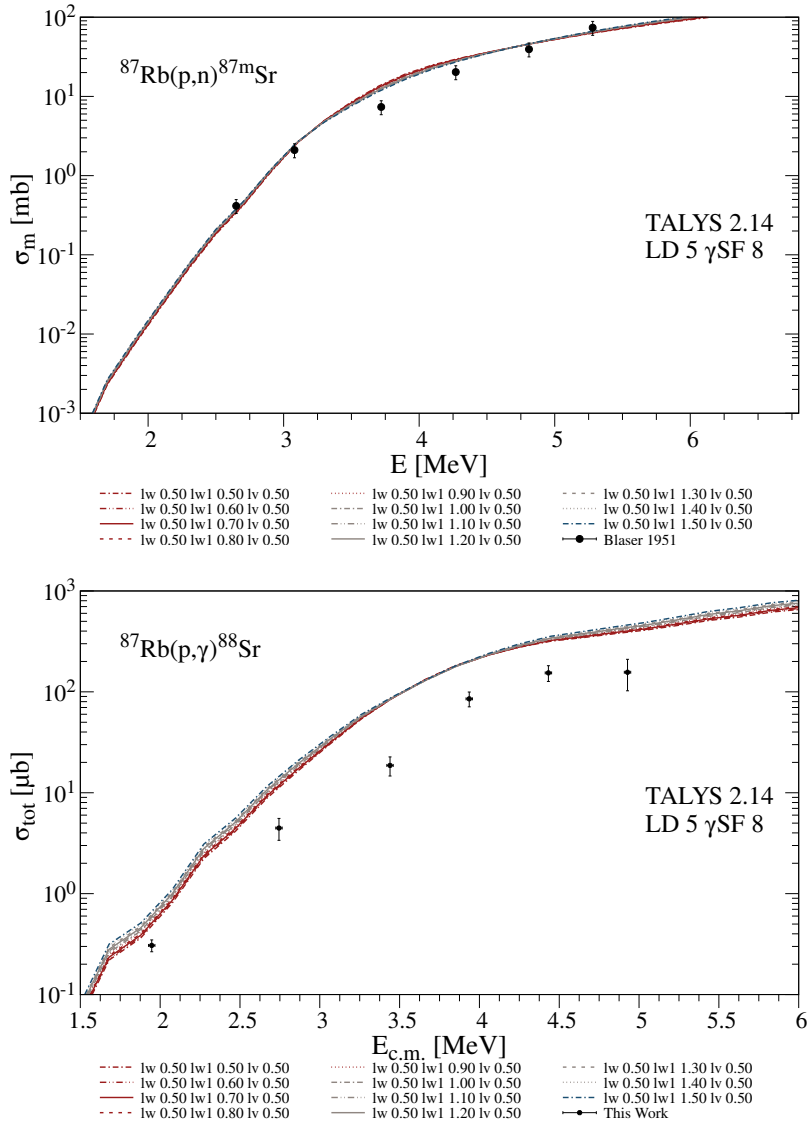

Figure B.10: Variation of $lwadjust = lvadjust = 0.5$ with different values of $lw1adjust$, employing γ-ray strength model 8 for proton-induced reactions on ^{87}Rb. The upper panel shows the predicted isomeric (p, n) cross sections in comparison with the experimental data from Reference [139]. The overall energy dependence is reproduced reasonably well, although not all data points are accurately described. A similar behavior is observed in the lower panel, which compares the predicted and experimental cross sections for the (p, γ) reaction.

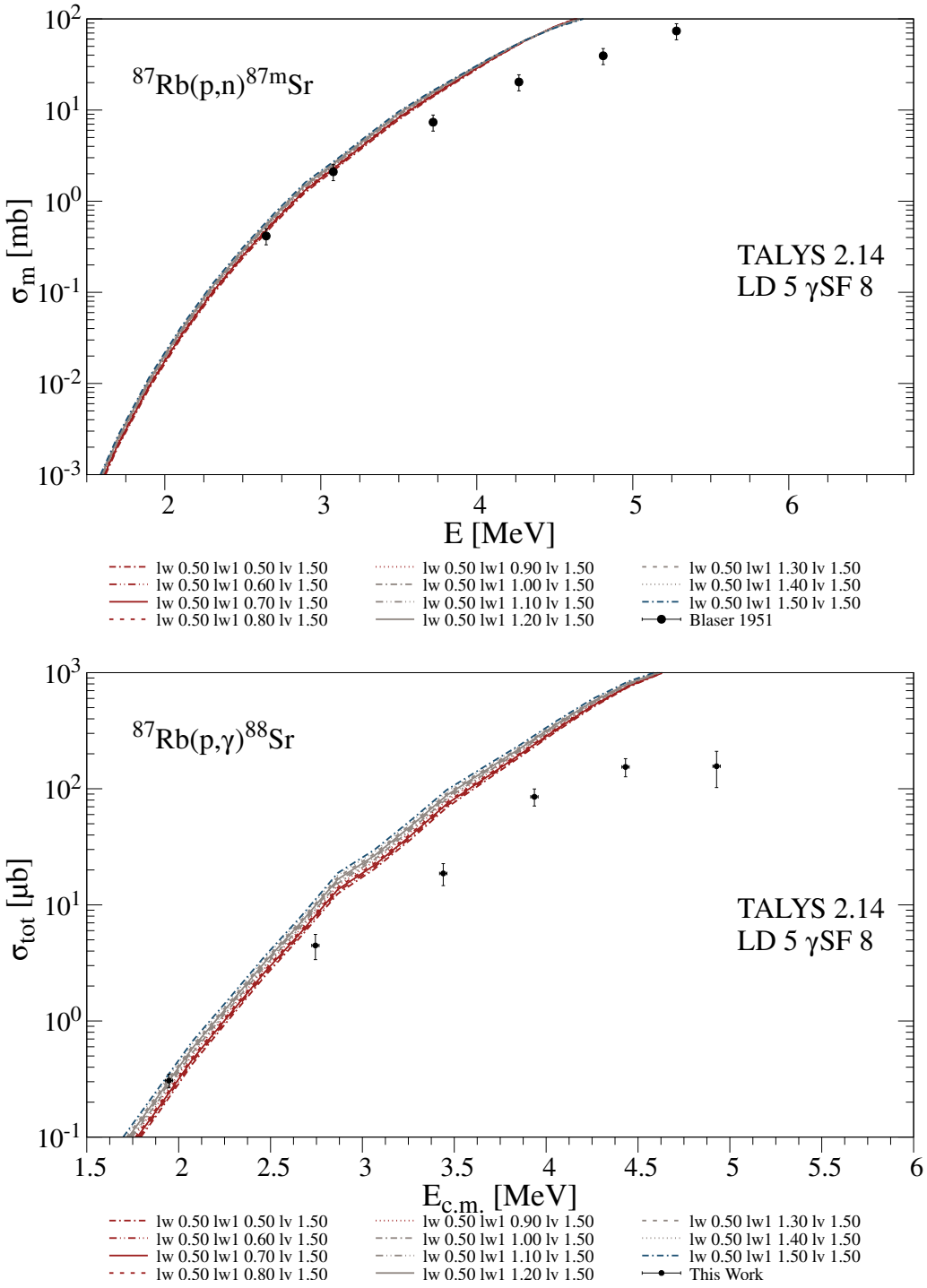

Figure B.11: The same as before with *lwadjust* = 0.5 and *lvadjust* = 1.5.

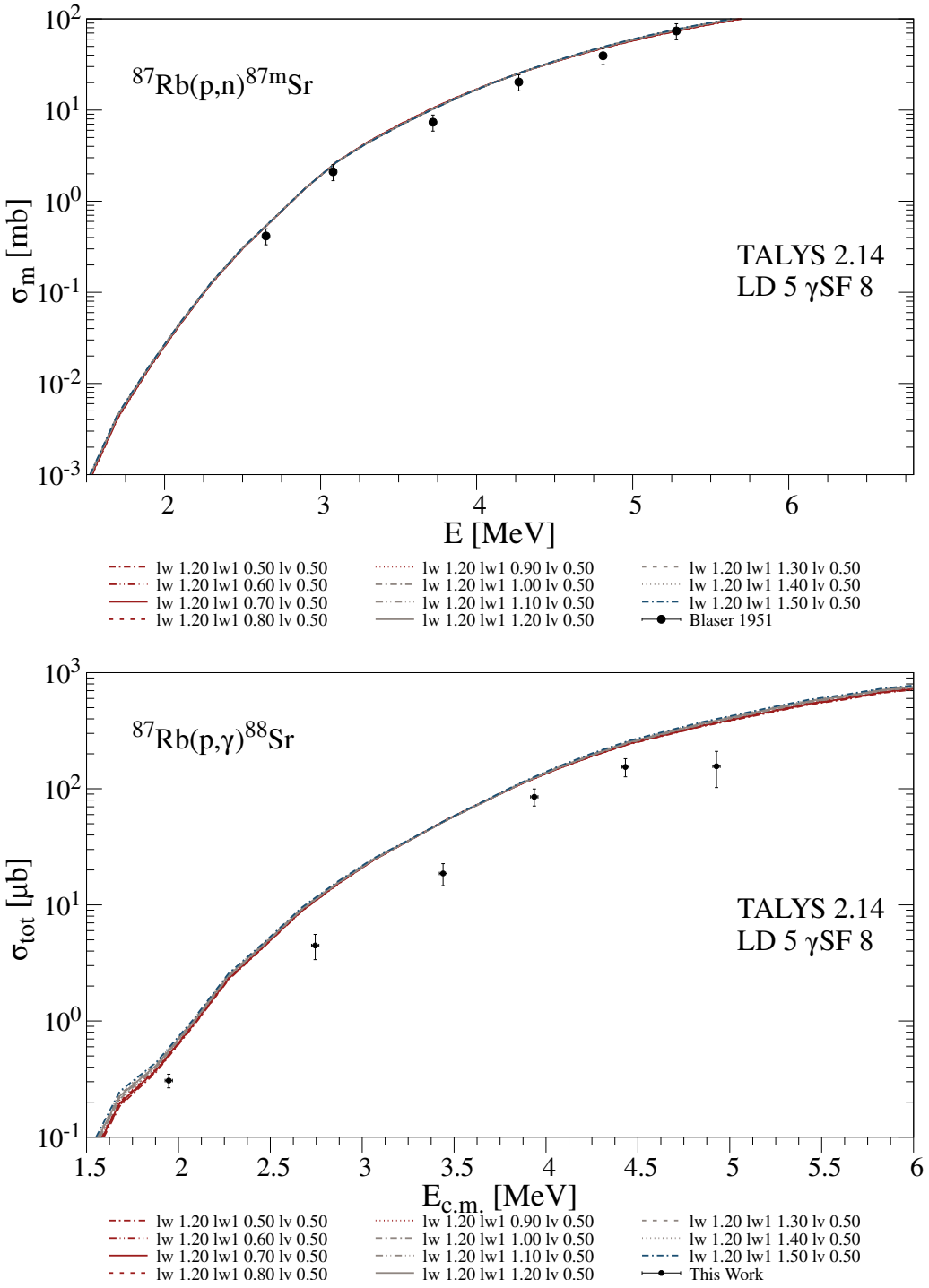

Figure B.12: The same as before with *lwadjust* = 1.2 and *lvadjust* = 0.5.

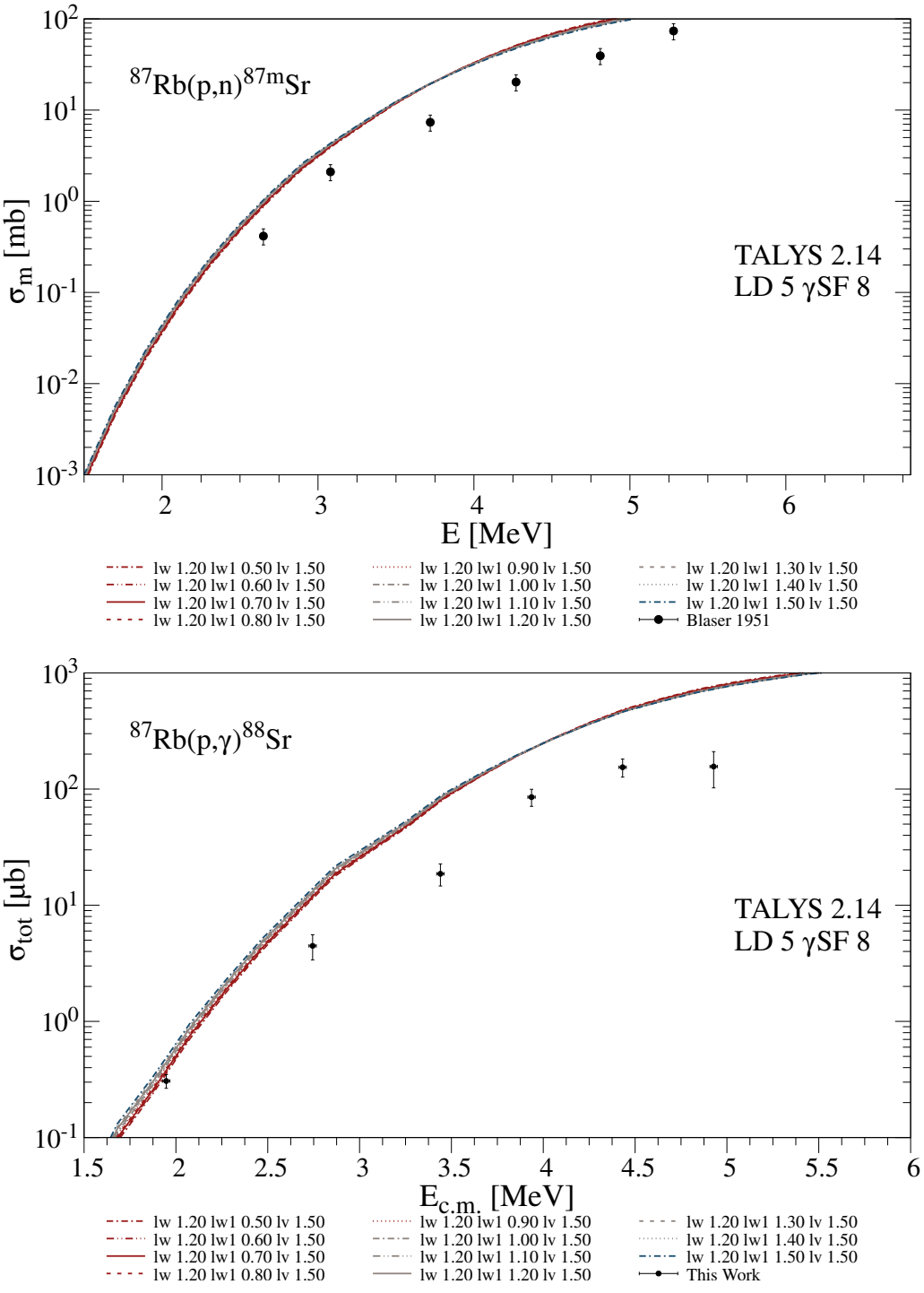

Figure B.13: The same as before with *lwadjust* = 1.2 and *lvadjust* = 1.5.

B.3 Variations of *lwadjust*, *lvadjust* and *lv1adjust*

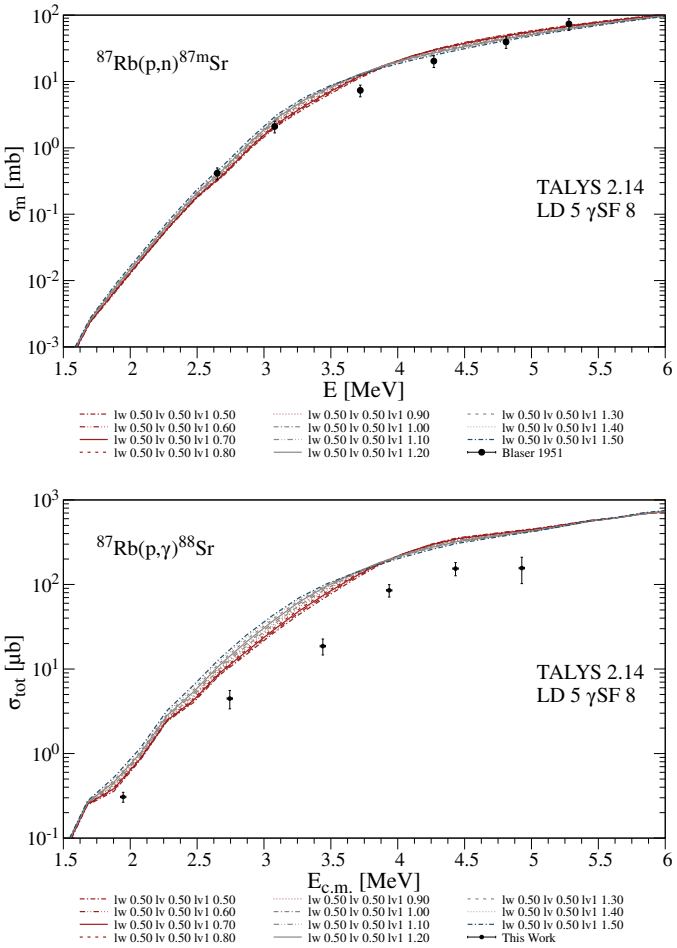

Figure B.14: Variation of $lwadjust = lvadjust = 0.5$ with different values of $lv1adjust$, employing γ-ray strength model 8 for proton-induced reactions on ^{87}Rb. The influence on predicted cross sections is slightly greater than for variations of $lw1adjust$ in the presented energy region. The upper panel shows the predicted isomeric (p, n) cross sections in comparison with the experimental data from Reference [139]. The overall energy dependence is reproduced reasonably well, although not all data points are accurately described. A similar behavior is observed in the lower panel, which compares the predicted and experimental cross sections for the (p, γ) reaction.

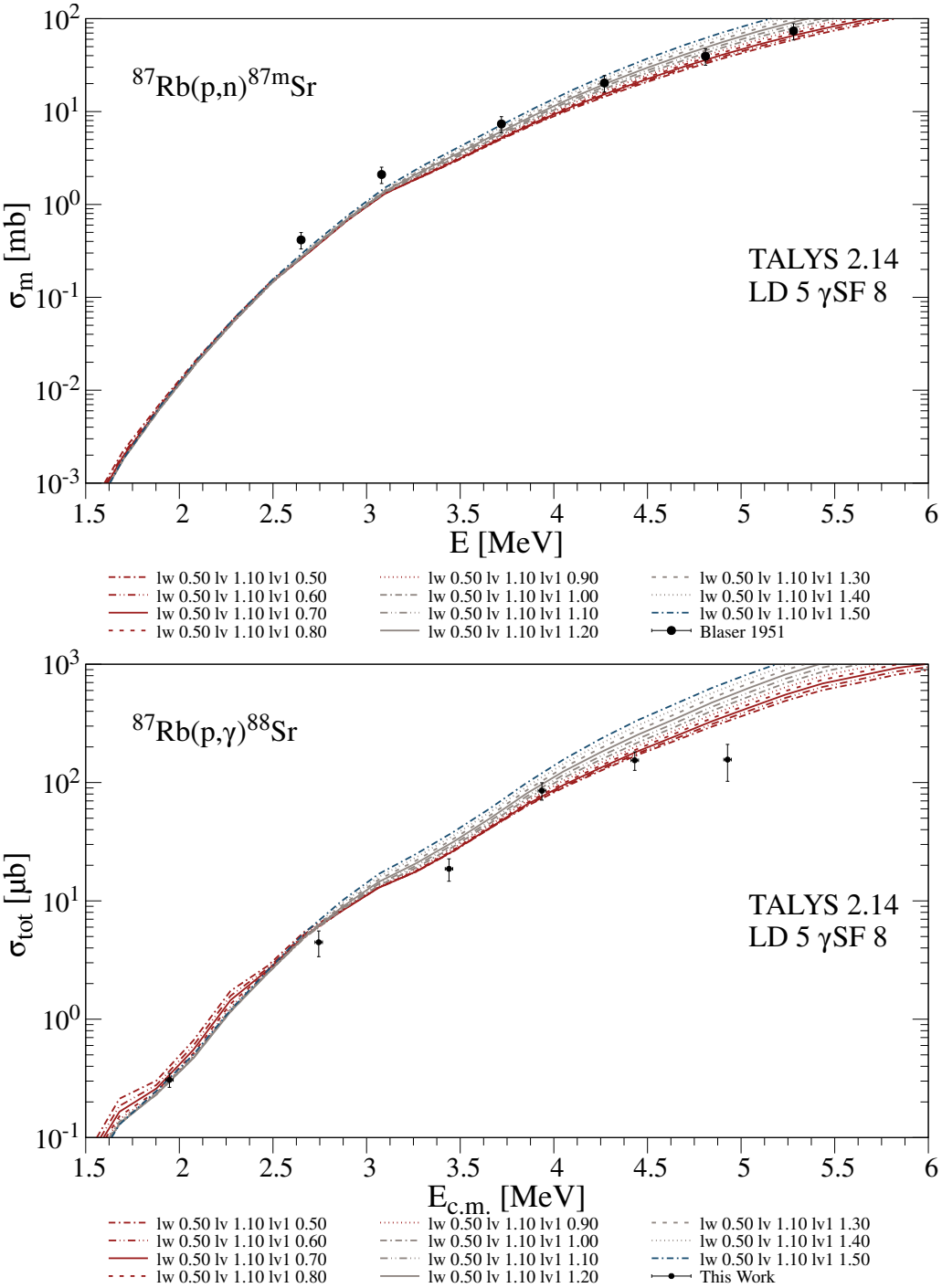

Figure B.15: The same as before with $lwadjust = 0.5$ and $lvadjust = 1.1$.

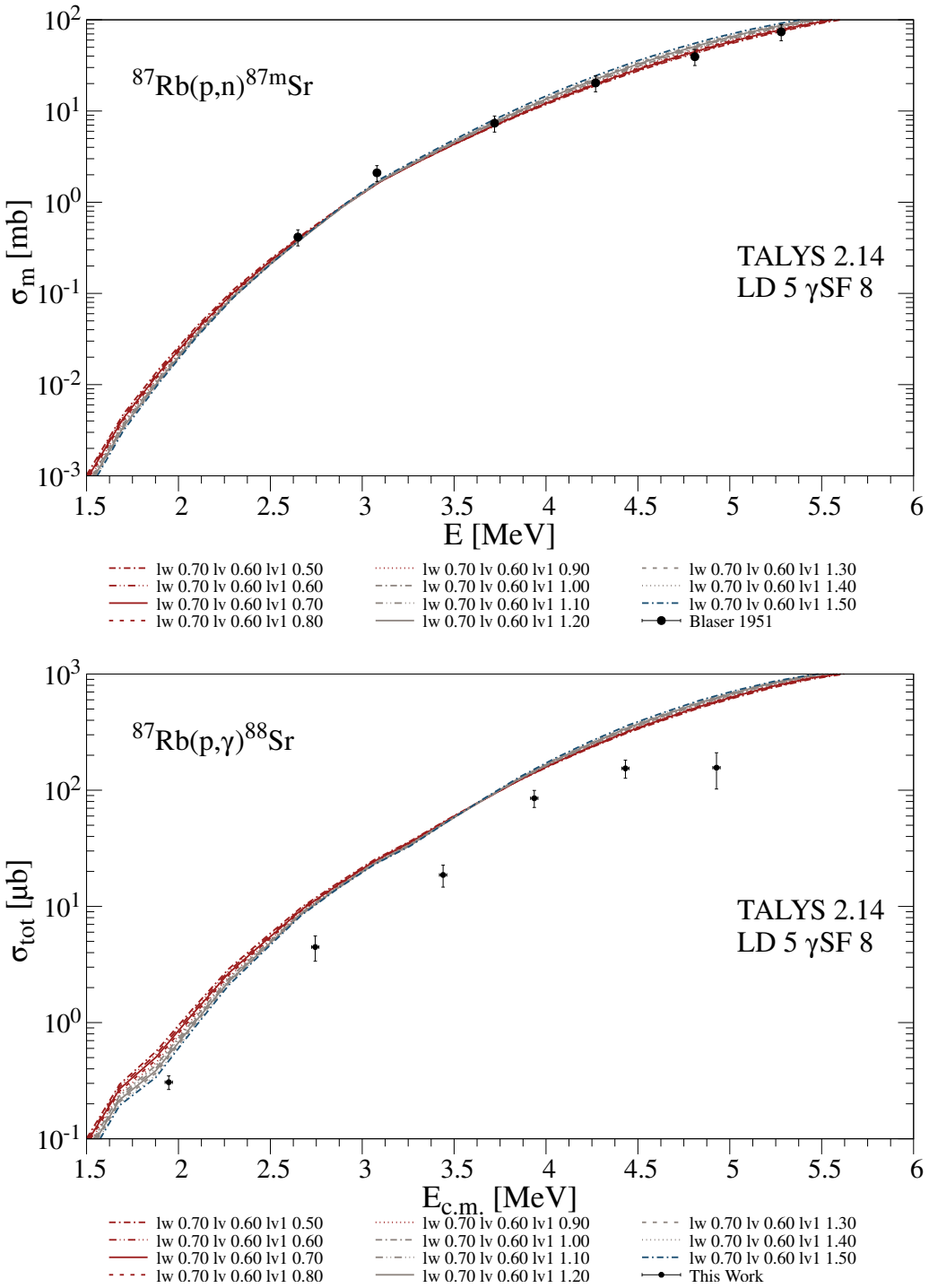

Figure B.16: The same as before with *lwadjust* = 0.7 and *lvadjust* = 0.6.

B.4 Variations of *lwadjust*, *lwsoadjust* and *lvadjust*

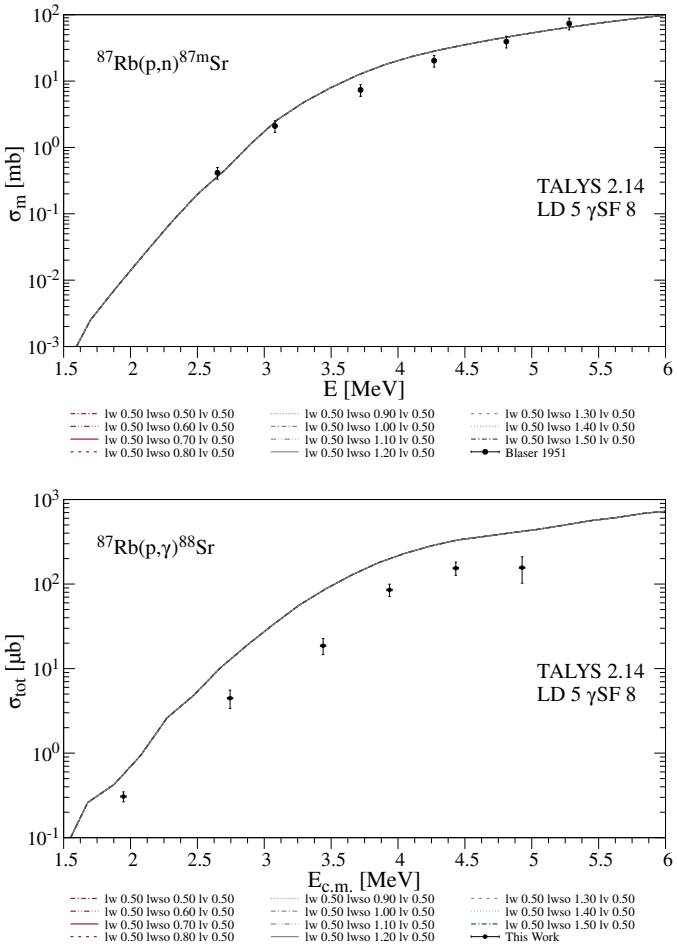

Figure B.17: Variation of $lwadjust = lvadjust = 0.5$ with different values of $lwsoadjust$, employing γ-ray strength model 8 for proton-induced reactions on ^{87}Rb. The upper panel shows the predicted isomeric (p, n) cross sections in comparison with the experimental data from Reference [139]. The lower panel shows the comparison of the predicted to experimental cross sections for the (p, γ) reaction. The influence of varying $lwsoadjust$ is negligible.

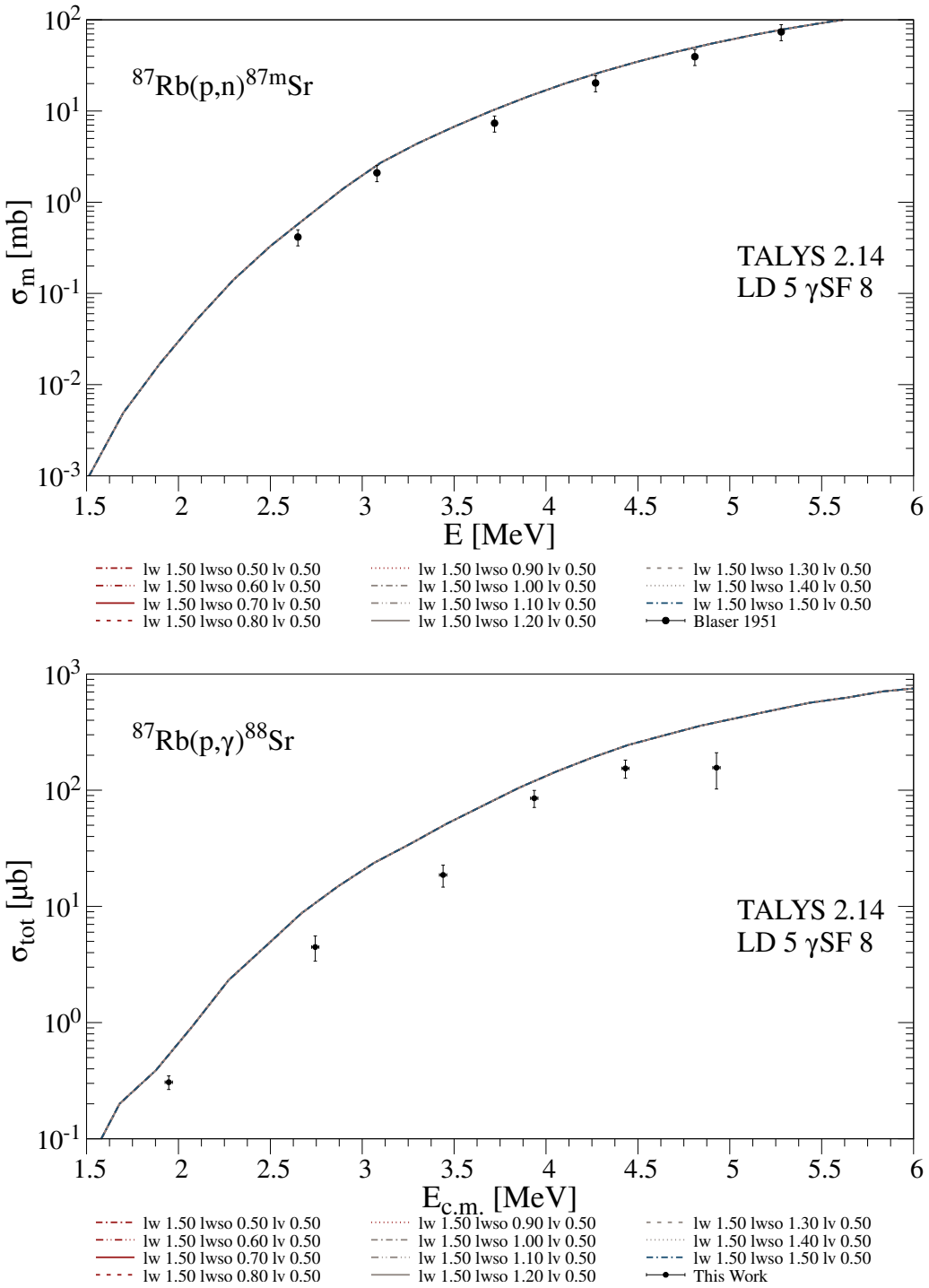

Figure B.18: The same as before with *lwadjust* = 1.5 and *lvadjust* = 0.5.

B.5 Variations of *lwadjust*, *lvadjust* and *lvsoadjust*

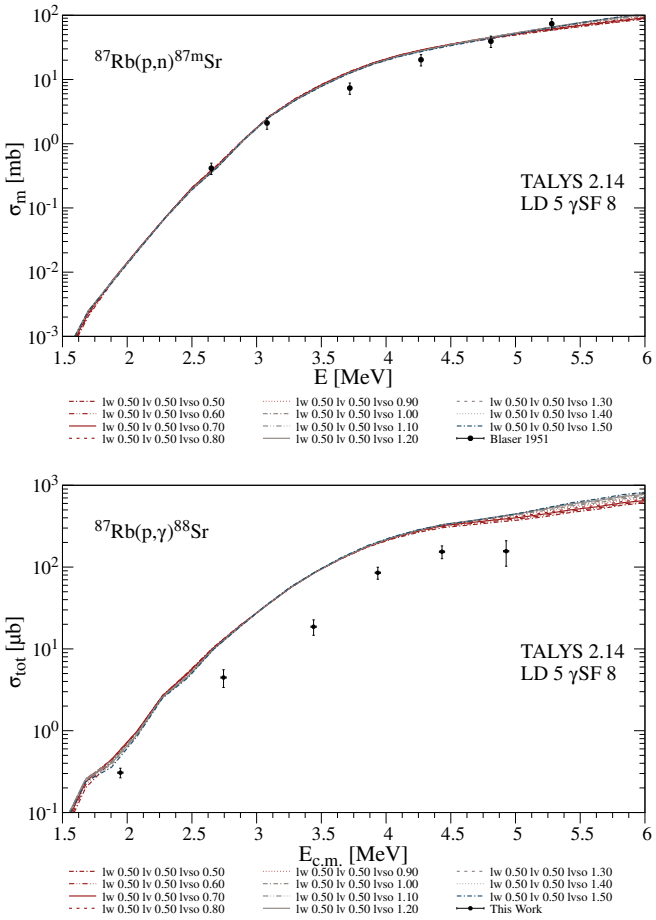

Figure B.19: Variation of $lwadjust = lvadjust = 0.5$ with different values of $lvsoadjust$, employing γ-ray strength model 8 for proton-induced reactions on ^{87}Rb. The upper panel shows the predicted isomeric (p, n) cross sections in comparison with the experimental data from Reference [139]. The lower panel shows the comparison of the predicted to experimental cross sections for the (p, γ) reaction. The influence of varying $lwsoadjust$ is negligible.

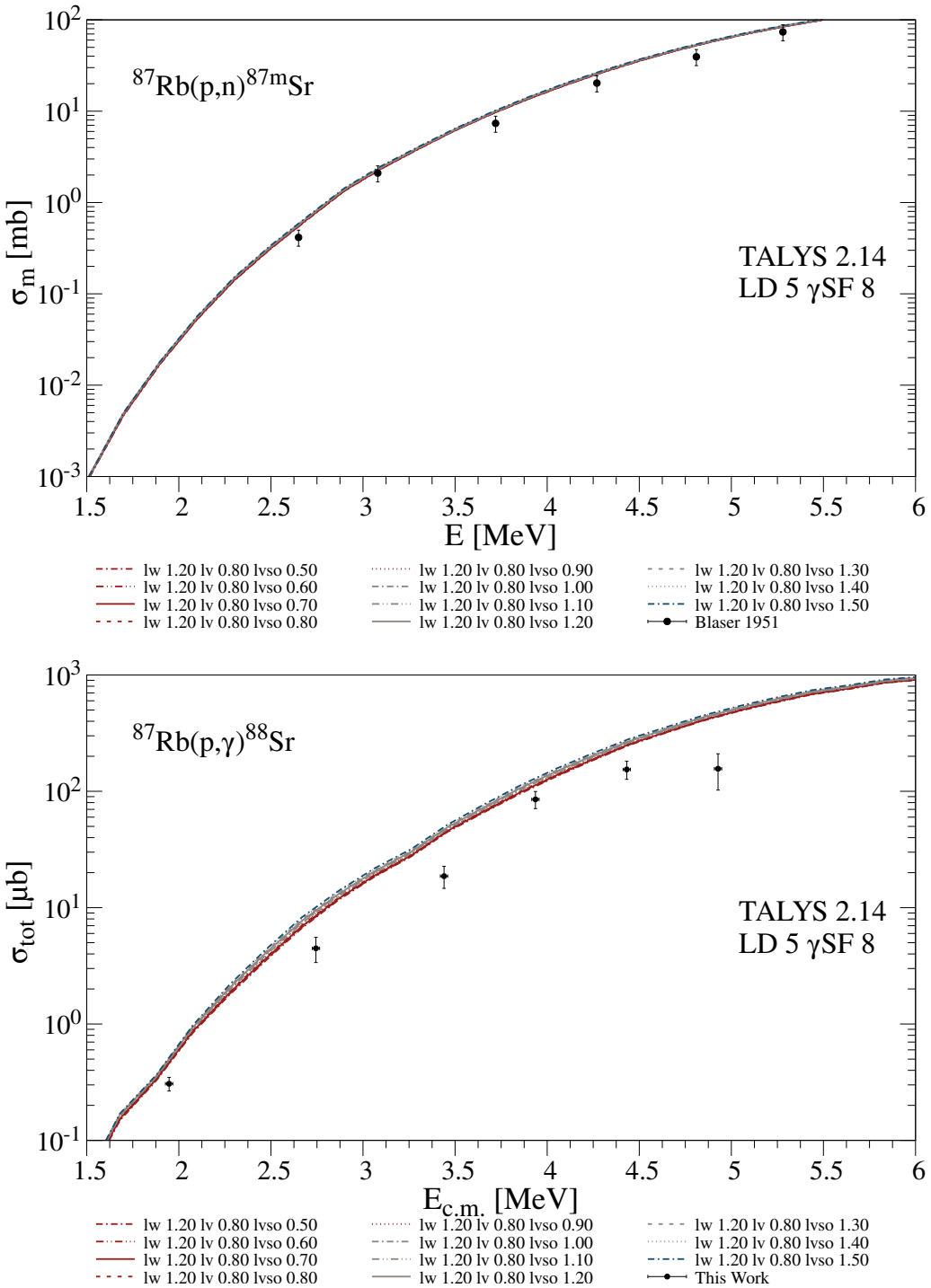

Figure B.20: The same as before with *lwadjust* = 1.2 and *lvadjust* = 0.8.

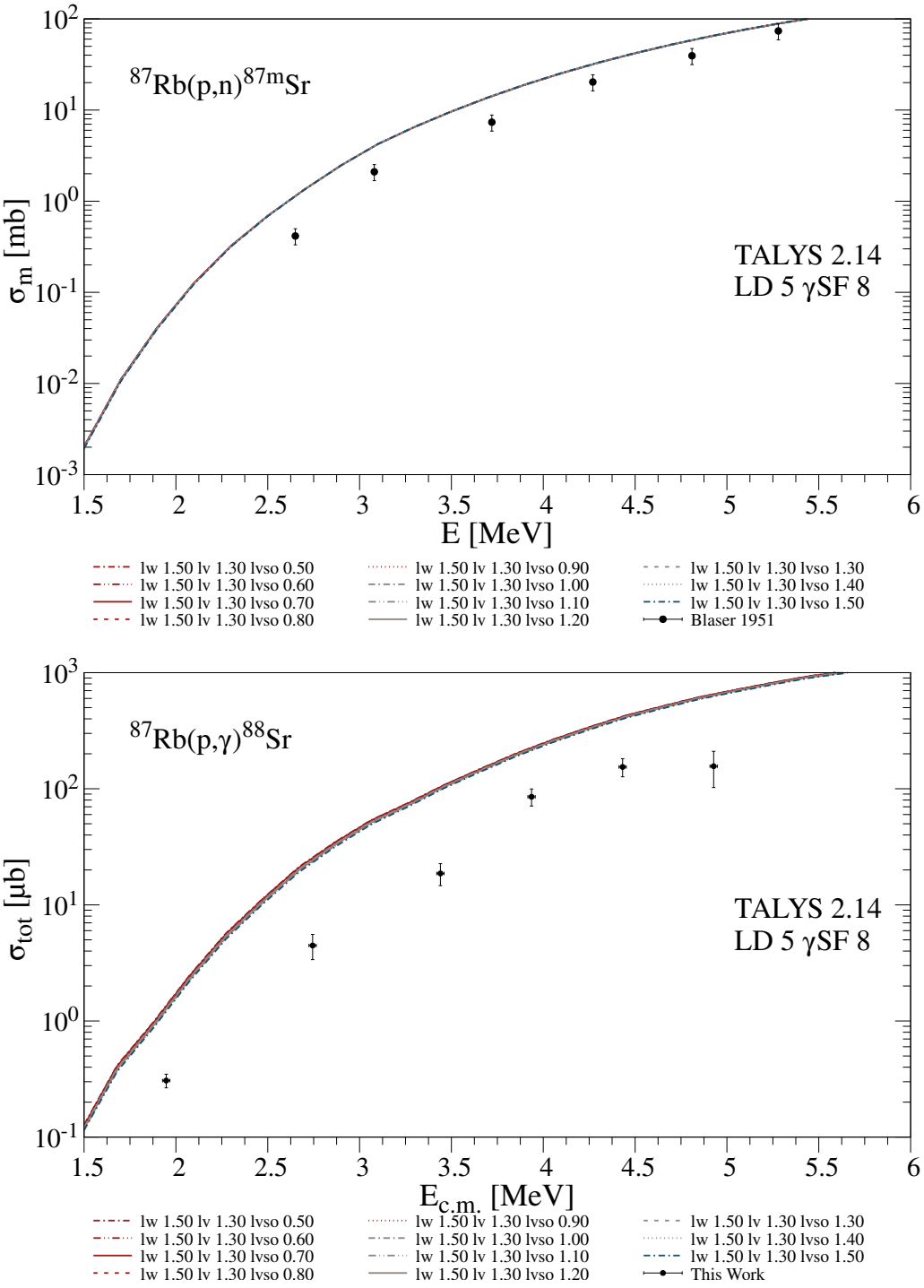

Figure B.21: The same as before with *lwadjust* = 1.5 and *lvadjust* = 1.3.

B.6 Variations of *lwadjust* and *lvadjust* utilizing γ-strength model 10

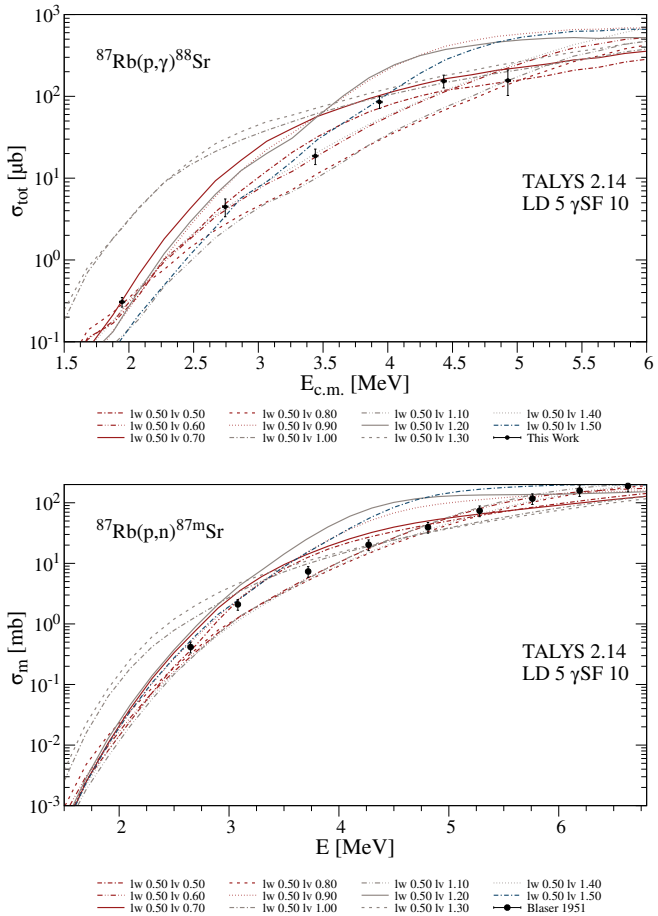

Figure B.22: Variation of *lwadjust* = 0.5 with the altered *lvadjust* for proton-induced reactions on ^{87}Rb. utilizing γ-ray strength model 10.

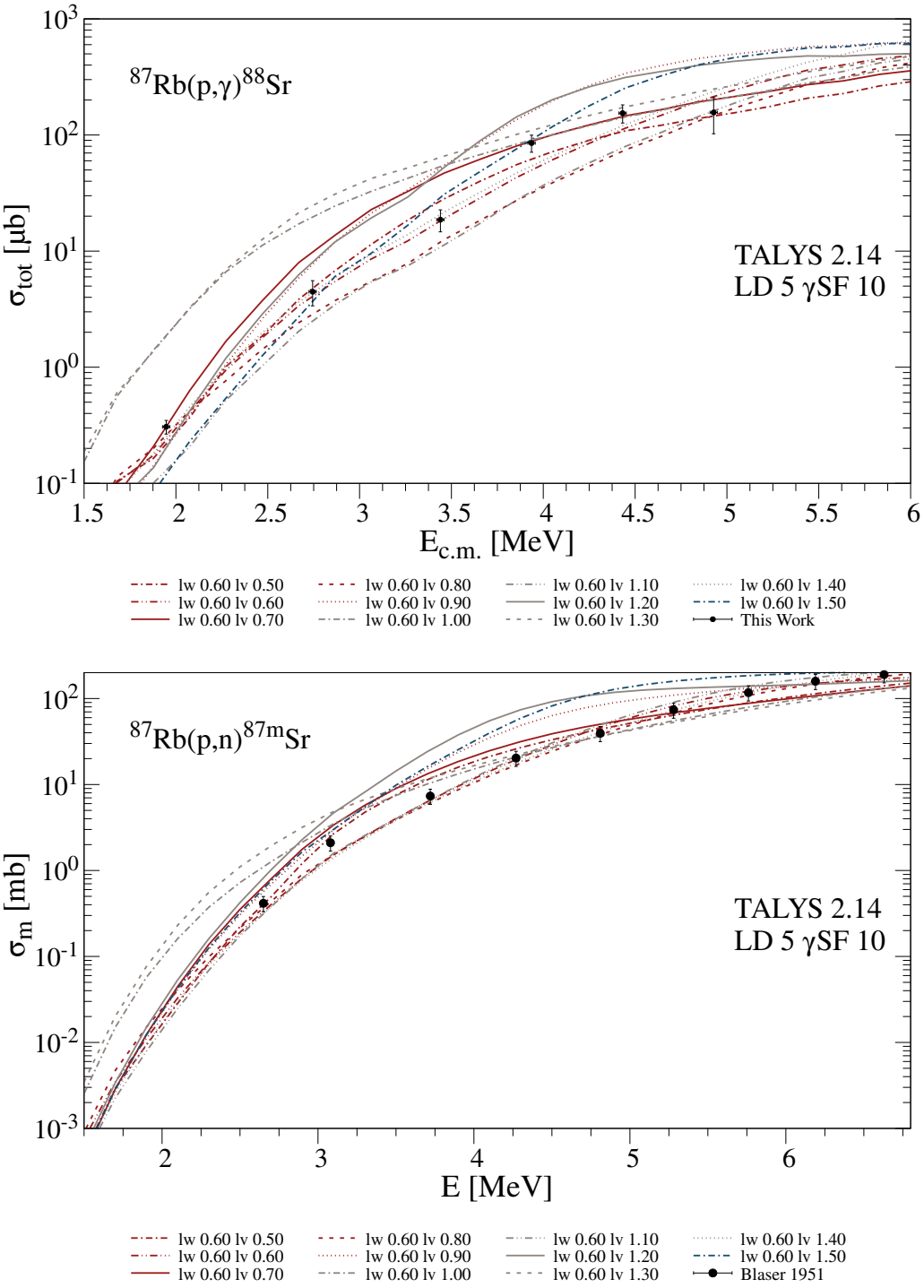

Figure B.23: The same as before with $lwadjust = 0.6$.

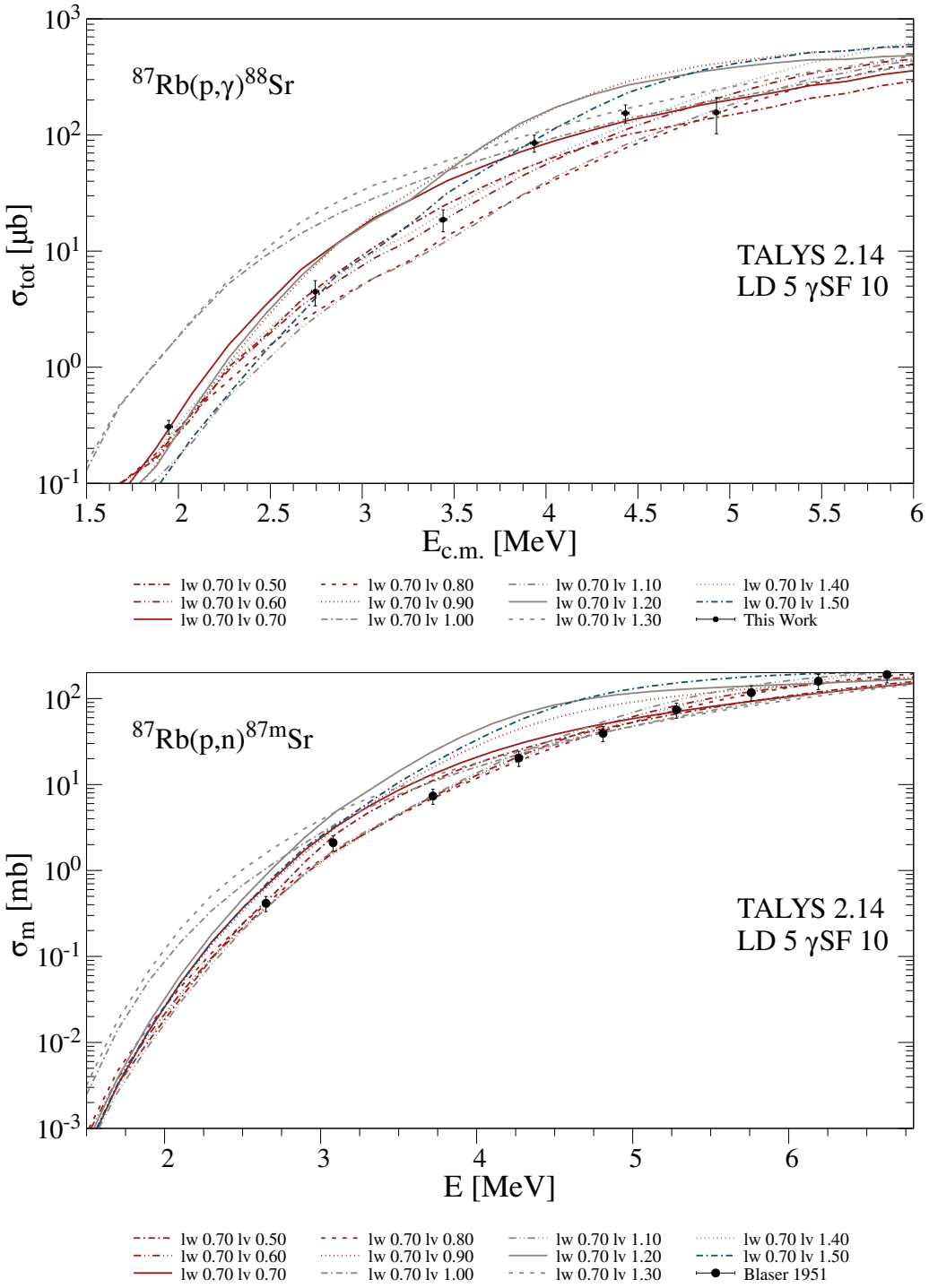

Figure B.24: The same as before with *lwadjust* = 0.7.

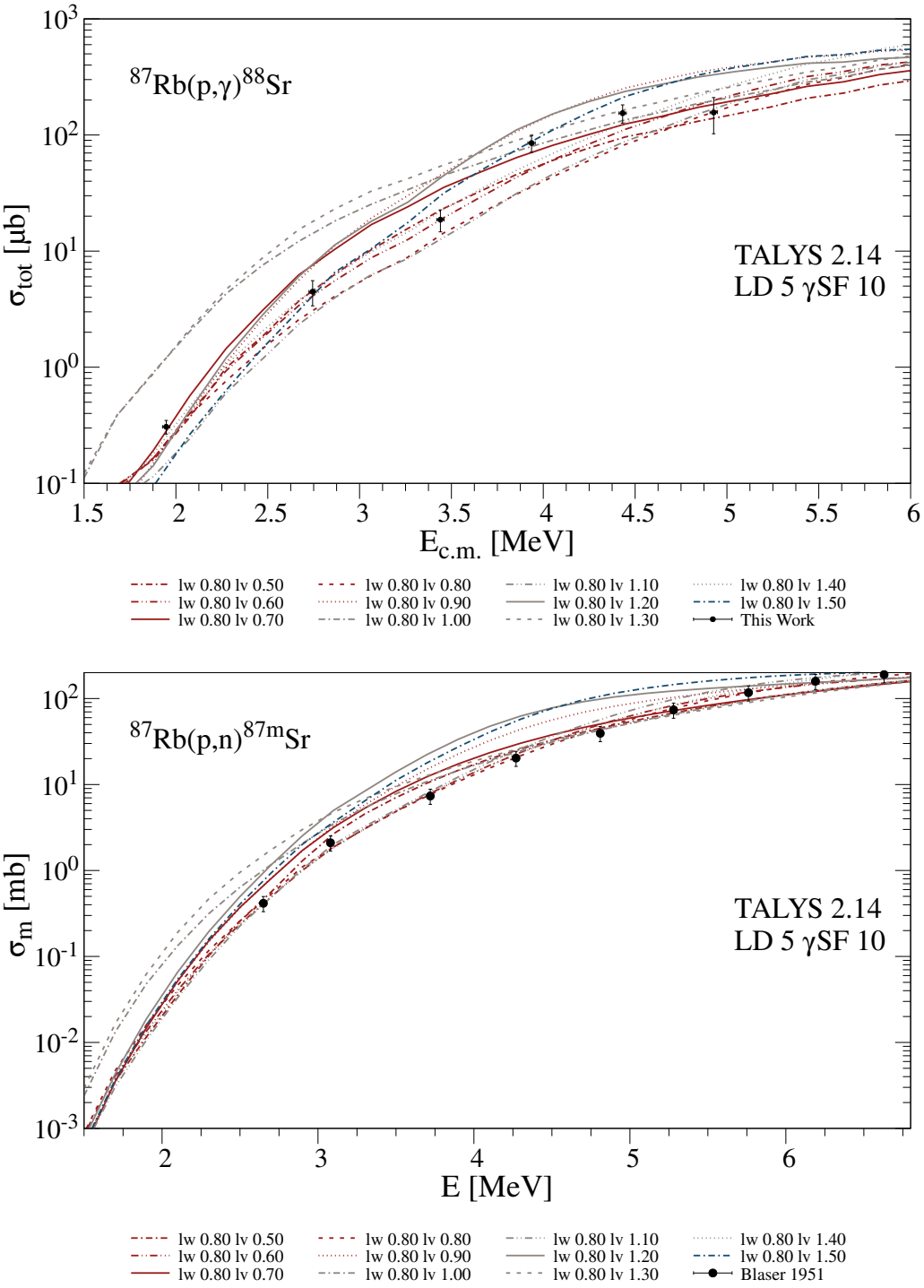

Figure B.25: The same as before with $lwadjust = 0.8$.

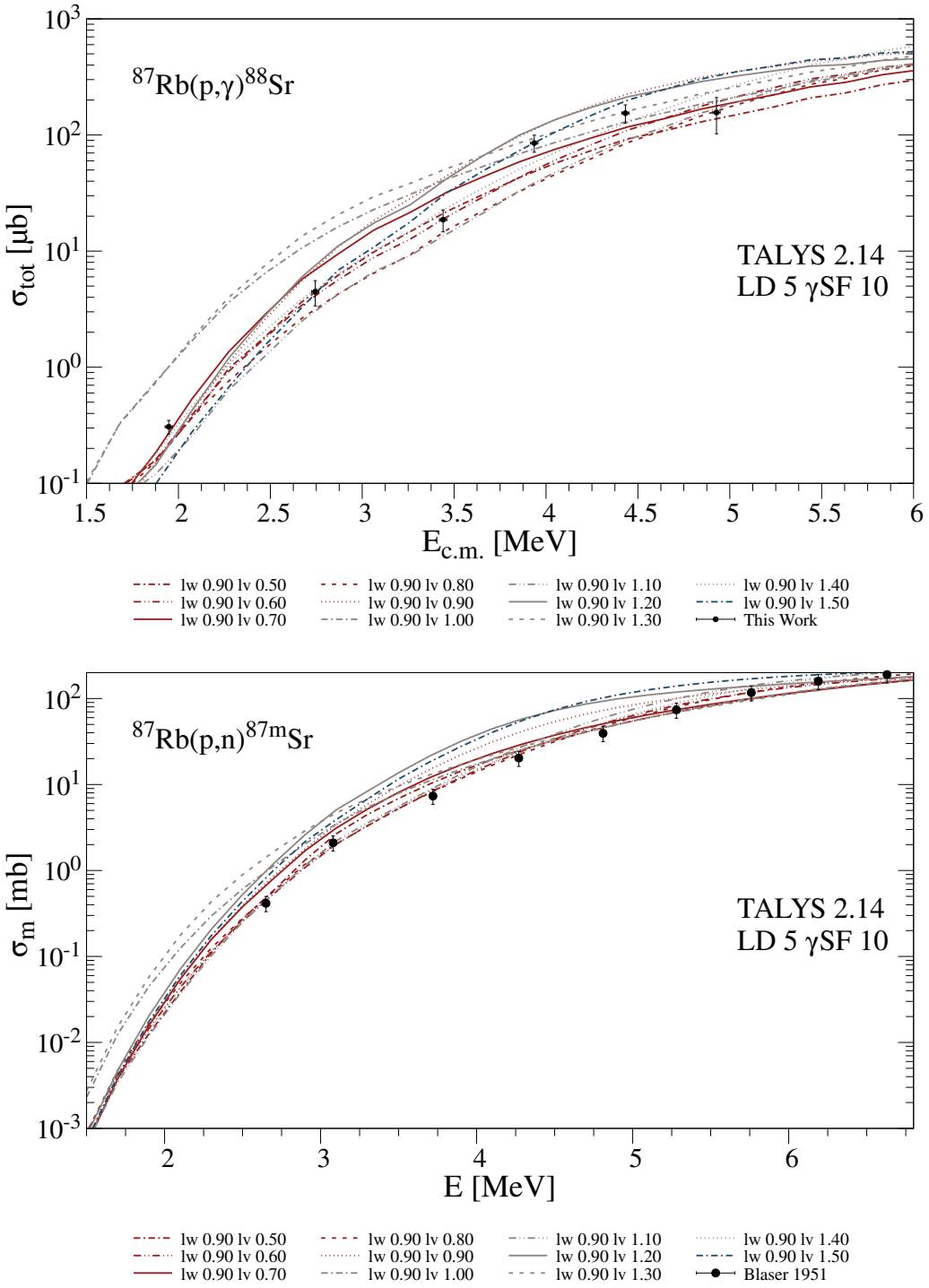

Figure B.26: The same as before with *lwadjust* = 0.9.

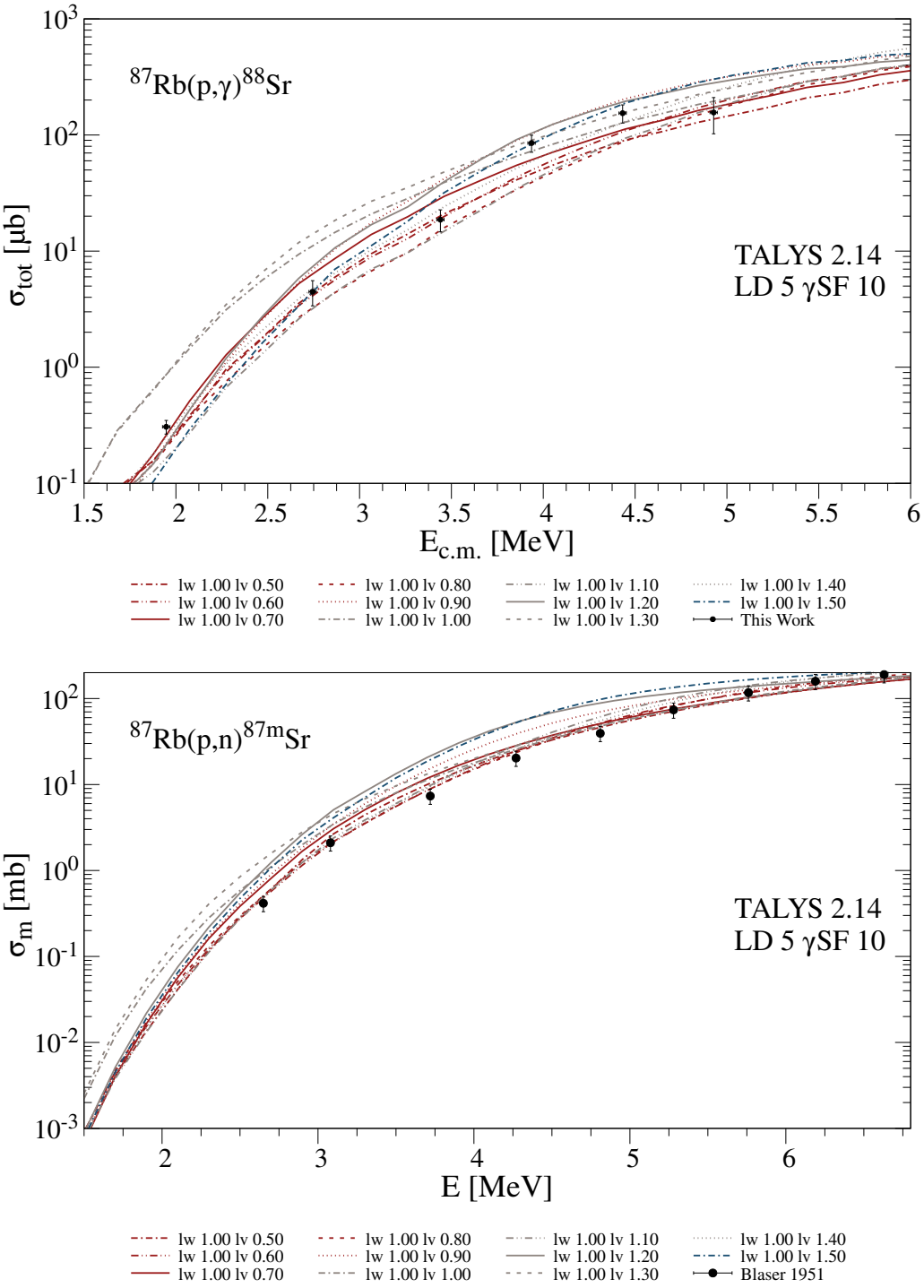

Figure B.27: The same as before with *lwadjust* = 1.0.

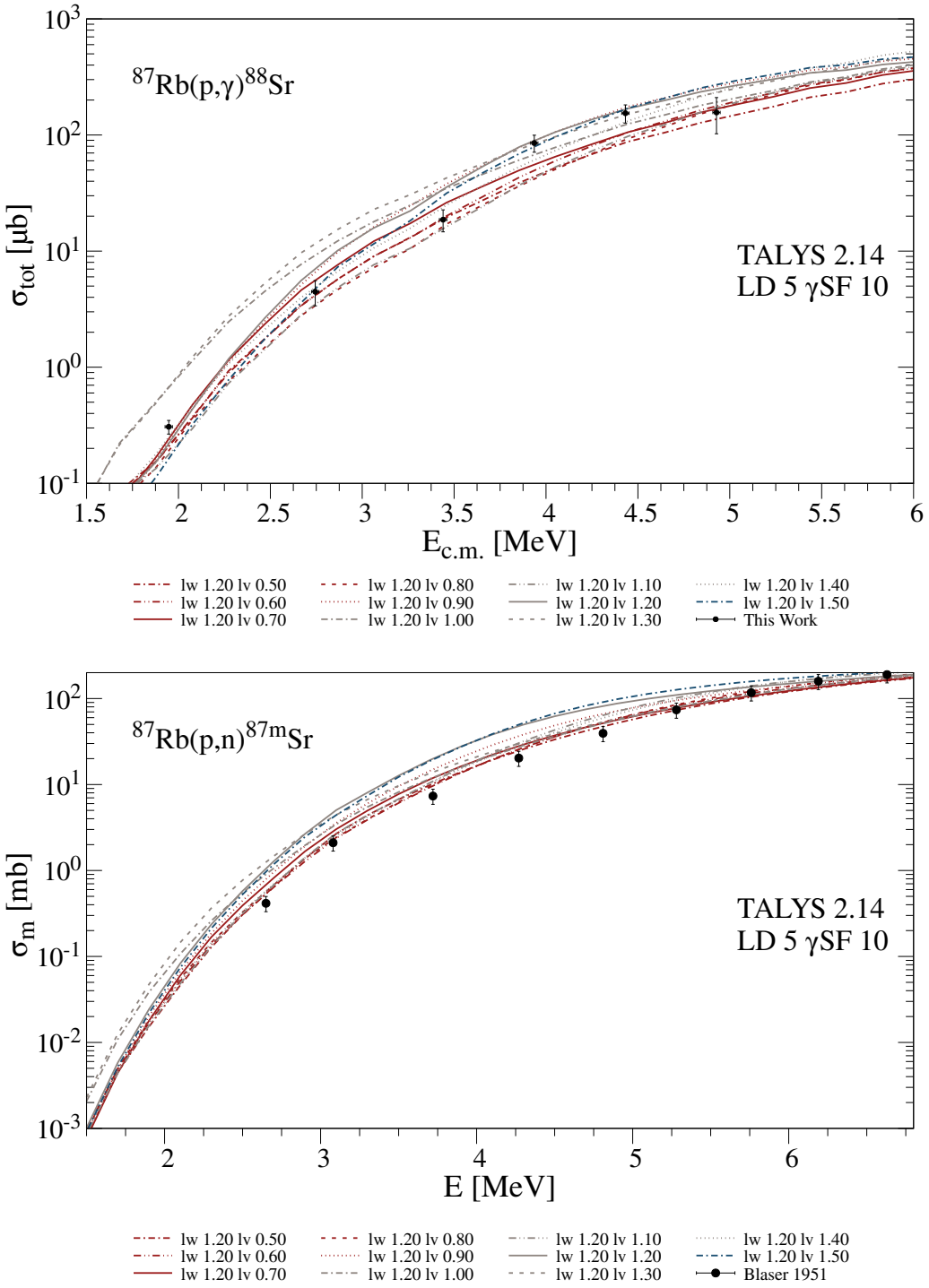

Figure B.28: The same as before with *lwadjust* = 1.2.

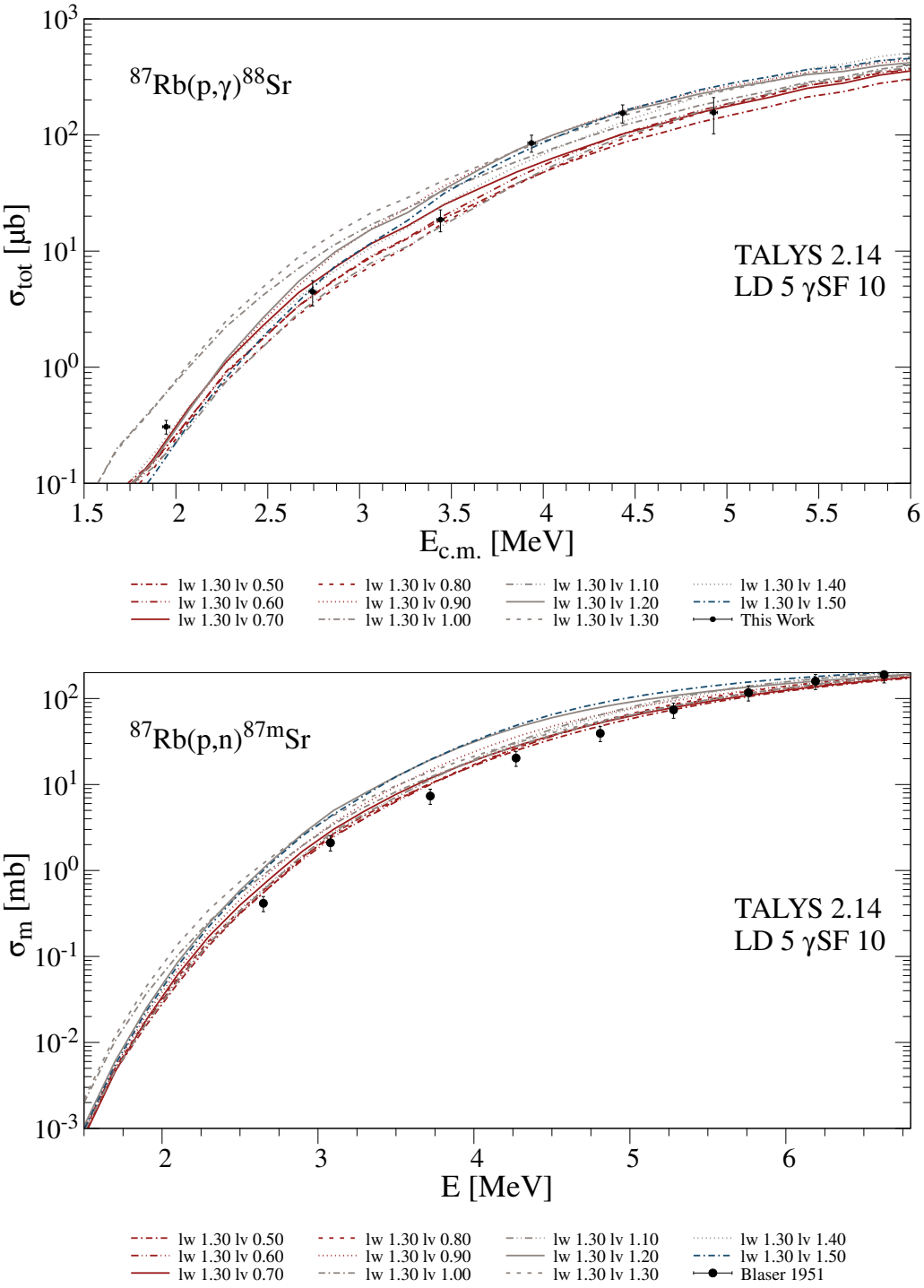

Figure B.29: The same as before with $lwadjust = 1.3$.

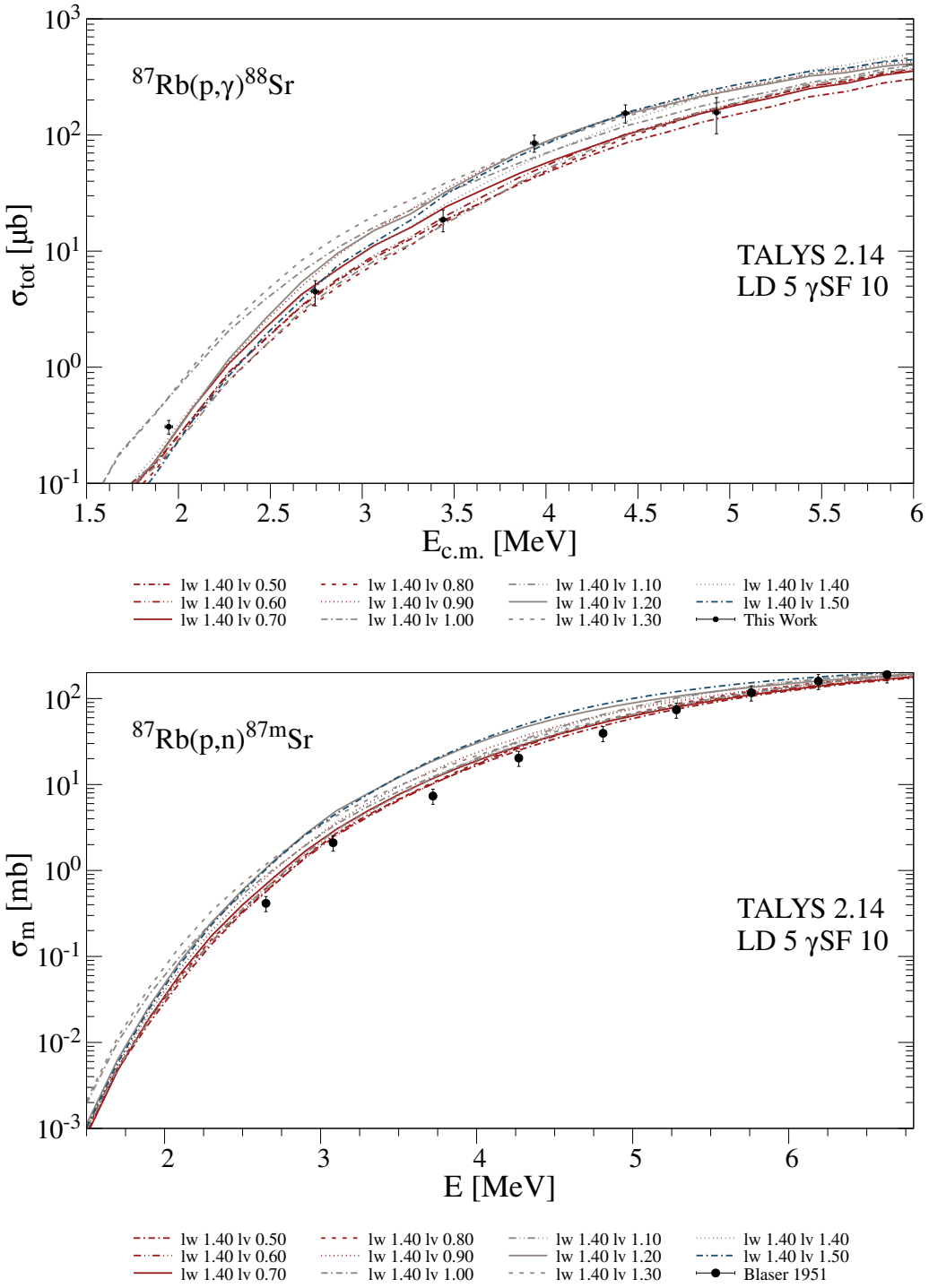

Figure B.30: The same as before with *lwadjust* = 1.4.

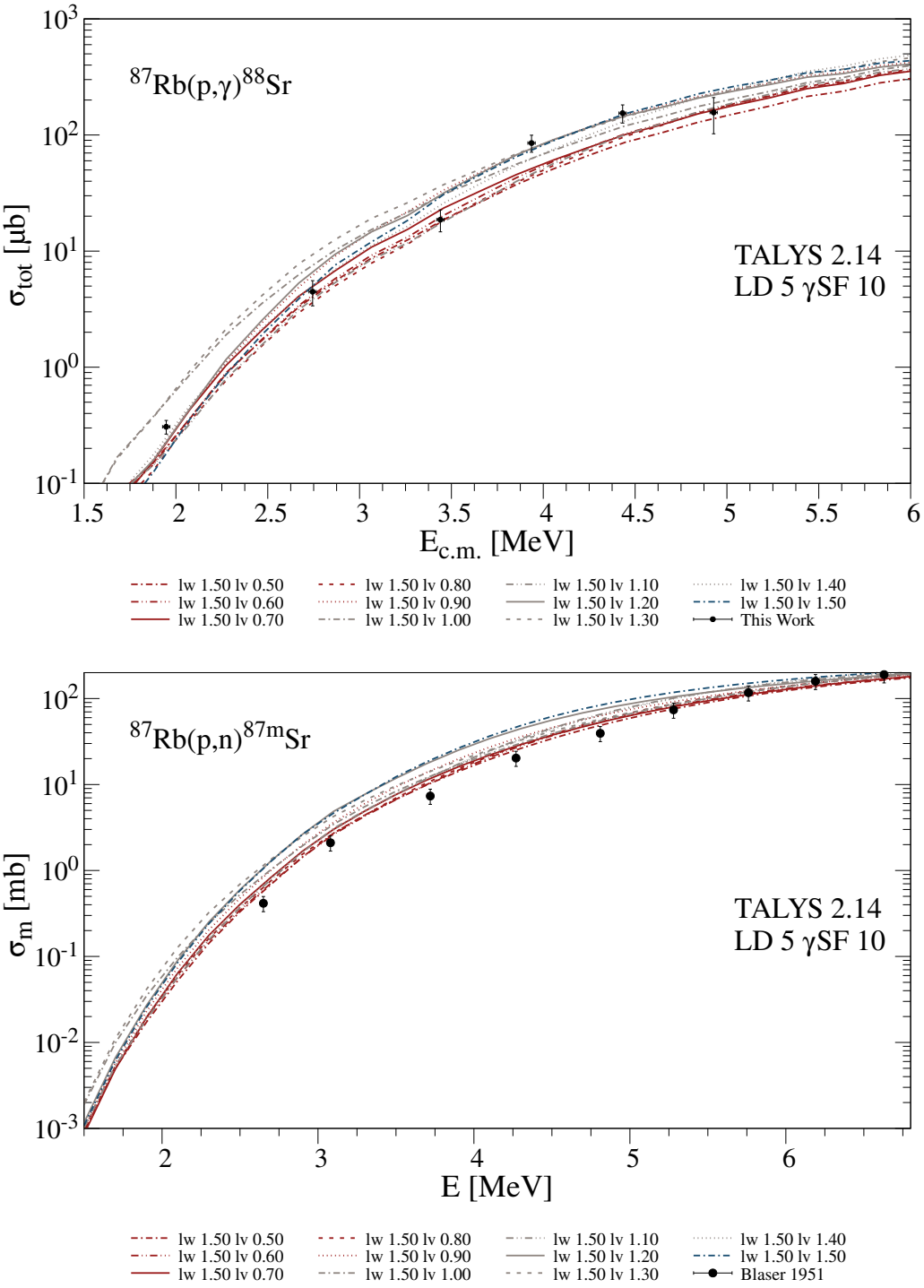

Figure B.31: The same as before with *lwadjust* = 1.5.

B.7 Variations of *lwadjust*, *lw1adjust* and *lvadjust* utilizing γ-strength model 10

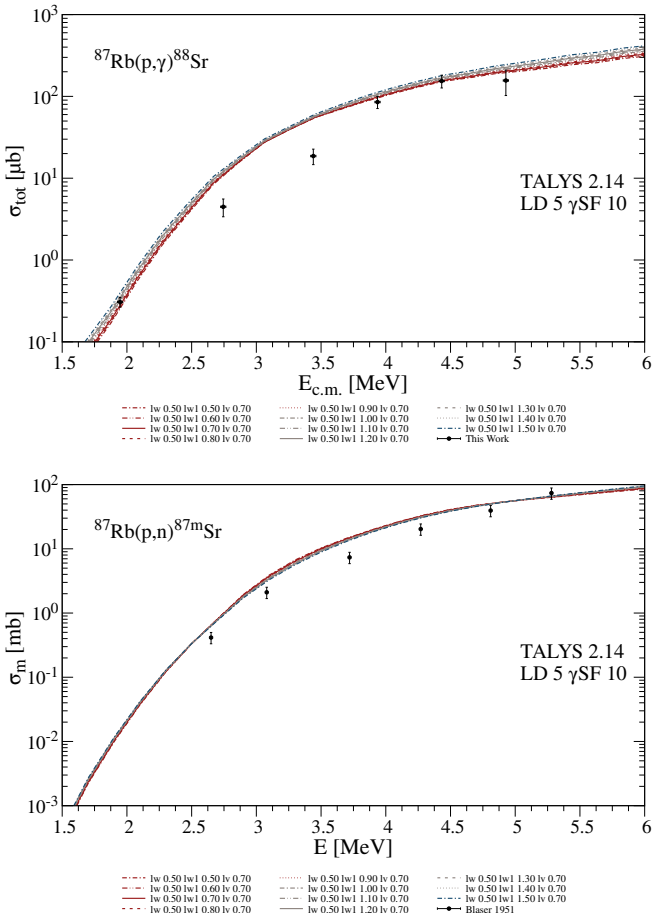

Figure B.32: Variation of *lwadjust* = 0.5 and *lvadjust* = 0.7 with different values of *lw1adjust*, employing γ-ray strength model 8 for proton-induced reactions on ^{87}Rb. The upper panel shows the predicted isomeric (p, n) cross sections in comparison with the experimental data from Reference [139]. The overall energy dependence is reproduced reasonably well, although not all data points are accurately described. A similar behavior is observed in the lower panel, which compares the predicted and experimental cross sections for the (p, γ) reaction.

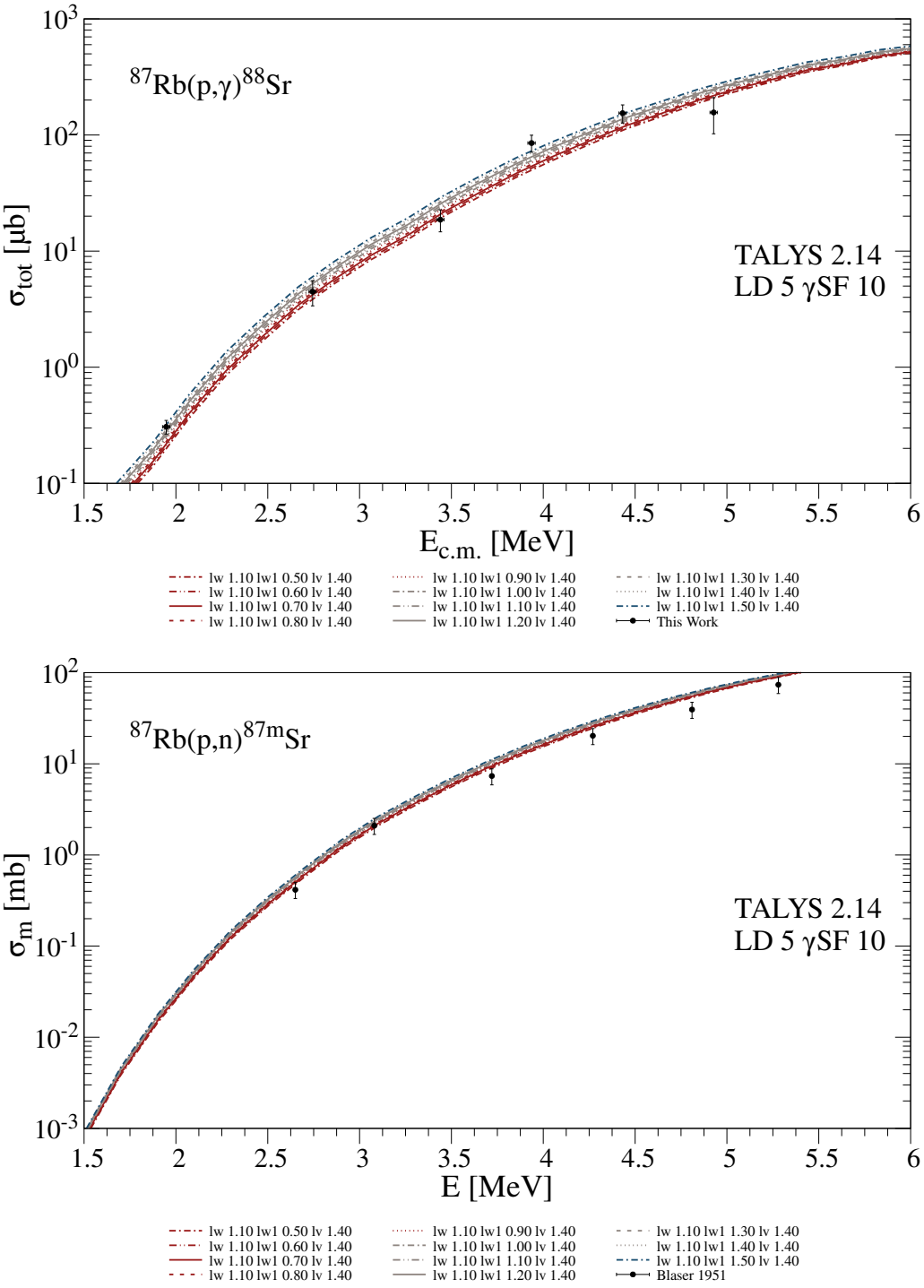

Figure B.33: The same as before with *lwadjust* = 1.1 and *lvadjust* = 1.4.

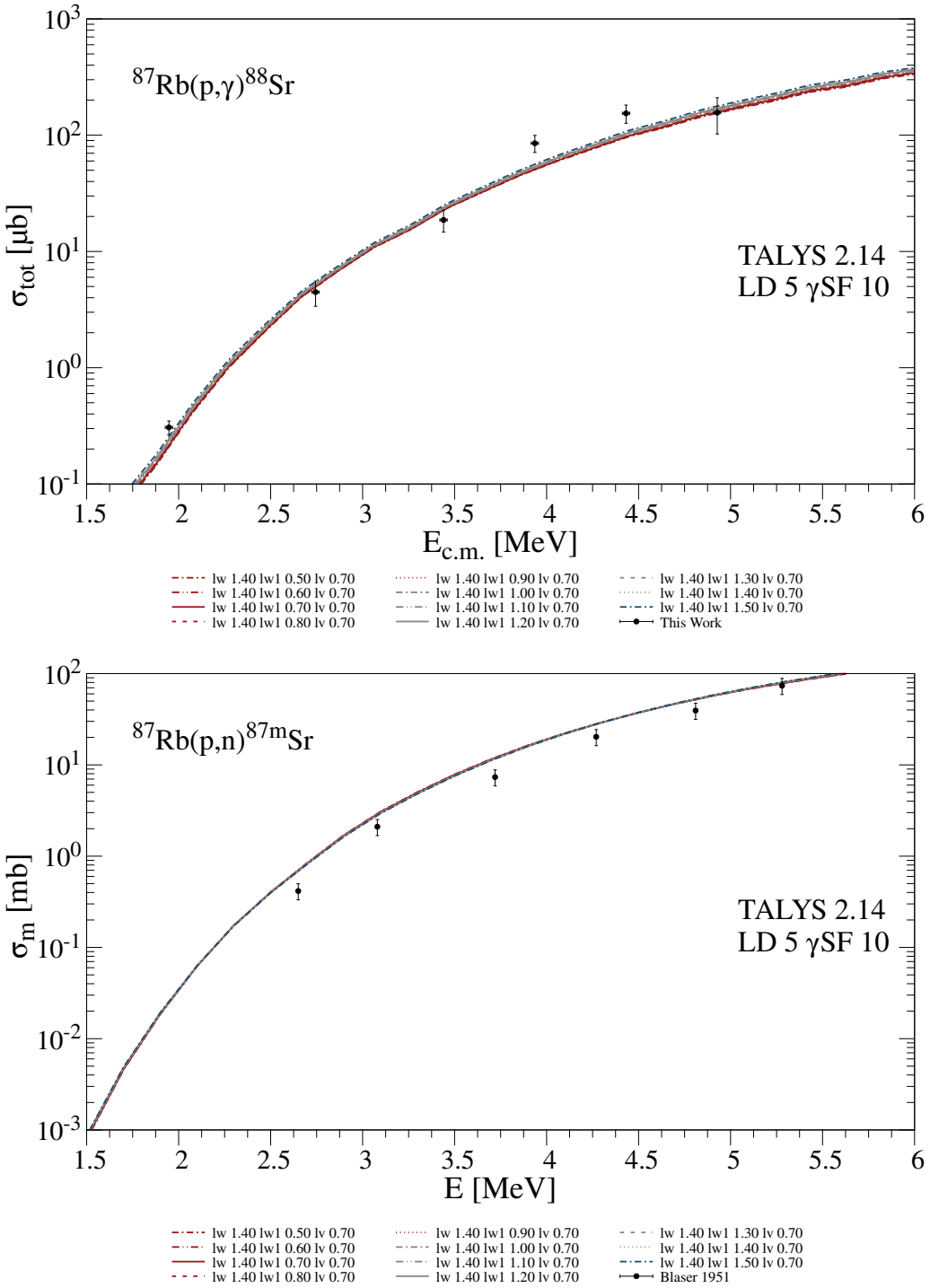

Figure B.34: The same as before with *lwadjust* = 1.4 and *lvadjust* = 0.7.

B.8 Variations of *lwadjust*, *lvadjust* and *lv1adjust* utilizing γ-strength model 10

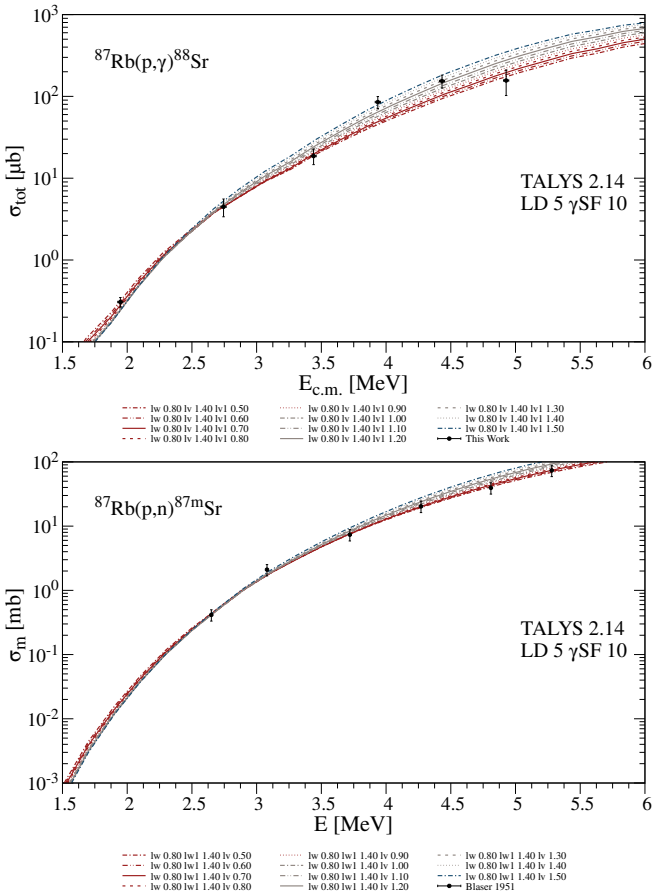

Figure B.35: Variation of $lwadjust = 0.8$ and $lvadjust = 1.4$ with different values of $lv1adjust$, employing γ-ray strength model 10 for proton-induced reactions on ^{87}Rb. The influence on predicted cross sections is slightly greater than for variations of $lwv1adjust$ in the presented energy region. The upper panel shows the predicted isomeric (p, n) cross sections in comparison with the experimental data from Reference [139]. The overall energy dependence is reproduced reasonably well, although not all data points are accurately described. A similar behavior is observed in the lower panel, which compares the predicted and experimental cross sections for the (p, γ) reaction.

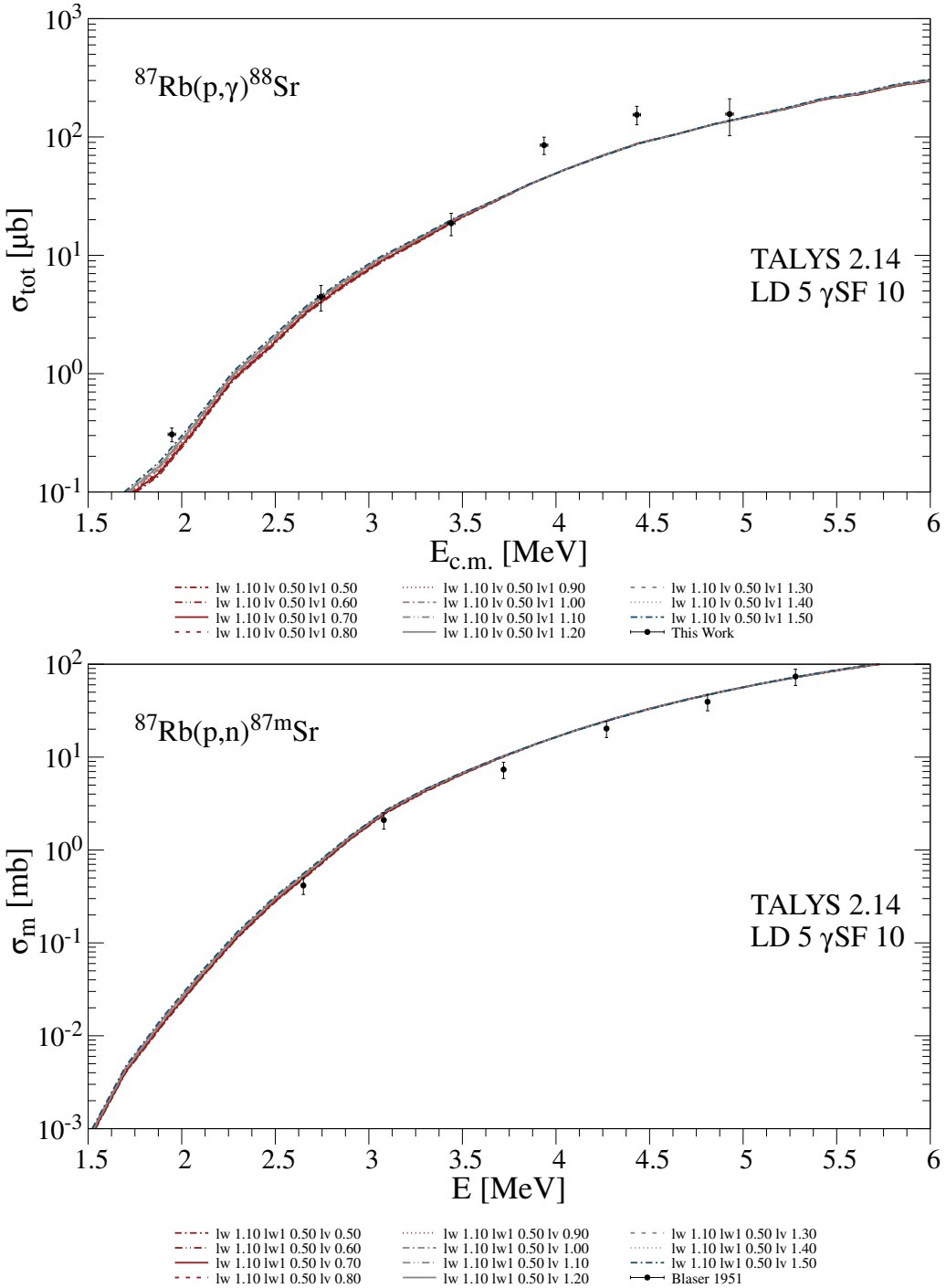

Figure B.36: The same as before with *lwadjust* = 1.1 and *lvadjust* = 0.5.

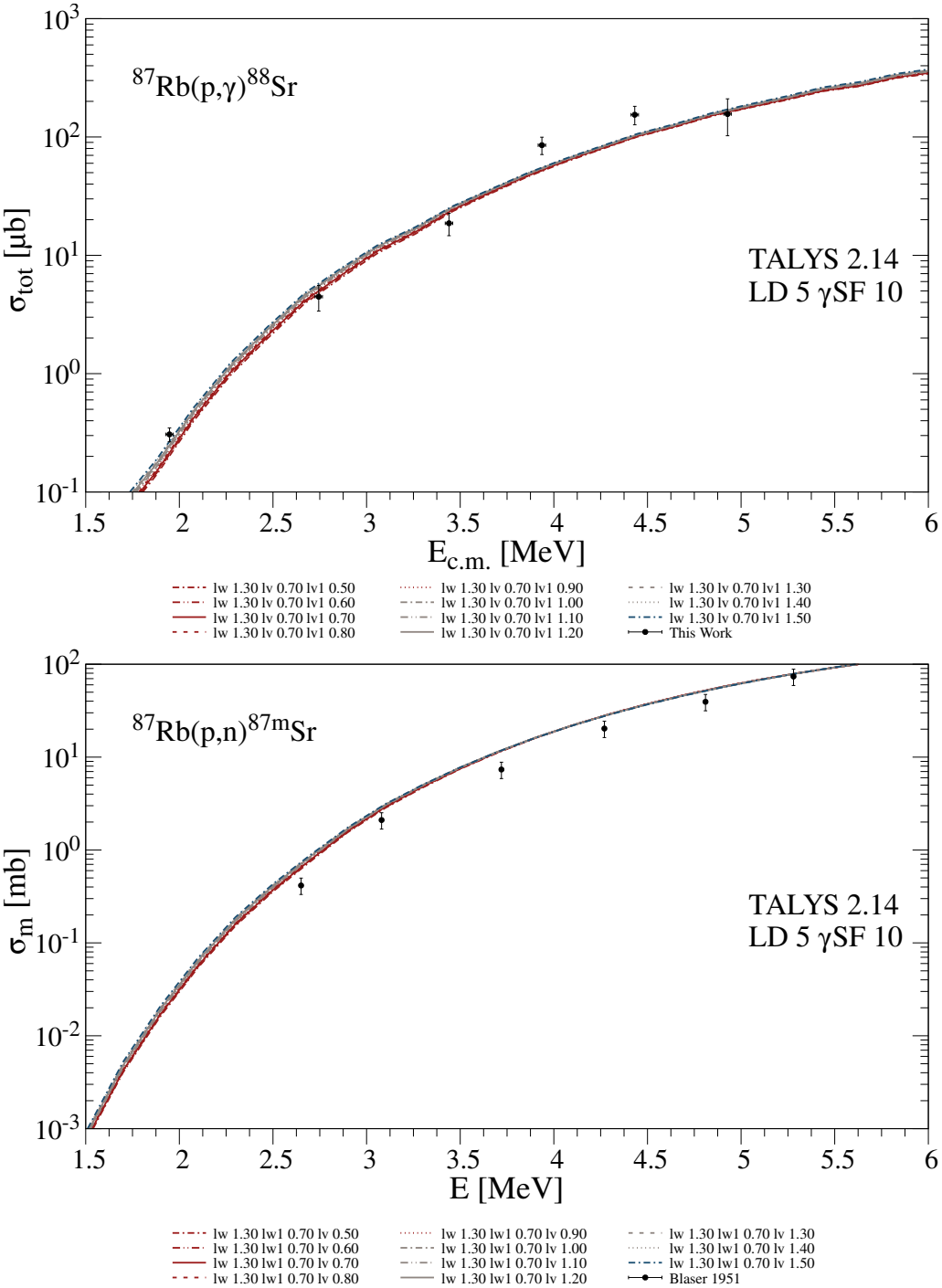

Figure B.37: The same as before with $lwadjust = 1.3$ and $lvadjust = 0.7$.

B.9 Variations of *lwadjust*, *lw1adjust*, *lvadjust* and *lv1adjust* utilizing γ-strength model 10

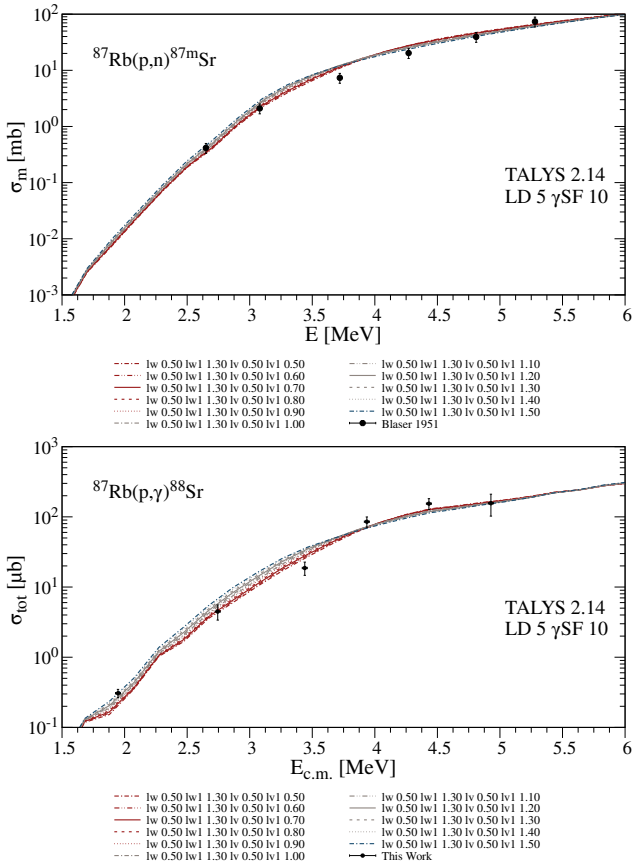

Figure B.38: Variation of $lwadjust = 0.5$, $lw1adjust = 1.3$ and $lvadjust = 0.5$ with different values of $lv1adjust$, employing γ-ray strength model 10 for proton-induced reactions on ^{87}Rb.

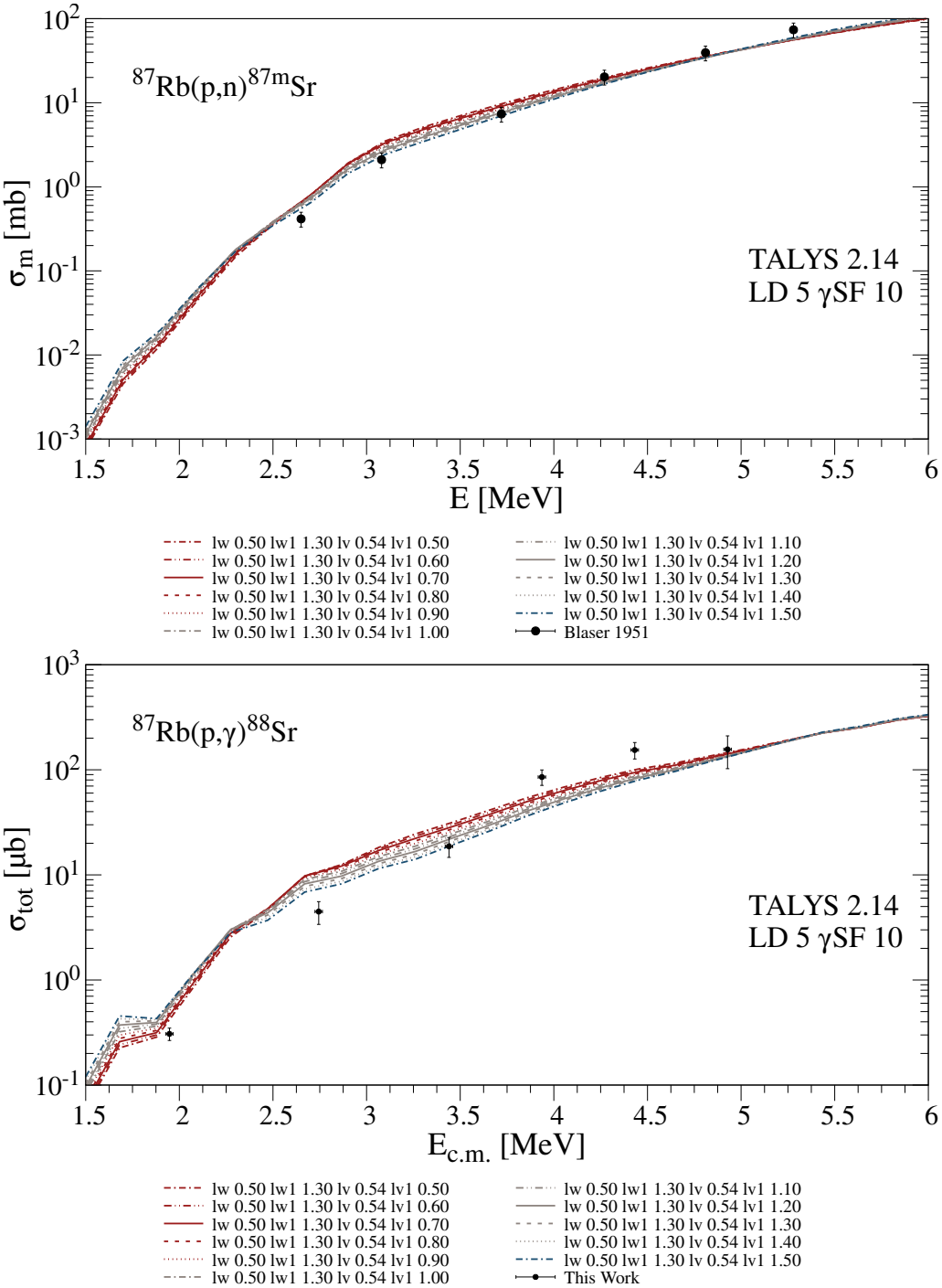

Figure B.39: The same as before with $lwadjust = 0.5$, $lw1adjust = 1.30$ and $lvadjust = 0.54$.

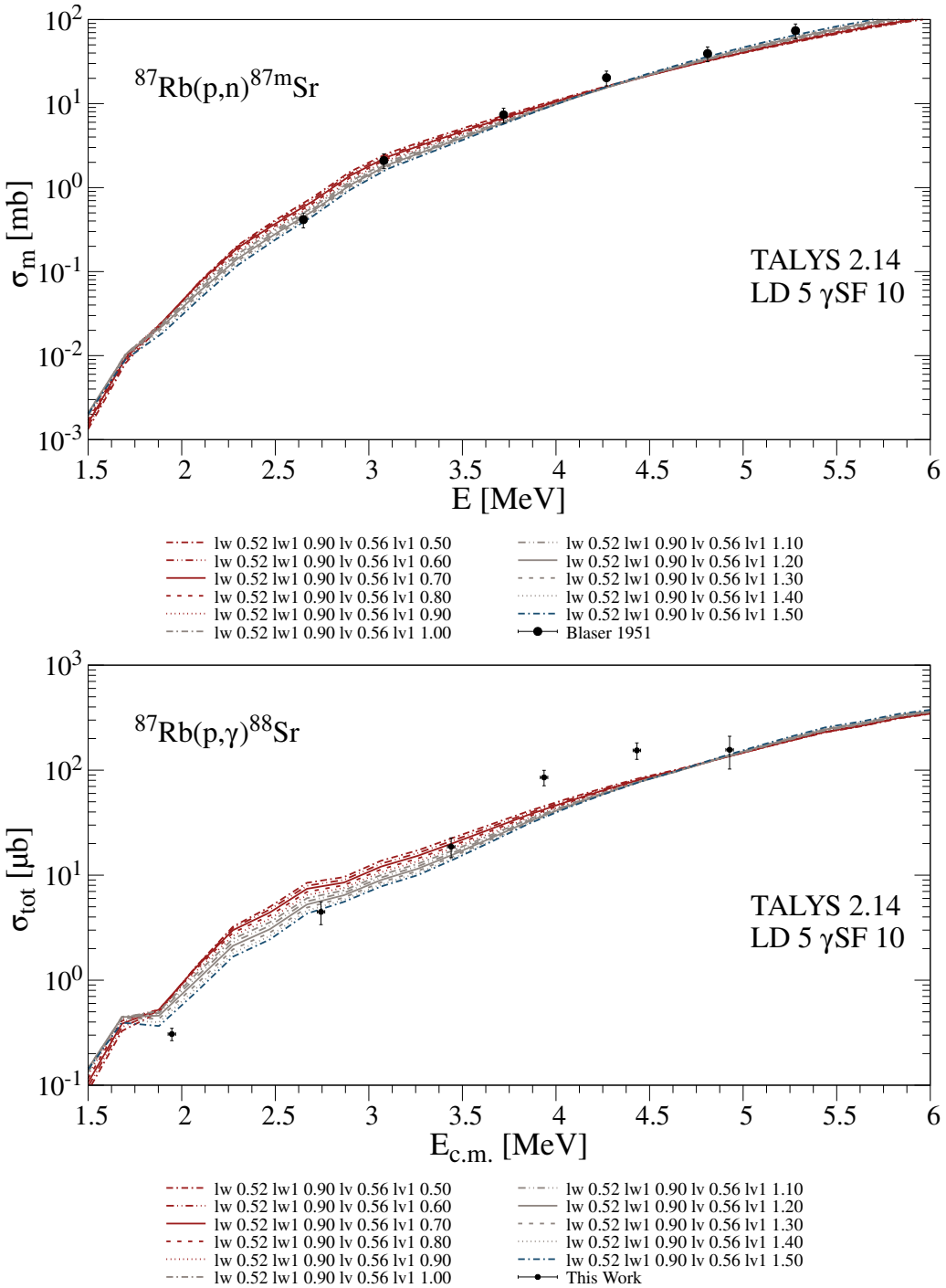

Figure B.40: The same as before with $lwadjust = 0.52$, $lw1adjust = 0.90$ and $lvadjust = 0.56$.

Acknowledgements

Diese Arbeit wäre ohne viele Personen nie zustande gekommen, weswegen ich mich bedanken möchte.

Vielen Dank an Prof. Dr. Andreas Zilges, der nicht nur mein Doktorvater ist, sondern auch die Person, die mir überhaupt eröffnet hat, dass man mit einem Master of Education promovieren kann. Ohne ihn hätte ich nicht gewusst, dass das möglich ist. Ich bin ihm für die vielen Möglichkeiten, die er ermöglicht, dankbar: Experimente planen und durchführen zu können, an vielen Konferenzen teilnehmen zu dürfen, um Netzwerke aufzubauen, zu pflegen und in den wissenschaftlichen Austausch auf nationaler und internationaler Ebene gehen zu können. Wir waren zwar nicht immer bei Dingen einer Meinung, aber durch eine angemessene Diskussionskultur und der Fähigkeit, trennen zu können zwischen persönlicher Ansicht, Gremienarbeit und beruflicher Perspektive, ist dennoch immer ein gutes Miteinander gelungen. Das ist etwas, was vielen Menschen nicht gelingt.

Ich bedanke mich für die Übernahme des Zweitgutachtens bei Prof. Dr. Yury Litvinov, der auf meine Anfrage sehr enthusiastisch zugestimmt hat, diese Aufgabe zu übernehmen.

Bei den zahlreichen Mitarbeiter*innen im Institut für Kernphysik möchte ich mich auch sehr bedanken. Zum einen beim Targetlabor in Person Andrey Blazhev, ohne den sehr viel Expertise zu Targets fehlen würde. Er hat immer ein offenes Ohr, wenn man Ideen hat und über Probleme mit Targets Rücksprache halten muss. Vielen Dank an die Teams der Elektronik- und Feinmechanikwerstätten sowie dem ganzen Beschleunigerteam. Ihr seid der Herzschlag, der das Experiment leben lässt. Einen großen Dank auch an die beiden guten Seelen der Verwaltung: Sabine Hingott und Heike Röhnelt. Auch in stressigen Zeiten habt ihr alles unter Kontrolle und den Überblick.

Für die Übernahme des Prüfungsvorsitzes bedanke ich mich sehr gerne bei Prof. Dr. Peter Schilke. Auch für die gelungene Zusammenarbeit in den Gremien der Physik möchte ich mich herzlich bedanken. Durch engagierte Personen wie ihm wird vieles in Bewegung gesetzt. Er hat immer ein offenes Ohr für Anliegen und die Ruhe, um auch komplizierte Situationen für Studierende gut zu lösen.

Ein gleiches großes Dank wie an Peter geht an Dr. Petra Neubauer-Guenther. Du hast immer offene Ohren, auch wenn du noch so viel Arbeit hast, für jedes Anliegen hast du Ideen, wie allen schnell und sinnvoll geholfen werden kann. Vielen Dank dafür. Du bist die gute Seele in der Physik ohne die so vieles auf der Strecke bleiben würde, weil niemand Dinge so schnell wie du mitdenkt und erledigt, bevor es aufkommt. Danke für die tolle, unvergessliche, arbeitsintensive Zeit an der Prüfungsordnung.

At this point, I must apologize in advance, I will certainly forget to mention some people by their names. Nevertheless, deep in my heart I'm grateful and thankful for you.

First I want to thank all the great people I met at so many international conferences. Kaitlin, Lorenzo, Artemis, Sophie, Zsolt, Sándor, Nikola, Thanassis, Luca, Charles, Axel, Luis, Mila, Guy, Chris, and so many more. It is always fun and often feels more like a class reunion than a cold conference. I always enjoy discussing science with you. Many friendships arose and I can happily say, I will come and visit you, some time soon!

Für den tollen Zusammenhalt und die sehr angenehmen Arbeitsatmosphäre möchte ich mich bei der gesamten AG Zilges bedanken. Ich habe mich direkt zu Beginn meiner Masterarbeit gut

aufgehoben und willkommen gefühlt. Die Wandertage und Weihnachtsmarktbesuche finden nie ohne irgendwelche Diskussionen über Physik statt. Bewahrt euch diese Leidenschaft im Herzen.

Für viele gemeinsame Konferenzanreisen und -Aufenthalte möchte ich mich auch bei Benedikt Machliner und Martin Müller bedanken. Es war auch dank euch, nie langweilig und die ein oder andere gute Idee konnten wir immer mitnehmen und umsetzen. Des Weiteren möchte ich mich bei Sarah Prill und Anna Bohn bedanken, mit denen ich den Großteil meiner gesamten Zeit in einem Büro saß und sitze. Ihr habt immer ein offenes Ohr, gute Ideen und auch schon mal die ein oder andere Ablenkung parat gehabt, wenn es nötig war. (Leider kann ich hier keine Karteikarten einfügen...) Ein weiterer Dank geht an Florian Kluwig, Markus Müllenmeister und Michael Weinert, die es immer schaffen, mit mehr oder weniger schlechten Witzen, die Stimmung aufzulockern und einem immer mit Rat und Tat an der Seite stehen. Und sei es nur bei der Frage, ob man sich noch einen Kaffee holt.

Ein ganz großes Dank gilt auch der Fachschaft. Jedes Engagement kann und sollte etwas zum Besseren bewegen und das zeigt besonders der Einsatz von vielen Studierenden für Studierende in Gremien. Manche Diskussionen dauern intern und dann auch in den Gremien zwar lange, aber es wird immer eine Lösung gefunden, mit der alle beteiligten leben können und das ist in der gesamten Fachgruppe Physik eine gute Errungenschaft. Behaltet das bei. Ihr seid einer der verrücktesten, liebenswertesten, offensten Haufen Menschen, den ich kenne.

Ich möchte mich bei meinem Quizteam bedanken, 5 Kölsch für Tisch 3. Ihr habt immer an mich geglaubt und die Montagabende mit euch sind einfach immer toll. Danke Benne, Laura, Lena und Lukas. Aber auch ein großes Danke an Sven und Nico, ohne die Montagsabends nicht eine solche Institution wäre. Danke an meine regelmäßigen Bouldermenschen, Lisa, Jana, Feli und Silvan. Ohne den Ausgleich, wäre mein Kopf bestimmt geplatzt. Danke an Saskia, für die wunderbare Freundschaft seit der Schule. Ein Dr. kommt nun selten allein – hoffentlich. Thanks a lot to Kaitlin, who read the whole thesis despite being an astronomer. When are you visiting again? Wann steht eigentlich das nächste Konzert an, Annemarie? Danke fürs immer da sein, Tiramisu vorbeibringen und spontan auf (gewonnene) Konzerte gehen. Danke an die Schlawinen für unvergessliche Erlebnisse und den Spaß, seit wir zusammengeworfen worden sind, beim Skifahren. Auch wenn ich lange nicht mehr da war, danke an die Fußball-Runde für viel Sonne und frische Luft, wenn man doch wieder zu viel im Büro und Keller war.

Danke an Herrn Esser und Frau Meuter, die mein Interesse für Physik die Schulzeit hindurch hochgehalten haben.

Und mit der größte Dank gilt wahrscheinlich meinen Eltern. Ohne dich, Papa, hätte ich die Liebe für Physik nicht schon in der Grundschule entdeckt. Was so ein Schaltkreis auf einer Plexiglasplatte alles auslösen kann. Wir haben hoffentlich bald die erste Doktorin in der Familie. Und Mama: Du hast mir gezeigt, dass man stets für sich einstehen soll und man mit viel Willen alles schaffen kann. Danke für eure jahrelange Unterstützung in allem, was ich getan habe und noch vorhabe. Ohne euch wäre das alles nicht gegangen.

Und danke an Philipp. Fürs da sein, zuhören, ablenken, in den Arm nehmen, versuchen, Essen zu machen, rumalbern. Du hast mir immer wieder hochgeholfen, um weiterzumachen. Danke.